

Environment and Cost Comparison of Warm Mix Asphalt Technology Application in Turkey

Halit Ozen¹, Kemal Karakuzu², Ibrahim Sel²

Abstract

In Turkey which is provided with highways in passenger transport by 95%, and 92% of freight transport Hot Mix Asphalt (HMA) is used in large quantities in especially municipalities. In recent years, several studies have been carried out to develop a new product which is more environmentally friendly and energy saving that can be used instead of HMA due to increasing environmental awareness and high fuel costs in the World. Thanks to "Warm Mix Asphalt Technology" (WMA), which was placed the first field experience in Germany in 1999, asphalt mixture can be produced at lower temperatures ranging from 20°C-50°C than HMA. Using WMA also provide significant advantages such as extension of performance life of pavement, reduction of greenhouse gas emission, contribution to worker health, extension of construction season and carrying to long distance. WMA is very newly technology for our country yet which is used in especially USA and among Europe countries and was applied a test road as trial in only Ankara and Sivas.

In this research study, literature information is given about WMA and advantages and disadvantages are listed on issues such as environment, fuel consumption and workmanship as compared with HMA. Production cost of WMA is calculated by using "Unit Cost Calculation Method" for our country conditions and demonstrated differences from HMA in terms of materials and equipment. In addition, in case of accessing under the our country conditions which is used WMA rates in the developed countries in the world is calculated monetary value that can bring benefits in terms of environmental and fuel consumption and importance of the WMA usage is revealed.

Keywords: *Economical Aspect, Environmentally Friendly, Warm Mix Asphalt, WMA*

1. INTRODUCTION

Hot Mix Asphalt (HMA) is the one of the most widely used pavements in the World. In recent years, due to increasing environmental awareness, several studies have been carried out on the objectives of improving the performance of pavement materials and increasing the laying productivity and resource efficiency. Thanks to the newly developed Warm Mix Asphalt (WMA) technology, these objectives can be achieved in lower production temperatures [1]

WMA can be produced and paved in lower temperatures as compared with traditional HMA. Warm mix asphalt technology can reduce the viscosity of bitumen and subsequently increase the workability of the final asphalt mixtures. As a result, the pavements can be produced at temperature between 100-140°C without sacrificing the quality. The low temperature production has various positive effects, including reduction of greenhouse gas emission, lower energy consumption, improving working conditions, better workability and compaction condition [2]

The viscosity of asphalt mixtures and the temperature needed for coating of aggregates with bitumen can be greatly reduced using WMA technology, including adding chemical, organic and/or water-based additives to the mixture during the production phase. Therefore, the production temperature of WMA can be much lower than that of HMA, which is normally between 140-180°C [3].

2. HISTORY OF WMA

Most of the field practice related with pavement is still using HMA process in the world. In recent years, WMA technology has gained a great acceptance in many countries especially in Europe and United State of America. The first survey related with WMA technology dates back to 1956 [4]. At the University of Iowa (USA), binding property of bitumen was noticed and asphalt mixture was produced by applying steam into bitumen.

This process was began to be named as the WMA technology together with production of WAM-Foam by Shell Bitumen Co.Ltd in 1996 and also Sasobit additive was produced by Sasol Wax Co.Ltd. Some countries began to research WMA technology to reduce high fuel cost and take advantages from WMA than earlier other many countries [5].

Especially in countries such as USA and Germany greenhouse gas effect debate on going for many years was ended up with acceptance of Kyoto Protocol which was included the restriction of emission gases in 1997 and also studied which was carried out on the field practice has been increased with this agreement.

¹ Corresponding author: Yildiz Technical University, Department of Civil Engineering, 34220, Esenler/Istanbul, Turkey. ozen@yildiz.edu.tr

² Bursa Orhangazi University, Department of Civil Engineering, 16310, Yildırım/Bursa, Turkey, kemal.karakuzu@bou.edu.tr

First field experiment in Germany was applied by using Asphamin additive in 1999 and also an application was carried out by some researchers firstly in USA in 2004 by using Asphamin additive [6]. After these first attempts, applications have increased in many states. In 2007, in Belgium, France, Germany and Norway were made in many different highways and the results were same or even better than USA trials [3].

Trial application was made in all 50 states in USA at the end of 2011. In 2009 19,2 million tons WMA mixture was paved with the support of American Federal Highway Administration (FHWA). 13% of all asphalt mixes were carried out by using 47,2 million ton WMA [7].

The quantity of produced WMA in the USA, Europe and Canada in 2011 is given Table 1 [8].

Table 1. WMA production amount in 2011

Country	Ton
Romania	126.000
Finland	690.000
France	1.259.000
Luxemburg	7.000
Holland	300.000
Spain	125.000
Switzerland	600.00
Sweden	850.000
USA	70.000.000
Japan	111.000
Canada	600.000

3. ADVANTAGES OF WMA

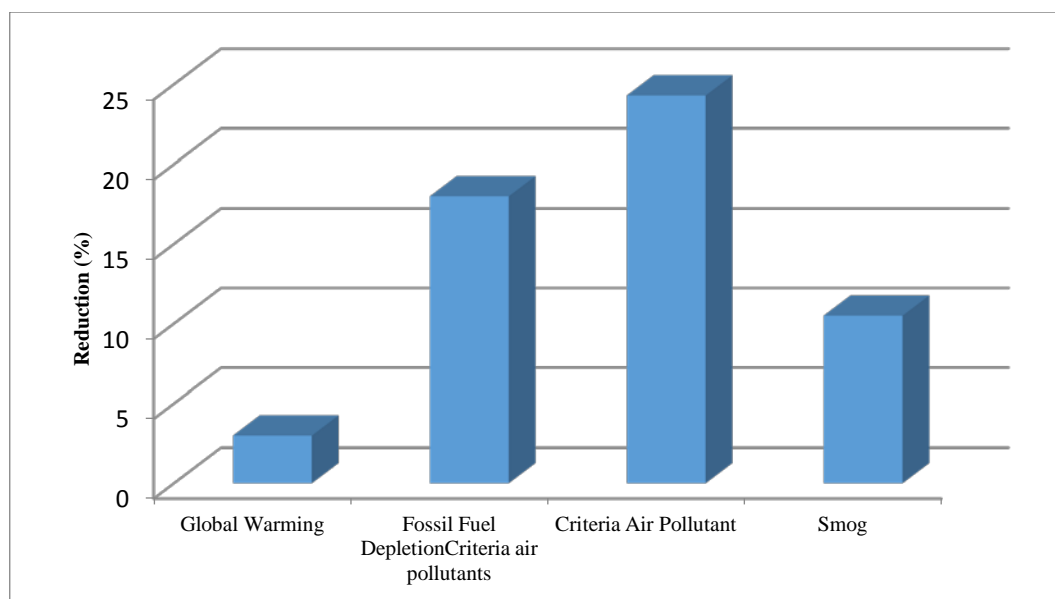
Environmental Benefits

Thanks to WMA technology, asphalt mixtures can be produced at lower temperatures than HMA. Due to the fact that greenhouse gas emissions are directly proportional with temperature, a considerable amount of emission and odor reduction are observed. Reducing in emissions with using WMA is shown in Table 2 which is detected in several studies [9]

Table 2. Reduction in emission

	Vaitkus et al. (2009) [10,11]	Bueche (2009) [12]	Larsen (2001) [13]	D'angelo et al. (2008) [3]	Evotherm website (2011)
CO₂	%30-40	%30-40	%31	%15-40	%46
SO₂	%35	-	-	%20-35	%81
VOC	%50	%50	-	%50	%30
CO	%10-30	-	%29	%10-30	%63
NO_x	%60-70	-	%62	%60-70	%58
Particle	%20-25	-	-	%25-55	-

According to Table 2, WMA can ensure great decreasing reach up to 70%. Benefits of WMA on environment are assessed in a study of Marwa Hassan [14] In the light of this information on *Graphic 1* WMA provides a reduction at global warming 3%, fossil fuel consumption 18%, air pollution 23,6% and toxic gas 9,5%.



Graphic 1. Percentage improvement due to use of WMA

Releasing the low emission gas has positive effect on employee health. According to a study that was conducted in 2003, it is observed that the oxygen saturation rate of the workers in the blood is quite low than normal [15] gas emissions can be very dangerous for workers especially in closed areas such as tunnels.

Economic Benefits

- Providing energy saving in the rate of 20-35% according to HMA by the help of decreasing the production temperature
- Allowing the use of Reclaimed Asphalt Pavement (RAP) in the rate of 30%
- Due to low production temperature, aggregate and bitumen are less damaged and occurred less crack on pavement. Also aging occur later

Ease of Application

- Increasing in the workability due to low viscosity
- Easing of compaction
- Allowing to pave at lower temperatures and extend of paving season
- Increasing worker productivity and paving quality due to low temperatures during paving
- Longer haul distances on account of the fact that allow paving at lower temperature. By this means economically competition fortune to find new market
- Early opened to traffic [2]

4. DISADVANTAGES OF WMA

WMA studies generally have been mentioned about advantages of WMA technology, but it also has many disadvantages. It can be expressed that WMA is not worse than HMA according to field data and laboratory experiment. However due to fact that the first field application to be made in 1999 and service life of asphalt mixtures range from 15 to 20 years or more, this cannot express absolute idea about WMA long term performance.

Although the production cost of the WMA is lower, if the total life cycle cost is higher than HMA, WMA lost its advantage in the face of HMA. Thus life cycle cost analysis should be performed well. Asphalt contractors reported that WMA should not be adapt due to just low emission and fuel saving [16.]

Due to WMA additives and modification cost in the plant arise extra cost in the production phase. If the production is made in a low fuel cost country, these additional cost will reset the fuel saving due to low fuel cost [17].

One of the most important criteria for the production of WMA is the presence of moisture. Production of warm mix asphalt at low temperatures may cause to dry of aggregates insufficiently [18]. This situation leads to insufficient cohesion between the bitumen and aggregate and peeling as well. It also has not been surveyed enough yet on the warm mix asphalt because of being new technology. Due to the fact that environmental impact of asphalt additives, performance and life cycle cost analysis are not performed. There are many questions to answer [9].

5. ECONOMICAL ANALYSIS

Data used in calculation

To calculate the cost of asphalt mixture is used from “Road, Bridge, Tunnel, Bitumen Mixture, Maintenance and Traffic Affairs Unit Price List in 2012, 2013 and 2015” that is published by General Directorate of Highway in Turkey (KGM). In this study, some additives which are chosen Sasobit from chemical additives, Rediset from organic additives and Advera from water based technologies and are used in appropriate proportions and cost comparison is evaluated in accordance with HMA. All calculations are based on the preparation of 1 ton asphalt mixture.

In the calculations, selected samples gradation rates are determined by designed with aggregates which are crushed and sieved in highways according to the specification and the ratio frequently used. Aggregate mixing ratio which is prepared on the basis of Highway Technical Specification is shown in Table 3[19].

Table 3. Aggregate design ratio

Sieve mm	Design (%)	Specification (%)
19,1	100	100
12,7	90	83-100
9,5	80	70-90
4,75	45	40-55
2	15	10-20
0,42	15	10-20
0,177	8	6-15
0,075	7	4-10

B 50/70 penetration bitumen is used producing by TÜPRAŞ Refinery in İzmit for design. Dates 23.12.2015 for 2015, 27.12.2013 for 2013 and 20.11.2012 for 2012 are chosen for cost comparison. Oil price is determined on the basis of dollar, additive price also determined on the basis of euro. Petrol (<http://tr.investing.com/commodities/crude-oil>), bitumen (www.tupras.com.tr), dollar and euro values (www.tcmb.gov.tr) are demonstrated in the following Table 4.

Table 4. Petrol, bitumen, dollar and euro values in different years

	2012	2013	2015
Petrol (Barrel/Dollar)	96,49	97,69	38,10
Bitumen (TL/Ton)	1100,00	1293,00	381,78
1 Dollar (TL)	1,80	2,15	2,92
1 Euro (TL)	2,32	2,84	3,20

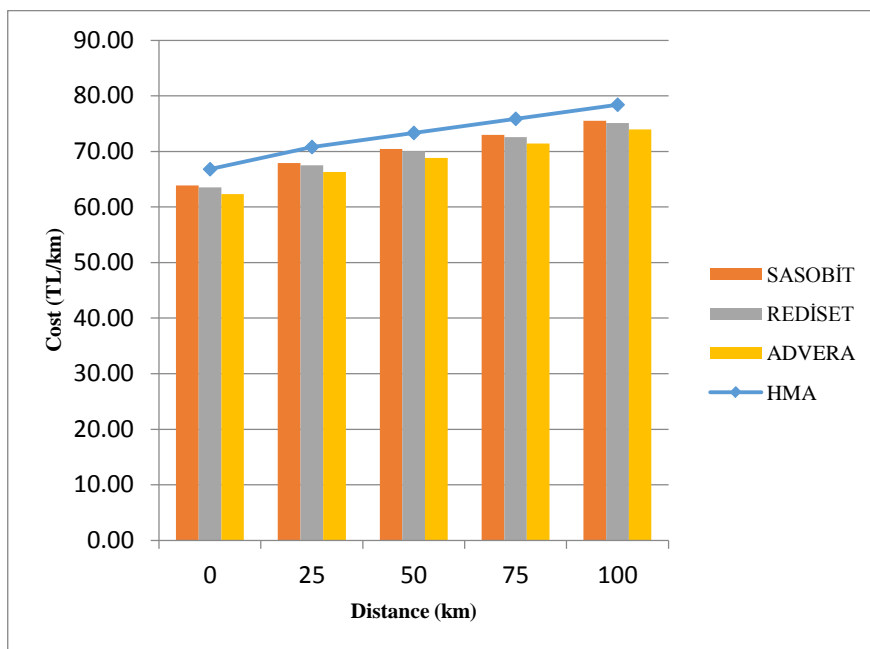
Table 5 shows that bitumen and additive ratio which is used in asphalt mixtures. Additives are added to the mixture as a percentage by weight of bitumen.

Table 5. Bitumen and additive ratio used in mixture

	BSK	Sasobit	Rediset	Advera
Bitumen (%)	4,8	4,2	4,46	4,5
Additive (%)	-	3,0	2,0	5,0

5.1. Comparative cost

Costs depending on the distance and production are illustrated in Graphic 2, Graphic 3 and Graphic 4 respectively in 2012, 2013 and 2015 by calculating for per ton asphalt mixture production. Each kind of asphalt mixture is compared as related with cost that arising as a result of haul to 0, 25, 50, 75 and 100 km.

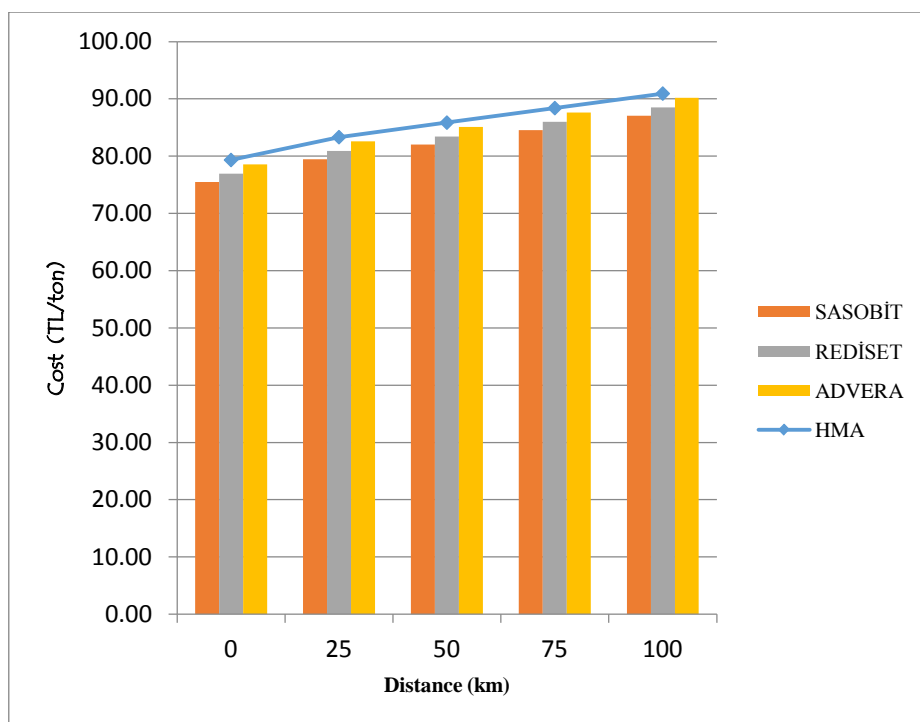


Graphic 2. Asphalt mixture costs in 2012

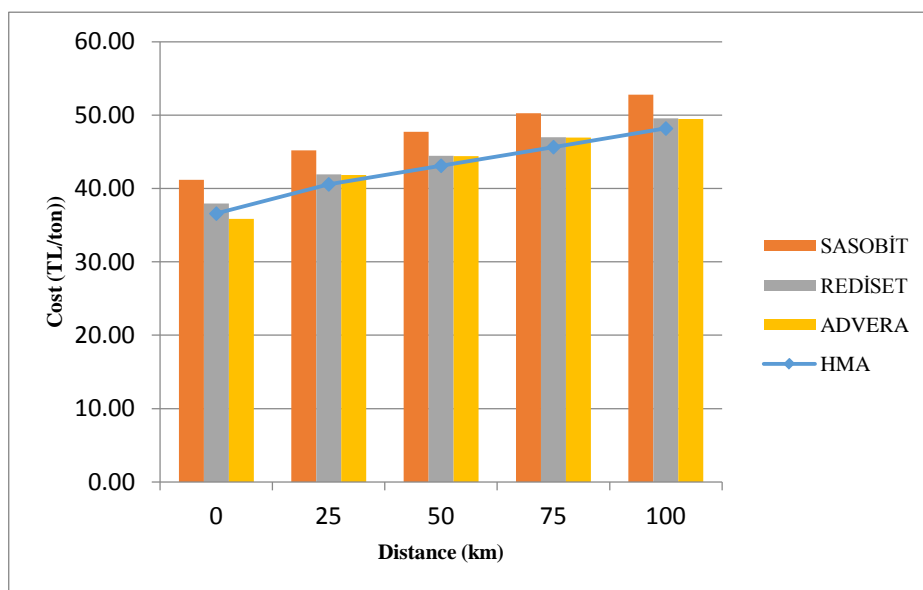
According to the Graph 2, Graph 3 and Graph 4, WMA cost is lower than HMA cost due to higher petrol price. So, using of WMA is more advantageous than HMA economically in 2012. Although there was no any serious uprising in oil price in 2013, increasing of Euro exchange caused decreasing the cost difference between WMA and HMA but it is also seen that WMA is more economical to use in this situation.

In 2015, HMA became cheaper than WMA due to the fact that oil price was diminished and cost of bitumen was cheaper. In addition, this causes to be more costly of WMA by the reason of WMA additive owing to increasing of euro exchange rate. In this case WMA is lost its economic advantage

The amount of produced HMA is shown in Table 6 over the years in Turkey [20]. HMA production amount has not been announced yet in 2015 but it is estimated to be the same as the year 2014 [21].



Graphic 3. Asphalt mixture costs in 2013



Graphic 4. Asphalt mixture costs in 2015

Table 6. The amount of produced asphalt over the years (HMA: Hot Mix Asphalt, CMA: Cold Mix Asphalt)

	Year	HMA (million ton)	Sealing (km ²)	CMA (x1000 ton)	Bitumen consumption (x1000 ton)
Highway, Urban and Rural roads	2012	98,3	294,9	1819	2809
	2013	46,2	216,3	1050	2820
	2014	30,9	203,8	805,7	2216

According to Table 6, in case of using the HMA instead of WMA technology savings are provided 170.8 million TL in 2012 and 181.1 million TL in 2013 TL in our country conditions. Usage of WMA lead to loss about 39,2 million TL because of the fact that WMA has lost its advantage in the face of HMA. HMA plants need some modifications to produce the WMA in according for every WMA technology kind. This case adds the extra cost to production because of the fact that WMA technology has not been used yet in Turkey.

6. CONCLUSION

WMA technology is a great opportunity for the development of the asphalt industry. Due to better workability and compactibility features, it is revealed that WMA has equal or even better performance than HMA in the light of the researches. Producing of mixture at the lower temperatures also ensure an advantage to delay of aging of bitumen, decrease of thermal and fatigue cracks and reduce emission gasses significantly. In this way it is provided a positive impact on working condition and employee's healthcare.

WMA has a serious disadvantage despite all positive aspects. Inability of identifying of long term performance of WMA, lack of sufficiently widespread in our country and throughout the world, and to be based on the HMA of existing asphalt technology are affected to WMA against HMA adversely. Also the modification required for producing WMA imposes severe additional costs for manufacturers.

WMA shows it's the most important impact on usage of reclaimed asphalt pavement. Re-cycling of asphalt pavement which is completed the service life is not only contribute to the economy but also reduce damage to environment.

Changing of petrol prices from year to year, make it risky to make long term investment on WMA technology. Moreover, manufacturers are worry about which technic is more advantageous and useful due to being numerous additive materials and production techniques.

In later years, WMA would be a good alternative with respect to HMA with increasing of environmental awareness throughout the world

REFERENCES

- [1]. Kheradmand, B., Muniandy, R., Hua, L. T., Yunus, R. B., & Solouki, A. (2014). An overview of the emerging warm mix asphalt technology. *International Journal of Pavement Engineering*, 15(1), 79-94, Malesia
- [2]. Zaumanis, M. (2010). Warm mix asphalt investigation. Riga Technical University, Denmark
- [3]. D'Angelo, J., Harm, E., Bartoszek, J., Baumgardner, G., Corrigan, M., Cowser etc (2008). Warm-Mix asphalt: European practise. American Trade Initiatives, Washington, DC
- [4]. Dokandari, P. A., & Topal, A. (2015). Effects of Warm Mix Asphalt Additives on Aging Characteristics of Bituminous Mixtures. *Periodica Polytechnica Civil Engineering*, 59(4), 475-486.
- [5]. Button, J.W., Estakhri, C. ve Wimsatt, A., (2007). A Synthesis of Warm-Mix Asphalt. FHWA Report 0-5597-1, Texas Transportation Institute.
- [6]. Croteau, J.M. and Tessier, B., (2008). "Warm Mix Asphalt Paving Technologies: a Road Builder's Perspective", Transportation Association of Canada, Ottawa, Canada
- [7]. Öztürk, H.I, (2013). Quantification Of Quality Of Foamed Warm Mix Asphalt Binders And Mixtures. PhD Teisses Michigan State Universitesi, ABD
- [8]. Asphalt in Figures, 2011. European Asphalt Pavement Association, Brussel
- [9]. Rubio, M. C., Martinez, G., Baena, L. ve Moreno, F., (2012). "Warm mix asphalt: an Overview", *Journal of Cleaner Production*, 24: 76-84.
- [10]. Vaitkus, A., _Cygus, A., Laurinavi_cius, A., Perveneckas, Z., 2009a. Analysis and evaluation of possibilities for the use of warm mix asphalt in Lithuania. *The Baltic Journal of Road and Bridge Engineering* 4 (2), 80-86
- [11]. Vaitkus, A., Vorobjovas, V., _Ziliut, L., 2009b. The Research on the Use of Warm Mix Asphalt for Asphalt Pavement Structures. Road Department, Vilnius Gediminas
- [12]. Bueche, N., 2009. Warm Asphalt Bituminous Mixtures with Regards to Energy, Emissions and Performance Young Researchers Seminar (YRS) LAVOC-CONF-2010-002, Torino, Italy
- [13]. Larsen, O.R., 2001. Warm Asphalt Mix with Foam e WAMFoam. IRF 2001 Partie B: Thèmes Techniques, S.00469. Kolo Veidekke, Norway
- [14]. Hassan, M. (2009). Life-Cycle Assessment Of Warm-Mix Asphalt: An Environmental And Economic Perspective. Lousiana Universitesi, USA
- [15]. Çoksevim, B. ve Türk, M., (2003). "Asfaltlama İşçilerinde Kan Gazları Değerleri", *Türkiye Klinikleri Tıp Bilimleri*, 23:1-4
- [16]. Kristjansdottir, O., (2006). Warm Mix Asphalt for Cold Weather Paving, Report No. WA-RD 650.1, University of Washington, Seattle, Washington
- [17]. Hurlley, G.C. and Prowell, B.D. , (2005). Evaluation of Sasobit for use in warm mix asphalt. Report 05-06, Auburn : National Center for Asphalt Technology
- [18]. Dasa, P. K., Tasdemir, Y. ve Birgissona, B. (2012). Evaluation of fracture and moisture damage performance of wax modified asphalt mixtures. *Road Materials and Pavement Design*, 13, 142-155.
- [19]. Güngör, A. G., Orhan, F., Ve Kaşak, S., (2008) Bitümlü Sıcak Karışım Aşınma Tabakalarının Performanslarının İleri Deneyler İle Belirlenmesi, Ankara
- [20]. ASMÜD, (2015). Türkiye'de Rakamlarla Asfalt, <http://www.asmud.org.tr/asfalt.php?sayfa=25> [Cited at 15.03.2016]
- [20]. Özcan, A., (2015). Asfalt Sektörü Büyümesini Sürdürecektir. *Yol Teknolojileri Dergisi*, 1309-6095 (36):44-48

Forming of Carbon Fiber Reinforced Composite Materials By Using of Stretch Apparatus

Omer Bayraktar¹, Abdulmecit Guldas¹, Mustafa Goktas²

Abstract

At shaping of composite materials that are obtained from woven fiber, except for filament winding method, all the techniques are carried out by the way fiber fabric is laid on a surface diagonally and then it is shaped. At the products produced with the method of laying fabric layers on a surface, a non-uniform structure between fiber and matrix material may occur. Long fibers that are laid freely cannot be placed in matrix material lineally. Therefore, when pressure is (loads are) applied on the composite, force is not distributed to all fibers evenly. Thus, as some fibers exposed to more stress than others they are broken or deformed primarily. This situation results lower mechanical features for composite material than expected. Woven fabrics produced from the fibers will be formed by stretching fabric instead of laying on a surface freely. This stretching process will be performed by a stretching tool which is designed and manufactured. When the woven fabric is stretched by stretching apparatus, sealing problems has occurred in the vacuum bagging process. This problem solved by applying resin to the leaking areas. In this way, when pressure (load) is applied to composite material, pressure distributed evenly to all fibers.

***Keywords:** Stretch apparatus design, Carbon fiber, Composite structural design*

1. INTRODUCTION

Carbon fiber reinforced polymer (CFRP) composites have been widely utilized and studied due to their excellent properties, including high specific strength, modulus, thermal and electrical conduction, corrosion resistance, good dimension and stability, etc. [1-2]. Composite structures are typically used as the form of laminate. Therefore, the strength and failure mechanism of laminate structure become the most important problem for designers and users.

In recent applications of composite laminates, only classic failure criteria such as the maximum stress/strain, Tsai–Hill, and Tsai–Wu criteria have been considered during the static analyses of composite structures. For this reason, the local failure in a region of the fiber and/or matrix under a particular stress combination cannot be calculated [3-4]. On the other hand, the initial fiber failure is the main design criterion to ensure the structural safety of a composite structure. In other words, the failure of a single fiber represents the total failure of the structure. However, this design criterion is too redundant and conservative, and it is laborious to describe the progressive failure of the fiber and/or matrix under increasing static loads or cyclic fatigue loads [5].

Today, at shaping of composite materials that are obtained from woven fiber, except for filament winding method, all the techniques are carried out by the way fiber fabric is laid on a surface diagonally and then it is shaped. At the products produced with the method of laying fabric layers on a surface, a non-uniform structure between fiber and matrix material may occur. Long fibers that are laid freely cannot be placed in matrix material lineally. Therefore, when pressure is (loads are) applied on the composite, force is not distributed to all fibers evenly. Thus, as some fibers are exposed to more stress than others they brake or deform primarily. This situation results lower mechanical features for composite material than expected. Some research show that compressive stress may be as high as 1700 MPa at local region of composite materials [5].

2. THEORIES FOR REDUCING THE INITIAL FAILURE OF COMPOSITE LAMINATES

In order to eliminate the failure of a single fiber, the load occurring on the material must be distributed to all fibers evenly. In order to achieve this, all the fibers must be linearly aligned. The fibers which are produced with laid freely on a surface cannot be regularly aligned during application. However, the effect of the most important error may be reduced by aligning the fibers in the same direction during production. In this paper, woven fabrics produced from the fibers will be formed by stretching fabric instead of laying on a surface freely. This stretching process will be performed by a stretching tool that will be designed and manufactured. With the use of this method, fibers will be both homogeneously dispersed and linearised in a certain direction in the matrix. By this way, when pressure (load) is applied to composite material, it will be possible that pressure will be distributed evenly to all fibers.

¹ Corresponding author: Gazi University, Department of Manufacturing Engineering, 06500, Teknikokullar/ANKARA, Turkey.
omerbayraktar@gazi.edu.tr

²Gazi University Technical Sciences Junior technical college Ankara /TURKEY

Compressing and pulling the fiber bundles which are in the form weave will not linearise the all fibers. As the linear fibers will encounter the load instead of the curved fibres when compressing the woven fabric, the curved fabrics will not become linear. To overcome this issue, a design of a stretching equipment which on one end works as a fixed jaw and the other side has two rolls with adjustable distance has been considered. Visual diagram of the stretch equipment designed on this context is shown in Fig.1.

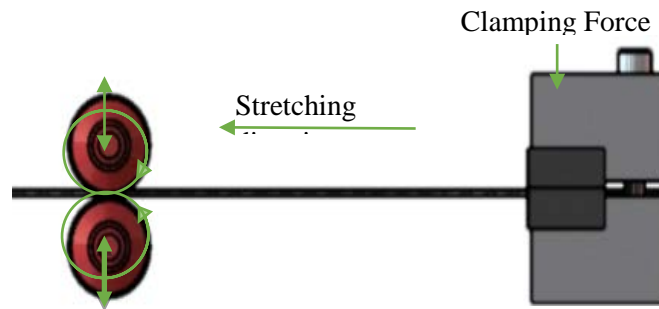


Figure 1. Visual scheme of stretching apparatus

3. DESIGNING OF STRETCH APPARATUS

After the conception, the design of the mechanism in 3D was performed (Figure 2). The distance between the rolls and the pressure are obtained by turning the crank handle shown in Figure 2 which provides up and down movement to the movable jaw. To perform this process, the drive plate and the movable jaw are fixed to each other by columns. Up and down movements have been provided to the mechanism by the bolts using timing belts and pulleys between the drive plate and fixed jaw.

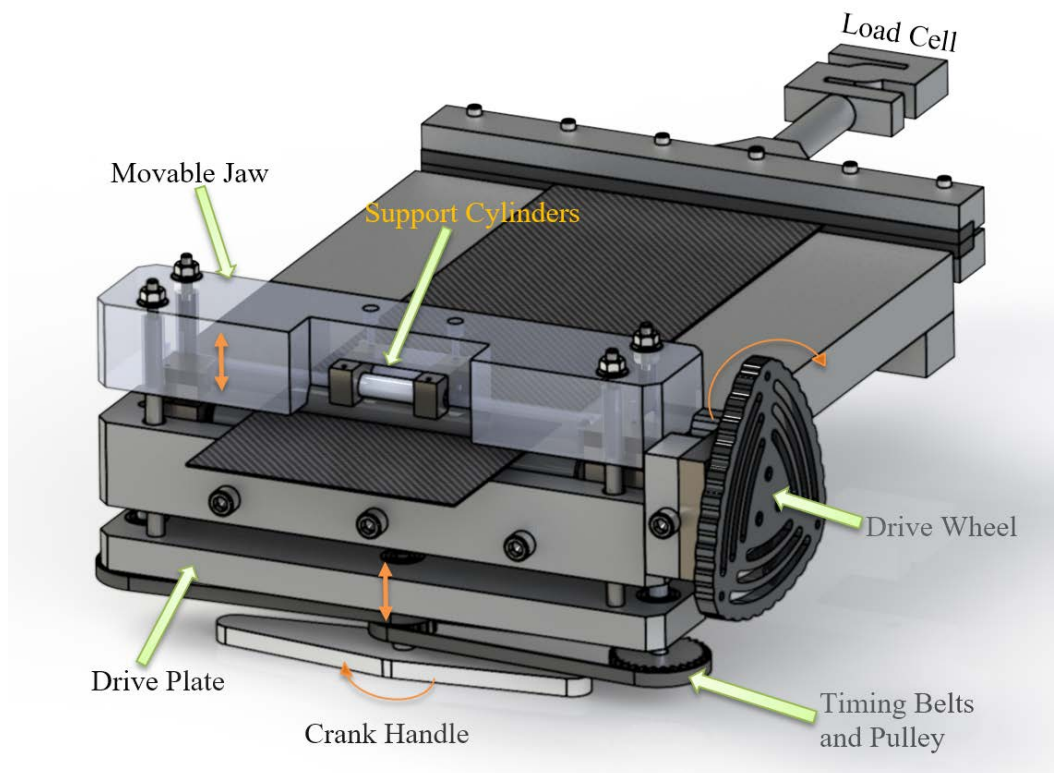


Figure 2. Designed stretching apparatus

Various measures have been taken in mind during the design stage for the problems which might occur during production stage. Firstly the support cylinders shown in Figure 2. has been designed. This part is designed to prevent bending while the rollers produce perpendicular pressure to each other. These support rollers are also located in the lower rollers. The movement of the rollers are provided with the small gear box shown in Figure 3. However, the distance between the gears

in the gearbox needs to be adjustable due to the rollers having variable distance. The design was carried out to make the distance adjustments quick and easy (Figure 3).

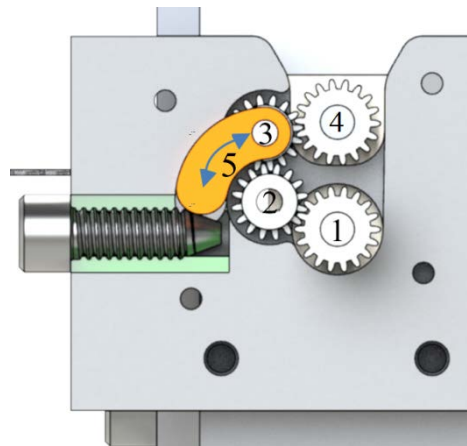


Figure 3. Gearbox located on the apparatus

The design stage of the gearbox shown in Figure 3 is as follows;

- ✓ Parts number 1 and number 4 are fixed to the ends of the rolls.
- ✓ As the gear no 4 is linked to the movable jaw, it is removable and attachable. Therefore, the upper side of this gear in the gearbox is left open.
- ✓ Gear no 3 installation is made on the part no 5
- ✓ The slot of number 5 is opened so that it can rotate around gear number 2
- ✓ The movement of number 5 is provided with a tapered screw working as a gauge.
- ✓ The gear shaft of number 1 is fixed with a drive gear shown in Figure 2. and the rotational movement of the rolls are provided with this gear.



Figure 4. System which provides movement to the movable jaw

Desired tensioning force can be applied to the load cell by placing load cell to the designed stretch apparatus. Also, a vacuum system has been adapted to impregnate resin with vacuum method to the fiber or fabric which is stretched with the apparatus. Thus, composite materials can be manufactured by using the vacuum method on the stretching apparatus. The stretching apparatus manufactured according to the design shown in Figure 5.



Figure 5. Stretch apparatus (a: stretching apparatus, b: a digital display of load cell).

4. MATERIALS AND METHODS

Epoxy is impregnated and composite is created by using the vacuum infusion method on unidirectional woven carbon fiber fabric with the help of the stretch apparatus which was designed and manufactured.

4.1. Material

4.1.1. Woven fiber

In this study, GURIT UT-C300 brand unidirectional woven carbon fiber fabric is used as matrix material to create samples.

Table 1. UT-C300 Uni-directional woven fabric properties

Warp stretching				Weft			
Primary Fibre Type	Fiber g/km	Tex	Theoretical g/m ²	Filament Type	Fiber g/km	Tex	Theoretical g/m ²
Carbon 12k	800		300	PE	10	3	

4.1.2. Epoxy resin

Prime 20LV manufactured by GURIT is used as epoxy resin. For curing, Prime 20LV fast hardener by the same manufacturer is used. This resin is designed for various types of resin transfer moulding and due to having low viscosity, it is suitable for use in large-scale part manufacturing. Generally, it is used in production of parts such as wind turbine blades and yacht hulls.

4.2. Equipments

4.2.1. SEM study

The observation of the fracture surface is evaluated with a Jeol JSM-6060LV scanning electron microscope to determine linearity of fibers.

4.2.1. Load Cell

Stretch force measured with GERATECH brand SH-10K models are placed on stretching apparatus. Measured value of tension is controlled via digital screen. The stretch apparatus mechanism was locked when desired strength is reached.

4.3. Method for manufacturing process

Composite materials which were desired to be produced with stretching apparatus have been manufactured by using vacuum infusion method (Figure 6). Resin impregnated samples have been kept in 22°C condition for 24 hours for curing. Thereafter, they were incubated in an oven with 50°C for 16 hours. During this process in total of 5 samples (4 pre-stressed and 1 stress-free) were manufactured. Two from each sample were produced in order to test the stability and repeatability of the testing equipment. The samples have been manufactured using uni-directional carbon fiber fabric with a width of 220mm. Tension values used during production are 0 N, 200 N, 300 N, 450 N and 680 N.

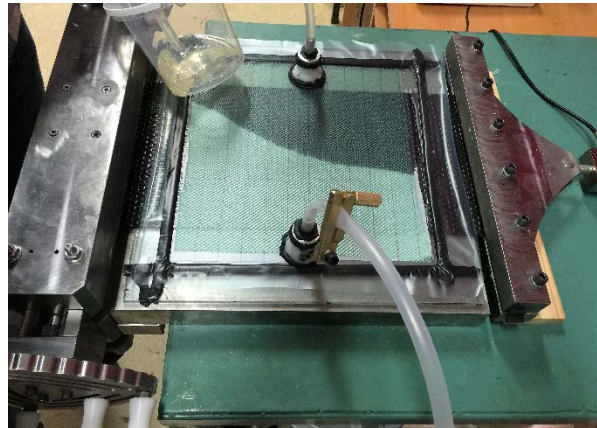


Figure 6. Vacuum infusion process

5. RESULTS

Surfaces of the specimens were examined by SEM to compare the fiber linearity with respect to the stretch apparatus methods as shown in Fig. 7-11. Increasing linearity proportional to the pre-tension was observed on the SEM images of the samples with the pre-tension values of 0 N, 200 N, 300 N, 450 N and 680 N. The undrawn fiber (0 N) was curved, warped and the fiber directions differ from each other (Figure 7). In literature, after examining SEM images, it has been determined that samples manufactured without pre-tension have similar situation. [7-9]. Curvatures of fibers are relatively decreased but are still aligned in different directions after stretching and linearising with 200N pre-tension. (Figure 8.a,b) When the samples with 300 N pre-tension value were observed, fibres with curvatures were disappeared but the alignment were respectively different (Figure 9). A homogenous property, linear and same directional fibers were observed when 450 N pre-tension values was examined as shown in Figure 10. However, fracture surface was located in the central part and relatively resin-free regions of the sample when examining Figure 11.b.

When observing the fracture surfaces of the materials manufactured by the designed and manufactured stretch apparatus using resin impregnation method, linearization increase in fibers was found up to 450 N pre-tension. However, a decrease of space between fibers were observed after pre-tension values of 450 N due to very tight package which occurred by high stress levels. Since the penetration of resin to the shrunken space becomes harder, epoxy resin amount on unit cross section has decreased. We believe that, the mechanical properties of the composite material will be effected negatively due to decrease on resin which hold the fiber together.

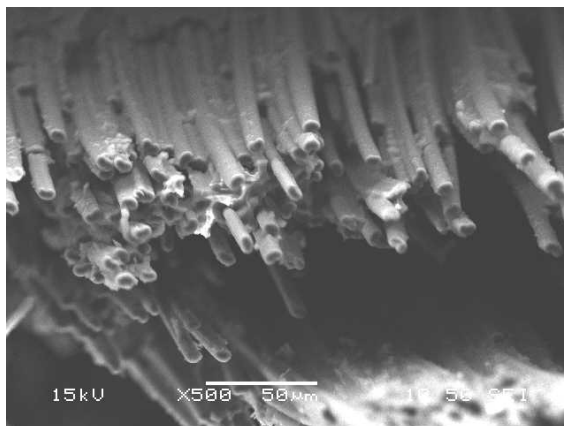


Figure 7. The SEM image of sample manufactured with the pre-tension values of 0 N (undrawn)

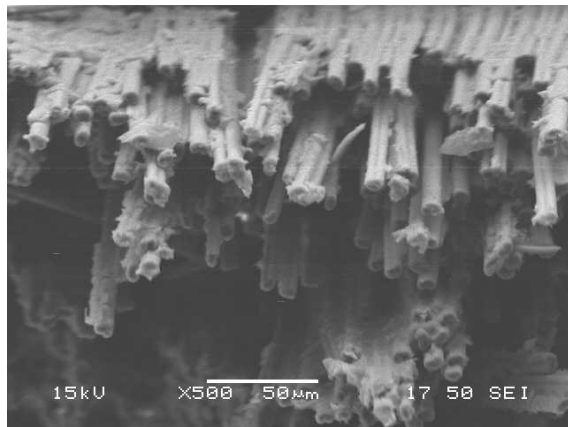


Figure 8. The SEM image of sample manufactured with the pre-tension values of 200 N

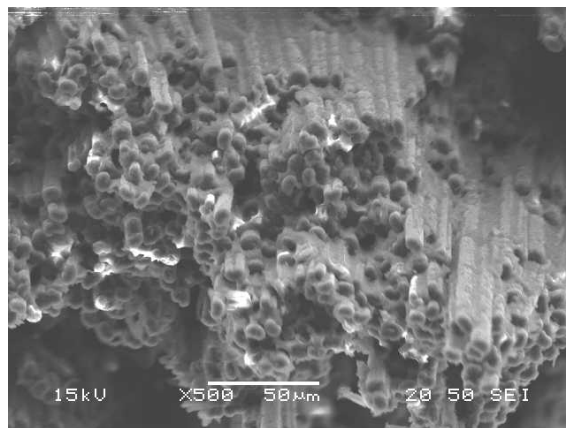


Figure 9. The SEM image of sample manufactured with the pre-tension values of 300 N

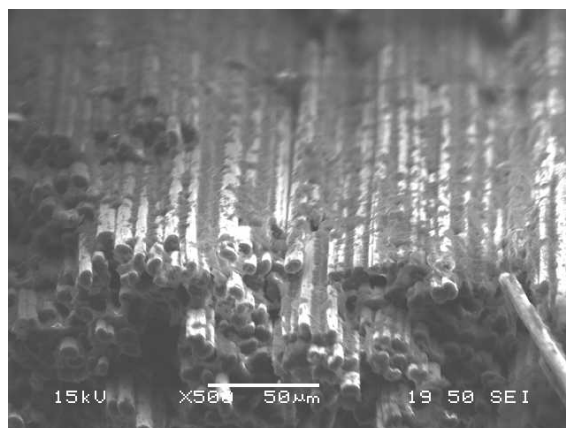
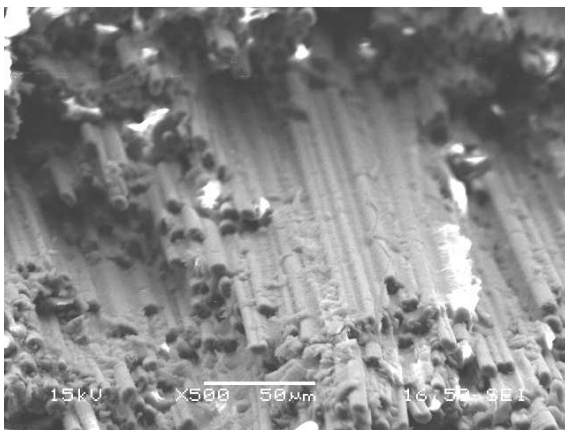
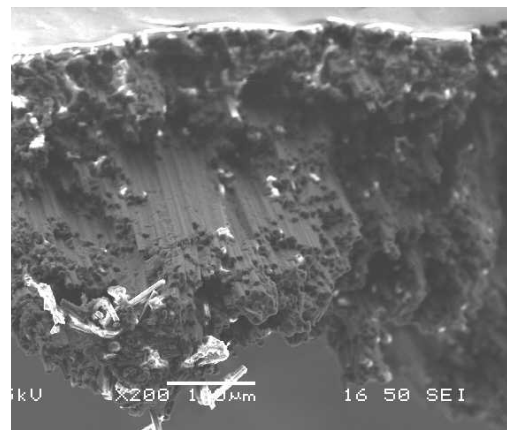


Figure 10. The SEM image of sample manufactured with the pre-tension values of 450 N



(a)



(b)

Figure 11. The SEM images of samples manufactured with the pre-tension values of 600 N

6. CONCLUSIONS

After observing SEM images, it has been determined that the designed stretch apparatus is successful in linearization of fibers

Linearity of fibers are at maximum value on 450N pre-tension and values over 450N produce the same results, therefore values over 450N are considered unnecessary.

Fibers become tight package shape with the increase of pre-tension.

Resin-free regions occur due to tight packaging on values over 450N.

It should be examined that how these linearity gaining fibers effect the materials endurance.

ACKNOWLEDGMENT

This study is supported by TUBITAK with the project number 214M649. We are grateful for the support given by TUBITAK for this project.

REFERENCES

- [1]. S.H. Han, H.J. Oh, S.S. Kim, "Evaluation of fiber surface treatment on the interfacial behavior of carbon fiber-reinforced polypropylene composites" Composite Part B Engineering, Vol. 60., pp. 98–105, 2014.
- [2]. S. Wana, X. Huanga, P. Qiua, S. Baia, L. Chena, "The effect of short carbon fibers on the thermoelectric and mechanical properties of p-type CeFe₄Sb₁₂ skutterudite composites", Materials & Design, Vol. 67., pp. 374-384, 2015.
- [3]. Z. Hashin, "Failure criteria for unidirectional fiber composites", J Appl. Mech., Vol. 47, pp. 329–34, 1981.
- [4]. A. Puck, H. Schürmann, "Failure analysis of FRP laminates by means of physically based phenomenological models", Composites Science and Technology, Vol. 62, pp. 1633-1662, 2002.
- [5]. C.-S. Lee, J.-H. Kim, S.-k. Kim, D.-M. Ryu, J.-M. Lee, "Initial and progressive failure analyses for composite laminates using Puck failure criterion and damage-coupled finite element method", Composite Structures, Vol. 121, pp. 406–419, 2015.
- [6]. K. W. Gan, M. R. Wisnom, S. R. Hallett, "Effect of high through-thickness compressive stress on fibre direction tensile strength of carbon/epoxy composite laminates", Composites Science and Technology, Vol. 90, Pp. 1–8, 2014.
- [7]. Y. Wei, Q. An, X. Cai, M. Chen, W. Ming, "Influence of Fiber Orientation on Single-Point Cutting Fracture Behavior of Carbon-Fiber/Epoxy Prepreg Sheets", Materials 2015, Vol. 8(10), pp. 6738-6751, 2015.
- [8]. D. Leea, J. W. Limb, S. Nama, I. Choic, D. G. Leea, "Method for exposing carbon fibers on composite bipolar plates", Composite Structures, Vol. 134, pp. 1–9, 2015.
- [9]. G. Wua, L. Maa, Y. Wang, L. Liu, Y. Huang, "Interfacial properties and impact toughness of methylphenylsilicone resin composites by chemically grafting POSS and tetraethylenepentamine onto carbon fibers", Composites Part A: Applied Science and Manufacturing, Vol. 87, pp. 1-8, 2016.

Depth Estimation From the Magnetic Anomalies of the Northern end of the Fethiye-Burdur Fault Zone (FBFZ), SW Turkey

M. Nuri Dolmaz¹

Abstract

The study focuses on the depth estimation of magnetic anomalies of the northern end of the Fethiye-Burdur Fault Zone (FBFZ) in SW Turkey. Obtaining of the source depths could contribute to understanding underground causative bodies, tectonic and geological structures of the area. The power spectrum techniques were applied to the residual aeromagnetic data. Depth to bottom of deepest magnetic source in the study area, one block of 100 km dimensions, reaches a maximum depth of 15.94 km. This value corresponds to the Curie point. Then the power spectrum method was also applied to the RTP data in two places in and around the Burdur Lake and the depths of 6.8 km in the north and 2.1 km in the south were obtained for the causative magnetic bodies. It is interpreted by looking at the shape of the anomalies, which are adjacent anomalies that the causative body is two-headed structure and placed in the sediment accumulation of the Burdur graben in SW Turkey. It can also be suggested that the magnetized body gained its magnetization during a normal polarity time oriented in about N-S direction as inclined to the north.

Keywords: Aeromagnetic data, Power spectrum, Burdur basin

1. INTRODUCTION

The SW Turkey that mainly controlled by the processes associated with the Africa-Anatolia plate convergence zone is a tectonically active region. One of major tectonic features of SW Turkey is NE-SW trending the strike slip Fethiye-Burdur Fault Zone (FBFZ). Several NW-SE trending active normal faults cut across this NE-SW trending major structure [1]. The FBFZ in SW Turkey, a complex geological structure, is an active plate boundary connecting to different tectonic provinces (Fig. 1). Collision tectonic regime is dominant between the Eurasian and African plates. The zone is formed by northward movement of the African Plate and westward escape of the Aegean-Anatolian block. The FBFZ is about 300 km in length characterizing as a combination of a number of normal faults in SW Turkey.

Along the fault zone the Plio-Quaternary sediments and deposits are cut with the stepwise active faults, branch of FBFZ. Locally, the folding and dipping Quaternary sedimentary beds and sandy and mud dykes and also eruptions of H₂S gases can be seen along the fault zone [2]. The Burdur fault is one of the most important active fault zones in the region and generated two large destructive earthquakes in October 1914 (Ms = 7.0) and May 1971 (Ms = 6.2) causing serious damage and casualty [3]. Due to new tectonic system, the different stress field has been occurring the Burdur fault and the tension cracks have formed in east and west side of Burdur Lake [4]. Recent GPS data indicate that the Aegean plate in the northern part of the FBFZ extends with a velocity of 3 cm/year in SW direction and however, there is no significant extension/movement in the south of the FBFZ within the Isparta Angle area [5].

In this study it is focused on the depth estimation from the magnetic anomalies of the northern end of the FBFZ of SW Turkey. For this purpose, the power spectrum techniques were applied to the residual aeromagnetic data. The depth to bottom of deepest magnetic source for one block of 100 km dimensions in the study area is estimated. The power spectrum method was also applied to the RTP data in two places in and around the Burdur Lake and therefore the depths of the causative magnetic bodies were obtained.

¹ Corresponding author: Suleyman Demirel University, Department of Geophysical Engineering, 32200, Isparta, Turkey.
nuridolmaz@sdu.edu.tr

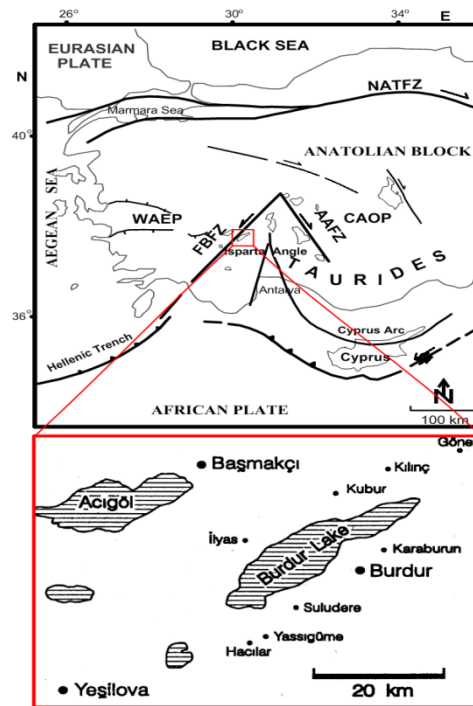


Figure 1. Simplified tectonic map of western Turkey and adjoining regions (modified after [6]) and geographic location of the study area (below) (modified from [7]). Abbreviations: NATFZ, North Anatolian Transform Fault Zone; FBFZ, Fethiye-Burdur Fault Zone; AAFZ, Afyon-Akşehir Fault Zone; EFZ, WAEP, West Anatolian Extensional Province; CAOP, Central Anatolian Ova Province. Coastlines and lakes are also shown.

2. METHODS

The aeromagnetic data were provided by the General Directorate of Mineral Research and Exploration of Turkey (MTA) and the International Geomagnetic Reference Field (IGRF) for the 1982.5 was then removed from the aeromagnetic anomalies using the program of [8]. Magnetic data have positive and negative anomalies due to the polarity of the magnetic sources with the Earth's induced magnetic field. For this purpose, first of all the anomaly data were reduced the (north) magnetic pole, utilizing the FFTFIL program [9]. Total field magnetic data are transformed into the magnetic pole [10]. Figure 2 shows the reduced to pole (RTP) total field aeromagnetic anomaly map of the study area. The aeromagnetic anomaly map has several magnetic anomalies and their intensities are about 100 nT.

Geophysicists frequently have used prism models to calculate the total field magnetic anomalies due to geological structures [11]. The relationship between the spectrum of magnetic anomalies and the depth of a magnetic source has been proven by [12] by analyzing statistical properties of patterns of magnetic anomalies. The power spectrum method of [12] is based on the assumption that the sources are considered to be independent collections of rectangular vertical prisms. The radial average of the power spectrum of magnetization is constant for random magnetization. [13] implied that the rectangular prism is an optimum geometrical shape, not a required geologic model.

To estimate the source depths of the magnetic data for this study, power spectrum analyses were done according to the methods of [12] and [13]. The depth to bottom (DTB) of the structure for magnetized layer (z_b) is calculated from the centroid depth (z_0) and the top depth (z_t) using the equation ($z_b = 2z_0 - z_t$) [13].

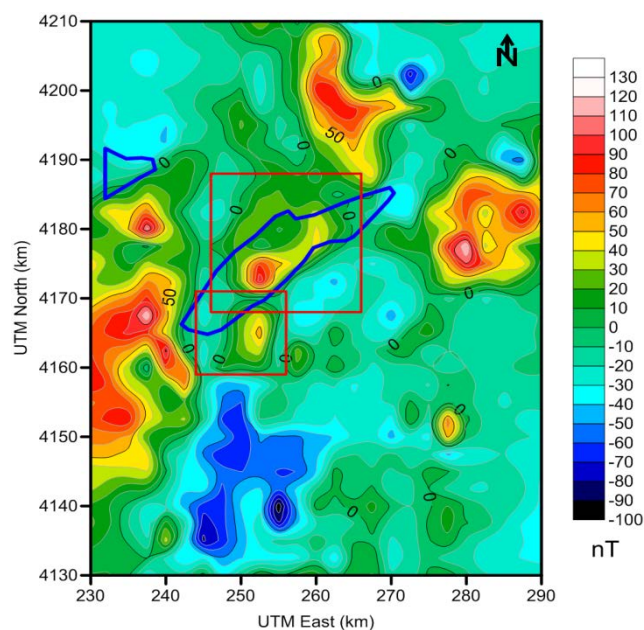


Figure 2. Reduced to pole (RTP) total field aeromagnetic anomaly map of the study area. Red rectangles show the data subregions to estimate depths.

3. RESULTS AND DISCUSSION

The NE-trending FBFZ which limits the Western Anatolia to the south has left lateral oblique in character and is exposed for 400 km in the SW-Anatolia. According to field observations and fault plane solutions of recent earthquakes, the Burdur fault is a left lateral oblique fault and consists mainly of several NE-trending fault systems [2]. In this study, it is focused on depth estimation of the causative bodies of magnetic anomalies in the northern end of the FBFZ in SW Turkey. Obtaining of source depths could contribute to understanding underground magnetized structures of the area. Total field aeromagnetic data of the area were processed and interpreted for the present study. The power spectrum techniques were applied to the residual aeromagnetic data which were already reduced to the north magnetic pole (RTP). One block of 100 km dimensions is used to estimate deepest magnetic source. From centroid depth of 9.53 km and top depth of 3.12 km (Fig. 3), the deepest depth is calculated as 15.94 km for this block by means of equation ($z_b = 2z_0 - z_t$). Then the power spectrum method was also applied to the RTP data in two places (Fig. 2) in and around the Burdur Lake to estimate the average depth of magnetic sources which causes to the magnetic anomalies. Two source depths for the causative magnetic bodies in subsurface are calculated such as 6.8 km in the north and 2.1 km in the south.

In the study area, the magnetized layer reaches a maximum depth of 15.94 km from the power spectrum of magnetic anomalies. Under this layer, the crust has virtually non magnetic properties. The variance reductions determined for different depths suggest that the Burdur seismic activity is confined to the upper crust [14]. This condition is consistent with our results. Looking at the shape of the anomalies, I suggest that the causative body is two-headed structure and places in the sediment accumulation of the Burdur graben in SW Turkey. It can also be suggested that the magnetized body gained its magnetization during a normal polarity time, oriented in about N-S direction as inclined to the north.

4. CONCLUSIONS

Determination of the depths from magnetic anomalies could contribute to understanding subsurface causative bodies, tectonic and geological structures of the area. At the conclusion of the power spectrum of the magnetic data in the northern end of the FBFZ, two bottom depths for the causative magnetic bodies in subsurface were calculated such as 6.8 km in the north and 2.1 km in the south. It is interpreted by looking at the shape of the anomalies that the causative body is two-headed unified structure in the Burdur graben of SW Turkey. The magnetized structure was shaped in the sediment accumulation of the graben and it gained its magnetization during a normal polarity time, oriented in about N-S direction as inclined to the north. Depth to bottom of deepest magnetic source in the study area, named also Curie point depth, was estimated at 15.94 km in the study area.

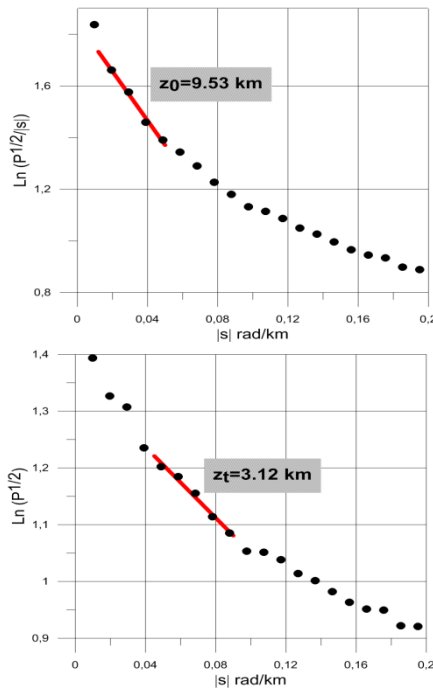


Figure 3. Examples of power spectrum for depth estimation. $|s|$ is the wavenumber and $P^{1/2}$ is the power spectrum

ACKNOWLEDGMENT

I thank the General Directorate of the Mineral Research and Exploration (MTA) of Turkey for use of the aeromagnetic data.

REFERENCES

- [1]. E. Altunel, A. Barka, and S. Akyüz, "Palaeoseismicity of the Dinar fault, SW Turkey," *Terra Nova*, 11, 297-302, 1999.
- [2]. F. Yağmurlu, N. Özgür, S. Pavlides, A. Chatzipetros, Z. Kamacı, A. Pınar, M. Şentürk, K. Uysal, and E. Şener, "Seismotectonic features of Aegean-Peloponnisos plate and the position of the Fethiye-Burdur Fault Zone, SW Turkey," The 33rd IGC 6-14 August, Oslo-Norway, 2000.
- [3]. N.N. Ambraseys and J.A. Jackson, "Faulting associated with historical and recent earthquakes in the Eastern Mediterranean region," *Geophys J. Int.*, 133, 390-406, 1998.
- [4]. Ş. Şahin, "Distribution of stress in Southwestern Anatolia and its Influence on the Burdur Fault," *İst. Üniv. Müh. Fak. Yerbilimleri Dergisi*, 17(1), 1-9, 2004.
- [5]. S. McClusky, S. Balassanian, A. Barka, C. Demir, S. Ergintav, I. Georgiev, O. Gurkan, M. Hamburger, K. Hurst, H. Kahle, K. Kastens, G. Kekelidze, R. Ring, V. Kotzev, O. Lenk, S. Mahmoud, A. Mishin, M. Nadariya, A. Ouzounis, D. Paradissis, Y. Peter, M. Prilepin, R. Reilinger, I. Sanli, H. Seeger, A. Tealeb, M.N. Toksöz, and G. Veis, "Global positioning system constraints on plate kinematics and dynamics in the eastern Mediterranean and Caucasus," *Journal of Geophysical Research-Solid Earth*, 105, 5695-5719, 2000.
- [6]. M.N. Dolmaz, "An aspect of the subsurface structure of the Burdur-Isparta area, SW Anatolia, based on gravity and aeromagnetic data, and some tectonic implications," *Earth Planets and Space*, 59(1), 5-12, 2007.
- [7]. T. Taymaz and S. Price, "The May 12 Burdur Earthquake Sequence, SW. Turkey: a synthesis of seismological and geological observations," *Geophys. J. Int.*, 108, 589-603, 1992.
- [8]. S.R.C. Malin and D.R. Barraclough, "An algorithm for synthesizing the geomagnetic field," *Computers and Geosciences*, 7, 401-405, 1981.
- [9]. T.G. Hildenbrand, *FFTFIL: A Filtering Program Based on Two dimensional Fourier Analysis*, U.S.G.S. Open File Report, pp. 83-237, 1983.
- [10]. V. Baranov, "A new method for interpretation of aeromagnetic maps: pseudo-gravimetric anomalies," *Geophysics*, 22, 359-383, 1957.
- [11]. B.K. Bhattacharyya, "Continuous spectrum of the total magnetic field anomaly due to a rectangular prismatic body," *Geophysics*, 31, 97-121, 1966.
- [12]. A. Spector and F.S. Grant, "Statistical models for interpreting aeromagnetic data," *Geophysics*, 35, 293-302, 1970.
- [13]. Y. Okubo, J.R. Graf, R.O. Hansen, K. Ogawa, and H. Tsu, "Curie Point Depths of the Island of Kyushu and Surrounding Areas, Japan," *Geophysics*, 53, 481-494, 1985.
- [14]. S. Över, H. Yılmaz, A. Pınar, S. Özden, U.C. Ünlügenç, and Z. Kamacı, "Plio-Quaternary Stress State in the Burdur Basin, SW-Turkey," *Tectonophysics*, 588, 56-68, 2013.

Repeated Low-Velocity Impact Behavior of Particle-Reinforced Metal Matrix Composites

Recep Ekici¹

Abstract

This study investigates the response of particle-reinforced metal matrix composites to repeated low-velocity impacts. Finite Element Method (FEM) was used to model the single and repeated low-velocity impact analyses of SiC particle-reinforced aluminum 6061 matrix composites. The numerical impact tests were carried out for the same total impact energy as single and repeated impacts. Three different total impact energies were chosen as 9, 15 and 24 J for the single impacts while the impact energy combinations of repeated impacts are chosen as 3+3+3, 5+5+5 and 8+8+8 J. Also, single and repeated impacts were performed for same particle size (70 μm) and two different particle volume fractions (10 and 30%). The effects of particle volume fraction and impact energy on the single and repeated impact behavior were explained by the contact force history, the central transverse deflections, and the residual stress and plastic strain distributions. In general, the repeated impacts induce an increase at the peak contact force and a shortening at the impact time due to an intensive strain-hardening in the metal matrix. Repeating of the impact makes the structure stiffer, reduces the central transverse deflections and affects the equivalent residual stress and plastic strain distributions. When the volume fraction (V_f) is increased, the peak contact force increases whereas the impact time decreases. Also, the maximum residual stress distributes uniformly in the impact region, the transverse strain bands disperse laterally and the level of plastic strain reduces.

Keywords: *Low-velocity repeated impact, particle-reinforced metal matrix composite, finite element analysis, drop-weight test.*

1. INTRODUCTION

Particle reinforced metal matrix composites (PRMMCs) are attractive materials in structural and advanced engineering applications for a long time. The property combinations obtained from metal and ceramic phases provide them important advantages in their service life. The high strength/weight ratio, high specific modulus, low coefficient of thermal expansion, and excellent wear resistance, high service temperature and isotropic properties make PRMMCs one of the best choices for applications such as automobile components, aerospace structures, mining equipments and turbine blades. The conventional materials don't have the combinations of these properties [1-4].

PRMMCs are exposed to static and dynamic loading conditions along their service life. In contrast to static loading, the mechanical behavior can be quite different under dynamic loading [5]. Because, the impact is a sudden dynamic loading, and may cause failure in structure which has no enough time to respond. Therefore, the response against impact loading is an important design parameter for using PRMMCs with confidence in working conditions [6-8].

In PRMMCs, the base micro-structural parameters such as particle volume fraction, size, shape and distribution can be affected the impact behavior [9-10]. In addition to these, the type of impact (being low- or high-velocity impact, oblique and repeated impact) will affect the response of the composite structure. However, PRMMC structures can be subjected to external repeated impact loads under heavy operating conditions such as the brake disks and engine pistons. This may affect the mechanical performance of the composite structures and cause severe damages as well. In order to enhance the structural safety of the devices and make sure a longer service life, the repeated impact responses of PRMMCs should be clarified [11].

In literature, most studies were conducted on the single-impact properties of PRMMCs at different impact energy levels [1,9-10,12-13], instead of multiple or repeated impact loading conditions. However, there are few studies concerning repeated impacts, and they are mainly focused on experiments [11,14].

The aim of this study is to investigate the dynamic behavior of SiC particle-reinforced Al matrix composites under repeated impacts. Numerical modeling was performed by Finite Element Method (FEM). Repeated and single low-velocity impact analyses were carried out with the same total impact energy. The effects of single and repeated impacts as well as particle volume fraction on the dynamic behaviors of PRMMCs were comparatively explained by the computational results.

¹Corresponding author: Erciyes University, Department of Mechanical Engineering, 38039, Melikgazi/Kayseri, Turkey.
rekici@erciyes.edu.tr

2. FINITE ELEMENT MODEL

Numerical modeling, single and repeated impact analyses of SiC particle-reinforced Al 6061 metal matrix composites were carried out by using the non-linear finite element method (FEM). In analyses, ABAQUS/Explicit [15] finite element software was used. The geometry of PRMMC and impactor were cylindrical and hemispherical, respectively. Axisymmetric modeling was used for simplifying the problem. Composite FEM models had 20 mm radius and 7 mm height, and were circumferentially clamped (Fig. 1). However, the top and bottom edges of the composite structure were free. An axisymmetric circular rigid impactor was modeled in a 5.045 kg mass and a 10 mm radius. The impact velocity and mass were assigned at a reference point on the center of impactor (see Fig.1). PRMMCs were modeled with axisymmetric eight-noded solid square elements in a size of 70 μm . Also, the impactor was also modeled with rigid two-noded shell elements. Therefore, PRMMC model was meshed with 28600 finite elements, and the impactor was meshed with 500 un-deformable finite elements.

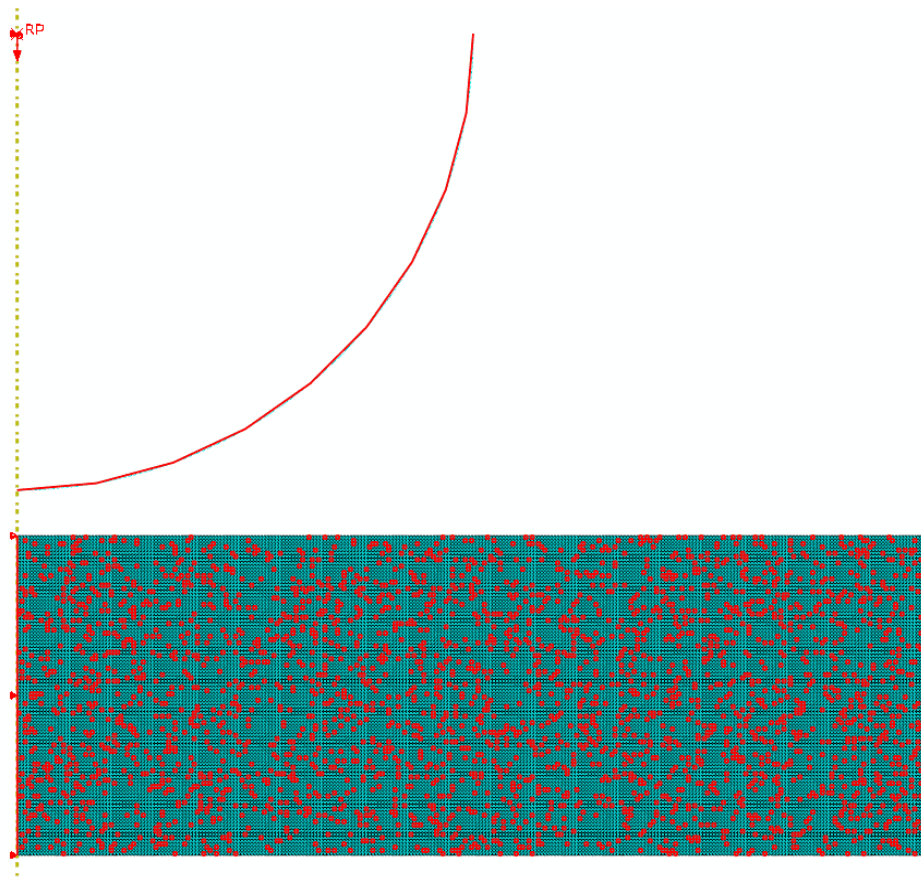


Figure 1. FEM model of the impactor and a PRMMC specimen ($V_f = 10\%$) with the random particle distribution.

In present study, the PRMMC composite material consists of a random distribution of ceramic SiC particles embedded within an Al 6061 alloy metal matrix for achieving a real PRMMC structure. The mechanical properties of Al 6061 alloy and ceramic SiC is given in Table 1. Numerical specimens were constituted in two different particle volume fractions ($V_f = 10$ and 30%). Al 6061 matrix was assumed as an elastoplastic material, whereas SiC (Silicon Carbide) particles were behaved elastic, and any failure of constituents was not considered.

Table 1. Mechanical properties of Al 6061 and SiC.

Property	Al 6061	SiC
Modulus of Elasticity (E), (GPa)	70	420
Poisson's ratio (ν)	0.33	0.17
Density (ρ), (kg/m ³)	2700	3100

In a developed algorithm for the random particle arrangement, the volume fraction of SiC particles in the composite structure is adjusted as a percentage of total finite element number (28600). Thus, a volume fraction of 10% for SiC particles corresponds to 2860 finite elements representing SiC particles. These 2860 elements are assigned randomly as

SiC particles among the total finite elements in the meshed region. So, SiC particle elements randomly change for each new analysis.

The repeated impact tests were conducted on the same location of PRMMC specimens with three impacts. The repeated impact energy combinations were 3+3+3, 5+5+5 and 8+8+8 J, whereas the single impacts were conducted on PRMMC specimens with total impact energies 9, 15 and 24 J. Among them, the impact tests performed for 3+3+3 J refer to three impacts on the same location of the specimen with 3 J impact energy each, while the 9 J impact test refers to a single impact on the specimen with 9 J impact energy.

3. NUMERICAL TEST RESULTS

The single and repeated impacts on PRMMCs were carried out for volume fractions of $V_f = 10$ and 30%. Fig. 2 a, b and c show the contact force histories of PRMMCs with $V_f = 10\%$ for total impact energies $E_{total} = 9$ J, 15 J and 24 J, respectively. It can be seen that both the impact time and the peak contact force increase with increasing total impact energy for all samples. Also, the peak contact force is reached in a longer time. PRMMCs exhibit a highly ductile behavior due to Al 6061 matrix and can absorb more impact energy since the contact time and contact force increase with increasing the impact energy. Hence, PRMMCs experience more plastic deformation with the increasing impact energy. The repeated impacts on the same location of PRMMC samples cause generally an increase at the peak contact force and a shortening at the impact time. With the repeating of impact, the peak contact force values are closer to those of the single impact. These show that PRMMC structures are subjected to an intensive strain-hardening during repeated impact.

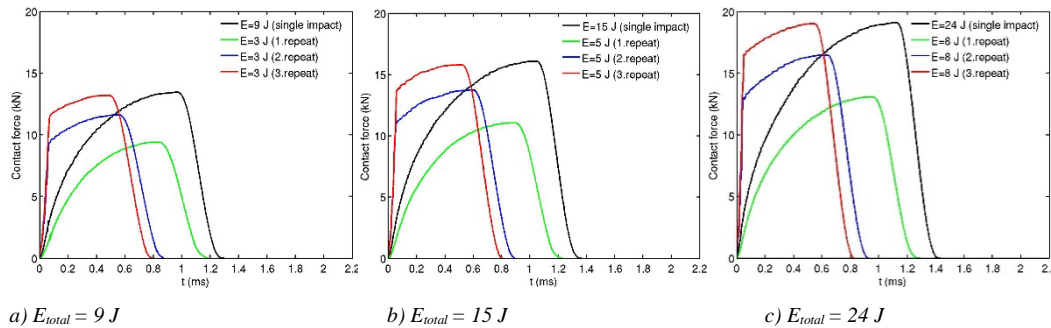


Figure 2. The contact force histories obtained from single and repeated impacts on PRMMCs ($V_f = 10\%$) for total impact energies a) $E_{total} = 9$ J, b) $E_{total} = 15$ J and c) $E_{total} = 24$ J

Fig. 3 also shows the effect of particle volume fraction (V_f) on the contact force histories of samples for total impact energy $E_{total} = 15$ J. It can be observed that as the volume fraction (V_f) is increased from 10 to 30%, the peak contact force increases, whereas the impact time reduces generally. PRMMCs behave stiffer as the particle volume fraction is increased and can absorb less impact energy.

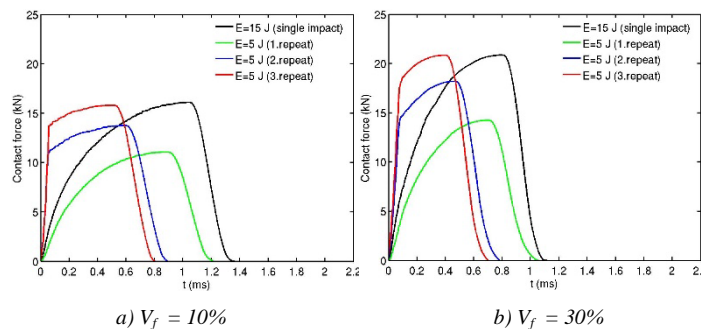


Figure 3. The contact force histories obtained from single and repeated impacts on PRMMCs for volume fractions a) $V_f = 10\%$ and b) $V_f = 30\%$.

After the impact completed, the residual equivalent (Mises) stress and equivalent plastic strain (PEEQ) distributions through the cross-section of PRMMC specimens (having $V_f = 10\%$) can be seen in Fig. 4 for the total impact energy $E_{total} = 15$ J. Fig. 4 a, b and c show the equivalent stress and plastic strain distributions after the 1st, 2nd and 3rd impact for the impact energy of 5 J each, respectively, while Fig. 4 d shows the equivalent stress and plastic strain distributions after the single impact for the impact energy of 15 J. To be more apparent of the residual stress and strain distributions, the elastic ceramic particles in matrix are removed. The maximum residual stress through the cross-section underneath the indenter changes considerably more intensive. Ceramic particles in the metal matrix affect significantly the equivalent residual stress and plastic strain distributions. Also, the intensity of the maximum residual stress distribution enlarges gradually toward the back face of PRMMC after each repeat of the impact. For the repeated impact sample it is observed lots of transverse strain bands under the impact region, whereas it is seen less strain bands in the cross-section of single impacted sample. The strain bands concentrate on the transition region of deformation and move to right side due to extending deformation region with repeating impact. In addition, the plastic strain gradually increases in PRMMC structures. Thus,

this causes the strain-hardening and decreases the ductility, which increases the chance of brittle failure of composite structure.

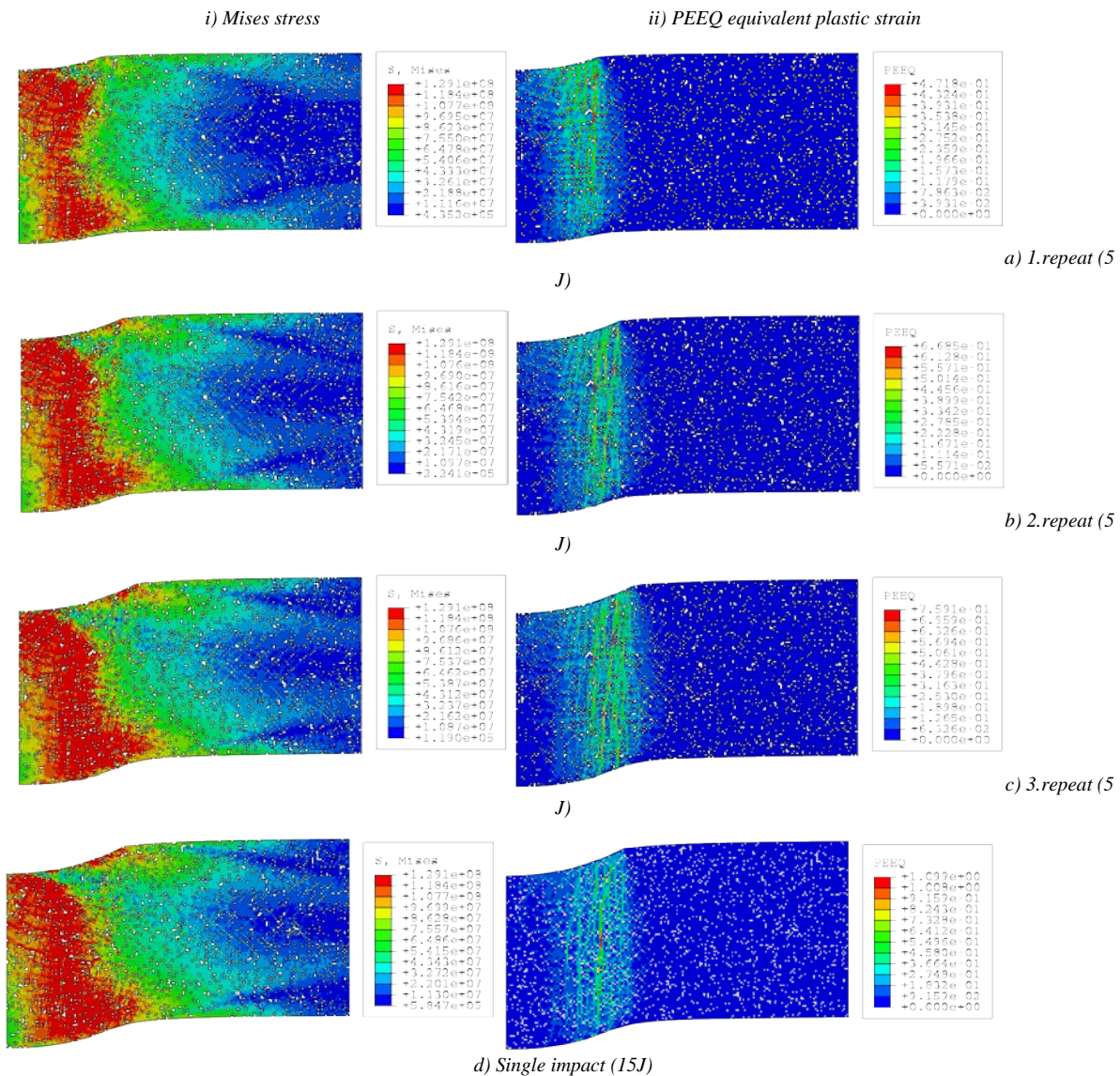


Figure 4.(i) The residual equivalent (Mises) stress and (ii) Equivalent plastic strain (PEEQ) distributions through the cross-section of PRMMC specimens ($V_f = 10\%$) for $E_{total} = 15 J$. (a) 1.repeat (5 J), (b) 2.repeat (5 J), (c) 3.repeat (5 J) and d) single impact (15J).

Fig. 5 shows the effect of particle volume fraction on the residual equivalent Mises stress and the equivalent plastic strain distributions in PRMMC structures under the single impact with the total impact energy of $E_{total} = 24 J$. As the particle volume fraction increases, the maximum residual stress concentrates increasingly through the cross-section of PRMMC. The maximum residual stress distribution becomes completely uniform through the cross-section of PRMMC underneath the impact region for the particle volume fraction of 30%. The plastic strain distribution changes with the particle volume fraction. The thin transverse strain bands disperse laterally and the level of plastic strain decreases as the volume fraction increases. The stiffness of composite structure is lower and the impact load is carried mostly by metal matrix for lower volume fractions. Thus, the metal matrix undergoes higher plastic deformations and absorbs more impact energy. But, increasing the volume fraction of particles increases the stiffness, and the impact load is carried mostly by elastic SiC particles and the metal matrix absorbs lower impact energy.

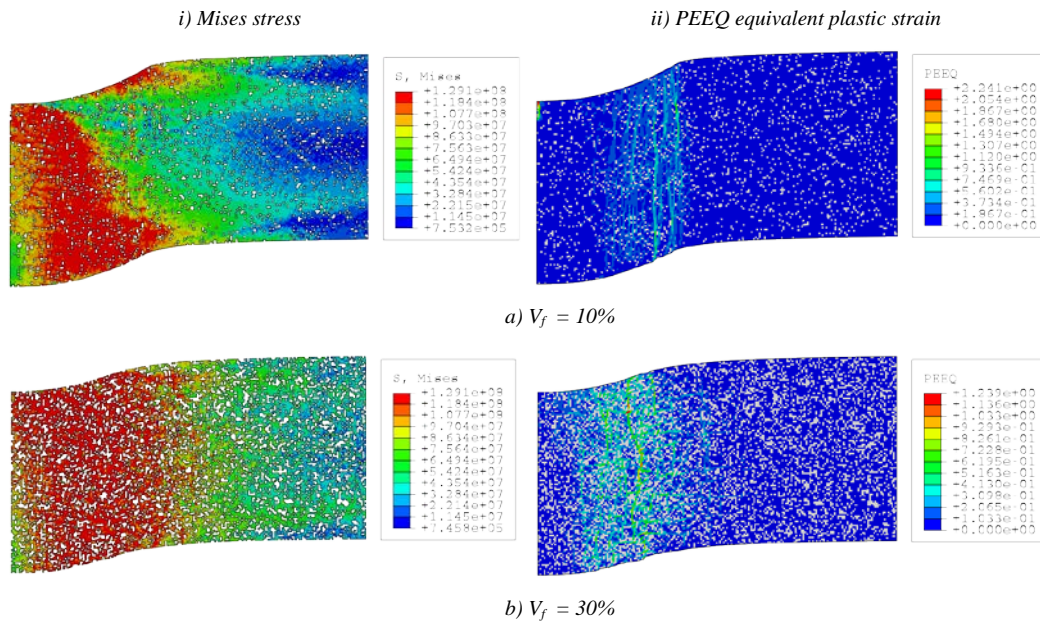
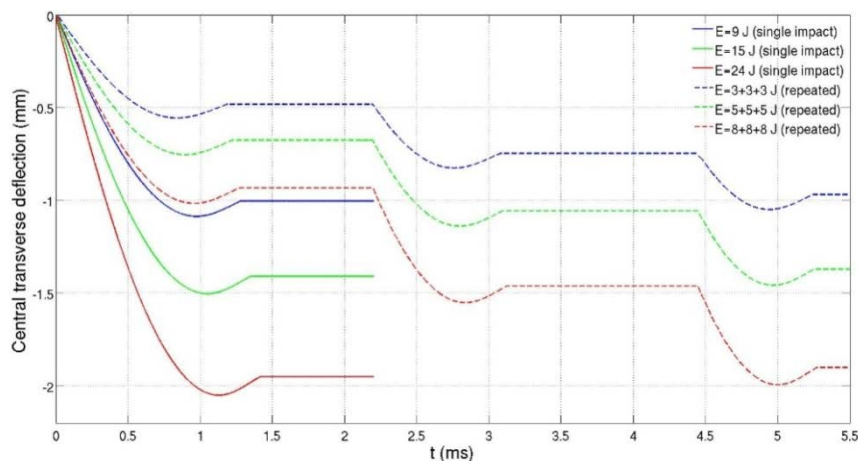


Figure 5.(i) The residual equivalent (Mises) stress and (ii) Equivalent plastic strain (PEEQ) distributions through the cross-section of PRMMC specimens under single impact with the total impact energy of $E_{total} = 24$ J. (a) $V_f = 10\%$, (b) $V_f = 30\%$.

Fig. 5 shows the central transverse deflection histories obtained from single and repeated impacts on PRMMCs for volume fractions $V_f = 10$ and 30% . The repeated impact loading causes a gradual increase in plastic deformation in the metal matrix of the composite structure. As a consequence of increasing plastic deformation the strain-hardening occurs in composite structure. Thus, PRMMCs become stiffer and the central transverse deflections generally reduce. It can be clearly seen from Fig. 5 (a) and (b) that the central transverse deflection values are greater under the single impact results. With the increasing impact energy, the PRMMC structures undergo more residual deformation to be able to absorb more impact energy. Thus, the central transverse deflection of composite structure as well as the impact time and the contact force increases when the impact energy increases. PRMMC structures behave stiffer and the central transverse deflection reduces when the particle volume fraction is increased. Thus, the capacity of the impact absorption of PRMMC structures decreases.



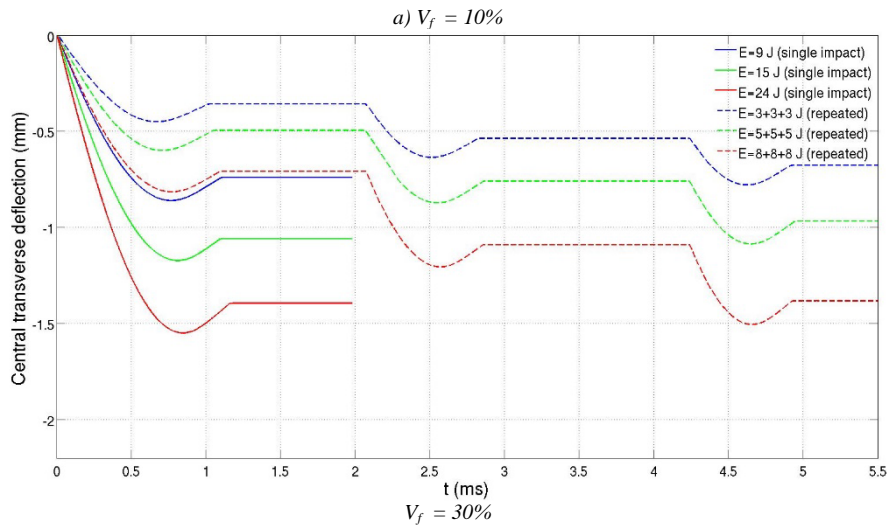


Figure 5. Central transverse deflection histories obtained from single and repeated impacts on PRMMCs for volume fractions a) $V_f = 10\%$ and b) $V_f = 30\%$.

4. CONCLUSIONS

In this study, finite element analyses were carried out to investigate behavior of PRMMCs under repeated and single low-velocity impact loading for the same total impact energy. The effects of particle volume fraction and impact energy on the repeated and single impact behaviors are explained by the contact force, the central transverse deflections, and the residual stress and plastic strain distributions. The impact time and the peak contact force increase with increasing total impact energy. Because, particle reinforced metal matrix composites exhibit a highly ductile behavior, and can absorb more impact energy by ductile Al 6061 matrix. The repeated impacts cause generally an increase at the peak contact force and a shortening at the impact time since PRMMC structures are subjected to an intensive strain-hardening. Repeating of the impact changes the equivalent residual stress and plastic strain distributions. The maximum residual stress distribution enlarges and the plastic strain gradually increases in PRMMC structures. Thus, this causes the strain-hardening and decreases the ductility and energy absorption capacity. In addition to these, PRMMCs become stiffer and the central transverse deflections generally reduce. As the volume fraction (V_f) is increased, the peak contact force increases, but the impact time reduces. Also, the energy absorption capacity and the central transverse deflections reduce due to increasing of stiffness. The maximum residual stress distribution becomes completely uniform underneath the impact region, the transverse strain bands disperse laterally and the level of plastic strain decreases.

REFERENCES

- [1]. A.M.S. Hamouda, M.S.J. Hashmi, Journal of Materials Processing Technology, Mechanical properties of aluminium metal matrix composites under impact loading, 56, 743-756, 1996.
- [2]. A.Sakthivel, R. Palaninathan, R. Velmurugan, P. Raghothama Rao, Production and mechanical properties of SiC_p particle-reinforced 2618 aluminum alloy composites, Journal of Materials Science, 43, 7047-7056, 2008.
- [3]. Chawla N and Chawla KK. Metal matrix composites. New York: Springer, 2006.
- [4]. Chawla KK. Composite materials-science and engineering, 2nd ed. New York: Springer, 1997.
- [5]. Duffy, J.: The dynamic Plastic Deformation of Metals: A review. Technical report Air Force Wright Aeronautical Laboratories, AEWAL-TR-82-4042, 1982.
- [6]. Sakthivel A, Palaninathan R, Velmurugan R, et al. The effect of silicon carbide particulates on tensile, fatigue, impact and final fracture behaviour of 2618 aluminium alloy matrix composites. Int J Aerosp Innov, 3, 193-205, 2011.
- [7]. Tirtom I, Guden M and Yildiz H. Simulation of the strain rate sensitive flow behavior of SiC-particulate reinforced aluminum metal matrix composites. Comp Mater Sci 2008; 42: 570-578.
- [8]. Deshmanya IB and Purohit GK. Development of models for predicting impact strength of Al7075/Al₂O₃ composites produced by stir-casting. Int J Advance EngSci Tech, 11, 238-252, 2011.
- [9]. S. Ozden, R. Ekici and F. Nair, Investigation of impact behaviour of aluminium based SiC particle reinforced metal-matrix composites, Compos Part A Appl Sci, 38, 484-494, 2007.
- [10]. R.Ekici and M.Kaburcuk, Low-velocity impact behavior of Al 6061/SiC particulate metal matrix composites, Journal of Composite Materials, 49 (7), 853-871, 2015.
- [11]. D.F. Cao, L.S. Liu, Q.W. Li and S.X. Li, Compressive Properties of SiC Particle-Reinforced Aluminum Matrix Composites Under Repeated Impact Loading, Strength of Materials, 47 (1), 61-67, 2015.
- [12]. Z. H. Tan, B. J. Pang, B. Z. Gai, et al., "The dynamic mechanical response of SiC particulate reinforced 2024 aluminum matrix composites," Mater. Lett., 61 (23- 24), 4606-4609, 2007.
- [13]. L. H. Dai, L. F. Liu, and Y. L. Bai, "Effect of particle size on the formation of adiabatic shear band in particle reinforced metal matrix composites," Mater. Lett., 58 (11), 1773-1776, 2004.
- [14]. J. Lai and W. Sun, Dynamic damage and stress-strain relations of ultra-high performance cementitious composites subjected to repeated impact, Sci. China Technol. Sci., 53 (6), 1520-1525, 2010.
- [15]. ABAQUS/Explicit (Version 6.8). Finite Element Software, www.simulia.com (accessed 2008).

Economical and Environmental Investigation of Thermally Insulated and Non-Insulated Building in Osmaniye. Turkey

Coskun Ozalp¹, Bulent Yaniktepe¹, Canan Aladag¹, Mustafa Soyler¹

Abstract

In this paper, economical and environmental performance of thermally insulated and non-insulated for a sample building located in Osmaniye, Turkey is presented. Thermal performance of building is determined according to Turkish Standard 825 (TS 825) "Thermal Insulation Requirements for Buildings". The yearly energy needs of the building (Q) rating limited energy needs (Q') then it is investigated whether compliance with standards. The total heat transfer coefficients used in the building construction elements are evaluated as recommended in TS825 equations and contained with exception the principle and provision of the standard.

Keywords: *thermal insulation, building, degree-day concept*

1. INTRODUCTION

Energy demand in the world especially in developing countries has been increasing rapidly due to economic and population growth. Increasing energy demand has led to increasing energy consumption and causes economical and environmental impacts such as budget deficit global warming, air pollution etc.

Turkey is the one of the developing countries according to the statistical data of international statistical institute. Due to the limits of Turkey's domestic energy sources energy demand depends on energy imports. At present, around 75% of the total energy demand is being met by imports and causes an increase in the budget deficit. As a result of increasing in population of urban areas in Turkey, the numbers of commercial and residential buildings in cities have risen rapidly. The existing building stock which accounts for approximately 36% of the final energy consumption of total Turkey energy demand in 2008, has the big potential to provide significant opportunities for energy saving [1]. In terms of final energy consumption the building sector represents the second-largest energy consumer accounting for and the building sector's emissions are 32% of the total national energy-related CO₂ emissions. However the building sector in Turkey presents significant opportunities for cost-effective energy and CO₂ savings estimated at some 30-50% of the current levels [1]. Various national legal acts regulations and standards on energy efficiency in building have been compiled for heating energy conservation predominantly such as Standard of Thermal Insulation Requirements for Buildings (TS 825) [2]. Building Energy Performance (BEP) and the Regulation on Heat Insulation in Buildings for New Buildings. According to the results the calculation procedure described in TS 825 based on ISO 9164 and partly on EN 832 is highly accurate and precise for heating period [3].

Energy performance of building is performed for different countries with considering climate zones [4, 5, 6,7]. Economical and environmental impacts of energy consumption are given in [9, 10, 11].

Environmental impact of thermal insulation thickness is investigated by Comakli and Yuksel [8]. They determined decreasing of CO₂ emissions by optimum insulation thickness for the one of the coldest city of Turkey, Erzurum. They determined that CO₂ emissions amount decreased about 50% with using optimum insulation thickness. In this paper, economic and environmental performance of thermally insulated and non-insulated for a sample building located in Osmaniye, Turkey is presented.

2. RESULTS AND DISCUSSION

Turkey is classified into four climatic zones considering heating energy requirement by using degree-day concept in TS 825. Statistical data on each climatic zone are presented in Table 1. The city of Osmaniye, in south Turkey is in the first degree-day region according to TS 825 (Figure 1). The sample building with four floors investigated in this paper is located representing located in Osmaniye (37°49.73"N, 36°14'59.91"E, and 118m altitude). Osmaniye represents a Mediterranean climate (hot and humid summer and warm winter).

¹ Corresponding author: Osmaniye Korkut Ata University, Department of Energy Systems Engineering, 80000, Osmaniye, Turkey.
coskunozalp@osmaniye.edu.tr

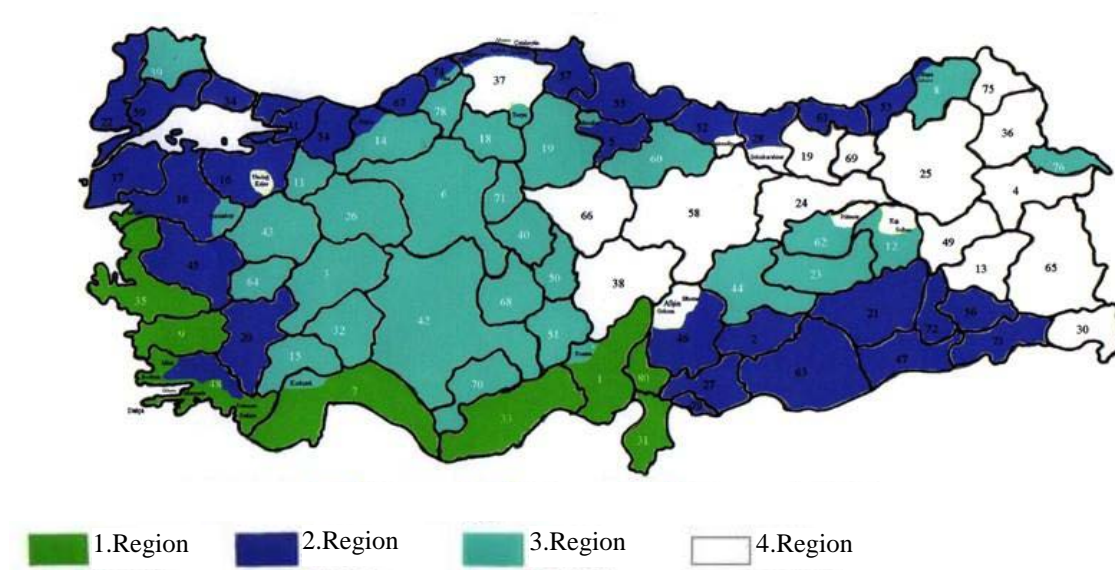


Figure 1. Provinces of Turkey according to degree day regions

Building specifications is given in below. Shape of building is rectangular form and ventilating type is selected as natural ventilating.

Ground Floor:

Area: 182 m²

Volume: 546 m³

Wall Surface Area: 189 m²

Reinforced Concrete Wall: 63 x 0.3 = 18.9 m²

Beams: 6.9 m² x 2.70 = 18.63 m²

Total reinforced concrete: 18.9 + 18.63 = 37.53 m²

Metal Door: 1x2.1 = 2.1 m²

Other doors: 3x0.8x2.1 = 5.04 m²

Total Door area: 5.04 + 2.1 = 7.14 m²

Windows;

North: 1.8 x 1.5 x 2 = 5.4 m²

East: (1.5 x 2.20) + (2 x 1.8 x 1.5) + (2 x 0.5 x 0.5) + (1.5 x 1.8) = 11.9 m²

West: 1.5 x 1.8 = 2.7 m²

South: 13.1 m²

Total Window area: 33.1 m²

Total Wall Area: 189 m² - (33.1+7.14 +37.53) m² = 111.23 m²

First Floor (Same as for 2.3 and 4. floors) :

Area: 198 m²

Volume: 594 m³

Wall surface area: 205.8 m²

Reinforced concrete wall: 68.6 x 0.3 = 20.58 m²

Walls: 5 m² x 2.70 = 13.5 m²

Total reinforced concrete wall: 20.58 + 13.5 = 34.08 m²

PVC door: (2.1 x 0.8) + (2.1 x 0.7) + (2x2.1x0.8) = 6.51 m²

Windows;

North: 7.92 m²

East: 14.06 m²

West: 3.96 m²

South: 16.8 m²

Total Windows area: 42.74 m²

Total Wall Area: 198 m² – (34.08+6.51 +42.74) m² = 122.47 m²

Total areas for building :

Floor area: 182 m² (Soil contacted floor)

Σ volume: 2922 m³

Σ reinforced concrete wall area: 173.85 m²

Σ brick wall area: 601.11 m²

Σ PVC door area: 31.08 m²

Σ metal door area: 2.1 m²

Σ Windows area: 204.06 m²

Total Windows area and direction for heat gain

ΣNorth: 37.08 m²

ΣEast: 68.14 m²

ΣWest: 18.54 m²

ΣSouth: 80.3 m²

Σ windows area: 204.06 m²

Table 1. Monthly average outdoor temperatures (°C) for each climatic zone [2]

	1. Zone	2. Zone	3. Zone	4. Zone
January	8.00	3.30	1.30	-5.20
February	9.30	4.50	2.00	-4.10
March	11.50	7.20	5.00	-1.30
April	15.70	12.60	9.80	5.10
May	20.60	17.80	14.10	10.10
June	25.40	21.90	18.10	13.50
July	28.00	24.40	21.10	17.20
August	27.20	23.80	20.60	17.20
September	23.30	19.60	16.50	13.20
October	18.10	14.10	11.30	6.90
November	13.30	9.10	6.50	1.30
December	9.40	4.90	2.60	-3.00

Building structure properties are given in Table 2 for calculating of total thermal permeability resistance. Surface transmission resistance are taken 0.13 and 0.04 m²K/W for internal and external conditions respectively.

Table 2. Building structure properties for thermally insulated wall

	Component Number	Materials	Thick.(m)	Thermal Cond. (W/m.K)
BRICK WALL	1)	Solo Made Using Gypsum Plaster	0.005	0.51
	2)	Slurry	0.020	1.6
	3)	Horizontal Perforated Brick	0.190	0.36
	4)	Slurry	0.025	1.6
	5)	Polystyrene Foam Particulate	0.05	0.04
REINFORCED CONCRETE WALL - BEAMS	1)	Solo Made Using Gypsum Plaster	0.005	0.51
	2)	Lime Mortar. Lime - Cement Mortar	0.02	1.0
	3)	Reinforced Concrete Wall + Columns	0.2	2.5
	4)	Polystyrene Foam Particulate	0.05	0.035
	5)	Slurry	0.025	1.6
TERRACE CEILING	1)	Solo Made Using Gypsum Plaster	0.005	0.51
	2)	Lime Mortar. Lime - Cement Mortar	0.02	1.0
	3)	Reinforced Concrete Wall + Columns	0.22	2.5
	4)	≤3 as Backlash; Width <300 mm	0.22	0.36
	5)	Reinforced Concrete Wall + Columns	0.08	2.5
	6)	Mastic Asphalt Coating	0.01	0.7
	7)	Extruded Polystyrene Foam	0.06	0.03
	8)	Slurry Screed	0.07	1.4
SOIL CONTACT BOTTOM	1)	Artificial Stones	0.01	1.3
	2)	Slurry Screed	0.07	1.4
	3)	Mastic Asphalt Coating	0.005	0.7
	4)	Extruded Polystyrene Foam	0.04	0.03
	5)	Reinforced Concrete Wall + Columns	0.10	2.5
	6)	Sand. Gravel. crushed stone	0.40	0.7
	7)	Rough Concrete	0.10	1.65
	1)	Slurry	0.025	1.6
	2)	Reinforced Concrete Wall + Beams	0.22	2.5
	3)	≤3 as Backlash; Width <300 mm	0.22	0.36

LEAVE BOTTOM	4)	Reinforced Concrete Wall + Beams	0.08	2.5
	5)	Polystyrene Foam Particulate	0.03	0.035
	6)	Slurry Screed	0.07	1.4
	7)	Derived From Coniferous Trees	0.01	0.13

The annual heating energy need for the sample building is calculated with the following equations[3].

$$Q_{year} = \sum Q_{month} \quad (1)$$

$$Q_{month} = [H \cdot (\theta_i - \theta_e) - \eta_{month}(\phi_{i,month} + \phi_{i,solar})] \cdot t \quad (2)$$

The specific heat loss of the building (H) is found with the addition of the heat loss realized via the transmission and convection (H_T) and heat loss realized via the ventilation (H_v)[3].

$$H = H_T + H_v \quad (3)$$

The heat loss realized via the transmission and convection is calculated with the equation below. In this equation

$$H_T = AU + l U_l \quad (3)$$

In this equation “l” shows the length of the heat bridge in unit of meter. In this study energy bridge is ignored for sample building. The heat loss realized via the natural ventilation is calculated with

$$H_v = 0.33 n_h \cdot V_h \quad (4)$$

In this equation n_h is shows air exchange rate and V_h shows ventilated volume and it is equal to $0.33 V_{gross}$. Monthly internal gains $\phi_{i,month}$ in equation (2) is less equal to $5x A_n$ (A_n is net usage area and is equal to $0.32x V_{gross}$). Monthly solar energy gain is calculated with equation (17) in TS825 standard. All the glasses in building are colorless insulation glass unit for solar energy gain. Insulation material is not used for the calculation of non-insulated condition. Annual heating energy needs per usage area in the sample building is 24.50 kWh/m^3 for the thermally non-insulated walls. Annual and monthly heating energy need are given in Table 3. Since heat gain is greater than heat loss heating energy need is not given for the months May to October. The highest heat loss required to be for the sample building is found as $Q^1 = 10.19 \text{ kWh/m}^2$. The annual heating energy need must be less than the required highest value. For this reason. This sample building without insulation is not appropriate to the TS825.

Table 3. Monthly and annual heat loss and heat gain. Non-insulated case

Months	Heat Loss		Heat Gain					
	H (W/K)	$T_i - T_e$ ($^{\circ}\text{C}$)	$H \cdot (T_i - T_e)$ (W/K) $^{\circ}\text{C}$	$\Phi_{i,month}$ (W)	$\Phi_{s,month}$ (W)	$\Phi_{T,month}$ (W)	γ_{month}	η_{month}
January	10.6		32857	3349	8024	0.24	0.98	64,782,991
February	10.0		30997	4146	8821	0.28	0.97	58,166,294
March	7.4		22938	4784	9459	0.41	0.91	37,143,624
April	3.2		9919	5385	10060	1.01	0.63	9,282,564
May	0	0	0	5918	10593	0	0	0
June	0	0	0	6162	10837	0	0	0
July	0	0	0	6023	10698	0	0	0
August	0	0	0	5737	10412	0	0	0
September	0	0	0	5030	9705	0	0	0
October	0.5		1550	4186	8861	5.72	0	0
November	6.0		18598	3217	7892	0.42	0.91	29,591,516
December	9.7		30067	2938	7613	0.25	0.98	58,595,999

$$Q_{year} = \sum Q_{month} = 257,563,577 \text{ kJ}$$

$$Q_{year} = 71603 \text{ kWh}$$

$$Q = \frac{Q_{year}}{V} = \frac{71603}{2922} = 24.50 \text{ kWh/m}^3$$

$$Q^1 = 14.1 \times \frac{1408}{2922} + 3.4 = 10.19$$

Particulate polystyrene 5 cm thick foam is used as insulation material for thermally insulated wall. Annual and monthly heating energy need is given in Table 4 for thermally insulated wall. Annual heating energy needs per usage area in the

sample building is 9.59 kWh/m^3 for the thermally insulated walls. Since the annual energy need is less than the highest heat loss required insulation thickness is appropriate to TS825 standard.

Table 4. Monthly and annual heat loss and heat gain. Non-insulated case

Months	Heat Loss			Heat Gain					
	H	$T_i - T_e$	$H \cdot (T_i - T_e)$	$\Phi_{i, \text{month}}$	$\Phi_{g, \text{month}}$	$\Phi_{T, \text{month}}$	γ_{month}	η_{month}	$Q_{i, \text{mon}}(\text{kJ})$
	(W/K)	($^{\circ}\text{C}$)	(W/K) $^{\circ}\text{C}$	(W)	(W)	(W)			
January		10.6	18368		4729	9404	0.51	0.86	26,646,792
February		10.0	17328		5854	10529	0.61	0.81	22,808,563
March		7.4	12823		6754	11429	0.89	0.67	13,388,566
April		3.2	5545		7603	12278	2.21	0.36	2,915,627
May		0	0		8355	13030	0	0	0
June		0	0		8699	13374	0	0	0
July		0	0		8503	13178	0	0	0
August		0	0		8099	12774	0	0	0
September		0	0		7101	11776	0	0	0
October		0.5	866		5910	10585	12.22	0	0
November		6.0	10397		4542	9217	0.89	0.67	10,942,076
December		9.7	16808		4147	8822	0.52	0.85	24,130,356
	1732.8			4675					

$$Q_{\text{year}} = \sum Q_{\text{month}} = 100,832,568 \text{ kJ}$$

$$Q_{\text{year}} = 28031 \text{ kWh}$$

$$Q = \frac{Q_{\text{year}}}{V} = \frac{28031}{2922} = 9.59 \text{ kWh/m}^3$$

$$Q^1 = 14.1 \times \frac{1408}{2922} + 3.4 = 10.19$$

Figure 2 shows the insulated and non-insulated case with monthly energy needs. While monthly energy need is 9,282,564 kJ for non-insulated case, 2,915,627 kJ for insulated case in April. Percentage of decreasing of energy need is 68.5%. Annual energy need is 24.50 kWh/m^3 for non-insulated wall and 9.59 kWh/m^3 for insulated wall.

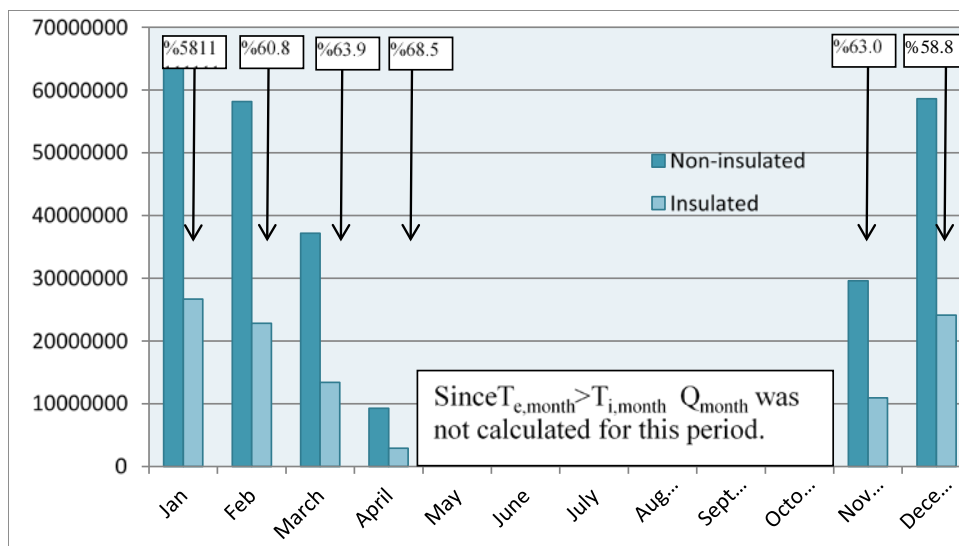


Figure 2. Comparison of insulated and non-insulated wall with respect to monthly energy need.

Calculation of Payback period:

Screw price, stucco price, dubels price are not included in the calculation of payback period

Table 5. Specifications of insulation material

Material	k (W / mK)	Cy (\$ / m3)
XPS	0,032	60
EPS	0,033	80

Cy : Unit price of insulation material

Cost of Insulation;

$$1) \text{ Brick wall (EPS) : } C_{\text{ins}} = C_{y,x} = 60 \text{ \$ / m}^3 \times 0.04 \text{ m} = 2.4 \text{ \$ / m}^2$$

$$2.4 \text{ \$ / m}^2 \times 601,11 \text{ m}^2 = 1442,64 \text{ \$}$$

$$2) \text{ Reinforced concrete (EPS) : } C_{\text{ins}} = C_{y,x} = 80 \text{ \$ / m}^3 \times 0.04 \text{ m} = 3.2 \text{ \$ / m}^2$$

$$3.2 \text{ \$ / m}^2 \times 173.85 \text{ m}^2 = 556.32 \text{ \$}$$

$$3) \text{ Roof (XPS) : } C_{\text{ins}} = C_{y,x} = 60 \text{ \$ / m}^3 \times 0.05 \text{ m} = 3.0 \text{ \$ / m}^2$$

$$3.0 \text{ TL / m}^2 \times 198 \text{ m}^2 = 594.0 \text{ \$}$$

$$4) \text{ Basement (XPS) } = C_{\text{ins}} = C_{y,x} = 60 \text{ \$ / m}^3 \times 0,05 \text{ m} = 3,0 \text{ \$ / m}^2$$

$$3.0 \text{ TL / m}^2 \times 182 \text{ m}^2 = 546 \text{ \$}$$

$$5) \text{ Leave bottom (EPS) } = C_{\text{ins}} = C_{y,x} = 80 \text{ \$ / m}^3 \times 0.04 \text{ m} = 3.2 \text{ \$ / m}^2$$

$$3.2 \text{ \$ / m}^2 \times 15.80 \text{ m}^2 = 50.56 \text{ \$}$$

$$\sum C_{\text{ins}} = 3189.544 \text{ \$ TL}$$

Annual energy need for non-insulated case = 71603 kWh

Annual energy need for insulated case = 28031 kWh

Difference between non-insulated and insulated case = 43572 kWh

Natural Gas saving = 4095.111 m³

Total price of natural gas per year = 1228.5 \$

Payback period = 2.5 years

The amount of CO₂ = 43572 x 0.234 = 10195 kg per year

3. CONCLUSION

In this study the economic and environmental comparison of thermally insulated and non-insulated buildings is investigated in Osmaniye. Thermal performance of building is determined according to Turkish Standard 825 (TS 825) “Thermal Insulation Requirements for Buildings” Annual energy need is 24.50 kWh/m³ for non-insulated building and 9.59 kWh/m³ for insulated building. The payback period is 2.5 years for the insulation cost. Reduction of CO₂ is estimated 10195 kg per year after the insulation of sample building.

REFERENCES

- [1]. Turkish National Committee Energy Report 2011
- [2]. *Thermal Insulation Requirements for Buildings*, TS825
- [3]. S. Dilmac, and N. Kesen “A comparison of new Turkish insulation standard (TS825), ISO 9164, EN 832 and German regulation .” *Energy and Buildings* 35 161-174, 2003
- [4]. Yang, Joseph C. Lam, C.L. Tsang “ Energy performance of building envelopes in different climate zones in China” *Applied Energy* 85 (2008) 800–817
- [5]. M. N. Inanici, F. N. Demirbilek Thermal performance optimization of building aspect ratio and south window size in five cities having different climatic characteristics of Turkey *Building and Environment* 35 (2000) 41-52
- [6]. Z. Yılmaz., Evaluation of energy efficient design strategies for different climatic zones: Comparison of thermal performance of buildings in temperate-humid and hot-dry climate *Energy and Buildings* 39 (2007) 306–316
- [7]. N. Eskin , H. Turkmen Analysis of annual heating and cooling energy requirements for office buildings in different climates in Turkey *Energy and Buildings* 40 (2008) 763–773
- [8]. K. Comaklı, B. Yuksel Environmental impact of thermal insulation thickness in buildings *Applied Thermal Engineering* 24 (2004) 933–940
- [9]. N. Yamtraipat, J. Khedari., J. Hirunlabh, J. Kunchornrat Assessment of Thailand indoor set-point impact on energy consumption and environment *Energy Policy* 34 (2006) 765–770
- [10]. Grace K.C. Ding, Sustainable construction—The role of environmental assessment tools *Journal of Environmental Management* 86 (2008) 451–464
- [11]. T. Esin, A study regarding the environmental impact analysis of the building materials production process (in Turkey), *Building and Environment* 42 (2007) 3860–3871

Wireless Sensor Network Design for Seedling Production

Mehmet Erkan Yuksel¹, Ruya Samli²

Abstract

Seedling production in some countries has remained outside the interests of Information Technology (IT) industry for many years. Production environment is evaluated and run in a traditional and uniform manner. Producers can not use information regarding the soil management, irrigation methods, physical and geographical variables of agricultural land, plant production techniques, the agribusiness effectively, efficiently and towards production. Integrating emerging technologies into the cultivation of seedlings by taking into consideration the economic and environmental policies is an important requirement. Therefore, next generation technologies such as computing, sensing, monitoring/surveillance and evaluation, decision support systems can be used in seedling production activities for the purpose of increasing efficiency, preventing waste of resources, minimizing the environmental pollution resulting from production, reducing the input usage (i.e., chemicals such as fertilizers and pesticides) and increasing the gross yield of product (to provide high-quality and high-quantity products). From this point of view, in this study, we propose an overview of useful, energy-centric wireless sensor network (WSN) design that enable application developers to study soil dynamics based on data gathered at regular intervals, to improve irrigation efficiency by using collected information as feedback, to scale up as needed without re-planning as compared to traditional wired sensor networks, and to significantly extend the production system and network lifetime. We hope that our design will lead to develop data evaluation techniques, to discuss the optimum characteristics of decision support systems, and to perform more efficient irrigation practices using an energy efficient WSN for seedling production.

Keywords: *Wireless sensor networks, sensor node, intelligent irrigation, seedling production*

1. INTRODUCTION

Plant growth is often limited by water deficiency. Even under mild water deficit, shoots may stop growing completely while roots continue to grow [1]. In this sense, the regular supply of water is essential to plant growth as plants are made out of more than 90% water. When grown in containers, plants have only a limited volume of substrate and do not have the ability of mature trees to search for water from below the soil surface. On the other hand, too much water can damage the plants because of water logging which makes the roots not breathe. The water requirement of seedlings depends on the seedling age, the amount of sunlight and the soil type [2].

Water scarcity is a challenge for agriculture and plantation forestry in many parts of the tropical and temperate regions in the world. Thus, water saving technologies that enhance plant growth in various soils are required [3]. In this context, the decision support systems transmitting data regarding soil (soil nutrients, minerals, soil moisture, gaseous substances in the soil), growing site (temperature, rainfall, humidity, light intensity and so on) and seedling simultaneously to producers by means of wireless communication technology are needed in order to use land efficiently and to enhance the quality seedling production. In this way, as producers know how much water seedlings need, they would use water wisely. In addition, an irrigation system using wireless communication technology will increase seedling quality which is certainly more important than its quantity, as poor quality seedlings will never reach the growth potential of high quality ones in the field. Thus, in practice it is preferable to plant fewer high quality seedlings rather than many poor quality ones. In recent years, considerable studies on the seedling production have been conducted due to the increased environmental awareness and at the same time the increased emphasis on the spatial planning and design [4].

Inputs (chemicals, fertilizer, mineral, etc.) needed by seedlings in a nursery are usually applied in the same amount. This approach may result in land not to receive inputs in a balanced way. On the contrary, a wireless communication technology determining, analyzing and managing factors varying temporally and spatially on the land in terms of the optimum gain, sustainability and environmental protection is an important application for seedling production. This application has benefited from several technologies such as global positioning system (GPS), geographic information systems (GIS), remote sensing, automatic control, advanced data processing techniques, and telecommunications. In instance, when the seedling producers determine the variability of their land using information and communication technologies, they may apply inputs more effectively and efficiently [5-7].

¹ Corresponding author: Mehmet Akif Ersoy University, Department of Computer Engineering, 15030, Burdur, Turkey. erkanyuksel@mehmetakif.edu.tr

² Ruya Samli, Istanbul University, Department of Computer Engineering, Istanbul, Turkey, ruyasamli@istanbul.edu.tr

Continuous developments in information and communication technologies, integrated circuits, hardware, digital electronics and micro-electro-mechanical systems (MEMS) allowed the design, production and development of multifunctional, small-size wireless sensor circuits with low cost and energy saving. Thanks to their ever increasing capabilities such as being in continuous interaction with the environment, sensing physical phenomenon (temperature, humidity, pressure, light, sound, visuals, acceleration etc.), ability to carry out functions such as data gathering, processing and storage, transferring real-time data to the related central systems, intercommunication and collaborative working, they enabled the WSNs to be created [8-10].

In recent years, WSNs have been an important technology used in seedling production. They contribute to the development of decision support systems that enable seedling producers to treat appropriately to the characteristics of nursery and seedlings. In this study, an energy-centric WSN providing the desired water in every area and at every moment is designed. Sensor nodes in the WSN transmit real-time information to data collection centers in different points of irrigation systems. WSN that are low-cost, energy efficient and long-life, provide seedling producers to obtain great benefits and significant gains. Data collection relating to availability of soil water, soil productivity, biomass yield, soil compaction, crop yield, plant water status, local climate data, insect-disease- weed invasion will be easier by means of the designed WSN. Hence, the sensed data regarding soil, plants and the environment is processed and sent to decision support system for helping about which treatments/methods seedling producers have to apply.

2. RELATED STUDIES

In several studies conducted in a laboratory [11], in a commercial greenhouse [12] and in outdoor condition [13], traditional wireless network was used to transfer sensor data to a computer. In these studies, real-time sensor data taken from the wireless networks were used for irrigation management decisions. Cayanan et al. [11] used a non-commercial wireless transmitter ("Poseidon" wireless module) in conjunction with a custom MATLAB PC interface. The MATLAB program sent data requests to the wireless modules every 20 minutes. The system controlled water delivery via drip irrigation lines based on volumetric water content of the coconut coir substrate using capacitive sensors (ECH₂O-TE, Decagon Devices). Lea-Cox et al. [12] utilized a noncommercial wireless system developed by Carnegie Mellon Robotics Institute (Pittsburgh, PA, USA) with ECH₂O series sensors at a commercial cut-flower greenhouse operation. The battery and solar powered wireless nodes activated the sensors once every minute and recorded the average every 5 minutes.

Rong-Hua Ma et al. [14] designed a wireless remote weather monitoring system based on Micro-Electro-Mechanical Systems (MEMS) and WSN technologies comprising sensors for the measurement of temperature, humidity, pressure, wind speed and direction, integrated on a single chip. Ayala et al. [15] developed a long-range wireless mesh network system for weather monitoring in unfriendly geographic conditions. It consists of three main parts: Remote Terminal Units (RTUs), Base Terminal Units (BTUs) and a Central Server (CS). The RTUs share a wireless network from a single point-to-point communication. A BTU controls the traffic within the network and has a Ku band satellite link. Data is stored in a CS and sent to the end user in a web portal.

Ayday and Şafak [16] developed a moisture distribution map obtained through the integration of a WSN with a GIS (Geographic Information System). The wireless nodes with moisture sensors were located at predetermined locations; geographic coordinates of these points were obtained with GPS and then, all the information was evaluated using the GIS. Pierce and Elliot [17] monitored an agricultural weather and an on-farm frost using WSNs established at regional and on-farm remotely and in real-time. Thus they aimed to improve efficiency and efficacy of targeted management practices.

Perkins et al. [18] introduced a low cost, low power, self-organizing sensor network developed by Motorola Labs. The system can be used to sense agricultural, environmental and process parameters. Gomide et al. [19] designed a mobile field data acquisition system that was developed to collect data for crop management and spatial-variability studies. This system has collected related data during sowing, planting and yielding, improving the performance of crop production and monitoring physical and biological characteristics of soil-water-plant-atmosphere by examining the rationality of input usage. Mahan and Wanjura [20] developed a wireless, infrared thermometer system for in-field data collection. The system consisted of infrared sensors, programmable logic controllers and low power radio transceivers to collect data in the field and transmit it to a remote receiver outside the field. Shinghal et al. [21] improved irrigation performance for potato crop production. They calculated and interpreted agricultural parameters like depth of water, soil water tension and system capacity etc. for irrigation management system to maintain optimum soil water tension for better crop yield and increase the application efficiency of irrigation system. O'Shaughnessy and Evett [22] provided auto-irrigation scheduling by determining crop canopy temperatures using infrared thermometer thermocouples located on a center pivot lateral.

Damas et al. [23] developed and tested a distributed, remotely controlled, automatic irrigation system. In this system, each sub-region was monitored and controlled by a control sector. Communication was done through a WLAN network. They found 30–60% saving in water usage. Evans and Bergman [24] used wireless sensors in linear-move and center-pivot irrigation systems to assist irrigation scheduling using combined on-site weather data, remotely sensed data and grower preferences. Cugati et al. [25] developed an automated fertilizer applicator for tree crops. The system consisted of an input module for GPS and real-time sensor data acquisition, a decision module for calculating the optimal quantity and spread pattern for a fertilizer, and an output module to regulate the fertilizer application rate. A Bluetooth network was used data communications among the modules.

Considering the mentioned studies above, this study aims to design an energy efficient WSN that is capable of ideal sensing, reliable data gathering, processing and analyzing tasks. It operates in an organized manner, provides energy from

the sun which is a renewable energy source, performs synchronization depending on weather conditions, has long operating life for deploying in a specific nursery with sprinkler or drip irrigation by considering the limitations of WSNs' structural characteristics and the difficulties in the application areas.

3. WIRELESS SENSOR NETWORK DESIGN

In our study, we designed an energy efficient WSN for seedling production. Figure 1 illustrates the WSN. It consists of low-cost, low-power, small-size wireless sensor nodes and multifunctional coordinators as shown in Figure 2 and Figure 3, respectively.

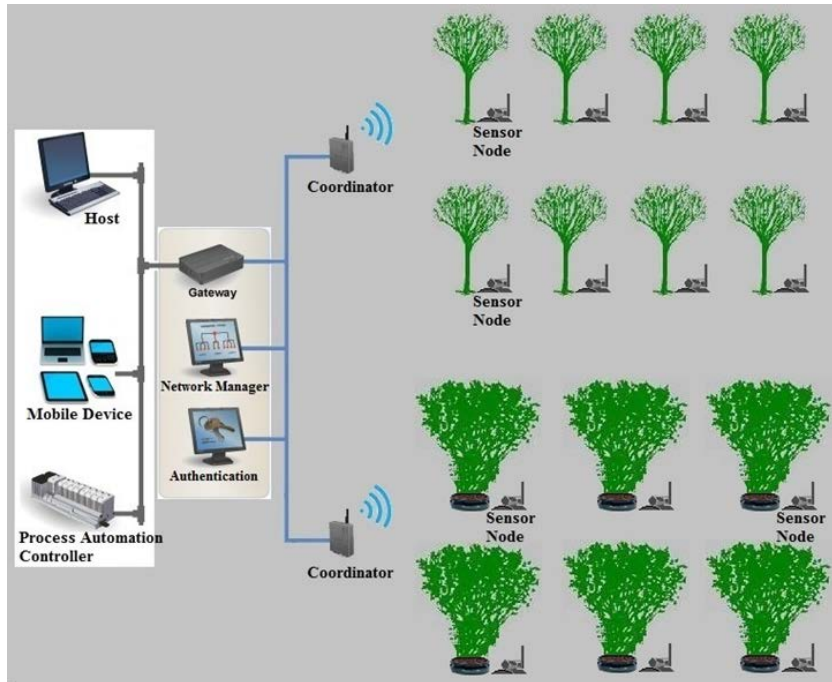


Figure 2. Our design of WSN for seedling production

All devices used in our WSN have small size solar panels. They are compatible with Wi-Fi, Bluetooth, IEEE 802.15.4 standards and can adapt to different network topologies such as mesh, star and point-to-multi-point. Wireless sensor nodes can make short-range or long-range data transmission and send data to the coordinator via single-hop or multi-hop communications. They make synchronization with coordinators according to their battery levels and weather conditions. They have the ability of monitoring environmental events such as weather conditions (temperature, humidity, pressure, light intensity, solar radiation) and soil status (soil moisture and temperature). Wireless sensor nodes perform simple data processing, work collaboratively together in a distributed manner so as to accomplish a common task, and help to control the amount of water flow.

As shown in Figure 2, our wireless sensor nodes have a power generator unit with our own original design consisting of a solar panel, rechargeable battery and battery fuel gauge, compared to other sensor nodes' power sources (i.e Mica, Mica2, MicaZ, IRIS, EYES, Telos/Tmote SKY, etc.). Thanks to the software running on its hardware, each of nodes uses dynamic power management technique depending on its own local operations (sensing, computing, data processing, communication). The software also monitors the battery charge status of the node and performs the synchronization process with coordinator.



Figure 2. Our wireless sensor node prototype for seedling production

In our study, we used two different energy sources in the power unit of our wireless sensor nodes and coordinators. One of these energy sources is a rechargeable Lithium Iron Phosphate (LiFePO₄) battery which is unaffected by the

environmental factors. When compared to other batteries used in existing wireless sensor nodes, LiFePO₄ batteries have many superior characteristics such as self-balance, simplified battery management system and battery charger, longer cycle life, high temperature performance. They have fast "forced" charging, large overcharge tolerance, higher energy density. They have been proven as the safest, durable and the most environmental friendly batteries.

During literature researches, we found out that there are not any solar panels on wireless sensor nodes and coordinator devices used in WSN applications designed for seedling production. Rarely, we observed that there are large-size of the solar panels integrated onto the several fixed gateways. From this point of view, in our study; we used small-size solar panel (for harvesting energy from sunlight) as a secondary energy source for wireless sensor nodes and coordinators (Figure 3) that are greatly different from the existing devices mentioned in the literature in terms of hardware features.

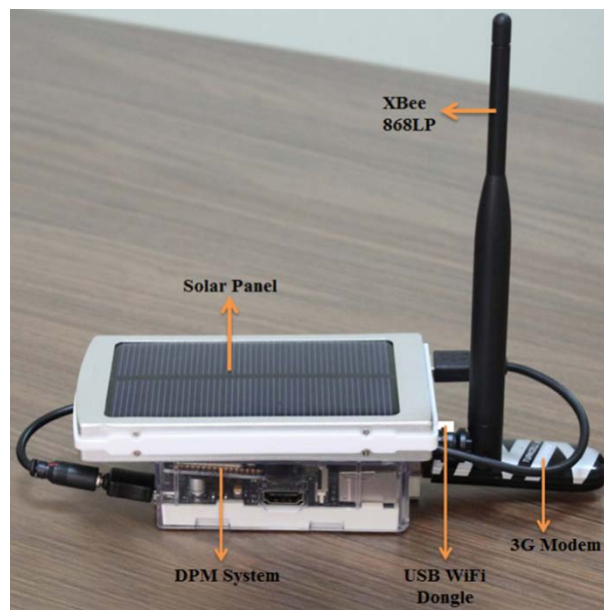


Figure 3. Our coordinator prototype in the WSN

We used "Raspberry Pi" single-board computer as a coordinator device in the WSN designed for seedling production. Coordinator is a small (credit-card sized), low-cost (€30), multifunctional, and has the feature of high-level sensor platform. It has a power generator unit with our own design consisting of a solar panel and rechargeable battery, and uses dynamic power management technique to perform tasks energy efficient. It runs Arch Linux operating system, MariaDB relational database management system and Apache Web Server. It has the ability of transferring data collected from sensor nodes to a server on the Internet, mobile devices or end users over the WLAN or cellular modems. It is possible to analyze data stored in the coordinator through a web interface on the server from anywhere, at any time.

As shown in Figure 3, our coordinator contains Bluetooth, Ethernet, XBee 868LP, Wi-Fi, 3G communication modules and various connection interfaces depending on the WSN topology and operations carried out in the seedling area (i.e., controlling water flow). Data transmission between sensor nodes and coordinator is done by the XBee 868LP radio. Coordinator connects to the WLAN through USB Wi-Fi adapter. A 3G modem is used to access to the coordinator over the Internet. Seedling data sent from wireless sensor nodes are stored in MariaDB database management system running on the coordinator. The coordinator sends data to other coordinators via multi-hop communication or directly to the server on the Internet (main data collection center). The Apache HTTP Server installed on the coordinator allows users to access stored information from anywhere, at any time, on any device connected to the Internet (i.e. mobile phone, PDA, laptop etc.). In brief, coordinator devices work as a gateway, router, controller, HTTP server and local data gathering center in the designed WSN.

In the current study, deployed wireless sensor nodes and coordinators in the monitored region are grouped depending on the irrigation area. They are established in accordance with the international standards and upbringing conditions of the young seedlings. The distance between coordinators and nodes, and the distance between each group of sensor nodes are all changeable. Preliminary results are not now available. After implementing the system, we will examine the reliability, efficiency, security and usability of our WSN and to what extent this system embodied each of them. There is a need to know and analysis the long-term behavior of our WSN system. Most of the applications reported in this paper have short experimental periods. However, unlike these studies, we will improve some critical issues such as extending lifetime of the WSN, reliability of measurements, performance of collaborative working in real environments, data gathering and analysis, longer testing and experimentations.

4. CONCLUSION

The applications of WSNs are many and varied. The collaboration of sensing, processing, communication and actuation is an important synergy to exploit the potential of the WSNs. The development of similar applications has attracted considerable research efforts in the last years, because WSNs are very suitable for distributed data collecting and monitoring in tough environments. In this study, we presented an energy-centric WSN design as a most relevant and alternative application in agriculture and nursery industry. Our study aims the integration of WSNs into seedling production to provide new features that have the potential to be an economically and technically viable replacement to wired networks, to improve operations by providing early warning of equipment failures and a predictive maintenance tools, to develop data evaluation techniques, to improve energy management of WSN. We hope that the value of this integration will be best realized when combined with agronomic knowledge using the detailed information produced by decision support systems.

REFERENCES

- [1]. C. M. van der Wee, W.G. Spollen, R. E. Sharp, and T.I. Baskin, "Growth of arabidopsis thaliana seedlings under water deficit studied by control of water potential in nutrient-agar media", *Journal of Experimental Botany*, vol. 51, pp. 1555-1562, Sept. 2000.
- [2]. A. Mbora, J.-P. B. Lilleso, and R. Jamnadass, *Good Nursery Practices: A Simple Guide*, World Agroforestry Centre, Nairobi, Kenya, 2008.
- [3]. J. Six, C. Feller, K. Denef, S. M. Ogle, J. C. D. Sa, and A. Albrecht, "Soil organic matter, biota and aggregation in temperate and tropical soils-effects of no-tillage", in *Proc. 11th International Nitrogen Workshop, 9-12 Sept. 2001*, Reims, France, pp. 755-775.
- [4]. I. F. Akyildiz, W. Su, Y. Sankarasubramaniam, and E. Cayirci, "Wireless sensor networks: a survey", *Computer Networks*, vol. 38, pp. 393-422, 2002.
- [5]. F. L. Lewis, *Wireless Sensor Networks, Smart Environments: Technologies, Protocols, and Applications*, D. J. Cook (Ed.), S. K. Das (Ed.), NJ, USA: John Wiley & Sons, 2005.
- [6]. V. Raghunathan, C. Schurgers, S. Park, and M. B. Srivastava, "Energy efficient design of wireless sensor nodes", *Wireless Sensor Networks*, C. S. Raghavendra (Ed.), K. M. Sivalingam (Ed.), T. Znati (Ed.), Chapter 3, NY, USA: Springer, 2004.
- [7]. D. Rakhmatov and S. Vrudhula, "Energy management for battery-powered embedded systems", *ACM Transactions on Embedded Computing Systems*, vol. 2, pp. 277-324, 2003.
- [8]. N. Patwari, J. N. Ash, S. Kyperountas, A. O. Hero, R. L. Moses, and N. S. Correal, "Locating the nodes: cooperative localization in wireless sensor networks", *IEEE Signal Processing Magazine*, vol. 22, pp. 54-69, 2005.
- [9]. K. Langendoen and N. Reijers, "Distributed localization in wireless sensor networks: a quantitative comparison", *Computer Networks*, vol. 43, pp. 499-518, 2003.
- [10]. G. Mao, B. Fidan, and B. D. O. Anderson, "Wireless sensor network localization techniques", *Computer Networks*, vol. 51, pp. 2529-2553, 2007.
- [11]. D. Cayanam, M. D. Feliciano, and Y. Zheng, "Development of an automated irrigation system using wireless technology and root zone environment sensors", *Acta Horticulturae*, vol. 797, pp. 167-171, 2008.
- [12]. J.D. Lea-Cox, F. R. Arguedas-Rodriguez, A. G. Ristvey, D. S. Ross, and G. Kantor, "Wireless sensor networks to precisely monitor substrate moisture and electrical conductivity dynamics in a cut-flower greenhouse operation", *Acta Horticulturae*, vol. 893, pp. 1057-1063, 2010.
- [13]. R. Cardell-Oliver, K. Smettem, M. Kranz, and K. Mayer, "A reactive soil moisture sensor network: Design and field evaluation", *International Journal of Distributed Sensor Networks*, vol. 12, pp. 149-162, 2005.
- [14]. R. Ma, Y. Wang, and C. Lee, "Wireless remote weather monitoring system based on MEMS technologies", *Sensors*, vol. 11, pp. 2715-2727, 2011.
- [15]. M. Toledano-Ayala, G. Herrera-Ruiz, G. M. Soto-Zarazua, E. A. Rivas-Araiza, R. D. Bazan Trujillo, and R. E. Porras-Trejo, "Long-range wireless mesh network for weather monitoring in unfriendly geographic conditions", *Sensors*, vol. 11, pp. 7141-7161, 2011.
- [16]. C. Ayday, and S. Safak, "Application of wireless sensor networks with GIS on the soil moisture distribution mapping", in *Proceedings of 16th International Symposium GIS Ostrava 2009. Seamless Geoinformation Technologies*, 25-28 January 2009, Ostrava, Czech Republic, pp.123-132.
- [17]. F. J. Pierce and T.V. Elliott, "Regional and on-farm wireless sensor networks for agricultural systems in Eastern Washington", *Computers and Electronics in Agriculture*, vol. 61, pp. 32-43, 2008.
- [18]. M. Perkins, N. Correal, and B. O'Dea, "Emergent wireless sensor network limitations: a plea for advancement in core technologies", in *Proceedings of the 1st IEEE International Conference on Sensors*, Orlando, Florida, USA, pp. 1505-1509, 2002.
- [19]. R. L. Gomide, R. Y. Inamasu, D. M. Queiroz, E. C. Mantovani, and W. F. Santos, "An automatic data acquisition and control mobile laboratory network for crop production systems data management and spatial variability studies in the Brazilian center-west region", *ASAE Paper No.*: 01-1046. The American Society of Agriculture Engineers, St. Joseph, Michigan, USA, 2001.
- [20]. J. Mahan, and D. Wanjura, "Upchurch, design and construction of a wireless infrared thermometry system", *The USDA Annual Report*. Project Number: 6208-21000-012-03, 2004.
- [21]. K. Shinghal, A. Noor, N. Srivastava, and R. Singh, "Wireless sensor networks in agriculture: For potato farming", *International Journal of Engineering Science and Technology*, vol. 2, pp. 3955-3963, 2010.
- [22]. S. A. O'Shaughnessy, and S. R. Evett, "Canopy temperature based system effectively schedules and controls center pivot irrigation of cotton", *Agricultural Water Management*, vol. 97, pp. 1310-1316, 2010.
- [23]. M. Damas, A. M. Prados, F. Gomez, and G. Olivares, "HydroBus® system: fieldbus for integrated management of extensive areas of irrigated land", *Microprocessors and Microsystems*, vol. 25, pp. 177-184, 2001.
- [24]. R. Evans, and J. Bergman, "Relationships between cropping sequences and irrigation frequency under self-propelled irrigation systems in the Northern Great Plains", *USDA Annual Report*. Project Number: 5436-13210-003-02, 2003.
- [25]. S. Cugati, W. Miller, and J. Schueller, "Automation concepts for the variable rate fertilizer applicator for tree farming", in *The Proceedings of the 4th European Conference in Precision Agriculture*, 14-19 June 2003, Berlin, Germany, 2003.

Landslide Monitoring with GNSS-PPP on Steep-Slope and Forestry Area: Taşkent Landslide

Ismail Sanliogu¹, Mustafa Zeybek², Cemal Ozer Yigit³

Abstract

Landslide area occurs on steep-slope and forestry. Generally, investigations are pursuing on the difficult topographical area for monitoring a landslide. GNSS measurements and analysis are providing very accurate, large content, scope and reliable information to monitoring movements on ground surface. Most techniques are not possible produce safe results for stability of the slope in forestry area. GNSS measurement techniques are the most reliable technique to monitoring slopes. This paper is aimed to present landslide monitoring with Global Navigation Satellite System (GNSS) measurements and to compare performance of Precise Point Positioning (PPP) method and rapid-static GNSS solution. Study area is located on the Middle of Taurus mountain chains. Three epoch GNSS campaigns for monitoring were performed on the study site from 2011 to 2012. For the purpose of detecting surface movement, ground monitoring points conducted on reachable areas and clean sky view in complex and dense forestry topography. In this study, GNSS data were processed by post-processed PPP method and rapid static GNSS solution for the purpose of comparison. Abrupt heavy rainfalls in area resulted 4m displacement top-scarp of landslide area. The landslide toe moved forward averagely 1-2 m between campaigns. Processing results show that differences between PPP-derived and rapid-static-derived displacement are within dm level. As a conclusion, in case of limited GNSS receiver, post-processed static PPP method can be used as an efficient alternative to the rapid-static GNSS method to detect displacement caused by landslide.

Keywords: *Landslide Monitoring, GNSS, Slope Stability, 3D Deformation.*

1. INTRODUCTION

A landslide is the movement of rock, debris or earth down a slope. They result from the failure of the materials which make up the hill slope and are driven by the force of gravity. Landslides are known also as landslips, slumps or slope failure. Landslides are an important subject for research in this respect to the amount of landslides among many natural disasters, causing loss of life and property in many countries. Research in Turkey has shown that landslides are only second to earthquakes in terms of their quantifiable losses [1].

The corporations and scientists have studied to reduce damage and prevent disasters. Many techniques have been used to monitoring landslides and to reduce (or prevent) the effects of such natural disasters. Monitoring techniques based on such systems as the Global Navigational Satellite Systems (GNSS), interferometric synthetic aperture radar (InSAR) and terrestrial laser scanning (TLS) can be used for geomatics investigations of land movements and landslides ([2], [3], [4]). The use of these methods in monitoring landslides has become commonplace following the development of GPS systems in the 2000s, which enabled a level of precision that could generate coordinate data with sensitivity of a few centimeters ([5],[6], [7], [8]). The scientists have been studied static and rapid-static GNSS surveying methods in these papers. At the last decade the scientists have been increasingly used web based precise point positioning (PPP) method in the landslide or deformation monitoring. ([9], [10], [11], [12], [13], [14]). When conventional surveying techniques as electronic distance meters (EDM), azimuth and angle surveying, levelling, and satellite based techniques were compared, GNSS have cut out many difficulties. The using of GNSS systems have furnished additional contributions with ease at the landslide surveying. Also, user does not need extra GNSS processing software when using PPP method.

In this paper we have compared differences between PPP-derived and rapid-static-derived displacement by using GNSS surveying. The aim of this investigation is to find out how PPP method affects deformation analysis or landslide monitoring.

2. USED GNSS SURVEYING METHODS

Static method sometimes called static surveying, is used surveying projects that require high accuracy. In this method, each receiver at each station logs data continuously for a pre-planned length of time. The duration of data collection, however, should be long enough for the post processing software to resolve the integer ambiguity. Most new generation receivers and processing software are capable of resolving the integer ambiguity with small amount of data. However, a higher accuracy for the baseline components can be achieved by collecting data for a longer period of time more than an hour.

¹ Corresponding author: Selçuk University, Engineering Faculty, Geomatics Engineering Department, Konya, Turkey, sanlioglu@selcuk.edu.tr

² Selçuk University, Engineering Faculty, Geomatics Engineering Department, Konya, Turkey, mzeybek@selcuk.edu.tr

³ Department of Geodetic and Photogrammetric Engineering, Gebze Technical University, Gebze 41400, Turkey, cyigit@gtu.edu.tr

Rapid static was a method developed for dual frequency receivers. A new algorithm was developed to reduce the amount of data needed to resolve integer ambiguity. Recently, because of modifications in processing algorithms and because a larger number of satellites are available, the amount of data needed can be reduced even with single frequency receivers. Field requirements and procedure for fast static are same as those for static except for the short session lengths. However, rapid static is only suitable for low order control surveys [15]. In this study, landslide displacements have come around averagely 1-2 m between campaigns. So rapid static surveying has been preferred.

GNSS-PPP is a most popular and powerful positioning technique based on processing observation from a single GNSS receiver. The method has become very preferable in terms of positioning performance, ease of use and low cost since there is no need to simultaneously observation from any reference station. When compared to Differential GNSS method, PPP method has an advantages and disadvantages. Rizos et al. ([16]) explained the detailed comparison between PPP and differential GNSS. PPP ([17]) method requires precise satellite orbit and precise satellite clock corrections and also need to be accounted, among others, satellite and antenna phase wind up, geophysical models, such as ocean loading- solid earth and polar tides-plate tectonics. The achievable PPP precision is very much a function of the implementation and accuracy of the models used in the PPP software ([18]). Detailed information about software packages and web based GNSS software's are given by Huber et al. ([19]). More details on the PPP algorithms, models and specifications can be found in ([20]).

In this study, CSRS-PPP software is used to process all observation files due to its free online service. CSRS-PPP software developed by the Geodetic Survey Division of the Natural Resources Canada (NRCan) is a web-based application used for single GNSS receiver positioning [21].

3. STUDY AREA

Study area is located on the Middle of Taurus mountain chains. The landslide, which occurred on slopes with elevations ranging between 1,400 m and 1,600 m and approximately 40% slope of landslide hill in the Sazak Valley, flowed in a northerly direction. It occurred in an area covering approximately 50 ha, its 40-ha section is forestry and farmland. The study area is approximately 10 ha in size. According to GNSS data from previous years, the annual movement was as high as 2 m. The landslide region is in the Taşkent district, which is approximately 130 km from Konya and situated at the southernmost tip of the district. A site location map of the study area is shown in Fig. 1.

Findings obtained during fieldwork indicate that there are frequent mass movements such as landslides and rock falls in the area. The traces left by these natural disasters on the topography are visible to the naked eye, and these natural phenomena continue to alter the topography. Landslides in the area cause serious economic damage to telephone lines, roads and the sheeting and retaining walls that protect roads and agricultural activities. Moreover, rock falls resulting from the geological structure of the Taşkent region are quite frequent. Rock falls also inflict significant amounts of material damage and create fear among the populace. The road that crosses this area is a major artery that connects Taşkent to the town of Balçılar and seven other villages. Landslides damage this road every winter and sometimes block Access ([13])

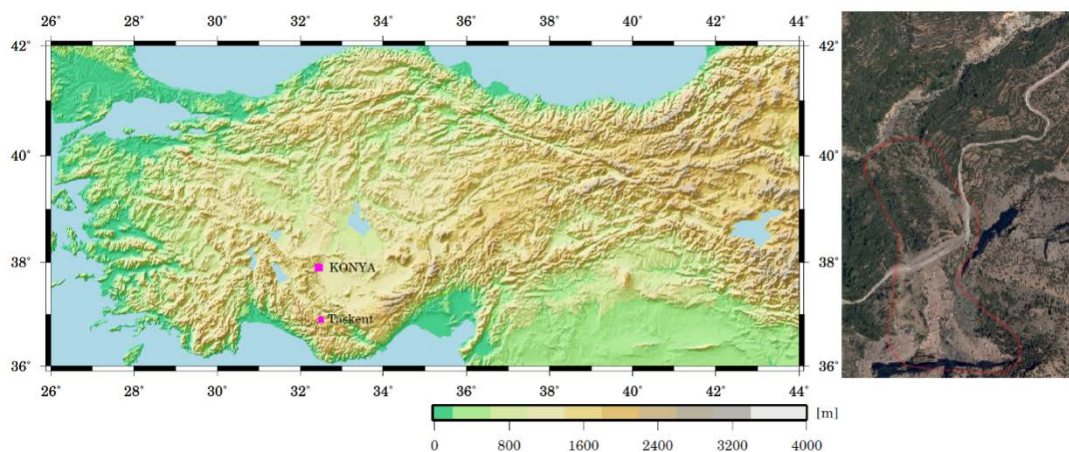


Figure 1: Location map of the study area and landslide region in Taşkent

3.1 Reference Network

The reference network had been established for landslide monitoring. The reference network consists of four reference points that are all built in stable regions outside the landslide area. These points cover 240 ha and are 625 m, 725 m, 1379 m, and 2287 m away from the active landslide area. The static GNSS surveying method was performed for eight hours and sampling intervals were set to 5 second and the elevation mask angle was 10°. The reference stations also checked with Turkish National Permanent GPS Network (TNPGN) reference frame for stability using precise ephemeris. The TNPGN stations were AKSI, KAMN, KNYA, SARV and 65km, 70 km, 121 km and 28 km, from the average of reference station coordinates, respectively. The reference network points can be seen on Figure 2.

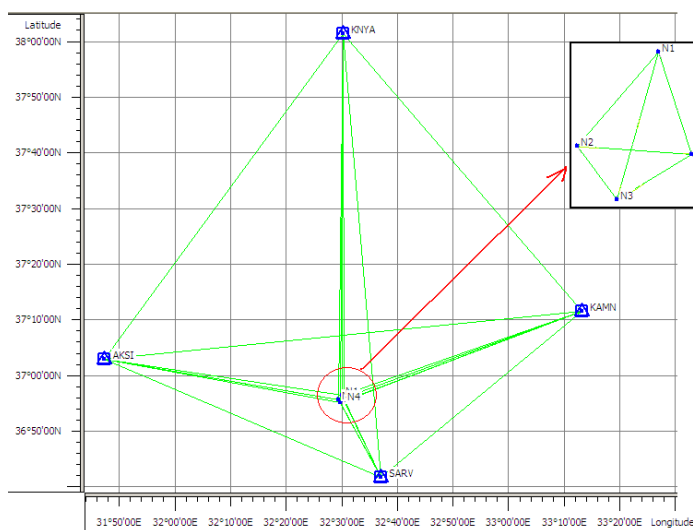


Figure 2. Used Turkish National Permanent GPS Network Stations and stable points

For the purpose of detecting surface movement, ground monitoring points conducted on reachable areas and clean sky view in complex and dense forestry topography. The rover stations at the deformations points and stable points had collected data via 5 second interval, 10° elevation mask angle. The duration of data collection was minimum 30 minutes as rapid-static GNSS surveying method. The measurements had been obtained at three periods by Javad Triumph, Topcon HiperLite and HiperPro GNSS dual frequency receivers. The first period observations had been completed at 26 November 2011, the second period is 23 April 2012 and the third period is 12 June 2012. The GNSS network baselines have been processed by Leica Geo-office 5.0 software. The processing parameters have been given at the table 1. Although all GNSS receivers had collected Glonass observations, processing software had given error messages at processing time of all Glonass observations. So Glonass observations hadn't been used at the processing.

Table 1. The processing parameters of rapid-static method.

Parameters	Option
Cut-off Angle	10 ⁰
Ephemeris	Broadcast
Solution Type	GPS Phase: All Fix
Frequency	L1+L2
Tropospheric Model	Hopfield
Ionospheric Model	Computed model

The network has been adjusted as minimally constrained with one point fixed at ITRF-96 datum and at 2005.00 reference epoch. The confidence interval has been typically stated at the 95% confidence level. To determine movements with a static model, a functional model, solved according to the least-squares method, was constituted for each observation period. The test statistic value computed from the difference vector and covariance matrix was compared with the F-distribution. As a result, moving points and movements were computed ([6],[22]).

4. RESULTS AND DISCUSSION

The observations were obtained at 35 stations (4 stable point, 31 object point) at the first period. Because of debris stream at the time of landslide, three station benchmark had get lost in study area at the second period. The five station benchmark had been established before third period. Consequently 32 station coordinates, existent at all periods, have been compared. Figure 3 shows horizontal deformation vectors and vertical displacements between first and second period obtained by rapid-static method. Also figure 4 shows horizontal deformation vectors and vertical displacements between second and third period obtained by rapid-static method. The coordinates have been given Transversal Mercator Projection, each 3° of longitude in width and central meridian 30° east.

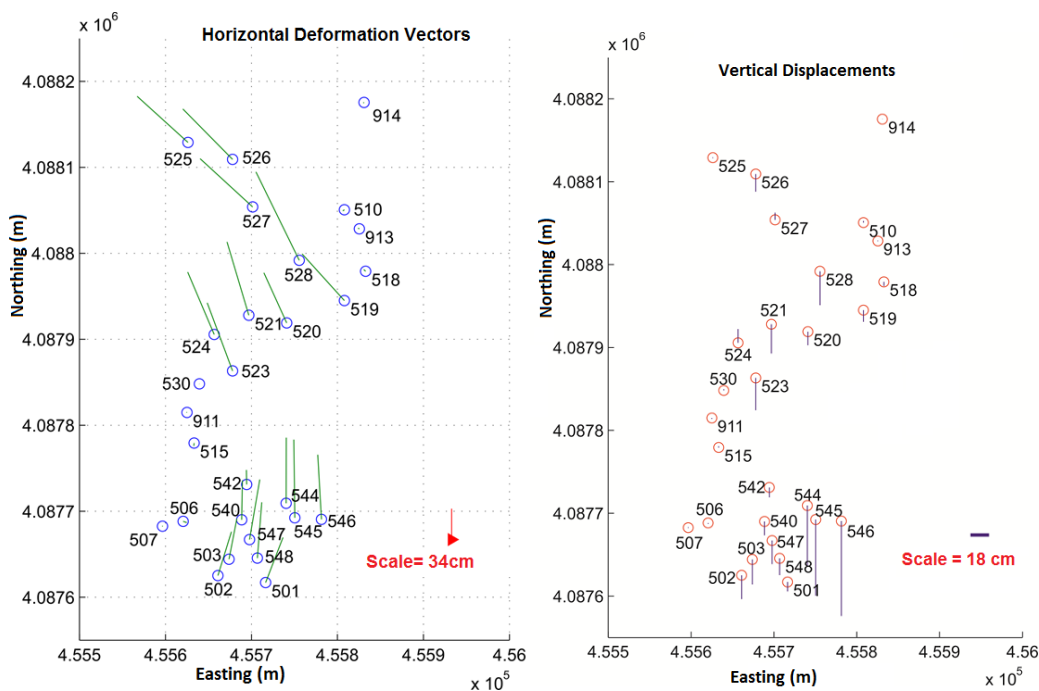


Figure 3: The horizontal deformation vectors and vertical displacements between 1. period and 2. period obtained by rapid-static method.

The near values to zero indicate stable points among object points. Point movements generally have resulted with northern movement. These results may be correlation with slope, aspect, underground waters, distance to river and road. The moving points have also descended hill through slope. Because rainfall and melting snow waters getto increase the intensity of landslide, the displacements had been determined as the biggest values in the winter and spring season. The rain and melting snow waters have created a pressurised discharge of water that enters the landslide area through underground leakage in spring. The reduced resistance of the clay, shale and slope debris is believed to be the primary reason behind the formation of the landslide. Mass movement typically occurs on the circular sliding surface [3].

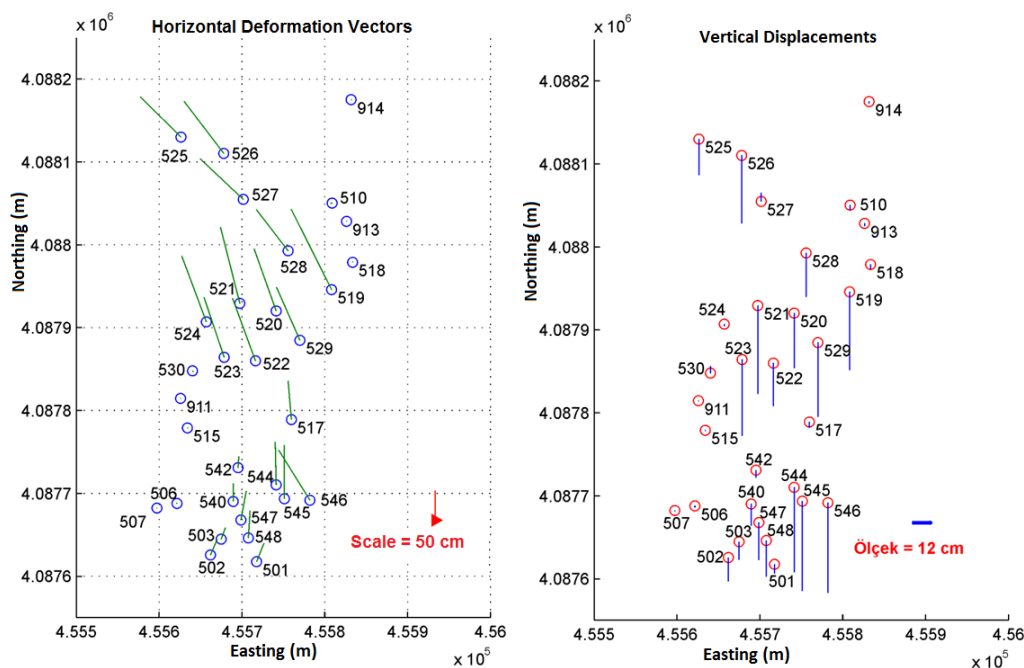


Figure 4. The horizontal deformation vectors and vertical displacements between 2. period and 3. period obtained by rapid-static method.

Then all observations have been processed and adjusted by PPP method. The processing parameters of PPP method have been used as shown in Table 2. The differences among periods have been computed and their results are given in Table 3 according to projection coordinates system.

Table 2. The processing parameters of PPP method

Parameter Name	Option	Parameter Name	Option
<i>User dynamics</i>	STATIC	TZD random walk (mm/hr^{^(1/2)})	5
<i>Observation processed</i>	CODE&PHASE	Marker->ARP distance (m)	1.426
<i>Frequency observed</i>	L3	Cutoff elevation (deg)	10
<i>Satellite orbits</i>	PRECISE	Ocean loading coefficients	NOT FOUND
<i>Satellite product input</i>	CLK-RINEX	Surface meteorological data	
<i>Ionospheric model</i>	L1&L2	Temperature (deg C)	4.55 (GPT model)
<i>Marker coordinates</i>	ESTIMATED	Pressure (Mb)	843.05 (GPT model)
<i>Troposphere zenith delay(TZD)</i>	ESTIMATED	Relative humidity(%)	50.00 (Default)
<i>Clock interpolation</i>	YES	Tropospheric models	
<i>Parameter smoothing</i>	NO	Hydrostatic delay	Davis(GPT)
<i>Satellite clock interval (s)</i>	30	Wet delay	Hopf(GPT) init
<i>Pseudorange sigma (m)</i>	2	Mapping functions	GMF
<i>Carrier phase sigma (m)</i>	0.015		

Table 3. The displacements according Precise Point Positioning Method

Between 1. period and 2. period				Between 2. period and 3. period			
501	0.79	0.35	-0.19	501	0.47	0.15	-0.19
502	0.60	0.61	0.12	502	0.54	-0.29	-0.65
503	0.77	0.15	-0.35	503	0.39	0.11	-0.13
506	0.00	0.11	-0.12	506	0.05	-0.03	0.01
507	0.00	0.12	-0.02	507	0.02	0.00	-0.12
510	0.06	-0.10	-0.03	510	-0.04	-0.03	-0.06
515	-0.04	-0.01	0.04	515	0.01	0.00	-0.05
518	0.05	0.02	-0.15	518	0.02	-0.13	-0.10
519	1.21	-0.51	-0.49	519	1.43	-0.81	-0.43
520	1.31	-0.16	-0.49	520	1.93	-0.68	-0.49
521	1.59	-0.33	-0.52	521	1.82	-0.73	-0.22
523	1.30	-0.30	-0.45	523	1.42	-0.26	-0.55
524	1.57	-0.29	-0.37	524	2.01	-1.72	0.25
525	1.27	-0.74	-0.09	525	1.44	-0.88	0.06
526	1.48	-0.80	-0.45	526	1.70	-0.90	-0.33
527	1.13	-0.66	-0.05	527	1.42	-1.05	-0.21
528	1.25	-0.66	-0.51	528	1.50	-0.68	-0.54
530	-0.02	-0.09	0.03	530	0.07	0.15	0.02
540	0.62	0.05	-0.06	540	0.37	0.03	-0.22
542	0.22	-0.02	-0.19	542	0.24	0.03	-0.13
544	Not computed			544	1.17	-0.14	-0.76
545	1.63	0.02	-1.01	545	1.25	0.00	-0.79
546	1.54	-0.15	-1.37	546	1.48	-0.53	-0.60
547	1.06	0.51	-0.05	547	0.89	-0.15	-0.82
548	1.05	0.21	-0.34	548	0.65	0.13	-0.28
N1	0.00	0.01	-0.06	N1	0.01	0.01	0.08
N2	0.01	-0.01	0.02	N2	-0.02	0.00	-0.10
N3	0.01	-0.01	-0.03	N3	-0.01	0.01	-0.09
N4	0.01	-0.04	-0.02	N4	-0.01	0.00	-0.06
911	0.05	0.02	0.02	911	-0.01	-0.03	-0.12
913	0.00	-0.08	-0.18	913	0.02	0.05	0.03
914	0.03	-0.11	-0.10	914	0.01	-0.03	-0.02

The stable points according to rapid-static method are N1,N2,N3,N4 and 911, 93, 914 traverse points and 506, 507, 510,515, 518, 524, 53 object points. Generally the obtained results by PPP methods have resembled the results of rapid-static methods. But according to PPP method, some of these points have been seen moving averaged 10-15 cm especially to the vertical direction. We know that the positioning by GNSS on vertical direction always have been problem because of GNSS satellite constellation and design. It is argued that the collect time of object point's data is not adequate. This collect time has to be increased as an hour or two hours.

5. CONCLUSIONS

In this study, GNSS data were processed by post-processed PPP method and rapid static GNSS solution for the purpose of comparison. The landslide toe moved forward averagely 1-2 m between campaigns. Processing results show that differences between PPP-derived and rapid-static-derived displacement are within dm level. As a conclusion, in case of limited GNSS receiver, post-processed static PPP method can be used as an efficient alternative to the rapid-static GNSS method to detect displacement caused by landslide.

Especially if PPP method is used in landslide monitoring with static GNSS surveying, time of collect data has to be minimal an hour or two hours for correct determining of vertical displacements. Also in long term landslide monitoring, the deformation analysis has to be made at common reference epoch or at semi-kinematic datum, using the latest realization of ITRF.

ACKNOWLEDGMENT

This study was supported by the Scientific and Technical Research Council of Turkey (TÜBİTAK) (project number 111Y307) and by the Selçuk University Scientific Research Projects Coordinator (project number 11101028). The authors also thank production editor for editing and the Natural Resources Canada for providing CSRS-PPP service.

REFERENCES

- [1]. Akıncı H, Doğan S, Kılıçoğlu C, Keçeci SB., Samsun İl Merkezinin Heyelan Duyarlılık Haritasının Üretilmesi. *Electronic Journal of Map Technologies* vol:2, Issue:3:pp:13–27 (In Turkish), 2010
- [2]. Akgun A, Kincal C, Pradhan B., Application of remote sensing data and GIS for landslide risk assessment as an environmental threat to Izmir city (west Turkey). *Environmental Monitoring and Assessment*, Vol:184 Issue:9 pp:5453–5470. 2012
- [3]. Zeybek M, Şanlıoğlu İ., Accurate determination of the Taşkent (Konya, Turkey) landslide using a long-range terrestrial laser scanner. *Bulletin of Engineering Geology and the Environment*, .vol:74, Issue:1, pp:61-76, 2014
- [4]. Zhu W, Zhang Q, Ding XL, Zhao CY, Yang CS, Qu FF, Qu W., Landslide monitoring by combining of CR-InSAR and GPS techniques. *Advances in Space Research* Vol:53, Issu:3, pp:430–439, 2014
- [5]. Gili J.A., Corominas, J., Rius, J., Using Global Positioning System techniques in landslide monitoring, *Engineering. Geology*, vol:55 Issue:3, pp:167-192, 2000
- [6]. Yalçınkaya M, Bayrak T., Comparison of static, kinematic and dynamic geodetic deformation models for Kutlugün Landslide in Northeastern Turkey. *Natural Hazards* Vol:34 Issue:1, pp:91–110, 2005
- [7]. Hastaoğlu K.O. and Sanli, U., Accuracy of GPS rapid static positioning: application to Koyulhisar landslide, central Turkey, *Survey Review*, vol:43, Issue: 321, pp:226-240, 2011
- [8]. Hastaoğlu K.O. and Sanli, U., Monitoring Koyulhisar landslide using rapid static GPS: a strategy to remove biases from vertical velocities, *Natural Hazards*, Vol:58, Issue:3, pp:1275-11294, 2011b
- [9]. Calais E, Han JY, Demets C, Nocquet JM. Deformation of the North American plate interior from a decade of continuous GPS measurements, *Journal of Geophysical Research Solid Earth* Vol: 111, Issue: B6, pp:1_23, 2006
- [10]. Ohta Y, Ohzono M, Miura S, Iinuma T, Tachibana K, Takatsuka K, Miyao K, Sato T, Umino N., Coseismic fault model of the 2008 Iwate-Miyagi Nairiku earthquake deduced by a dense GPS network. *Earth Planets Space*. Vol:60, No:12, pp:1197_1201 2008
- [11]. M. Lytvyn, C. Pöllabauer ; M. Troger , K. Landfahrer , L. Hörmann, C. Steger, *Real-Time Landslide Monitoring Using Single-Frequency PPP: Proof of Concept*, [Satellite Navigation Technologies and European Workshop on GNSS Signals and Signal Processing \(NAVITEC\), 2012 6th ESA Workshop on, pp:1-6, 5-7 December 2012.](#)
- [12]. Li P and Zhan X., Integrating GPS and GLONASS to accelerate convergence and initialization times of Precise Point Positioning. *GPS Solutions*, vol:18, Issu:3, pp:461-471, 2014
- [13]. Yiğit, C.Ö., Experimental assessment of post-processed kinematic Precise Point Positioning method for structural health monitoring, *Geomatics, Natural Hazards and Risk*, vol:7, No:1, pp:360-383, 2016
- [14]. R. M. Capilla, J. L. Berné, A. Martín and R. Rodrigo., Simulation case study of deformations and landslides using real-time GNSS precise point positioning technique, *Geomatics, Natural Hazards and Risk*, 2016, <http://dx.doi.org/10.1080/19475705.2015.1137243>
- [15]. Michigan School of Technology Web-page [on-line] Available: http://www.tech.mtu.edu/courses/su4100/Course_Material
- [16]. Rizos, C., Janssen, V., Roberts, C., Grinter, T., GNSS: Precise Point Positioning PPP versus DGNSS. *Geomatics World* (October), pp.18–20, 2012
- [17]. Zumberge JF, Heflin MB, Jefferson DC, Watkins MM, Webb FH., Precise Point Positioning for the efficient and robust analysis of GPS data from large networks. *Journal of Geophysical Research*, vol. 102, pp.5005_5017,1997
- [18]. El-Mowafy, A. ,Analysis of Web-Based GNSS Post-Processing Services for Static and Kinematic Positioning Using Short Data Spans. *Survey Review*, 43(323), 535–549. , 2011 doi:10.1179/003962611X13117748892074
- [19]. Huber, K., Heuberger, F., Abart, C., Karabatic, A., Weber, R. and Berglez, P., *Precise Point Positioning-Constraints and Opportunities*, Fig Congress, Sydney, Australia 11-16 April, 2010
- [20]. Kouba, J., Héroux, P., Precise Point Positioning Using IGS Orbit and Clock Products, *GPS Solutions*. Vol.5, pp: 12-28, 2001
- [21]. The Canadian Spatial Reference System (CSRS) Precise Point Positioning (PPP) tool web page (on-line) Available: (<https://webapp.geod.nrcan.gc.ca/geod/tools-outils/ppp.php>).
- [22]. Koch KR *Parameter estimation and hypothesis testing in linear models*. Springer-Verlag, Berlin, 1999

Biography: İsmail Şanlıoğlu is Assoc. Prof. Dr. of Geomatics Department, Engineering Faculty, Selçuk University, Konya, Turkey. He is a graduate of the Selçuk University with a Master of Science in Geodetic Science and Surveying in 1998 and a Ph.D. in Geomatics Science (emphasis in GNSS processing and using IGS products) in 2004. He has been researching applications of GNSS, height and geoid determination, landslide and sinkhole monitoring, reference frames, processing and adjustment of GNSS observations. He is a member of Turkish Federation of Surveyors.

Estimation of Uniaxial Compressive Strength From Point Load Strength, Porosity Dry Density and P-Wave Velocity

A. Bozdogan^{*1}, I. Ince¹ and M. Fener²

Abstract

The prediction of the uniaxial compressive strength (UCS) from indirect methods is widely used for the preliminary investigations. In this study, the possibility of predicting the UCS from the physical-strength properties (dry density, porosity, P-wave velocity and point load test) was investigated for magmatic rocks. For this purpose, magmatic rocks were collected from 59 different locations in Anatolia of Turkey. The UCS and the physical-strength tests were carried out on the samples in the laboratory. The UCS values were correlated with the physical-strength values and strong relations were obtained. We used dry density (ρ_d), porosity (n) and point load strengths (PLT) values of magmatic rocks in this model. This model is very reliable ($R^2 = 0.832$) for predetermination of uniaxial compressive strengths of magmatic rocks.

Keywords: Magmatic rocks, Porosity, Statistical model, Uniaxial compressive strength

1 INTRODUCTION

The uniaxial compressive strength (UCS) is an experiment that commonly used in the rock mechanics and engineering geology designs. However in some situations, preparing sample for this experiment and performing the experiment is costly and time consuming. As a result of this, for the estimation of rocks' UCS values; alternative experiments (i.e. point load index test, Schmidt hammer rebound value etc.) and/or the analytical and empirical relationships between various mechanical and physical properties have been developed.

While these analytical and empirical relationships are being generated, the UCS value is estimated with different methods (i.e. simple regression analysis, multiple regression analysis etc.) by using one or more properties of rock's index, strength, weathering etc. properties. The relationship between UCS and index-strength properties was investigated by many researchers such as porosity [1], P-wave velocity [2]-[5], dry unit weight [6] and PLT [7]-[12].

In previous studies, the uniaxial compressive strength of various rock groups was trying to be estimated by using different approach methods. The aim of this study is estimation of the uniaxial compressive strength (UCS) of the magmatic rocks, whose strength values vary in wide range, by using powerful software, SPSS Statistics-21.

2. MATERIAL AND METHOD

For the experimental studies, representative block samples of approximately 20x30x30 cm dimensions were collected from different of magmatic rocks outcropped in Anatolia. Physical properties (i.e. dry density (ρ_d) and porosity (n)) were determined on specimens prepared from each magmatic rocks (ISRM, 2007). Then the uniaxial compressive strength (UCS), and P-wave velocity (V_p) determinations were performed in accordance with test methods suggested by ISRM [13]. Diametral point load test (PLT) was performed according to the standard ASTM [14].

3. RESULTS AND DISCUSSION

3.1 Index-Mechanical Properties

Values for index properties (ρ_d , n and V_p), strength properties (UCS and PLT) of the samples used in this study were determined. Table 1 presents the statistical data obtained from these values. While dry density of the samples vary between 1.23-2.69 gr/cm³, porosity values range between 0.46% and 36.83%. The P-wave velocities and point load strength index of the samples were determined to be between 0.70 and 5.38 km/s. and 0.70 and 10.40 MPa respectively. The UCS found to be between 6.19 and 144.10 MPa.

Table 1. Descriptive statistics of data used in the analysis.

Variables	Data	Mean	Std. deviation	Variance	Minimum	Maximum
n - %	59	2.03	0.41	0.17	0.46	36.83
ρ_d - gr/cm ³	59	15.59	11.01	121.191	1.23	2.69

Vp – km/s	59	3.36	1.11	1.23	0.70	5.38
PLT - MPa	59	4.59	2.78	7.72	0.70	10.40
UCS - MPa	59	52.04	35.30	1246.0	6.19	144.10

3.2 Statistical Analysis

In order to describe, the relationships between UCS with index and strength properties of the magmatic rocks, regression analysis was accomplished and empirical equations have been developed. The appropriate equation and the coefficient of correlation (R^2) were determined for each test results (Table 2). The plots of the UCS as a function of index and strength properties are demonstrated (Figure 1).

Table 2. Predictive models for assessing the UCS from index and PLT.

Equation no	Equation type	Predictive models	R^2
1	Power	$UCS = 10.723 PLT^{1.0084}$	0.8544
2	Exponential	$UCS = 0.8529e^{1.8806 pd}$	0.8088
3	Exponential	$UCS = 115.52e^{-0.07 n}$	0.8091
4	Exponential	$UCS = 3.8987e^{0.6815 Vp}$	0.7732

Multiple regression analysis was conducted using index and PLT to estimate uniaxial compressive strength in magmatic rocks. Confidence interval for the analysis was determined as 95% and the analysis was performed using the programmer SPSS Statistics-21. In order to determine the best subsets to be used for the multiple regression analysis, a forward analysis was made by the programmer SPSS Statistics-21. Statistical data obtained from different models produced from different subsets were determined.

It is required that p value should be smaller than 0.05 for the reliability of the regression analysis for the significance level of 5% ($\alpha=0,05$) of the chosen subsets. In determining the best subset that complies with this requirement, the one with the highest R^2 value is preferred.

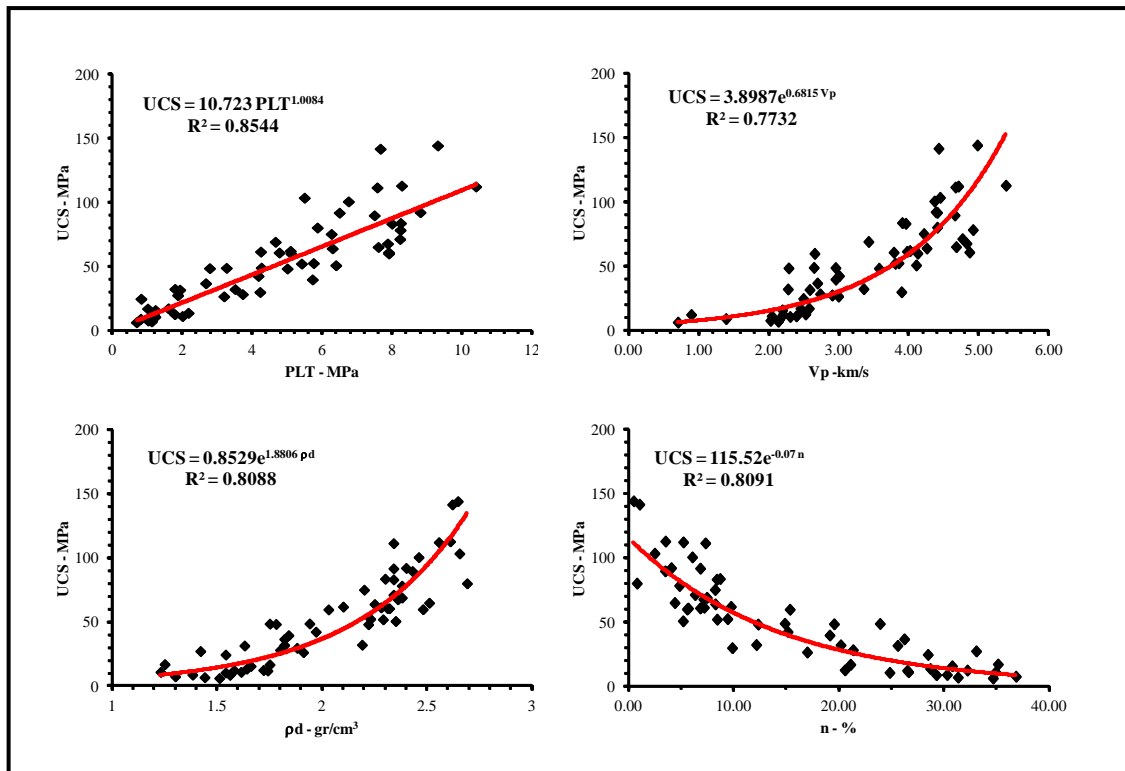


Figure 1. The relation between UCS with index and PLT obtained from simple regression.

In Table 3, rock properties which fell within the model that ensured the case above were determined as subset. The most appropriate subset determined to estimate uniaxial compressive strength by means of multiple regression analysis consists

of independent variables of PLT, n and ρ_d . Statistical results for multiple regression analysis made with independent variables of this subset were given in Table 4.

Equation formulated according to the data obtained from Table 4 was given in Equation 1.

$$UCS = -115.836 + 6.363PLT + 0.909n + 61.416\rho_d \text{ (Equation 1)}$$

The analysis of variance for the validation of the regression equation was performed and the results were given in Table 5. In this test, a 95% level of confidence was chosen. The statistical model developed has proved itself that it is securely employable to estimate the uniaxial compressive strength ($F=90.701$, $p=0.000 < \alpha$) the basis of 5% importance level ($\alpha=0.05$).

Table 3. Results of the best subsets regression.

R ²	Adjusted R Square	p	PLT	ρ_d	Vp	n
0.827	0.821	0.000	x	x		
0.794	0.787	0.000	x		x	
0.804	0.797	0.000	x			x
0.800	0.793	0.000		x	x	
0.778	0.770	0.000		x		x
0.761	0.753	0.000			x	x
0.828	0.819	0.000	x	x	x	
0.832	0.823	0.000	X	X		X
0.806	0.795	0.000		x	x	x
0.807	0.796	0.000	x		x	x
0.831	0.822	0.000	x	x	x	x

Table 4. The statistical results of multiple regression analysis.

Model	Unstandardized Coefficients		Standardized Coefficients	t	p
	β	Std. Error	Beta		
(Constant)	-115.836	51.654		-2.243	0.029
PLT	6.363	1.517	0.501	4.194	0.000
ρ_d	61.416	20.498	0.716	2.996	0.004
n	0.909	0.759	0.284	1.198	0.236

Table 5. The analysis of variance of regression model for UCS.

Model	Sum of Squares	Degree of freedom	Mean square	F	p
Regression	60116.937	3	20038.979	90.701	0.000
Residual	12151.334	55	220.933		
Total	72268.270	58			

The multiple regression models for the prediction of the UCS were then developed (Figure 2). When the Figure 2 is examined, it can be seen that there is a high correlation coefficient ($R^2: 0.832$) between the estimated and actual values.

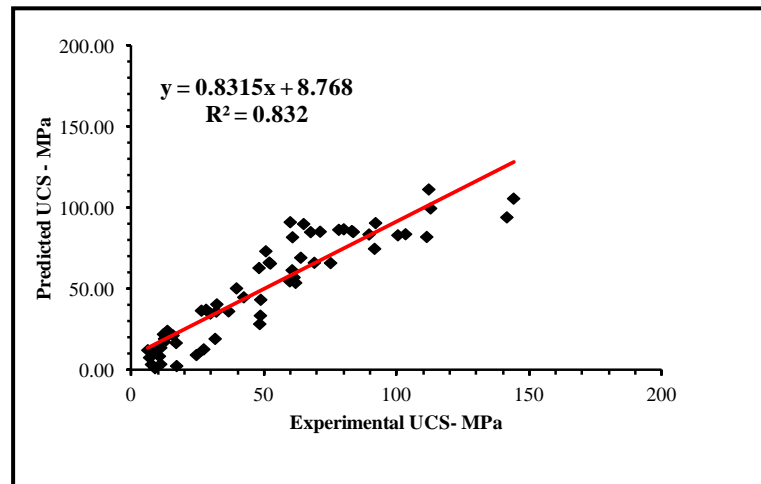


Figure 2. The relationship between the actual and estimated values of UCS.

4 CONCLUSION

In rock mechanics and engineering geology designs, uniaxial compressive strength (UCS) is extensively used as parameter. Despite the easy determination of UCS, this is a time consuming and expensive method. By practical experiments, the modelling of UCS values of magmatic rocks, which spread in various regions around the world, is important.

Based on the analyses, the following main conclusions were drawn.

- a. The most suitable variables for regression analysis were determined to be the values for point load strength index (PLT), dry density (ρ_d) and porosity (n) by testing various subsets representing different index and mechanical properties of intact rock.
- b. A fairly reliable statistical model ($R^2 = 0.832$) was developed to estimate uniaxial compressive strengths.
- c. The most importantly, the equation developed in this study could be used to predetermine the uniaxial compressive strengths of magmatic rocks widely used as a rocks in the Anatolian (Turkey) as well as other regions.

REFERENCES

- [1]. V. Palchik, Y.H.Hatzor, "The influence of porosity on tensile and compressive strength of porous chalks," *Rock Mechanics and Rock Engineering*, vol.,37(4), pp 331-341,2004.
- [2]. S.Kahraman, "Evaluation of simple methods for assessing the uniaxial compressive strength of rock," *Int. J. Rock Mech. Min. Sci.* vol.,38, pp 981-994,2001.
- [3]. B. Minaeian, K. Ahangari, "Estimation of uniaxial compressive strength based on P-wave and Schmidt hammer rebound using statistical method," *Arabian Journal of Geosciences*, vol., 6(6), pp 1925-1931,2013.
- [4]. R. Altindag, "Correlation between P-wave velocity and some mechanical properties for sedimentary rocks," *J South Afr Inst Min Metall*, vol.,112, pp 229-237,2012.
- [5]. A. Azimian, R. Ajalloeian, L. Fatehi, "An empirical correlation of uniaxial compressive strength with p-wave velocity and point load strength index on marly rocks using statistical method," *Geotechnical and Geological Engineering*, vol., 32 (1), pp 205-214,2014.
- [6]. K. Diamantis, E. Gartzos, G. Migiros, "Study on uniaxial compressive strength, point load strength index, dynamic and physical properties of serpentinites from Central Greece: test results and empirical relations," *Engineering Geology*, vol., 108, pp 199-207,2009.
- [7]. K.T. Chau, R.H.C. Wong, "Uniaxial compressive strength and point load strength of rocks," *Int J Rock Mech Min Sci Geomech Abst.*, vol.,33(2), pp 183-188,1996.
- [8]. H.J. Smith, "The point load test for weak rock in dredging applications," *Int J Rock Mech Min Sci.*, vol., 34(3-4), 295 p., 1997.
- [9]. S. Kahraman, O. Günaydın, M. Fener, "The effect of porosity on the relation between uniaxial compressive strength and point load index," *Int J Rock Mech Min Sci.*, vol., 42(4), pp 584-589,2005.
- [10]. M. Fener, S. Kahraman, A. Bilgil, O.Günaydın, "A comparative evaluation of indirect methods to estimate the compressive strength of rocks," *Rock Mech Rock Eng.*, vol., 38(4), pp 329-343,2005.
- [11]. M. Kohno, H. Maeda, "Relationship between point load strength index and uniaxial compressive strength of hydrothermally altered soft rocks," *Int. J. Rock Mech. Min. Sci.*, vol., 50, pp 147-157, 2012.
- [12]. S. Kahraman, "The determination of uniaxial compressive strength from point load strength for pyroclastic rocks," *Engineering Geology*, vol., 170, pp 33-42,2014.

- [13]. ISRM, "The complete ISRM suggested methods for rock characterization, testing and monitoring: 1974-2006. In: Ulusay, Hudson (eds) Suggested methods prepared by the commission on testing methods," *International Society for Rock Mechanics*. ISRM Turkish National Group, 2007, Ankara, Turkey, p 628.
- [14]. ASTM (American Society for Testing Materials), "Standard Test Method for Determination of the Point Load Strength Index of Rock (D5731-05)," 2005.

The Effect Of Reciprocating Extrusion Pass Number Of Aluminum 6061 Based Composites Microstructure

Fatma Nazlı Sari¹, Veysel Erturun¹, Mehmet Baki Karamis¹

Abstract

In this study Aluminum 6061 (Al) matrix reinforced with SiC metal matrix composites (MMC) were manufactured by powder metallurgy. Besides unreinforced aluminum alloy (Al 6061) samples were manufactured for comparing microstructure of Al 6061 MMCs. The purpose of this study is to investigate the effect of reciprocating extrusion (RE) pass number for microstructures of Al MMCs. RE is a kind of severe plastic deformation (SPD) method for obtaining improved material structures. Different extrusion pressures and RE pass numbers were investigated for the changes in hardness value of samples. The Al MMC and Al 6061 alloy samples microstructures were examined by Scanning Electron Microscope (SEM).

Keywords: *Metal matrix composites reciprocating extrusion, Al 6061, microstructure*

1. INTRODUCTION

Metal Matrix Composites (MMCs) are suitable for applications requiring combined strength, thermal conductivity, damping properties and low coefficient of thermal expansion with lower density [1].

Particulate reinforced aluminum alloy composites are attractive materials for automotive, aeronautic and aerospace applications due to their low density, high Young's modulus and strength and high wear resistance [2]. Achieving uniform distribution of reinforcement is the most important work. These aluminum alloy matrix composites can be produced by powder metallurgy routes followed by secondary forming processes, such as extrusion and rolling [3]. The factors that determine properties of composites are volume fraction, microstructure, homogeneity and isotropy of the system and these are strongly influenced by proportions and properties of the matrix and the reinforcement. Abdulhaqqet.al. [4, 5], Hutchings [6] and Lloyd et.al. [7] explored the significance of hard ceramic particles in increasing the bulk hardness of Al-MMCs. Howel et.al. [8] and Venclat.al. [9], reasoned the improvement of the hardness of the composites to the increased particle volume fraction. Deuiset.al. concluded that the increase in the hardness of the composites containing hard ceramic particles not only depends on the size of reinforcement but also on the structure of the composite and good interface bonding [10].

Among them Al6061 alloy is highly corrosion resistant, extricable in nature and exhibits moderate strength. It finds vast applications in the fields of construction, automotive and marine fields. They have been studied extensively because of their technological importance and their exceptional increase in strength obtained by precipitation hardening. [11].

Severe plastic deformation (SPD) can lead to emergence of microstructural features and properties in materials which are fundamentally different from the ones well known for conventional cold deformation [12]. Reciprocating extrusion (RE) is one of the finest severe plastic deformation (SPD) processes for developing mechanical features and eliminating the pores in the structures of aluminum matrix composites (AMCs). [13,14].

¹Corresponding author: Erciyes University, Department of Industrial Design Engineering , 38039, Kayseri/Turkey,
fnasari@erciyes.edu.tr

2. MATERIALS AND METHODS

2.1. Materials

In the present study, AA 6061 aluminum alloy powder (10 μm in size) was used as a matrix material. AA 6061 powder was mixed with SiC particles (20 μm size) in a volume fraction of 5% for 1 h using a shaker-mixer. Unreinforced samples were also used for observing the changes of microstructure. The mixed composite powders were cold compacted at a pressure of 20 bar and then sintered at 600 °C under Ar atmosphere at 10 bar pressure

All the billets that were prepared using powder metallurgy methods have dimensions of 29.5 mm diameter and 42 mm height as shown in Figure 1. These billets were extruded reciprocatingly at 400 °C. The extrusion ratios are 10:1.

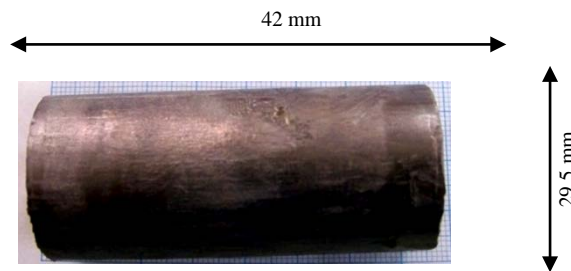


Figure 1. Sintered AA6061 Billet

2.2. Method

Figure 2 shows the schematic of the RE process. A die, two punches and two containers in a symmetrical design compose the RE system. Extrusion has been carried out repeatedly in the directions of up and down till the desired number of passes is obtained. With the last extrusion, in the meantime, punch B is removed to yield an extruded sample with a 10 mm diameter. The meaning of 0 passes is that the billets are inserted into the container A and then extruded into a sample with a 10 mm diameter. Pass can be called also with the term of cycle.

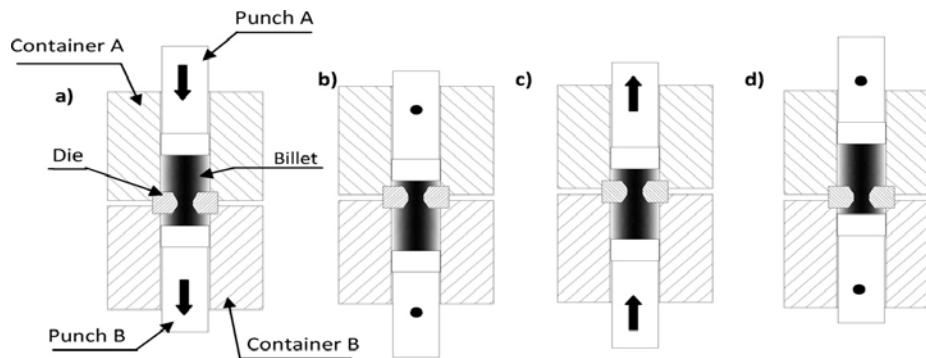


Figure 2. Schematic illustration of reciprocating extrusion (a) starting to step 1 (b) end of step 1 (c) start of step 2 (d) end of step 2.[13].

The reciprocating extrusion (RE) pressure range of unreinforced samples with different cycles at 400 °C are shown in Table 1. Unreinforced samples were reciprocated with 1 to 4 pass cycles respectively.

Table 1. RE pressure range of unreinforced AA 6061 samples with different cycle

Sample Number	RE Cycle Number			
	1	2	3	4
	RE Pressure (bar)			
A3	30			
A4	40 -70	14 -44		
A5	26 -47	25- 40	25- 45	

A6	26-47	25-47	29-43	18-47
----	-------	-------	-------	-------

Microstructure of unreinforced samples are shown in Figure 3 scanning electron microscope (SEM -Leo 440 WDX). images show different microstructures of unreinforced AA 6061 samples with different pass cycles. Table 2 shows RE pass cycle and pressure values for reinforced samples AA6061/SiC20 $\mu\text{m}/5$.RE temperature was 400 °C.

Table 2. RE pressure range of AA 6061/SiC/5 samples with different pass cycles

Sample Number	RE Cycle Number							
	0	1	2	3	4	5	10	15
	RE Pressure (bar)							
A13	48							
A15	48							
A16	48							
A17	48							
A22	48							
A2		30						
A7		52	56					
A8		65	53	58				
A9		65	45	55	55			
A12						70		
A14						70		
A19						70		
A11							70	
A18							70	
A21							70	
A10								70
A20								70

As mentioned above in Table 1 and Table 2 samples were finally extrudes as a rod with a 10 mm diameter at 350 °C with constant pressure of 48 bar. The extruded rod is shown in Figure 4. In order to examine the microstructures of samples, metallographic specimens were cut off from the extruded rod.

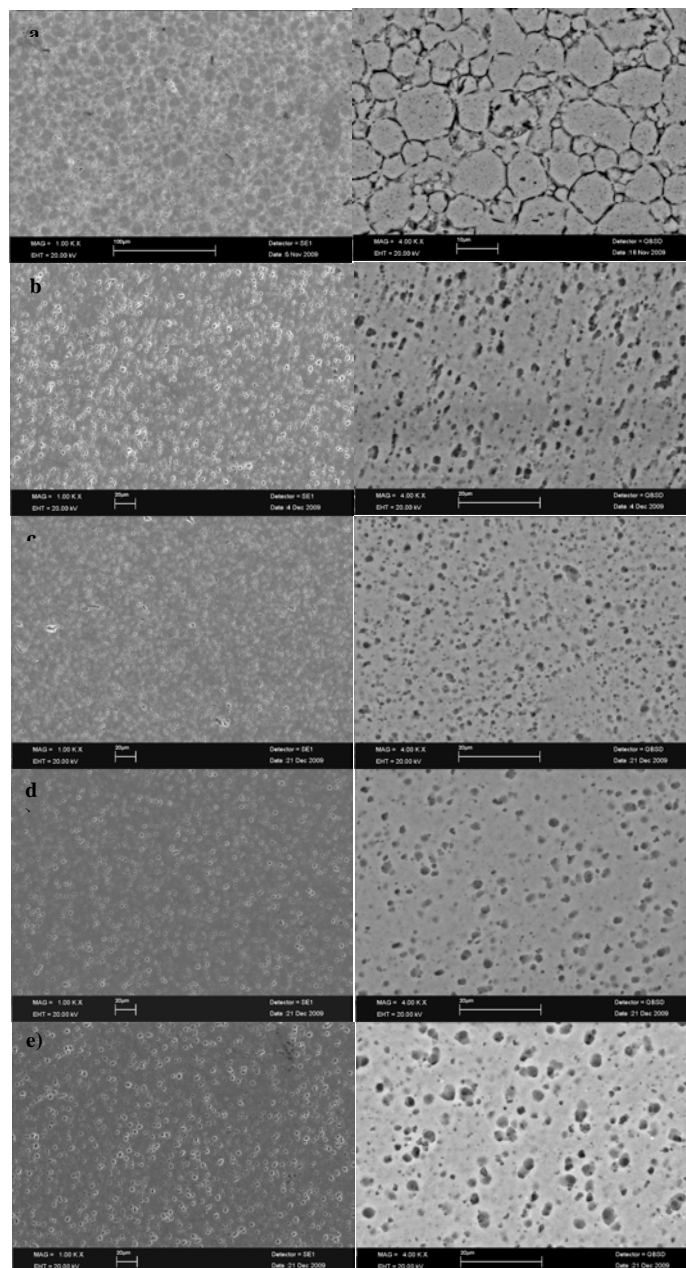


Figure 3. Microstructure of AA6061 samples. (a) Billet, (b) 1 pass, (c) 2 passes, (d) 3 passes (e) 4 passes

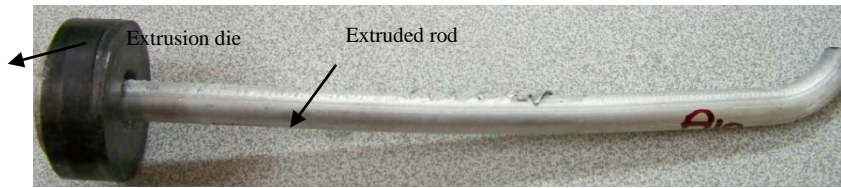


Figure 4. An Extruded composite sample

3. RESULT AND DISCUSSION

Examining billet sample microstructure in Fig 3 (a) which was not extruded AA 6061 powder particles can be seen clearly. However, after 1 RE cycle powder particles are gained as a whole matrix and cannot be detected with SEM images. After over deformation with increasing RE cycles it is not possible to detect matrix grain boundaries. As a result of this examination increasing RE cycle cannot be commented as a grain refining parameter.

In Figure 5 microstructure of reinforced samples AA6061/SiC $20 \mu\text{m}/5$ are shown. Figure 5 (a) shows the composite billet microstructure that was not reciprocally extruded. Figure 5(b) to Figure 5 (h) show composite microstructures which have different RE cycles.

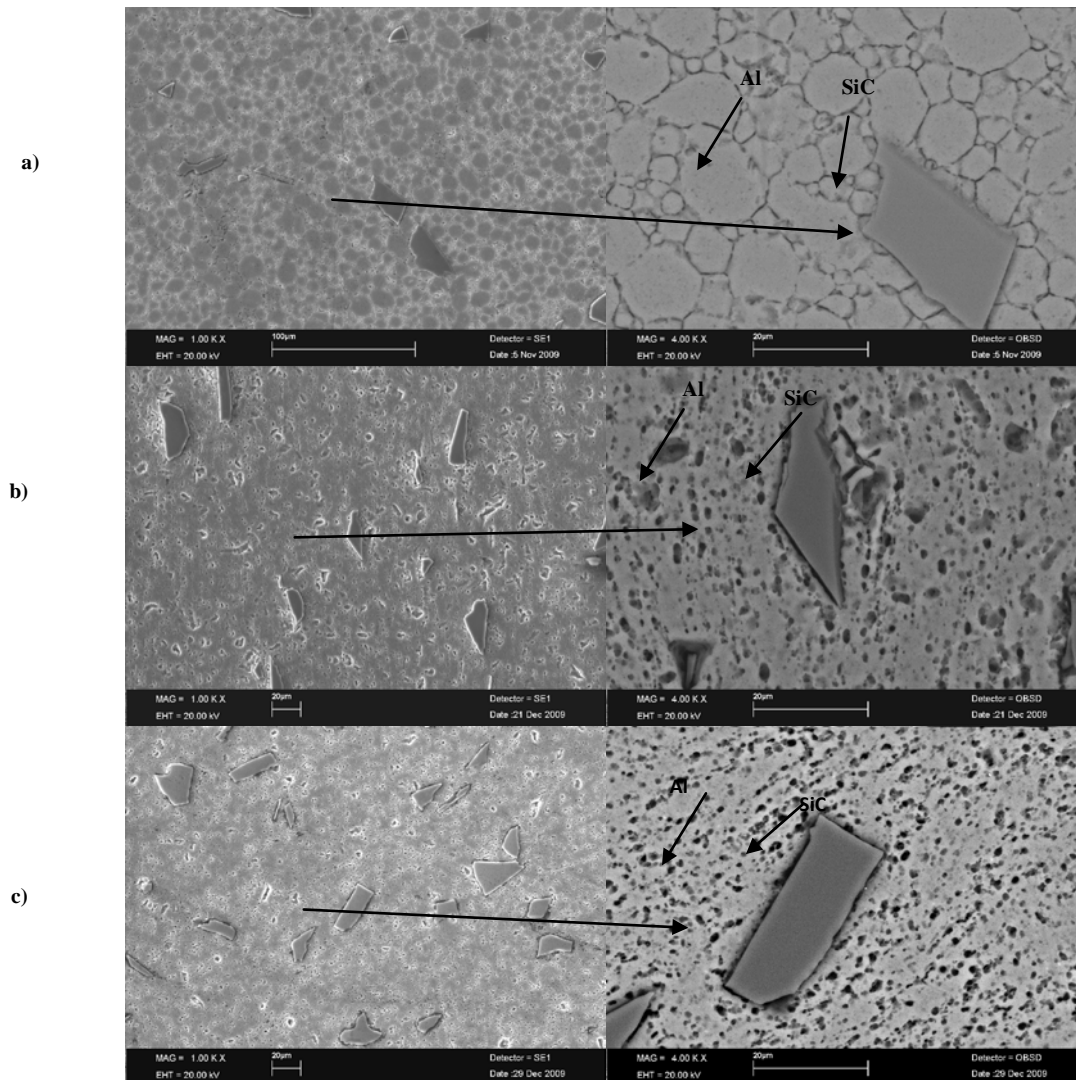


Fig. 5. Microstructure of AA6061/SiC $20 \mu\text{m}/5$ composite (a) Billet (b) 1 pass (c) 2 passes

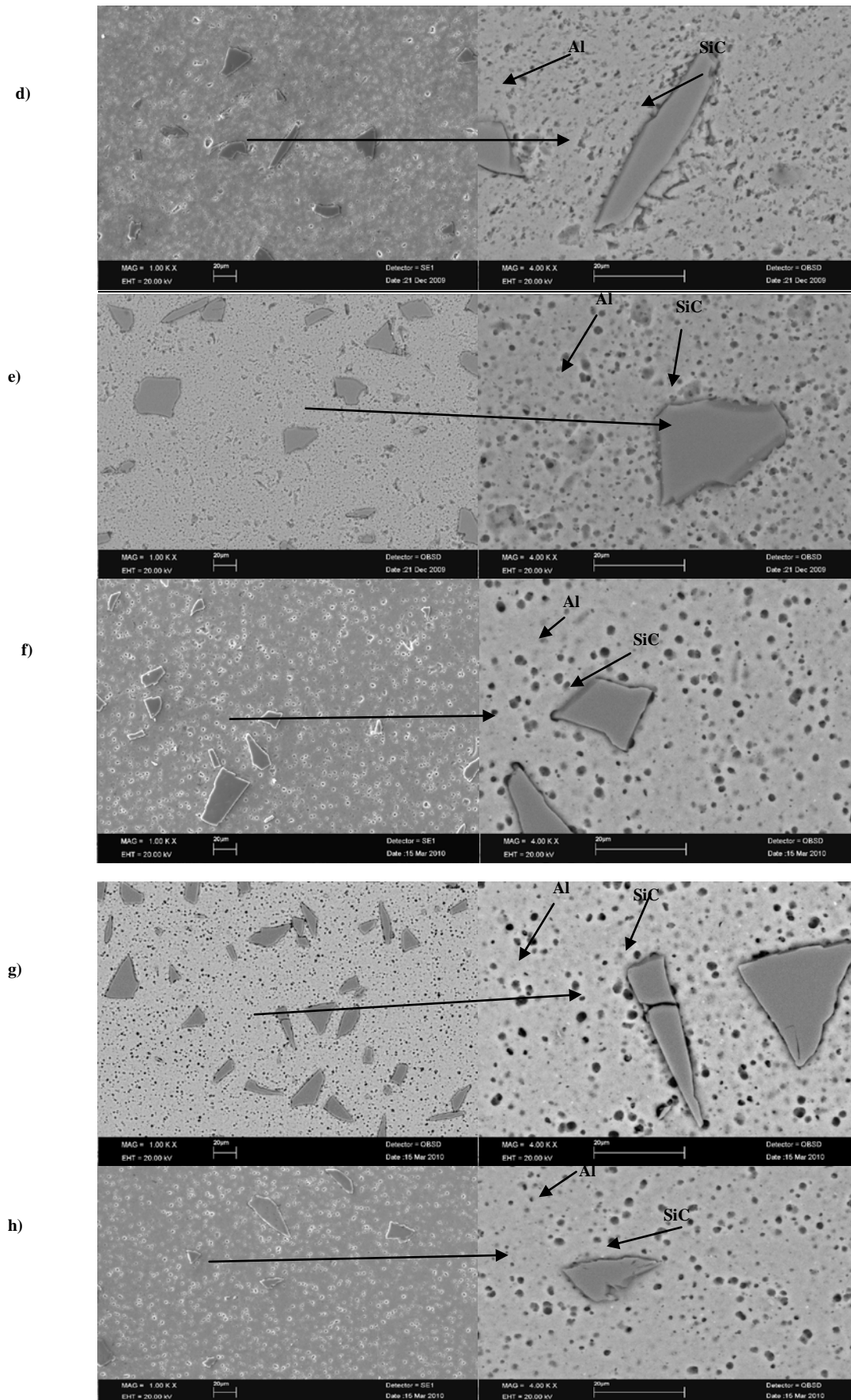


Fig. 5. Microstructure of AA6061/SiC 20 μm/5 composite (d) 3 passes (e)4 passes (f)5 passes (g) 10 passes (h) 15 passes

The microstructures which are shown in Figure 5 (b) to Figure 5 (h) it is clearly seen that matrix and SiC particles compacted together. In other word it can be concluded that there are no space between matrix and SiC particles. AA 6061 powder boundaries which are seen in Figure 5 (a) nearly disappeared after 1 RE cycle. It is understood that if RE cycle increased also deformation effect increases resulting in compact powder grains. When 10 cycles reciprocatingly extruded composite's microstructure is examined (Fig.5 (g)) there are cracks on the SiC particle because of extrusion. In Figure 5 (h) the microstructure was obtained after 15 RE cycles. Al powder grains could not be displayed with big scales by SEM technique. To sum up grain boundaries could not be observed so it cannot be briefly explained that grains were refined.

Hardness measurements were conducted on all the billets and extruded samples using Brinell scale are shown in Table 3. Table 3 is plotted by means of RE cycles. Hardness measurements are mean values.

Table 3. Brinell Hardness of AA 6061 and AA6061/SiC 20 μm/5 composite samples

Sample Number:	RE Cycle Number	Hardness (BSD)	Mean Value
AA 6061 samples			
A3 billet	0	49	49
A3	1	49	49
A4	2	49	
A5	3	49	
A6	4	48	
AA6061/SiC 20 μm/5 composite samples			
A2 billet	0	63	63
A2	1	53	55
A7	2	56	
A8	3	54	
A9	4	54	
A12	5	58	
A11	10	56	
A10	15	58	

Hardness value of unreinforced samples are 49 BSD and mean value for reinforced samples is 55 BSD. By increasing the RE passes, the hardness of the composites was not increased. It can be concluded that hardness can be increased by means of reinforcement.

4. RESULT AND DISCUSSION

To investigate the effect of reciprocating extrusion (RE) pass number for microstructures of Al MMCs reinforced and unreinforced samples were manufactured by sintering.

1. It was not possible to observe grain boundaries when RE cycles increased.
2. Deformation of samples are increased with increasing RE cycles causing matrix in compact structure so in high SEM scales grain boundaries could not be displayed.
3. SiC reinforcement increased AA6061 hardness but with RE cycles hardness were not increased effectively. Generally, the effect of process temperature (350 °C) on the grain size is more efficient than that of the pass number. Because the process temperature is above the recrystallization temperature of the material.

ACKNOWLEDGMENT

The authors would like to thank the Scientific and Technological Research Council of Turkey (TUBITAK) and Erciyes University, for their financial support of this study under project numbers: 108M562.

REFERENCES

- [1]. A. Kr. Mishra, R. Sheokand, Dr. R. K. Srivastava, "Tribological Behaviour of Al 6061/SiC Metal Matrix Composite by Taguchi's Techniques.", *International Journal of Scientific and Research Publications.*, vol.2, pp. 1-8, Oct. 2012.
- [2]. D.Poirier, R. A.Drew, M. L.Trudeau, R. Gauvin. "Fabrication And Properties Of Mechanically Milled Alumina/Aluminum Nanocomposites". *Materials Science and Engineering: A*, vol. 527(29), pp.7605-7614, Nov. 2010.
- [3]. R. R. Fard, F. Akhlaghi, "Effect Of Extrusion Temperature On The Microstructure And Porosity Of A356-SiC P Composites". *Journal Of Materials Processing Technology*, vol.187-188, pp.433-436, June.2007.
- [4]. Abdulhaqq A. Hamid, P.K. Ghosh, S.C. Jain, Subrata Ray, "The Influence of Porosity and Particles Content On Dry Sliding Wear Of Cast in situ Al(Ti)-Al₂O₃(TiO₂) Composite", *Wear*, vol.265(1-2), pp.14-26, June.2008.
- [5]. Abdulhaqq A. Hamid, P.K. Ghosh, S.C. Jain, S. Ray, "Influence Of Particle Content And Porosity On The Wear Behaviour Of Cast in situ Al(Mn)-Al₂O₃(MnO₂) Composite", *Wear*, vol.260 (4-5), pp. 368-378, Feb.2006.
- [6]. I.M .Hutchings, "Tribological Properties Of Metal Matrix Composites", *Mater. Sci. Technol*, vol.10, pp.513-517, Dec.1994.
- [7]. D.J. Lloyd, "Particle Reinforced Aluminium and Magnesium Matrix Composites", *International Materials Reviews*, vol.39, pp.1-23, July.1994.
- [8]. G.J.Howell, A.Ball, "Dry Sliding Wear Of Particulate-Reinforced Aluminium Alloys Against Automobile Friction Materials", *Wear*, vol.181-183, pp.379-390, Feb.1995.
- [9]. A.Venci, I.Bobi, Z. Mijskovi, "Effect Of ThixoCasting And Heat Treatment On The Tribological Properties Of Hypoeutectic Al-Si Alloy", *Wear*, vol.264 (7-8), pp. 616-623, March.2008.
- [10]. R.L.Deuis, C.Subramaniam, J.M.Yellup., "Abrasive Wear Of Aluminium Composites—A Review", *Wear*, vol.201 (1-2), pp.132-144, Dec.1996
- [11]. P .K.Jayashree, M.C .Gowri Shankar, K.Achutha, S.S. Sharma, S. Raviraj , "Review on Effect of Silicon Carbide (SiC) on Stir Cast Aluminium Metal Matrix Composites", *International Journal of Current Engineering and Technology*, vol.3(3), pp.1061-1071, August.2013.
- [12]. R.Z. Valiev, "Paradoxes of Severe Plastic Deformation ", in *Proc. NANOSPD2*, 2002, pp.109-117.
- [13]. M.B. Karamis, F.N. Sari, V. Erturun, "Friction and Wear Behaviors of Reciprocatingly Extruded Al-SiC Composite ", *J.Mater. Process. Tech nol.* vol.212, pp. 2578-2585, July. 2012.
- [14]. M.B. Karamis, V. Erturun, F.N. Sari, "Investigation On Effects Of Reciprocating Extrusion Process On Microstructure Of AA 6061 Based Composites". *Mater. Sci. Technol.* vol.28(12), pp.1379-1384, July ,2012.

BIOGRAPHY

Fatma Nazlı Sarı is an assistant professor at Erciyes University in the Department of Industrial Design Engineering. She received her phd degree in 2016 at Erciyes University in Department of Mechanical Engineering.

Transmission Properties of Metallic Photonic Crystals in One-Dimension

Ali Cetin¹, Nurettin Bilgili²

Abstract

In this study, we have theoretically examined transmission properties of metallic photonic crystals in one dimension by using OptiFDTD software based on finite-difference time-domain approximate method. The light can be controlled by fixing the geometry and refractive indexes in photonic crystals. In our investigation the suitable thickness and layer refractive indexes are optimized. Thus, optical transparency is investigated in this photonic structure.

Keywords: *Metallic photonic crystal, FDTD method, Refractive index, Optical transparency.*

1. INTRODUCTION

Photonic crystals (PCs) are artificially multilayer optical structures which dielectric constants periodically change. The most important feature of these structures is the existence of bandgaps (PBGs). In these bandgaps (or frequency bands), electromagnetic waves are prohibited from propagating through the structure [1]. This special feature of photonic crystals motivates the scientists and engineers to control the flow of light in the realization of modern photonic devices. Because of these interesting features photonic crystals have been great interest and many theoretical and experimental applications progressively carried out [2] – [4]. Photonic crystals are used as antenna, micro strip, solar cells, optical waveguide, etc [5] – [8].

According to ability of the light confinement, PCs can be periodic in one, two or three dimension. One dimensional photonic crystal has attracted extensive studies because of easily fabricated and simply theoretical investigation. In one dimensional photonic crystal, dielectric constants are periodic in one dimension and usually composed of alternating high and low refractive index layers.

First experimental study on the one dimension periodic structures performed by Rayleigh in 1887 [9], who observed reflection of a narrow band of light from a periodic stratified medium illuminated at different angles. In 1970's Yeh and Yariv [10], [11] demonstrated the existence of bandgaps. In 1987, John [12] and Yablonovitch [13] firstly generated two and three dimension PCs independently. Since the end of 1980's, great interests were attracted by the works on photonic crystals.

The materials used for photonic crystals are usually dielectric materials or superconductors. But also metallic materials can be used in photonic crystals. These structures named metallic photonic crystals (MPCs). In metallic photonic crystals different metallic or metallic-dielectric structures lined up. Generally metals are reflective over wide range frequencies [14]. However transmission of bulk metal can be changed by optimizing the thickness and refractive indexes of layers for making transparent aimed at frequency regions.

In this study transmission properties of transverse electric field (TE) component are theoretically investigated in metallic photonic crystals. To create the electromagnetic source, design and change the properties of metallic photonic crystal and to simulate transmission graphs of TE, OptiFDTD software [15] is used. OptiFDTD software uses finite-difference time-domain method.

2. THEORY AND METHOD

Researches on PCs use different techniques such as the transfer matrix method (TMM) [16], the plane wave method (PWM) [17] and the finite-difference time-domain method (FDTD) [18]. Because of simplicity FDTD method is widely used.

In FDTD method, Maxwell equations [19] are solved in complex geometries. The FDTD method is discrete in both time and space.

Maxwell equations in isotropic linear medium is [20],

¹Eskişehir Osmangazi University, Department of Physics, Eskişehir/ Turkey. acetin@ogu.edu.tr

²Eskişehir Osmangazi University, Department of Physics, Eskişehir/ Turkey. nurettinbilgili@gmail.com

$$\begin{aligned}\nabla \times \mathbf{H} &= \varepsilon \frac{\partial \mathbf{E}}{\partial t} + \sigma \mathbf{E} \\ \nabla \times \mathbf{E} &= -\mu \frac{\partial \mathbf{H}}{\partial t} + \sigma_m \mathbf{H}\end{aligned}\tag{1}$$

Where, ε is the dielectric permittivity, σ is the medium conductivity, μ is the permeability of the medium and σ_m is the magnetic loss of the medium. In one dimensional case, suppose the TEM wave goes along z direction. Because of this,

$$\frac{\partial}{\partial x} = \frac{\partial}{\partial y} = 0$$

Eq. (1) changed into

$$-\frac{\partial H_y}{\partial z} = \varepsilon + \frac{\partial E_x}{\partial t} + \sigma E_x\tag{2}$$

$$\frac{\partial E_x}{\partial z} = \mu + \frac{\partial H_y}{\partial t} + \sigma_m H_y\tag{3}$$

In one dimensional photonic crystal every structure can be assume as a node. One dimensional cellular integer time step and half-integer values of \mathbf{E} and \mathbf{H} field component in each node domain are; k (z coordinates of the space component samples) and n (sampling time axis t) for E_x and $k + 1/2$ and $n + 1/2$ for H_y .

Then Eq. 2 and 3 become

$$E_x^{n+1}(k) = \frac{1 - \frac{\sigma(m)\Delta t}{2\varepsilon(m)}}{1 + \frac{\sigma(m)\Delta t}{2\varepsilon(m)}} \times E_x^n(k) - \frac{\frac{\Delta t}{\varepsilon(m)}}{1 + \frac{\sigma(m)\Delta t}{2\varepsilon(m)}} \times \frac{H_y^{n+1/2}(k + \frac{1}{2}) - H_y^{n+1/2}(k - \frac{1}{2})}{\Delta z}\tag{4}$$

$$H_y^{n+1/2}(k + \frac{1}{2}) = \frac{1 - \frac{\sigma(m)\Delta t}{2\mu(m)}}{1 + \frac{\sigma(m)\Delta t}{2\mu(m)}} \times H_y^{n-1/2}(k + \frac{1}{2}) - \frac{\frac{\Delta t}{\mu(m)}}{1 + \frac{\sigma(m)\Delta t}{2\mu(m)}} \times \frac{E_x^n(k + 1) - E_x^n(k)}{\Delta z}\tag{5}$$

If the medium is lossless $\sigma = \sigma_m = 0$ then Eq. 4 and 5 shown simply

$$E_x^{n+1}(k) = E_x^n(k) - \frac{\Delta t}{\varepsilon \Delta z} \left[H_y^{n+1/2}(k + \frac{1}{2}) - H_y^{n+1/2}(k - \frac{1}{2}) \right]$$

$$H_y^{n+1/2}(k + \frac{1}{2}) = H_y^{n-1/2}(k + \frac{1}{2}) - \frac{\Delta t}{\mu \Delta z} [E_x^n(k + 1) - E_x^n(k)]$$

Transmission coefficient is

$$t = \frac{E_t(t)}{E_i(t)}\tag{6}$$

Where $E_i(t)$ is incident wave and $E_t(t)$ is transmitted wave.

From FDTD method we solved Maxwell equations discretely in time. To obtain frequency domain information at any location we have to use Fourier transform of time domain information at that location. If we use Fourier transform,

$$\begin{aligned}F_i(k) &= FFT\{E_i(t)\} \\ F_r(k) &= FFT\{E_r(t)\} \\ F_t(k) &= FFT\{E_t(t)\}\end{aligned}\tag{7}$$

Where k is the number corresponding to each point of Fourier transform sequence? If we take Eq. 7 into Eq. 6 formula of transmission of structure occur.

$$R = \frac{|F_t(k)|^2}{|F_i(k)|^2}\tag{8}$$

3. MODELLING AND SIMULATIONS

Firstly we consider a photonic crystal structure shown in Figure 1.

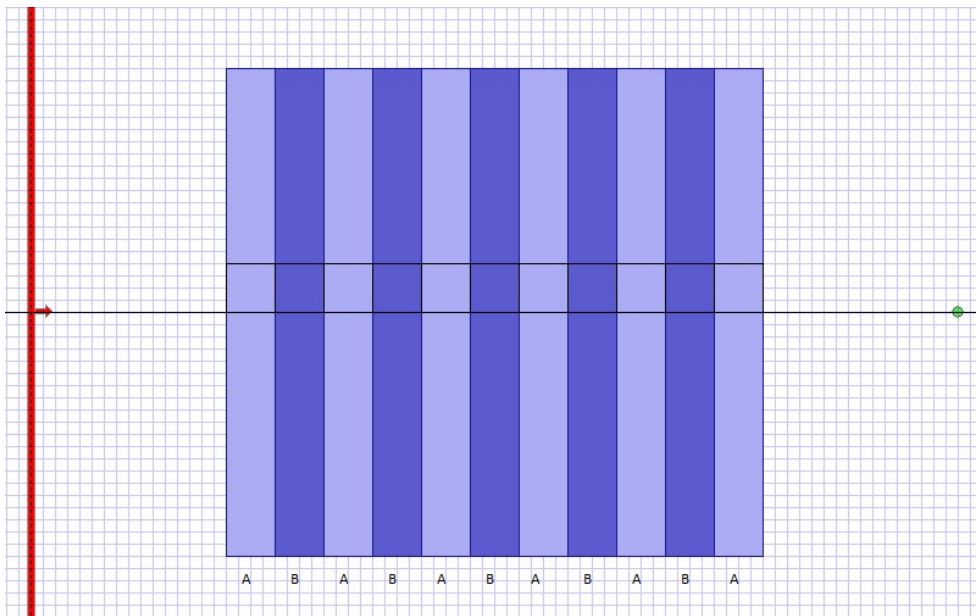


Figure 1: Layout of Photonic Crystal Structure

Where A and B represent Silicon dioxide and Nickel whose refractive indexes are $n_A = 1.44$, $n_B = 3.38$ [21] and thicknesses $d_A = 500 \text{ nm}$, $d_B = 500 \text{ nm}$ respectively. The input plane taken to Gaussian modulated continuous wave whose wavelength is $1.55 \mu\text{m}$ and propagate along z direction.

Figure 2 shows the transmittance of the TE_y from structure that has got 11 layers and each layer thicknesses is 500 nm . In this structure maximum peak occurred at $1.4 \mu\text{m}$.

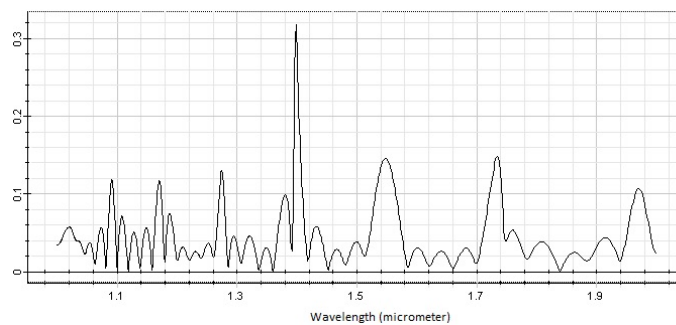


Figure 2: Transmittance graph of structure which layer thicknesses are 500 nm

In Figure 3 the transmittance of TE_y shown when we change the thicknesses of the structures to 1000 nm . In this structure, maximum peak occurred at $1.4 \mu\text{m}$ but value of the peak decreases.

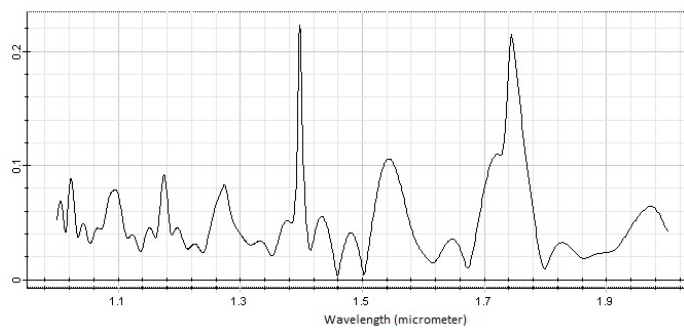


Figure 3: Transmittance graph of structure which layer thicknesses are 1000 nm

In Figure 4 the transmittance of TE_y shown when we change the thicknesses of the structures to 1250 nm . In this structure, maximum peak occurred at $1.4 \mu\text{m}$ to but value increases.

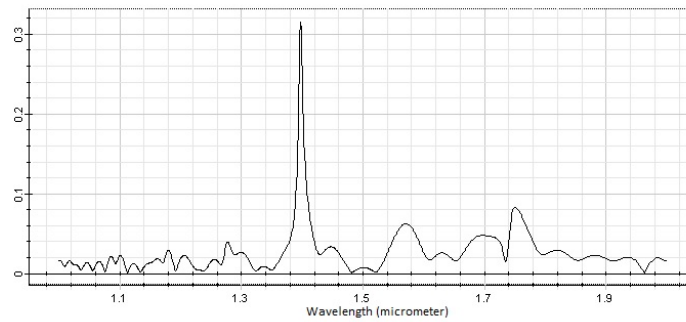


Figure 4: Transmittance graph of structure which layer thicknesses are 1250 nm

In Figure 5, the transmittance of TE_y shown when we change the low refractive index material (Silicon dioxide) to Lithium Niobate $n = 2.21$. Maximum peak increase at $1.4 \mu m$.

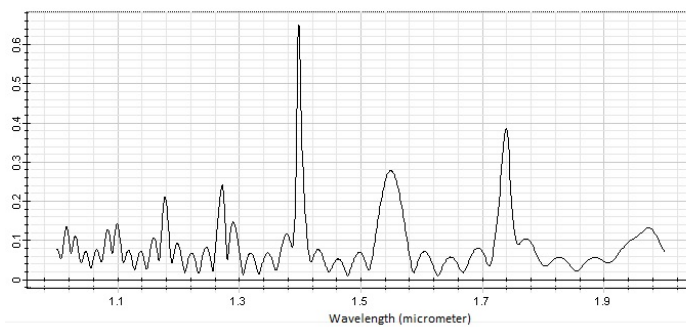


Figure 5: Transmittance graph of Lithium Niobate-Nickel structure

In Figure 6 the transmittance of TE_y shown when we change the low refractive index material (Lithium Niobate) to Titanium Dioxide $n = 2.45$. Maximum peak increase and reach the top value at $1.4 \mu m$.

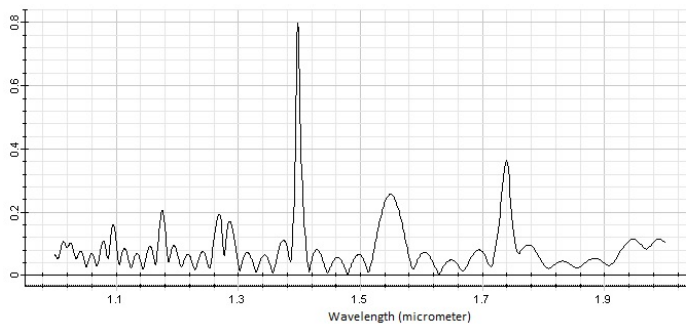


Figure 6: Transmittance graph of Titanium Dioxide -Nickel structure

4. CONCLUSIONS

We have presented theoretical studies of the transmission properties in 1D metallic photonic crystal. Our design simulations show that Silicon dioxide and Nickel PC have maximum transmission in infrared region of spectrum. As increase the thickness of layers from 500 nm to 1000 nm the transmission rate decreases. Then we increase the thickness of layer from 1000 nm to 12500 nm transmission rate increases. But maximum peak coordinates doesn't changed. By replacing the low refractive index material with higher refractive indexes materials the transmission of PC increases. The maximum value increase is 67 % in Titanium Dioxide -Nickel structure.

From our study we can say that electromagnetic waves can be controlled by changing variables of PC. Therefore some applications can be made such as solar cells, laser safety goggles, sunglasses for protection from UV, optical filters, optical sensors, optoelectronic and microwave devices, high-efficiency semiconductor lasers and so on.

REFERENCES

- [1]. Weizong, Chen, et al. "Analysis on band gap of one-dimensional photonic crystal." *Acta Photonica Sinica* 30.9 (2001): 1077-1080.
- [2]. Foresi, J. S., et al. "Photonic-bandgap microcavities in optical waveguides." *nature* 390.6656 (1997): 143-145.
- [3]. Sergeant, Nicholas P., et al. "Design of wide-angle solar-selective absorbers using aperiodic metal-dielectric stacks." *Optics Express* 17.25 (2009): 22800-22812.
- [4]. Patel, Jay S., and Kasra Rastani. "Electrically controlled polarization-independent liquid-crystal Fresnel lens arrays." *Optics letters* 16.7 (1991): 532-534.
- [5]. Chutinan, Alongkarn, Nazir P. Kherani, and Stefan Zukotynski. "High-efficiency photonic crystal solar cell architecture." *Optics Express* 17.11 (2009): 8871-8878.
- [6]. Guenneu, S., et al. "Numerical and theoretical study of photonic crystal fibers." *Progress In Electromagnetics Research* 41 (2003): 271-305.
- [7]. Nozhat, Najmeh, and Nosrat Granpayeh. "Specialty fibers designed by photonic crystals." *Progress In Electromagnetics Research* 99 (2009): 225-244.
- [8]. Yu, Junfei, et al. "Absorption in one-dimensional metallic-dielectric photonic crystals." *Journal of Physics: Condensed Matter* 16.7 (2004): L51.
- [9]. I. A. Sukhoivanov, I. V. Guryev, *Photonics crystals, physics and practical modeling*, Springer, 2009.
- [10]. P. Yeh, A. Yariv, and C. Hong, "Electromagnetic propagation in periodic stratified media. I. General theory," *J. Opt. Soc. Am.*, vol. 67, pp. 423-438, 1977.
- [11]. A. Yariv and P. Yeh, *Optical waves in crystals: Propagation and control of laser radiation*, Wiley, New York, 1984.
- [12]. John, Sajeev. "Strong localization of photons in certain disordered dielectric superlattices." *Physical review letters* 58.23 (1987): 2486.
- [13]. Yablonovitch, Eli. "Inhibited spontaneous emission in solid-state physics and electronics." *Physical review letters* 58.20 (1987): 2059.
- [14]. Scalora, M., et al. "Transparent, metallo-dielectric, one-dimensional, photonic band-gap structures." *Journal of Applied Physics* 83.5 (1998): 2377-2383.
- [15]. <http://www.optiwave.com>
- [16]. Pendry, J. B., and A. MacKinnon. "Calculation of photon dispersion relations." *Physical Review Letters* 69.19 (1992): 2772.
- [17]. Hui, Wang, and Li Yong-Ping. "An eigen matrix method for obtaining the band structure of photonic crystals." (2001): 2172-2178.
- [18]. Z. Zang, S. Satpathy, "Electromagnetic wave propagation in periodic structures: Block wave solution of Maxwell equations", *Phys. Rev. Lett.* 65 (21) (1990) 2650-2653.
- [19]. Mur, Gerrit. "Absorbing boundary conditions for the finite-difference approximation of the time-domain electromagnetic-field equations." *Electromagnetic Compatibility, IEEE Transactions on* 4 (1981): 377-382.
- [20]. Yee, Kane S. "Numerical solution of initial boundary value problems involving Maxwell's equations in isotropic media." *IEEE Trans. Antennas Propag* 14.3 (1966): 302-307.
- [21]. Palik, Edward D. "Handbook of optical constant of solids." Vol. 3. Academic press, 1998.

Multi-Functional Sensor Applications Based on Metamaterial Absorber Designed by Meander-Line Resonator

*Elif Eda Dalkilinc*¹, Olcay Altintas¹, Oguzhan Akgol¹, Muharrem Karaaslan¹*

Abstract

In this study, we present a multifunctional sensor applications based on metamaterial absorber at microwave regime. The proposed structure consists of a meander line type resonator (MLR) topology. Pressure, density and humidity sensing applications are achieved by proposed metamaterial absorber. These applications numerically examined in a full wave commercial simulation software. Since linearity of the sensor depend on resonance frequency shifts, operating frequency band of the structure are chosen carefully. X band is very suitable for sensing ability of proposed structure and it provides linearity depending on pressure, density and humidity. The proposed structure is obtained by placing a sensor layer between two dielectric layers and it is also called sandwich model. Back layer is covered by metallic plate and front layer is designed by MLR. So, we observed sensing ability of the proposed structure due to dielectric changes of the sample placing sensor layer. Moreover, proposed model has wide range application areas such as medical, biological, agricultural in microwave frequency band.

Keywords: Absorber, sensors, X-band

1. INTRODUCTION

Metamaterials (MTMs) are structures having many unusual electromagnetic properties such as simultaneous negative refraction, negative permittivity and negative permeability. The first theoretical study on MTMs was achieved by Veselago in 1968 [1]. After about 30 years, Pendry et al. put this theoretical study into practice with the help of an artificial construction which has split rings [2]-[3]. Negative permittivity and negative permeability were obtained by Pendry et al. in 1996 and 1999, respectively. In 2000, Smith et al. performed first double negative material (DNG) with the split rings and wires [4]. In recent years, because of the some advantages of MTMs such as easy fabrication, low loss and configurable for desired applications, many technological devices such as sensors, absorbers and polarization converters are rebuild by using MTMs [5]-[9].

In this paper, we offer a multi-functional sensor applications based on a MTM absorber. The architecture of proposed MTM sensor consists of meander-line resonator (MLR) topology. The sensor has pressure, density and humidity sensing ability at X-band microwave regime. All the sensing abilities give us a linear response between at 9 GHz - 10 GHz. Pressure sensing ability is tested by distance between two plates of the structure.

Density sensing ability is simulated by Arlon type dielectric materials which have different density values. Three type of Arlon dielectric materials are placed at the sensor layer as AR 300, AR 350 and AR450, respectively and linear response is obtained. In addition, humidity sensor application is achieved by proposed sensor structure. The epsilon and loss tangent values which correspond to percentage humidity of silt loam are taken by the literature. These variables are defined as new materials and placed at the sensor layer in the simulation study. Besides the sensor features, the proposed model can be used as an absorber at X - band microwave frequency. It has many potential application areas such as medical, biological and agricultural.

2. DESIGN OF THE PROPOSED SENSOR

We offer a sandwich model sensor structure based on metamaterial absorber. The proposed model consists of copper meander line resonator topology and sandwich layer between two FR4 dielectric substrate with a thickness, loss tangent and relative permittivity of 1.6 mm, 0.02 and 4.3 respectively. Back of the structure is covered by copper metal plate which is conductivity of 5.80001×10^7 S/m as shown in Figure 1(a). The structure fixed at 22.86 mm \times 10.16 mm rectangular loop due to X-band waveguide dimension and L1, L2, h and w is 5 mm, 4.33 mm, 6.6 mm and 0.4 mm, respectively as shown in Figure 1(b).

¹Corresponding author: Iskenderun Technical University, Department of Electrical and Electronics Engineering, 31200 Iskenderun/Hatay, Turkey, elifedadalkilinc@gmail.com

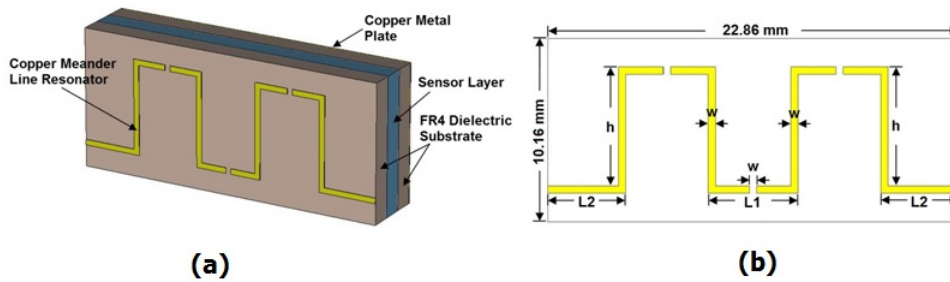


Figure 3. (a) Perspective view and (b) dimensions of the proposed structure

3. SIMULATION STUDY

Three sensor applications are developed by the simulation study for proposed structure based on metamaterial absorber. Sensor layer is defined as air-gap for pressure sensor application. When thickness of the sensor layer which is filled by air increases or decreases, capacitive effect is changed in the structure. Resonance frequency shifts are caused by this fact. Proposed sensor structure responses linear frequency shifts against different thickness values and it has also perfect absorption activity for each air-gap thickness as shown in Figure 2(a).

All the sensor applications have near perfect absorption activity. Perfect absorption can be expressed as zero reflection and transmission. Transmission is set to zero thanks to a metal plate which is cover back of the structure and reflection is prevented at the resonance frequency.

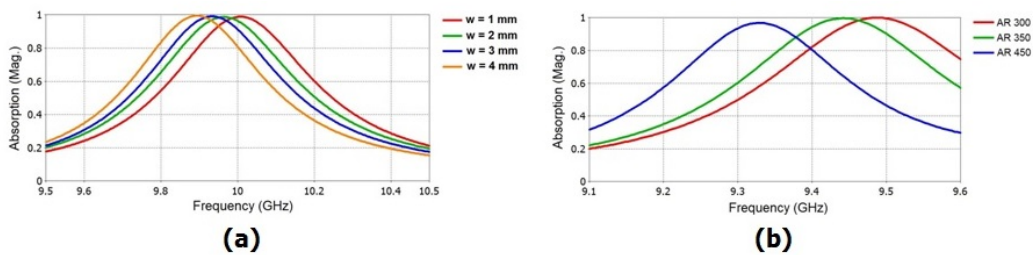


Figure 2. Simulation study results of (a) pressure sensor and (b) density sensor applications

Density sensor application is realized by the Arlon type dielectric materials. Arlon 300, Arlon 350 and Arlon 450 have a density of 2.07 g/cm^3 , 2.2 g/cm^3 , 2.4 g/cm^3 , respectively. Linear response is obtained in the simulation study after these types of materials are placed in sensor layer as shown in Figure 2(b). The structure has also perfect absorption activity at between 9 GHz - 9.5 GHz.

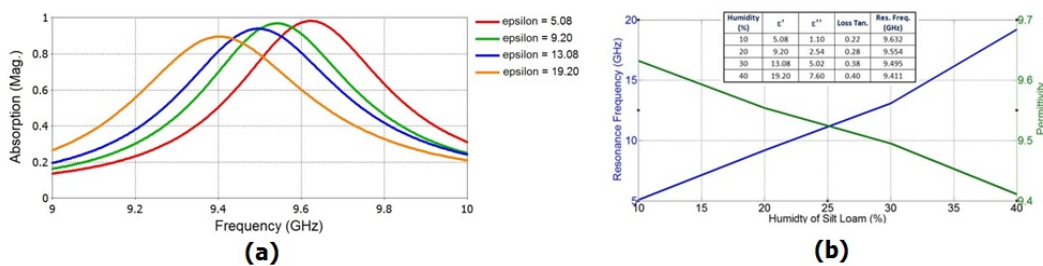


Figure 3. Simulation study result of (a) humidity sensor application and (b) its linearity graph

Some electromagnetic properties of humid silt loam is taken by the literature for humidity sensing application. The permittivity values of 5.08, 9.20, 13.08 and 19.20 correspond to humidity of %10, %20, %30 and %40 respectively. Near perfect absorption activity is obtained in this application as shown in Figure 3(a). The resonance frequencies are shown in Figure 3(b) due to the ratio of percentage change in humidity of silt loam.

4. CONCLUSION

In this study, three sensor applications based on metamaterial absorber are realized at X - band microwave frequency regime. The sensor structure is sandwich type and it is designed by using meander-line topology. Simulation studies are realized by placing the sample in the sensor layer of the structure. Linear responses are obtained for pressure, density and humidity sensing applications. In addition, absorption results are near perfect for each application. Proposed structure can

be used in many application areas such as medical, agricultural and defense industry. Besides, it can be easily fabricated and rearranged for different sizes.

ACKNOWLEDGMENT

We would like to thank the Scientific and Technological Research Council of Turkey (TUBITAK 114E295 and 113E290) for its financial support.

REFERENCES

- [1]. V. G. Veselago, "The electrodynamics of substances with simultaneously negative values of ϵ and μ ," *Sov. Phys. Usp.*, Vol. 10, No. 4, p. 509–514, 1968.
- [2]. J. B. Pendry, A. J. Holden, W. J. Stewart, I. Youngs, "Extremely low frequency plasmons in metallic mesostructures," *Physical Review Letters*, Vol. 76, p. 4773–4776, 1996.
- [3]. J. B. Pendry, A. J. Holden, D. J. Robbins, W. J. Stewart, "Magnetism from conductors and enhanced nonlinear phenomena," *IEEE Transactions on Microwave Theory and Techniques*, Vol. 47, p. 2075–2084, 1999.
- [4]. D. R. Smith, W. J. Padilla, D. C. Vier, S. C. Nemat-Nasser, S. Schultz, "Composite medium with simultaneously negative permeability and permittivity," *Physical Review Letters*, Vol. 84, p. 4184–4187, 2000.
- [5]. F. Dincer, M. Karaaslan, S. Colak, E. Tetik, O. Akgol, O. Altintas, C. Sabah, "Multi-band polarization independent cylindrical metamaterial absorber and sensor application", *Modern Physics Letter B*, vol. 30, p. 1650095, 2016.
- [6]. M. Karaaslan and M. Bakir, "Chiral metamaterial based multifunctional sensor applications," *Progress In Electromagnetics Research*, Vol. 149, p. 55-67, 2014.
- [7]. F. Dincer, O. Akgol, M. Karaaslan, E. Unal, and C. Sabah, "Polarization angle independent perfect metamaterial absorbers for solar cell applications in the microwave, infrared, and visible regime," *Progress In Electromagnetics Research*, Vol. 144, p. 93-101, 2014.
- [8]. W. Withayachumnankula, K. Jaruwongrungrueeb, A. Tuantranont, C. Fumeaux, and D. Abbotta, "Metamaterial-based microfluidic sensor for dielectric characterization," *Sensors and Actuators A: Physical*, Vol. 189, p. 233–237, 2013.
- [9]. F. Dincer, M. Karaaslan, E. Unal, and C. Sabah, "Dual-band polarization independent metamaterial absorber based on omega resonator and octa-star strip configuration," *Progress In Electromagnetics Research*, Vol. 141, p. 219-231, 2013.

Pressure and Density Sensor Applications Based on Perfect Metamaterial Absorber

Elif Eda Dalkilinc¹, Olcay Altintas¹, Emin Unal¹, Muharrem Karaaslan¹

Abstract

In this paper, we present a numerical study of pressure and density sensor applications based on perfect metamaterial absorber at microwave regime. The proposed structure consists of three resonators having a split ring resonator topology (SRR) placed in an FR4 dielectric substrate. Numerical studies have realized by a commercial full wave simulation program for pressure and density sensing applications. Linearity is the key factor for sensor applications to measure sensitivity of the sample properly. Linear results for pressure and density sensor and perfect absorption activity are obtained by adjusting resonators sizes of proposed structure. The best suitable frequency range for proposed metamaterial absorber is determined as X band due to linearity factor. The sensor layer is placed between two dielectric layers which is called sandwich layers. The back of the structure is covered by a metallic layer to eliminate transmission signal. We observed sensing ability of proposed structure due to constant changes at the resonance frequency and also investigate perfect absorber ability at different frequencies. In addition, proposed model has lots of application areas such as chemical, agricultural, medical in X band.

Keywords: Absorber, sensors, X-band

1. INTRODUCTION

Metamaterials (MTMs) have unusual features such as negative refraction index, strong optical activity, polarization conversion of electromagnetic waves. These properties of MTMs enable to develop signal absorbers, sensors, super lenses etc. MTMs have been investigated theoretically by Veselago in 1968 [1]. Veselago studied simultaneously negative values of permittivity and permeability in theory. After about thirty years, Smith and Kroll achieved to fabricate a MTM periodically with composed of a split ring resonator (SRR) and wires [2]. In the later years, many researchers developed various MTM applications [3]-[4].

In this study, we present multi-functional sensor applications based on a perfect metamaterial absorber (MA) which sense pressure and density according to different environmental parameters. Sensing ability of proposed MA structure is analyzed numerically. Most important factors are the resonance frequency and linearity in proposed sensor applications. Proposed MTM sensor is sandwich type and back of the structure covered by metallic layer to obtain absorption activity. It has been developed by SRR topology at X band microwave frequency regime. Distance between sandwich layers called sensing layer is filled by air for pressure sensor application. Thickness of sensor layer is changed to observe pressure sensing activity. For density sensing activity, Arlon type materials which have different density values are used in the simulation study. Both sensor application have linear response feature and near perfect absorption activity. Proposed structure can be used in many potential applications such as medical and agricultural.

2. DESIGNING OF PROPOSED SENSOR

The proposed structure designed by a sensor layer at between two dielectric substrates called sandwich type sensor as shown in Figure 1(a). Front of the structure has three identical resonator designed by SRR topology and back of the structure is covered by copper type metal plate which is conductivity of 5.80001×10^7 S/m to eliminate transmission. Dielectric substrates are FR4 type dielectric materials having a thickness, loss tangent and relative permittivity of 1.6 mm, 0.02 and 4.3 respectively. Overall dimension of the structure is arranged as 22.86 mm \times 10.16 mm due to X band waveguide size. The resonator dimension is 5.8 mm, 6 mm, 0.5 mm, 0.35 mm, 0.4 mm, 2.9 mm which represents x, y, w, k, d and z, respectively as shown in Figure 1(b).

¹Corresponding author: Iskenderun Technical University, Department of Electrical and Electronics Engineering, 31200 Iskenderun/Hatay, Turkey, elifedadalkilinc@gmail.com

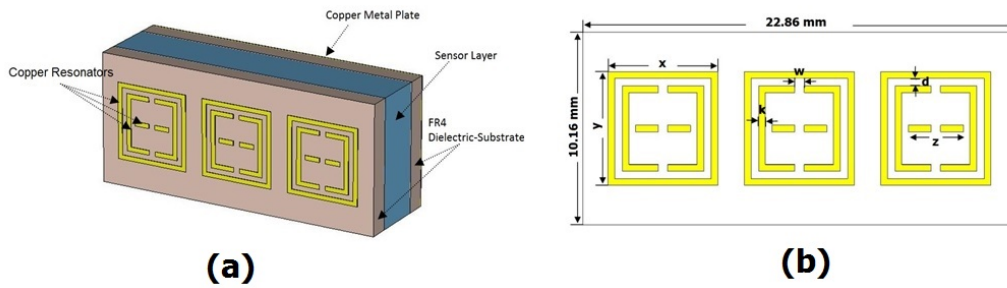


Figure 4. (a) Perspective view and (b) dimensions of the proposed structure

3. SIMULATION STUDY

Simulation studies of proposed sensor structure have been realized by full wave commercial electromagnetic solver simulation program. To obtain perfect signal absorption, transmission and reflection of the signal must be prevented absolutely. Transmission of the signal is set to zero thanks to metal plate at back of the structure. Reflection of the signal is absorbed by resonator of the structure at certain ratio.

Pressure sensor application is achieved by changing thickness of sensor layer which is filled by air-gap. Resonance frequency of the proposed structure shifts to left about 30 MHz for each equal increment of thickness of sensor layer as shown in Figure 2(a). It means that the structure has linearity for pressure sensing application. In addition, proposed pressure sensor absorbs the signals perfectly.

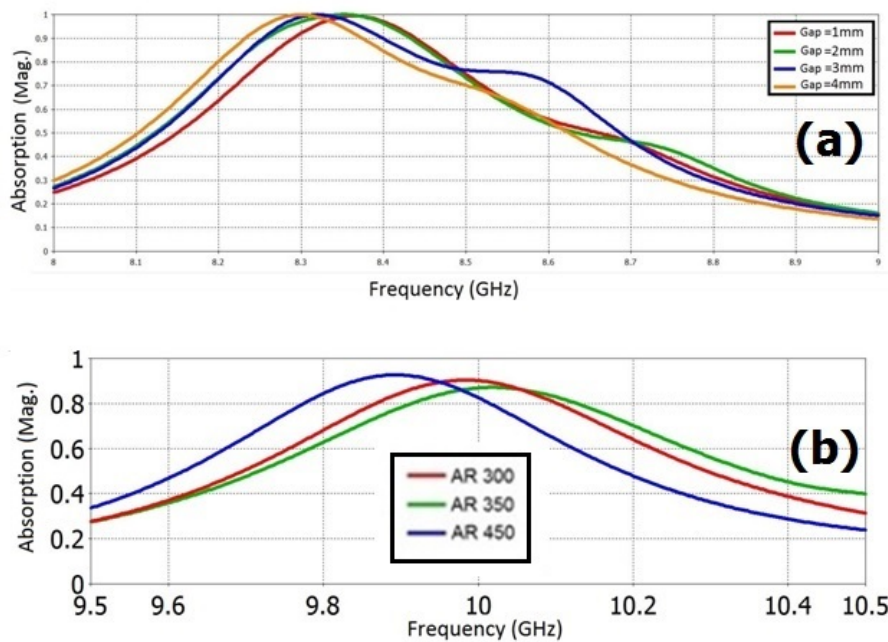


Figure 2. (a) Simulation study results of (a) pressure sensor and (b) density sensor applications

Arlon 300, 350 and 450 which are densities of 2.07 g/cm^3 , 2.2 g/cm^3 and 2.4 g/cm^3 have been used for density sensing application. These materials placed in sensor layer have a great impact on resonance frequency of structure. When the density of the sensor layer increases, the resonance frequency shifts linearly to the left as shown in Figure 2(b). It demonstrates that the density sensing activity is achieved by proposed structure and signal absorption is near perfect.

4. CONCLUSION

In this paper, pressure and density sensor application is numerically realized by perfect metamaterial absorber at X-band microwave regime. The sandwich type proposed sensor structure is designed by SRR topology. We observed that sensing ability of the proposed structure is due to dielectric changes of a sample placing sensor layer. Both sensor application has linear response and perfect signal absorption activity. Moreover, proposed model has wide range application areas such as medical, biological, agricultural in microwave frequency band.

ACKNOWLEDGMENT

We would like to thank the Scientific and Technological Research Council of Turkey (TUBITAK 114E295 and 113E290) for its financial support.

REFERENCES

- [1]. V. G. Veselago, "The electrodynamics of substances with simultaneously negative values of ϵ and μ ," *Sov. Phys. Usp.*, Vol. 10, No. 4, p. 509–514, 1968.
- [2]. D. R. Smith and N. Kroll, "Negative Refractive Index in Left-Handed Materials", *Physical Review Letters*, vol. 85, no. 14, p. 2933-2936, 2000.
- [3]. F. Dincer, M. Karaaslan, S. Colak, E. Tetik, O. Akgol, O. Altintas, C. Sabah, "Multi-band polarization independent cylindrical metamaterial absorber and sensor application", *Modern Physics Letter B*, vol. 30, p. 1650095, 2016.
- [4]. M. Karaaslan and M. Bakir, "Chiral metamaterial based multifunctional sensor applications," *Progress In Electromagnetics Research*, Vol. 149, p. 55-67, 2014.
- [5]. G. Barbillon, "Plasmonic nanostructures prepared by soft UV nanoimprint lithography and their application in biological sensing," *Micromachines*, Vol. 3, p. 21–27, 2012.
- [6]. C. Sabah, H. Tugrul Tastan, F. Dincer, K. Delihacioglu, M. Karaaslan, and E. Unal, "Transmission tunneling through the multilayer double-negative and double-positive slabs," *Progress In Electromagnetics Research*, Vol. 138, p. 293-306, 2013.
- [7]. E. Ekmekci, and G. T. Sayan, "Multi-functional metamaterial sensor based on a broad-side coupled SRR topology with a multi-layer substrate," *Applied Physics A: Materials Science & Processing*, Vol. 110, No. 1, p. 189–197, 2013.
- [8]. F. Dincer, C. Sabah, M. Karaaslan, E. Unal, M. Bakir, and U. Erdiven, "Asymmetric transmission of linearly polarized waves and dynamically wave rotation using chiral metamaterial," *Progress In Electromagnetics Research*, Vol. 140, p. 227-239, 2013.

Determination of Potential Groundwater Pollution by Drastic Model and Gis in Mersin, Turkey

Olcay Gülcicek¹, Zeynel A. Demirel¹

Abstract

Mersin is situated in the Mediterranean region of Turkey. The study area is located between latitude 37° 0' 13" - 36° 43' 27" and longitude 34° 29' 44" - 35° 0' 13". Mersin is one of the rapidly growing and industrializing coastal cities. Depending on the rapid growth and industrialization, the demand for drinking and irrigation water is increasing day by day. Mostly water required for industrial facilities and agricultural activities is obtained from the wells. The DRASTIC model is developed by US-EPA and NWWA to determine potential for water contamination in 1987. The DRASTIC model that is based on the geological and hydrogeological information, is used to determine the potential contamination of groundwater against pollutants.

In this study between in the region Mersin and Tarsus, potential of groundwater pollution were detected using DRASTIC model with Geographic Information System (GIS). As a result of DRASTIC model, the coastal areas were identified as high potential for contamination. DRASTIC index was higher in coastal regions. The high drastic index indicates a high sensitivity to contamination. In the areas that have high DRASTIC index; intensive land use, industrialization, agricultural activities and fuel storage areas are available. Accidents that may occur in these regions, the extreme use of agricultural chemicals, lack of infrastructure, would be inevitable groundwater contamination.

Keywords: DRASTIC, Groundwater pollution, Mersin, GIS.

1. INTRODUCTION

The hydrologic cycle describes the continuous movement of water above, on, and below the surface of the Earth. A large part of the freshwater on Earth is located underground [1]. Although groundwater exists everywhere under the ground, some parts of the saturated zone contain more water than others. An aquifer is an underground formation of permeable rock or loose material which can produce useful quantities of water when tapped by a well. Aquifers come in all sizes and their origin and composition is varied. They may be small, only a few hectares in area, or very large, underlying thousands of square kilometres of the earth's surface. They may be only a few metres thick, or they may measure hundreds of metres from top to bottom. [2,3].

Mersin is a rapidly growing and industrializing coastal city. This is due to the rapid growth and industrialization, the demand for drinking and irrigation water use is increasing every day. Water needed for industrial plants and agricultural activities mostly is obtained from the down shallow or deep wells. Water resources in this area were reported to intensive demands, stresses and pollution risks [4]. The long industrial history of Mersin city has results in complex patterns of pollution that impact on the underlying groundwater quality. The dominant industries are textile, cement, food and industrial metal manufacturing like chromium. Population dynamics and agricultural activities in this region have important implications from the groundwater chemistry.

Groundwater contamination assessment methods divide a geographical region into sub-areas in terms of their vulnerability to groundwater contamination; thereafter, effective groundwater protection measures are conducted in areas prone to pollution [5].

Groundwater vulnerability is defined as the tendency of contaminants to reach a specified position in the groundwater system after introduction at some location above the uppermost aquifer [6,7,8].

In any given area, the groundwater within an aquifer, or the groundwater produced by a well, has some vulnerability to contamination from human activities [7]. The concept of groundwater vulnerability to contamination was developed by Margat (1968) [9]. It derives from the assumption that the physical environment may provide some degree of protection of groundwater against human impacts, especially with regard to pollutants entering the subsurface [10]. Many methods have been developed to assess groundwater vulnerability. The overlay/index methods that is one of these methods, combine factors controlling the movement of pollutants from the ground surface into the saturated zone.

The DRASTIC method is one of the overlay/index methods, assess groundwater vulnerability to a wide range of potential contaminants and is a powerful tool for assessing groundwater vulnerability and is widely used [5, 7, 11, 12, 13, 14, 15, 16, 17, 18, 19]. The data the DRASTIC method requires are easily available, which makes it suitable for regional-scale assessments [20].

¹ Corresponding author: Mersin University, Engineering Faculty, Department of Environmental Engineering, Turkey.
olcay.gulcicek@gmail.com, olcayozcer@mersin.edu.tr

In the literature, DRASTIC model and GIS software were used to create groundwater vulnerability maps which are in the aquifers that provide drinking and potable water [21, 22, 23, 24, 25, 26, 27, 28] and in the areas where dense population, industry and agricultural activity [29, 30, 31, 32, 33].

In recently studies were identified to affected the groundwater quality with anthropogenic activities (agricultural, industrial, and domestic) and seawater intrusion. Also, the Karaduvar region was found to contaminated with aromatic hydrocarbons [34, 35, 36, 37, 38].

Fundamental information is required to characterize the existing groundwater pollution in this area in order to establish a sustainable groundwater-use policy. For this purpose, between in the region Mersin and Tarsus, geological and hydrogeological data were collected and potential of groundwater pollution were detected using DRASTIC model with Geographic Information System (GIS). As a result of DRASTIC model, the coastal areas were identified as high potential for contamination. DRASTIC index was higher in coastal regions. The high DRASTIC index indicates a high sensitivity to contamination. In the areas that have high DRASTIC index; intensive land use, industrialization, agricultural activities and fuel storage areas are available. Accidents that may occur in these regions, the extreme use of agricultural chemicals, lack of infrastructure, would be inevitable groundwater contamination.

2. MATERIALS AND METHODS

2.1. Material

2.1.1. Site Description

Mersin is situated in the Mediterranean region of Turkey. The study area is located between latitude $34^{\circ}37'$ and $34^{\circ}57'$ and longitude $36^{\circ}45'$ and $37^{\circ}00'$. The study area is situated in a region with a typical Mediterranean climate. Wet and mild winters, combined with dry and hot summers are typical for the coastal zone around the Mediterranean Sea. Average annual temperature in the area is 18.6°C . The difference in the temperatures between winter and summer is fairly small, as is characteristic of the Mediterranean climate. Yearly average of rainfall is about 600–650mm. Showers start in October and continue till mid-April. Maximum rainfall is in December.

The area of the study area is 1410 km^2 , in the west; Bekiralanı, Kepirli, Çiftlik, Kaleköyü, the east; Hacıbozan, Alifakı, Kelahmet, Ağzıdelik, the north; Gözne, Karadiken, Ulas, in the south; coastline forms a boundary to the workspace. The study area satellite image in Figure 2.1, the digital maps that prepared using MapInfo 9.5 GIS software is shown in Figure 2.2.

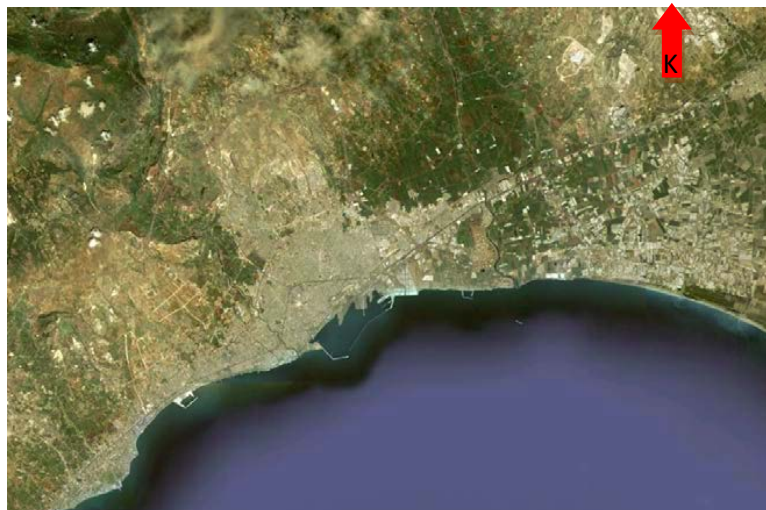


Figure 2.1. Satellite Image of the study area.

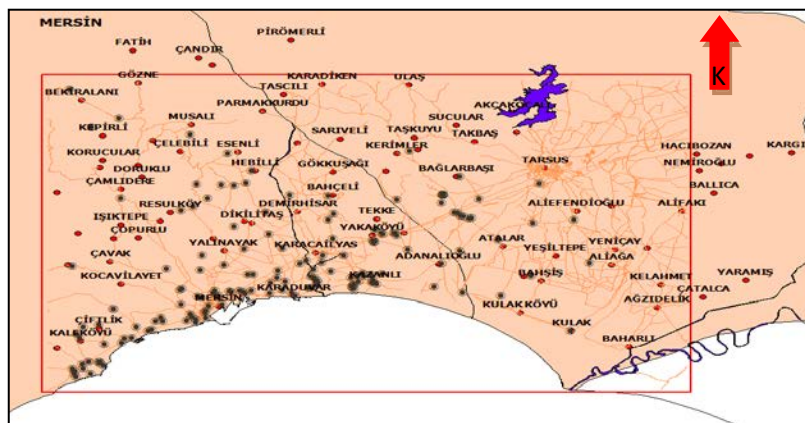


Figure 2.2. Digitized map of the study area (by MapInfo).

2.1.2. Geology and Hydrogeology

The Mersin–Tarsus region (MTR) is bounded by the Taurus Mountains on the northern side and by the Mediterranean Sea on the southern side. The southern portion of the MTR area is a delta plain made up of sediments mainly from Berdan River in the east and partly by Deliçay, and Müftü Creeks in the west direction. Topographic structure in the north of the investigated area (Taurus Mountains) is rugged with altitudes ranging from 300 to 1,100 m.

Rocks and unconsolidated deposits in the area can be divided into four geological units [39]: (1) Paleozoic schist and marble; (2) upper cretaceous Mersin ophiolitic melange; (3) tertiary units; (4) quaternary basin-fill deposits. The oldest rock unit of the MTR is Karahamzalı Formation of Paleozoic Age, which consists of marble, schist and quartzite. Mersin ophiolitic melange (upper cretaceous) is generally found in the northern part of the study area within deep canyons and shows serpentization. Ophiolitic melange contains various rocks with differing compositions including gabbro, harzburgite, verlite, dunite, clinopyroxenite, diabase, and radiolarite. Ophiolitic melange also contains substantial amounts of chromite mineralizations with chromite (Cr_2O_3) contents ranging between 52–60%. Tertiary units are composed of oligomiocene girdirli formation, lower-middle Miocene karaisali formation and guvenc, formation, middleupper Miocene kuzgun formation, and upper Miocene– Pliocene handere formation. Tertiary rocks consist of a succession of marine, lacustrine, and fluvial deposits, which display transitional characteristics both vertically and areally in the study area [40].

The basin-fill deposits vary greatly in lithology and grain-size, both vertically and areally. Accordingly, the hydraulic properties of these deposits can differ greatly over short distances, both laterally and vertically. The gravel and sand deposits of alluvium form the most productive aquifers in the study area. Although almost all of the wells drain the alluvial aquifer the Mersin aquifer consists of quaternary sands and gravel-sand it is recharged mainly by direct infiltration from precipitation.

In the study area, groundwater abstracted from the coastal aquifer is the principal source of water for agricultural, domestic, and industrial uses. Aquifers in the coastal plain are mostly confined or semi-confined in nature due to the presence of clay-silt layers or lenses within the fluvio-deltaic sequence [39].

2.1.3. DRASTIC Model

Various techniques and methodologies have been developed to evaluate environmental impacts associated with groundwater pollution and the concept of aquifer vulnerability is one of them.

Maps are produced from a set of decisional criteria linked to a number of physical parameters but the choice depends on the model used for it. Vulnerability maps can be calculated with the aid of a GIS. GIS allows spatial data gathering and, at the same time, gives a means for data processing, such as geo referencing, integration, aggregation, or spatial analysis [41]. The National Water Well Association [42] developed the DRASTIC model to assess aquifer sensitivity by combining data sets. The DRASTIC model was originally developed as an easy-to-use tool for aquifer vulnerability assessment encompassing diverse hydrogeologic settings based on vulnerability index. The DRASTIC vulnerability index is useful at a regional scale, to prioritise areas into high, moderate and low vulnerability regions, which could be followed up by detailed field investigations. The model is rigid in the assignment of ratings and weights to the model parameters.

Each a letter of the "DRASTIC" represents the required parameters for modelling. These parameters are :

- **D**epth to water
- **R**echarge
- **A**quifer media
- **S**oil media
- **T**opography
- **I**mpact of the vadose zone
- **H**ydraulic Conductivity

These parameters are divided into various hydrological media in itself, and the hydrological media is scored according to the ability of pollutants transmission. Also, each Drastic parameter has a own unique the weight value (Table 2.1-2.2-2.3-2.4-2.5-2.6-2.7) . Drastic index is calculated from these data. The index of each a point shows the contamination potential by other points (Table 2.8). From these parameters a DRASTIC index or vulnerability rating can be obtained. The higher the value for the DRASTIC index, the greater the vulnerability of that location of an aquifer [7].

$$Index(Di) = DrDw + RrRw + ArAw + SrSw + TrTw + IrIw + CrCw \quad (1)$$

(Where w = weight, r = rank)

D- Depth to Water: Depth to Water affects the time available for a contaminant to undergo chemical and biological reactions such as dispersion, oxidation, natural attenuation, sorption etc. A low depth to water parameter will lead to a higher vulnerability rating.

Table 2.1. Ranges and ratings of depth to water-table

(Adapted from US EPA, 1985)

Depth to water (ft) (D)	
Ranges	Ratings
0-5	10
5-15	9
15-30	7
30-50	5
50-75	3
75-100	2
>100	1
Drastic weight : 5	

R- Net Recharge: Net Recharge is the amount of water which enters the aquifer. This value can be calculated on an annual or monthly basis with data available. Although recharge will dilute the contaminant which enters the aquifer, recharge is also the largest pathway for contaminant transport. Therefore, the amount of recharge is positively correlated with the vulnerability rating. Net Recharge can be calculated using climate data by applying a mass balance on the water.

Table 2.2. Ranges and ratings of depth to Recharge (Adapted from US EPA, 1985)

Recharge (in) (R)	
Ranges	Ratings
0-2	1
2-4	3
4-7	6
7-10	8
>10	9
Drastic weight : 4	

A - Aquifer Media: Aquifer Media is used to produce a rating based on the permeability of each layer of media. High permeability allows more water and therefore more contaminants to enter the aquifer. Therefore a high permeability will yield a high vulnerability rating.

Table 2.3. Ranges and ratings of depth to aquifer media (Adapted from US EPA, 1985)

Aquifer Media (A)	
Ranges	Ratings
Coarse shale	2
Metamorphic / igneous	3
Degraded metamorphic / igneous	4
Glacier	5
Bedded lime / sandstone	6
Coarse sand stone	6
Coarse lime stone	8
Sand and gravel	8
Basalt	9
Karstic	10
Drastic weight : 3	

S - Soil Media: Soil media is affects the transport of the contaminant and water from the soil surface to the aquifer. Some of the interactions with soil have already been stated, but for review, the soil media can affect the types of reactions which can take place. Sorption phenomena, for example, can be affected by the structure of the soil surface. Additionally, different soils will provide better habitats for microorganisms which can potentially biodegrade the contaminant.

Table 2.4. Ranges and ratings of depth to soil media (Adapted from US EPA, 1985)

Soil Media (S)	
Ranges	Ratings
Fine or not	10
gravel	10
sand	9
Torf	8
clay	7
Sandy loam	6
loam	5
Silty loam	4
Clay loam	3
fertilizer	2
Non-shrink clay	1
Drastic weight : 2	

T- Topography: The topography of the land affects groundwater vulnerability because the slope of the land is an important factor in determining whether the contaminant released will become run-off or infiltrate the aquifer. With a low slope, the contaminant is less likely to become run-off and therefore more likely to infiltrate the aquifer.

Table 2.5. Ranges and ratings of depth to topography (Adapted from US EPA, 1985)

Topography (m) (T)	
Ranges	Ratings
0-10	10
10-20	9
20-30	5
30-60	3
60-100	1
Drastic weight : 1	

I - Impact of Vadose Zone: The vadose zone is the typical soil horizon above and below the water table, which is unsaturated or discontinuously saturated. If the vadose zone is highly permeable then this will lead to a high vulnerability rating.

Table 2.6. Ranges and ratings of depth to impact of vadose zone (Adapted from US EPA, 1985)

Impact of Vadose Zone (I)	
Ranges	Ratings
Impermeable layer	1
Silt / clay	3
Sedimentary schist	3
Lime stone	3
Sandstone	6
Bedded lime / sandstone	6
Sand and gravel alluvium	6
Sand and gravel	8
Basalt	9
Karstic	10
Drastic weight :: 5	

C-Hydraulic Conductivity: The hydraulic conductivity relates the fractures, bedding planes and intergranular voids in the aquifer. These components become pathways for fluid movement, and likewise pathways for contaminant movement once a contaminant enters the aquifer. The hydraulic conductivity is positively correlated with the vulnerability rating.

Table 2.7. Ranges and ratings of depth to hydraulic conductivity (Adapted from US EPA, 1985)

Hydraulic Conductivity gpd/ft ² (C)	
Ranges	Ratings
1-100	1
100-300	2
300-7	4
700-1000	6
1000-2000	8
>2000	10
Drastic weight : 3	

Table 2.8. Drastic Index Values .

	Index Values
Low	$DI \leq 100$
Middle	$100 < DI \leq 140$
High	$140 < DI \leq 200$
Very High	$200 < DI$

2.2. Methods

In this study aim, the wells in the study area (between Mersin-Tarsus) , determination of the pollution potential of the region and showing the contamination create the thematic map. The determination of the potential for contamination, was used DRASTIC model developed by US-EPA and NWW (National Water Well Association) .

In the study, literature review was conducted in order to be rated according to each well Drastic parameters. According to obtained data coordinates, transferred to Geographic Information System (GIS) and were obtained DRASTIC parameter maps .The depth of the water table was calculated from well profiles for all wells. Visual HELP program was used to calculate the amount of groundwater recharge. Rainfall data of the past years , required to calculate the amount of groundwater recharge, information was entered into the Visual HELP program.Vadose zone and aquifer properties of each wells were identified by the wells profile data and the identified profiles of wells were rated by the DRASTIC model.

The study area soil map was compared according to the coordinates of the wells and the soil type was determined for the each well. According to soil types of wells were converted to polygons and was facilitated to selection of the wells that were in the same soil type.

3. RESULTS AND DISCUSSION

3.1. Results of DRASTIC

Data (depth of the water table ,net recharge, aquifer material, soil type, topography , impact of vadose zone, hydraulic conductivity) required by the DRASTIC program, according to the coordinates it was transferred onto digital maps using MapInfo 9.5 program. By the kriging interpolation method in the DRASTIC program were estimated the values of the dataless points.By the obtained data with interpolation results were calculated the Drastic indexes for the dataless points.In order to determine the hydrogeological characteristics of previously in this study area of State Hydraulic Works (DSI), Rural Services (STS) and the the individual wells data were evaluated .

3.1.1. Water Table Depth

Water table depth was determined to as shown in Figure 3.1, red> yellow> green> blue. When the specified red areas on the map was assessed according to distance from the water table, the red areas were lower than the potential contamination compared to other regions.

Yellow regions were determined to have more pollution potential than the red regions. Likewise, the green regions were determined to have more pollution potential than the yellow regions. The most sensitive areas of contamination were shown blue in the Figure 3.1.

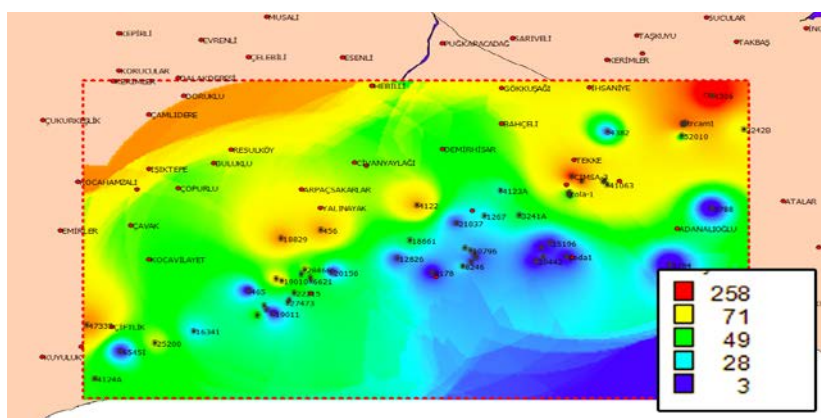


Figure 3.1. Thematic map showing the depth of the water table (meters).

3.1.2. Results of recharge, aquifer material, soil type, topography , impact of vadose zone, hydraulic conductivity.

The amount of annual groundwater recharge in the study area with the help of the Visual HELP software was found to be 3.0458 mm. In the calculation of groundwater recharge was recognized that rainwaters infiltrated homogeneous in each region (Fig 3.2).

The groundwater flow in the study area was determined in the southeastward from northwest. Of the study area; Aquifer media, topography, vadose zone and hydraulic conductivity values of the material were transferred onto a digital map with the MapInfo GIS software program.

3.2. Results of DRASTIC Index

By the map, that created by the DRASTIC indexes, was determined the distribution of the pollution potential of the between the Mersin -Tarsus region (Fig.3.2). By the obtained DRASTIC thematic map (Fig.3.2) was identified as high pollution potential of coastal areas .

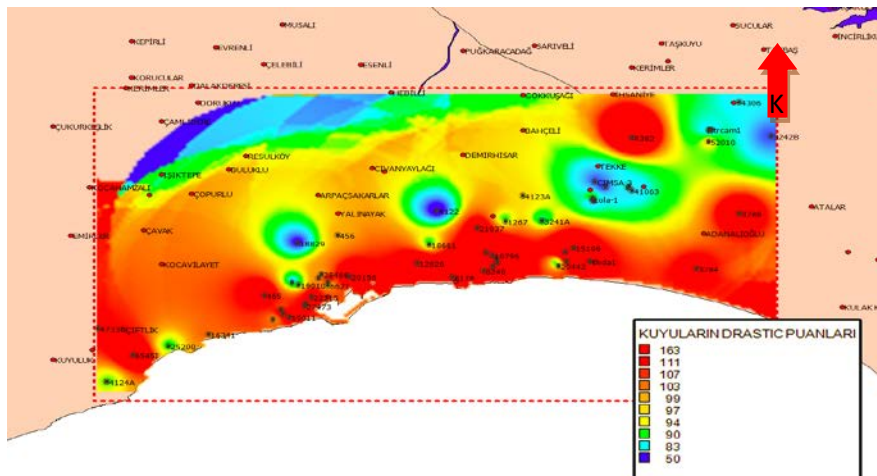


Figure 3.2 Vulnerability distribution map (DRASTIC Index) of groundwater contamination.

4. CONCLUSIONS

The study suggests that the DRASTIC model can be used for prioritization of vulnerable areas in order to prevent the further pollution to already more polluted areas. There is a need to develop a system that can be used to identify areas where attention or protection effort is required.

The DRASTIC model, which is used for preparing the pollution potential map, can be used as a screening tool to see whether a particular area is more or less vulnerable to groundwater pollution. High vulnerable water zones are usually difficult to monitor, as it requires the drilling of many monitoring wells, which is very expensive. The vulnerability map produced in this study gives a decision maker a very comprehensive idea of areas that need to be closely monitored, as well as those areas which are less likely to become contaminated and require less intensive monitoring.

There should be a detailed and frequent monitoring in high and very high vulnerable zones in order to monitor the changing level of pollutants.

Groundwater contamination potential distribution map in study area that derived from DRASTIC index, (Figure 4.1) was transferred on Google Earth .

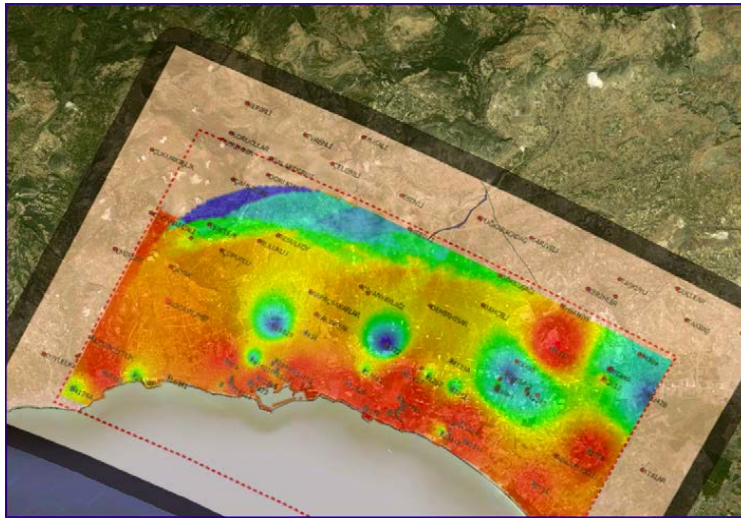


Figure 4.1. Vulnerability map (DRASTIC Index) of groundwater contamination on the digital map.

In the Figure 4.1 is shown risk of groundwater contamination, according to it is high Drastic index.

As a result of DRASTIC model, the coastal areas were identified as high potential for contamination. DRASTIC index was higher in coastal regions. The high drastic index indicates a high sensitivity to contamination. In this study, in the high DRASTIC index areas should be noted that presence of land use, industries, agriculture and oil storage areas. In these areas, it is inevitable that contaminate of groundwater. Accidents that may occur in these regions, the extreme use of agricultural chemicals, lack of infrastructure, would be inevitable groundwater contamination. The study suggests that the DRASTIC model can be used for prioritization of vulnerable areas in order to prevent the further pollution to already more polluted areas. There is a need to develop a system that can be used to identify areas where attention or protection effort is required.

High vulnerable water zones are usually difficult to monitor, as it requires the drilling of many monitoring wells, which is very expensive. The vulnerability map produced in this study gives a decision maker a very comprehensive idea of areas that need to be closely monitored, as well as those areas which are less likely to become contaminated and require less intensive monitoring. The mapping technique used for this analysis is a qualitative method of describing the occurrence and distribution of groundwater pollution. Before performing any activities that can cause of groundwater contamination, should be used this map as a reference will prevent the contamination of groundwater.

REFERENCES

- [1].](2013) USGS, Natural Processes Of Ground-Water And Surface-Water Interaction [Online]. Available: http://pubs.usgs.gov/circ/circ1139/htdocs/natural_processes_of_ground.htm
- [2]. (2013) *Environment and Climate Change Canada* [Online]. Available: <http://www.ec.gc.ca/eau-water/default.asp?lang=En&n=300688DC-1#sub2>
- [3]. Afşin, M., Kayabalı, K. "Uygulamalı Hidrojeoloji", 4. Baskı, Gazi Kitabevi, Ankara, (2004), 682 S.
- [4]. Demirel, Z., "The history and evaluation of saltwater intrusion into a coastal aquifer in Mersin, Turkey (2004)", *Journal of Environmental Management*, 70(3), pp.275-282
- [5]. Neshat, A. Pradhan, B. DadrasM. "Groundwater vulnerability assessment using an improved DRASTIC method in GIS", *Resources, Conservation and Recycling* 86 (2014) 74–86.
- [6]. Worrall, F., Besien, T., 2005. The vulnerability of groundwater to pesticide contamination estimated directly from observations of presence or absence in wells. *J. Hydrol.* 303 (1–4), 92–107.
- [7]. Rahman, A., 2008. A GIS based DRASTIC model for assessing groundwater vulnerability in shallow aquifer in Aligarh, India. *Appl. Geograp.* 28 (2008), 32–53.
- [8]. Bai, L., Wang, Y., Meng, F., 2011. Application of DRASTIC and extension theory in the groundwater vulnerability evaluation. *Water Environ. J.* 26 (2012), 381–391.
- [9]. Margat, J., 1968. Vulnérabilité des nappes d'eau souterraine à la pollution. Bases de la cartographie, (Doc.) 68 SGC 198 HYD, BRGM, Orleans, France.
- [10]. Tilahun, K., Merkel, B.J., 2010. Assessment of groundwater vulnerability to pollution in Dire Dawa, Ethiopia using DRASTIC. *Environ. Earth Sci.* 59 (2010), 1485–1496.
- [11]. Knox, R.C., Sabatini, D.A., Canter, L.W., 1993. *Subsurface Transport and Fate Processes*. Lewis Publishers, USA.
- [12]. Osborn, N.I., Eckenstein, E., Koon, K.Q., 1998. Vulnerability assessment of twelve major aquifers in Oklahoma. Oklahoma Water Resources Board Technical Report 98-5.
- [13]. Kim, Y.J., Hamm, S., 1999. Assessment of the potential for groundwater contamination using the DRASTIC/EGIS technique, Cheongju area, South Korea. *Hydrogeol. J.* 7 (2), 227–235.
- [14]. Al-Adamat, R.A.N., Forster, I.D.L., Baban, S.M.J., 2003. Groundwater vulnerability and risk mapping for the basaltic aquifer of the Azraq basin of Jordan using GIS, Remote sensing and DRASTIC. *Appl. Geograp.* 23, 303–324.
- [15]. Hamza, M.H., Added, A., Rodriguez, R., Abdeljaoued, S., Mammou, B., 2007. A GIS based DRASTIC vulnerability and net recharge reassessment in an aquifer of a semi-arid region (Metline-Ras Jebel-Raf Raf aquifer, Northern Tunisia). *J. Environ. Manage.* 84, 12–19.

- [16]. Leone, A., Ripa, M.N., Uricchio, V., Deak, J., Vargay, Z., 2009. Vulnerability and riskevaluation of agricultural nitrogen pollution for Hungary's main aquifer using DRASTIC and GLEAMS models. *J. Environ. Manage.* 90, 2969–2978.
- [17]. Voudouris, K., Kawakis, N., Polemio, M., Karelas, K., 2010. Assessment of intrinsic vulnerability using DRASTIC model and GIS in the Kiti aquifer, Cyprus. *Eur. Water* 30, 13–24.
- [18]. Hallaq, A.A., Elaish, B.A., 2011. Assessment of aquifer vulnerability to contamination in Khanyounis Governorate, Gaza Strip – Palestine, using the DRASTIC model within GIS environment. *An-Najah Univ. J. Res. – Nat. Sci.* 25, 2011
- [19]. Fraga, C.M., Fernandes, L.F.S., Pacheco, F.A.L., Reis, C., Moura, J.P., 2013. Exploratory assessment of groundwater vulnerability to pollution in the Sordo River Basin, Northeast of Portugal. *Revista Escola de Minas, Ouro Preto* 66 (1), 49–58.
- [20]. Thapinta, A., Hudak, P.F., 2003. Use of geographic information systems for assessing groundwater pollution potential by pesticides in Central Thailand. *Environ. Int.* 29, 87–93.
- [21]. Lynch, S. D., Reynders, A. G., & Schulze, R. E., "Preparing input data for a national-scale groundwater vulnerability map of southern Africa". Document ESRI 94 (1994).
- [22]. Osborn NI, Eckenstein E, Koon KQ Vulnerability assessment of twelve major aquifers in Oklahoma. Technical Report, Oklahoma Water Resources Board, Tulsa, OK., (1998). pp: 98–95.
- A. Added, M.H. Hamza "Evaluation of the vulnerability in Metline aquifer (Northeast of Tunisia), ESRI User Conference, San Diego, USA (1999)
- [23]. Demirkıran, O. "Ovaçay Havzasındaki Akiferlerin Kirliliğe Duyarlılığının Belirlenmesinde Yeraltısu Seviye Değişimlerinin Etkisi", Toprak Gübre ve Su Kaynakları Merkez Araştırma Enstitüsü, Ankara, (2012).
- [24]. R. Al-Adamant, I. Foster and S. Baban, "Groundwater Vulnerability and Risk Mapping for the Basaltic Aquifer of the Azraq Basin of Jordan Using GIS, Remote Sensing and DRASTIC," *Applied Geography*, Vol. 23, No. 4, (2003) pp. 303-324.
- [25]. Babiker IS, Mohamed MAA, Hiyama T, Kato K A GIS-based DRASTIC model for assessing aquifer vulnerability in Kakami-gahara Heights Gifu Prefecture, central Japan. *Sci Total Environ* , (2005), 345:127–140.
- [26]. Yıldırım, M., Topkaya, B. "Antalya Kentindeki İçme Suyu Kaynaklarının Kirlenme Potansiyelinin Uzaktan Algılama ve Coğrafi Bilgi Sistemleri Kullanılarak Belirlenmesi", Akdeniz Üniversitesi Çevre Mühendisliği Bölümü, Antalya, (2000).
- [27]. Erdem, E. "Mersin-Tarsus Arasında Alüvyon Akiferde Yeraltı Suyu Kirliliğinin Fotometrik Ölçümler ile Araştırılması", Yüksek Lisans Tezi, Mersin Üniversitesi Fen Bilimleri Enstitüsü Jeoloji Mühendisliği Ana Bilim Dalı, Mersin, (2006) pp 100
- [28]. Navulur, K.C.S., Engel, B.A. "Predicting spatial distribution of vulnerability of Indiana State aquifer system to nitrate leaching using a GIS", USA, (1997).
- [29]. Thirumalaivasan D, Karmegam M, Venugopal K AHP- DRASTIC: software for specific aquifer vulnerability assessment using DRASTIC model and GIS. *Environ Modell Softw* (2003) ,18:645–656.
- [30]. Secunda S, Collin ML, Melloul AJ Groundwater vulnerability assessment using a composite model combining DRASTIC with extensive agricultural land use in Israel's Sharon region. *J Environ Manage* 54:39–57, (1998)
- [31]. Almasri M., "Assessment of intrinsic vulnerability to contamination for Gaza coastal aquifer, Palestine", *Journal of Environmental Management* , Volume 88, Issue 4, September, , (2008), P. 577–593.
- [32]. Remesan R., Panda R.K. " Groundwater vulnerability assessment, risk mapping, and nitrate evaluation in a small agricultural watershed: Using the DRASTIC model and GIS" *Environmental Quality Management*, [Volume 17, Issue 4](#), (2008), pp: 53–75.
- [33]. Hatipoğlu, Z., Bayarı, C.S "Geostatistical estimation of hydraulic conductivity and effective porosity distribution: A case study of Mersin-Tarsus coastal and hillside aquifers" *Jeoloji Mühendisliği Dergisi*, Volume 29, Issue 2, 2005, Pages 1-9
- [34]. Demirel, Z., Külege, K. "Monitoring of spatial and temporal hydrochemical changes in groundwater under the contaminating effects of anthropogenic activities in Mersin Region, Turkey " *Environmental Monitoring and Assessment* , Volume 101, Issue 1-3, January 2005, Pages 129-145
- [35]. Güler, C. , Kaplan, V., Akbulut, C. "Spatial distribution patterns and temporal trends of heavy-metal concentrations in a petroleum hydrocarbon-contaminated site: Karaduvar coastal aquifer (Mersin, SE Turkey) " *Environmental Earth Sciences*, Volume 70, Issue 2, September 2013, Pages 943-962
- [36]. Kurt, M.A. , Güler, C., Alpaslan, M., Akbulut, C. "Determination of nitrate and nitrite origins in the soils and ground waters of the area between mersin-tarsus (Turkey) using geographic information systems " *Carpathian Journal of Earth and Environmental Sciences*, Volume 7, Issue 4, 2012, Pages 181-188
- [37]. Güler, C. , Kurt, M.A., Alpaslan, M., Akbulut, C. "Assessment of the impact of anthropogenic activities on the groundwater hydrology and chemistry in Tarsus coastal plain (Mersin, SE Turkey) using fuzzy clustering, multivariate statistics and GIS techniques " *Journal of Hydrology*, Volume 414-415, 11 January 2012, Pages 435-451.
- [38]. Güler, C. , Kurt, M.A., Korkut N., "Assessment of groundwater vulnerability to nonpoint source pollution in a Mediterranean coastal zone (Mersin, Turkey) under conflicting land use practices", *Ocean & Coastal Management* 71 (2013) . 141-152
- [39]. Şenol, M., S. ahin, S., , Duman, T.Y., 1998. Adana-Mersin Dolayının Jeoloji Etüd Raporu. MTA, Ankara.
- [40]. Burrough, P. A., & McDonnell, R. A. (1998). *Principals of geographical information systems*. Oxford: Oxford University Press.
- [41]. Aller, L., Bennet, T., Lehr, J. H., Petty, R. J., & Hacket, G. (1985). *DRASTIC: A standardized system for evaluating groundwater pollution using hydrological settings*. Ada, OK, USA: Prepared by the National water Well Association for the US EPA Office of Research and Development.

Biography:

Dr. Olcay Gülçiçek

She was born in 1985 in North Cyprus. After she completed basic education in N. Cyprus, she studied Environmental Engineering Department between the years 2002-2006 in the Mersin University. Immediately after, she was awarded a master's degree (in 2008) and a doctorate degree (in 2014), respectively.

In Department of Environmental Engineering between the years 2008-2014, she worked as a research and teaching assistant.

Currently, she works as a Laboratory Expert in the same department.

Investigation on Effect of Tool Geometry on the Surface Roughness in Machining AISI D2 Steel

*Metin Zeyveli*¹

Abstract

In this study, machining tests were carried out surface quality on AISI D2 steel. The machining tests were performed through single point turning using coated cemented carbide tools with traditional nose radius and wiper nose radius at four different cutting speeds (70, 130, 190, 250 m/min), four different feed rates (0.05, 0.1, 0.15, 0.20 mm/rev) and 1 mm constant depth of cut without using coolant. The influences of nose radius, cutting speed and feed rate on surface roughness and chip formation were investigated. Cutting speed significantly affected the machined surface roughness values. Surface roughness was most sensible to changes in cutting tool geometry from the other parameters. Wiper geometry were provided lower surface roughness at higher cutting speed and third feed rate value, according to the standard geometry.

Keywords: ANOVA, Wiper, Machining, Surface Roughness, AISI D2.

1. INTRODUCTION

Tool steels are widely subjected to machining operations. A large portion of machining operations carried on tool steels belongs to the die and mould sector. Due to their high wear resistance, high toughness and good hardening properties, AISI D2 tool steels are widely used for making of dies and moulds for cutting, bending, deep drawing, spinning, cold extrusion and plastic injection moulding [1].

Surface roughness is related to surface finish one of the machinability criteria and plays an important role on the part's fatigue life, corrosion behaviour and crack propagation rate [2]. Surface roughness of a machined part depends on many factors that can be grouped as follows: a) geometric factors, b) work material factors and c) vibration and machine tool factors [3]. In machining, there are various parameters. Some of them like cutting speed and feed rate can be controlled, while the other parameters like tool geometry, tool wear, chip forms and tool-workpiece couple cannot be controlled [4].

In the past studies were carried out on the machinability of AISI D2 steel and cold work tool steel. Reginaldo et al. [5] carried out studies FEM (finite element analyses) studies in order determine and improve machining performance. They compared the FEM results with the experimental ones. Khaider et al. [6] examined tool wear and cutting force variations depending on the workpiece hardness and cutting speed in the machining of hardened materials. They also examined the relation between surface roughness and cutting parameters like cutting speed and feed rate. Lima et al. [7] evaluated the machinability of materials of various hardness levels using different cutting tools. They reported that at low cutting speed and high feed rate, the surface roughness values increased while at high cutting speed and low feed rate it decreased. They also reported that machining of AISI D2 steel of 58 HRC using mixed alumina cutting tools led to the surface roughness values as low as to those obtained by grinding. Arsecularatne et al. [8] determined the optimum cutting speed and feed rate ranges in machining of hardened materials using PCBN cutting tools. In their study, it was revealed that flank wear was the dominant wear mode and that the acceptable long tool life and higher metal removal rate were obtained at low speeds. Grzesik et al. [9] investigated the influence of ceramic tool nose radius on surface roughness when machining hardened low chromium alloy steel. Two different surface topographies were obtained using standard and wiper geometries at 0.1 and 0.2 mm/rev feed rates, respectively. Özel et al. [10] carried out studies in order to examine the machinability of cold work tool steel using ceramic cutting tools with wiper nose radius as cutting tool nose design influenced the roughness and productivity. For this purpose, they developed multi linear regression analyses and artificial neural network model and predicted the surface roughness and tool flank wear. Davim et al. [11] examined the machinability of cold work tool steel using ceramic cutting tool and the determination of constant starting cutting parameters for their experimental study was based on orthogonal array. Amin et al. [12] investigated the influence of pre-heat treatment of hardened AISI D2 cold work tool steel on surface roughness, chatter and tool performance when end milling. Their results showed that surface roughness values of pre-heat treated workpiece were lower than 0.4 μm .

The aim of this study was to determine optimum cutting parameters when machining AISI D2 steel for different cutting parameters. Machining tests were carried out through single point turning method at various cutting speeds, feed rates and depth of cuts using cutting tools of various nose radii. The Taguchi Method was applied to the test result. Surface roughness and tool wear mechanism were considered as the quality characteristic factor.

¹Corresponding author: Karabuk University, Department of Mechatronics Engineering, 78100, 100. Yil /Karabuk, Turkey.
mzeyveli@karabuk.edu.tr

2. EXPERIMENTAL METHOD

The main aim of this experimental work was the establishment of the correlation between cutting parameters and machinability, such as surface roughness, cutting speed, feed rate, dept of cut and tool wear, tool noise radii and material. For this purpose experimental study focused on measurement of the surface finish of AISI D2 workpieces materials obtained by dry turning with different cutting parameter levels. The workpiece material was high chromium cold work tool steel D2 (AISI) with the following chemical composition (Table 1). Its hardness was 225 HV.

Table 1. Chemical composition of experimental pieces (mass%).

Element	C	Si	Mn	Cr	Mo	V
Content	1.55	0.30	0.40	11.80	0.80	0.80

The geometry of the workpiece bars used allowed a clamping with a length of 30 mm, to obtain a cylindrical turning length (L) with a 250 mm, with a initial diameter of 50 mm (D) corresponding to ratio (L/D) 4. These bars were machined under dry condition. Table 2 gives the machining parameters used.

Table 2. Machining Parameters and levels used in the experiments

Level	Cutting velocity Vc (m/min)	Feed rate f (mm/rev)	Tool nose radius R _e mm)	Tool type	Dept of cut ap (mm)
1	70	0,05	0.4	Standart	1
2	130	0,1	0.8	Wiper	
3	190	0,15			
4	250	0,2			

The machine tool used for the turning tests was a Taksan TMC 500V type of CNC turning centre. This machine tool was equipped with 10 kW motor drive and variable spindle speed up to 6000 rpm. Two types of multi layer CVD coated cemented carbide cutting tools were used for the machining tests. The top layer was Al₂O₃ and this is followed by TiCN and TiC. One group of these tools had standard nose radius while the other had wiper nose geometry. Both types of tools had the nose radius values of 0.4 and 0.8 mm (Figure.1).

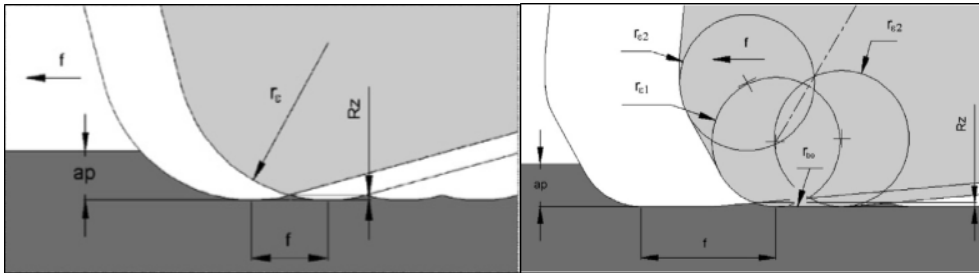
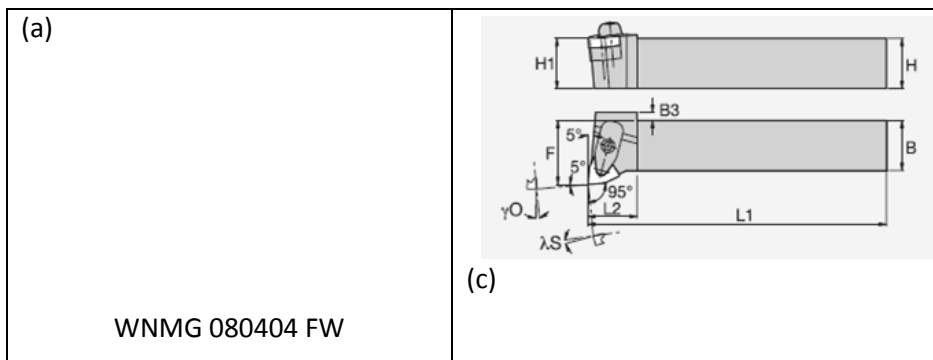


Figure 1. Conventional and Wiper tool geometry

The insert geometry was WNMG 080408-WP P20 commercial quality produced by Walter. These cutting tools were rigidly attached to a tool holder (DWLN R/L 2020K08KC040) and this provided the following cutting geometry: rake angle -6°

□ (negative), 5□clearance



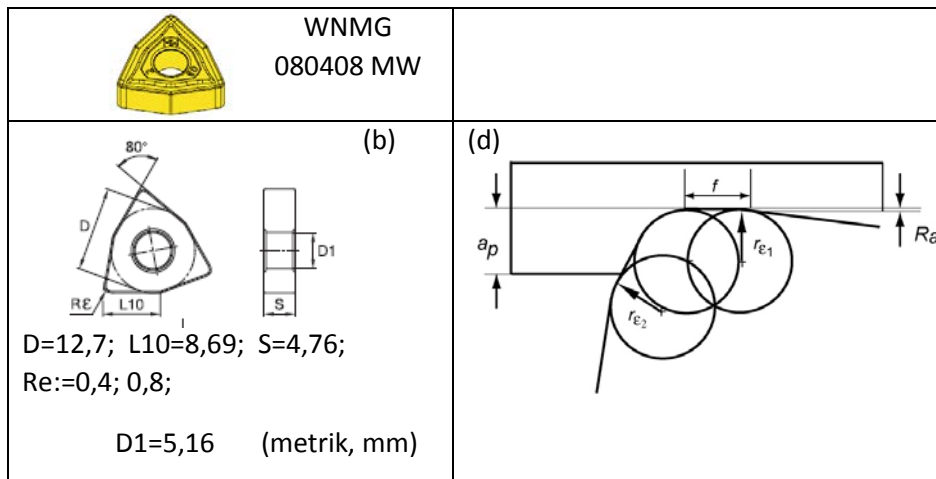


Figure 2. Cutting tool and tool holder geometry

The measurement of the arithmetic roughness average (R_a) on turned surfaces, was made by a profilometer Marsurf PS1, with a cut off of 0.8 mm, according ISO/DIS 4287/1E. Three surface roughness measurements were made by rotating the machined surface 120° . The average of the three measurements was taken as R_a values.

In this research, orthogonal array was applied for the execution of the plan of experiments, for four levels, whereby the levels are the values taken by the factors. The factors to be studied and the attribution of the respective levels are indicated in Table 1. The chosen array was 13 degrees of freedom regarding the number and levels of control factors and the number of the desired interactions between control factors. A Standard Taguchi experimental plan with notation L16 (215) was chosen [5].

In order to allow the analysis of the variance, each test was repeated two times, corresponding a total of 54 tests. The main purpose of ANOVA is the application of a statistical technique to identify the effect of factors. Results from ANOVA can determine very clearly the impact of each factor on the outputs. The parameter symbols typically used in orthogonal array and ANOVA are described in [7].

3. RESULT AND DISCUSSION

3.1. Surface Roughness

After each individual test, Arithmetic average roughness (R_a) of the machined surfaces was measured three times using a Marh M1 profilometer with a cut-off of 0.8mm (in accordance to ISO/DIS 4287/1E). Figure 3 shows the surface roughness graph on the 0.4 mm standard tool nose radius. It can be seen generally cutting speed increasing the surface roughness is decreasing but it has not been a significant change of surface roughness with the increasing cutting speed. However, on the contrary of the cutting speed with the increasing feed rate demonstrated a very significant increase in surface roughness. This situation shows the feed rate changes are more effective on the surface roughness. Minimum surface roughness value was obtained on the 0.1 mm/rev feed rate and 250 m/min cutting speed.

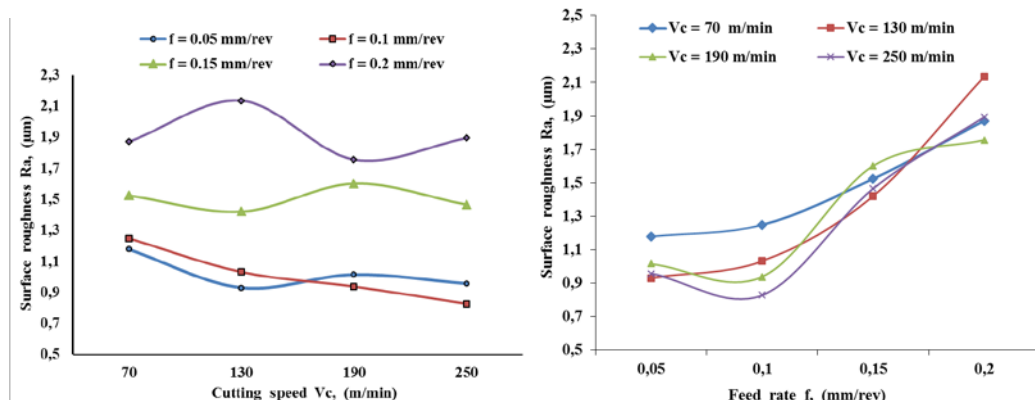


Figure 3. Surface roughness of 0.4 mm standard tool nose radius

The results show (Figure 4) on the experiments in 0.4 mm wiper tool nose radius. It has been seen that the cutting speed had the greatest effect on the surface roughness. In generally cutting speed increasing the surface roughness is decreasing.

While the cutting speed is greater effect on the surface roughness but feed rate is little influence. The surface roughness increases with the feed rate increases. According to the graph lowest surface roughness value was obtained on the 0.1 mm/rev feed rate and 250 m/min cutting speed.

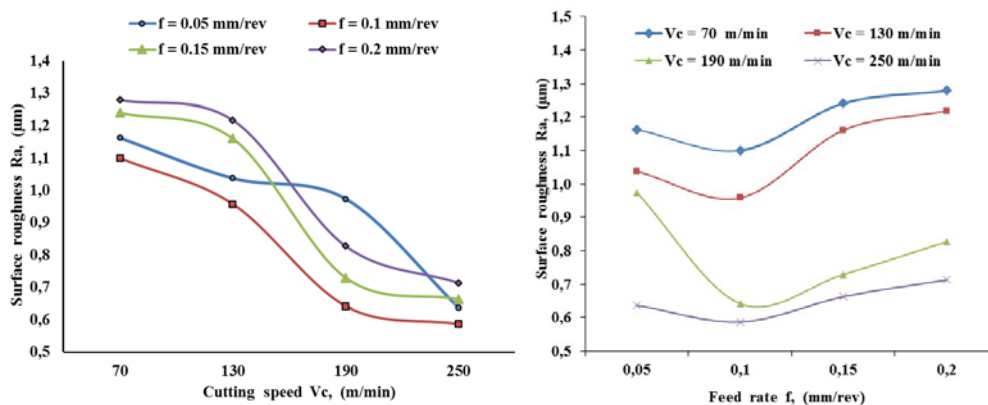


Figure 4. Surface roughness of 0.4 mm wiper tool nose radius

Figure 5. and Figure 6. shows the surface roughness graph on the 0.8 mm standard tool nose radius and 0.8 mm wiper tool nose radius respectively. It can be seen cutting speed increasing the surface roughness is not decreasing all of the feed rate. Generally the cutting speed and feed rate changing the surface roughness is varies in all the parameters. Minimum surface roughness value was obtained 0.8 mm standard tool nose radius on the 0.1 mm/rev feed rate and 130 m/min cutting speed while 0.8 mm wiper tool nose radius was obtained on the 0.1 mm/rev feed rate and 250 m/min cutting speed.

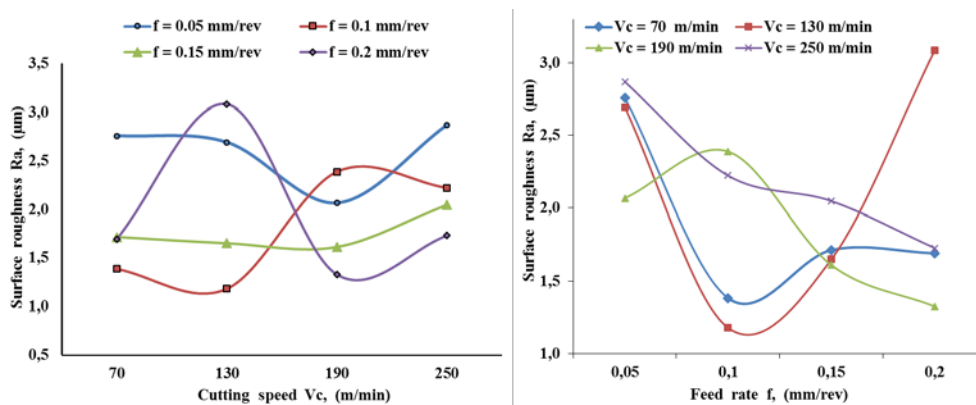


Figure 5. Surface roughness of 0.8 mm standard tool nose radius

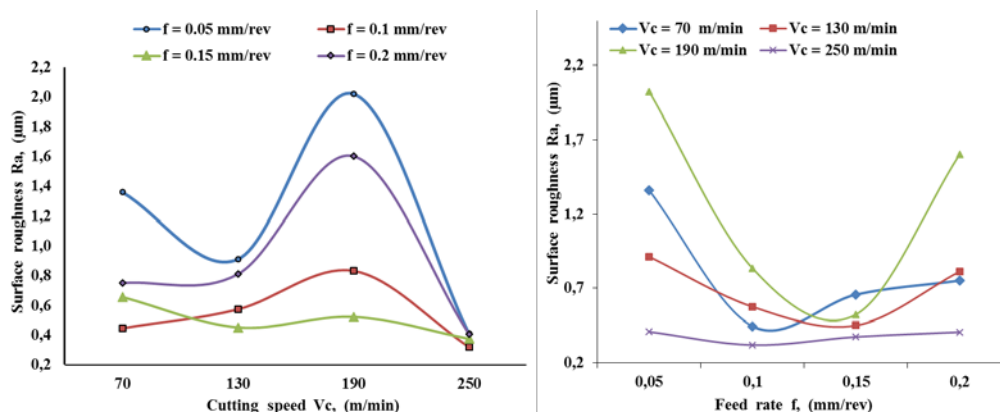


Figure 6. Surface roughness of 0.8 mm wiper tool nose radius

3.1. Anova Analysis

Without taking into account the category of S/N ratio, the larger S/N ratio points to the better performance characteristic. And so, the optimum level of the process parameters is the level with the highest S/N ratio. In addition, analysis of variance (ANOVA) was conducted to see which process parameters were statistically significant. After the analysis (S/N

and ANOVA), a confirmation experiment was performed to verify the optimum process parameters acquired from the parameter design

Table 3. ANOVA results for S/N ratios of the surface roughness.

Source	Degrees of freedom (DoF)	Sequential sum of squares (SS)	Mean sum of squares (MS)	F-test	P-coefficient	PCR (%)
Cutting speed	3	84.065	28.022	5.25	0.033	15.16
Feed rate	3	22.871	7.624	1.43	0.313	1.60
Nose radius	1	0.786	0.786	0.15	0.712	0.00
Tool type	1	292.472	292.472	54.80	0.000	65.62
Residual error	7	37.357	5.337	--	--	17.18
Total	15	437.552				100

From the values in Table 3, it can be seen that the tool type factor (PRC= 65.62 %) has statistical significance on the surface roughness. The effect of cutting speed on Ra is 15.16%. That is to say, Ra is more sensible to the changes in the tool type than the other machining parameters.

4. CONCLUSIONS

The machining tests using conventional and wiper tools were carried out at various machining parameters on AISI D2 cold work tool steel. Taguchi method was also applied for the selection of optimum cutting conditions. The following conclusions can be drawn from this study:

The statistical analyses showed that the most important factors on surface roughness was tool type (conventional and wiper) and this was followed by cutting speed and feed rate.

The ANOVA analysis carried out for surface roughness S/N ratio indicated that 0.8 mm wiper tool, 250 m/min cutting speed and 0.1 mm/rev feed rate were the optimum machining conditions.

According to the ANOVA analyses results, tool type among the others had the highest influence (65.62 %) on surface roughness.

This present work showed that Taguchi optimisation technique prior to multi factorial experimental tests can be effectively used for selection of optimum parameters.

ACKNOWLEDGEMENTS

This study has been supported by the Department of Karabuk University Scientific Research Project. Project Number: KBÜ-BAP-16/1-YD-033.

REFERENCES

- http://www.matweb.com/search/datasheettext.aspx?matguid=bcbf506c860444a08a1ff23635b6815f
- By Dr. Mike S. Lou, Dr. Joseph C. Chen & Dr. Caleb M. Li Surface Roughness Prediction Technique For CNC End-Milling Journal of Industrial Technology • Volume 15, Number 1 • November 1998 to January 1999
- Boothroyd, G. and Knight, W. A., (1989), Fundamentals of Machining and Machine Tools, Second Edition, Marcel Dekker Inc., New York.
- Huynh, V. M. and Fan, Y., (1992), "Surface-Texture Measurement and Characterization With Applications To Machine-Tool Monitoring", The International Journal of Advanced Manufacturing Technology, 7, pp.2-10.
- Reginaldo T. Coelho, Eu-Gene Ngb, M.A. Elbestawi, Tool wear when turning hardened AISI 4340 with coated PCBN tools using finishing cutting conditions, International Journal of Machine Tools & Manufacture 47 (2007) 263–272
- doi:10.1016/j.ijmhm.2009.11.011, Khaider Bouacha a,b,*, Mohamed Athmane Yallese b, Tarek Mabrouki c, Jean-François Rigal , Int. Journal of Refractory Metals & Hard Materials,
- J.G. Lima a, R.F. A´vila a, A.M. Abraˆo a, M. Faustino b, J. Paulo Davimb,*, Hard turning: AISI 4340 high strength low alloy steel and AISI D2 cold work tool steel, Journal of Materials Processing Technology 169 (2005) 388–395
- J.A. Arsecularatne a,*, L.C. Zhang a, C. Montross b, P. Mathewc, On machining of hardened AISI D2 steel with PCBN tools, Journal of Materials Processing Technology 171 (2006) 244–252
- W. Grzesik, T. Wanat, Surface finish generated in hard turning of quenched alloy steel parts using conventional and wiper ceramic inserts, International Journal of Machine Tools & Manufacture 46 (2006) 1988–1995
- Tugrul Ozel a,*, Yigit Karpat a, Luis Figueira b, J. Paulo Davimb, Modelling of surface finish and tool flank wear in turning of AISI D2 steel with ceramic wiper inserts, Journal of Materials Processing Technology 189 (2007) 192–198
- J. Paulo Davim *, Luis Figueira, Machinability evaluation in hard turning of cold work tool steel (D2) with ceramic tools using statistical techniques, Materials and Design 28 (2007) 1186–1191

- [12]. *A.K.M. Nurul Amina, Shuriani Binti Dolaha, Marlina Binti Mahmuda, M.A. Lajis*, Effects of workpiece preheating on surface roughness, chatter and tool performance during end milling of hardened steel D2, *journal of materials processing technology*, 201 (2008) 466–470

A New Weathering Classification for Rock Mass Using Rock Engineering System and its Application

Samet Berber¹, Nurcihan Ceryan¹, Sener Ceryan¹

Abstract

Description and classification of weathered rocks are necessary to obtain the changes of its engineering properties. In this study, a new approach suggested to evaluate rock masses was suggested to determine weathering degree of rock mass. For this, Rock Engineering System (RES) was applied to evaluate of weathering state of rock mass. In geotechnical practice, understanding the most effective parameters in engineering system and their relationships is important in order to obtain an optimum design for the engineering system. The applications of Rock Engineering System (RES) an approach to quantifying the intensity and dominance of parameters, method in the analysis of complicated engineering processes have been widespread. Development of a quantitative weathering system using RES is the main purpose of the study to overcome the lack of a comprehensible qualitative weathering system. In the new approach, reduction in uniaxial compressive strength, the ratio of rock to soil, weathering state of discontinuity surface, protection of the rock mass structure, comparison of rock material weathered to depth with joint waviness and frequency of discontinuity were used as input parameter. In this study, the new classification system suggested was applied to volcanic rocks from NE Turkey and the result of the application was compared with the other classification system of weathered rock mass used commonly in literature.

Keywords: *Rock mass, Weathering, Classification, Rock Engineering System, volcanic rock, NE Turkey*

1. INTRODUCTION

The engineering behavior of rock depends not only on stress state and stress history but also on the physical and chemical change of the rock due to weathering. Thus, it is important for geotechnical engineers to estimate quantitatively the changes during weathering. Various stages in the reduction process of a rock to soil can be recognized and can be used to form the basis of engineering classifications of weathered rocks. Description and classification of weathered rocks are necessary to obtain the changes of its engineering properties. The first step in classification is to determine the parameters of rocks related to classification purpose and to define the rock according to these parameters and properties [1]. Defining the weathered rocks for the purpose of engineering goals is make sense to determine the degree of weathering effect, extend and characteristics in detail at that moment [1]. There are mainly two topics about the classification systems of weathered rock mass. One of them is the qualitative weathering system. The qualitative weathering systems, are mainly based on the visual definition of the geological properties, the index properties and the basic mechanical test that can be applied also in the field ([1]. Also, the engineering properties of these rocks are able to be predicted in a range by these classifications. However, this range of the engineering properties predicted for each weathering grade can overlap with the range of these properties predicted at the boundaries [2]. Also, the qualitative weathering classifications do not allow the numerical relationships to be established between the weathering grade and the engineering properties of the rock. The other drawback of the qualitative weathering classification is that the properties used in these systems are subjective (depending on the user), and that the distant properties are used for each weathering grade and the separation of them from the others [2]. In the present, the most widely used weathering classification system among qualitative classification system in the literature were suggested by IAEG[3] (Fig.1). The other type of classification system for weathered rocks is quantitative system. Rock mass rating system suggested by Price [4] is an example for quantitative system (Table 1)

¹ Corresponding author: Department of Geological Engineering, Balikesir University, Balikesir, Turkey sametberber@balikesir.edu.tr

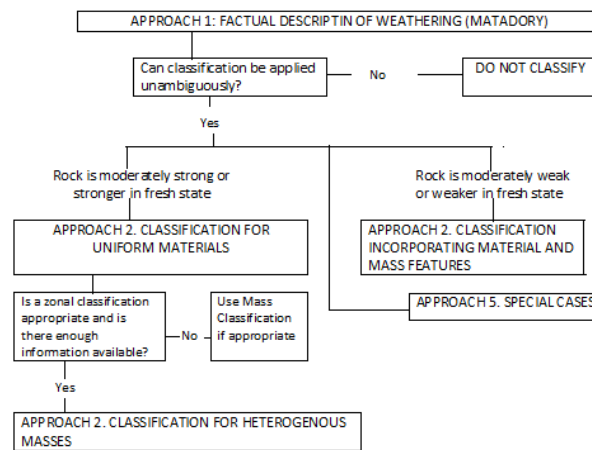


Figure 1. The approach for the classification system of weathered rocks [3]

Price [4] suggested a ratings (quantitative) system for the description of rock mass weathering (Table 1). The system is based on visual impression. However, an approach which seems to be successful for many engineering applications is the use of a rating system to place a rock mass within a classification. Accordingly, it is suggested that giving a grade to a rock mass in a weathering classification related to engineering significance might be most appropriately undertaken by a ratings system. It is able to establish the numerical relationship between the weathering rating and strength properties of rock masses

Table 1. Rating for all rocks materials and joint (and relict discontinuities) in all rocks [4] (Prp: Proportion)

Prp	Fresh	Discolored (some loss of strength)	Friable (and discolored) (considerable loss of strength, geotechnically an engineering soil, $\sigma_{ci} < 1.25$ MPa)	
4/4	40	0	0	
3/4	30	5	5	
2/4	20	10	10	
1/4	10	15	15	
0	0	20	20	
Igneous rocks-joint only			All discontinuities in all type of rocks	
Prp	Unweathered	Surface stained	Rock material weathered to depth > joint waviness	Proportion of discon-tinuities present as relict in geotechnical soil
4/4	20	0	0	-20
3/4	15	5	5	-15
2/4	10	10	10	-10
1/4	5	15	15	-5
0	0	20	20	0
Sedimentary and metamorphic rocks (including limestone)- Ratings for joint and bedding or foliation planes				
Prp	Unweathered	Surface staining or	Rock material weathered to depth > joint	

		modified by solution	waviness or open by solution
4 / 4	20	0	0
3 / 4	15	5	5
2 / 4	10	10	10
1 / 4	5	15	15
0	0	20	20

Development of a quantitative weathering system is the main purpose of the study to overcome the lack of a comprehensible quantitative weathering system. These system was obtained using interaction matrix. The parameters used in these matrix are reduction in uniaxial compressive strength, the ratio of rock the soil, weathering state of discontinuity surface, protection of the rock mass structure, comparison of rock material weathered to depth with joint waviness and frequency of discontinuity. In this study, also, the new classification system was applied to volcanic rocks exposed on the excavated slopes on Kurtun-Torul district of Gumushane-Giresun road (Fig. 1). In this study, firstly, the geotechnical units were separated from using the lithological features, the weathering state and the frequency of discontinuity. The uniaxial compressive strength of rock material value and the geotechnical properties of discontinuities on the said geotechnical units used in this study were taken from [5]. In the study performed Akgun and Ceryan [5], the mechanical properties of the said geotechnical units were obtained by Hoek-Brown failure criterion [6]. Then, the weathering rating (Wres) was obtained by using RES system and it was compared with Price's rating system [4] and the qualitative weathering classification suggested by IAEG [3]. In addition, the relationship between the weathering rate (Wres) and mechanical properties the geotechnical units investigated.

2. METARIAL AND METHODS

2.1. Geological Setting

In the study area, the oldest rocks are Turonian-Santonian andesite and its pyroclastic that interbedded with dark red colored clayey limestone, sandy limestone and tufts [7]. This series rocks called as Catak Formation that concordantly overlies Kızılkaya Formation, is consist of mainly Turonian?-Santonian dacite and its pyroclastic with some sedimentary rock lenses[7]. Sarosman Granitoid aged Campanian-Maastrichtian Caglayan Formation concordantly covers all these series. All these rocks concordantly overlie Travertine aged Quaternary (Figure 2).

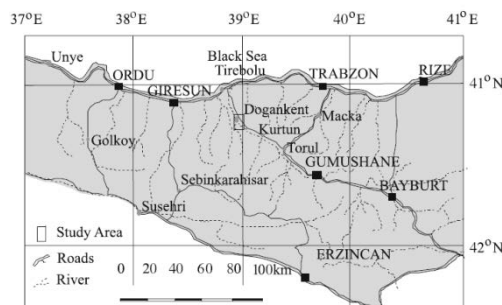


Figure 1. Location map of the study area

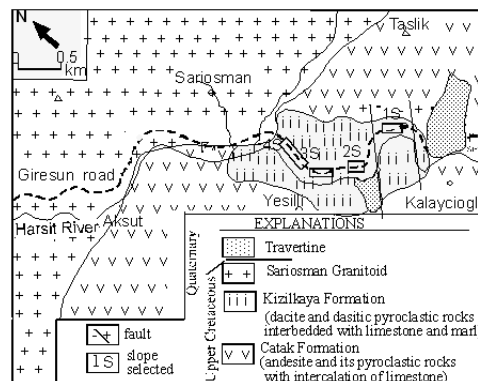


Figure 2. Geology map of the study area [7].

2.2. The Rock Engineering System and the creating of the quantitative classification system for weathered igneous rocks

It is known that some parameters will have a greater effect on any natural system than others. The approach for quantifying the intensity and dominance of parameters is achieved by Hudson [8] by coding the interaction matrices and working the interaction intensity and dominance of each parameter. The general characteristic of the approach is shown conceptually in Fig 3a ([8], [9]). To understand the interactivity of the parameters described previously, a systematic study is carried out "how the variation of one of the factors may cause modifications in the others". These parameter interactions can be evaluated using a matrix display (Hudson 1989) where the parameters are listed along the main diagonal of a

square matrix and the interactions considered in the off-diagonal boxes of the matrix as given Fig. 3b ([8], [9]). The main parameters, P_i , are given along the leading diagonal with parameter construction as the last box, as highlighted in Fig 3b. From the construction of the matrix, it is clear that the row passing through P_i , represents the influence of P_j on all the other parameters in the system. Conversely, the column through P_i , represents the influence of the other parameters, i.e., the rest of the system on P_j . Once the matrix has been coded approximately, the sum of each row and each column can be found. If the influence of P_i on the system is thought, the sum of the row values as the 'cause' and the sum of the column terms as the 'effect' are termed as designated coordinates (C, E). To quantify the different importance of the interactions, a coding method is required ([8], [9]).

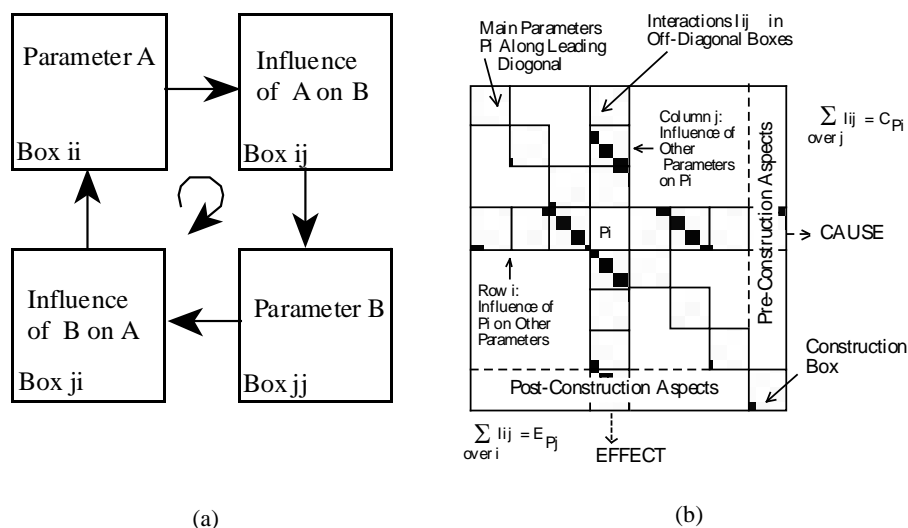


Figure 3. 2x2 interaction matrix with leading diagonal terms (a) and Summation of coding values in the row and column through each parameter to establish the cause and effect co-ordinates (b)[8]

In the approach for creating the weathering classification, reduction in uniaxial compressive strength, the ratio of rock to the soil, weathering state of discontinuity surface, protection of the rock mass structure, comparison of rock material weathered to depth with joint waviness and frequency of discontinuity were used as input parameters for set developing the interaction matrix. When developing the interaction matrix, the generic matrix coding method is employed. There are five categories into which the mechanism can be classified, ranging from zero to four, corresponding to 'no', 'weak', 'medium', 'strong' and 'critical' interactions, respectively (Table 2). The cause-effect plot is helpful to understand the role of each factor within a project and may be used in decision stage of an engineering project. It can be shown in Figure 6 that the most important factors affecting the instability of the slopes in the study area are reduction in uniaxial compressive strength, discontinuity frequency and weathering state of discontinuity surface. And the more interactive parameters are the ratio of rock to the soil, reduction in uniaxial compressive strength and weathering state of discontinuity surface (Fig. 3).

Table 2. Interaction Matrix coded for the weathering degree

	C _i						
P1	5	4	3	2	1	3	18
4 P2	3	2	2	1	3	15	
2 3 P3	1	4	1	4	15		
1 2 1 P4	1	1	3	9			
2 3 3 2 P5	1	2	13				
1 1 1 " 2 P6	2	9					
0 0 0 0 0 0 P7	0						
E _i	10	14	12	10	11	5	17 79

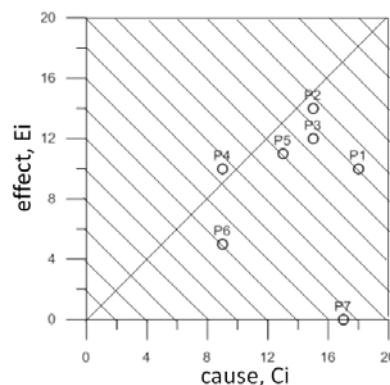


Figure 3. Cause versus effect for weathering degree

(P1: reduction in uniaxial compressive strength, P2: the ratio of rock to the soil, P3: weathering state of discontinuity surface, P4: the rock mass structure, P5: rock material weathered to depth, P6: frequency of discontinuity and P7: weathering degree)

After definition of the relative interactive intensity as a measure of the significance of the parameters, the actual parameter values were measured and assigned. For this reason, a detailed input data is required. To provide such data, an extensive field work were carried out. The data about the relevant parameters was collected from the geotechnical unit investigated and then the parameter values were selected from Table 3. The ratings of the each parameters taken from Table 3 were given in Table 4.

Table 3. Definition and rating of the parameters used to create the weathering classification suggested

Reduction in uniaxial compressive strength (P1) and weathering state of discontinuity surface (P3)			Rock/soil ratio (P2)		
Wc (R _f /R _w)	Description	Rating	Rock/soil (%)	Rating	
<1.1	fresh	1	>90	1	
1.1-1.5	Slightly weathered	3	90-70	2	
1.5-2.0	Moderately weathered	5	70-50	4	
>2.0	Highly weathered	7	50-30	6	
			30-10	8	
			<10	9	

Rock Mass structure (P4)	Rating
The blocs are interconnect firmly each other	1
The blocks are cornered and interconnect each other.	2
Mass structure is preserved. But the blocks tend to divide each other	4
Corestones are beginning breaking and may be significant for investigation and construction Rock framework still locked	6
May behave as soil although relict fabric may be significant. Weak grade will control behavior of soil mass.	8
Mass structure isn't Preserved	9

Rock material weathered to depth (P5)		Frequency of discontinuity (P6)		
Comparison of rock material weathered to depth with joint waviness	Rating	Jv	Description	Rating
Rock material weathered to depth > joint waviness	1	<1	Massive	1
Rock material weathered to depth equal to joint waviness	3	1-3	Blocky	3
Rock material weathered to depth > joint waviness	5	3-10	Very Blocky	5
(Rf: Shimidt hammer rebound value for unweathered rock materials, Rw: Shimidt hammer rebound value for discontinuity surface, Wc; weathering degree ([10])		10-30	Blocky/Disturbed	7
		>30	Disintegrated	9

(Jv: Volumetric joint count number)

In Table 4, in addition, the compressive strength of rock materials (UCSm), Volumetric joint count (Jv), Geological Strength index (GSI), Rating of rock materials according to Price's system (Rm), definition of weathering degree

according to IAEG [3], and the compressive strength and deformation modulus of rock mass were given. The said properties of the geotechnical units were taken from Akgun and Ceryan [5].

In order to obtain weathering degree of the geotechnical units there is need the weight factor (a_i) for various each parameters. The weight factor can be calculated using the Equation 1 ([9])

$$a_i = \left(\frac{C_i + E_i}{\sum (C_i + E_i)} \times 100 \right) / (P_{\max}) \quad (1)$$

Where $(C_i + E_i)$ is cause +effect value of parameter, total $(C_i + E_i)$ is the total of all lines and columns except P7 in interaction matrices, P_{\max} is maximum value of parameter i measured at the field.

Having established both the value scaled from the C + E histogram for each parameter and its rating for each geotechnical units, the Weathering Rating, W_{res} , can be calculated employing the Equation 2 ([9])

$$W_{res} = \sum_{i=1}^6 a_i P_{ij} \quad (2)$$

Where i refers to parameters (from 1 to 6), j refers to geotechnical unit, a_i is the value scaled from the C + E histogram for each parameter and P_{ij} is the rating assigned to different classes of parameter values. The maximum possible value of W_{res} is 100.

The weight factor (a_i) was obtained as 2,8368 for P1, 2,2855 for P2, 2,7356 for P3, 1,497 for P4, 3,4042 for P5 and 1,1032 for P6.

Table 1. The strength and deformation properties, volumetric joint count, Geological Strength Index, weathering degree obtained with Price's system [4] and IAEG [3] of the geotechnical units [5] and, the rating of the parameters selected and the Weathering Rate

SN	jnt	UCSi	Jv	GSI	Rm	Rd	Rw	WD*	UCSm	Em	P ₁	P ₂	P ₃	P ₄	P ₅	P ₆	Wres
1	1	152	2.72	42	20	40	60	MW	1.11	3155	3	4	5	4	2	3	49.8
	2	184	6.04	57	65	60	125	F	7.98	9725	1	1	5	1	1	5	33.2
	3	171	3.91	62	60	50	110	SW	7.17	9976	3	2	5	2	1	5	42.6
	4	152	5.91	52	60	40	100	SW	2.69	5610	3	2	5	2	1	5	42.6
2	5	196	3.66	65	80	60	140	F	10.5	11857	1	1	3	1	1	5	27.7
	6	110	1.83	49	20	40	60	MW	1.51	4720	5	4	7	6	1	3	60.5
	7	86	24.85	33	20	20	40	HW	0.27	1759	7	8	7	6	5	7	96.5
	8	117	6.09	39	20	30	50	HW	0.64	2654	5	6	5	6	5	5	77
3	9	114	10.8	30	20	20	40	HW	0.26	1581	5	6	7	6	3	7	79.5
	10	133	2.83	53	35	40	75	MW	2.558	5942	5	4	5	4	3	3	58.9
	11	161	5.47	48	35	30	65	MW	2.01	4456	3	4	5	4	1	5	50.2
	12	163,1	4.72	49	35	40	75	MW	2.21	4720	3	4	5	4	1	5	50.2
	13	181,6	5.47	61	65	50	115	SW	6.92	9418	3	2	3	2	1	5	37.1
	14	163,1	5.48	58	35	50	85	MW	4.81	7924	3	4	5	2	1	5	47.2
4	15	103,7	4.97	35	20	30	50	HW	0.39	2108	5	8	7	6	5	5	87.1

16	185,6	4.84	54	35	40	75	F	3.88	6295	1	1	3	1	1	5	27.7
17	97	5.42	53	35	40	75	SW	1.87	5862	7	2	5	2	1	5	54
18	138	3.43	68	60	50	110	SW	9.51	14092	3	2	5	2	1	5	42.6
19	100	3.5	43	20	30	50	MW	0.79	3342	7	8	7	8	5	5	95.7
20	114,1	4.44	39	20	20	40	MW	0.257	1581	5	8	7	8	5	5	90.1
21	164	6.28	46	35	30	65	SW	1.7	3972	3	2	5	2	1	5	42.6
22	119	8.05	39	20	30	50	MW	0.66	2654	3	4	5	6	1	5	53.2

(SN: Slope number, Jnt: Geotechnical unit, UCSi: the compressive strength of rock materials (MPa), Jv: Volumetric joint count, GSI: Geological Strength index, Rm: Rating of rock materials according to Price's system [4], Rd: Rating of discontinuity surface, Rw: according to Price's system [4], WD*: weathering degree according to IAEG system, UCSm and Em: the compressive strength and deformation modulus of the geotechnical units (MPa), P₁, P₂, P₃, P₄, P₅ and P₆: the obtained rating of the parameter selected in this study, Wres: The Weathering Rating)

The Weathering Rating, Wres, obtained by the new approach suggested in the study was compared with Price's system [4] and IAEG system [3] (Fig. 4 and Eq. 3). The relationships between Wres and the mechanical properties of the geotechnical units were investigated, additionally (Eqs. 3-6)

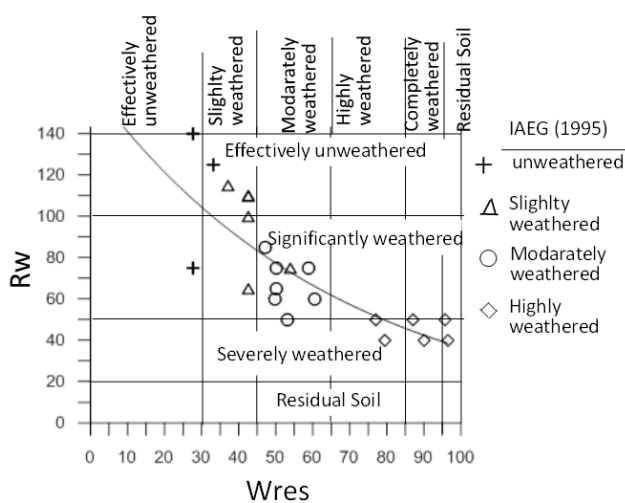
$$Rw = 163.79 e^{0.0115Wres} (R^2 = 0.706) \quad (3)$$

$$GSI = 76.36 e^{0.0083Wres} (R^2 = 0.636) \quad (4)$$

$$UCSm = 27.3 e^{-0.0483Wres} (R^2 = 0.754) \quad (5)$$

$$Em = 18.776 e^{-0.0248Wres} (R^2 = 0.661) \quad (6)$$

Where, Rw is the weathering rating of rock mass according to Price's system [4], GSI is Geological Strength Index, UCSm is the uniaxial compressive strength of rock mass (MPa) and Em is the deformation modulus of rock mass (GPa).



(a)

(Rw: the weathering rating of rock mass according to Price's system [4],

GSI is Geological Strength Index,

UCSm: the uniaxial compressive strength of rock mass (MPa),

Em: the deformation modulus of rock mass (GPa),

Wres: the Weathering Rating suggested in this study

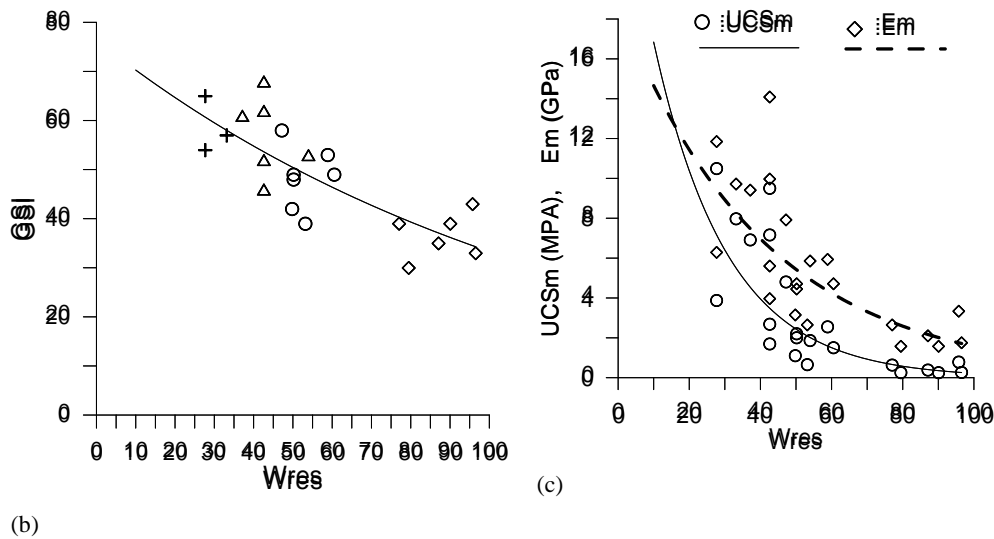


Figure 4. the comparison of the Weathering Rating /Wres) to IAEG system and Price's system (a), the relationships between Wres and mechanical properties including the uniaxial strength (b) and the deformation modulus (c)

3. RESULTS AND DISCUSSION

In this study, a quantitative weathering system was suggested to overcome the lack of a comprehensible quantitative weathering system. For this, RES was used. In the interaction matrix to define quantitative weathering degree, reduction in uniaxial compressive strength of rock materials and discontinuity surface materials (P1, P3), the ratio of rock the soil (P2), protection of the rock mass structure (P4), rock material weathered to depth (P5) and frequency of discontinuity (P6) were used as input parameter. According to the cause-effect diagram, the most important factors affecting the instability of the slopes in the study area are reduction in uniaxial compressive strength, discontinuity frequency and weathering state of discontinuity surface. And the more interactive parameters are the ratio of rock to the soil, reduction in uniaxial compressive strength and weathering state of discontinuity surface. The weight factor was obtained as 2,8368 for P1, 2,2855 for P2, 2,7356 for P3, 1,497 for P4, 3,4042 for P5 and 1,1032 for P6.

In this study, the new classification system suggested was applied to volcanic rocks from NE Turkey and the result of the application was compared with Price's system and IAEG system used commonly in literature. As a result, it can be said that suggested, the weathering Rating, Wres, representing the quantitative weathering degree, suggested in this study is compatible with IAEG system and there are the meaningful statically relationships between Wres and the rating of weathering obtained with Price's system.

In this study, the relationships between the weathering grade and mechanical properties of the twenty-two geotechnical units, described at five rock slopes were selected were investigated. A meaningful relationships between the rock mass strength properties and the Weathering Rating were obtained (Equations 12-16). The uniaxial compressive strength and deformation modulus (Em) of the geotechnical unit decreases with rating Wres. (Equations 3-6) (Figure 4b-c).

4. CONCLUSION

In this study, a new quantitative definition of the weathering degree for rock mass was suggested. The new index, the Weathering Rating, Wres, was obtained using Rock Engineering System. In order to form the Weathering Rating, reduction in uniaxial compressive strength of rock materials and discontinuity surface materials, the ratio of rock the soil, protection of the rock mass structure, rock material weathered to depth and frequency of discontinuity were used as input parameter in interaction matrix. The Weathering Rating is compatible with Price's system and IAEG system. IAEG system is qualitative system and Price's system was commonly applied to the sedimentary rocks such the limestone, marl and clay stone. On the other hand, this system is numerical and can be improved in whole rock. It was concluded that the GSI values, uniaxial compressive strength and deformation properties of the dacite units in the area could be estimated with a high reliability and quickly by using the Weathering Rating, Wres, suggested in this study. To test these obtained results for the other magmatic rocks will be helpful.

REFERENCES

- [1]. Ceryan, S. *Weathering Indices for Assessment of Weathering Effect and Classification of Weathered Rocks: A Case Study from NE Turkey*. *Earth Sciences* (Editor: Imran A. Dar), ISBN 978-953-307-861-8, InTech Publication, 2012, p.19-44.
- [2]. Ceryan, S., Tudes S. and Ceryan N, "A new quantitative weathering classification for igneous rocks", *Environmental Geology*, 55, 1319-1336, 2008
- [3]. IAEG "The description and classification of weathered for engineering purposes" Geological Society Engineering Group Working Party Report. *Quarterly Journal of Engineering Geology*, 1995 28, 207-242.
- [4]. Price, D. G., "Weathering and Weathering Processes", *Quarterly Journal Engineering Geology*, 1995, 28, 234-252
- [5]. Akgun, A. and Ceryan S. Estimating of the Mechanical Properties of Rock Masses by the Rating System Representing Rock Mass Weathering: A case study". *9th International Congress on Advances in Civil Engineering*, 27-30 September 2010 Karadeniz Technical University, Trabzon, Turkey, p.1-6, 2010
- [6]. Hoek, E, Carranza-Tore. C. and Corkum. B. "Hoek-Brown failure criterion -2002 Edition". In: *Proceedings of the Fifth North American Rock Mechanics Symposium 20002*, Vol 1, Toronto, Canada, pp 267-273
- [7]. Ceryan, N. "Relationships between Excavatability of Rocks and GSI: An Example Study from the Rock Masses Exposed Along Gumushane-Giresun (NE Turkey) Motonvay". *9th International Congress on Advances in Civil Engineering*, 27-30 September 2010 Karadeniz Technical University, Trabzon, Turkey, p.1-6
- [8]. Hudson, J.A. *Rock engineering systems: theory and practice*. Ellis Horwood, Chichester, 1992
- [9]. Ceryan, N. and Ceryan S., "An application of interaction matrix method for slope failure susceptibility zoning: Dogankent settlement area (Giresun, NE Turkey)", *Bulletin of Engineering Geology and Environment*, 200867,375-385,
- [10]. Gokceoglu, C., Aksoy. H. "New approaches to the characterization of clay-bearing, densely jointed and weak rock masses". *Engineering Geology*, 2000, 58, 1-23

Bark Beetle Species (Scolytinae) Of Ordu, Turkey

Yafes Yildiz¹, Belgen Yiğit²

Abstract

In this study, bark beetles of Ordu forests were investigated. For this purpose, at appropriate times in the field with the pheromone traps and trap trees in the collection of species, determination of some important species biology to be studied. Identification of the species kept and the specimens, As a result of studies 8 bark beetle species have been identified in the regions and provide suggestions to reduce the amount of insect damage.

Keywords: *Bark beetle, Ordu, Scolytinae, Turkey*

1 INTRODUCTION

The subfamily Scolytinae is a fairly large family (Coleoptera: Curculionidae), with more than 6000 described species, is one of the largest groups of Coleoptera [1]. 107 species belonging to Scolytinae were known from Turkey [2]. Adults can be minute, with a body length of little more than 2 mm, although *Dendroctonus micans* Kugelan, which is the biggest species of bark beetles in Turkey, body length can reach 10 mm. Bark beetle species typically cause secondary damage but during occasional outbreaks they are capable of killing relatively vigorous trees [2, 3]. The adult beetles are the primary tunnellers and make breeding galleries in the wood under the bark of a wide range of trees where the eggs are laid. The larvae then make small lateral galleries where they live and feed [4]. Scolytinae is one of the most important insect groups in Turkey due to their damage to forest trees. In recent years, an important increase has been observed on damage level of bark beetles by their outbreaks [5, 6].

There are some records of Scolytinae species associated with forest of the Ordu region of Northern Turkey, but these species have not been studied extensively. The aim of the study was to determine the bark beetle fauna and host plants of species in the forests of Ordu region.

2. MATERIAL AND METHODS

Surveys were conducted the forests of the Ordu region of Northern Turkey between 2014 and 2015. Scolytinae species were collected from different forest sites in Ordu provinces. In addition, altitude and geographical coordinates were also noted. Besides forest stands, specimens were also collected from trunks deposited in forest depots. Trees weakened by other insects or drought were used to determine the Scolytinae fauna. These trees were selected by observing damage symptom and signs like holes in the bark, resin flows, and yellowish or brownish color on crown. Using entrance holes and sawdust around the stems as a guide, main galleries were opened. Collected specimens were labeled with date, location, and forest characteristics of the sampling area. Bark sections and shoots infested by Scolytinae species were placed in plastic boxes and taken to the laboratory. All samples are now deposited at the Entomology laboratory of Bartın University, Forestry Faculty, Bartın, Turkey.

3. RESULT AND DISCUSSION

As a result, 8 bark beetles species were determined. Species were confirmed according to the classifications in Pfeffer [7]. Information on the examined materials is provided in the following order: Host plant/pheromone trap, province and collecting date.

Hylastes ater (Paykull, 1800)

Material examined: Pheromone traps Çambaşı /Döngeri; 17.03.2014, Çambaşı/Çukuralan; 01.06.2014, Mesudiye/Avoroz; 18.07.2014, Mesudiye/Yazlık; 18.08.2014

Host Plant: *Picea abies*, *P. jezoensis*, *P. obovata*, *P. orientalis*, *Pinus slyvestris*, *P. brutia*, *P. rotundata*, *P. strobus*, *P. nigra nigra*, *P. leucodermis*, *P. cembra*, *P. koraiensis*, *Abies nordmanniana*, *A. bormmülleriana* [7, 8].

Distribution: Central and Northern Europe, Balkan States, Asia Minor, Caucasus, Siberia [7].

¹ Corresponding author: Bartın University, Department of Forest Engineering, 74100, Bartın, Turkey. yildiz@bartin.edu.tr

² Bartın University, Department of Forest Engineering, 74100, Bartın, Turkey.

Turkish records: Bursa, Karabük, Eskişehir, Antalya, Ankara, Artvin, Burdur, Kahramanmaraş, Kars, Kırşehir, Ordu, Sinop ve Trabzon' da üzerinde rastlanmıştır [9, 10, 11, 12].

***Dendroctonus micans* Kugelann, 1794**

Material examined: *Picea orientalis* Çambaşı: 17.03.2014, 20.04.2014, 30.06.2014 Ulubey: 17.05.2014; Gölköy: 16.07.2014

Host Plant: *Picea abies*, *P. sitchensis* ve *P. orientalis*, *P. breweriana*, *P. engelmannii*, *P. glauca*, *P. jezoensis*, *P. mariana*, *P. obovata*, *P. omorika*, *P. pungens* [13].

Distribution: Australia, Belgium, Czechoslovakia, Denmark, Finland, France, Germany, Hungary, Italy, Netherlands, Norway, Poland, Romania, Sweden, Switzerland, Turkey, Russia, Yugoslavia [13].

Turkish records: Trabzon, Artvin, Giresun [8].

***Pityophthorus pityographus* (Ratzeburg, 1837)**

Material examined: Pheromone traps Çambaşı /Kaleboynu; 30.06.2014, Çambaşı / Tekmezar, 02.08.2014

Host plants: *Abies alba*, *Picea abies*, *P. omerica*, *Larix decidua*, *Pinus sylvestris*, *P. strobus*, *P. rotundata*, *P. mugo*, *P. cembra*, *Pseudotsuga menziesii* [7].

Distribution: Central Europe, Bosnia and Herzegovina, Serbia, Macedonia and Bulgaria [7].

Turkish records: Ankara, Artvin, Bolu, Bursa, Düzce, Giresun, İstanbul, Karabük, Kastamonu, Sinop, Trabzon [2].

***Pityogenes bidentatus* (Herbst 1783)**

Material examined: Pheromone traps Çambaşı /Taşmezar; 17.03.2014, *Picea orientalis* Çambaşı/Gerce ovası; 20.05.2014, Çambaşı /Hevrek; 18.06.2014, Çambaşı / Madala 17.07.2014

Host plants: *Pinus sylvestris*, *P. nigra balcanica*, *P. nigra cevennensis*, *P. nigra nigra*, *P. strobus*, *p. mugo*, *P. rotundata*, *P. sibirica*, *Picea obovata*, *P. orientalis* [7].

Distribution: Central and North Europe, Caucasus, Anatolia [7].

Turkish records: Antalya, Artvin, Giresun, Ordu ve Trabzon [8].

***Pityokteines curvidens* (Germar, 1824)**

Material examined: Pheromone traps Mesudiye/ Avaroz; 18.07.2014, Çambaşı / Tekmezar; 02.08.2014

Host plants: *Abies alba*, *A. cephalonica*, *A. borisii regis*, *A. nordmanniana* subsp. *bornmulleriana*, *A. cilicica*, *A. nordmanniana* subsp. *equitrojani*, *A. nordmanniana*, *A. firma*, *A. sachalinensis*, *Cedrus libani*, *Picea abies*, *P. orientalis*, *Larix decidua*, *Pinus sylvestris* [2, 7, 8, 14].

Distribution: Caucasus, Corsica, Italy, the Balkans, Turkey, Japan [7, 14].

Turkish records: Bursa-Uludağ, Bursa- Nergizpınar, Ayancık, Devrek, Karabük, Küre, Bartın, Düzce, Bolu-Gerede, Mudurnu, Ankara-Kızılcahamam, Çanakkale-Bayramiç, Bucak-Sobyay, Bucak-Karlık, Akseki, Manavgat-Cevizli [2, 8, 9, 14, 15, 16, 17, 18, 19, 20].

***Ips sexdentatus* (Boerner, 1776)**

Material examined: Pheromone traps Kabadüz.; 30.04.2014, 16.05.2014, 01.06.2014, 18.06.2014, 30.06.2014, 17.07.2014, 02.08.2014, 24.08.2014; Pheromone traps Gölköy: 02.05.2014, 17.05.2014, 03.06.2014, 18.06.2014, 01.07.2014, 16.07.2014, 05.08.2014, 20.08.2014; Pheromone traps Ulubey: 02.05.2014, 17.05.2014, 03.06.2014, 18.06.2014, 01.07.2014, 16.07.2014, 05.08.2014, 20.08.2014; Pheromone traps Mesudiye: 18.05.2014, 04.06.2014, 19.06.2014, 03.07.2014, 18.07.2014, 03.08.2014, 18.08.2014, 05.09.2014

Host plants: *Pinus sylvestris*, *P. nigra*, *P. leucodermis*, *P. sibirica*, *P. koraiensis*, *P. brutia*, *Picea orientalis*, *Abies nordmanniana* subsp. *bornmulleriana*, *A. nordmanniana* [7, 9, 10, 11, 12, 21, 22, 23].

Distribution: Europe, Caucasus, Turkey, Siberia, Korea, Japan, North China [7, 21].

Turkish records: Artvin, Trabzon, Rize, Giresun, Samsun, Ayancık, Küre, Karabük, Ankara, Kızılcahamam, Soğuksu, Bolu, Düzce, Eskişehir, Bursa, Balıkesir-Dursunbey, Uşak, İzmir, Manisa, Denizli, Akseki, Muğla, Gölhisar, Erzurum, Sarıkamış [9, 10, 11, 12, 20, 22, 23].

***Ips typographus* (L, 1758)**

Material examined: Pheromone traps Çambaşı/İkidere-Gerce ovası-Kaleboynu; 17.03.2014, Çambaşı/Armutlan- Hevrek-Çelikkıran; 20.04.2014, Ulubey/Hapancık tepesi; 17.05.2014, Çambaşı /Sarıoba-Madala- Kürt Mehmet boğazı; 17.07.2014, Mesudiye / Yaylacık; 03.08.2014, Mesudiye/Avaroz; 18.08.2014, Mesudiye /Kopar – Muzdere; 05.09.2014

Host plants: *Picea orientalis*, *Picea abies*, *P. omorica*, *Pinus mugo*, *P. rotundata*, *P. cembra*, *P. peuce*, *P. leucodermis* [7].

Distribution: Central Europe, Bosnia and Herzegovina, Serbia, Macedonia and Bulgaria [7].

Turkish records: Sapanca- Gökdağ, Trabzon-Maçka, Artvin, Ardanuç, Borçka, Murgul, Şavşat, Yusufeli, Arhavi ve Ardahan-Posof [11].

***Trypodendron lineatum* (Olivier, 1795)**

Material examined: Pheromone traps Çambaşı /Çelikkıran; 30.04.2014, Çambaşı/Kale Boynu; 16.05.2014, Mesudiye; 20.05.2014, Çambaşı/İkidere; 30.06.2014, Çambaşı/Sarıoba; 17.07.2014, Mesudiye/Çoğran; 18.08.2014

Host plants: *Picea abies*, *P. orientalis*, *Abies alba*, *A. bornmülleriana*, *A. nordmanniana*, *Pinus brutia*, *P. silvestris*, *P. montana*, *P. strobus*, *P. cembra*, *Cedrus libani*, *Larix decidua*, *L. sibirica*, *Tsuga*, *Pseudotsuga*, *Thuja*, *Juniperus*, *Sequoia* [2, 8].

Distribution: Europe, North Africa, Siberia, Japan, Mediterranean, North America [21].

Turkish records: İstanbul, Bursa, Antalya, Düzce, Bolu, Karabük, Tokat, Giresun, Trabzon, Rize, Artvin [11].

Consequently, bark beetles are very important pests for forests of the region due to their damage. Many dead trees were observed as well as trees weakened by bark beetle species. Among the determined species, *I. sexdentatus*, *I. typographus* and *Dendroctonus micans*, cause economically important damage.

ACKNOWLEDGMENT

We express our sincere appreciation to Bartın University, Coordinatorship of Scientific Research Projects for their financial support by project which numbered as 2013.2.109.

REFERENCES

- [1]. M.Eroğlu, H. Alkan-Akıncı, and G.E. Özcan, Kabuk böceği Salgınlarının Nedenleri ve Boyutları. *Orman ve Av Dergisi*. 5:27-34, 2005
- [2]. E. Selmi, *Türkiye Kabuk Böcekleri ve Savaşı*, İstanbul Üniversitesi Yayınları, İstanbul, 1998
- [3]. P. Can, Türkiye Ormanlarında Son Yıllarda Görülen Kabukböcekleri (Coleoptera, Scolytidae) Sorunu Üzerinde Bir Değerlendirme. *Orman ve Av*. 82: 4-11, 2005.
- [4]. D.S. Hill, *The Economic Importance of Insects*, Chapman & Hall, London, 1997
- [5]. S. İnaç and B. Laz, Kahramanmaraş Andırın Kızılcım Ormanlarında Zarar Yapan Büyük Orman Bahçivani (*Blastophagus piniperda* Lin.)'na Karşı Feromon Denemesi ve Sonuçları. 4: 73-80, 2001.
- [6]. O. Sarıkaya and M. Avcı, Kabuk Böceklerine Karşı Ormanlarımızda Alınabilecek Koruyucu Önlemler. *Orman Mühendisliği Dergisi*. 1-2-3: 26-31, 2006.
- [7]. A. Pfeffer, *Zentral und westpaläarktische Borken und Kernkäfer*, Naturhistorisches Museum, Basel, 1995.
- [8]. H. Çanakçıoğlu and T. Mol, *Orman Entomolojisi, Zararlı ve Yararlı Böcekler*, İstanbul Üniversitesi Orman Fakültesi Yayınları, İstanbul, 1998.
- [9]. İ. Tosun, Akdeniz Bölgesi, *İğne Yapraklı Ormanlarda Zarar Yapan Böcekler ve Önemli Türlerin Parazit ve Yurtucuları Üzerine Araştırmalar*, İstanbul, 200 pp, 1975.
- [10]. O.A. Sekendiz, *Abies nordmanniana* (Stev.) Spach. 'nın Doğu Karadeniz Bölümü Ormanlarındaki Zararlı Böcekleri İle Koruma ve Savaş Yöntemleri. OGM Yayınları, 1991.
- [11]. B. Yüksel, Türkiye'de Doğu Ladini (*Picea orientalis* (L.) Link.) Ormanlarında Zarar Yapan Böcek Türleri ile Bunların Yurtucu ve Parazitleri, Doğu Karadeniz Ormanlık Araştırma Enstitüsü, Teknik Bülten No: 4, 143 pp, 1998.
- [12]. B. Yüksel, G. Tozlu and M. Şentürk, *Sarıkamış Sarıçam (Pinus sylvestris L.) Ormanlarında Etkin Zarar Yapan Kabuk Böcekleri ve Bunlara Karşı Alınabilecek Önlemler*. T.C. Orman Bakanlığı Doğu Akdeniz Ormanlık Araştırma Müdürlüğü, Teknik Bülten No: 3, Orman Bakanlığı Yayın No: 107, DAOA Yayın No: 8, 66 pp, 2000.
- [13]. J.C. Grégoire, *The greater European spruce beetle. In: Dynamics of forest insect populations* (Ed. by Berryman, A.), pp. 455-478. Plenum Publishing Corporation, New York, USA, 1988.
- [14]. K.E. Schedl, *Borkenkäfer aus der Türkei*, II. Mitteilung 190. Beitrag zur Morphologie and Systematik der Scolytoidea. 34: 184-188, 1961.
- [15]. A. Toper, Bartın ve Karabük Ormanlarındaki Göknarlarda Zarar Yapan *Pityokteines curvidens* (Germ.) (Coleoptera, Scolytidae)'in Biyolojisi. Doktora Tezi, ZKÜ, Bartın, 130 pp, 1999.
- [16]. A. Toper, Bartın ve Karabük Ormanlarında Göknar Ağaçlarında Zarar Yapan *Cryphalus piceae* (Ratzeburg) ve *Pityokteines curvidens* (Germar) (Coleoptera, Scolytidae)'in Bazı Biyolojik Özelliklerinin Karşılaştırılması. In: Türkiye 4. Entomoloji Kongresi Bildirileri, Aydın, pp. 111-118, 2000.
- [17]. A. Toper, The amount of damage and importance of *Pityokteines curvidens* (Germar) (Coleoptera, Scolytidae) feeding on fir in Bartın and Karabük forests in the western Blacksea region, Turkey. In: Third Balkan Scientific Conference, Study, Conservation and Utilisation of Forest Resources Proceedings, Sofia, pp. 54-64, 2001.
- [18]. A. Toper Kaygın, Batı Karadeniz Bölümünde *Abies bornmülleriana* Matff. Ağaçlarında Tespit Edilen Bazı Zararlı Böcekler ve Bunların Önemi. Gazi Üniversitesi Orman Fakültesi Dergisi. 3: 153-164, 2003.
- [19]. Z. Şimşek and N. Öner, Ilgaz-Yenice Orman Ekosisteminde Bulunan Kabuk Böceklerinin Salgın Yapmasında Meşcere Yapısı ve İklim Koşullarının Etkisi. II. Ulusal Karadeniz Ormanlık Kongresi Bildirileri, pp. 696-706, 2002.

- [20]. Y. Yıldız, Bartın ve Karabük Ormanlarının Scolytidae Faunası ve Bazı Önemli Türlerin Biyolojilerinin Belirlenmesi. Bartın, 2012.
- [21]. A. Kolk and J.R. Starzyk, *The Atlas of Forest Insect Pests*. The Polish Forest Research Institute, 705 pp, 1996.
- [22]. M. Defne, *Ips sexdentatus* Boerner Kabuk Böceğinin Çoruh Ormanlarındaki Durumu Ve Tevhit Ettiği Zararlar. *İ.Ü. Orman Fakültesi Dergisi*. 4: 80-91,1954.
- [23]. C. Chararas, *Picea orientalis*'e Arız Olan *Ips sexdentatus* ve Diğer Kabuk Böcekleri. *Ormanlık Araştırma Enstitüsü Dergisi*, 12:3-37, 1966.

Physical, Mechanical and Radiational Properties of Heavyweight Concretes Used for Structural and Radiation Shielding Purposes

Süleyman Ozen¹, Cengiz Sengul², Uner Colak², Mehmet Ali Tasdemir², Iskender Atilla Reyhancan²

Abstract

Heavyweight concrete is widely utilized as counterweight and shielding against radiation. Commonly, the heavyweight concrete is prepared by using high density aggregates. Similar to regular concrete, aggregates take approximately 75% of total volume in heavyweight concrete. This paper presents an experimental study that was carried out to investigate the influence of heavyweight aggregate type on the physical and mechanical properties, fracture behaviour under bending, and radiation shielding performance. Concrete samples were prepared by using iron ore, steel mill scale, two types of barite, steel slag which are heavyweight constituents available in Turkey and magnetite as a natural mineral heavyweight aggregate imported from the Netherlands. In all concrete samples prepared, water/cement ratio, cement content, maximum aggregate size, and the combined grading of aggregate used in the mixture were kept constant. In addition to the mechanical properties such as compressive strength, modulus of elasticity and splitting tensile strength, the fracture behaviour under bending was also investigated. Experimental observations show that the type of heavyweight constituents used affects the properties of heavyweight concretes. In terms of basic mechanical properties, the best performances were obtained when iron ore and steel slag were used while the highest fracture energy values were reached in concretes with steel mill scale, magnetite or the mixture of steel slag and iron ore. The second objective of this research study was to evaluate the radiation shielding properties of heavyweight concrete with iron ore, steel mill scale and two types of barite or steel slag used as aggregates. The experimental results showed that the attenuation coefficient varied from 0.224 to 0.265 1/cm. Based on this observation, it is concluded that there is reasonably good agreement between the theoretical values and experimental results of linear attenuation coefficients. This is a promising result that can be used to design heavyweight concretes using proper mix of ingredients against radiation fields with given characteristics.

Keywords: heavyweight concrete, radiation shielding, mechanical properties

1. INTRODUCTION

The utilization of radiation in diverse applications has been extended in recent years. Radiation is a form of energy transport either by electromagnetic waves or particles. Radiation has been beneficially utilized, however, it could create health risks for the users if necessary precautions are not taken. In order to avoid any undesired consequence, radiation sources should be confined in adequate structures with relevant strength and shielding characteristics. Proper shielding will create a medium for radiation to interact densely so that transmission to the other side is reduced significantly. Thus, adverse effects on human health are avoided [1].

Mainly, materials having high specific gravity are used for this purpose. Lead and heavy-weight concrete, which have these characteristics, are commonly used. But heavy-weight concrete is more preferred than the other especially due to its cost and mechanical properties. It is widely used in radiotherapy facilities and nuclear power plants in order to store and utilize radioactive materials. Heavy-weight concrete is a type of concrete which has the property of high radiation shielding, due to its unit weight which is more than 2.6 kg/dm³. As the unit weight of the concrete increases, the shielding performance against radiation increases. Presence of high Z, atomic number, elements also improve the shielding capability of materials against electromagnetic waves.

Various studies about heavyweight concretes have been performed according to the needs and application areas of the industry in the past. These investigations mostly focus on how the mechanical and shielding properties of heavyweight concretes change depending on the type of aggregate used.

Akyüz [2] made a concrete design by using barite aggregate in mixtures in order to shield against gamma rays and he carried out a comprehensive study on these concretes. As a result of experiments, while the amount of barite increased, strength did not improve, but the shrinkage decreased. Substantial increase in barite causes a rise in the linear attenuation coefficient. Coşkun [3] also investigated properties of concretes produced by using barite and the corresponding effects of this type of aggregate on radiation shielding. He studied the physical properties of concretes containing barite that have been designed to reach both an adequate workability and the theoretically calculated target radiation shielding. Kılınçarslan et al. [1] produced concretes of three different strength classes C20, C30, and C40 by using barite and

¹ Corresponding author: Uludag University, Department of Civil Engineering, 16059, Nilüfer/Bursa, Turkey. sozen@uludag.edu.tr

²Istanbul Technical University, Department of Civil Engineering, 34469, Sarıyer/İstanbul, Turkey. cengizsengul@yahoo.com

conventional aggregate. Physical and mechanical properties of these concrete samples were investigated and radiation attenuation coefficients were calculated.

Oudo [4] aimed to produce high-performance heavyweight concrete providing radiological protection, structural integrity and durability. He prepared 15 different concrete mixtures including the coarse aggregates of barite, magnetite, goethite and serpentine with addition of 10% silica fume, 20% fly ash and 30% blast-furnace slag of total content of cement in each mixture. He determined values of compressive strength of mixtures at 7, 28 and 90 days. Gamma ray sources such as ^{137}Cs and ^{60}Co radiation sources were used in radiation transmission tests. Experimental results showed that high performance heavy-weight concrete including magnetite coarse aggregate with 10% silica fume had the highest compressive strength and the shielding efficiency enhanced with increasing ratio of fine magnetite aggregate.

Ling and Poon [5] made a concrete design to research high temperature effects on heavyweight concrete containing barite and cathode ray tube funnel glass. They obtained the mechanical properties of heavyweight concrete after exposure to high temperature (25, 300, 500, 600, and 800 °C). At 25°C, barite concrete had higher density than granite concrete (normal) but compressive strength was decreased slightly. At 300°C, both density and strength of barite concrete were decreased significantly as compared with the granite concrete. After 600°C, explosion occurred on surface of concrete specimens.

Gonzales-Ortega et al. [6] evaluated behavior of concretes containing electric arc furnace slags (EAF) as aggregates. They produced 6 concrete mixtures. Four of them were made using EAF slags, one was produced as conventional concrete and the last one was designed as heavyweight concrete with barite aggregates. Concrete produced with EAF slag had the compressive strength similar to that of conventional concrete and higher compressive strength than that of concrete with barite. They obtained that attenuation coefficient was the highest for barite concrete and was the lowest for conventional concretes when concrete specimens were exposed to gamma rays.

Apart from the shielding applications, heavy-weight concretes are also used in the production of counterweight members as catenary support and in devices such as washing machines. In addition, heavyweight concrete is utilized for increasing the weight of immersed tubes constructed on the seafloor.

This work aims at determining both the mechanical properties and the radiation shielding properties of heavyweight concretes. The investigated mechanical properties include compressive strength, modulus of elasticity, tensile strength, bending strength and fracture energy. Understanding these properties plays a crucial role for ensuring safe and reliable use of heavyweight concretes in the construction of load carrying structural elements.

Heavyweight aggregates such as magnetite, barite, iron ore, steel mill scale, and steel slag were used in concretes produced for experimental study. After the physical properties of aggregates were investigated, concrete mixtures were produced for preliminary experiments. Design properties and workabilities of the concretes were investigated. Finally, concrete productions were carried out based on the selected mixture proportions. Physical and mechanical experiments were performed on concrete samples produced with six different heavyweight aggregates (i.e. magnetite, iron ore, steel mill scale, two types of barite, and steel slag). In order to investigate the shielding properties, all concrete samples except those produced with magnetite aggregate were irradiated by γ -ray emitted from a point source of Cesium (Cs-137) (at 662 KeV) and the corresponding linear attenuations were found both theoretically and experimentally.

2. MATERIAL AND METHODS

2.1. Materials

In this study, magnetite, iron ore, steel slag, steel mill scale, and two types of barite (barite 1 and barite 2) were used in the production of different types of heavyweight concretes. Crushed sand was also used in concretes including steel slag. The same type of cement (CEM I 42.5) was used in all mixtures and water/cement ratio was kept constant. In addition, superplasticizer was added to the mixtures to ensure workability. The range of the densities of heavyweight aggregates were as follows: Steel mill scale (0-2, 2-4 and 4-8 mm): 4.8 – 4.96 kg/dm³, Barite1 and 2 (0-2, 1-2, 2-4 and 4-8 mm): 3.94 - 4.25 kg/dm³, iron ore (0-2, 2-4 and 4-8 mm): 4.24- 4.39 kg/dm³, magnetite (0-2 and 0-8 mm): 4.73-5.13 kg/dm³, steel slag (0-3 mm): 3.60 kg/dm³. Oxide compositions of steel mill scale, iron ore, steel slag and crushed sand are given in Table 1.

Table 1. Chemical properties of the aggregates

Oxide Composition (%)	Steel Mill Scale	Iron Ore	Steel Slag	Crushed Sand	Barite I	Barite 2	Magnetite
CaO	-	26.25	3.74	52.59	-	-	-
SiO ₂	1.56	16.18	4.03	1.12	-	-	-
Al ₂ O ₃	-	2.33	2.17	-	-	-	-
Fe ₂ O ₃	97.52	42.28	75.60	2.67	-	-	-

Fe ₃ O ₄	-	-	-	-	-	-	97,7
MgO	-	4.28	2.13	0.25	-	-	-
K ₂ O	0.06	0.29	0.08	0.10	-	-	-
Na ₂ O	0.04	0.25	0.07	0.05	-	-	-
SO ₃	0.32	-	-	0.45	-	-	-
BaSO ₄	-	-	-	-	92.4	61.64	-
CaCO ₃	-	-	-	-	1.5	19.38	-
Loss on Ignition	5.14	6.13	11.48	42.74	6.1	18.98	2.3

Pycnometer method was used to measure water absorption capacity and density of concrete specimens. Table 2 shows values of water absorption and density of aggregates used in mixtures. Except for crushed limestone sand, water absorptions of all heavyweight aggregates were less than 0.8 %.

Table 2. Density and water absorption of aggregates in mixtures

Types of Aggregate	Gradation (mm)	Density (kg/dm ³)	Water Absorption
			(%)
Steel Mill Scale	0 – 2	4,96	0,1
	2 – 4	4,80	0,4
	4 – 8	4,93	0,4
Barite 1	0 – 2	4,06	0,8
	1 – 2	4,12	0,4
	2 – 4	4,25	0,3
	2 – 8	4,16	0,5
Barite 2	0 – 2	4,08	0,3
	2 – 4	4,00	0,2
	4 – 8	3,94	0,2
Iron Ore	0 – 2	4,24	0,2
	2 – 4	4,33	0,1
	4 – 8	4,39	0,4
Magnetite	0 – 2	5,13	0,3
	0 – 8	4,73	0,2
Steel Slag	0 – 3	3,60	0,3
Crushed Sand	0 – 4	2,70	1,0

2.2. Mixtures

2.2.1. Aggregate Content

All aggregates were used as dry surface-saturated condition. Concretes produced were designated by the mixture codes of T, D, B1, B2, M and G. T and D show the concretes produced with steel mill scale and iron ore, respectively. B1 and B2 refer to the concretes produced with the combinations of Barite 1 and Barite 2, respectively. M expresses the concrete produced with magnetite and G is used to represent the concrete produced with steel slag, iron ore and crushed sand. Apart

from other concrete mixtures, iron ore was added to the last concrete mixture to ensure the required unit weight and crushed sand was added for the sufficient workability of fresh concrete.

In the small size prefabricated members, the maximum aggregate size was kept constant and was limited to 8 mm because coarse aggregates cause several problems regarding the homogeneity [7]. For each type of aggregate, grading in concrete mixtures was selected by taking Fuller Parabola as reference. Fuller parabola is calculated as follows using Eq. (1):

$$P = 100 \times \sqrt{\left(\frac{d}{D}\right)} \quad (1)$$

In this equation, "D" is the maximum aggregate size and "d" shows any aggregate size between 0.25 and 8 mm.

2.2.2. Concrete Mixtures

Heavyweight concrete mixtures were prepared by using six different heavy aggregates of five different mineralogical origins in this study. Crushed sand, as a conventional aggregate, was used together with high contents of heavy aggregates (steel slag and iron ore) in the last concrete mixture. A total of six different concrete mixtures were produced. Cement content and effective water/cement ratio were kept constant for each concrete mixture. The mixture proportions of the concretes produced are shown in Table 3.

Table 3. Mix proportions of concrete mixtures and fresh concrete properties

	M	T	D	B1	B2	G
Cement, kg/m ³	551	546	559	550	550	551
Water, kg/m ³	154	153	156	154	154	154
Water/Binder	0.28	0.28	0.28	0.28	0.28	0.28
Super Plasticizer, kg/m ³	16	20	18	15.36	16.5	40.9
Aggregate 0-2 mm, kg/m ³	1163	1243	1364	2028	1503	1571
Aggregate 2-4 mm, kg/m ³	870	902	696	552	305	228
Aggregate 4-8 mm, kg/m ³	1039	927	706	35	751	480
Concrete Unit Weight, kg/m ³	3793	3820	3447	3334	3278	3012
Air Content (%)	3.30	4.7	2.26	3.52	3.58	5.62
Flow (cm)	40	50	47	60	60	50

3. EXPERIMENTS

3.1.1. Mechanical and Fracture Properties

At 72 days, compressive, splitting tensile and bending strengths, moduli of elasticity, fracture energies, experimental and theoretical linear attenuation coefficients of T, D, B1, B2 and G concretes were determined except for concrete type M. Only compression and bending tests were carried out on M where compressive and bending strengths, modulus of elasticity and fracture energy were determined. For each type of concrete, compression tests were carried out on three cylindrical specimens having a diameter of 100 mm and height of 200 mm. Modulus of elasticity for each concrete mixture was calculated from the stress strain curve up to the 35% of maximum stress. Compressive strengths and the moduli of elasticity of the different mixtures are presented in Fig. 1.

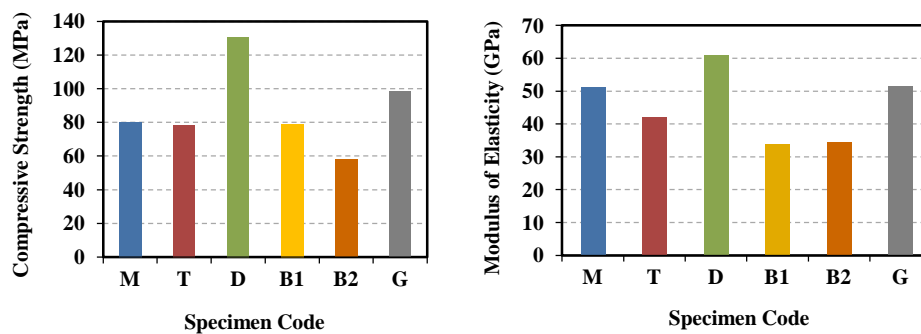


Fig. 1. Compressive strengths and the moduli of elasticity of the mixtures

Six disc specimens having a diameter of 150 mm and height of 60 mm were produced for Splitting tensile tests. Splitting tensile strength of concretes were calculated using Eq. (2) as follows:

$$f_{ct} = \frac{2 \times F}{\pi \times L \times D} \quad (2)$$

In this equation, f_{ct} is splitting tensile strength, F is fracture force, L is loading strip length and D is cross-section size of the concrete sample. Splitting tensile strength values for different mixtures are shown in Fig. 2.

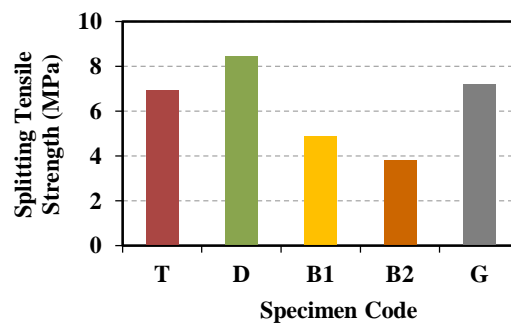


Fig. 2. Splitting Tensile Strength of Concretes

Three point bending tests were carried out on five beam specimens having 70 x 70 x 280 mm dimensions for each mixture. The tests were performed under displacement control, using INSTRON 5500R closed loop testing machine having a 100 kN capacity. During the experiment, the deflection was obtained from an LVDT placed under the beam and the crack mouth opening displacement was measured by a displacement transducer at the same time.

The bending strength (F_{net}) of notched beams for three point bending test was calculated by using Eq. (3) as follows:

$$F_{net} = \frac{3 \times P \times L}{2 \times B \times (H - a)^2} \quad (3)$$

In this equation P , L , B , H and a are maximum load, span, effective span, beam width, beam height, and notch depth, respectively.

Fracture energy (G_f) is the energy required to form a crack of unit area on a plane parallel to the crack direction [8] and its unit is N/m or Joule/m². Values of fracture energy were calculated from the area under load-deflection curve in accordance with the method proposed by RILEM TC 50-FMC [8] using Eq. (4) as follows:

$$G_f = \frac{W_0 + m \cdot g \cdot \delta_0}{A_{lig}} \quad (4)$$

In this equation, W_0 is the area under load-deflection curve (N/m), m is the weight of the span between beam supports (N), g is gravitational acceleration, δ_0 is the deflection of beam at collapse and A_{lig} is the effective cross-section area of the notched beam ($A_{lig} = (H - a) \cdot b$).

The Bending Strength and the fracture energies obtained for different heavyweight concrete mixtures are given in Fig. 3.

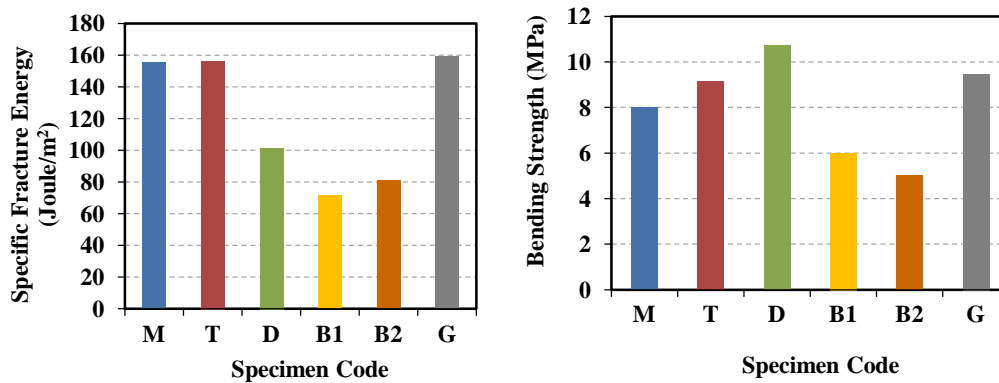


Fig. 3. Fracture Energies and Bending Strengths of Different Heavyweight Concrete Mixtures

The Load-crack mouth opening displacement curves obtained from testing of different concrete mixtures are presented in Fig. 4.

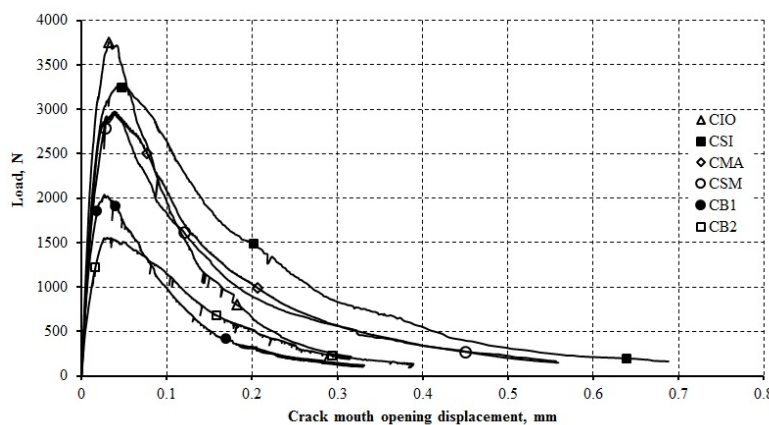


Fig. 4 Typical load-crack mouth opening displacement curves for concretes investigated

3.1.2. Radiation Transmission Experiments

Radiation transmission experiments were carried out on concrete specimens produced with five different aggregates and linear attenuation coefficients (μ) were investigated. 6, 15, 21, and 30 cm thick specimens were used for each concrete mixture for the experiment. Radiation transmissions of the specimens exposed to γ ray were measured. ^{137}Cs radioisotope (Cesium-137) was used as the γ ray source. Cesium-137 radioisotope emits photons having 662 keV energy. γ spectroscopy analysis was carried out with High Purity Germanium Detector (HPGe). Photons were counted on PC by using Genie 2000 program. Linear attenuation coefficients of each concrete mixture were calculated using Eq. (5) as follows:

$$\mu = \frac{\ln(I_0/I)}{x} \quad (5)$$

In this equation, μ is linear attenuation coefficient, I_0 is counted value when there is no concrete between radioactive source and detector, I is counted value when there are specimens of concrete with different thickness between radioactive source and detector, and x is thickness of concrete specimen exposed to radiation.

The linear attenuation coefficients obtained for different mixtures are shown in Fig 5. These coefficients vary in direct proportion with unit the weight of the concrete. Also, there is an inverse proportion between the linear attenuation coefficient and radiation transmission.

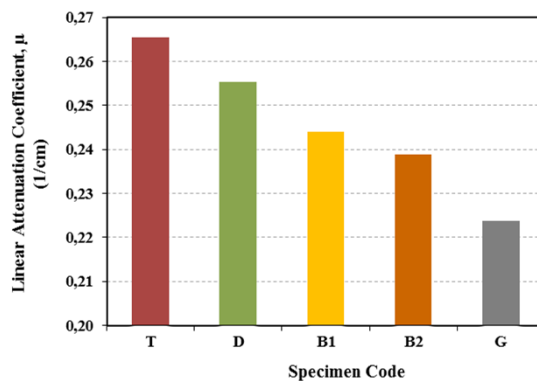


Fig 5. Linear Attenuation Coefficients of Concrete

After radiation transmission experiment, the theoretical linear attenuation coefficients of concretes were calculated using XCOM online database in this work [9]. Calculations were performed based on the chemical compositions of the constituents for each concrete. The experimental and theoretical linear attenuation coefficients obtained for different mixtures are shown in Figure 6. They are in reasonably good agreement. The theoretical values are slightly above the experimental results. Slight variations may be originated from the use of finite size of slabs in experiments and inhomogeneities and uncertainties associated with compositions and densities.

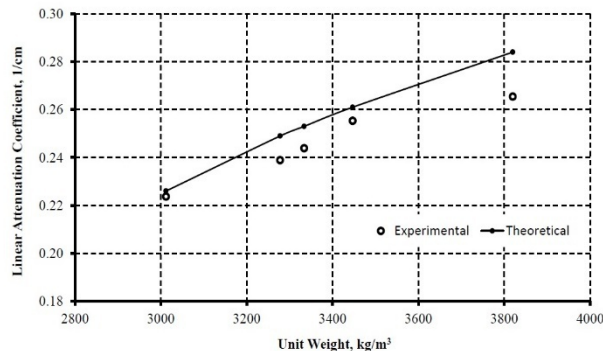


Fig. 6. Relation between the unit weight and the linear attenuation coefficient of concrete tested

4. RESULTS AND CONCLUSION

Based on the results obtained in this study, the following conclusions can be drawn:

Cylindrical compressive strength of the concretes containing iron ore is significantly higher than those of all the other mixtures. Compressive strength of the concrete mixture produced with iron ore and steel slag is also high compared to the rest of the mixtures except the mixture with only iron ore aggregates. The presence of Fe_2O_3 or Fe_3O_4 in concretes with iron ore, magnetite, steel mill scale and steel slag may play an important role in high values of compressive strength. Concrete containing barite 2 aggregate gave the lowest compressive strength among all mixtures.

The change in modulus of elasticity has a similar trend as the compressive strength. Moduli of elasticity of concretes produced with iron ore were the highest. Moduli of elasticity of concretes containing barite aggregates were significantly lower than those of the others. There is no considerable effect of BaSO_4 content in concrete with barite 1 and barite 2 in terms of modulus of elasticity.

Similarly, the splitting tensile strengths of concretes produced with iron ore are higher than the other mixtures. As seen in the other mechanical properties, concretes produced with barite have lower tensile strengths. Concrete with barite 1, which has a density higher than that of barite 2, has a comparatively higher splitting tensile strength.

Bending strengths of concretes produced with iron-ore is higher than others. As in the compressive and splitting tensile strengths, concretes containing barite aggregates have the lowest bending strength values.

The radiation transmission decreases with increasing concrete thickness for all concrete mixtures. The linear attenuation coefficient increases with increasing unit weight of concrete. There is reasonably a good agreement between theoretical and experimental attenuation coefficient. So, radiation shielding is directly related to the unit weight of concrete.

REFERENCES

- [1]. Kılınçarslan, Ş.; Başıyigit, C., Akkurt, İ. Investigation of Heavyweight Concrete with Barite Aggregates for Radiation Shielding, *Journal of The Faculty of Engineering and Architecture of Gazi University*, 22(2): 393-399. (2007).
- [2]. Akyüz, S.: "Heavyweight concrete with barite aggregate for protecting structures against Gamma Rays", *ITU Journal*, Vol 35, Year 35, Number 5, Page: 59-69, (1977).
- [3]. Coşkun, A.: Use of Barite Aggregate in Heavy-weight Concrete and Study of Concrete Properties. Master Thesis, Afyon Kocatepe University, 2010.
- [4]. Ouda, A. S.: Development of High Performance Heavy Density Concrete Using Different Aggregates for Gamma-Ray Shielding. *Progress in Nuclear Energy*. 79, 48-55 (2015).
- [5]. Ling, T. C.; Poon C. S.: High temperatures properties of barite concrete with cathode ray tube funnel glass. *Fire Mater.* 38, 279–289 (2014).
- [6]. Gonzales-Ortega, M. A.; Segura, I.; Cavalaro, S.H.P.; Toralles-Carbonari, B.; Aguado, A.; Andreello, A.C: Radiological protection and mechanical properties of concretes with EAF steel slag. *Construction and Building Materials*. 51, 432–438 (2014).
- [7]. Mindess S.; Young J.F.: *Concrete*. Prentice-Hall, Englewood Cliffs, NJ 07632, pp. 596– 599, 1981.
- [8]. RILEM Technical Committee 50-FMC 1985. Draft Recommendation Determination of the fracture energy of mortar and concrete by means three point bend test on notched beams. *Materials and Structures*, 18(4), 287-290.
- [9]. Berger, M.J., Hubbell, J.H., Seltzer, S.M., Chang, J., Coursey, J.S., Sukumar, R., Zucker, D.S., and Olsen, K., XCOM: Photon Cross Section Database (version 1.5). [Online] Available: <http://physics.nist.gov/xcom>. National Institute of Standards and Technology, Gaithersburg, 2010, MD.

Prediction of Evapotranspiration with Daily Meteorological Data Using M5 Model Tree

Yunus Ziya Kaya¹, Fatih Unes², Mustafa Mamak³

Abstract

Evapotranspiration is an important term for hydrological design and agricultural yield. Although it has a great impact on the efficiency of hydrological design calculations such as dam water level changes and agricultural yield, evapotranspiration (ET) process and accuracy of ET models are not clear enough. This study consists two parts. For each part of the study, the same data set including namely Solar Radiation (SR), Wind Speed (U), Air Temperature (T), Relative Humidity (RH) and ET parameters is employed. The data set is achieved from De Soto County, Florida, USA. In the first part, M5 model tree (M5T) is built up and 1716 daily meteorological data is used for training the model and 571 daily meteorological data for testing the model. In the second part of the study, the Ritchie empirical formula is applied to the data set. For comparison of the results Mean Square Error (MSE), Mean Absolute Error (MAE) and determination coefficient (R) statistics are used. According to the comparison it is found that M5T gives better solutions than Ritchie empirical formula and it is possible to employ M5T successfully to the ET modelling. **Keywords:** evapotranspiration, M5 model tree, prediction, Ritchie, statistical modeling

Keywords: evapotranspiration, M5 model tree, prediction, Ritchie, statistical modelling

1. INTRODUCTION

Water losses due to evapotranspiration take a basic role in our local scales, regional, even in our environment. Evapotranspiration is an important part of agricultural yield and hydraulic design. Irrigation engineers need to consider ET as a determinative parameter for planning an irrigation field. Although it effects human life quality directly or indirectly, information about evapotranspiration is not clear enough as it is due to meteorological parameters. Generally it is assumed that energy & aerodynamic equations give most accurate solutions for ET as a result of these equations are based on physics rules and rational relationships [1]. In this study Ritchie empirical formula is used because of this formula is based on physics rules and rational relationships. For the reason ET is hard to calculate with high accuracy, some different methods have been suggested as described by [1], [2].

In the past decade, some new methods are used to predict evapotranspiration, reference evapotranspiration or evaporation such as artificial neural networks [3], fuzzy logic [4], support vector machines [5] and M5T [6], [7]. In this study M5T which is a decision tree method is used to determine evapotranspiration. Daily meteorological parameters RH, T, SR and U is used as input and ET is used as output of the model. M5T model results and Ritchie formula results are compared with daily recorded ET values. Both-M5T and Ritchie-results are compared using MSE, MAE and correlation coefficient statistics. According to the statistical investigation it is seen that M5T method performs better than Ritchie formula for the forecasting daily ET.

2. MATERIALS and METHODS

2.1. Data Set Used

Daily meteorological data set is achieved from De Soto County, Florida, USA station which is located with 27°10'42" latitude and 81°46'23" longitude. Location of the station is marked in Figure 1. Data set is downloaded from U.S. Geological Survey website [8]. SR, RH, U, T and ET are the parameters of the data set downloaded. Units of parameters are given by turns as W/m², percent, m/s, C°, mm. Data set consists of 2287 daily data between 2004-2010 years. 1716 daily (approximately % 75 of data set) data is used for training M5T and remaining 571 daily data is used for testing it. And also Ritchie formula is applied to the test set.

¹ Corresponding author: Osmaniye Korkut Ata University, Department of Civil Engineering, 80000, Merkez/Osmaniye, Turkey. yunuszkaya@osmaniye.edu.tr

² Iskenderun Technical University, Department of Civil Engineering, 31200, Iskenderun/Hatay, Turkey. fatihunes66@gmail.com

³ Osmaniye Korkut Ata University, Department of Civil Engineering, 80000, Merkez/Osmaniye, Turkey. mmamak@osmaniye.edu.tr

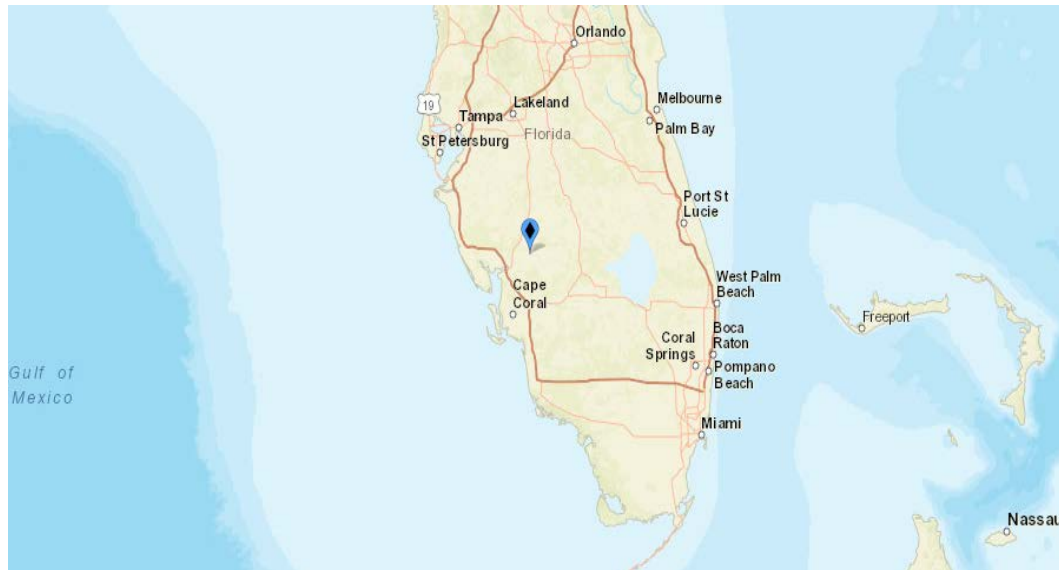


Figure 1. Location of data set station

2.2. M5 Model Tree

Model trees have constant values at their leaves as a concept of regression trees [9]. M5T is a decision tree which has regression functions at the terminal nodes. Model occur one root node and according to the problem complexity/data set specifications, nodes are built up. Splitting data set into subsets for M5T is based on getting lower values of standard deviation as a measure of error at each node [7]. Standard deviation reduction formula (SDR) is given below as;

$$SDR = sd(T) - \sum \frac{|Ti|}{|T|} sd(Ti) \quad (1)$$

At equation 1; “sd” represents standard deviation, “T” symbolized a set of examples that get at the node and “Ti” symbolized subset of examples that have the *i*th effect of the potential set. As a result of splitting process, child nodes always have less standard deviation values than the main nodes. One more result of splitting process is producing a large tree which may cause overfitting. To handle overfitting problem M5T structure must be pruned. For further information about M5T, readers are referred to [10].

2.3. Ritchie Formula

Ritchie method is described by [11] as below;

$$ET = \alpha_1 [3.87 \times 10^{-3} R_s (0.6T_{\max} + 0.4T_{\min} + 29)] \quad (2)$$

At equation 2; “ R_s ” symbolized solar radiation, “ T_{\max} ” and “ T_{\min} ” represent maximum and minimum temperatures. α_1 is a coefficient which is calculated as below;

$$5 < T_{\max} \leq 35 \text{ } ^\circ\text{C} \quad \alpha_1 = 1.1 \quad (3)$$

$$T_{\max} > 35 \text{ } ^\circ\text{C} \quad \alpha_1 = 1.1 + 0.05(T_{\max} - 35) \quad (4)$$

$$T_{\max} < 5 \text{ } ^\circ\text{C} \quad \alpha_1 = 0.01 \cdot \exp[0.18(T_{\max} + 20)] \quad (5)$$

2.4. Evaluation Criteria

Results of ANFIS model and Hargreaves-Samani equation are evaluated using MSE, MAE, R and R^2 values. These values are calculated as follows:

$$MSE = \frac{1}{N} * \sum_{i=1}^n (f_i - y_i)^2 \quad (2)$$

$$MAE = \frac{1}{N} * \sum_{i=1}^n |f_i - y_i| \quad (3)$$

$$R = \frac{\sum_{i=1}^n (x_i - \bar{X}) \cdot (y_i - \bar{Y})}{\sqrt{\sum_{i=1}^n (x_i - \bar{X})^2} \cdot \sqrt{\sum_{i=1}^n (y_i - \bar{Y})^2}} \quad (4)$$

Error! Bookmark not defined. Where, “ f_i ” represents predicted values and “ y_i ” represents actual values for equation 2&3. “ x_i ” shows i th actual value, “ y_i ” shows i th predicted value, \bar{x} represents x_{mean} and \bar{y} represents y_{mean} at equation 4.

3. RESULTS and DISCUSSIONS

In this study authors mainly investigated the ability of M5T method for prediction of daily ET. For the evaluation, distribution graphs of daily Ritchie formula ET outcomes and daily M5T results are drawn. Also scatter chart is drawn for Ritchie formula and M5T method. Final comparison is done using MSE, MAE and correlation coefficient statistics and results are shown in Table 1.

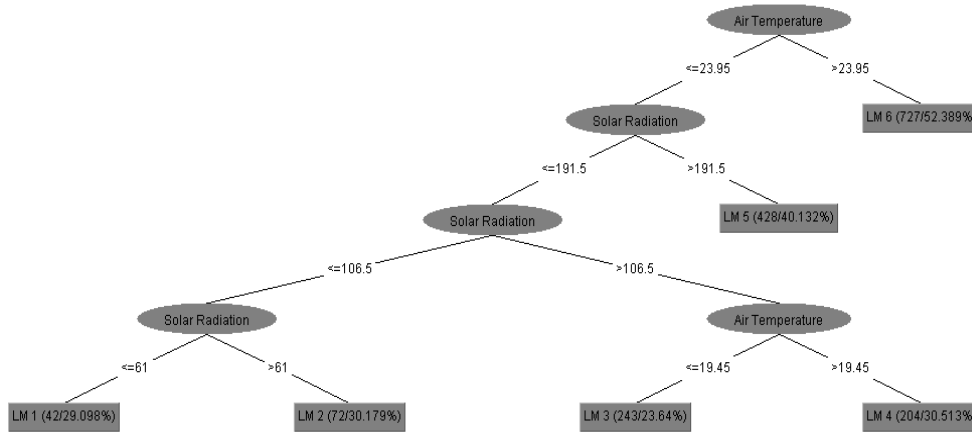


Figure 2. M5T structure

It is seen in Figure 2 that T is the root node of the structure which means T is the main parameter of the tree. There is no effect of RH & U parameters in this structure and also it is possible to see regression functions at terminal nodes.

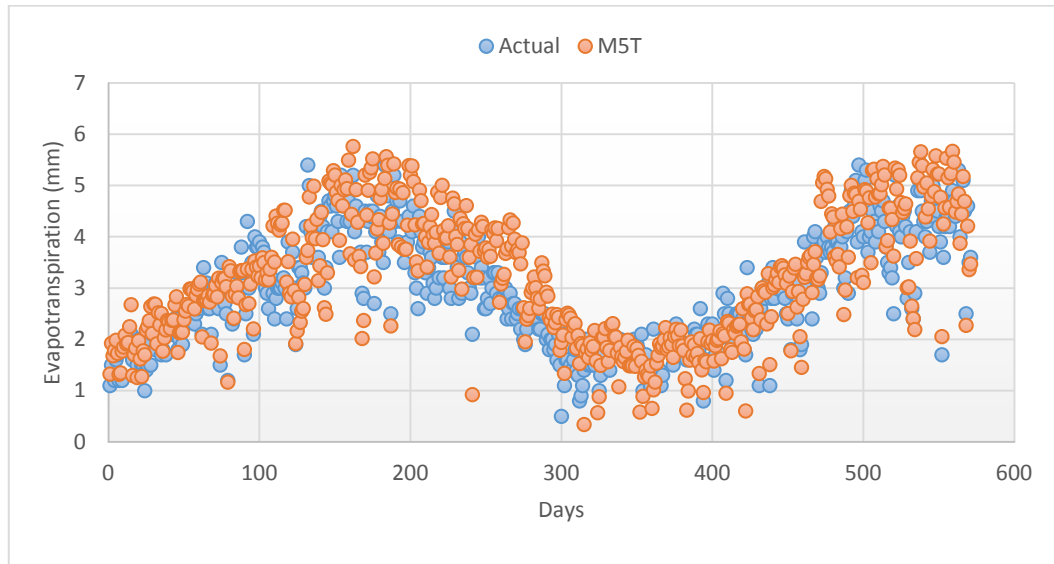


Figure 3. Distribution graph of daily M5T method results

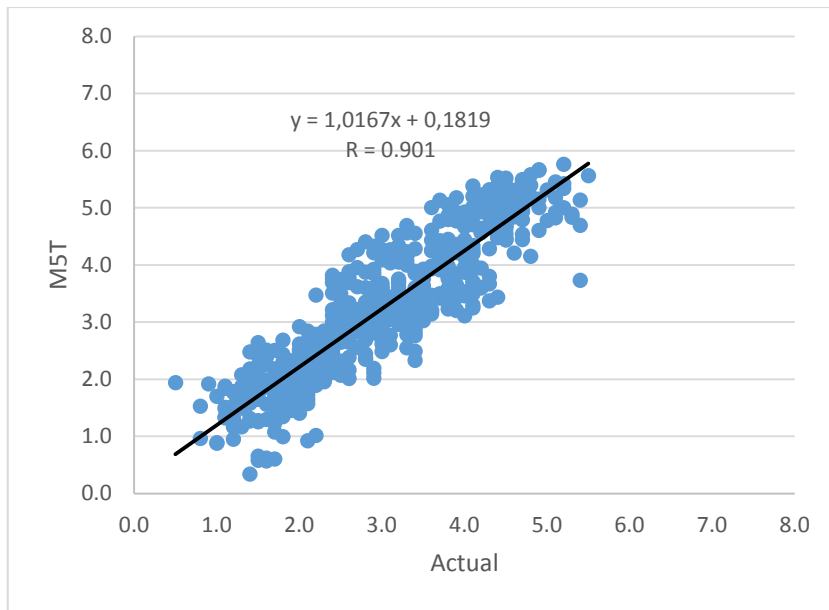


Figure 4. Scatter chart of M5T method results

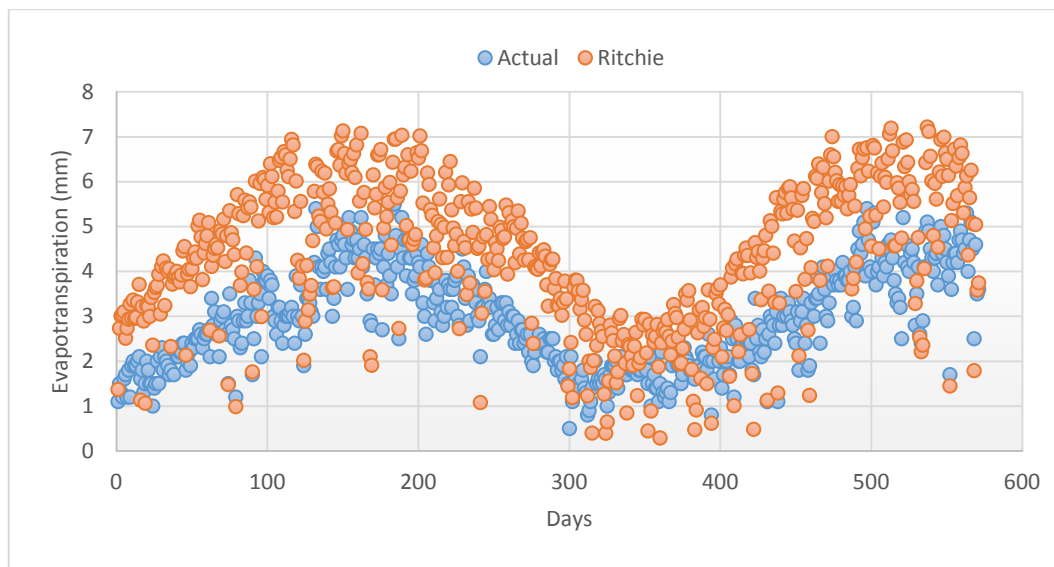


Figure 5. Distribution graph of daily Ritchie formula results

As it is drawn in Figure 3&5 it is seen that distribution of M5T results are looking closer to the actual values. For the seeing results statistically scatter charts are drawn and it is understood that M5T gives better solutions (R is 0.901) than Ritchie empirical formula. Any daily missing value is not used in model creating process to extinguish missing values effect on results.

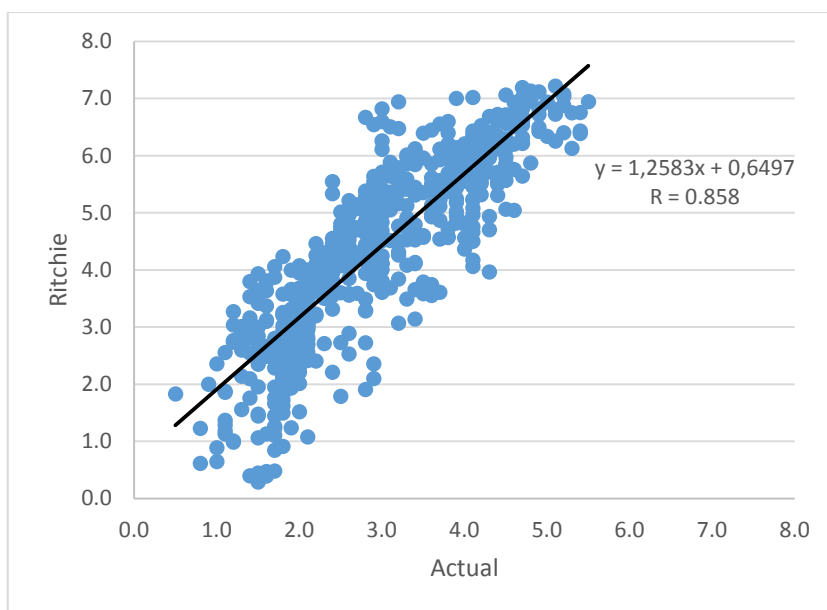


Figure 6. Scatter chart of Ritchie formula results

Table 1. Comparison of Ritchie equation and M5T results statistically

	M5T	Ritchie
R	0.901	0.858
R ²	0.811	0.737
MSE	0.338	2.733
MAE	0.459	1.476

Statistical investigation parameters which are MSE, MAE, R, R² are calculated and given in Table 1.

4. CONCLUSION

The potential of M5T data mining method and Ritchie empirical formula is investigated for the forecasting daily ET by comparing results with observed daily ET. Although M5T method's R and R² statistics are close to Ritchie formula's R and R² values, the error calculations showed that MSE and MAE values of M5T method is much more lower than Ritchie formula. Therefore it is understood it is possible to use M5T method for modelling ET and it gives better solutions than Ritchie empirical formula. In this study parameter effect on M5T method is not investigated as detailed but according to the results it is seen that M5T method neglected the RH and U parameters when building the tree. Parameters effect on M5T and ET could be investigated as a part of another study.

REFERENCES

- [1]. Jensen, M.E., Burman, R.D. & Allen, R. G. *Evapotranspiration and Irrigation Water Requirements*, New York, USA: ASCE Manuals and Reports on Engineering Practices no. 70., ASCE, 1990.
- [2]. Brutsaert, W. H. *Evaporation into the Atmosphere*, Dordrecht, The Netherlands: D. Reidel Publishing Company, 1982.
- [3]. O. Kisi, "Evapotranspiration modelling from climatic data using a neural computing technique," *Hydrological Process.*, vol. 21, pp. 1925-1934, 2007.
- [4]. O. Kisi, "Fuzzy genetic approach for modelling reference evapotranspiration," *Journal of Irrigation and Drainage Engineering.*, vol. 136, pp. 175-183, March, 2010.
- [5]. O. Kisi, M. Cimen, "Evapotranspiration modelling using support vector machines," *Hydrological Sciences.*, vol. 54(5), pp. 918-928, October 2009.
- [6]. O. Kisi, "Pan evaporation modelling using least square support vector machine, multivariate adaptive regression splines and M5 model tree," *Journal of Hydrology.*, vol. 528, pp. 312-320, June 2015.
- [7]. M. Pal, S. Deswal, "M5 model tree based modelling of reference evapotranspiration," *Hydrological Processes.*, vol. 23, pp.1437-1443, March 2009.
- [8]. (2015) U.S. Geological Survey website. [Online]. Available: <http://www.usgs.gov/>

- [9]. I.H. Witten and E. Frank, Data Mining: Practical Machine Learning Tools and Techniques with Java Implementations, Morgan Kaufmann, San Francisco, 2005.
- [10]. J.R. Quinlan, "Learning with continuous classes," Proceedings of Australian Joint Conference on Artificial Intelligence, World Scientific Press: Singapore, 1992, 343-348.
- [11]. J. W. Jones, J.T. Ritchie, Ed., Crop growth models: Management of farm irrigation system, G.J. Hoffman, T.A. Howel, and K.H. Solomon, eds., ASAE monograph No. 9, ASAE, St. Joseph, Mich., 1990, pp. 63-89.

Estimating Evapotranspiration Using Adaptive Neuro-Fuzzy Inference System and Hargreaves-Samani Method

Yunus Ziya Kaya¹, Fatih Unes², Mustafa Mamak³

Abstract

Information about evapotranspiration (ET) is limited even though water losses due to evapotranspiration is an important process for hydrological design and agricultural yield. Solar Radiation (SR), Air Temperature (T), Wind Speed (U) and many other meteorological parameters have an impact on evapotranspiration. In this study 2287 daily meteorological SR, T, U and Relative Humidity (RH) data from De Soto County, Florida, USA are used for modelling ET. In the first part of the study an adaptive neuro-fuzzy inference system (ANFIS) model is created using 1716 daily data for training model and remaining 571 daily data is used for testing model. In the second part of the study Hargreaves-Samani empirical formula is applied to the data set. Mean Square Error (MSE), Mean Absolute Error (MAE) and determination coefficient (R) statistics are calculated for the evaluation of results. According to the analysis, it is seen that ANFIS has better performance than Hargreaves-Samani empirical formula and for modelling ET.

Keywords: *adaptive neuro fuzzy inference system, estimation, evapotranspiration, Hargreaves-Samani, modelling*

1. INTRODUCTION

Knowledge of evapotranspiration losses is an important parameter for the hydrological design and agricultural yield. Designers of many hydraulic constructions, such as dam or irrigation channel construction designers, need to know how much water will be lost due to ET after construction is built up. An irrigation engineer needs to consider ET as a determinative parameter for satisfactory agricultural yield, for the reason ET has an impact on crop water need.

Many different methods have been suggested to calculate ET by Brutsaert & Jensen [1], [2]. Generally, using combination of energy balance and aerodynamic equations, gives most accurate solutions because of this equations are based on physics rules and rational relationships [2]. In this study Hargreaves-Samani empirical equation is used to determine ET as this equation is based on physics rules and rational relationships. Hargreaves-Samani equation is employed for calculation of ET in some studies [3], [4], [5]. On the other hand some neuro-computing techniques such as adaptive neuro-fuzzy inference system, fuzzy genetic approach, artificial neural networks are proposed for modelling reference evapotranspiration, evaporation, monthly/daily evapotranspiration [5], [6], [7].

In this paper ability of ANFIS model and Hargreaves-Samani formula for prediction of ET is investigated, results are compared using MAE, MSE and R. According to the investigation, it is found that ANFIS model has higher accuracy than Hargreaves-Samani for estimation ET.

2. MATERIALS and METHODS

2.1. Data Set Used

Daily climatic data of De Soto County station which is located Florida, USA with latitude 27°10'42" and longitude 81°46'23" are used. Data set is downloaded from U.S. Geological Survey website [8]. Data set is including SR, ET, U, T, RH parameters and it consists of six years data (2004-2010). First, respectively, 75 percent of daily records is used for training ANFIS model and remaining 25 percent for testing the model. Hargreaves-Samani calculations are made for the same daily test set with ANFIS model.

¹ Corresponding author: *Osmaniye Korkut Ata University, Department of Civil Engineering, 80000, Merkez/Osmaniye, Turkey.*
yunuszkaya@osmaniye.edu.tr

² *Iskenderun Technical University, Department of Civil Engineering, 31200, Iskenderun/Hatay, Turkey.* fatihunes66@gmail.com

³ *Osmaniye Korkut Ata University, Department of Civil Engineering, 80000, Merkez/Osmaniye, Turkey.* mmamak@osmaniye.edu.tr

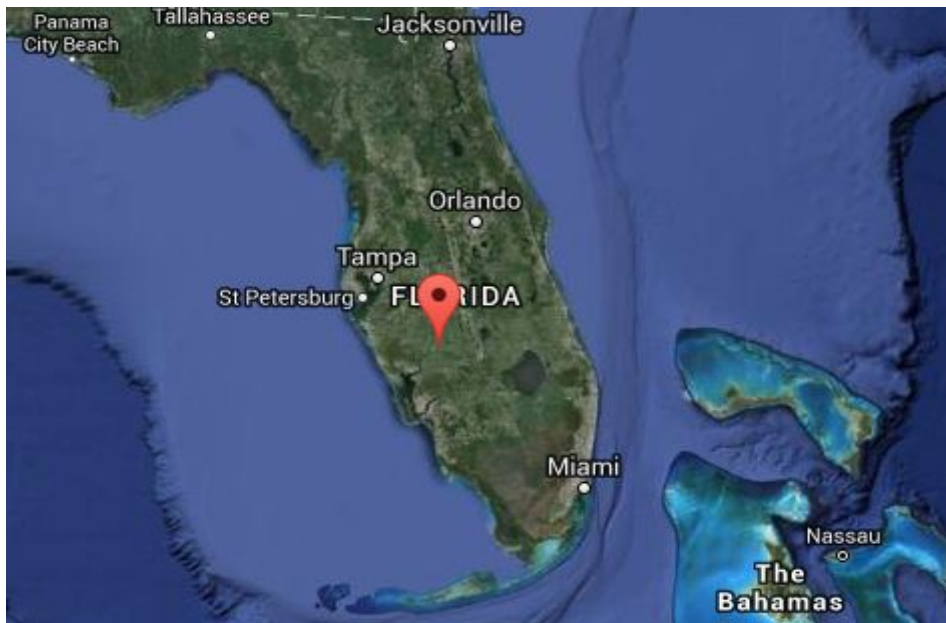


Figure 1. Location of data set station

2.2. Adaptive Neuro-Fuzzy Inference System

Fuzzy set concept first introduced by Zadeh [9]. Since then, fuzzy sets systems are improved to apply practical/physical cases. It is possible to introduce fuzzy sets as logical models which is occurred “If-Then” rules and membership functions. Fuzzy models let users to define physical problems linguistic and according to the linguistic definition, models let users to make transparent interpretation and analysis. An ANFIS is a fuzzy inference system carried out in the framework of adaptive networks [10]. Sugeno model which was suggested by Takagi and Sugeno [11] is in use to create an ANFIS model.

In this study Subtractive Clustering Method of ANFIS is used for ET prediction. SR, U, T, RH meteorological variables are applied as input and ET as output. Calibration of model is done as trial. Readers are referred to [12] for further information about ANFIS structure.

2.3. Hargreaves-Samani Equation

Necessary parameters for calculation of daily ET with Hargreaves-Samani equation are daily maximum temperature (T_{max}), daily minimum temperature (T_{min}) and extraterrestrial solar radiation (R_s) [13]. The equation which is used for calculation is given below;

$$ET = 0,0135.0,408R_s(T + 17,8)(1)$$

Where, “T” represents daily mean temperature in Hargreaves-Samani equation.

2.4. Evaluation Criteria

Results of ANFIS model and Hargreaves-Samani equation are evaluated using MSE, MAE, R and R^2 values. These values are calculated as follows:

$$MSE = \frac{1}{N} * \sum_{i=1}^n (f_i - y_i)^2 \tag{2}$$

$$MAE = \frac{1}{N} * \sum_{i=1}^n |f_i - y_i| \tag{3}$$

$$R = \frac{\sum_{i=1}^n (x_i - \bar{x}) \cdot (y_i - \bar{y})}{\sqrt{\sum_{i=1}^n (x_i - \bar{x})^2} \cdot \sqrt{\sum_{i=1}^n (y_i - \bar{y})^2}} \tag{4}$$

Error! Bookmark not defined.Where, “ f_i ” represents predicted values and “ y_i ” represents actual values for equation 2&3. “ x_i ” shows i th actual value, “ y_i ” shows i th predicted value, \bar{x} represents x_{mean} and \bar{y} represents y_{mean} at equation 4.

3. RESULTS and DISCUSSIONS

In the first part of the study authors focused on ANFIS and Hargreaves-Samani results separately. Firstly ANFIS results are compared with recorded daily ET values. Distribution graph and scatter chart (Figure 2&3) are drawn to show accuracy of ANFIS results and then same graphs (Figure 4&5) are drawn for Hargreaves-Samani empirical equation results. In the second part of the study relation between ANFIS results and empirical equation is investigated and a table is created to see the comparison (Table 1).

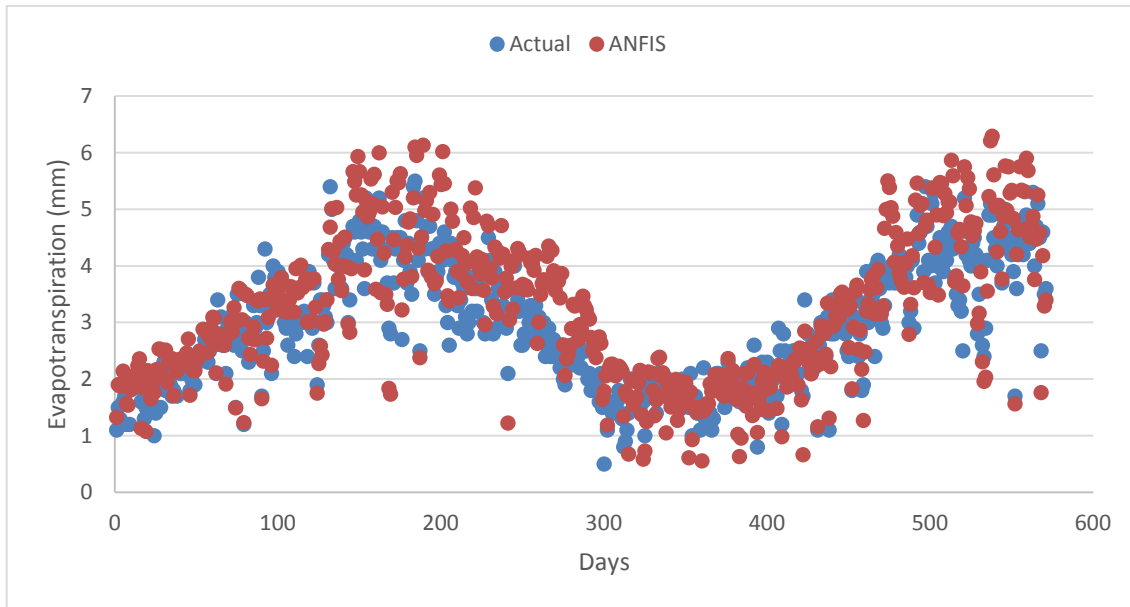


Figure 2. Distribution graph of daily recorded ET and daily ANFIS results

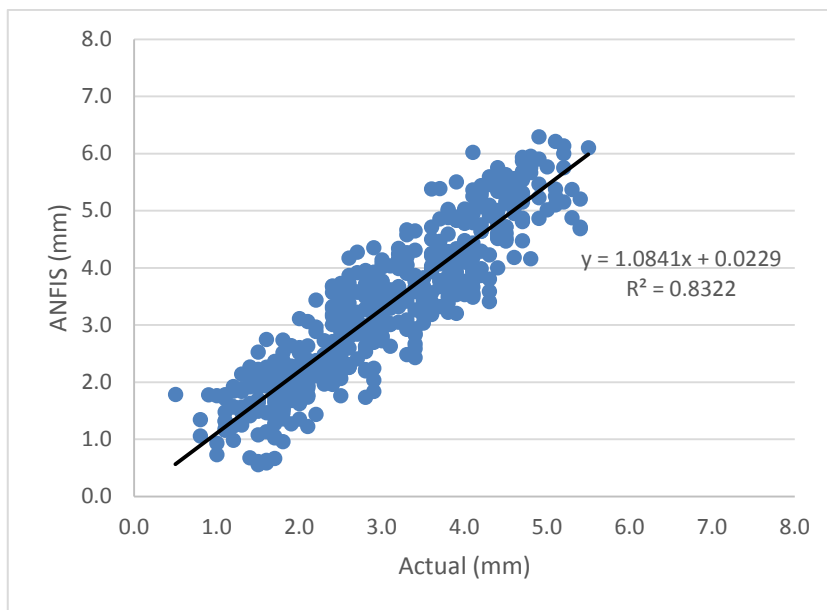


Figure 3. Scatter chart of daily recorded ET and daily ANFIS results

Distribution graphs (Figure 2&4&6) are given to see how results are meaningful and what is the daily changes between ANFIS predictions, empirical equation outcomes or actual values.

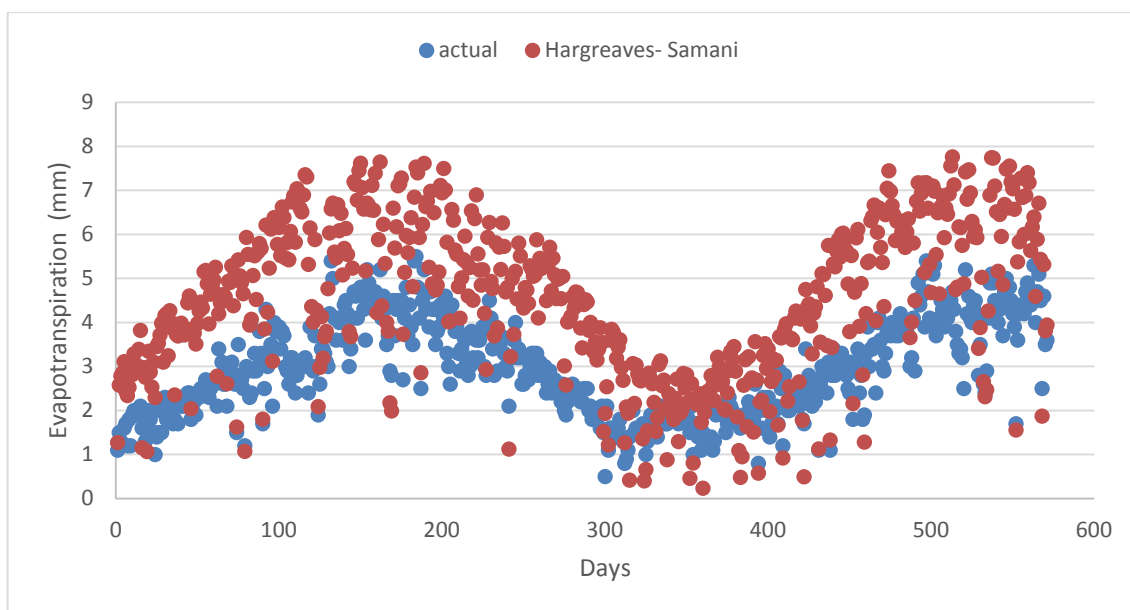


Figure 4. Distribution graph of daily recorded ET and daily Hargreaves-Samani equation results

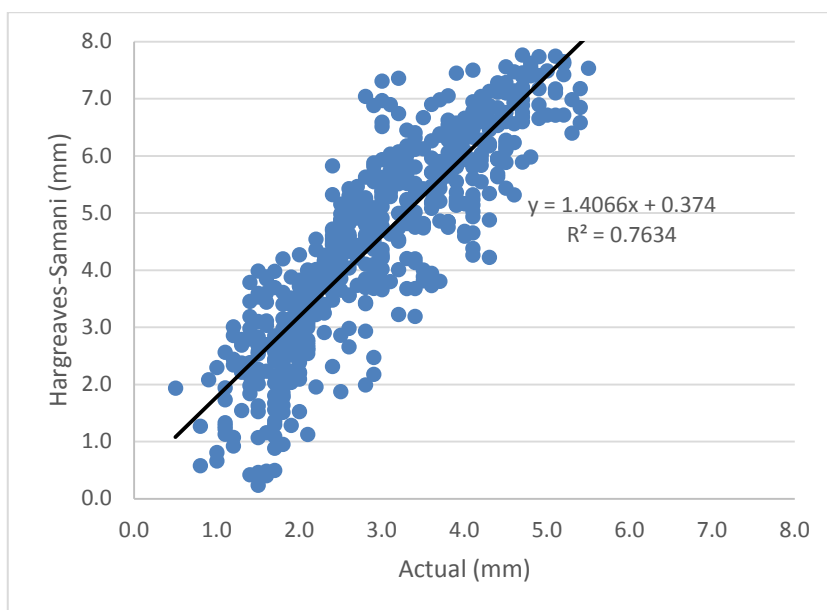


Figure 5. Scatter chart of daily recorded ET and daily Hargreaves-Samani results

It is shown in Figure 3. and Figure 5. that ANFIS model has a better R^2 value which is 0,8322 than Hargreaves-Samani equation. And also R^2 values are given in Table 1. with error calculations.

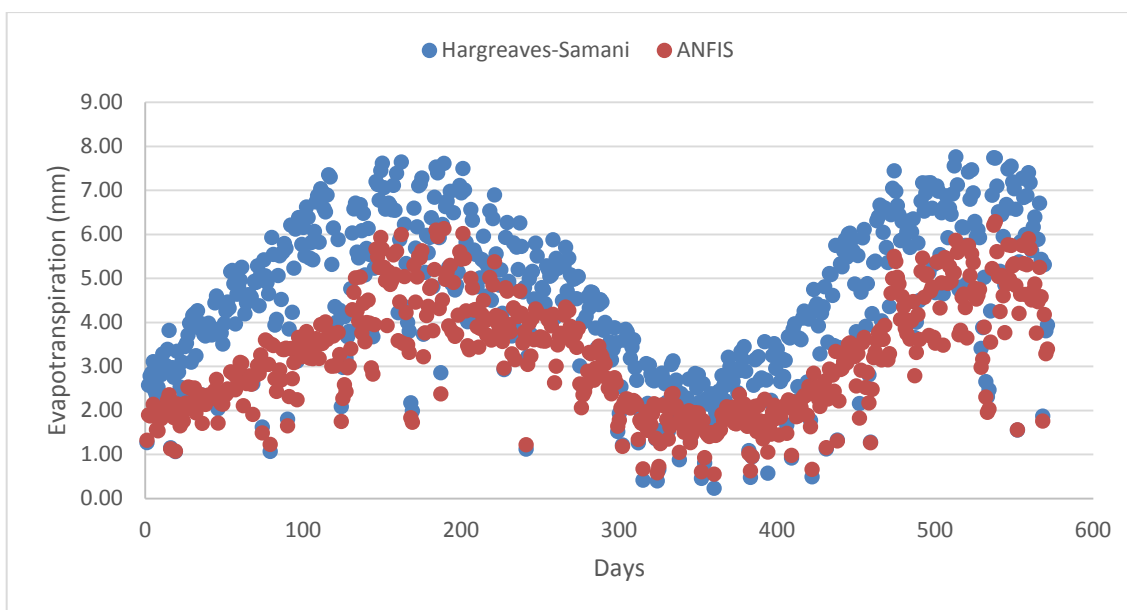


Figure 6. Distribution graph of daily Hargreaves-Samani and ANFIS results

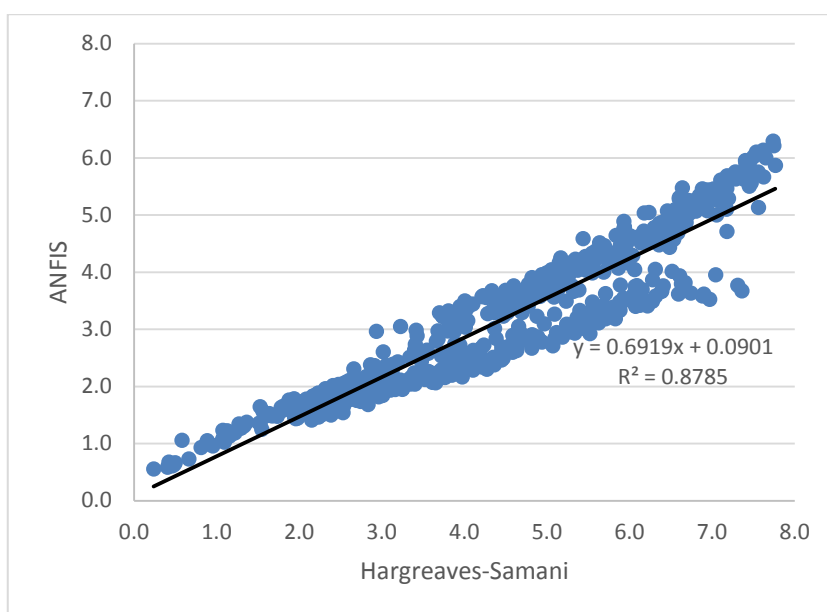


Figure 7. Scatter chart of daily Hargreaves-Samani and ANFIS results

Comparison between Hargreaves-Samani equation and ANFIS is done to show the how ANFIS model consequences are close to Hargreaves-Samani empirical equation. Any daily missing data is not used in creating ANFIS model process. These missing records are deleted from data set. Therefore there is no missing value effect on daily predictions.

Table 1. Comparison of Hargreaves-Samani and ANFIS results statistically

	ANFIS	Hargreaves-Samani
R	0.9122	0.8737
R ²	0.8322	0.7634
MSE	0.3619	3.3833
MAE	0.4725	1.6314

4. CONCLUSION

The potential of ANFIS model and Hargreaves-Samani equation for the forecasting ET is questioned in this study by comparing results with observed ET. According to the statistical analyses it is seen that ANFIS model gives results with high accuracy. Also it is understood from the statistical results, ANFIS model is much trustier than Hargreaves-Samani empirical equation. Even it is seen ANFIS model consequences are better than Hargreaves-Samani for prediction ET, ANFIS results are also compared with Hargreaves-Samani equation results using R^2 statistic and it is seen that there is high relation between each method.

REFERENCES

- [1]. Brutsaert, W. H. *Evaporation into the Atmosphere*, Dordrecht, The Netherlands: D. Reidel Publishing Company, 1982.
- [2]. Jensen, M.E., Burman, R.D. & Allen, R. G. *Evapotranspiration and Irrigation Water Requirements*, New York, USA: ASCE Manuals and Reports on Engineering Practices no. 70., ASCE, 1990.
- [3]. O. Kisi, M. Cimen, "Evapotranspiration modelling using support vector machines," *Hydrological Sciences.*, vol. 54(5), pp. 918-928, October 2009.
- [4]. M. Pal, S. Deswal, "M5 model tree based modelling reference evapotranspiration," *Hydrological Process.*, vol. 23, pp. 1437-1443, March 2009.
- [5]. O. Kisi, "Fuzzy genetic approach for modelling reference evapotranspiration," *Journal of Irrigation and Drainage Engineering.*, vol. 136, pp. 175-183, March, 2010.
- [6]. E. Dogan, "Reference evapotranspiration estimation using adaptive neuro-fuzzy inference system," *Irrigation and Drainage.*, vol. 58, pp. 617-628, March, 2008.
- [7]. O. Kisi, "Daily pan evaporation modelling using multi-layer perceptrons and radial basis neural networks," *Hydrological Process.*, vol. 23, pp. 213-223, 2009.
- [8]. (2015) U.S. Geological Survey website. [Online]. Available: <http://www.usgs.gov/>
- [9]. L.A. Zadeh, "Fuzzy Sets," *Inf Control.*, vol. 8(2), pp. 338-353, 1965.
- [10]. L.Y. Wei, T.L. Chen, T.H. Ho, "A hybrid model based on adaptive-network-based fuzzy inference system to forecast Taiwan Stock Market," *Expert Systems with Applications.*, vol. 38(11), pp. 13625-13631, 2011.
- [11]. T. Takagi, M. Sugeno, "Fuzzy identification of systems and its applications to modelling and control," *IEEE Transactions on Systems, Man and Cybernetics.*, vol. 15, pp.116-132, 1985.
- [12]. J.S.R. Jang, "ANFIS: adaptive-network-based fuzzy inference system," *IEEE Transactions on Systems, Man and Cybernetics.*, vol. 23(3), pp. 665-685, 1993.
- [13]. G.H. Hargreaves, "Moisture availability and crop production," *Trans ASAE.*, vol. 18(5), pp. 980-984, 1975.

Finite Element Analysis of Infilled RC Frames Under Lateral Loads

M. Omer Timuragaoglu^{1}, Adem Dogangun¹, Ramazan Livaoglu¹*

Abstract

The effects of infill wall on the dynamic behaviour of reinforced concrete (RC) buildings have been studied after second quarter of twentieth century by different researchers. Since they are widely used for various purposes in all over the world and it is known that they enhance the global behaviour of structures including stiffness, load bearing capacity and strength, infill walls are assumed as non-structural elements in general. Since infill walls consist of different materials such as mortar and brick having different mechanical properties, it becomes more difficult to clarify the behaviour. The purpose of this study is to investigate and explain the behavior of brick and gas concrete infilled RC frames. For this reason, full scaled, one bay and one storey RC frames with and without infill wall are constructed and tested experimentally under lateral loads and analyzed numerically using non-linear finite element analysis (FEA). In conclusion, the results of FEA models were evaluated of whether these numerical approaches can estimate the behavior of infill wall on the RC frame and wall-frame interaction or not. On the other hand, efficiency of different concrete material models is also scrutinized. The study showed that infilled RC frame, compared with bare frame, improves the global behaviour of the structure considering stiffness, load bearing capacity and strength.

Keywords: *Finite Element Method, Infill wall, RC frame*

1 INTRODUCTION

Reinforced concrete (RC) frame structures with masonry infill walls are widely used in moderate to high seismic zones. Masonry or infill walls have been used in structures for different reasons such as dividing places, fire resistance and thermal isolation. The performance evaluation of infilled RC frames have been a significant challenge for engineers. According to the available experimental [1-5] and analytical studies [6-9], considering stiffness, strength, ductility and energy dissipation capacity of infilled frame, it is expected by the wall to affect the performance and behaviour of structure. Increasing the mass and stiffness of structure are the mostly known main influences of infill wall on the structure. The period of a structure or frame with infill wall, under earthquake loads, will be considerably different than that of bare frame, since the mass and stiffness of the frame/structure changes.

In studies of damage assessment after earthquakes and when damages occurred in structures due to misapplication are investigated, soft storey mechanism is witnessed due to underuse or non-use of infill wall especially in ground or first floor. In addition, it has been long known that using ribbon window in infill wall for lighting of basement floor causes short columns to occur. The shear force, occur in short columns, becomes more than that of considered in calculations and shear fracture happens in column for this reason. This application of infill wall, on one hand, when demonstrating the influence of infill wall on the stiffness of the frame, on the other hand, reveals the negative effect of arrangement of infill wall on the behaviour of structure.

Finite element modeling technique of the structures is a powerful tool for engineers to evaluate, explain and understand the behaviour of any system. Finite element method (FEM) is a numerical solution method which searching for approximate solution of different engineering problems. Different researchers used FEM to model infilled RC frames [10-12]. In the present study, nonlinear behavior of brick and gas concrete infilled RC frames is investigated by using FEM. For this reason, full scaled, one bay and one storey RC frames with and without infill wall are constructed and tested experimentally under lateral loads analyzed numerically by using non-linear finite element analysis (FEA). The results obtained from experimental tests and numerical analyses indicate that infill walls increase the strength and stiffness of infilled RC frames.

¹ Corresponding author: Uludağ University, Dept. of Civil Eng. 16059, Nilüfer/Bursa, Turkey. omertao@uludag.edu.tr

2. EXPERIMENTAL INVESTIGATION

2.1. Prototype of Test Specimen

In this study, two bare frame and two infilled RC frame specimens are analyzed: gas concrete infill wall and hollow brick infill wall frames. A one-storey one-bay RC frame was selected as a prototype structure. The height/length (h/l) ratio for infill walls was selected to be 1/1.25. Infill walls are constructed as brick and gas concrete infill wall. The frames were designed in accordance with the provisions of Turkish Earthquake Code (TEC'07). The test specimens were chosen to be 1/1 scale. The design details for the frame specimens are shown in Figure 1. The columns and beam were selected to be 0.2x0.25 m and 0.25x0.2 m, respectively. A minimum reinforcement of 6 ϕ 14 is used for columns while a reinforcement of 3 ϕ 12 for bottom and 2 ϕ 12 for top of beam is selected as shown in Figure 1. Confinement reinforcement, which is required by TEC'07, is used both along the columns and beam. The details of confinement in columns and beam is shown in Figure 1. For the base of the frame, 4x0.6x0.4 m dimensions were selected. The base is fixed to the ground with shear connectors. The test specimen shown in Figure 1, is subjected to lateral cyclic loads. The loads are applied to the system by increasing the amplitude in each cycle as shown in Figure 2.

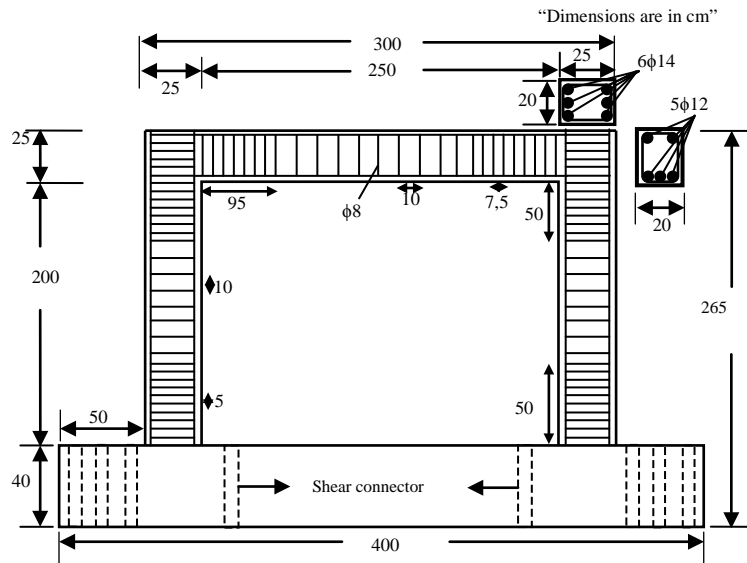


Figure 1. Dimensions and reinforcement details of the test specimens

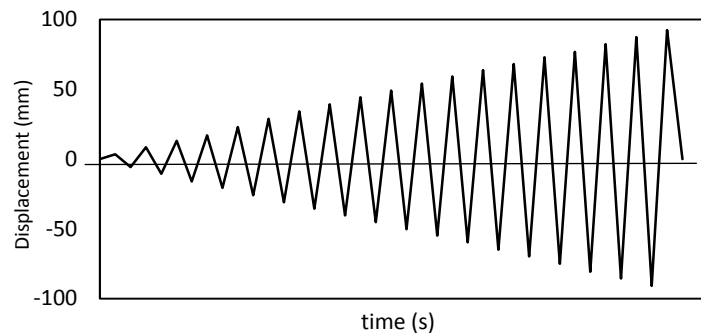


Figure 2. Displacement amplitudes used in laboratory and FEA tests

2.2. Material Properties

The compressive strength for the concrete used for frame with gas concrete infill wall is identified as 20 MPa whereas compressive strength for concrete used for frame with brick infill wall is 25 MPa and elasticity modulus are defined as 20 000 and 28 000 MPa, respectively. The compressive strength for gas concrete and brick infill wall are determined as 1 and 4.1 MPa, respectively. On the other hand, the modulus of elasticity for gas concrete and hollow brick masonry are estimated as 800 MPa and 1000 MPa, respectively.

3. MODELING OF INFILLED RC FRAMES

In finite element modeling of infilled RC frames, RC frame, infill wall and wall-frame interaction is modeled separately. Abaqus [13] finite element analysis (FEA) program is used in the analysis. Since the aim of the study is to investigate the

effect of infill wall on reinforced concrete (RC) frame, RC is modeled as solid, homogeneous and single material in FEA to represent behaviour of both concrete and reinforcement. Besides, RC modeled as homogeneous and single material in order to shorten the computational time. Three different confined concrete mathematical models are used in the analysis to compare the effectiveness of material models. These mathematical models are Popovics [14], Saenz [15] and Thompson and Park models. Detailed explanation of material models are available in the literature.

In this study, infill walls are accepted as homogeneous material and the unit and mortar effects are neglected in the analysis. Concrete Damage Plasticity (CDP) model which is available in FE program (Abaqus), is used to represent the behaviour of infill wall. The concrete damaged plasticity model in Abaqus, provides a general capability for modeling concrete and other quasi-brittle materials in all types of structures (beams, trusses, shells, and solids) and uses concepts of isotropic damaged elasticity in combination with isotropic tensile and compressive plasticity to represent the inelastic behavior of concrete. Thus CDP model is applied to model infill wall in the analysis. The mathematical model of infill wall is given by Tao et.al. [16]. Detailed explanation of the mathematical model can be found in mentioned study.

In addition to RC and masonry infill wall, an interaction between wall and surrounding frame is defined since it is the interaction that shows the influence of infill wall on the frame. Different elements (spring, tie, hard contact) have been used to represent the behaviour between wall and frame. In this study, surface based cohesive behavior is used. This model is defined as surface interaction feature and is used to model the traction-separation behaviour in the interface. Traction separation criterion used in FEA considers linear elastic behaviour and this behaviour is expressed as:

$$t = \begin{Bmatrix} t_n \\ t_s \\ t_t \end{Bmatrix} = \begin{bmatrix} K_{nn} & K_{sn} & K_{tn} \\ K_{ns} & K_{ss} & K_{nt} \\ K_{nt} & K_{st} & K_{tt} \end{bmatrix} \begin{Bmatrix} \delta_n \\ \delta_s \\ \delta_t \end{Bmatrix} = K \delta \quad (1)$$

The nominal traction stress vector, t , consists of three components (two components in two-dimensional problems): t_n , t_s and (in three-dimensional problems) t_t , which represent the normal (along the local 3-direction in three dimensions and along the local 2-direction in two dimensions) and the two shear tractions (along the local 1- and 2-directions in three dimensions and along the local 1-direction in two dimensions), respectively. The corresponding separations are denoted by δ_n , δ_s and δ_t [13].

3.1. Calibration of Models

Concrete and reinforcement are not modeled separately. On the contrary, they are modeled as a homogeneous, single material for simplicity in the analysis. Interaction between infill wall and surrounding frame is modeled using surface based cohesive behavior. This interaction type is used to model the separation in interface according to traction-separation criteria. In the traction-separation model, linear elastic behaviour is approved until damage started. The base of the frame is modeled as fixed and there is no gravity load on the frame. The load is applied laterally to the cross-section area of the beam (Figure 3).

Material parameters used for calibration in this model, for infill wall, is given in Table 1. These parameters are: dilation angle ψ , eccentricity ϵ , the ratio of initial equibiaxial compressive yield stress to initial uniaxial compressive yield stress f_{b0}/f_{c0} , the ratio of the second stress invariant on the tensile meridian to that on the compressive meridian k and viscosity parameter χ . The first two parameters are used for shape of the potential flow while f_{b0}/f_{c0} and χ are used to define the shape of yield function. Viscosity parameter (χ) is used to regularize the viscoplastic material.

Table 1. Material parameters used for Concrete Damaged Plasticity

Dilation angle	Eccentricity	f_{b0}/f_{c0}	k	Viscosity Parameter
1	1	1.16	0.6667	0.004

Since various parameters are effective in modelling, it is rather difficult to calibrate a model in analysis. However, the experimental test results simplified the calibration process during the finite element analysis.

4. FINITE ELEMENT ANALYSIS RESULTS AND DISCUSSION

In this section, force-displacement curves obtained from FEA and failure modes for brick and gas concrete infilled RC frame are compared with the available experimental test data. At first, base shear and displacement characteristics of specimens is scrutinized. Later, the failure modes of both experimental and numerical results are compared with each other. Lastly, the efficiency of three different mathematical models, used for modeling of RC frame, are investigated.

4.1. FEA Results of Brick infilled RC Frame

In this study, full scale, one bay and one storey infilled RC frame systems are modeled and analyzed under lateral loads. Two types of infill walls are used namely: gas concrete and brick. The experimental data for brick infilled RC frame is taken from a study carried out in KTU laboratories [17] which has the same geometry and dimensions of gas concrete infilled RC frame. The experimental test mechanism and modeling of infilled RC frame are seen in Figure 3.

The results obtained from the FEA of brick infilled RC frame system is compared with experimental test data in Figure 4. It is obvious that the results obtained from experimental tests and FEA are well-suited until reaching load bearing capacity of the system considering each of the concrete material models. After this point, mathematical models behave differently. Saenz model is failed because of a sudden decrease in stress in softening regime of stress-strain curve. On the other hand, Popovics and Thompson - Park models differ from each other and experimental results, although results of Popovics model are lower than Thompson-Park model results. It is clear that Popovics model gives closest results to the experimental tests. However, after load carrying capacity, load carrying capacity is still higher than experimental results.



Figure 3. Experimental test and numerical analyze of infilled RC frame

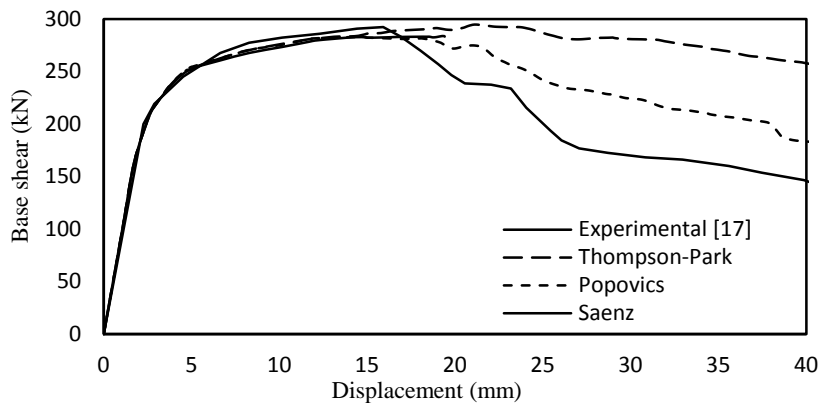


Figure 4. Comparison of force-displacement curves for brick infilled RC frame

Failures in frames generally occur as plastic hinges in columns and column-beam joints. These types of failure happen in weak frame with strong infill walls. The failure types observed in frames from the experimental and finite element analysis results for brick infilled RC frame are shown in Figure 5. In the experiment of brick infilled RC frame, the wall is fallen down. It is obviously seen from the figure that plastic hinges occurred in column-beam joints is also formed in the nonlinear FEA of infilled RC frame.

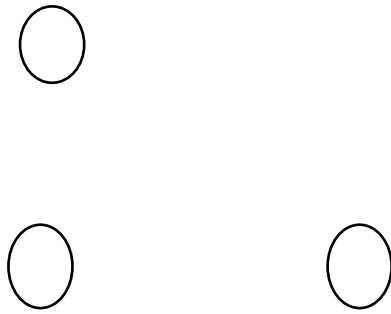


Figure 5. Comparison of failure types occurred in experimental test and numerical analysis for brick infilled RC frame

5. FEA Results of Gas Concrete infilled RC Frame

The results obtained from the FEA of gas concrete infilled RC frame system is compared with experimental results in Figure 6. It can be seen from the figure that experimental and numerical results are compatible with each other. It is clear that nonlinear finite element analysis in all three concrete material models are able to represent the initial rigidity of the system. On the other hand, lateral load bearing capacity of nonlinear analysis deviate from those of the experimental tests with a certain ratio of %15-20 in all material models. After system reaches its load carrying capacity, a displacement of approximately 27mm, numerical results of mathematical models changes significantly.

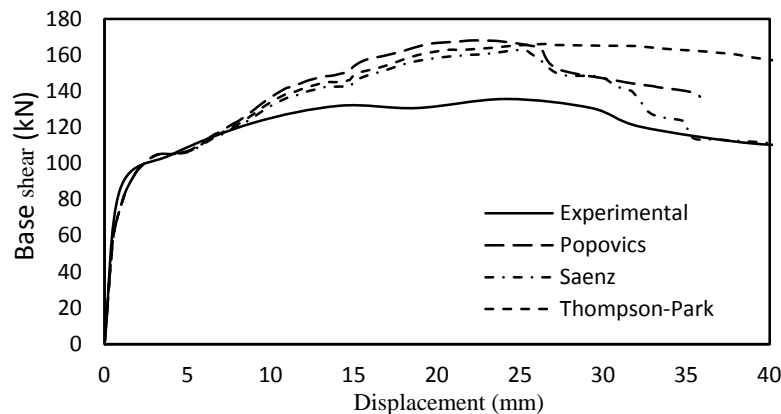


Figure 6. Comparison of force-displacement curves for gas concrete infilled RC frame

The failure types observed in frames from the experimental and finite element analysis results for gas concrete infilled RC frame are shown in Figure 7. It is obviously seen from the figure that plastic hinges occurred in column-beam joints in experimental test is also formed in the nonlinear FEA of infilled RC frame. On the other hand, since infill wall is modeled as a solid and homogeneous element, the failure types developed in units or mortar beds cannot be seen in FEA. When force-displacement curves of brick and gas concrete infilled RC frames are compared, it will be seen that initial stiffness of both gas concrete and brick infilled RC frames are close to each other. On the other hand, while the gas concrete wall provides more ductility to the frame, brick infill increases load carrying capacity of the frame twice of gas concrete wall.

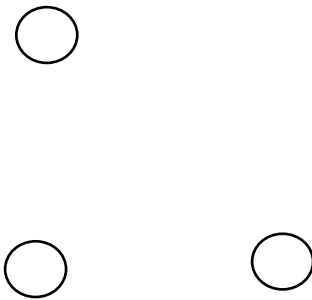


Figure 7. Comparison of failure types occurred in experimental and numerical tests for gas concrete infilled RC frame

6. CONCLUSION

This paper compares nonlinear finite element analysis (FEA) results of brick and gas concrete infilled RC frames with the available experimental test results. The failure mode occurred in the simulations are also investigated according to commonly considered failure modes available in literature. Furthermore, the efficiency of different mathematical models of confined concrete is scrutinized. The conclusions, reached up at the end of the study, are specified below:

The numerical results obtained from modeling of brick and gas concrete infilled RC frames are well suited with the experimental test data especially when considering the initial stiffness of the system. After achieving the lateral load carrying capacity, numerical results show different deviation from not only each other but also experimental results.

Failure mode occurred in frame in experimental tests, which happens as plastic hinge in column or column-beam joint, is also formed in the finite element analysis (FEA) results on almost same time.

Three different stress-strain relationships for concrete are used to compare the influence of mathematical models. These models are Popovics, Saenz and Thompson-Park models. The nonlinear FEA results show that mathematical model can change the behaviour of infilled RC frame. Additionally, mathematical models used in the analysis gave close result until load carrying capacity of system. After this point, the result obtained from concrete models diverge from each other.

It is understood from the experimental tests and numerical analysis that infill wall has a positive influence on the behaviour of infilled RC frame considering initial stiffness, strength, and lateral load carrying capacity of the system.

REFERENCES

- [1]. S. V. Polyakov, "On the interaction between masonry filler walls and enclosing frame when loading in the plane of the wall". Translation in earthquake engineering, Earthquake Engineering Research Institute (EERI), San Francisco, 1960.
- [2]. B. S. Smith, *Lateral stiffness of infilled frames*. Proceedings of the American Society of Civil Engineering, Journal of Structural Division, 1962, 88(6).
- [3]. B. S. Smith, *Behavior of square infilled frames*. Proceedings of the American Society of Civil Engineering, Journal of Structural Division, 1966, 92(1).
- [4]. A. E. Fiorato, M. A. Sözen, and W. L. Gamble. *An investigation of the interaction of reinforced concrete frames with masonry filler walls*. Report No. UILU-ENG 70-100, Dept. of Civ. Eng., University of Illinois at Urbana-Champaign, 1970.
- [5]. A. B. Mehrabi, P. B. Shing, M. Schuller, and J. Noland. *Experimental evaluation of masonry-infilled RC frames*. Journal of Structural Engineering, 122(3), 228–237, 1996
- [6]. T. C., Liauw and K.H., Kwan. *Nonlinear behaviour of non-integral infilled frames*. Computers and Structures, 18(3), 551-560, 1984.
- [7]. A. Saneinejad and B. Hoobs. *Inelastic design of infilled frames*. Proceedings of the American Society of Civil Engineering, Journal of Structural Engineering, 1995, 121(4).
- [8]. P. G. Asteris. "A method for the modelling of infilled frames (Method of contact points)". *11th World Conference on Earthquake Engineering*, 1996, Mexico.
- [9]. A. B. Mehrabi and P.B. Shing. *Finite element modelling of masonry infilled reinforced concrete frames*. ASCE Journal of Structural Engineering, 123(5), 604-613, 1997.
- [10]. P.G. Asteris. *Finite element micro-modeling of infilled frames*. Journal of Structural Engineering, 8(8), 1-11, 2008.
- [11]. M. Resta, A. Fiore and P. Monaco. *Non-linear finite element analysis of masonry towers by adopting the damage plasticity constitutive model*. Advances in Structural Engineering, 16(5), 791-803, 2013.
- [12]. Y. Tao, J.F. Chen, T. Stratford and J.Y. Ooi. "Numerical modelling of a large scale model masonry arch bridge". *In Proc. of the 14th International Conference on Structural Faults + Repair*. 2012.
- [13]. Abaqus 2013. ABAQUS Documentation, Dassault Systèmes, Providence, RI, USA.
- [14]. S. Popovics. *A numerical approach to the complete stress-strain curve of concrete*. Cement and Concrete Research, 3(5), 583-599, 1973.
- [15]. L.P. Saenz. *Discussion of Equation for the stress-strain curve of concrete by Desayi P, Krishnan S*. ACI Journal; 61:1229–1235, 1964.
- [16]. Y. Tao, J.F. Chen, T.J. Stratford and J.Y. Ooi. Numerical modelling of a large scale model masonry arch bridge paper presented at structural faults and repair, Edinburgh, United Kingdom, 2012.

- [17]. M.E. Arslan. "Deprem kumaşıyla güçlendirilen çevrimsel yük etkisindeki dolgu duvarlı betonarme çerçevelerin davranışlarının deneysel ve teorik olarak incelenmesi". Doctoraldissertation, Karadeniz TechnicalUniversity, Trabzon, 2013.

Evaluation of the Compressive Strut Model for Analytical Modelling of Infilled Reinforced Concrete Frames

Mehmet Omer Timuragaoglu¹, Adem Dogangun¹, Ramazan Livaoglu¹

Abstract

Masonry infill walls have been largely used for various reasons in reinforced concrete (RC) frames for a long time. Several buildings suffer damage and many of them collapse due to failure of infill walls in earthquakes in all over the world. The effects of infill wall on the frame under lateral loads have been studied by researchers for over fifty years. Despite the wide usage of infill walls in RC frame buildings, the effects of them on the frame are not included in analysis because of the fast degradation in strength, stiffness and energy dissipation capacity of infill wall. In consequence of broad experimental studies, it is approved by the researchers that the behaviour of infill walls under lateral loads can be represented by replacing the wall with a diagonal compression strut. In the present study, a full scaled, one bay and one storey RC frames, which are previously tested experimentally under lateral loads, are simulated and analyzed using finite element method by replacing the wall by one, two or three compressive strut in order to investigate the efficiency of the strut models. The analysis results show that compressive strut model is a simple, easy and effective way of represent the global behaviour of infill wall.

Keywords: *Compressive strut, Finite Element Method, Infill wall, RC frame*

1. INTRODUCTION

Infill walls have been widely used in reinforced concrete (RC) structures such as thermal and sound isolation, creating living spaces etc. The availability and applicability of infill wall to the structure is also made infill wall the most preferred element in structures. On the other hand, in earthquakes happened in all over the world, many building suffer damage and many people injured or lost their life due to failures occurred in infill walls. Additionally, collapse of buildings is seen due to significant failures occurred in infill wall. For all reasons above, a serious increase is seen to understand the influence of infill wall on structures in the last two decades.

Extensive experimental ([1]-[7]) and analytical ([8]-[12]) studies have been performed. According to the results of these studies different analytical approaches are proposed to idealize the behaviour of infill wall. The most significant and representative one is the equivalent compressive strut model in which the wall is replaced with different number of struts in each directions. Reference [1] suggested to model the infill wall replaced by an equivalent diagonal strut. Reference [6] suggested a diagonal strut model, with a different arrangement, placing one end of strut downward the top joint. Reference [10] proposed two strut model to estimate the behaviour of infill wall on the frame. Reference [11], in order to idealize the behaviour of compression area, recommended multi strut model. Reference [12], by taking strength and rigidity decrease in infill wall into account, suggested six strut model to predict the reaction of infilled steel frame under seismic loads. In this model, only three struts are active in analysis in one direction. Reference [13], based on studies conducted on concrete masonry infilled steel frames, proposed a three strut model. In this model, each masonry infill wall is replaced by three struts with force-deformation characteristics based on the orthotropic behavior of the masonry infill.

In the present study, the efficiency of analytical models suggested by different researchers are investigated using Finite Element Method (FEM). For this reason, a one-storey one-bay gas concrete infilled RC frame is selected. In order to compare the analytical approaches, one, two and three equivalent struts are used in models. The experimental test data are used to calibrate analytical results. The analysis results obtained from strut models show that equivalent strut model is an easy and simple method to estimate the global behaviour of infill wall on the RC frame. The main advantages of multi strut models, despite increasing the complexity, is that these models can represent the global behaviour of the frame more accurately than single strut model.

2. EXPERIMENTAL PROGRAM

2.1. Prototype of Test Specimen

In this study, an infilled RC frame specimen is tested and analyzed under lateral loads. A one-storey one-bay RC frame was selected as a prototype structure. The height/length (h/l) ratio for infill walls was selected to be 1/1.25. RC frame is constructed with gas concrete infill wall. The frame was designed in accordance with the provisions of Turkish Earthquake Code (TEC'07). The test specimen was chosen to be 1/1 scale. The design details for the frame specimen is

¹ Corresponding author: Uludağ University, Department of Civil Engineering, 16059, Nilüfer/Bursa, Turkey. omertao@uludag.edu.tr

shown in Figure 1. The columns and beam were selected to be 0.2x0.25 m and 0.25x0.2 m, respectively. A minimum reinforcement of 6φ14 is used for columns while a reinforcement of 3φ12 for bottom and 2φ12 for top of beam is selected as shown in Figure 1. Confinement reinforcement, which is required by TEC'07, is used both along the columns and beam. The details of confinement in columns and beam is shown in Figure 1. For the base of the frame, 4x0.6x0.4 m dimensions were selected. The base is fixed to the ground with shear connectors. The test specimen shown in Figure 1, is subjected to lateral cyclic loads. The loads are applied to the system by increasing the amplitude in each cycle as shown in Figure 2. The compressive strength for concrete used for frame is 20 MPa and elasticity modulus is 20 000 MPa. The compressive strength for gas concrete infill wall is determined as 1 MPa. On the other hand, the modulus of elasticity for gas concrete masonry wall is taken as 800 MPa.

details of the test specimens

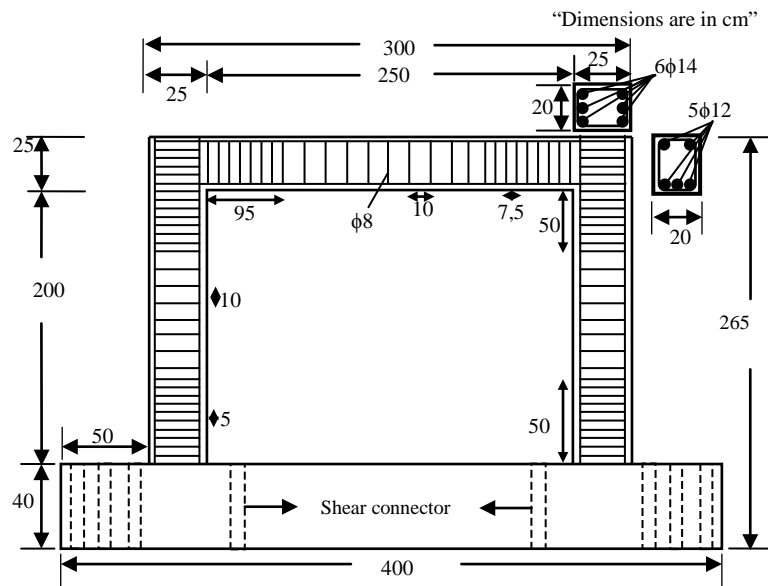


Figure 1. Dimensions and reinforcement

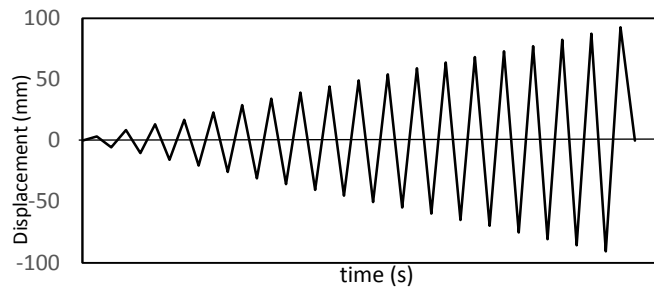


Figure 2. Displacement amplitudes used in laboratory and FEA tests

Under lateral cyclic loading, the equivalent diagonal strut model has gained a wide acceptance by researchers. Reference [1] suggested to model the infill wall replaced by an equivalent diagonal strut. The actual system and the equivalent model for infill wall is shown in Figure 3a and b, respectively. In this method, it is accepted that infill wall, under seismic forces, acts like a diagonal strut. This diagonal strut has an effective width (w) and a thickness (t_w) same of infill wall. Afterwards, Reference [14], based on diagonal strut model, proposed an equation to specify the width of the equivalent diagonal strut as:

$$w = \frac{d_m}{3}$$

(1)

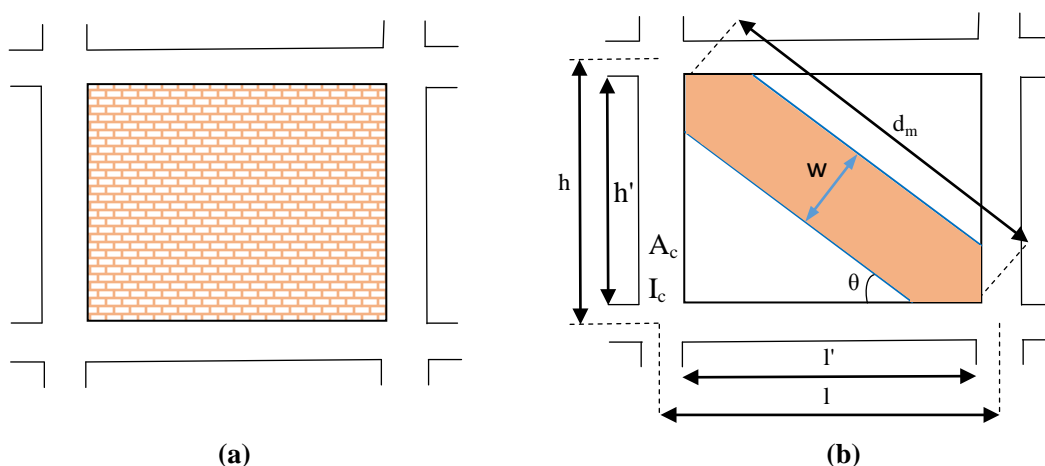


Figure 3. (a) Actual system (b) Equivalent model for infill wall

Reference [2] conducted wide scale experimental tests on infilled steel frames and found out that the ratio of diagonal strut width to the diagonal length (w/d_m) varies between 0,1-0,25. In these test, the evaluation of width of equivalent strut is determined as a function of relative panel to frame stiffness parameter (λ_h) defined as:

$$\lambda_h = \sqrt[4]{\frac{E_m t \sin 2\theta}{4E_c I_c h'}} \quad (2)$$

where E_m =modulus of elasticity of the masonry panel; $E_c I_c$ =flexural rigidity of the columns; t = thickness of the infill panel and equivalent strut; h' = height of infill panel; and θ = angle, whose tangent is the infill height to length aspect ratio, defined as:

$$\theta = \tan^{-1}\left(\frac{h'}{l'}\right) \quad (3)$$

Reference [5] found out the width of the equivalent strut by conducting a series of tests on infilled steel frames:

$$w = 0.16\lambda_h d_m \quad (4)$$

Reference [15], considering stress distribution, expressed an equation for strut width depending on contact length between infill wall and surrounding frame.

$$w = \frac{1}{2}\sqrt{(Z_1)^2 + (Z_h)^2} \quad (5)$$

$$Z_1 = \frac{\pi}{\lambda_1} \quad \text{and} \quad Z_h = \frac{\pi}{2\lambda_h} \quad (6)$$

where Z_1 and Z_h are contact lengths of beam and column with infill wall, respectively. Reference [8] specified an equation for effective width of the strut by using data obtained from experimental studies on steel frames.

$$w = \frac{0.95h' \cos \theta}{\sqrt{\lambda_h}} \quad (7)$$

On the other hand, Reference [16] expressed that a high value of equivalent strut width means a stiffer structure and therefore a potentially higher seismic response. They proposed a simple and constant value for the calculation of equivalent strut width, given by

$$w = 0.25d_m \quad (8)$$

According to Reference [17], based on experimental and analytical studies, equivalent strut width can be calculated as:

$$w = 0.175(\lambda_h h)^{-0.4} d_m \quad (9)$$

Variation of equations explained above for the calculation of equivalent diagonal strut width are illustrated in Figure 4. In this figure, the angle, θ , in the equation proposed by Reference [8], is taken as 25° and 50° for practical purposes. As it is

clearly seen from the figure, equations (1) and (8), suggested Reference [14] and Reference [16], respectively, are independent of relative panel-frame stiffness parameter (λ_h). However, according to equations (4), (7) and (9), w/d_m ratio is decreasing when panel-frame stiffness parameter (λ_h) increasing. The equation (9), which is also proposed by Reference [17], gives close result to the equation (7) with an angle equal to 50. Additionally, these equations give highest values when the panel-frame stiffness parameter (λ_h) is between 1 and 1.7. On the other hand, equation (4), suggested by Reference [5], gives the lowest ratios as panel-frame stiffness parameter (λ_h) increasing. The equation (8), recommended by Reference [16], seems to be an average equation that can be used in the calculation of equivalent diagonal strut.

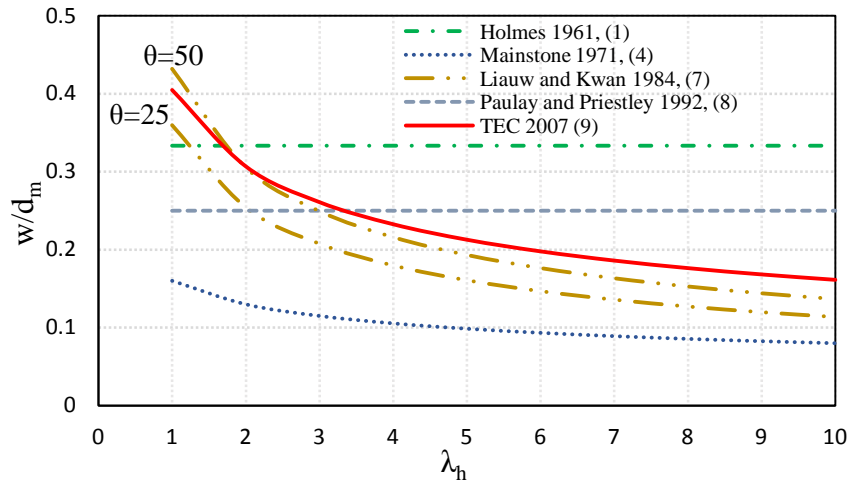


Figure 4. Variation of w/d_m ratio depending on relative panel-frame stiffness parameter (λ_h)

Although single strut model is easy, practical and capable of representing the global behavior of infill wall, it may not capture the behaviour between the wall and surrounding frame. Hence, the moment and shear force occurred in the frame cannot be expressed accurately and plastic hinges developed in the structure cannot be located in the model [10]. For these reasons, researchers suggested multi strut models based on equivalent diagonal strut to idealize the behaviour accurately. Reference [1] suggested to model the infill wall replaced by an equivalent diagonal strut. The actual system and the equivalent model for infill wall is shown in Figure 1a and b, respectively. Reference [10] proposed two strut model to estimate the behaviour of infill wall on the frame as shown in Figure 5a. Reference [13], based on studies conducted on concrete masonry infilled steel frames, proposed a three strut model as illustrated in Figure 5b

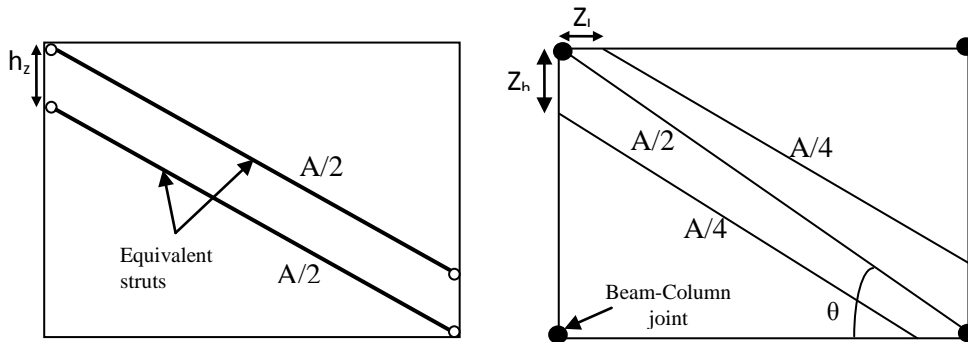


Figure 5. (a) Two strut model [10] (b) Three strut model [13]

3. FINITE ELEMENT ANALYSIS AND COMPARISON OF RESULTS

In the present study, the efficiency of compressive strut approaches, used to represent the behaviour of infill wall, are investigated. In the analysis, the struts are modeled as linear-elastic while the frame is considered as non-linear. One, two and three struts are used to compare the analysis results of strut models. The effective width of strut is calculated by using Eq. (8). Equations (2) and (6) are used to calculate the contact lengths between the wall and surrounding frame.

The reduced storey drift (Δ_i) of any column or structural wall shall be determined by Eq. (10) as the difference of displacements between the two consecutive stories. On the other hand, effective storey drift (δ_i) of columns or structural walls at the i 'th storey of a building shall be obtained for each earthquake direction by Equation (11). In these equations, d_i and d_{i-1} represent lateral displacements obtained from the analysis at the ends of any column or structural wall at stories i and $(i-1)$ under reduced seismic loads. R denotes structural behaviour factor.

$$\Delta_i = d_i - d_{i-1} \tag{10}$$

$$\delta_i = R\Delta_i \tag{11}$$

The maximum value of effective storey drifts ($(\delta_i)_{max}$) obtained for each earthquake direction by Eq.(11) at columns or structural walls of a given i 'th storey of a building shall satisfy the condition given by Eq.(12):

$$\frac{(\delta_i)_{max}}{h_i} \leq 0.02 \tag{12}$$

Combining equation (11) into equation (12), equation (13) will be produced. Thus reduced storey drift (Δ_i) will be obtained depending upon structural behaviour factor (R) and storey height (h).

$$\Delta_i \leq \frac{0.02h_i}{R} \tag{13}$$

The limitations specified by TEC'07 is used in the analysis by changing the structural behaviour factor in order to compare the limits with experimental and analytical results (Figure 6). The height of the storey is taken as 2.25 meter. The force-displacement curves obtained from finite element analysis (FEA) of one strut model for gas concrete infilled RC frame are shown in Figure 6. The experimental and analytical results can be seen in the figure. Furthermore, the limits of Turkish Earthquake code (TEC'07) is also added to the figure according to Eq. (13) by changing structural behaviour factor. By comparing the experimental results with analytical one, it seen from Figure 6a that using one compression strut instead of infill wall cannot represent the initial stiffness of the system while structural behaviour factor can be identified ($R \approx 4$) from figures 6b, c and d. Structural behaviour factor is obtained by determining the conjunction of TEC'07, experimental and analytical results.

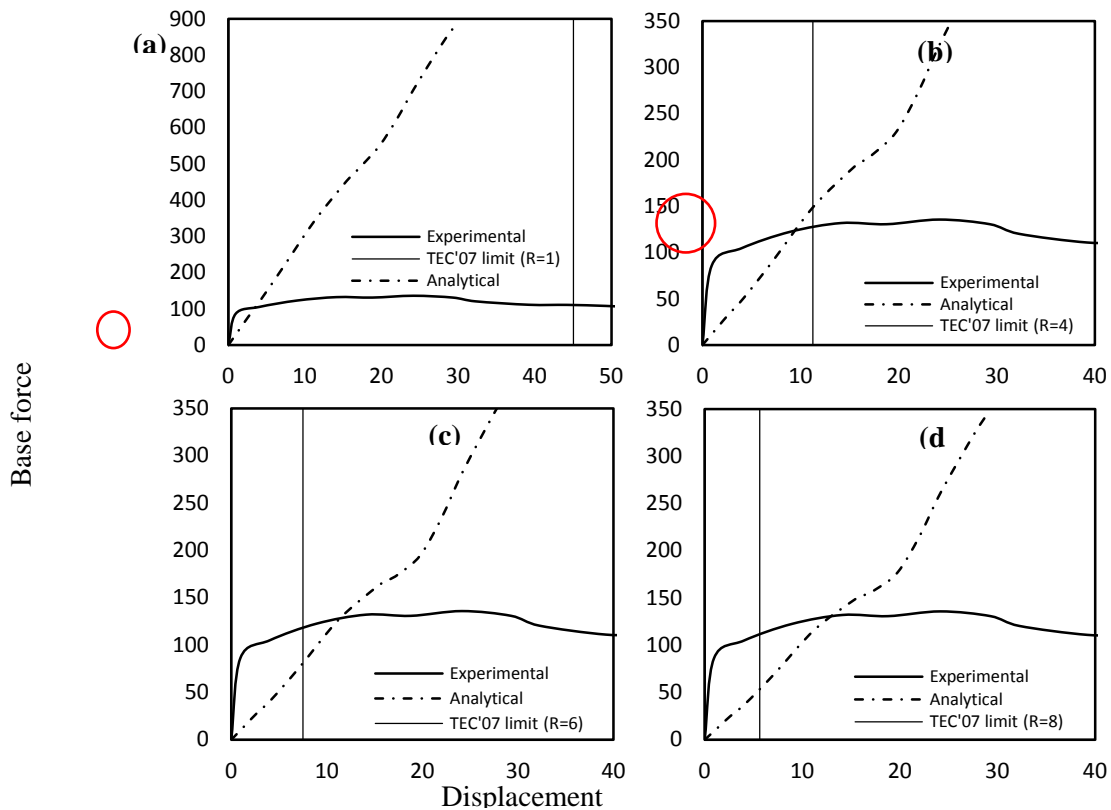
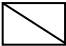
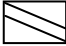



Figure 6. Force-displacement curves for one strut frame for different R values

When applying the same procedure of one strut model to two and three strut models, the analysis results obtained from two and three strut models are given in Table 1. In this table, NDL and HDL denote nominal ductility level and high ductility level, respectively. From the results given in Table 1, it is understood that increasing the number of strut will result in a better representation of ductility although it increases the complexity. On the other hand, three strut model best estimates the initial rigidity of the system although its computational time is more than other strut models. Using only one diagonal strut cannot represent the effect of masonry because this model cannot estimate the internal forces formed in the frame. Difference between one and multi strut models is that multi strut models are capable of transfer the forces occurring between infill walls and surrounding frame. But using only one compression strut is acceptable when bond

strength between wall-frame interfaces is very low. It should be noted that stiffness may significantly change depending on the contact length for multi strut models.

Table 1. Analysis results obtained from strut models for gas concrete infilled RC frame

One strut		Two struts		Three struts	
Gas concrete infilled frame	NDL (R=4)	HDL (R=6)	HDL (R=8)		

The damages occurred after experimental tests and analytical results of gas concrete infilled RC frame is shown in Figure 7. The damage locations, when experimental and analytical results of figure 7 are compared, clearly different especially parallel to the strut. This is because the strut model, although able to represent the global behaviour of infilled frame, cannot estimate local behaviour of both infill wall and frame. It is seen from the analysis results that plastic hinge is formed in the middle of both columns while it is not formed in experimental test results. It should be noted that failure modes occurred in the infill wall cannot be represented with compressive strut models.

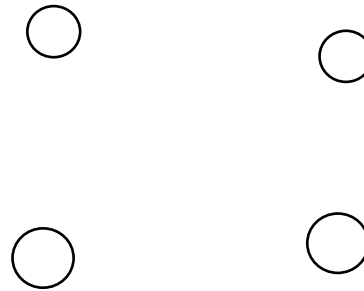


Figure 7. Analysis results of one strut models for gas concrete infilled RC frame

4. CONCLUSIONS

The efficiency of different strut models is investigated in the paper. For this purpose, one bay, one storey, gas concrete infilled RC frame is constructed and tested under lateral loads. In modeling, struts are modeled elastically while frame is modeled as 3D solid elements. Three different strut configurations are used in models to understand the efficiency of strut models. The analysis results in this paper show that the experimental response of infilled frame under lateral loads can properly be described with proposed analytical methods.

The results of this paper indicate that single strut model has a simple and easy method for application to the structure and gives an acceptable estimation of stiffness of infilled RC frame. In addition, single strut model cannot represent the local failure occurring in the surrounding frame. A better representation of stiffness of the system is obtained by using multi strut model although it increases the complexity. In these models, the interaction between infill wall and surrounding frame is better represented. It is this interaction that specifies the influence of infill wall on the frame. When this interaction or contact length is bigger, the contribution of infill wall on frame considering strength, stiffness and lateral load carrying capacity

Using compressive diagonal struts instead of infill wall provides obvious advantages in terms of computational time and efficiency. Their formulas are based on physical representation of infill frame. Additionally, equivalent strut width and contact lengths should be carefully determined in order to accurately estimate the behaviour of infilled frame under lateral loading.

It must be noted that the equivalent strut approach is valid for infill walls without openings. Thus, equivalent strut method for infill walls with openings should be investigated experimentally and analytically.

REFERENCES

- [1]. S. V. Polyakov, "On the interaction between masonry filler walls and enclosing frame when loading in the plane of the wall". Translation in earthquake engineering, Earthquake Engineering Research Institute (EERI), San Francisco, 1960.
- [2]. B. S. Smith, *Lateral stiffness of infilled frames*. Proceedings of the American Society of Civil Engineering, Journal of Structural Division, 1962, 88(6).
- [3]. B. S. Smith, *Behavior of square infilled frames*. Proceedings of the American Society of Civil Engineering, Journal of Structural Division, 1966, 92(1).
- [4]. A. E. Fiorato, M. A. Sözen, and W. L. Gamble. *An investigation of the interaction of reinforced concrete frames with masonry filler walls*. Report No. UILU-ENG 70-100, Dept. of Civ. Eng., University of Illinois at Urbana-Champaign, 1970.
- [5]. R. J., Mainstone. *On the stiffnesses and strengths of infilled frames*. Proceedings of Institution of Civil Engineers, 1971, Supplement (IV), 57-90.
- [6]. R. Zarnic and M. Tomazevic. *An experimentally obtained method for evaluation of the behavior of masonry infilled RC frames*. Proceedings of 9th World Conference on Earthquake Engineering, 1988, Tokyo, Japan.

- [7]. A. B. Mehrabi, P. B. Shing, M. Schuller, and J. Noland. *Experimental evaluation of masonry-infilled RC frames*. Journal of Structural Engineering, 122(3), 228–237, 1996
- [8]. T. C., Liauw and K.H., Kwan. Nonlinear behaviour of non-integral infilled frames. Computers and Structures, 18(3), 551-560, 1984.
- [9]. A. Saneinejad and B. Hoobs. Inelastic design of infilled frames. Proceedings of the American Society of Civil Engineering, Journal of Structural Engineering, 1995, 121(4).
- [10]. F. J. Crisafulli. Seismic Behaviour of Reinforced Concrete Structures with Masonry Infills. PhD Thesis, 1997, University of Canterbury, New Zealand.
- [11]. C. A. Symakezis and V. Y. Vratsanou. Influence of infill walls to R.C. frames response. Proceedings of 8th European Conference on Earthquake Engineering, 1986, Lisbon, Portugal.
- [12]. C. Z. Chrysostomou, P. Gergely, and J. F. Abel. Non-linear seismic response of infilled steel frames. Proceedings of 10th World Conference on Earthquake Engineering, 1992, Madrid, Spain.
- [13]. W. W. El-Dakhkhni, M. Elgaaly and A. A. Hamid. Three strut model for concrete masonry-infilled steel frames. ASCE, Journal of Structural Engineering, 2003, 129(2), 177-185.
- [14]. M. Holmes. Steel Frames with Brickwork and Concrete Infilling. Proceedings of the Institution of Civil Engineers, 1961, London, Part 2, 19, 473-478.
- [15]. M. R. A. Kadir. The structural behaviour of masonry infill panels in framed structures, PhD thesis, 1974, University of Edinburgh.
- [16]. T. Paulay and M. J. N. Priesley. Seismic Design of Reinforced Concrete and Masonry Buildings. John Wiley, New York, USA, 744 pp, 1992.
- [17]. CODE, Turkish Earthquake. Specification for structures to be built in disaster areas. Ministry of Public Works and Settlement Government of Republic of Turkey, 2007.

Improved Greedy Algorithms

Sema Kayhan¹

Abstract

This paper proposes a robust greedy algorithms which utilizes Lorentzian robust weighting function and partially known support as a prior knowledge to reconstruct sparse signals. The greedy algorithms Orthogonal Matching Pursuit (OMP), and Compressive Sampling Matching Pursuit (CoSaMP) are modified to use robust weighting of the residuals and robust estimation. The resulting algorithms show better performance than the standard greedy algorithms for impulsive noise environments and outliers.

Keywords: *Compressed sensing, Greedy Algorithms, Signal reconstruction*

1. INTRODUCTION

Compressed sampling (CS) has received a lot of research interest recently. The major goal of Compressed sensing (CS) is to recover a high dimensional sparse signal from its low dimensional linear measurements. The standard CS theorem is based on a sparse signal model and uses an underdetermined system of linear equations. Obviously, know that if the measurement matrix satisfies the condition so called restricted isometry property (RIP), the sparse signal can be exactly (or approximately) recovered through truly designed recovery algorithms [1]. $x \in \mathbb{R}^N$, have a K sparse input, via the linear measurements,

$$y = \Phi x \quad (1)$$

where $\Phi \in \mathbb{R}^{m \times N}$ represents a random measurement (sensing) matrix, and $x \in \mathbb{R}^N$, represents the compressed measurement signal. A K sparse signal vector consists of most K nonzero indices. With the setup of $K < M < N$, the task is to reconstruct x from y (as \hat{x}) using a small number of measurements in addition to achieve good reconstruction qualification [2], [3].

Greedy Algorithms like Matching Pursuit (MP), Orthogonal Matching Pursuit (OMP), the Regularized OMP (ROMP), and Compressive Sampling Matching Pursuit (CoSaMP) are low complexity reconstruction methods are used nowadays. The simple idea behind the usage of greedy method is to find the support for unknown signal sequentially. The support includes indices of non-zero elements of a sparse signal. For example, CoSaMP algorithm is based on the idea of iteration to find the approximation of the original signal. In each iteration, the current approximation produces a residual, which it is the part of the treated signal that has not been approximated yet [4]. OMP algorithm constructs an approximation by using an iteration process. At each iteration, the locally optimum solution is found. This is done by finding the column vector in A which most closely resembles a residual vector [5]. In this paper, greedy algorithms are modified adding robust weight function [6] to calculate the residue and prior known information [7] in reconstruction process.

2. ROBUST GREEDY ALGORITHMS WITH PARTIALLY KNOWN SUPPORT

In this section, first we describe the robust version of two greedy algorithms: OMP and CoSaMP by introducing M -regression and Lorentzian estimation function. Second, partially known support is included in recovery process.

A linear regression model can be written for the CS problem as, $y = \Phi x + e$, here Φ is the known $M \times N$ random measurement matrix, Φ^* denotes the transpose of Φ , and Φ^\dagger denotes the pseudo-inverse $\{(\Phi^* \Phi)^{-1} \Phi^*\}$ and $x \in \mathbb{R}^N$ is the regression coefficients which is K sparse signal, consists of K nonzero indices. Let the support set $T \subset \{1, 2, \dots, N\}$ denotes the set of nonzero component ($K = |T|$), indices of x (i.e. $sup(x) = \{i | x_i \neq 0\}$), and noise term, e . When robust weight function is used, then the estimating equation can equation can be solved using IWRLS approach at each iteration of the algorithm,

$$\hat{x}_{t+1} = (\Phi^T W_t \Phi + \lambda I)^{-1} \Phi^T W_t y \quad (2)$$

In this study the Lorentzian weight function is used. It is given as,

$$w(e, \sigma) = \frac{2}{(2\sigma^2 + e^2)} \quad (3)$$

¹ Corresponding author: Gaziantep University, Department of Electrical Electronics Engineering, 27000, Gaziantep, Turkey.
skoc@gantep.edu.tr

where $e = y_i - \Phi_i^* x$.

Algorithm 1: CoSaMAlgorithm for Signal Recovery

Input *CSmatrix* Φ , *measurements* y , *sparsity* K , *partialknownsupport* T_0 *level*

Output: $\hat{x}_{1 \times N}$

Iteration index $t = 0$,

Initialize: $x_{T_0}^t = \Phi_{T_0}^\dagger y$, $x_{T_0^c}^t = 0$, $r = y - \Phi_{T_0} x^t$,

$$K = K - |T_0|$$

repeat:

$t = t + 1$

Calculate Lorentzian robust weighted residue, e ;

$$e(r, \sigma) = \frac{2}{(1 + r^2/\sigma^2)^2}, \quad \sigma = 1.4826MAD(r)$$

Expands support set T_f ,

$$T_f = \text{supp}(\|(\Phi^\dagger e)\|_{2K})$$

Form a new support set T^{t+1}

$$T = [T_f \cup \text{supp}(x^{t-1})],$$

estimate the x^t using ridge regression estimation equation (1) and update the residual,

$$x^t = \text{RidgeReg}(y, \Phi_T, x^{t-1}),$$

$$x^t(T_0) = 0, \text{ and } T_b = [\text{supp}(\|x^t\|_{K-|T_0|}) \cup T_0],$$

$$r = y - \Phi_{T_b} (\Phi_{T_b}^\dagger y)$$

until $\frac{\|x^t - x^{t-1}\|}{\|x^t\|} \leq \delta$ or $t > t_{\max}$

$$\hat{x}_{1 \times N} = \Phi_T^\dagger y \text{ and } \hat{x}_{T^c} = 0$$

Algorithm 2: OMPAlgorithm for Signal Recovery

Input *CSmatrix* Φ , *measurements* y , *sparsity* K , *partialknownsupport* T_0 *level*

Output: $\hat{x}_{1 \times N}$

Iteration index $t = 0$,

Initialize: $x_{T_0}^t = \Phi_{T_0}^\dagger y$, $x_{T_0^c}^t = 0$, $r = y - \Phi_{T_0} x^t$, $T^t = 0$,

$$K = K - |T_0|$$

repeat:

$t = t + 1$

Calculate Lorentzian robust weighted residue, e ;

$$e(r, \sigma) = \frac{2}{(1 + r^2/\sigma^2)^2}, \quad \sigma = 1.4826MAD(r)$$

Form a new support set T^t

$$T^t = [T^{t-1} \cup \text{supp}(\|(\Phi^\dagger e)\|)],$$

estimate the x^t using ridge regression estimation equation (1) and update the residual,

$$x^t = \text{RidgeReg}(y, \Phi_T, x^{t-1}), \quad r = y - \Phi_T x^t$$

until $|T^t| \geq K$

$$\hat{x}_{1 \times N} = \Phi_T^\dagger y \quad \text{and} \quad \hat{x}_{\overline{T}} = 0$$

Orthogonal Matching Pursuit with partially known support (ROMP-PKS) algorithm finds the support for unknown signal sequentially. At each iteration, algorithm selects the column of measurement matrix which is most strongly correlated with the remaining part of y , and subtracts off this contribution from the remaining part of y and then iterates on the residual. The pursuit algorithm repeats this procedure several times until all the coordinates are arranged in the evaluated support set. The performance of the algorithm can be improved by inclusion of the prior known support and by using robust weighting of the residuals and robust estimation of regression instead of solving a least squares problem at each iteration.

3. EXPERIMENTAL WORKS

The simulations illustrate the performance of the modified CoSaMP and OMP algorithms. Figure 1 illustrates ROMP-PKS, RCoSaMP-PKS results for 256X 256 Lena test image, in the presence of α -stable noise = 1.5.



Figure 1. Comparison of various reconstruction algorithm results for Lena test image, in the presence of α -stable noise = 1.5 (a) R-OMPPS, R-SNR = 31.96 (b) R-CoSaMPPS, R-SNR= 33.18

Table 1 shows the recovery time performance of the proposed algorithms and standart greedy algorithms for a synthetic sparse signal for different signal length N.

Table 1. Reconstruction times (in seconds)

N	128	256	512	1024
CoSaMP	0.0025	0.0032	0.0037	0.0063
RCoSaMP-PKS	0.0083	0.0045	0.0097	0.0318
OMP	0.0042	0.009	0.013	0.0025
ROMP-PKS	0.0522	0.0508	0.0997	0.2708
SP	0.0024	0.0027	0.0332	0.0688

4. CONCLUSION

In this paper, greedy algorithms OMP and CoSaMP are improved by using Lorentzian weight function during residue updating and including partially known support during the reconstruction process. Proposed algorithms needs less number

of samples and reconstructions is more robust than the standard algorithms in noisy case and give better reconstruction performance.

REFERENCES

- [1]. Compressed sensing by Terence Tao, University of California, Los Angeles, (2007). I. S. Jacobs and C. P. Bean, "Fine particles, thin films and exchange anisotropy," in *Magnetism*, vol. III, G. T. Rado and H. Suhl, Eds. New York: Academic, 1963, pp. 271–350.
- [2]. Subspace Pursuit for Compressive Sensing Signal Reconstruction, Wei Dai, Member, IEEE, and Olgica Milenkovic, Member, IEEE, 5, May (2009).
- [3]. Parichat Sermwuthisarn, Duangrat Gansawat, "Impulsive noise rejection method for compressed measurement signal in compressed sensing" , Sermwuthisarn et al. *EURASIP Journal on Advances in Signal Processing* 2012, 2012:68.
- [4]. Needell, D., Tropp, J. A. (2008) CoSaMP: iterative signal recovery from incomplete and inaccurate samples. *Appl Comput Harmonic Anal.* 26 (3) 301–321.
- [5]. J. A. Tropp, J. A., Gilbert, A. C. (2007) Signal recovery from random measurements via orthogonal matching pursuit. *IEEE Trans. Inf. Theory.* 53 (12) 4655–4666.
- [6]. Razavi, S. A., Ollila, E., Koivunen, V. (2012) Robust greedy algorithms for compressed sensing, In *Proc. 20th European Signal Processing Conference (EUSIPCO'12)*, 969-973.
- [7]. Carrillo, R. E., Polania, L.F., Barner, K. E. (2010) Iterative algorithms for compressed sensing with partially known support, in *Proc., IEEE ICASSP, Dallas, TX, 3654-3657, 2010.*

Recent LTE Simulation Tools

Zafer Albayrak¹, Cumhur Torun²

Abstract

In recent years, LTE (Long-Term Evolution) wireless cellular networks has attracted the attention of many researchers. In LTE cellular network, one of the most important issues considered by researchers is to improve QoS (Quality of Service). Performances of protocols depends on network throughput, end to end delay and packet drop. Performance analysis of improved protocols can be tested using simulation tools. In this study, for wireless cellular network, OPNET, OMNeT++ and NS3 network simulators were examined and briefly compared.

Keywords: LTE, Simulation, NS3, OPNET, OmNET++.

1. INTRODUCTION

Whereas the first mobile phones used to allow only for phone call and SMS messages, they now use broadband internet route thanks to the rapid development of mobile technology and cellular networks. Each stage in the evolution of the cellular network is defined as a generation. The difference between each generation represents a higher level in the advancements in air interface and the services offered to users. LTE communication is the fourth generation communication technology, the standards of which is defined by the 3GPP (The 3rd Generation Partnership Project) and which has a complete IP-based communication infrastructure [1].

One of the easy and effective ways used in the analysis of communication networks is the simulation method which is used in various fields. Using the simulation, the network connections, nodes and the traffics generated in the network can be designed in a way similar to those in the real world. The conditions which may be impossible to generate in real life due to financial or other constraints can be easily observed in the network simulators. Since performing experiments by changing queue management algorithms inside the devices on the nodes may be too costly and troublesome in hardware terms, these conditions can be tested with network simulators.

2. BACKGROUND

The fourth generation (4G) cellular network is named as LTE (Long Term Evolution). The LTE system architecture was designed in accordance with the principles of packet switching circuit starting from the air interface (see Fig. 1). Unlike the previous cellular networks, there is a circuit switched architecture in the LTE systems. All network operations are configured in a way to conform to the packet switching system [2]. The LTE communication has a completely IP-based communication infrastructure. It achieves a data download speed of 100Mbps and higher and a data upload speed of 50Mbps or higher with at most 5ms delay (see table 1). The scalable bandwidths used vary from 1.4MHz up to 20MHz [3]. When LTE and the third generation network structures are compared with each other, it is seen that some structures, which are available in the third generation communication systems, are not used in the LTE. The RNC (Radio Network Controller) functions in the third generation are available within the eNodeB (Evolved Node B) unit in LTE. Besides, there is aGW (Access Gateway) unit in LTE instead of the SGSN (Serving GPRS Support Node) and (Gateway GPRS Support Node) nodes, which are available in the third generation systems [4]. In this way, the scarcity of the exchange units used simplifies the network architecture and reduces the exchange costs.

¹ Corresponding author: Karabuk University, Department of Computer Engineering, 78050, Karabuk, Turkey. zalbayrak@karabuk.edu.tr

² Karabuk University, Department of Computer Engineering, 78050, Karabuk, Turkey. cumhurturun@gmail.com

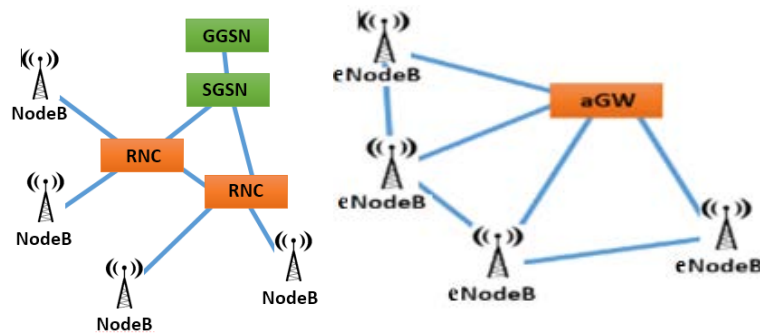


Figure 1. (a) Third Generation Network Architecture (b) LTE Network Architecture

Table 1. Features of LTE Technolog

Maximum data rate (for a bandwidth of 20 MHz)	Downlink: 100Mbps and upper Uplink: 50Mbps
Subscriber movement speed	Supports a range from low speeds such as 0 and 15 km/h up to a high speed of 500 km/h
Control layer delay	< 100ms
User layer delay	< 5ms
Control layer capacity (for a bandwidth of 5 MHz)	Greater than 200 users per cell
Cell coverage	Whereas the most commonly used coverage is 1-30 km, the cell coverage is supported up to 100 km.
Available bandwidths	1.4, 3, 5, 10, 15, 20 MHz

In the studies conducted, the timer algorithms in the queues were tested using the NS-3 and LTE-Sim simulation software for the LTE cellular networks. Within these studies, similar results were obtained from the two simulation software. NS-3 offers a rich source to make a network simulation with the sample applications available in its storage site and using the open source codes. LTE-Sim [5] constitutes a better alternative for beginner users in the Google groups. Both simulator software uses open source codes and run over open source operating systems [6].

In order to compare the performance of LTE and WiMAX systems, the Opnet Modeler network simulation program was utilized. In the study conducted, the LTE and WiMAX systems were compared over four scenarios and it was found that LTE showed better results in terms of parameters such as delay and response time. OPNET Modeler is a network simulation software which has a graphical interface. Since it has a graphical interface, preparing the network environment is relatively easy compared to other software [7]. OMNeT++ simulation software was utilized to evaluate the performances of the LTE and LTE-A systems [8]. In order to examine the radio access technologies in LTE and UMTS wireless cellular network systems, the QualNet simulation software was utilized [9].

3. SIMULATION TOOLS

Network simulation refers to the modeling of the network environment by means of a computer and the monitoring and testing of how the network will operate without a physical installation. Network simulators are used in order to perform network simulations in accordance with the TCP and OSI reference models.

Network simulators are divided into two groups (see table 2), including open source and commercial. In commercial software, users are allowed to purchase the software by paying for the whole software or just for the packages necessary for themselves. OPNET is an example for this type of software. Different packages have been created based on the type of the simulation to be made in OPNET and you may buy them separately. The commercial simulators have both advantages and disadvantages. The fact that both the software and the documentation created for the software are generated by expert personnel may be considered as an advantage. However, the open source network simulators have disadvantages in this

respect and, generally, there is not a sufficient number of experts working on the documents. The upgrades of the software are released with many additional features, which may make it difficult to keep track of the newly added features or lead to serious problems in understanding the previous codes without proper documentation.

In open source network simulator, everyone can make contributions to the software and has the opportunity to find the errors. The interface is open to development. Due to their flexibility, they can reflect the latest developments of the new technologies faster than the commercial network simulators. However, the shortcomings such as the lack of wholly-systematic and full documentation and version control supports may lead to serious problems and may restrict the applicability and lifetime of the open source network simulators.

Table 2. Types of Simulation Software

	Simulation Software
Commercial	OPNET, Matlab, QualNet
Open Source	NS2, NS3, OMNeT++

3.1. OPNET Modeler

OPNET Modeler is an object-oriented program, which provides a visual simulation environment for the modeling of communication systems and communication networks. The behavior and performance analyses of the modeled systems are achieved by discrete-event simulation method. Opnet has a broad library and involves the models of the network protocols such as ATM (Asynchronous Transfer Mode), TCP/IP, and the products generated by the leading companies in the networking industry. It can be used for examining the communications networks, devices, protocols and applications [10].

The biggest advantage of OPNET is that it allows for creating models of new protocols and products with the help of its editors and adding them to the model library. Also, since it is a commercial software provider, it offers a relatively very strong visual and graphic support for OPNET users. It is used to form a network topology from the physical layer to the application layer thanks to its graphic editor interface. OPNET Modeler's interface is given in Figure 2 below.

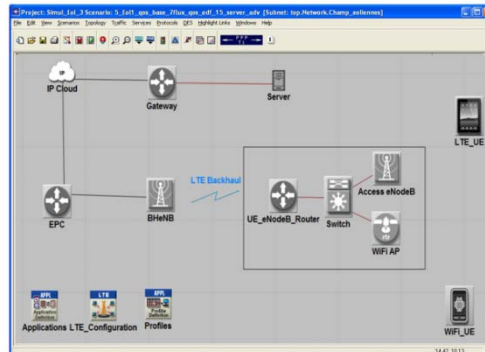


Figure 2. OPNET Modeler Interface

Opnet Modeler gives support to LTE since the release of its version 17.5. OPNET Modeler provides an easy, flexible and comprehensive simulation platform with its pre-defined core functions and standard node models. It allows for a modeling on almost all the basic features of LTE. Opnet modeler has a graphical interface and, thanks to this feature, a modeling environment can be created quickly. The features of OPNET are listed below [11];

- Rapid discrete event simulation engine,
- Object-oriented modeling,
- Scalable wireless simulation support,
- Customizable wireless modeling,
- 32-bit and 64-bit parallel simulation kernel,
- Grid computing support,
- Integrated, GUI-based debugging and analysis,
- Open interface for the integration of external component libraries.

3.2. OMNeT++

OMNeT++ is a network simulator licensed to use the open source, which is based upon graphical user interface and component. Its primary application area is the communication networks. OMNeT++ has a flexible architecture with successful results in areas such as information systems, queuing systems, hardware architectures and, even, business processes. Like NS2 and NS3, OMNeT++ is also a discrete event simulator and has a component-based architecture. Its components are referred to as modules and programmed using C++. The components are then mounted to the larger components and models using a high-level language.

Since OMNeT++ is designed to provide a component-based architecture, the models or modules of OMNeT++ can be reused or can be mounted to the components. The modules can be reused and the main features of OMNeT++ can be combined in various ways. The components of OMNeT++ are as follows;

- Simulation kernel library
- NED topology description language compiler (NEDC)
- Graphical network editor for NED files (gned)
- GUI for playing the simulation (Tkenv)
- Command-line user interface for playing the simulation (Cmdenv)
- Drawing tool for graphic output vector (Plove)
- Visualization tool with graphic output scalar (Scalars)
- Model documentation tool (opp_neddoc)
- Auxiliary tools (makefile creation tool)

The OMNeT++'in interface is given in Figure 3 below.

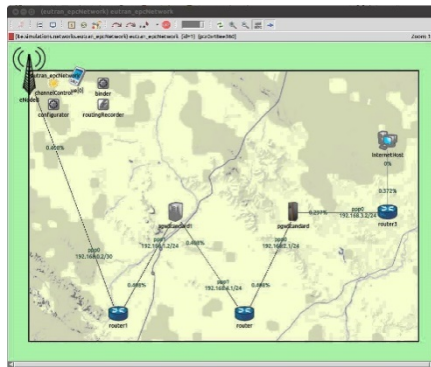


Figure 3. OMNeT++ Interface

OMNeT++ can run over Linux, other Unix-like systems and Windows (XP, Win2K, 7, 8). SimuLTE is an innovative simulation tool that uses OMNET++ framework to simulate LTE and LTE-Advanced systems. It is written in C++. SimuLTE is in the form of an open source project running on the OMNeT++ and INET Framework [12].

SimuLTE can be used on any system compatible with OMNeT++ (Windows, Linux or Mac OS X). The following software must be installed for the simulation tool;

- OMNeT++ v4.6,
- INET-Framework v2.3.

3.3. NS-3

NS-3 a discrete event simulator with open source network which is aimed for research and educational purposes. NS-3 is licensed under the GNU GPLv2 license and can be used for research and development [13].

NS-3 is designed to replace NS-2. NS-3 does not constitute an updated version of NS-2. NS-3 is a new simulator and is not retrospectively compatible with NS-2. The difference between NS-3 and NS-2 are listed below;

- Different software kernel: NS3 kernel is written in C++ and Python coding interface. NS-2 is written in OTcl.
- Factuality: Its protocol components are designed in a way to be close to the actual computers.
- Virtualization support: Used by lightweight virtual machines compared to the NS-2.
- Monitoring architecture: A monitoring and statistics collection framework has been developed in NS3 simulation kernel.

LENA (LTE-EPC Network SimulAtor) is developed for the NS-3 LTE module. LTE-EPC model has two main components. These components are as follows;

- LTE Model: This model includes Radio Protocol Stacks (RRC, PDCP, RLC, MAC, PHY) between UEs and eNB nodes,
- EPC Model: This model involves the core network interfaces and protocols between SGW, PGW and MME.

EPC model provides tools for the simulation of end-to-end IP connection over LTE model. Multiple eNodeBs are connected to one SGW / PGW node and the data flow is over the SGW and PGW [14].

The image created according to the NS3 simulation result file is given in Figure 4 below.

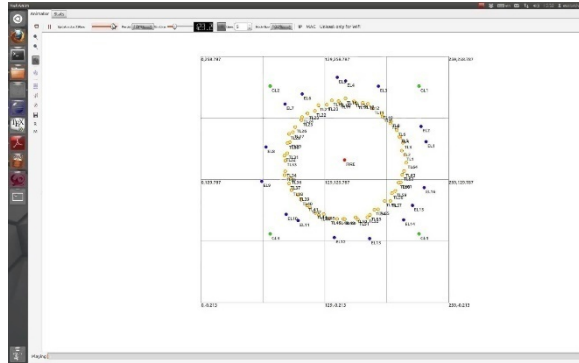


Figure 4. NS3 Interface

4. CONCLUSION

It is almost impossible to model a network environment fully with all details. On the other hand, it is important to pay attention to some details, which seriously affects the results. Therefore, software has detail levels. Among the software studied, OPNET Modeler has a higher detail level. OMNeT++ and NS-3, however, provide a moderate detail level.

Considering the descriptions of the simulation and the studies conducted, it can be concluded that the best option for studies is the NS-3 and OMNeT++.

NS-3 is the most commonly used simulators for academic researches; however, its complicated architecture is generally criticized. Nevertheless, it has many users who try to solve problems arising in the preparation of a simulation thanks to its actively used e-mail lists and forums.

OMNeT++, on the other hand, is gaining popularity in the academic and industrial world. It also has a powerful graphical interface. However, it has a lower number of external models and user base compared to the NS-3.

In addition to being a commercial simulation software, OPNET Modeler provides a whole simulation solution and meets the needs of industrial researchers who want to quickly create reliable simulations.

REFERENCES

- [1] Muntean, Vasile Horia, and Marius Ottesteanu. "WiMAX versus LTE-An overview of technical aspects for next generation networks technologies." *Electronics and Telecommunications (ISETC), 2010 9th International Symposium on*. IEEE, 2010.
- [2] Andersson, Karl, S. Al Mahmud Mostafa, and Raihan Ul-Islam. "Mobile VoIP user experience in LTE." *Local Computer Networks (LCN), 2011 IEEE 36th Conference on*. IEEE, 2011.
- [3] Nakamura, Takaharu. "LTE and LTE-Advanced: Radio technology aspects for mobile communications." *General Assembly and Scientific Symposium, 2011 XXXth URSI*. IEEE, 2011.
- [4] Dahlman, Erik, et al. *3G evolution: HSPA and LTE for mobile broadband*. Academic press, 2010.
- [5] Piro, G. "LTE-Sim-the LTE simulator." (2013).
- [6] Subramanian, Ramprasad, et al. "Survey Of Lte Downlink Schedulers Algorithms In Open Access Simulation Tools Ns-3 And Lte-Sim." *International Journal of Wireless & Mobile Networks 7.2* (2015)
- [7] Torad, Mohammed, A. El Qassas, and Hadia Al Henawi. "Comparison between LTE and WiMAX based on system level simulation using OPNET modeler (release 16)." *Radio Science Conference (NRSC), 2011 28th National*. IEEE, 2011
- [8] Andreozzi, Matteo Maria. "LTE and LTE-Advanced evaluation through innovative simulation tool." (2011)
- [9] Kaur, Simrandeep, and Dharmaraja Selvamuthu. "Adaptive joint call admission control scheme in LTE-UMTS networks." *Communication, Networks and Satellite (COMNETSAT), 2014 IEEE International Conference on*. IEEE, 2014.
- [10] Zaki, Yasir, et al. "Multi-QoS-aware fair scheduling for LTE." *Vehicular technology conference (VTC spring), 2011 IEEE 73rd*. IEEE, 2011.

- [11] Pan, Jianli, and Raj Jain. "A survey of network simulation tools: Current status and future developments." Washington University in St. Louis, Tech. Rep (2008).
- [12] Viridis, Antonio, Giovanni Stea, and Giovanni Nardini. "SimuLTE-A modular system-level simulator for LTE/LTE-A networks based on OMNeT++." Simulation and Modeling Methodologies, Technologies and Applications (SIMULTECH), 2014 International Conference on. IEEE, 2014.
- [13] Henderson, Thomas R., et al. "Network simulations with the ns-3 simulator." SIGCOMM demonstration 14 (2008).
- [14] N. Baldo, M. Requena, M. Miozzo, R. Kwan, "An open source model for the simulation of LTE handover scenarios and algorithms in ns-3"

A Classification Method for Images Containing Human Using Face-Body Relation

Fatih Aslan¹, Irfan Kosesoy²

Abstract

Classifying images have been one of the most studied topics in image processing for several purposes such as pose estimation, face detection, object recognition etc. Also, images of people on the Internet may contain nudity that are considered offensive by some people and more importantly used to tempt and abuse children or vulnerable. The goal of the study is to detect nude images more accurately and effectively. For this purpose, after obtaining faces in an image, related bodies are estimated according to general face-body ratio. Obtained body areas are checked one by one using three different color spaces together for the best skin pixel detection – YCrCb, HSV, and NormRGB. To classify, total number of skin pixels and total pixels are respectively calculated for each body area and checked against a threshold that is relative to face-body ratio of current body. Since the method works only vertical bodies and some bodies may be deviated from vertical line of corresponding faces, a number of rotations were used in the study in order to detect non-vertical images. For testing, randomly chosen images were taken and categorized by human eye first and given to the generated algorithm. The accuracy has been observed by the generated algorithm over classic methods, which evaluate a whole image, for the same test images. The main reason of using face-based rotational nudity classification is that skin pixels that are on faces increase nudity ratio and must be eliminated when giving decision. Another advantage of this method is to avoid the time wasted on searching whole image, instead specific areas are taken into consideration with the help of increased technology in face detection.

Keywords: *image classification, color spaces, face detection, nudity detection, face-body ratio.*

1. INTRODUCTION

Image classification has been widely studied and many applications have been conducted on images in order to make sense of them for several reasons – e.g. detecting objects, gathering information about crops, implementing face detection and so on.

Particularly, detecting images that contain human would be evaluated whether they might be considered as nude. This is absolutely necessary because children must be protected from accidentally or voluntarily in sake of their physical or psychological development as well as some people may not want to see such offensive images [1]. Currently for the classification there are some parental programs working on text basis and some programs disabling all image traffic flowing from the Internet. These are not favored because visual objects are main aspects of web pages and textual filters cannot work on plain images only giving information about pages.

There has been numerous studies on this subject. These are focuses on body structure, image retrieval, and skin color region [1]. Using prior body structure for nudity based classification, researches in [2] and [3] first try to detect skin color regions and then convert the detected regions into a predefined body. In [4], color or texture aspects of an image are acquired and then a pattern classifier resolves the recognition results. In [5], instead of directly analyzing an image, a database which is classified beforehand is used. An image is labeled as nude when the number of pre-classified images from the database reach to a threshold.

When detecting nudity in classical methods using skin color, the nudity ratio is calculated through dividing the number of detected skin pixels by the number of all pixels. It is obvious that these methods do not classify images containing large amount of skin color that is not considered nude – e.g. frames that show only faces have large amount of skin pixels as classical methods mistakenly label such an image as nude. Also, an additional feature is required to identify skins whether they belong to human. In this work, in order to deal with these problems, faces are detected and ignored by cropping related body area of an individual detected face. In addition to this cropping procedure, a number of rotations are applied each image in case a face and its related body have different orientations.

¹ Corresponding author: Yalova University, Department of Computer Engineering, 77100, Merkez/Yalova, Turkey. fatih.aslan@yalova.edu.tr

² Yalova University, Department of Computer Engineering, 77100, Merkez/Yalova, Turkey. irfan.kosesoy@yalova.edu.tr

In our previous work [6], a ratio gained by dividing total number of skin pixels by the number of faces on an image was used to classify images. This time, instead of working on whole image, part of images are taken into account as it is more accurate and efficient to deal with small regions of image that are belong to a detected face. Such small regions of an image can be estimated according to the ratios of different parts of body [7]. The estimation of a body area is considered vertically for a detected face. For this reason, a number of rotations are applied for increased accuracy.

2.BACKGROUND

2.1.Skin Color

As the most important aspect of an image, color has been exhaustively been used in image segmentation. Objects can be recognized based on color variation in images [8].

In this work, nudity means that sexual organs or most part of the body is open to public. It is evident to measure nudity of an image using skin color as the base feature [8][9]. Since nudity has different meanings and implications in different contexts, the proposed method can be adopted for them by changing the threshold value mentioned below.

In literature, there are many studies about color-based image classification. It must be taken into consideration that skin colors in grey-scale images cannot be detected, therefore gray scale images are ignored. Skin colors need to be detected in order to construct a method in the classification phase of pixels whether they stand for skin or not.

Many methods have been proposed to estimate skin color in literature. One of the simplest and fastest methods is the classification done by using pre-determined range to evaluate a pixel instead of using complex methods such as ANN and Bayesian classifications. Because of its simplicity, easy deployment, and instantaneous structure, range classification has extensive usage.

In this work, different color spaces NormRGB, HSV, and YCbCr are used altogether for the classification instead of using pure RGB. These color spaces are briefly explained below.

2.2.NormRGB

NormRGB is one of the most widely used color spaces to detect skin color. R,G, and B values of each pixel are summed and each component is divided by this summation. New r, g, and b values are obtained as in Equation-1. Using these r,g, and b values, in Equation-2 the ranges that indicate skin colors are given [10].

$$\left. \begin{aligned}
 Base &= R + G + B \\
 r &= \frac{R}{Base} \\
 g &= \frac{G}{Base} \\
 b &= \frac{B}{Base}
 \end{aligned} \right\} \quad (1) \left. \begin{aligned}
 \frac{r}{g} &> 1.185 \\
 \frac{R.G}{Base^2} &> 0.107 \\
 \frac{R.B}{Base^2} &> 0.107
 \end{aligned} \right\}$$

(2)

The last component b can be omitted for simplicity and therefore the space dimension can be reduced as sum of the normalized values are 1 [11].

2.3.YCbCr

In this color space, the components Y, Cr, and Cb stand for the luminance, the chrominance and the red components of a pixel respectively – showing how much each component deviate from gray. The following equations related to YCbCr color space are taken from the algorithms developed by Chai and Ngan [12] :

$$\left. \begin{aligned}
 Y &= 0.299R + 0.587G + 0.114B \\
 Cb &= B - Y \\
 Cr &= R - Y
 \end{aligned} \right\} \quad (3)$$

In YCbCr color space, any pixel that satisfies the condition shown in Equation-4 is considered as skin pixel.

$$\left. \begin{aligned}
 Y &> 80 \\
 77 &< Cb < 127 \\
 133 &< Cr < 173
 \end{aligned} \right\} \quad (4)$$

2.4.HSV

The three subdivision components of HSV color space are hue, saturation, and value. Hue is the color type ranging from 0 to 360, saturation is the vibrancy of the color ranging from 0 to 100%, and finally value is the brightness of the color ranging from 0 to 100% [13].

$$H = \left\{ \begin{array}{ll} \text{undefined} & , \text{if } \max = \min \\ 60x \frac{G-B}{\max - \min} + 0 & , \text{if } \max = R \text{ and } G \geq B \\ 60x \frac{G-B}{\max - \min} + 360 & , \text{if } \max = R \text{ and } G < B, \\ 60x \frac{B-R}{\max - \min} + 120 & , \text{if } \max = G \\ 60x \frac{R-G}{\max - \min} + 240 & , \text{if } \max = B \\ S = \begin{cases} 0 & , \max = 0 \\ 1 - \frac{\min}{\max} & , \text{otherwise} \end{cases} & \\ V = \max & \end{array} \right\}$$

(5)

Equation 5 illustrates the pseudo-code for the transform from RGB color space into HSV color space [14]. For HSV color space, skin pixels are in the range shown below:

$$\left. \begin{array}{l} 0 \leq H \leq 50 \\ 0.23 \leq S \leq 0.69 \end{array} \right\}$$

(6)

As a demonstration of capturing skin pixels in the color spaces mentioned above, the image shown in Figure-1 (a) is examined for each color space. In Figure-1 (b), (c), and (d), a white pixel represents skin for the image. It is clear that the best skin detection for the image is gained by YCbCr color space though they are simultaneously used for more accurate evaluation.

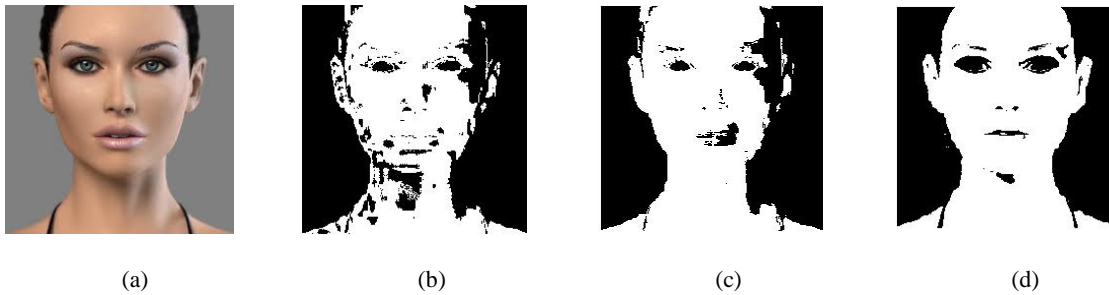


Figure 1. (a) Original Image, (b) NormRGB skin detection, (c) HSV skin detection, (d) YCbCr skin detection

2.5.Face-Body Relation

Since skin pixels can easily be detected, it is needed to go further and detect nudity through gaining help from face recognition techniques. Once a face detected in an image, a body area can be allocated for the face according to face-body ratio defined in [7]. The face-body ratio used in this work can be shown in Figure 2.

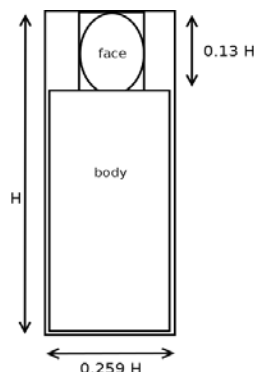


Figure 2. Face-Body ratio taken and adopted from [7]

In the proposed method, all the images are considered as vertical images. Even if real world images are not always vertical, this body area estimation increases accuracy in detecting nudity over classic methods that only find nude pixels of a whole image. To overcome the issue of not being vertical, a number of rotations are used.

3. NUDITY DETECTION

After explaining required and related topics for nudity detection, the proposed method is detailed in this section. The method is summarized in four stages as seen in Figure 3. After detecting skin pixels, some morphologic processes are applied to image and small regions are eliminated.

Since people in images may not be always aligned as vertical, a number of rotations are applied to images starting from -90 degree to +90 degree with 30 degree increments. This is applied in the first stage.

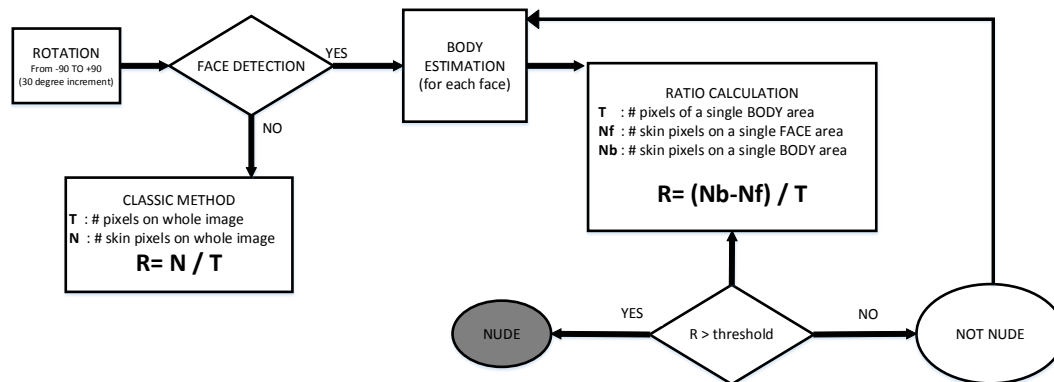


Figure 3. The proposed algorithm

In the second stage, general face detection tools are used and all faces of an image are identified. When no faces are detected, then classic methods are applied immediately. If any face found, then the algorithm goes into the third stage to estimate relational body areas as in section 2.2 for each face one by one. Although people in images are not always aligned as vertical, some body parts will be included in these estimated areas. By rotation, images having non-vertical bodies can be detected. As a result, nudity can be captured depending on to what extent bodies are vertical.

In the last stage, each body area that is calculated for a face will be taken into account individually. Here, skin pixels of the area are calculated firstly except the pixels belonging to the face. This subtraction eliminates inaccurate results for images that are mostly covered by faces such as a passport photo. Afterwards, the nudity ratio is computed through dividing this total number of non-face skin pixels by total number of pixels. At the end, the ratio is compared with a predefined threshold. If the ratio reaches to the threshold then the image is nude and vice versa. This process is applied for each face in an image, until reaching the last face. There must be a logical order for those faces to be taken. Vertically lower faces have higher priority over faces appearing on the upper part of an image. This process is applied until all the faces are taken into consideration. If any partial estimated area says the image is nude, then the algorithm stops working and the result is positive indicating nudity. After taking each face into consideration, next rotation is applied with the same procedure till last rotation.

Also, to decrease inaccurate results, subsequent estimated body areas do not include previously handled body areas – meaning that a body area is completely cropped from an image and the whole image is altered after a body area is estimated.

In addition, the threshold can be optionally determined according to audience – it is clear that threshold must be lower for a system that is mostly used by children.

4. RESULTS

To test the algorithm, 67 arbitrarily chosen images with varying resolution and context were used – they all have at least one face detected. By human eye, 54 of them labeled as nude with decreasing nudity rate and 13 are not nude. All of the images contain people. Also, the three color spaces NormRGB, HSV, and YCbCr were applied together in order to increase accuracy while obtaining skin pixels.

The threshold was chosen as 0.18 for both classic nudity detection method and the proposed method after exhausted experiments during implementation.

Shown how the images were classified for both classic nudity detection and the face-based nudity detection methods in the order. The number of True Positive (TP) and False Negative (FN) are the same. The main goal in the suggested method is to prevent images from being misclassified as nude. Hence, TP and FN values will be the same. However, when looked at the number of False Positive (FP) and True Negative (TN) images, it can be concluded that the suggested classification method is more successful than the classic method.

The overall accuracy results are 68 and 75 for classic and suggested methods respectively. As a result, the significant improvement by 7% can be seen for the test images and the threshold value 0.18.

5. CONCLUSION

The main goal of this work is to eliminate the error rate of classic nudity detection method which misclassifies nude images because of skin pixels that do not considered as nude. For this purpose, face areas which are never considered nude are detected and subtracted when calculating nudity ratio. The other aim of this work is applied by rotating images in order to detect possible non-vertical bodies when estimating body areas belonging to a face. According to the obtained results and the threshold value, the method is successful. Also, this method gives speedy results in contrast with classic methods because this method never evaluates whole image – only estimated body areas of a detected face will be cropped and used.

Using the proposed method, real time images such as streaming videos or web browser images can be efficiently filtered.

For future studies, instead of estimating body areas for faces, body posture can be detected and checked against nudity as skin pixels are obvious.

REFERENCES

- [1] Zhang, Jing, et al. "An approach of bag-of-words based on visual attention model for pornographic images recognition in compressed domain." *Neurocomputing* 110 (2013): 145-152..
- [2] Forsyth, David A., and Margaret M. Fleck. "Identifying nude pictures." *Applications of Computer Vision, 1996. WACV'96., Proceedings 3rd IEEE Workshop on*. IEEE, 1996..
- [3] Fleck, Margaret M., David A. Forsyth, and Chris Bregler. "Finding naked people." *Computer Vision—ECCV'96*. Springer Berlin Heidelberg, 1996. 593-602.
- [4] H. Zheng, M. Daoudi, and B. Jedynek, "Blocking Adult Images Based on Statistical Skin Detection," vol. 4, no. 2, pp. 1–14, 2004.
- [5] Wang, James Ze, et al. "System for screening objectionable images." *Computer Communications* 21.15 (1998): 1355-1360..
- [6] Kosesoy, Irfan and Aslan, Fatih "Face-Based Nudity Detection From Skin Color," in *International Conference on Innovative Trends in Science, Engineering and Management*, 2014.
- [7] Herman, Irving P. *Physics of the human body*. Springer, 2016.
- [8] Ap-Apid, Rigan. "An algorithm for nudity detection." *5th Philippine Computing Science Congress*. 2005..
- [9] Lin, Yu-Chun, Hung-Wei Tseng, and Chiou-Shann Fuh. "Pornography detection using support vector machine." *16th IPPR Conference on Computer Vision, Graphics and Image Processing (CVGIP 2003)*. Vol. 19. 2003..
- [10] Gomez, Giovanni, and E. Morales. "Automatic feature construction and a simple rule induction algorithm for skin detection." *Proc. of the ICML workshop on Machine Learning in Computer Vision*. 2002..
- [11] Subban, Ravi, and Ravishankar Mishra. "Rule-based face detection in color images using normalized RGB color space—A comparative study." *Computational Intelligence & Computing Research (ICCIC), 2012 IEEE International Conference on*. IEEE, 2012..
- [12] Chai, Douglas, and King N. Ngan. "Face segmentation using skin-color map in videophone applications." *Circuits and Systems for Video Technology, IEEE Transactions on* 9.4 (1999): 551-564..
- [13] Su, Ching-Hung, Huang-Sen Chiu, and Tsai-Ming Hsieh. "An efficient image retrieval based on HSV color space." *Electrical and Control Engineering (ICECE), 2011 International Conference on*. IEEE, 2011..
- [14] Chaves-González, Jose M., et al. "Detecting skin in face recognition systems: A colour spaces study." *Digital Signal Processing* 20.3 (2010): 806-823..

Investigation on Combining Electrochromic Devices and Organic Solar Cells and their Application Areas: A review

Halil Esgin¹

Abstract

In this work, transparencies of organic-based solar cells (OSCs) and application areas have been studied. OSCs have various advantages such as cost effectiveness, low weight, and flexible, transparent and wearable photovoltaic. OSCs have been more demanding on the market than silicon-based or compound semiconductor-based solar cells due to ease of manufacturing and more application areas. The efficiencies of OSCs are about 10% in spite of all these advantages. However, large potential surface areas that covered by OSCs can collect solar energy to production a very huge amount of electricity. Recently, It should become more effectual and can compete with silicon technology by improving the performance of the OSCs. Furthermore, research on the combining electrochromic (EC) devices and transparent solar cells has been done. The convenience of OSC-EC devices has been analyzed and has been suggested as large energy-saving devices for building applications.

Keywords: *Electrochromic Devices, Organic solar cells, Transparency*

1. INTRODUCTION

Energy demand is rapidly increasing with the growing world population. Demanding on energy is expected to increase up to 40% by 2035 [1]. Needed energy in this day and age is provided by using fossil fuels and amount of the sources decreasing day by day. This trend is economically, environmentally and socially unsustainable. It is projected that emissions of CO₂ due to using traditional energy source will more than double by 2050 [2]. Furthermore, the point of environmental concern it is predicted that regenerative energy sources will play an important role by the change of energy policy due to higher cost and limited fossil source. In recent years, new technologies that are able to alternative for fossil fuels are emerging to meet rising energy consumption and trying to find low-cost and renewable sources.

Renewable-energy sources such as solar, wind, geothermal energies etc. represent inexhaustible energy to our world. All these sources on the Earth derive from the sun. Among all energy sources, solar energy is the most abundant source and has a dominant characteristic position due to its environmentally advantageous in comparison to any other renewable-energy source. Besides, solar energy provides a continuous stream of energy which warms us, provides plants to grow via photosynthesis, heats the land and sea differentially and so causes winds and consequently waves and, of course, rain leading to hydropower [3]. It produce energy from sunlight directly without deplete natural resources, emit CO₂ or other gaseous into air and generate waste products [4].

The solar energy that hits the earth's surface in one hour is about the same as the amount consumed by all human activities in a year [2]. Although this huge potential energy, rate of using solar cells to provide all consumption of energy was only about 3% by 2009 [5]. The major reason for less use of solar cells is that polycrystalline (pc) Si solar cells dominate the PV market much greater than 80% [6]. Pc-Si technology requires high cost, temperature and vacuum, and slow manufacture and large application areas [7]. These disadvantages making pc-Si solar cells unattractive.

Organic photovoltaics (OPVs) are promising devices for PV market due to their potential for cost-efficient and large area manufacturing, and incomparable applications, such as flexibility and transparency [8]. Large area manufacturing and chemical flexibility of organic materials increase its applicability to industry. Variety of easy and cost-effective techniques is used to manufacture organic-based photovoltaic devices. These techniques mainly consist of two groups: thermal evaporation and solution coating.

2. MATERIALS AND METHODS

This study comprises two technologies, which have different applications but have many similar characteristics. One is the organic solar cell; the other is the electrochromic device. At first it is hard to see what they have in common other than that they both interact with light. [9]

¹ Corresponding author: Bartin University, Central Research Laboratory, 74100, Bartin, Turkey. hesgin@bartin.edu.tr

2.1. Electrochromic Devices

Chemicals that can be electrochemically switched between different colours are said to be electrochromic. Electrochromic devices can change their color reversibly when a voltage is applied. Electrochromic materials exhibit a huge change in optical properties upon a change in either electric field. A small voltage applied to the windows will cause them to darken; reversing the voltage causes them to lighten [10]. These devices have seen great interest in researches because of their fascinating fundamental spectroelectrochemical properties and their commercial applications [11]. Electrochromic devices (EC) are frequently used in many application areas such as optical and electrical. These application areas of electrochromic materials contain their use in controllable light-reflective or transparent devices for optical information and storage, anti-glare car rear-view mirrors, sunglasses, protective eyewear, glare-reduction systems for offices, and 'smart windows' for use in cars and in buildings [12].

An electrochromic device can offer matchless benefits to the consumer by means of this property. User can control the amount of transmitted light and heat in electrochromic glasses (smart glass). Thus, huge amount of energy saving can be performed by EC glasses. Thereby, EC glasses present an opportunity for the buildings as energy-saving devices. EC windows can reduce energy consume of a building up to 25% of heating and cooling needs, 50% of lighting, and 30% of peak power demand by using effectively [13].

Development of these devices has been growing ever since that time. The history of smart glass goes back to 1704 when Diesbach discovered Prussian blue (hexacyanoferrate), which changes the color from transparent to blue under oxidation of iron [14]. Electrochromic optical switching devices known as "smart windows" and these devices can be used for a variety of applications. Regulation of incident solar energy and glare in buildings, vehicles, aircraft, spacecraft and ships is one of the most promising application areas [9].

Electrochromism results from the generation of different visible region electronic absorption bands on switching between redox states. The colour change is commonly between a transparent ('bleached') state and a coloured state, or between two coloured states. In cases where more than two redox states are electrochemically available the electrochromic material may exhibit several colours and be termed polyelectrochromic.

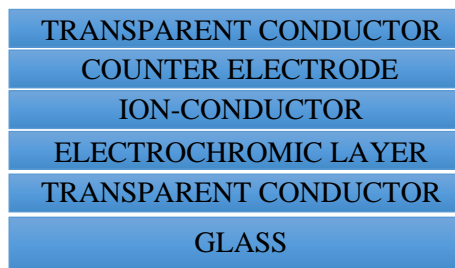


Figure 1. A typical electrochromic device

Figure 1 shows a typical EC device. This device includes a thin film of electrochromic layer, an ion-storage layer, and an ion-conductor layer sandwiched between two transparent conducting layers. This device is optically clear and transmits about 70 – 80% of the incident light when it's non-activated. The light transmission properties can be changed via changing applied voltage. It will remain in that state for a longer period of time without any applied voltage. On reversing the polarity, the device will return to its original transparent state. Although, there is still controversy about the detailed coloration mechanism, it is generally accepted that the injection and extraction of electrons and metal cations (Li⁺, H⁺, etc.) play an important role [15]. The performance characteristics of an EC device is a function of device parameters, but generally falls within the range specified in Table 1 [16].

Table 1. Performance characteristics of an electrochromic device

Characteristics of EC	Performance
Optical-transmittance visible-near-IR	1.0-80%
Switching voltage	0.5-3.0 V
Total injected charge	Up to 50 mc
Switching time	100 ms to 60 s

Memory	1-24 h
Cyclic lifetime	10K – 5M cycles
Projected lifetime	Up to 20 years
Operating temperature	-30 to 70°C
Total thickness of coatings	~2 μm

2.2. Organic Photovoltaics (OPVs)

Organic photovoltaic (OPV) research topics have become highly popular recently. The number of publications in this field of organic solar cells between 2000 and 2007 grew more than 10% of all photovoltaic publications dealing with OSCs. Moreover, 10% of publications in this field focused on OPVs in 2006[17].

Organic photovoltaics which contain at least one organic semiconductor or molecule in the active light absorbing layer have any whole definition, but typically called the third generation of PV technologies [18]. The all organic technologies can separate several areas: the small molecule, gas phase deposited solar cells [19] and the solution processed organic solar cells. The term solution processed organic solar cells includes the (i) all polymer cells [20] (ii) the small molecular organic solar cells, [21] and polymer/ fullerene based solar cells [22].

Tang reported the general structure of an OPV device in 1986 and it is described in Figure 2 [23]. It includes a substrate, a transparent conducting electrode such as indium-tin oxide (ITO), two organic light-absorbing layers, and a second electrode such as Ag.[18]

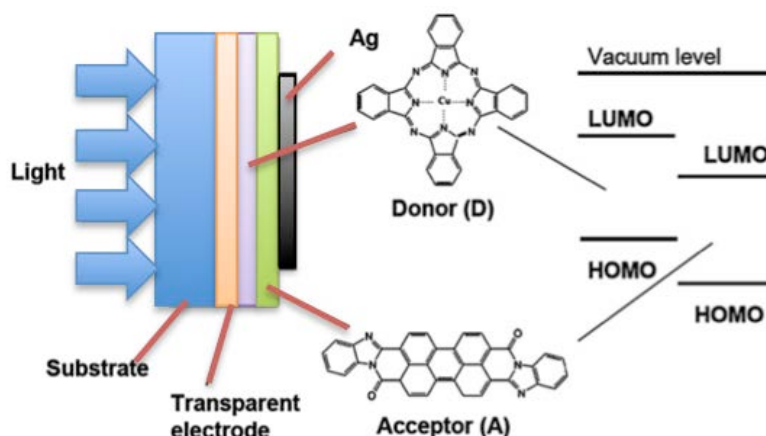


Figure 2. Cross-section of a bilayer organic photovoltaic [18]

Like all photovoltaics, OPVs convert light into electricity, by converting a flux of photons into a flux of charged particles to produce a current. Combination of many type materials made possible this conversion. These materials must have distinct electrical and optical characteristics that proper photovoltaic.

Solar cells must have these three steps:

- 1) Photons that have energy more than the semiconductor band gap must be incident on a semiconductor. Following exciting electrons to an unoccupied state above band gap, photons create electron-hole (e-h) pairs.
- 2) The electron-hole pairs are subsequently separated each other in the electrochemical potential of the solar cell.
- 3) Finally, the electrons and holes can be collected at opposite sides of the electrodes and they can recombine after the complete a circuit.

3 RESULTS AND DISCUSSION

3.1. Integration of OSC and EC

Compared to electrochromic technology, which has been under developing, energy saving with better efficiency can be provided by the integration of photovoltaic and electrochromic. Photovoltaic electrochromic device can change own color in electrochromic layer with using any additional electricity source. Diverse application areas of electrochromic devices can be generated by researches that integrate photovoltaic technology. This combined device may be used to automatically adjust the colors of electrochromic windows to reduce indoor heat and produce electricity.

PV-EC technology has become a new trend as an emerging technology due to energy saving is getting an important issue. PV-EC technology integrated in building application allows enormous energy saving, as reported by NREL [16] that 1 kWp of PV power can remove approximately 3 Wp of heat from a building envelope, while the same 1 kWp of PV used to activate a PV-EC window can avert 110 kWp [24].

The idea of combining a photovoltaic and electrochromic device (PV-EC) was first explored for an electrophotographic application [25]. An extension of that idea, which incorporates a PV device with an EC device [26] becomes even more compelling because the PV systems are being increasingly used in building facades [16].

There are two types of solar powered EC devices, silicon based PV-EC device [12]–[17] and dye-sensitized solar cell (DSSC) based PV-EC device [18]–[24].

In this paper, an innovative OSC-EC device [27] has been suggested. This device shown in Figure 3 schematically. This planar transparent OPV-EC design can meet energy requirement of EC device and produce electricity to climate buildings or meet energy necessity of any electronic devices. When sunlight enters the OSC-EC device, bulk heterojunction layer produce excitons. The OSC must be transparent in this design. Thus, this device could have huge application areas because of the transparency. Transparency of organic solar cells are under development since Lunt at al., demonstrated the first transparent NIR- absorbing luminescent solar concentrator with high transparency and minimal tinting [27].

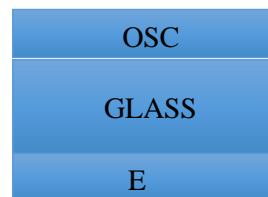


Figure 3. A schematic perspective view of new design OSC-EC device

4. CONCLUSIONS

Electrochromic devices and organic photovoltaics have some common properties due to interact with light. These devices have ability to transparency due to containing organic materials and transparent oxides. that electrolyte system which for the electrochromic can contain a variety of redox or ion storage layers. Billion square meters of building windows could benefit from the use of a solar-smart window. Saving and generating huge amount of energy can possible using this technology.

REFERENCES

- [1]. H. Huang, J. Huang. *Organic and Hybrid Solar Cells*, Springer, 2014.
- [2]. (2016) The IEA-PVPS website [Online] Available: www.iea-pvps.org.
- [3]. I. Dincer, "Renewable energy and sustainable development: a crucial review," *Renewable and Sustainable Energy Reviews.*, vol. 4, pp. 157-75, 2000.
- [4]. T. Tsoutsos, N. Frantzeskaki, V. Gekas, "Environmental impacts from the solar energy technologies," *Energy Policy.* vol. 33, pp. 289-96, 2005.
- [5]. B. P. Rand, H. Richter. *Organic Solar Cells: fundamentals, devices, and upscaling*, CRC Press, 2014.
- [6]. R. García-Valverde, J. A. Cherni, A. Urbina, "Life cycle analysis of organic photovoltaic technologies," *Progress in Photovoltaics: Research and Applications.*, vol. 18, pp. 535-58, 2010.
- [7]. V. Avrutin, N. Izyumskaya, H. Morkoç, "Semiconductor solar cells: Recent progress in terrestrial applications," *Superlattices and Microstructures.*, vol. 49, pp. 337-64, 2011.
- [8]. J. Suddard-Bangsund, C. J. Traverse, M. Young, T. J. Patrick, Y. Zhao, R. R. Lunt, "Organic Salts as a Route to Energy Level Control in Low Bandgap, High Open-Circuit Voltage Organic and Transparent Solar Cells that Approach the Excitonic Voltage Limit," *Advanced Energy Materials.*, vol. 6, pp. n/a-n/a, 2016.
- [9]. C. M. Lampert, "Towards large-area photovoltaic nanocells: experiences learned from smart window technology," *Solar Energy Materials and Solar Cells.*, vol. 32, pp. 307-21, 1994.

- [10]. G. G. T. Esat Pehlivan, "Titanium dioksit katkılı niobyum pentoksit filmlerin optik, yapısal ve elektrokromik özellikleri," *itü dergisi/c, fen bilimleri.*, vol. 5, pp. 49-55, 2007.
- [11]. R. J. Mortimer, "Electrochromic materials," *Chem Soc Rev.*, vol. 26, pp. 147-56, 1997.
- [12]. P. M. S. Monk, R. J. Mortimer, D. R. Rosseinsky. *Electrochromism: fundamentals and applications*, John Wiley & Sons, 2008.
- [13]. S. K. Deb, "Photovoltaic-integrated electrochromic device for smart-window applications," *National renewable energy laboratory golden, co.* vol.1, pp. 80401-3393, 2000.
- [14]. P. Monk, R. Mortimer, D. Rosseinsky. *Electrochromism and electrochromic devices*, Cambridge University Press, 2007.
- [15]. P. R. Somani, S. Radhakrishnan, "Electrochromic materials and devices: present and future," *Materials Chemistry and Physics.*, vol. 77, pp. 117-33, 2003.
- [16]. S. K. Deb, S. H. Lee, C. E. Tracy, J. R. Pitts, B. A. Gregg, H. M. Branz, "Stand-alone photovoltaic-powered electrochromic smart window," *Electrochimica Acta.*, vol. 46, pp. 2125-30, 2001.
- [17]. T. Ameri, G. Dennler, C. Lungenschmied, C. J. Brabec, "Organic tandem solar cells: a review," *Energy & Environmental Science.*, vol. 2, pp. 347-63, 2009.
- [18]. B. Kippelen, J.-L. Brédas, "Organic photovoltaics," *Energy & Environmental Science.*, vol. 2, pp. 251-61, 2009.
- [19]. P. Peumans, A. Yakimov, S. R. Forrest, "Small molecular weight organic thin-film photodetectors and solar cells," *Journal of Applied Physics.*, vol. 93, pp. 3693-723, 2003.
- [20]. C. R. McNeill, N. C. Greenham, "Conjugated-Polymer Blends for Optoelectronics," *Advanced Materials.*, vol. 21, pp. 3840-50, 2009.
- [21]. A. B. Tamayo, B. Walker, T.-Q. Nguyen*, "A low band gap, solution processable oligothiophene with a diketopyrrolopyrrole core for use in organic solar cells," *The Journal of Physical Chemistry C.*, vol. 112, pp. 11545-51, 2008.
- [22]. C. J. Brabec, S. Gowrisanker, J. J. M. Halls, D. Laird, S. Jia, S. P. Williams, "Polymer-fullerene bulk-heterojunction solar cells," *Advanced Materials.* vol. 22, pp. 3839-56, 2010.
- [23]. C. W. Tang, "Two-layer organic photovoltaic cell," *Applied Physics Letters.*, vol. 48, pp. 183-5, 1986.
- [24]. L.-M. Huang, C.-W. Hu, H.-C. Liu, C.-Y. Hsu, C.-H. Chen, K.-C. Ho, "Photovoltaic electrochromic device for solar cell module and self-powered smart glass applications," *Solar Energy Materials and Solar Cells.*, vol. 99, pp. 154-9, 2012.
- [25]. S. K. Deb, "A Novel Electrophotographic System," *Appl Opt.*, vol. 8, pp. 192-5, 1969.
- [26]. D. K. Benson, R. S. Crandall, S. K. Deb, J. L. Stone. "Stand-alone photovoltaic (PV) powered electrochromic window," Google Patents, 1995.
- [27]. Y. Zhao, G. A. Meek, B. G. Levine, R. R. Lunt, "Near-Infrared Harvesting Transparent Luminescent Solar Concentrators," *Advanced Optical Materials.* vol. 2, pp. 606-11, 2014.

Crystallization of Apatite

Nihal Derin Coskun¹, Veli Uz¹ Iskender Isik¹, Ali Issi¹, Ayse, Selcen Sahin¹, Pinar Cetinkaya²

Abstract

The crystallization of apatite has been an important research subject recently. In this research, calcium phosphate in the apatite structure occurring naturally was sintered at 1150°C. The crystallinity, crystal size and crystal growth of sintered apatite was investigated. Natural apatite has plate-shape crystals and spherical grains agglomerated with overlapping of plate-shape crystals. The sintered apatite crystals developed as rod-shaped crystals 20µm in length and which tend to grow along the c-axis. The aspect ratios of the crystals were determined as 7-10:1. The lattice parameters of the sintered apatite decreased, while the crystallinity increased 10%.

Keywords: *Apatite, Crystallization, Crystallinity, Sintering*

1. INTRODUCTION

Apatite, being chemical formula $\text{Ca}_5(\text{PO}_4)_3(\text{F}, \text{Cl}, \text{OH})$, is a phosphate mineral in a hexagonal structure. Apatite, occurring in nature geologically, is the most abundant as phosphate mineral on earth. OH-, F- and Cl- can be found at various percentages in apatite's canal zones [1]. Natural phosphate mineral occurs in the apatite structure such as fluorapatite, hydroxyapatite, and chlorapatite minerals. Recently, there have been significant studies conducted on apatite and potentially there will be a large area of utilization of apatite structures in the future [2,3]. Apatite has potential applications in biomedical materials, oxide cells of the solid fuel and luminescence materials [4,5]. Within the structure of apatite, one may find various elements with a wide range of ionic charges in crystallographic meaning. The ionic substitutions are particularly well determined in geologic apatites. In fact, apatite has a crystal structure that is able to substitute half of the elements on the periodic table within its atomic structure [1,6]. The mechanical properties of nanocrystals that are produced synthetically at 200°C are better than their traditionally solid-state sintered versions [7-9]. In the sintering of the apatite, conventional sintering techniques and hot press, spark plasma sintering (SPS) techniques are used [10-12]. The sintering of the apatite changes depends on the method of crystal production [13]. However, in the solid-state sintering are preferred temperatures between 1100-1250°C [14]. The apatite crystals tend to grow in structures of needle, rod-like and agglomerated layers [15,16]. In this study, the phosphate mineral occurring apatite form naturally was sintered at 1150°C and determined the lattice parameters, crystallinity, crystal sizes.

2. EXPERIMENTAL

The apatite mineral used in this study has been provided from the Mazıdağı in the Mardin Province. The chemical analyses were conducted by using Rigaku ZSX X-Ray fluorescence. The apatite samples were milled in ball mill by using alumina ball. Ground samples were shaped into 40x3 mm cylindrical pellets. The pellets were sintered at 1150°C. Sintering process was performed by using Nabertherm box kiln with 5°C/min. heating rate and one hour hold at peak temperature, then naturally cooling in air atmosphere. The phase analyses were carried out with a Rigaku Rint 2000 X-ray diffractometer. The phase analyses were performed at 30kV and 15mA (Cu-K α , $\lambda=1,541\text{\AA}$, $2\theta:5-70^\circ$, $2^\circ/\text{min}$. at a step size of 0.020). Phases were determined by MDI Jade 6.0 software. The crystallinity (Xc) of apatite crystals were calculated by using the XRD data according to the $X_c=1-(I_{112}/300/I_{300})$ equation. I300 is the intensity of (300) diffraction peak and I112/300 is the intensity of the hollow between (112) and (300) diffraction peaks of apatite [15-17]. The average crystallite size of the apatite was calculated by using the Scherrer's $X_s=(0.9 \lambda)/(FWHM \times \cos\theta)$ [15,17] formula. Xs is the average crystallite size (nm), λ is the wavelength (1.5406Å), FWHM is the full width at half maximum of the diffraction peak under consideration (rad), θ (degree) is the Bragg angle. In our study, the (002) and (310) diffraction peaks were used for calculation of the crystallite size. In microstructure analysis, powder and fractured surfaces of samples were analyzed by using Zeiss Supra 50VP (accelerating voltage=20kV) scanning electron microscope.

¹ Corresponding author: Dumlupınar University, Materials Science and Engineering, Kütahya/Turkey, nihal.dcoskun@dpu.edu.tr

² Inonu University, Faculty of Fine Arts and Design, Department of Ceramic, Malatya/Turkey, pinar.bicici@inonu.edu.tr

3.RESULTS

3.1.Chemical and mineralogical analysis

Natural phosphate consists of approximately 54% CaO, 28% P₂O₅ oxide (Table 1). Also, 5.4% of SiO₂ was identified.

Table 1.The chemical analysis of apatite

Oxides	SiO ₂	Al ₂ O ₃	CaO	Na ₂ O	P ₂ O ₅	LOI	Total
Weigth %	5.42	0.43	54.49	0.87	28.06	10.53	99.80

The X-ray diffraction patterns of apatite were given in Fig. 1. Since hydroxyapatite, carbonated apatite and fluorapatite peaks tend to overlap, it is difficult to distinguish them individually. According to mineralogical analyses, hydroxyapatite, carbonated apatite, fluorapatite, quartz and calcite minerals were identified. (112) the plane peak was unclear as a characteristic apatite peak on two-theta 32-33°. Therefore an interval of two-theta 31-35° was expanded in order to show the plane (112) in Figure 1. Between the two-theta values of 26-27°, the 100% peaks of quartz and calcite at 30° are significant. According to Scherrer equation, the calculation of crystallite size (002) and (310) is based on diffraction peaks. With reference to the peak that shows the a-axis plane reflecting plane (310), the crystallite size of the apatite was calculated as 11.69nm. The a-axis along of apatite's crystallite sizes was determined as ~12nm and the c-axis ~6nm. It was found that apatite crystals are a-axis along oriented plate-shaped formed crystals. The crystallinity of natural apatite was calculated as 77.70. The lattice parameters were found as 9.363Å on a-axis and 6.878Å on c-axis.

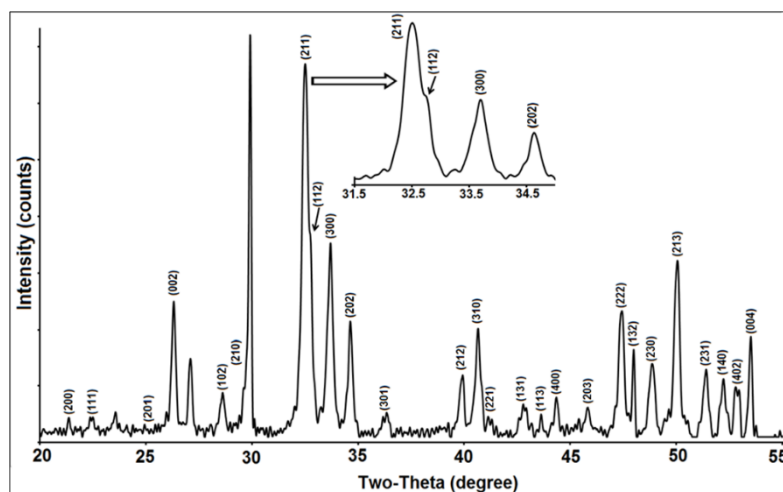


Figure. 1.X-ray diffraction patterns of apatite

The crystallites of bone apatites being rich in carbonate have the plate-shaped morphology [1,18]. In our natural apatite samples were observed very small sized plate-shaped crystals. The sizes of crystals are between 5-100nm (Fig. 2). Also, the nanometric crystals agglomerated into spherical agglomerates in the size of 50-100µm. The EDX analysis performed on apatite crystals revealed the presence of the elements of calcium, phosphorus and silicon. According to EDX analysis, apatite crystals contain %56.39 CaO, %33.87 P₂O₅ and % 9.74 SiO₂.

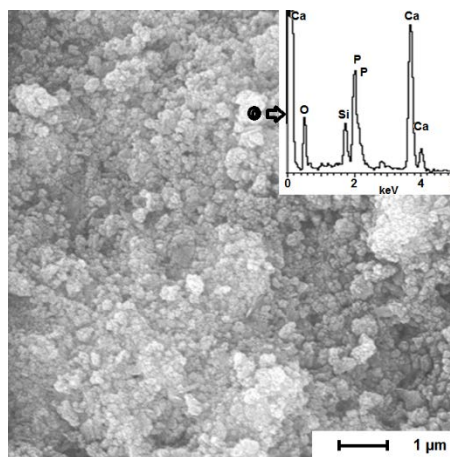


Figure 2. Microstructure of natural apatite

3.2. Phase analysis of sintered apatite

Pieters *et al.* (2010) indicated; (211) and (112) peaks in XRD peaks of the crystals produced by hydrolysis method showed expansion and single peak instead of two peaks with increasing Ca/P and CO₃ ratio. They determined that the crystallinity has decreased with increasing of CO₃ and expansion of peaks. Pieters *et al.* also stated that with an increasing ratio of CO₃ and Ca/P, the peak intensity has decreased [19]. The peaks of the apatite fired at 1150°C were more narrow and intense. The XRD peak in the natural apatite, which reflects the clearly nonvisible (112) plane was apparent at two-theta 32.7° in the XRD peak of fired apatite. The two-theta values were shown in Fig. 3 by broadening the values to 31-35° two-theta intervals. This peak overlaps the CaO (lime) peak and (112) plane apatite peak. The two-theta value that was observed at 30° for calcite peak and in 26-27° for quartz peak did not visible at 1150°C. The CaO (lime) peak, which occurs through the decomposition of calcite was determined at two-theta 32.40 and 54°. The narrowing and higher XRD peaks revealed that the size of crystallite and crystallinity increased. It was noticed that the c-axis oriented (002), (004) peaks, a-axis oriented (211), (300) and a-c-axis oriented (202), (203) peaks became prominently sharper on the sintered apatite. In regard to Miller indexes, if a-axis and c-axis oriented peak sharpens, the crystals would become larger along the a-axis and c-axis. However, the fact that c-axis oriented peaks were sharper than the a-axis peaks reveals that fired crystals tend to enlarge along the c-axis. The lattice perfection of apatite crystals and reduction in size ends up with the decrease of crystallinity and increase of the carbonate content. That is to say, as the carbonate content increases, the size and crystallinity reduce [19]. While the crystallinity of the natural apatite was 77.70, it was calculated as 88.00 on the sintered apatite with an approximate increase of 10%, which has shown that crystals become more ordered. The literature review confirmed that crystal formation and enlarging crystal size were caused by the decrease of the carbonate content on the apatite during sintering. By using the Scherrer equation (002) and according to (310) diffraction peaks, it can be determined that crystallite sizes get bigger. On the sintered apatite, the crystallite size (002) was 9.35nm, which is ~55% bigger than the unsintered apatite. According to the a-axis oriented peak that reflects the (310) plane, the size of the sintered apatite crystal became 16.94nm and that was ~41% bigger than the unsintered apatite. The calculation of crystallite sizes revealed that crystals were 15% bigger along the c-axis than the others along the a-axis. The lattice parameters of the sintered apatite reduced along the a-axis and c-axis. The calculated lattice parameters were specified as 9.305Å for a-axis and 6.839Å for c-axis. In regard to the lattice parameters of the unsintered apatite, the lattice parameters of the sintered apatite decreased 0.6%. Mohandes *et al.* (2014) calculated the cell parameters of apatite as 9.418-9.424Å along the a-axis and 6.884-6.879Å along the c-axis. They found out on the lattice structure they calculated that the unit cells of the specimens were longer along the c-axis. They stated that this finding reveals that nanorods show a crystal growth along the c-axis [20]. Eichert *et. al.* (2009) on the other hand measured the lattice parameters of hydroxyapatite they synthesized as 9.347-9.407Å for the a-axis and 6.862-6.881Å for the c-axis [10]. However the a-axis and c-axis oriented lattice parameters was smaller in our research.

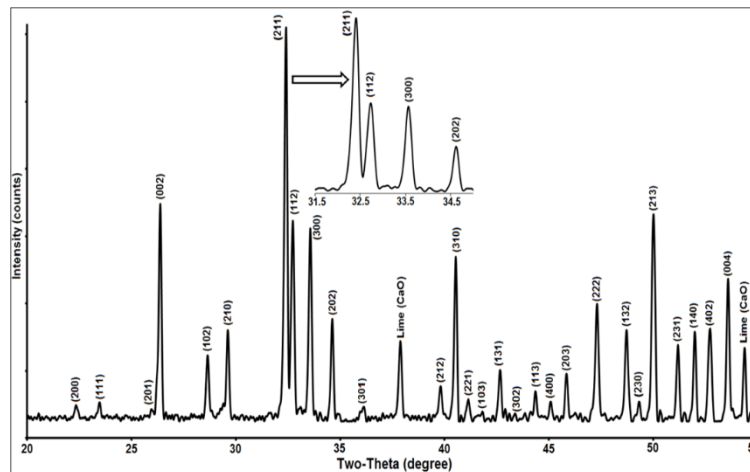


Figure 3. X-ray diffraction patterns of the sintered apatite

3.3. Microstructure of sintered apatite

The elongated rod-like crystals were identified in the microstructure of the sintered apatite. Furthermore, spherical lump crystals were observed. Very small apatite crystals gathering stacked and formed agglomerated lumps (Fig. 4A). And together with the long rod-like apatite crystals, hexagonal round-shaped crystals also developed. Some of the rod-like crystals were 0.2-0.5 μm in diameter and some 2-5 μm . Their length ranged between 3-20 μm . It has been stated that the c-axis width of the plate-shaped nanocrystal apatites was 200-400 \AA and the thickness 20-80 \AA . According to the Scherrer equation, the width of the (002) plane was calculated at 145-280 \AA and 50-70 \AA at (310) plane. It has been stated that the condensation started at approximately 850 $^{\circ}\text{C}$ and reached its maximum point at 1100 $^{\circ}\text{C}$ [21-23]. Hereunder, it has been seen that apatite crystals enlarge along both a-axis and c-axis, but develop along the c-axis more. According to the crystal size and enlarging style, phase analyses obtained from microscopic investigation, the results and the previous calculations correspond with each other. The aspect ratio of the enlarging rod-like crystals was determined as 7-10:1. The synthetically produced apatite crystals were agglomerated, rod-like, needle shaped and c-axis oriented [24-26]. The evolution of similar crystals, which occur after the sintering of natural apatite, at the same time, matches up with the information in the literature. In addition, crystals with sharp edges were detected on SEM photos (Fig. 4B) and EDX analyses revealed that their calcium content was relatively higher. The crystals, high in calcium content, were sharp edged and not exposed enough to grain-to-grain interaction. The EDX analysis performed on crystals revealed the existence of calcium and phosphate. It was determined that the rod-like crystals consist of ~55-57% CaO and ~43-44% P₂O₅. While the long rod-like crystals' P₂O₅ content was higher, the thick crystals' P₂O₅ was lower. According to this determination; while the Ca/P ratio in thin, long rod-like crystals was 1.25, it was 1.51 in thick crystals. Crystals with sharp edges contain 83% CaO and 17% P₂O₅. The high CaO consist of these crystal points the lime out which has been identified in XRD peaks. Nonetheless, the EDX analysis conducted on crystals collocated CaO and phosphate. The Ca/P ratio in these crystals was found ~5.

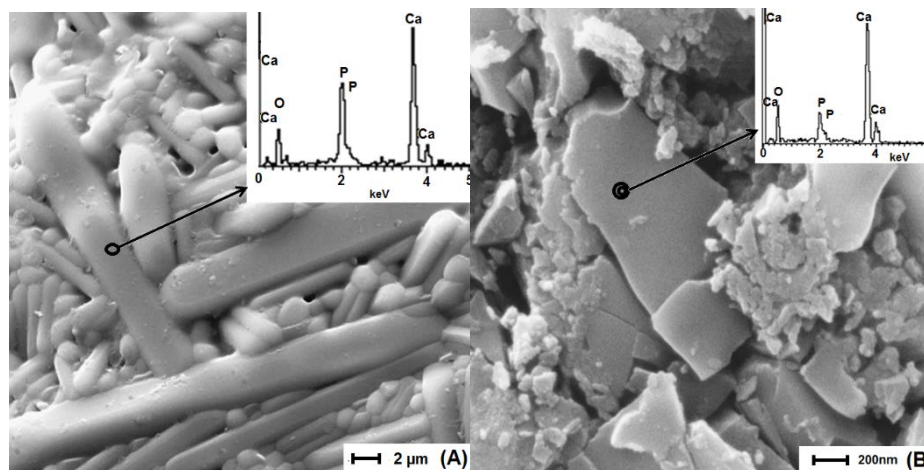


Figure 4. A and B. Apatite's microstructure sintered at 1150 $^{\circ}\text{C}$

4. CONCLUSIONS

- Natural phosphate is a cheap precursor source to be used for the production of rod-like apatite crystals and technological materials.
- Natural apatites are a-axis oriented plate-shaped crystals. After sintering, apatite crystals have grown along the a-axis and c-axis. Their growth along the c-axis compared with the growth along the a-axis and eventually rod-like crystals 20µm in size developed.
- After sintering, the lattice parameters of apatite reduced and it became 9.305Å along the a-axis and 6.839Å along the c-axis.
- Apatite's crystallinity percentage became 88.00 after sintering by increasing 10%.
- The crystal morphology exhibited a rod-shaped development after sintering. It has been determined that as in spherical grained crystals, after a long sintering process, they may grow and gain a rod-like shape.
- The calculation of Ca/P ratio was 1.25 in thin, long rod-like apatite crystals and 1.51 in thick crystals.
- In the case of longer sintering processes, the amount of rod-like crystals increased, thus a time-dependent crystal evolution research would be necessary.
- After sintering, the aspect ratio of apatite crystals was 7-10:1 and this determination validated that crystals grow along the c-axis.
- Calcite disintegrated and stood in the body by turning into CaO (lime). It should be considered that free CaO is a form of unhydrated lime and reacts with water. Thus, it tends to form OH⁻ ions and expand. The absence of quartz peak in the sintered apatite revealed the existence of both silica and phosphor in the crystal structure.
- In regard to removing the gangue minerals like quartz and calcite that accompany natural apatites by using the mineral processing methods, there would be a wide range of utilization areas for pure apatite crystals.

ACKNOWLEDGEMENT

We would like to thank to the administration of Dumlupınar University due to the support provided for this study under the Scientific research projects (BAP) with the project number of 2015-45.

REFERENCES

- [1]. B. Wopenka, J.D. Pasteris, *A mineralogical perspective on the apatite in bone*, Mat. Sci Eng 25, 131-43, 2005.
- [2]. J.R. Jones, *Review of bioactive glass: From Hench to hybrids*, Acta Biomater 9, 4457-86, 2013.
- [3]. M. Gruselle, *Apatites: A new family of catalysts in organic synthesis*, Organomet Chem 793, 93-101, 2015.
- [4]. H. Liu, L. Liao, et al., *Tunable luminescence properties and energy transfer of Ba₃NaLa (PO₄)₃F:Tb³⁺, Sm³⁺ phosphors with apatite structure*, Luminescence 169, 739-43, 2016.
- [5]. D.M. Lopez, et al, *Evaluation of apatite silicates as solid oxide fuel cell electrolytes*, Pow Sour. 195, 2496-06, 2010.
- [6]. W. Suchanek, et al, *Hydroxyapatite ceramics with selected sintering additives*, Biomater 18, 923-33, 1997.
- [7]. K. Tonsuaadu, et al, *A review on the thermal stability of calcium apatites*, Ther Anal Cal 110, 647-59, 2012.
- [8]. A.D. Bernache, et al, *Sintering of calcium phosphate hydroxyapatite Ca₁₀(PO₄)₆(OH)₂ I. Calcination and particle growth*, Eur Ceram Soc 23, 229-41, 2003.
- [9]. A.S. Kupiec, Z. Wzorek, *The influence of calcination parameters on free calcium oxide content in natural hydroxyapatite*, Ceram Int 38, 641-47, 2012.
- [10]. D. Eichert, et al, *Nanocrystalline Apatite-Based Biomaterials*, ISBN: 978-1-60741-212-0, Nova Sci Publ Inc, New York, 2009.
- [11]. K.A. Gross, L.L.M. Rodriguez *Sintered hydroxyfluorapatites. Part I: Sintering ability of precipitated solid solution powders*, Biomater 25, 1375-84, 2004.
- [12]. E. Landi, et al, *Influence of synthesis and sintering parameters on the characteristics of carbonate apatite*, Biomater 25, 1763-70, 2004.
- [13]. S. Ramesh, et al, *Sintering behavior of hydroxyapatite prepared from different routes*, Mat Des 34, 148-54, 2012.
- [14]. E. Champion, *Sintering of calcium phosphate bioceramics*, Acta Biomater 9, 5855-75, 2013.
- [15]. M.C. Wang, et al, *Characterization of calcium phosphate apatite with variable Ca/P ratios sintered at low temperature*, Ceram Int. 41, 1223-33, 2015.
- [16]. M.C. Wang, et al, *Crystalline size, microstructure and biocompatibility of hydroxyapatite nanopowders by hydrolysis of calcium hydrogen phosphate dehydrate (DCPD)*, Ceram Int 41, 2999-3008, 2015.
- [17]. S.C. Wu, et al, *Effects of heat treatment on the synthesis of hydroxyapatite from eggshell powders*, Ceram. Int 41 (2015) 10718-24.

- [18]. Y.X. Pang, X. Bao, *Influence of temperature, ripening time and calcination on the morphology and crystallinity of hydroxyapatite nanoparticles*, J Eur Ceram Soc 23, 1697-1704, 2003.
- [19]. I.Y. Pieters, et al, *Carbonated apatites obtained by the hydrolysis of monetite: Influence of carbonate content on adhesion and proliferation of MC3T3-E1 osteoblastic cells*, Acta Biomat 6, 1561-68, 2010.
- [20]. F. Mohandes, M.S. Niasari, M. Fathi, Z. Fereshteh, *Hydroxyapatite nanocrystals: Simple preparation, characterization and formation mechanism*, Mat Sci Eng C 45, 29-36, 2014.
- [21]. S. Raynaud, E. Champion, D.B. Assollant, J.P. Laval, *Determination of Calcium/Phosphorus Atomic Ratio of Calcium Phosphate Apatites Using X-ray Diffractometry*, J Am Ceram Soc 84/22, 359-66, 2001.
- [22]. A.D. Bernache, et al, *Sintering of calcium phosphate hydroxyapatite $Ca_{10}(PO_4)_6(OH)_2$ I. Calcination and particle growth*, J Eur Ceram Soc 23, 229-41, 2003.
- [23]. S. Raynaud, E. Champion, A. Bernache, *Calcium phosphate apatites with variable Ca/P atomic ratio II. Calcination and sintering*, Biomat 23, 1073-80, 2002.
- [24]. S. Raynaud, E. Champion, A.D. Bernache, P. Thomas, *Calcium phosphate apatites with variable Ca/P atomic ratio I. Synthesis, characterisation and thermal stability of powders*, Biomat 23, 1065-72, 2002.
- [25]. M.J. Lukic, et al, *Particularities in sintering behavior of Ca-deficient hydroxyapatite nanopowders*, Mat Let 68, 331-5, 2012.
- [26]. S. Pramanik, et al, *A Development of high strength hydroxyapatite by solid-state-sintering process*, Ceram Int 33, 419-26, 2007.

Factorial Design of Experiment Application and Statistical Analyse of Lignite Flotation

Oktay Sahbaz¹, Cengiz Karaguzel²

Abstract

Statistical design of experiments has been used in the mineral processing for providing the real optimum results by numerous authors. One of the methods is full factorial design of experiments. In this study, the main and interaction effects of parameters (collector amount, frother concentration and impeller speed) on lignite flotation were systematically investigated. The effects of collector amount (kerosene), frother concentration (AF65) and impeller speed on combustible recovery and ash rejection of lignite were investigated by the use of three-variable and two-level (2³) with 4 base point factorial design of experiment. The coal samples were subjected to the experiments with kerosene in a range of 600 to 1200 gr/t, AF65 in the range of 30 to 56 ppm and impeller speed in the range of 900 to 1400 rpm. It was obtained from the present study that collector and frother amounts were statistically significant parameters on combustible recovery, while the impeller speed with collector-frother interaction were significant on ash removal

Keywords: Flotation, Factorial design of experiment, lignite

1. INTRODUCTION

Coal is still one of the most important energy sources for Turkey [1]. The most of the coal is the lignitic type which has low calorific values. It has been used in power plants to generate the electricity, while small amount of it has been used in domestic use. Therefore, these lignitic type of coal is mostly put into a physical separation processes in washery by the use of many different kind of devices to provide coal having high calorific value. But the size of the coal particles limits the efficiency of physical processes. The performance of physical separation processes starts to decrease with the fine feeding is less than 0.5 mm. One of the most suitable processes is flotation for the fine coal size [2].

Flotation is a physico-chemical process which is used for beneficiation of not only coal but also metallic and industrial minerals. The method is used for water cleaning, removal of contaminant from various system as well. Besides, flotation is used for separation of fine coal particle mostly from the clay minerals in the entire world.

The performance of the method changes according to chemical parameters (collector, frother, depressant etc.), particle characteristics (liberation size, mineralogical features etc.) and qualification of devices (turbulence, air producing type etc.) used. Researchers have taken into consideration all these parameters to reach the optimum values which depend on the grade of floating product and the [3, 4, 5 and 6]. Because all parameters should be fixed in exact level to reach optimum results. Researchers generally use the classical design of experiments to obtain the most suitable results. In this type all parameters hold in exact level while the level of target parameter is changing. Classical methods for designing of experiments provide reasonable results to get main effect of parameters. But it is very hard to observe the interaction effect of parameters. In addition to this, some authors think that it is not possible to gain real main effects without using the statistical design and analyse [7].

Recently researchers have used the statistical techniques such as Taguchi design, full factorial design, Pluckt Burman design for obtaining the optimum results from the flotation experiments [8]. They have pointed out obtaining the optimum result by using the statistical methods.

Statistical experimental design is very useful tool to carry out any kind of experiments including mineral processing application for finding out the most suitable results with a less number of experiments. The factorial designed experiment has significant advantages over the classical one variable at a time technique due to the systematic and well organized behaviour. It is not only eliminate confounding of effects, but also helps for both determining the important variables to be controlled and measuring interactions. Statistical experimental design also brings the results of not only main effects of parameters also the interaction effects of them. Thus the effect of all parameters and interaction on coal flotation can be satisfactorily obtained by the use statistical design of experiment.

The main aim of the present study is to apply statistical design of experiments so called as full factorial design to obtain main and interaction effect of chosen parameters on lignite flotation. The parameters are tested is collector amount, frother amount and impeller speed.

¹ Corresponding author: Yildiz Technical University, Department of Environmental Engineering, 34220, Esenler/İstanbul, Turkey.
ocinar@yildiz.edu.tr

²Zenith Group, Sarajevo, Bosnia and Herzegovina, mkose@zenithgroup.ba

2. MATERIAL AND METHODS

2.1. Material

The lignite sample used in the experiment was obtained from Tuncbilek-Kutahya in the western part of Turkey. The sample size was reduced to under 500 μm by the use jaw crusher and roll crusher, respectively. Then particles were blended for homogenisation and stored in a hermetically sealed nylon bags with a capacity of 500 grams. The all representative samples had %14 of ash content. For the flotation tests; kerosene, sodium silicate and Aerofroth 65 (Cytec AF65) were used as a collector, depressant and frother, respectively. pH was naturally 7.5.

2.2. Method

Flotation test

Flotation experiments were conducted with mechanical flotation cell (MFC). MFC is commonly used flotation device in mineral processing. For instance in Turkey all flotation plants have this device for beneficiation of ore and coal. MFC includes two main parts which are an impeller and a cell. Impeller provides better contact of bubble and particle. In addition, air is vacuumed into the MFC by impeller turning in a high speed (1200 rpm). Vacuumed air is formed into bubbles by impeller and convenient hydrodynamic condition occurs. The second part of the MFC is the cell which provides suitable environment for bubble-particle attachment and separation of hydrophobic particle laden bubbles from the hydrophilic particles. Thus, hydrophobic particles are skimmed off at the top of the cell while hydrophilic particles are removed from the bottom of the cell.

In this study the MFC having the capacity of 2 l cell was used. The samples of 162 g were mixed with the 2 l of local tab water. The temperature during the experiments changed between 20 and 23 $^{\circ}\text{C}$. Since the flotation feed was produced using dry grinding in a shutter box, each sample was conditioned in water for 5 min following grinding to ensure complete wetting at required pH before any reagent addition was made. Then depressant (sodium silicate), collector (kerosene) and frother addition were done respectively. The conditioning for the depressant and kerosene were 5 and 10 min, respectively. And last a minute frother added to the pulp and flotation was started with opening the air vane. AF65 (Cytec Aerofroth 65) was used as the frother in subsequent tests. This is a polypropylene glycol based frother used in its commercial quality form "as received". Statistical design of experiment were used for carrying out the experiments.

Full factorial design of experiments

In this study, flotation tests were performed by using the full factorial center point repeated by experimental design. Three important parameters, which were collector, frother and impeller speed rate, were chosen as independent variables or design factors and two levels of these variables with their base points were used to generate namely 2^3 factorial design. The variables and their levels are given in the table. The higher level was designated as "+" while the lower one and mid-point were designated as "-" and "0", respectively. To convert from actual values (X_{actual}) to coded units (X_{coded}) the following equation can be used [9]:

$$X_{Coded} = [x_{Actual} - x_{Mean}] / [(x_{High} - x_{Low}) / 2] \quad (1)$$

where X_{high} is the highest value of any factor, X_{low} is the lowest value of the any factor and X_{mean} is the arithmetic value of X_{high} and X_{low} .

Recovery and ash content were chosen as responses. The main effect of any factor is the change in response produced by varying the level of the factors. It can be calculated by the below equation.

$$\text{Main effect of factor X} = (\text{Average response at } X_{high}) - (\text{Average response at } X_{low}) \quad (2)$$

In addition to above it is very important to find out the interaction effects that occurs when the difference in response between levels of any factor is not same as all levels of the other factor. This effect can only be found by the use of statistical design and by the Eq.3.

$$\text{Interaction effects of } X_1 \text{ and } X_2 = (\text{Average response at } X_1 X_2 \text{ high}) - (\text{Average response at } X_1 X_2 \text{ low}) \quad (3)$$

A full factorial design namely 2^3 with four mid points can geometrically be shown by a cube. In this case, responses can be placed the corners and X, Y and Z axes represent factor X_1 , X_2 and X_3 , respectively. The origin is the center of the cube and every side of cube is equivalent to two units, + and -. Design expert statistical programme (www.designexpert.com) was used to determine main and interaction effects with the confidence interval of 95%.

In this study, factorial design of experiments was used to determine main and interaction effects of three factors (n) which were kerosene, AF65 and impeller speed rate. Eight experiments were carried out for this determination by the use of Equation 4.

$$NoE = 2^n$$

(4)

Where NoE is the number of the experiments and n is the number of variables. To supply statistical significance and to estimate the variance (σ^2) and error additional four experiments were performed at the base level. The variance of the main and interaction effects are given by

$$Variance (Effects) = 4 \sigma^2 / 2^n$$

(5)

$$\text{Calculated main or interaction effects} / \sqrt{Variance (Effects)} \geq t_{3,0.025}$$

(6)

The 2^3 factorial design including the factors, levels and values are seen in Table 1. The regression equation with the main and interactive terms can be written with below formula.

$$Y = \beta_0 + \beta_1 X_1 + \beta_2 X_2 + \beta_3 X_3 + \beta_{12} X_1 X_2 + \beta_{13} X_1 X_3 + \beta_{23} X_2 X_3 + \beta_{123} X_1 X_2 X_3 \dots$$

(7)

where Y is response (recovery or ash content of lignite), β is the coefficients for main and interaction terms, X_1 is the collector, X_2 is the AF65 and X_3 is the impeller speed.

Table 1. 2^3 factorial design and parameters with their level

Flotation Factors	Low level (-)	Mid Level (0)	High Level (+)
X_1 , Collector, gr/t	600	900	1200
X_2 , Frother, ppm	30	43	56
X_3 , Impeller speed	900	1150	1400

3. RESULTS AND DISCUSSION

Flotation experiments done by using statistical experiment design on Tunçbilek lignite sample and results are shown as Table 2.

Table 2. Experiment Results

Experiment	X_1	X_2	X_3	Recovery	Ash
1	-1	-1	-1	28.96	11.48
2	+1	-1	-1	36.30	9.65
3	-1	+1	-1	36.87	10.40
4	+1	+1	-1	58.82	11.35
5	-1	-1	+1	28.48	12.05
6	+1	-1	+1	46.85	10.44
7	-1	+1	+1	52.37	11.74
8	+1	+1	+1	60.49	11.51
9	0	0	0	41.65	11.39
10	0	0	0	44.07	11.35
11	0	0	0	46.36	11.52
12	0	0	0	42.86	11.11

According to Table 2; the highest recovery value was obtained from experiment 8 done with high levels of chosen parameters. In addition the lowest ash content obtained from second experiment. F-test which is applied to figure out main and interaction effects of parameters is given in Table 3.

Table 3. Variance Analysis Results

	Ash		Combustible Recovery	
	F-value	p-value	F-value	p-value
X_1	31.57	0.0111	96.30	0.0022
X_2	8.13	0.0651	142.95	0.0013
X_3	34.91	0.0097	22.97	0.0173
X_{12}	73.85	0.0033	0.588	0.4989
X_{13}	3.93	0.1416	0.24	0.6561
X_{23}	0.08	0.7913	1.56	0.3002
X_{123}	8.36	0.0629	19.13	0.0221

F and p values are both for recovery and ash in Table 3. The higher F value is for parameters, the more effective it should be on recovery and ash which are dependent variables. That p value is smaller than 0.05 indicates that parameter is significant, in other words, it has a strong effect on the dependent variable statistically [10].

Accordingly, three parameters have a strong effect on the combustible recovery in the flotation study done via Tunçbilek sample. Also, triple effects of parameters are statistically significant on combustible recovery. While the biggest effect of parameter on the recovery is X_2 , namely the amount of frother, the amount of collector (X_1) has the second significant effect. And propeller speed (X_3) has the third one.

Regression analysis for combustible recovery is shown as Equation 7.

$$Y = 43.643 + 6.974X_1 + 8.495X_2 + 3.406X_3 - 3.106X_1X_2X_3 \quad (7)$$

According to Equation 7, while main effects of all parameters on combustible recovery, triple effect of them is negative. Hydrophobicity and recovery value of coal particles increase just as the amount of collector does. Enhancing the dosage of frother makes the combustible recovery increase as it provides stable and dense froth formation. Increasing the propeller speed makes the air quantity (hold-up) drawn in flotation cell enhance, and so it has stimulated the probability of encountering coal particles and bubbles resulting in increasing the amount of floating coal (recovery).

To the flotation studies carried out by Tunçbilek coal sample, it has been found that the most effective parameter on the amount of ash in the floating material is the mutual interaction between collector and frother (Table 3). The effects of collector amount and impeller speed are quite significant in the ash amount of floating material, but the main effect of the frother does not have a statistically significant value in 95% confidence interval.

That the main effect of frother amount is not high between the confidence interval detected statistically may be related to the amount of frother. In this study chosen frother levels are close to each other in terms of dosage, and that increasing of gas oil may have reduced the effect of frother. Even if the amount of frother went up, it would be less effective.

Regression analysis done for the amount of ash in the floating product is shown as Equation 8.

$$Y = 11.08 - 0.34X_1 + 0.36X_3 + 0.52X_1X_2 \quad (8)$$

That decreasing of ash amount in the floating material resulting from increasing collector amount may be defined as much more carboniferous materials' floating. The enhancement of propeller speed has brought about some killers are taken from the froth area by the increase of turbulence, and this has made the amount of ash in the floating material go up. The dense froth may cause more water to be transferred to froth zone and so, very little clay particles pass through the froth zone in the interaction between collector and frother. It may be defined that double effect leads to the increase of ash amount. Still, the proximity of ash values to one another prevents to evaluate exactly.

4. CONCLUSION AND SUGGESTIONS

In this study parameters which are effective in the flotation of coal samples brought from Kütahya Tunçbilek Region were tried to be determined via factorial experiment design method. Double and triple effects parameters to be determined by using statistical experiment design with classical method were also detected in addition to the main effects of combustible recovery and ash removal. In this study focused on combustible recovery, the sample, whose value of ash is quite low, but high-quality, has been tried to be used. Still, results related to the ash removal have been tried to be evaluated.

According to the results gained from this study;

- The most effective parameter on combustible recovery is the amount of frother. It followed by the amount of collector and propeller speed, respectively.
- Triple effects of parameters on combustible recovery are statistically significant.
- It has been found that the most effective parameter on ash removal is propeller speed. It has been also detected that the amount of collector has an important effect on ash removal. However, double effect, collector-frother, has the most effective one statistically..

It is seen that studying with high propeller speed has a great contribution on recovery flotation. It may be recommended that the type of frother should be suitable for flotation studies to be planned via particularly kerosene. Results should be optimised statistically as well in order to evaluate them as optimum ones. Steepest ascent method is suggested to be used for this.

ACKNOWLEDGMENT

The authors thank Prof. Dr. Sermet ANAGÜN for his great support about statistical analysis.

REFERENCES

- [1]. G. Ateşok and O. Kural, *Cevher Hazırlama El Kitabı -Kömür Teknolojisi*, 1st. ed., G. Önal, G. Ateşok and K.T.Perek, Ed. İstanbul, Turkey: yurt Madenciligi Geliştirme Vakfı, 2014.
- [2]. G. Özbayoğlu and M.Kemal, *Cevher Hazırlama El Kitabı -Kömür Zenginleştirme yöntemleri*, 1st. ed., G. Önal, G. Ateşok and K.T.Perek, Ed. İstanbul, Turkey: yurt Madenciligi Geliştirme Vakfı, 2014.
- [3]. Z. Aktas and E.T. Woodburn, *The effect of non-ionic reagent adsorption on the froth structure and flotation performance of two low rank British coals*, Powder Technology, Volume 83, Issue 2, May 1995, Pages 149-158.
- [4]. R.Jia, G.H. Harris and D.W. Fuerstenau, *The effect of non-ionic reagent adsorption on the froth structure and flotation performance of two low rank British coals*, Powder Technology, Volume 83, Issue 2, May 1995, Pages 149-158.
- [5]. Y. Cebeci, *The investigation of the floatability improvement of Yozgat Ayrıdam lignite using various collectors*, Fuel, Volume 81, Issue 3, February 2002, Pages 281-289
- [6]. Şahbaz, O., Öteyaka, B., Kelebek, Ş., Uçar, A., Demir, U.: Separation of unburned carbonaceous matter in bottom ash using Jameson cell. Sep. Purif. Technol. 62, 103-109, 2008.
- [7]. S. Anagun, Bileteral discussion with Prof. Dr. Sermet ANAGÜN about statistical analysis, Osmangazi University Industrial Engineering Department, 2009
- [8]. S., Kelebek, U., Demir, O., Şahbaz, A., Uçar, M., Cinar, C., Karaguzel, B.: Öteyaka, *The effects of dodecylamine, kerosene and pH on batch flotation of Turkey's Tuncbilek coal*. Int. J. Miner. Process. 88, 65-71, 2008.
- [9]. Design expert, www. stateease.com
- [10]. D.C., Montgomery and Runger G. C.: Applied Statistics and Probability for Engineers, fifth edition, USA, 2003.

Investigation of Modal Properties of a Plate Reinforced by Polyurethane Foam with Different Thicknesses

OrhanÇakar¹, Murat Sen²

Abstract

In this study, the effects of the thickness of polyurethane foam (PU), which is widely used in vibration isolation on plate vibrations, are investigated by using experimental modal analysis (EMA) and finite element (FE) methods. A number of test samples are prepared by applying the PU foam with different thicknesses onto one surface of a steel plate. The test samples, each with different PU foam coating thicknesses, are tested using the EMA technique. The samples are suspended by cords in order to satisfy certain free boundary conditions. The modal properties are determined by using measured frequency response functions. Additionally, the plates are modelled by ANSYS finite element software and vibration analysis is performed. The results have been comparatively presented. It is observed that PU foam affects the natural frequencies and modal damping of the plate.

***Keywords:** natural frequency, modal damping, modal test, polyurethane foam, vibration isolation*

1. INTRODUCTION

Excessive vibrations affect the dynamic of systems adversely. In this respect, it is extremely important to know how the dynamic forces on machine elements affect the machine performances and reliability. For this reason the natural frequencies, mode shapes and damping properties of systems have to be determined by performing dynamic analysis and the necessary preventions should be taken according to these results. Plate structures are widely used in many areas of engineering and it is very important to know their dynamic behaviors and to reduce the existing vibrations. One way to reduce the vibrations of a plate is to cover its one surface with some materials which have high damping capability such as PU foam, [1]. PU foam is extremely light in weight, its production cost is low, it can be applied to systems easily and it has high damping capacity. Due to its properties PU foam is commonly used in engineering applications and many studies have been made on the determination of dynamic properties of PU materials.

Zhang and Dupuis [2] performed an experimental work to investigate the dynamic characteristic of flexible PU foam used for automotive seats. For this aim, they mounted a rigid block on a 3 inch cube of foam material, which served as the only flexible component as a single degree of freedom system. They excited the experimental fixture by a small impulse at the top of the block and simplified the foam as a linear viscoelastic material. They analyzed the modal response and impact of modal parameters. Also, they identified the corresponding system parameters during the experimental data.

Viscoelasticity is an important feature of PU foam. Viscoelastic materials are characterized by a certain degree of rigidity of elastic solid materials. Also, they have damping capability like viscous fluids. In this regard, Deng et al. [3] made an experimental study to determine the viscoelastic properties of flexible PU foam material.

Numerous analytical models have been proposed to describe some properties of viscoelastic foams mathematically by utilizing many experimental studies made on viscoelastic materials. These modelling studies can be traced back to development of micro level constructive relations from the simple curve fitting method. The stress-strain relations are used in modelling processes and various modelling methods have been proposed. These methods use the combinations of spring and damper components [4]. Wiechert [5], Maxwell [6] and Kelvin [7] are modelling methods that are well known. Some of modelling methods have been obtained by utilizing the continuous mechanical system principles [8, 9]. Scarpa et al. [10] studied mechanical performance of auxetic PU foam for anti-vibration glove applications. In their study they used specimens produced from conventional gray open-cells PU foam with 30-35 pores/inch and 0.0027g/cm³ density. As a result they stated that auxetic PU foams can reduce vibration and compressive stresses significantly compared to conventional PU foams.

In this study, the effects of PU foam on the dynamic characteristics of plates are investigated. For this purpose, PU foam is applied to one surface of a square plate in various thicknesses and experimental modal analysis (EMA) is performed. Also, the plates reinforced with PU foam are modelled via ANSYS finite element (FE) software and vibration analysis is

¹ Corresponding author: Dept. of Mechanical Eng., Firat University, 23200, Elazığ, Turkey. cakaro@firat.edu.tr

² Dept. of Mechanical Eng., Firat University, 23200, Elazığ, Turkey. msen@firat.edu.tr

performed. The results obtained from FE solution are compared with the experimental results. In the following sections, the methods used in the study, the experimental equipment, experimental studies and results are given.

2. MATERIALS AND METHODS

In order to determine the dynamic behavior of the structures FE and EMA methods are effectively used. However, FEM, which is a numerical method, has some drawbacks. For example, it assumes material properties, the modeling of mechanical connections and supports are very hard and the accuracy of the solution is heavily dependent on the number and the type of elements used. After all, the results obtained from EMA are more accurate as long as the experimental setup is reliable. In the modal test, the structure under investigation is excited by a modal hammer or a shaker and the applied force and the responses of the structure are measured using force transducer and accelerometer(s), simultaneously. The frequency response functions (FRFs) are calculated by using a frequency analyzer. A typical modal test setup using modal hammer is seen in Figure 1. Usually the test piece is suspended by elastic cords to satisfy the free boundary conditions, which is reasonably easier and more trustworthy for comparing other boundary conditions.

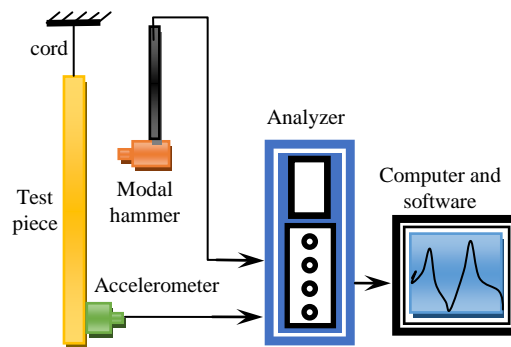


Figure 1. A Typical Modal Test Setup

The FRF specifies the dynamic characteristic of the system and expresses the relationship between input and output of the linear system. Although measured FRFs are mostly used to determine modal properties of the system, namely natural frequencies, mode shapes and modal damping they are also used for a wide range of application areas such as the verification of FE results, FE model updating, structural modification, coupling, un-coupling and so on, [11].

As given in equation (1) FRFs can also be calculated by using the dynamic characteristics of the structures determined from numerical methods [11]:

$$\alpha_{pq} = \sum_{r=1}^N \frac{\phi_{pr} \phi_{qr}}{\omega_r^2 - \omega^2 + i\eta_r \omega_r^2} \quad (1)$$

where α_{pq} is the FRF or receptance between coordinates p and q ; p and q are response and excitation co-ordinates, respectively; N is the number of modes; ϕ_{pr} and ϕ_{qr} are the elements of eigen-vectors related to the response and the excitation co-ordinates for mode r , respectively; ω_r is the natural frequency of the mode r ; ω is the frequency of excitation force.

In this study both EMA and ANSYS FE software are used to determine the dynamic properties of the plate reinforced by PU foam with different thicknesses. An AISI 1040 rectangular steel plate with 200x200x1 (mm³) dimensions is used for the study. The mechanical and physical properties of the test piece are given in Table 1.

Table 1. Mechanical and Physical Properties of AISI 1040 Material

Modulus of Elasticity (E)	Shear Modulus (G)	Poisson Ratio (ν)	Density (ρ)
200 GPa	80 GPa	0.3	7850 kg/m ³

There is no doubt that the reliability of the experimental results is highly dependent on the accuracy of test setup. Therefore, some calibration checks are made before measurements. Furthermore, the natural frequencies of the unreinforced test plate are calculated by using frequency formulae given by Leissa [12] to verify experimental and FE

results. Leissa [12] gave the analytical expressions of natural frequencies for different sized rectangular plates and various boundary conditions. The natural frequencies of the square plates can be calculated depending on the mechanical, geometrical and physical properties as:

$$\omega_i = \frac{\lambda_i}{a^2} \sqrt{\frac{D}{\rho}} \quad ; \quad i = 1, 2, \dots, n \quad (2)$$

where ρ and a represents the density of unit area [kg/m^2] and the width of the square plate [m], respectively. λ_i is the non-dimensional frequency parameter and the first five values of λ are 13.4728, 19.5961, 24.2702, 35.1565 and 63.6870, respectively. D is the flexural stiffness [N-m] and is given as:

$$D = \frac{Eh^3}{12(1-\nu^2)} \quad (3)$$

where E and ν are the modulus of elasticity [N/m^2] and Poisson ratio, respectively and h is the thickness of the plate [m].

After verification of the experimental results by the analytical and FE results, the modal parameters of the plate reinforced with different thickness of PU foam are determined by using experimental modal analysis.

3. EXPERIMENTAL STUDIES

Experimental studies in this research were carried out at Firat University, Machine Theory and Dynamics Laboratory. The test piece is partitioned with 50 mm intervals and 25 measurement points on the plate were determined. Then the plate was hinged to a stand from its two corners by using fiber strings to ensure free boundary conditions as seen in Figure 3.

Figure 3. Suspended Test Piece and Measurement Points

In the testing process, to excite the structure, a modal hammer (KISTLER, Model: 9724A2000 S/N 2069942) and to measure the response of the plate an ICP accelerometer (DYTRAN, Model: 3097A2 S/N2373) were used. For data acquisition and signal processing an OROS OR36 vibration analyzer and for the identification of modal parameters OROS Modal software were used. The test system are seen in Figure 4.

First, the accelerometer was located at the first node of the test piece (by using wax) because this node is very suitable for determining the dynamic properties of the plate over a wide frequency bandwidth for free boundary conditions.

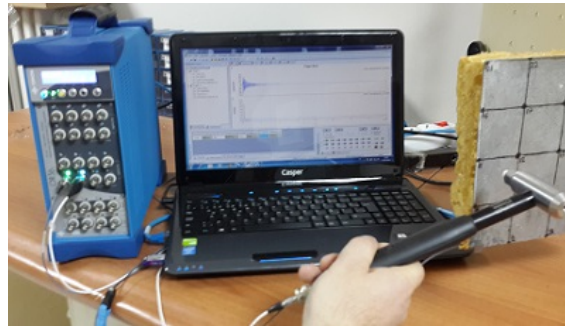


Figure 4. The Test Instruments and A Testing Process

Table 2. Measurement Parameters for Experimental Study

Parameter	
Frequency Bandwidth	0-2000 Hz
Frequency Resolution	1.25 Hz
Sampling Number	1600
Measurement Time	0.8 s
Windowing (response/impulse)	(uniform/uniform)

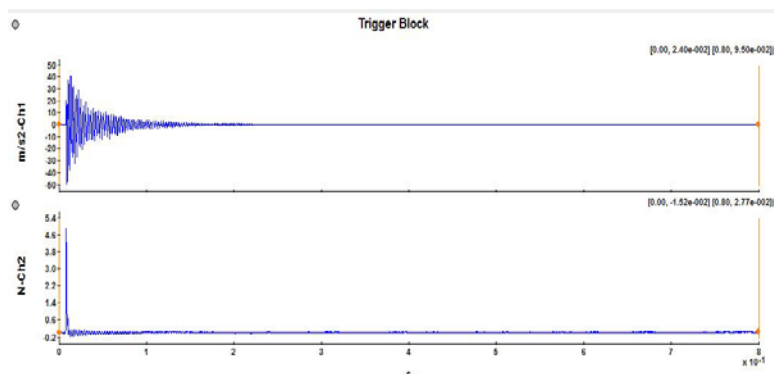


Figure 5. Time Signals of Force and Response.

Before the measurement some calibration tests such as repeatability and reciprocity checks were performed. The windowing function is an important parameter for Fourier transformation. In FRF measurements, a suitable windowing function is applied to response and force signals to satisfy periodicity so to avoid leakage problem. For example, in an impact test an exponential window function can be applied to the response signal when the signal is not dead in the measurement period after impact. But it should be pointed out that this windowing process brings additional damping to the measurements. This has extreme importance when the investigations, like this study, are made on the determination of the damping values of the system. In this study, the measurement parameters were selected so as to eliminate this adverse effect. In Figure 5, the time signals of the force and response for a measurement are given. As seen in the figure, the response is dead in the measurement period, therefore the windowing is not necessary. Note that a 10% negative delay was applied to the beginning of the measurement to satisfy periodicity and to not miss the beginning of the signals.

The test plate was sequentially hit at nodes 1 to 25 with the modal hammer and 25 FRFs were measured. Measurement parameters used for the test are given in Table 2. All of the 25 measured FRFs of the steel plate without PU foam, shortly unreinforced plate, are analyzed together by using Oros Modal software and the first five natural frequencies are given in Table 3. Also the results calculated by using the analytical method suggested by Leissa [12] and ANSYS FE software are given and compared in the same table. According to this comparison the experimental results are reliable.

Table 3. Natural Frequencies Obtained From Experimental, Analytical and Numerical Methods (Hz)

Mode	Experimental (Hz)	Leissa [12] (Hz)	Difference (%)	ANSYS (Hz)	Difference (%)
1	82.00	81.88	0.12	81.69	0.35
2	122.70	119.09	2.91	119.08	2.92
3	150.34	147.50	1.86	147.48	1.88
4	205.72	213.66	3.69	211.09	2.52
5	351.07	387.07	9.27	371.20	4.27

After confirming the experimental, numerical and analytical results, PU foam with thicknesses of 10, 20, 30, 40 and 50 mm were adhesively applied to one surface of the same plate respectively and EMA was performed for each reinforced thickness in order to determine the thickness effect of PU foam on the vibration characteristics of the plate. A PU reinforced plate structure under testing is seen in Figure 6.

The first natural frequency and damping values of unreinforced and PU reinforced plates obtained from EMA are given in Table 4. The natural frequencies obtained from ANSYS and the percentage of difference between results obtained from both methods are also given in the table. It can be said that the EMA and FE results are very close.

The change of the first natural frequency according to PU reinforcement thickness are plotted in Figure 7. From Figure 7, it can be said that the natural frequency increases almost linearly as the PU reinforcement thickness increases. The approximate linear equation between the first natural frequency f and the thickness of PU reinforcement t is estimated as,

$$f = 2.7359t + 57.823 \quad (4)$$

Note that the natural frequency of un-reinforced plate is excluded in the approximation equation.

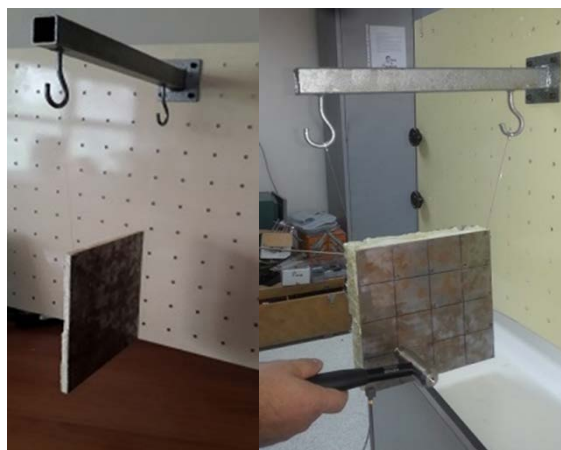


Figure 6. Plates Reinforced with PU Foam

Table 4. The First Natural Frequencies (Hz) and Damping Ratios for Different PU Reinforce Thicknesses

PU Foam Thickness (mm)	Experimental		ANSYS	Difference (%)
	ω_1 (Hz)	Damping (%)	ω_1 (Hz)	
0	82.00	0.37	81.69	0.03
10	86.66	0.26	83.25	3.93
20	110.22	0.97	97.24	11.77
30	140.42	1.43	124.08	11.63

40	167.27	3.10	156.65	6.34
50	194.93	5.58	189.99	2.53

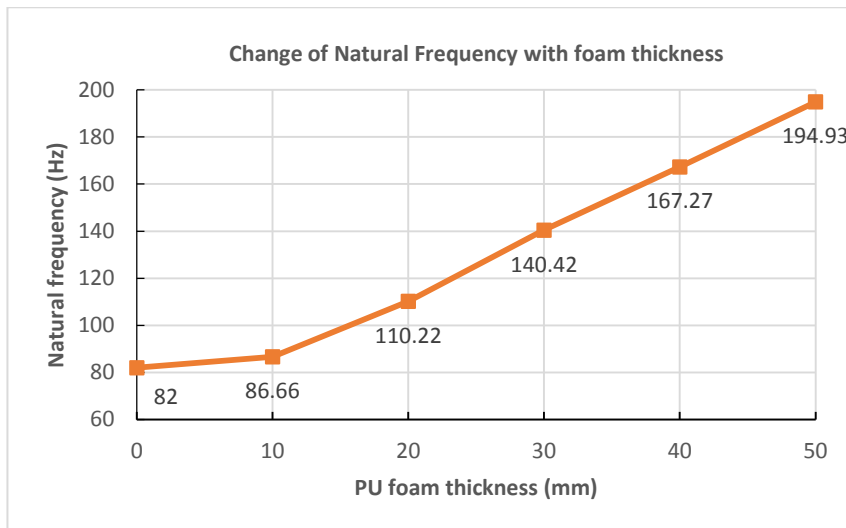


Figure 7. The change of the first natural frequency with PU foam thickness

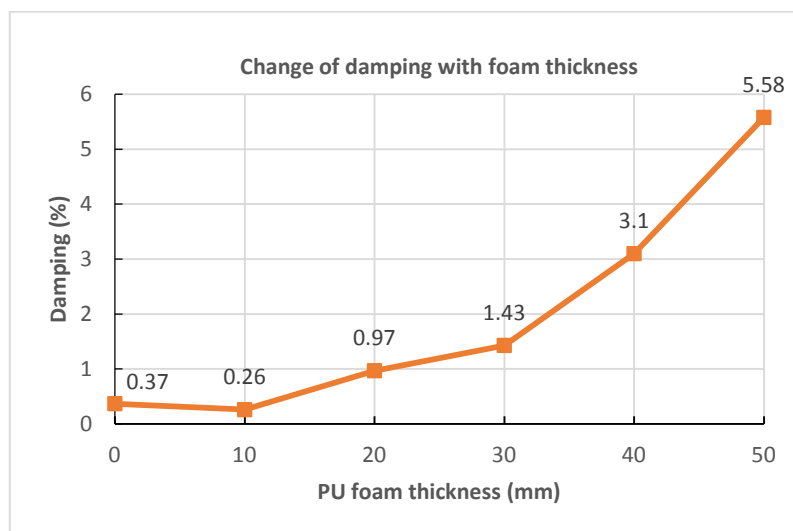


Figure 8. Damping Ratio of Reinforcement Thickness

The change of the damping value according to PU reinforcement thickness is plotted in Figure 8. It is also seen that the damping value increases as the PU reinforcement thickness increases. Interestingly, the damping of the plate reinforced with 10 mm PU foam is smaller than that of the unreinforced plate. This may be due to the effect of adhesive used to apply the PU foam to the plate. Nevertheless, it needs some additional investigations. On the other hand, the damping value for the 20 mm thickness disturbs the regularity of changing. By excluding this irregular value, an approximate polynomial equation for the change of damping value of the system with the thickness of the PU foam can be estimated as:

$$\zeta = 0.0038t^2 - 0.0925t + 0.812 \quad (5)$$

where ζ and t are the damping value and the thickness of PU foam, respectively.

4. CONCLUSIONS

Plates are widely used in engineering applications such as automotive industry, civil engineering construction, aerospace and aircraft structures, hydraulic systems, watercrafts etc. They may be exposed to very critical dynamic loads while operating. Therefore, if necessary, performing a detailed dynamic analysis for operating conditions and applying appropriate vibration isolation is very important for the system's performance. Recently, PU foam has been widely used for the vibration isolation of engineering structures. In this study, the effect of PU foam thickness applied to one surface of the plate on the vibration behavior was investigated experimentally.

Firstly, the modal properties of a square plate with $200 \times 200 \times 1$ (mm³) dimensions are determined by using EMA. The experimental results are verified with the results calculated by using the analytical method suggested by Leissa [12] and the results of ANSYS FE software. Then, 10, 20, 30, 40 and 50 mm PU foam were applied onto one surface of the plate respectively and EMA was performed for each plate. Also the plates reinforced with PU foam are modelled via ANSYS and the results are compared with the results obtained by EMA. Considering the results, an overall increase is observed in natural frequencies and damping ratio with the increase of PU reinforcement thickness for the same mode. However, contrary to expectations, it is observed that the damping ratio of the plate reinforced with 10 mm PU foam is lower than that of unreinforced plate. The reason for this is thought to be the change of dynamic characteristics of the system due to the effects of the adhesive layer between the reinforcement and the plate. It is concluded that some additional tests are necessary.

REFERENCES

- [1]. Sen M., Investigation Thickness Effects on Dynamic System Characteristics of Plates Reinforced with PU Foam, Master of Science, Firat University, Mechanical Engineering, 2016.
- [2]. Zhang L. ve Dupius R. Measurement and identification of dynamic properties of flexible polyurethane foam, *Journal of Vibration and Control*, 2010.S.
- [3]. Deng R., Davies P. and Bajaj A. K. Flexible polyurethane foam modeling and identification of viscoelastic parameters for automotive seating applications, *Journal of Sound and Vibration*, 252, 391–417, 2003.R. E. Sorace, V. S. Reinhardt, and S. A. Vaughn, "High-speed digital-to-RF converter," U.S. Patent 5 668 842, Sep. 16, 1997.
- [4]. P. Davies, R. Singh, A. K. Bajaj. 2002. Estimation of the dynamical properties of polyurethane foam through use of Prony series. *Journal of Sound and Vibration*. 264(2003) 1005-1043.
- [5]. Lodhia B.B. and Esat I.I. Vibration simulation of systems incorporating linear viscoelastic mounts using Pronyseries formulation, American Society of Mechanical Engineers, Petroleum Division, 81, 171–176, 1996.*FLEXChip Signal Processor (MC68175/D)*, Motorola, 1996.
- [6]. Ferry J.D. *Viscoelastic Properties of Polymers*, Wiley, New York, USA, 1970.Karnik, "Performance of TCP congestion control with rate feedback: TCP/ABR and rate adaptive TCP/IP," M. Eng. thesis, Indian Institute of Science, Bangalore, India, Jan. 1999.
- [7]. Gandhi F. and Chopra I. A time-domain non-linear viscoelastic damper model, *Smart Materials and Structures*, 5, 517–528, 1996.*Wireless LAN Medium Access Control (MAC) and Physical Layer (PHY) Specification*, IEEE Std. 802.11, 1997.
- [8]. Neilsen M.K., Krieg R.D. and Schreyer H.L. A constitutive theory for rigid polyurethane foam, *Polymer Engineering and Science*, 35 (5), 387–394, 1995.
- [9]. Coleman B.D. and Noll W. Foundations of linear viscoelasticity, *Review of Modern Physics*, 33 (2), 239–249, 1961.
- [10]. Scarpa F., Giacomini J., Zhang Y. and Pastorino P. Mechanical performance of auxetic polyurethane foam for antivibration glove applications, *Cellular Polymers*, 24 (5), 253-268, 2005.
- [11]. Ewins, D.J., *Modal Testing, Theory, Practice, and Application* (2nd Edition), Research Studies Press Ltd., 2000.
- [12]. Leissa A.W. The free vibration of rectangular plates, *Journal of Sound and Vibration*, 31, 257-293, 1973.

Economical and Social Dimensions of Reclamation in Textile and Clothing Sector: Turkish Case

Seher Kanat¹, Turan Atilgan²

Abstract

Textile and clothing sector has been maintaining Turkish economy's locomotive sector position for approximately forty years. Also, sector is one of the leading sectors of Turkey in terms of high international competitiveness. Almost one third of the sixty thousand textile and clothing enterprises operate in international markets especially by exportation. Reclamation constitutes one of the most significant dispute subjects in textile and clothing trade which enterprises have encountered. Reclamation, which occurs as a result of contrarian attitudes and behaviors towards contract terms, has serious negative social and economical effects on enterprises.

According to the World Trade Organization's data, Turkish textile sector is the fifth biggest supplier in the world whereas Turkish clothing sector is the seventh biggest supplier. With respect to Euratex data, Turkish textile sector is the second biggest supplier of European Union whereas Turkish clothing sector is the third biggest supplier. Reclamation is very important for Turkish textile and clothing sector which is one of the most significant suppliers of world's most important textile and clothing brands.

This study involves a field research in order to determine the dimensions and reasons of reclamation which Turkish textile and clothing enterprises experience during international trade. Besides, the study aims to specify precautions and solutions for reclamation.

Keywords: *Reclamation, Turkish textile and clothing sector, retailing in clothing sector, merchandising*

1. RECLAMATION CONCEPT

If a product or service doesn't conform to quality standards, the situation is named as reclamation. Textile sector frequently confronts with reclamation implementations [1]. Reclamation is implemented in textile and clothing sector due to the reasons such as; quality mistakes which are based on raw materials, quality mistakes which are based on finished goods, deadline delays, inconvenient working conditions, products which don't conform to standards and required properties.

Reclamation can be implemented as discount, return and compensation. If the sold product or service doesn't conform to quality standards, discount reclamation is implemented. In this case, the buyer demands a discount. This type of reclamation is also classified as quality cost. Return reclamation appears when the product is returned to the enterprise by the customer due to displeasure. Return reclamation can be solved in two ways: First, the returned product can be changed with a new product. Second, the returned product can be repaired and delivered to the customer. In compensation reclamation, the emerging loss, which is occurred during the utilization of product or service, is covered by producer [1].

2. ECONOMICAL AND SOCIAL DIMENSIONS OF RECLAMATION IN TURKISH TEXTILE AND CLOTHING SECTOR

Turkish textile and clothing sector frequently confronts with reclamation issue during exportation process. Buyers usually cut down the sale value due to the low-quality products and production faults. The enterprises confront with reclamation due to the reasons such as; measurement deviations in clothing products, fabrics which don't conform to required properties in terms of color, touching etc., improper accessories, color and shrinkage issues after washing, deadline delays and quality mistakes above 8% [2]. Cotton contamination can be indicated as another significant reclamation cause. Cotton is contaminated with nylon sack pieces and other substances during picking and transportation. Furthermore, mineral oils melt into cotton during gin process, yarn and fabric production. Thus, most of the Turkish exporters confront with reclamation because of low-quality clothing products which are produced with contaminated cotton [3]. When the yarn and fabric, which are produced from one bale contaminated cotton (one bale cotton costs 250 dollars), are transformed into clothing products; the loss turns into 350.000 dollars. Textile and clothing sectors have to pay million dollars reclamation because of contaminated cotton [4].

On the other hand, production implementations and issues of zipper producers, which are a part of accessories sector which is the sub-sector of clothing sector, are analyzed in a field study. More than half of the zipper producers indicate that they confront with reclamation issue [5].

¹ Corresponding author: Ege University, Department of Textile Engineering, 35100, Bornova/Izmir, Turkey, seher.kanat@ege.edu.tr

²Ege University, Department of Textile Engineering, 35100, Bornova/Izmir, Turkey, turan.atilgan@ege.edu.tr

As it can be seen, Turkish textile and clothing enterprises confront with reclamation issue during exportation process. Reclamation, which decreases the profitability of enterprises, causes economic and social burdens. Besides, there are a few studies about reclamation in the literature although it is a frequent issue. In this context, our research contributes to the gap within the literature.

This study involves a field research in order to determine the dimensions and reasons of reclamation which Turkish textile and clothing enterprises experience during international trade. Besides, the study aims to specify precautions and solutions for reclamation. In accordance with the aim of the research, successful textile and clothing enterprises, which operate and export in İzmir province, have been determined as target group. Interviews have been made with the marketing managers of these enterprises and a questionnaire form consisting of 12 main questions have been used.

2.1 The General Properties of Participating Enterprises

Sun Textile has been established in 1987 and it possesses 285 employees. It produces and exports clothing products for women and kids. There is knitting, fabric dyeing and finishing facility within the enterprise structure. The enterprise operates in Spain and United Kingdom markets. It possesses 20-25 million pieces production capacity per year.

Cu Textile has been established in 2006 and it possesses 130 employees. It produces and exports clothing products. The enterprise operates in European Union market. It possesses 8 million pieces production capacity per year.

Egedeniz Textile has been established in 1993 and it possesses 120 employees. It produces and exports clothing products. The enterprise operates in Japan, USA, Canada and United Arab Emirates markets. It possesses 200.000 pieces production capacity per year.

TYH Textile has been established in 2000 and it possesses 2650 employees. It produces and exports knitted clothing products. The enterprise operates in European Union market. It possesses 15 million pieces production capacity per year.

Üniteks Textile has been established in 1990 and it possesses 550 employees. It produces and exports knitted clothing products. The enterprise operates in European Union market. It possesses 30 million pieces production capacity per year.

Era Textile has been established in 1991 and it possesses 200 employees. It produces and exports clothing products. The enterprise operates in European Union market. It possesses 6 million pieces production capacity per year.

Roteks Textile has been established in 1986 and it possesses 210 employees. It produces and exports clothing products. The enterprise operates in European Union, Asia and America markets. It possesses 5 million pieces production capacity per year.

2.2 Reclamation Findings of Participating Enterprises

The survey offers 18 statements under 5 main questions which analyze the dimensions, reasons and solutions of reclamation. The participants are required to choose their agreement levels for each of these statements. In quinary likert scale never is coded as 1, rarely is coded as 2, occasionally is coded as 3, frequently is coded as 4 and always is coded as 5. The findings are given in Table 1, 2, 3, 4 and 5.

The participating enterprises indicate that reclamation has been implemented to their enterprises by their customers during international trade (Table 1). Besides, their enterprises have implemented reclamation to their suppliers. The imposed reclamation frequencies of enterprises are more than their implemented reclamation frequencies. On the other hand, the enterprises continue to work with brands which implement reclamation to them. However, their working possibilities with suppliers, which they implement reclamation, are less.

The participating enterprises specify that, their customers mostly implement reclamation due to the issues about deadline delays (Table 2). This issue is respectively followed by issues about product quality, issues about working conditions and issues about standards. However, issues about working conditions and standards are too rare. On the other hand, if the reclamation implementation reasons of enterprises are analyzed, it can be seen that issues about product quality take place on the top (Table 3). This issue is respectively followed by issues about deadline delays, issues about working conditions and issues about standards. Besides, two enterprises indicate that, they implement reclamation to their suppliers due to product and accessory loss.

The participating enterprises frequently solve their reclamation issues with discounts (Table 4). This solution is respectively followed by product return and legal procedure. However, legal procedure is rarely preferred. Discounts also take place on the top within the solutions of implemented reclamation (Table 5). In other words, suppliers solve their reclamation issue with discounts. This solution is respectively followed by product return and legal procedure.

Table 1. Distribution of participating textile and clothing enterprises according to reclamation implementations

Statements	N	Mean	Std. Deviation
Reclamation has been implemented to our enterprise by our customers.	7	3,00	1,0000
Our enterprise has implemented reclamation to our suppliers.	7	2,86	1,0690
Our enterprise continues to work with enterprises (brands) which implement reclamation to us.	7	4,43	0,5345
Our enterprise continues to work with suppliers which we implement reclamation.	7	3,86	1,0690

Table 2. Distribution of participating textile and clothing enterprises according to imposed reclamation reasons

Reasons	N	Mean	Std. Deviation
Issues about product quality	7	3,14	1,2150
Issues about deadline delays	7	3,71	0,9512
Issues about working conditions	7	1,14	0,3780
Issues about standards	7	1,14	0,3780

Table 3. Distribution of participating textile and clothing enterprises according to implemented reclamation reasons

Reasons	N	Mean	Std. Deviation
Issues about product quality	7	4,00	0,5774
Issues about deadline delays	7	2,71	0,7559
Issues about working conditions	7	1,57	0,9759
Issues about standards	7	1,43	0,5345

Table 4. Distribution of participating textile and clothing enterprises according to solutions of imposed reclamation

Solutions	N	Mean	Std. Deviation
Discount	7	3,71	0,9512
Product return	7	2,00	0,8165
Legal procedure	7	1,29	0,7559

Table 5. Distribution of participating textile and clothing enterprises according to solutions of implemented reclamation

Solutions	N	Mean	Std. Deviation
Discount	7	3,86	0,8997
Product return	7	2,57	1,2724
Legal procedure	7	1,57	0,7868

The participating enterprises are required to tell the precautions which they take in order to prevent reclamation in terms of customers and suppliers. The precautions can be summarized as below:

1. Quality control points within the production processes must be determined accurately and their numbers must be increased. The employees who will work at these points must be well-educated. Besides, faultless and qualified products must be delivered to final control by separating faulty products/semi-finished products at quality control points within production processes.
2. Quality assurance system of the enterprise and quality systems of suppliers must be strengthened jointly in order to decrease reclamation issues about product quality. Both the enterprise and the suppliers must assemble regular meetings about quality results.
3. Raw material problems must be decreased in order to reduce reclamation issues about deadline delays. Correct and accurate planning must be done in deadline determination. Also, possible risks must be taken into consideration. Besides, the production capacity of the enterprise must be controlled while receiving orders. The relations with customers must be improved. Therefore, additional time could be requested in deadline delays. The deadline delay issues which are based on suppliers must be solved with capacity increase. In necessary conditions, additional capacity must be created out of the enterprise. In other words, contract manufacturing can be used.
4. Detailed contracts must be signed with suppliers in order to prevent the reclamation issues which are based on suppliers. Also, the possible reclamation issues and their solutions (sanctions) must be written on the contract. The enterprise must be selective in order to provide long-term working conditions, which are proper to requested standards, with correct suppliers. The suppliers must be evaluated in order to supply accurate and qualified materials. The suppliers which cannot succeed the required results must be eliminated.
5. All required standards, which are demanded by customers, must be implemented both in the enterprise and in the suppliers in order to eliminate productional issues. Preproduction risk analyses must be carried out and necessary precautions must be taken. Possible issues must be prevented before they occurred.
6. The enterprise must accurately communicate with its customers in order understand the demands better. The production must be fulfilled according to these demands. Besides, the required demands must be transmitted to suppliers accurately, clearly and correctly.

3. RESULTS AND GENERAL EVALUATION

Nowadays, textile and clothing enterprises frequently confronts with reclamation issue which can be defined as the inappropriateness of sold products to required properties. This issue causes time losses, poor relations with customers and serious financial losses in terms of enterprises. Therefore, enterprises take precautions in order to prevent imposed and/or implemented reclamations.

According to our research results, enterprises indicate that reclamations have been implemented to them by their customers. Besides, their enterprises have implemented reclamation to their suppliers. On the other hand, the enterprises continue to work with brands which implement reclamation to them. However, they usually do not work with suppliers which they implement reclamation. This situation is proceeded from enterprises' customer retainment desire. Enterprises,

which try to survive under intensive rivalry conditions, do not want to lose customers. Therefore, they accept reclamations which have been implemented to them by their customers. However, they eliminate their suppliers, which they implement reclamation, in order to prevent the possible issues.

According to another result of our research, enterprises indicate that their customers mostly implement reclamation due to the issues about deadline delays and product quality. On the other hand they usually implement reclamation to their suppliers due to the issues about product quality. Sometimes, they can also apply reclamation in terms of deadline delays. When the solutions of imposed and implemented reclamations are analyzed it can be seen that discounts take place on the top. Enterprises and suppliers accept to decrease their profitability and sometimes they even accept to lose money. Product return is another solution for reclamation. However, this solution is occasionally implemented because these products can rarely be sold to another customer after repairment. Textile and clothing sector produces according to orders and its product ranges are very variable. Therefore, enterprises usually try to sell returned products in domestic market with low prices after removing their labels. Legal procedure is another solution which is used for solving reclamation issues. However, legal procedure is rarely used because it damages both the enterprises and the suppliers due to its long-term processes and high costs.

According to participating enterprises, quality control implementations take place on the top within the reclamation precautions. Quality control points within the production processes must be determined accurately and their numbers must be increased. In other words production must be fulfilled with minimum faults. Also, quality assurance system of the enterprise and quality systems of suppliers must be strengthened jointly. In addition to these, both the enterprise and the suppliers must assemble regular meetings about quality results. Therefore, the qualified production can be standardized and quality issues can be determined and solved at the beginning.

According to the obtained results, raw material problems must be decreased in order to prevent reclamation issues. Therefore, deadline delays can be reduced. Besides, production and supply plans must be done correctly and accurately. Also, possible risks must be taken into consideration. In necessary conditions, capacity of the enterprise must be increased and/or additional capacity must be created out of the enterprise. In other words, the enterprise must invest and/or outsource. Furthermore, all required standards, which are demanded by customers, must be implemented both in the enterprise and in the suppliers in order to eliminate productional issues. Preproduction risk analyses must be carried out and necessary precautions must be taken. Possible issues must be prevented before they occurred.

According to another research result, detailed contracts must be signed with suppliers in order to prevent the reclamation issues which are based on suppliers. Also, the possible reclamation issues and their solutions (sanctions) must be written on the contract. Besides, the enterprise must be selective in order to work with correct suppliers. The suppliers must be evaluated in order to supply accurate and qualified materials. The suppliers which cannot succeed the required results must be eliminated.

According to the participating enterprises, they must accurately communicate with their customers and suppliers. In fact, accurate, clear and correct communication is the best precaution for reclamation because faults and issues are based on misunderstandings. Therefore, the required properties and standards must be determined or notified accurately, clearly and correctly. Thus, misunderstandings and possible faults could be prevented.

To sum up, textile and clothing enterprises frequently confronts with reclamation issue. However, reclamation is a problem which has solutions. In this context, enterprises must communicate accurately and clearly with their customers and suppliers. Besides, they must take necessary precautions in order to prevent reclamation which causes losses in terms of financial and emotional damages.

REFERENCES

- [1] Yükcü S., What is reclamation?, <http://suleymanyukcu.com/?s=makale&kategoriNo=14> (Access Date: April 2016) (in Turkish)
- [2] Kayacık G., 2012, Reclamation issue of Turkish textile and clothing exporters, Dünya Newspaper, 03.11.2012, <http://www.dunya.com/yorum-inceleme/turk-tekstil-ve-hazir-giyim-ihracatcisinin-reklamasyon-sorunu-170184h.htm> , (Access Date: April 2016) (in Turkish)
- [3] İstanbul Chamber of Commerce, Denim fabric report, <http://www.ito.org.tr/Dokuman/Sektor/1-25.pdf> (Access Date: April 2016) (in Turkish)
- [4] Topçu T., 2003, Last days of contaminated cotton, Hedef Journal, No.113, http://www.itkib.org.tr/itkib/hedef/old_hedef/200305_mayis/ozelpamuk1.htm (Access Date: April 2016) (in Turkish)
- [5] Köksal M.H., 2001, Production implementations, issues and solutions in sub-sectors of clothing sector: a field study within zipper sector, Yönetim ve Ekonomi, Vol.8, No.2, p:69-79 (in Turkish)

Adsorption of Certain Pesticides in Apple Juice with Activated Carbon Produced From Pulp of Pomegranate Peel

Aziz Sencan¹, Merve Ciftci², Mustafa Karaboyacı¹, Mehmet Kılıç

Abstract

The pesticide residues in the fruits which used in the production of fruit juice and similar products, exceeds to the end product during the production process. The use of pesticides is under regulation by authorities around the World and In Europe the EU Commission & ESFA (European Food Standards Authority) and In Turkey 5. part of Turkish Food Codex Regulation designates the maximum residue limits (MRL). For this reason, in the juice production plants various methods have been applied to the fruit juice, for the removal of pesticides. One of the most effective method in this pesticides removing methods is to filter the juice with commercial activated carbon. In this study, the activated carbon used for the removal of pesticides was obtained from pomegranate pulp, which is occurring as a waste at the end of juice production process. Thus, a product occurring as a waste can be evaluate as a useful product again. Conversion of pomegranate pulp to activated carbon was conducted in an tubular type oven at 700 °C under nitrogen media. The obtained activated carbon was treated with apple juice, containing 100 µg/L carbendazim, thiacloprid and deltamethrin at different doses and pesticide removal performance of that new activated carbon was investigated. As a result, 90% of the carbendazim, 55% of thiacloprid and %86 of deltamethrin was removed from fruit juice with that new activated carbon. In addition, FT-IR spectrum were taken for the surface characterization of obtained activated carbon, before and after the adsorption experiments. Taking advantage of these spectrums, surface pesticide binding mechanism of activated carbon was explicated. The resulting activated carbon also used in removing pesticides from pomegranate juice, but it has shown opposite effects in the product quality. But it has no opposite effects on the quality of apple juice.

Keywords: *pomegranate peel adsorption, pesticides, activated carbon.*

1. INTRODUCTION

Agricultural pests are one of the reasons which causes decline of the fertile in agriculture. In order to eliminate these pests pesticide using has been required. Today over 1000 activate agents are using for the purpose of eliminating these pests. Fernandez-Alba and Garcia-Reyes have discovered new agents in their studies but the usage of other existing agents is prohibited or limited. It is true that using pesticides in agriculture is beneficial but these are also toxic compounds. The consumption of food which includes pesticides overly creates serious risks on human health [1,2]

Today the rate of pesticide residues in nourishment is so high that it threatens human health and for this reason this situation is needed to investigate. To designate the rate of pesticide residues in fruit juice that is consumed too much in the Turkey, investigating using synthetic medicine in products and comparing the results with normal limits in Turkish Food Codex Regulation is very essential for people's health.

Agricultural activities in the world and another human made improvements have increased usage of pesticides which pollutes water and environment. Pesticides are the most dangerous pollutions in the source of water and environment. In order to eliminate these dangerous pesticides lots of different methods have been tried such as coagulation/flocculation/sedimentation, membrane filtration. In these methods, efficiency has been obtained but these methods are very expensive. For the purpose of eliminating the toxic organic pollutions, using active carbon is the best model in treatment methods. Natural organic agents have been used to refine pesticides. Thanks to this method 98% refinery success has been gained [3].

Active carbon is a form of large inner surface and pore volume, generally it has %87-97 carbon. The rest of the part can include hydrogen, oxygen, Sulphur and azote. There can be 5 or 20 rate of harmless agents but before use it these agents should be moved away. This process is called ash content disappearing. Ash content should be between % 0.1-0.2 rate [4]. Active carbon is used for different purposes such as refining gases, water and waste water refine, metal industry, defense industry, weapon industry, bomb making, health sector. As you see, this active carbon can be used in every field [5]. Also it is used for liquid or gas phase. It can absorb lots of different molecules [6]. The pores are 0.2-1.0 cm³/g in an ideal carbon and its surface is 400-1000 m²/g. But it can exceed for special usages [7]. Pore size can be changed between 0.3 and thousands of monometers [8].

¹ Corresponding author: Süleyman Demirel University, Department of Chemical Engineering, 32260, Çünür/Isparta, Turkey. azizsencan@sdu.edu.tr

² Süleyman Demirel University, Department of Chemical Engineering, 32260, Çünür/Isparta, Turkey., mrvctfci@gmail.com

Carbon is used commonly for producing juice industry as a filter method in Turkey. Because there is no producing active carbon in Turkey, it is very expensive to use for eliminating pesticides and that's why it has not been preferred. Apple is a fruit that has been preferred from the point of producing in our country like others. Turkey has an important potential on this issue. Apple juice has had a large area on our export. Raw material quality has a big role on apple juice producing that is important for nourishment industry like other industrial fields. In apple juice producing, in order to market it is necessary to obtain some main criterias which are specified by FDA. The rate of pesticide is just one of these criterias. In this study we tried to produce active carbon from pulp of pomegranate peel and use it to remove pesticides in apple juice. Because carbon has an essential role in fruit juice producing.

2. MATERIALS AND METHODS

Pulp of pomegranate peels, which has taken from fabricate with the form of waste, have formed of main material of this study. All of the pomegranate peels have dried under room temperature. These peels have been activated with active carbon under N₂ gaze with 250°C, 400°C and 700°C about 30 minutes in ash oven. Pyrolyzed active carbon has been became smaller about 125 micron diameter. Different pesticides and pyrolyzed active carbon has been added to fruit juice. According to analysis results active carbon has an important role on eliminating pesticides in fruit juice. Other part of this study, with chemical treatment pyrolyzed active carbon and pesticides' adsorption in fruit juice has been analysed. 20 gr pulp of pomegranate peel has been added to %20 KOH solution and it has been mixed for 24 hours with 400 rpm. After chemical absorb operation, with the help of filter paper solutions have been moved away from water and dried. Dried pomegranate peels have been pyrolyzed for 30 minutes with 700 °C. And then pyrolyzed products have been watered with %5 HCl acid solution and pure water. At last they have been minimized with the rate of 125 micron diameter. Carbendazim and Thiocloprid agents have been prepared as a pesticide with 100ppb concentrations. Different dozes active carbon has been added after adding pesticide which has done to fruit juice with different concentrations. During different mixing durations, fruit juice sample has been analysed by using AOAC 2007 Pesticide Analyze Method and Quetchers kit. Analysis results have been gained with the help of LCMS-MS. Study has been ended up with these results.

3. RESULTS AND DISCUSSION

3.1 Adsorption studies of thermally activated carbon

In the chart above, the change in the amount of Carbendazim and Thiocloprid is observed during the period of 60min. The Adsorption capacity of Carbendazim is approximately 4 times more than Thiocloprid's .While the Activated Carbon is adsorbed nearly half of amount of Carbendazim at the first dose; on the other hand, the situation in Thicloprid is observed differently because of the another physical circumstances. During the definite time, at the beginning, a pesticide is formed quickly, but then dose is increased, so a pesticide was composed by slowly rather than be in quick.

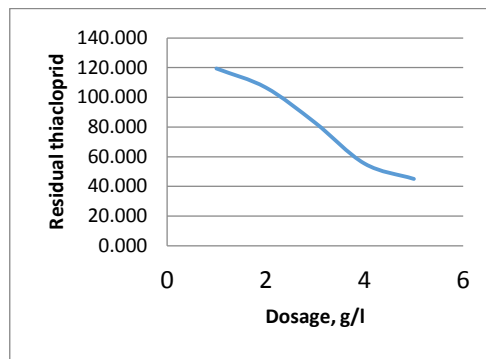
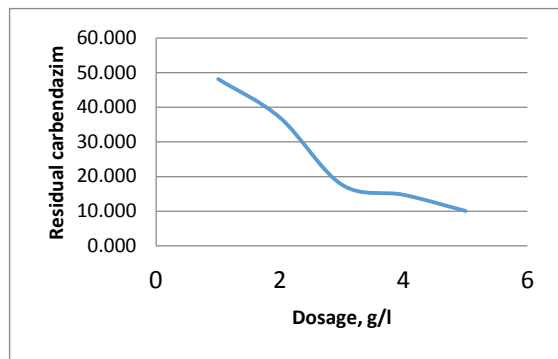


Figure 1a indicates that relation of 100ppb pesticide with activated carbon in 60 minutes. (carbendazim).

Figure 1b shows that the result of 100 ppb pesticide with activated carbon in 60 minutes. (thiaclopridin).

If we look at the above graph , for figure 2, after 5 g/l of activated carbon is added, the adhesion of the measurements about 88% was found to occur quickly after 5 minutes. As time progresses, It was observed that removal of pesticides occurs slowly. As a result, as shown in chart the active carbon has reached saturation 60 minutes later. According to graph, carbendazim was retained by activated carbon around %90 in our fruit juice sample. For Figure 2b, the pesticide is added to a mixture of 5 g/l and then 5 minutes later, activated carbon is obtained efficiency around %39. Again as time progresses, adhesion situation still continues. At the end of the 60 minutes, the yield around %55 was measured to obtain. If two graphics compared, in the beginning, at the first 5 minutes, figure 2a was really quick, but after that it takes place very slowly. On the other hand, figure 2b, first 5 minutes is really slow rather than other and then more quick than other. Considered as the yield, The activated carbon was found to better keep Carbendazim.

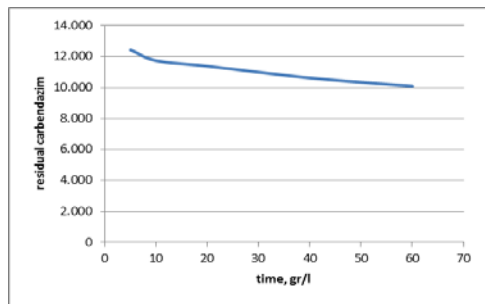


Figure 2a Carbendazim decreased concentration versus time (dosage:5g/l, initial carbendazim concentration 100 ppb)

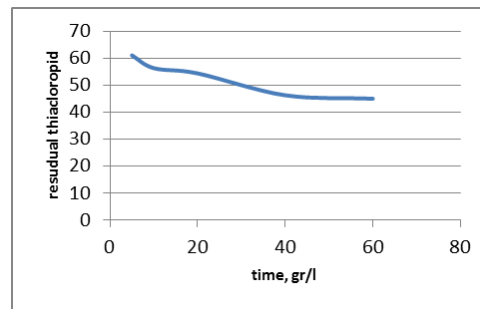


Figure 2b Thiaclopridin decreased concentration versus time (dosage:5g/l, initial thiaclopridin concentration 100 ppb).

3.2 Adsorption studies of chemically activated carbon with KOH

For figure 3a, when activated carbon is added into the sample first, The adsorption is occurred approximately 88% in 5min. As time progresses, the Adsorption continues to occur however it is progressing slowly. The adsorption is constant at the end of 60min and the yield is 90%. For figure 3b, after added the activated carbon to sample solution, at the first 5 min, the adsorption is occurred nearly %39. As time progresses, is slow. End of 60 min., total adsorption is nearly %55. Compared two charts, the adsorption in figure 3a for at the first 5min is faster and more efficient than figure 3b's. But after 5min later, the opposite is true. Carbendazim is adsorbed more in both samples which related with 2,5mg/l of activated carbon.

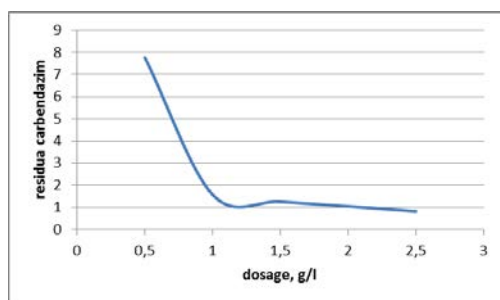


Figure 3a Carbendazim decreased concentration versus dosage (time: 60 min., initial carbendazim concentration 100 ppb, with KOH treatment)

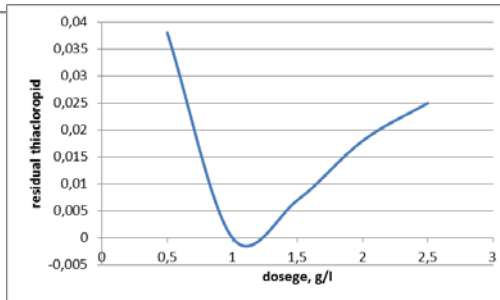


Figure 3b Thiaclopridin decreased concentration versus dosage (time: 2,5g/l, initial thiaclopridin concentration 100 ppb, with KOH treatment).

Looking at the chart above, for figure4: The first 5 minutes of pesticides kept largely (about 98%) it is realized. As time progresses, adhesion occurs slowly. And at the end of the 60 minutes, the total pesticide is measured around 98% it is largely in place of figure 4b. Adhesion event have occurred in 30 minutes thiacloprid which is in the juice completely passed into activated carbon site, and could be measured. Time progresses activated carbon held by a very small amount of pesticide that the measurement results are again released into the juice was observed. These results are fully consistent with the results in figure3b.

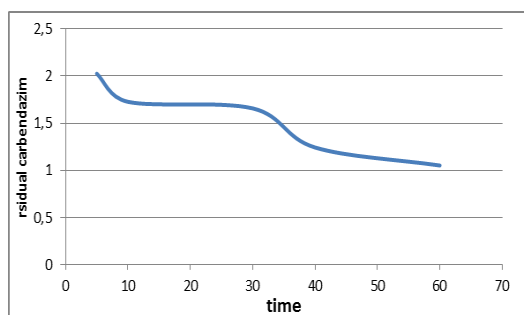


Figure 4a Carbendazim decreased concentration versus time (dosage:2,5g/l, initial carbendazim concentration 100 ppb, with KOH treatment)

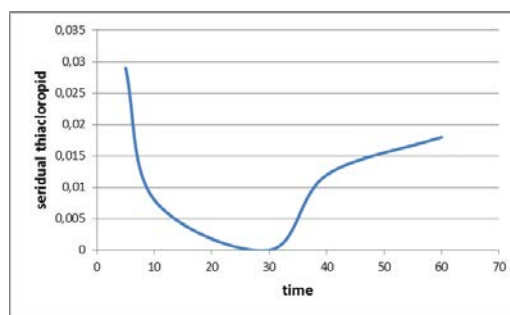


Figure 4b Thiaclopridin decreased concentration versus time (dosage:2,5g/l, initial thiaclopridin concentration 100 ppb, with KOH treatment).

As a result of studies it has completely changed the affinity of the treated activated carbon with KOH. Active carbon which is obtained only by Pyrolysis while carbendazim showed high affinity, the activated carbon obtained as a result of chemical activation with KOH showed against higher affinity in thiacloprid. [9] stated that and carbonate potassium hydroxide water and an oxidizing reagent rather than the role of an attractive long and narrow shaped themselves in the formation of micro pores at the same time, these alkaline earth compounds, with the formation of metallic particles mesopore to stop channelling features are committed with the work they have done. Adsorption is virtually complete in the first 20 minutes. Therefore, it is possible to express the adsorption occurs quickly. fast realization of the adsorption processes, means that the physical adsorption dominant one. A power which is effective in physical adsorption called Van Der Waals power. The chemical reaction between the adsorbate and adsorbent means chemical adsorption, and also occurs as a result of electron exchange. Bonding powers in physical adsorption with molecules, while chemical adsorption molecules are inside of it. Physical adsorption, has the biggest advantage is that it is reversible against chemical adsorption. So, the physical adsorbent is regenerated and re-used while the chemical regenerating adsorbent depends on the availability of interaction of adsorbate. While the interaction in physical adsorption occurs very quickly, interaction in chemical adsorption, is depending on the speed of the temperature varies. Therefore, the physical adsorption energy is lower, and both single and multi-layer, while energy of chemical adsorption, is high and can be single-layered,[10]. And the colour of the activated carbon obtained in both the fruit juice has not shown any effect on pH value. The same activated carbon in pesticide removal from pomegranate juice cause deterioration in colour, such negativity has been observed in apple juice.

4.CONCLUSION

After some studies which have been done, the activated carbon which is being performed with KOH, from apple juice, carbendazim-and thiacloprid that have the potential to be used to remove is observed. Especially, activated carbon by chemical activation, thiacloprid, yield was revealed %100 to be removed. Activated carbon which was obtained later should be investigated especially its effects on the product and also cost analysis should be searched, that's how its availability can be understood and used instead of resin.

REFERENCES

- [1]. Beyer, A. and Biziuk, M. 2008. Applications of sample preparation techniques in the analysis of pesticides and PCBs in food. *Food Chemistry*, 108, 669-680.
- [2]Kruve, A., Künnapas, A., Herodes, K. and Leito, I. 2008. Matrix effects in pesticide multi-residue analysis by liquid chromatography-mass spectrometry. *Journal of Chromatography A*, 1187, 58-66.
- [3]Bras, P., I., Santas, L., Alvas, A., 1999, Organochlorine Pesticides Removal By Pinus Bark Sorption, *Environmental Science and Technology*, 33, 631-634.
- [4]Choma J., Jaroniec M. (1987): "Materials Chem. Phys. 18, 409
- [5]Stoeckli H. F., Kraehenbuehl F. (1984): "The External Surface of Microporous Carbons, derived from Adsorption and Immersion Studies", *Carbon*, 22, 297
- [6]. Jaroniec M., Choma J. (1986) : *Materials Chem. Phys.* 15, 521
- [7]. Morgan I., Fink C. E. (1989): "Activated Carbon Production", *Chem. Ind. Eng.* 2, 219
- [8]. Küçükgül, E.Y., 2004. Ticari aktif karbon üretimi ve özelliklerinin belirlenmesi, DEÜ Mühendislik Fakültesi Fen ve Mühendislik Dergisi, 6, Sayı: 3 41-56
- [9]. Addoun, A., Dentzer, J., Ehrburger, P., 2002. Porosity of Carbons Obtained by Chemical Activation: Effect of the Nature of the Alkaline Carbonates. *Carbon*, 40, 1140-1143.
- [10]. Kılıç, M., 2004. Kurşun(II) ve Cıva(II) İyonlarının Biyokütle Üzerine Adsorpsiyonunun İncelenmesi.Süleyman Demirel Üniversitesi, Fen Bilimleri Enstitüsü, İnşaat Müh.Anabilim Dalı, Doktora Tezi, Isparta.

The Anion Dependence on the Corrosion Protection Effect of Polypyrrole Coating for Steel in Acidic Media

Seval Akpolat¹, Semra Bilgic²

Abstract

In this study the corrosion parameters of steel have been determined by Tafel extrapolation method in 1 M HCl, H₂SO₄ and H₃PO₄ media. Steel was coated with polypyrrole (PPy) in 0.1 M pyrrole +0.3 M oxalic acid solution by cyclic voltammetric method. It was found that this coating protects steel against corrosion. The open circuit potentials (E_{ocp}) determined for uncoated and coated steel electrodes indicate the shift toward the more positive values immediately after the formation of coatings open circuit potentials do not change depending on the immersion time. The corrosion parameters and percentage inhibition efficiencies of coated electrode were investigated according to immersion times in the same acid media. It was determined that in all acid media studied, the more immersion time, the more corrosion current densities and fewer percentage inhibition efficiencies were determined. It was found that the corrosion current density and inhibition efficiency variation order is H₂SO₄> H₃PO₄> HCl.

Keywords: Acid, coatings, corrosion, electropolymerization, polypyrrole

1. INTRODUCTION

The term of corrosion can be defined as the interaction of a metal with the surrounding environment, causing a slow, steady and irreversible deterioration in the metal in both physical and chemical properties. Corrosion is an electrochemical process which involves the transfer of electrons between a metal surface and aqueous electrolyte solution. Electrochemical corrosion is a major destructive process that results in destructive effects. The formation of rust on iron and steels and other corrosion products, cracks in aircraft, automobiles, boats, gutters, screens can be given as a few examples. Corrosion causes important material and economical losses due to particle or total replacement of equipment structures. Corrosion is a major factor in determining in the investment and production costs in the industry. According to some estimations, the cost of corrosion to a nation reaches to 3.5-5.0 % of the gross national product. Corrosion causes not only economic losses, but also social and these engage the safety and health of people working in industries or living in nearby towns.

Due to its different harmful effects, corrosion is an unwanted phenomenon,. There are several methods for protection of metals against corrosion. One of these methods is to add chemical substances or compounds called inhibitors to the medium these compounds prevent corrosion either by being adsorbed on the surface of metals or alloys, or by forming a protective layer, or by causing the formation of insoluble complex. However, most of these substances are toxic and using them is harmful for both human health and environment. For this reason, recently the researches have been focused on the use of non-toxic.

The protection of metals against corrosion via the use of polymeric coatings has been subject of undesirable research in recent years [1-4]. The advantages of polymeric coatings as compared to chemical inhibitors are the ease of their deposition, low toxicity, and low impact on the environmental and human health. The conductive polymers, which possess the electronic properties of semiconductors and processing advantages of conventional polymers, have widely been studied for corrosion protection during the last few years. Conducting polymers may function as organic inhibitors due to their great number of a π bonds, reducing the number of active sites on the metal surface through adsorption and acting as a barrier by decreasing the transport of corrosive agents. They also act as an electronic barrier and shift the potential of the coated material to a value where the kinetics of corrosion of underlying metal is lowered. Polyaniline [5,6], polypyrrole [7,8] and polythiophene [9] are the most important conductive polymers for the protection of corrosion.

In this study polypyrrole (PPy) was chosen as conductive polymer. The objective of this study is to determine the corrosion parameters of steel coated with PPy in 1M HCl, H₂SO₄ and H₃PO₄ media and to show the protection efficiencies and resistance of coating depending on the immersion time and to investigate the variation of the inhibition efficiency of PPy coating with increasing charges of anions in studied acid solutions.

¹ Gebze Commercial High Education School, 41400, Gebze, Turkey.

² Corresponding author: Ankara University, Faculty of Science, Department of Physical Chemistry, 06100, Besevler, Ankara, Turkey.
bilgic@science.ankara.edu.tr

2. MATERIALS AND METHODS

The chemical composition of the steel employed in this study is given in Table 1.

Table 1. The chemical composition (wt %) of studied steel electrode.

C	S	Cr	Si	Mn	Fe
0.130	0.004	12.400	0.650	0.510	86.310

The steel electrode of diameter was 4 mm, cut and embedded in a cold-curing resin on a methyl methacrylate basis (Technovit, Kulzer, Friedrichsdorf, Germany). Before each test the steel surface was abraded with a 1200 grid emery paper, washed bi-distilled water was sufficient for removing excess reactant from the coated steel, the emery paper was not used after the electrosynthesis of polymer coatings. Electropolymerization and corrosion tests were carried out in a three electrode cell.

The steel was used as an electrode located in the center of the cell, while SCE and platinum foil were used as reference electrode and counter electrode respectively, in the other parts of the cell. Bi-distilled water was used to prepare the solutions. Nitrogen was bubbled through the solutions before each experiment for up to 15–20 min to remove oxygen from the solution. The experiments were carried out using the system consisting of Wenking LB 75 L laboratory model potentiometer, Wenking VSG 72 model voltage-scanning generator, Yokogawa Technicorder Type 3077 recorder, BM 101 thermostat and electro mag-mixer. The corrosion parameters were determined by using Tafel extrapolation method [10].

Electrochemical corrosion measurements were performed in 1 M H₂SO₄ at room temperature. 0.3 M oxalic acid including 0.1 M pyrrole (Py) solution was used to coat both uncoated and coated-steel with a PPy film. Potential scan rate was initially kept at 2.5 mVs⁻¹ until the formation of Fe₂C₂O₄ on the steel surface.

3. RESULTS AND DISCUSSION

Fig 1 shows the cyclic voltammogram of uncoated steel in 0.3 M oxalic acid solution. The first scan and subsequent ten cycles of current–potential curves in 0.1 M pyrrole + 0.3 M oxalic acid can be seen from Figs 2a and 2b.

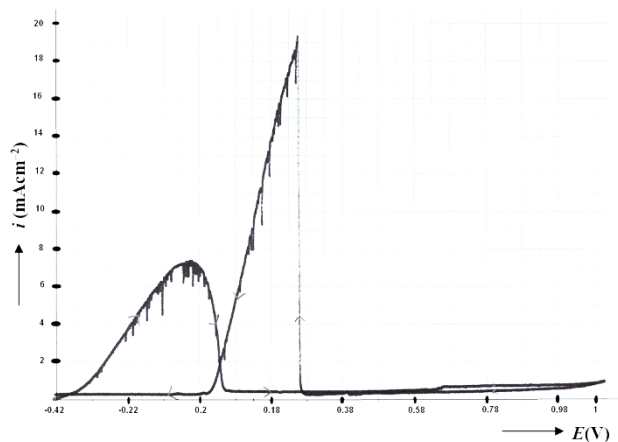


Figure 1. Anodic polarization curve of 12% Cr stainless steel in 0.3 M oxalic acid potential scan rate ($v = 20$ mV/s).

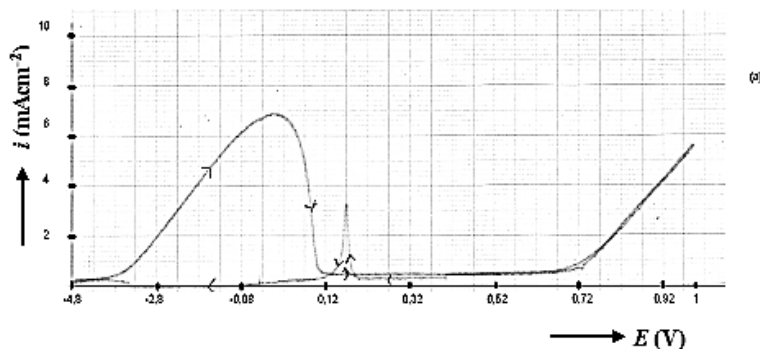


Figure 2a. The first scan curve of the steel in 0.1 M pyrrole + 0.3 M oxalic acid medium potential scan rate ($v = 20 \text{ mV/s}$)

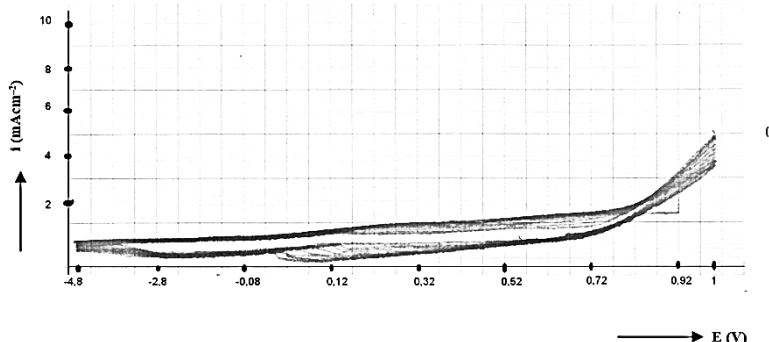


Figure 2b. The ten scan curves subsequently for steel in 0.1 M pyrrole + 0.3 M oxalic acid medium potential scan rate ($v = 20 \text{ mV/s}$).

As can be seen from Figs 1 and 2a, the passivation peak in the first scan was disappeared in the second scan due to the formation of PPy which prevents dissolution (Fig 2b). It can be said that the steel surface covered with PPy due to the change in the curve and a considerable decrease in the current. The open-circuit potentials of uncoated steel electrode are -460 , -440 and -480 mV whereas these potential values are -420 , -390 and -450 mV for PPy-coated electrode in 1 M HCl, H_2SO_4 and H_3PO_4 , respectively. These values of the open-circuit potentials of the steel electrode indicate the shift toward the more positive values immediately after the formation of coatings for each acidic medium. For the studied three acids, the variation of open-circuit potentials with immersion time can be seen in Fig 3. However, these values do not significantly change depending on the immersion time. This is consistent with the results of other researchers [11].

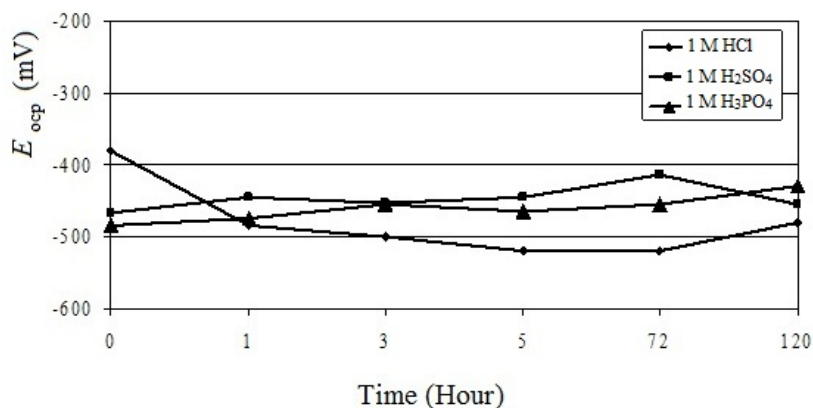


Figure 3. Open-circuit potentials vs immersion time for PPy-coated steel electrode in 1 M HCl, H_2SO_4 and H_3PO_4 media.

The corrosion parameters such as open-circuit potentials (E_{oxp}), anodic Tafel slopes (b_a), corrosion current densities (i_{corr}) and percent inhibition efficiencies ($\eta\%$) determined in these media are shown in Table 2.,

Table 2. Open circuit potentials (E_{oxp}), anodic Tafel slopes (b_a), corrosion current densities I_{corr} and percent inhibition efficiencies ($\eta\%$) obtained for uncoated steel and PPy-coated steel in various immersion time in a) 1 M HCl, b) 1 M H_2SO_4 and c) 1 M H_3PO_4 .

a)	Immersion Time (hour)	$-E_{\text{oxp}}$ (mV)	b_a (mV)	i_{corr} (mA/cm^2)	$\eta\%$
1 M HCl	uncoated	430	70	1.80	—
	immediately after immersion	380	55	0.25	86.1
	1	485	70	0.70	61.1
	3	500	80	1.05	41.6
	5	520	79	1.30	27.7
	72	520	70	1.50	16.6

	120	480	110	1.70	5.5
b) 1 M H₂SO₄	uncoated	390	110	6.00	—
	immediately after immersion	466	165	0.28	95.3
	1	445	148	0.30	95.0
	3	453	163	0.55	90.8
	5	445	144	0.75	87.5
	72	414	138	1.30	78.3
	120	454	160	1.60	73.3
c) 1 M H₃PO₄	uncoated	450	100	2.80	—
	immediately after immersion	485	125	0.125	95.5
	1	475	100	0.215	92.3
	3	455	75	1.00	64.3
	5	465	100	1.01	43.8
	72	455	75	1.59	43.2
	120	430	75	2.00	28.5

Percentage inhibition efficiency ($\eta\%$) and surface coverage degree (θ) were calculated by the use of following equation

$$\eta \% = \frac{i_{\text{corr}} - i'_{\text{corr}}}{i_{\text{corr}}} \times 100 \quad (1-a)$$

$$\theta = \frac{i_{\text{corr}} - i'_{\text{corr}}}{i_{\text{corr}}} \quad (1-b)$$

were i_{corr} and i'_{corr} are the corrosion current densities for uncoated and PPy-coated steel respectively.

According to the data in Table 2a, the E_{ocp} values obtained for uncoated steel in 1 M HCl medium shift more anodic potentials immediately after immersion. However, no regular variation can be seen for the other immersion times. Corrosion current density has been found to be 1.8 mAcm⁻² for uncoated steel while it has been found to be 0.25 mAcm⁻² immediately after coated PPy. Inhibition efficiency was determined as 86.1% immediately after coated PPy. An increase in corrosion current densities and a decrease in inhibition efficiencies have been seen with increasing the immersion time. However, the increase of corrosion current density approximates to the value for the uncoated steel at the end of fifth day. The values of percent inhibition efficiencies decrease with increasing immersion time; it has found to be 5.5% at the end of this period. Hence, it can be concluded that the protection effect of the coated steel becomes lower.

As can be seen from Table 2b, the E_{ocp} values obtained for uncoated steel in 1 M H₂SO₄ medium shift more negative values immediately after immersion and there is no regular change with increasing immersion time. The corrosion current densities increase and the percent inhibition efficiencies decrease depending on the immersion time. Higher inhibition efficiency has been determined in 1 M H₂SO₄ when compared to the value found for the PPy-coated steel in 1 M HCl. This also indicates that the PPy-coated steel has more protective effect.

Table 2c shows the obtained values of corrosion parameters such as E_{ocp} , b_a , i_{corr} and $\eta\%$ in 1 M H₃PO₄. As can be seen from this table, the values of E_{ocp} do not change significantly with increasing immersion time. The corrosion current density has been found to be 2.8 mAcm⁻² for uncoated steel whereas this value is 0.125 mAcm⁻² immediately after coating. However, an increase in i_{corr} and a decrease in inhibition efficiency have been found with increasing the immersion time. According to this table, PPy-coated steel supplies the 28.5% protection effect in 1 M H₃PO₄. The highest corrosion current density of uncoated steel electrode has been found to be in H₂SO₄ medium which is followed by H₃PO₄ and HCl media respectively. $\eta\%$ values vary in the same immersion times as follows:

$$\eta\% (\text{H}_2\text{SO}_4) > \eta\% (\text{H}_3\text{PO}_4) > \eta\% (\text{HCl})$$

$$\eta\% (\text{H}_2\text{SO}_4) > \eta\% (\text{H}_3\text{PO}_4) > \eta\% (\text{HCl})$$

In Figs. 4-6, the variation of $\eta\%$ values with immersion time for PPy-coated steel electrode can be seen in 1 M HCl, H_2SO_4 and H_3PO_4 media, respectively.

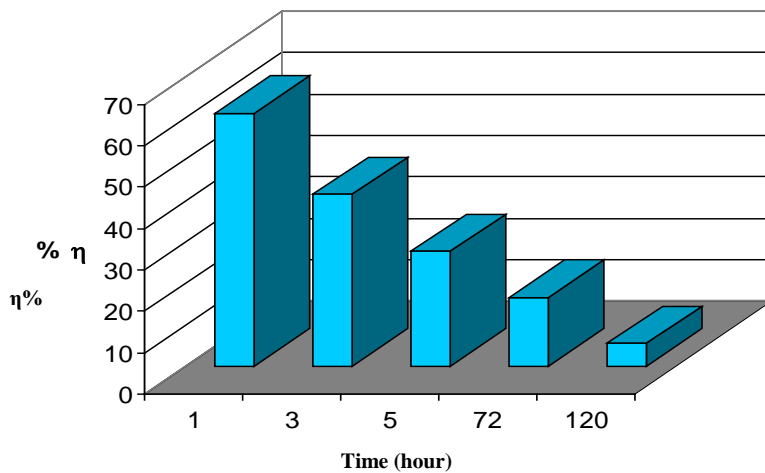


Figure 4. The $\eta\%$ values vs immersion time for PPy-coated steel electrode in 1 M HCl.

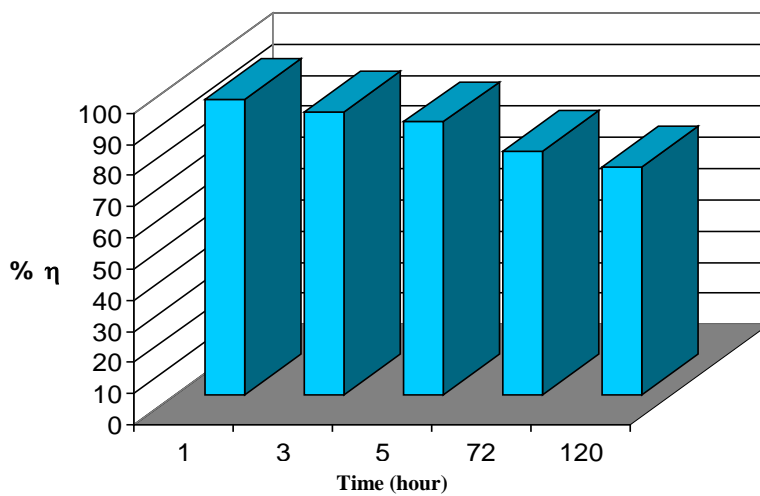


Figure 5. The $\eta\%$ values vs immersion time for PPy-coated steel electrode in 1 M H_2SO_4 .

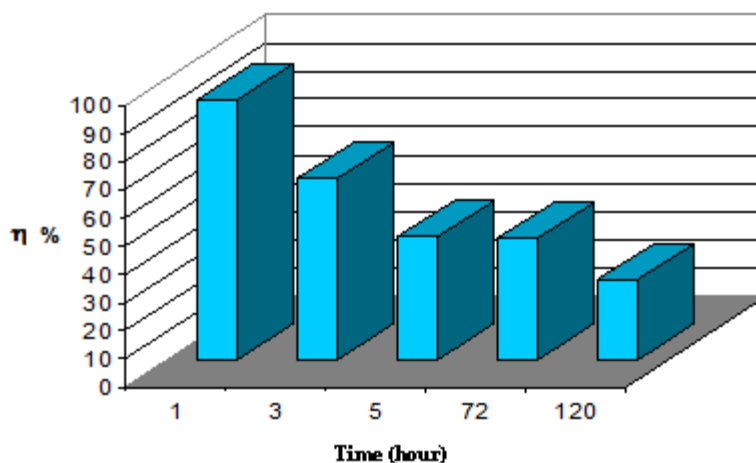


Figure 6. The $\eta\%$ values vs immersion time for PPY-coated steel electrode in 1 M H_3PO_4 .

The corrosion inhibition effect of chloride ions is due to their adsorption on the uncoated steel surface. Since the total Gibbs free energy of water-electrode, ion-electrode, ion-water interactions for the adsorption of Cl^- is, $\Delta G = -8.9$, Cl^- adsorbs on steel surface by contact adsorption [12]. Therefore, the corrosion rate is lower in HCl medium (Table 2a). As is known, the corrosive effect of these ions occurs rather under the coating. The higher corrosion rate of sulphate ions, however, can be explained by considering that sulphate ions are much bigger than chloride ions ($r_{SO_4^{2-}} = 2.30$, $r_{Cl^-} = 1.67$ Å) [13], hardly adsorb on the surface and consequently have less effect (Table 2b).

The protection of phosphate ions on the surface is rather through the formation of iron phosphate compounds. Because of its size ($r_{PO_4^{3-}} = 2.38$ Å), iron-phosphate compound which is partially formed unstable in acidic medium, provides higher protection than that of sulphate (Table 2c). This protective effect can be due to the buffering characteristic of phosphate at the narrow region of the nearest surface. This situation can counteract the protection conferred by sulphate through extending the life of the formed iron-phosphate compound.

For the PPY-coated electrode however, the Cl^- in the polymer is not effective in the control of surface. It is possible for pores to be open constantly due to the continuous motion of Cl^- ions in the polymer pores. Moreover, polymer enhances the corrosive effect of chloride by forming the sub-coating. Though PPY is formed even in the chloride solution, it is not too passive since Cl^- is aggressive and causes to pitting corrosion by settling under the formed passive film. These pits become more stable by the iron-oxalate precipitate; the film is decomposed through the motion of oxalate anions. There is not enough rapid O_2 formation for the maintenance of decomposed passive film in chloride medium. This finding has also been proved by Klimartin et al [14]. Sulphate ions lower the rate of corrosion development and prevent the contact of metal with solution either by penetration or closing the polymer pores at the polymer/solution interface. Hermas et al [15] specify that PPY film keeps the potential of stainless steel more stable and at higher positive values in sulfuric acid medium. Our findings for H_2SO_4 medium also confirm this conclusion. During the electropolymerization of PPY on steel surface, the corrosion of H_2SO_4 and H_3PO_4 can be prevented partially due to the formation of stable oxide layer; that is, PPY prevents the dissolution of steel. This is also reported by Kralzic et al [16]. Our findings also confirm these findings. The effect of phosphate should be close to that of sulphate however, due to the inclination of phosphate ions in the pores to form iron-phosphate, they could have caused the decomposition of polymer film rather than the protection. In this case, protective effect of phosphate is likely to be lower than sulphate.

3. CONCLUSIONS

The conclusions of this study can be drawn as follows:

1. Steel surface can be coated with PPY film via electropolymerization. This coating protects steel against corrosion in HCl, H_2SO_4 and H_3PO_4 media, but this is valid only for short span of time.
2. In all acidic media studied, the more immersion time, the more corrosion densities and fewer percentage inhibition efficiencies were determined.
3. The protective effect of PPY coating formed on steel surface exists mostly in H_2SO_4 medium, and this is followed by H_3PO_4 and HCl media, respectively.

REFERENCES

- [1] P. Ocón, A.B. Cristobal, P. Herrasti, E. Fatas, "Corrosion performance of conducting polymer coatings applied on mild steel," *Corros. Sci.*, vol. 47, pp. 649–662, Mar. 2005.
- [2] P.P. Deshpande, N.G. Jadhav, V.J. Gelling, D. Sazou, "Conducting polymers for corrosion protection: a review," *J. Coatings Technol. Res.*, vol. 11, pp. 473–494, July 2014.
- [3] R. Hasanov, S. Bilgiç, "Monolayer and bilayer conducting polymer coatings for corrosion protection of steel in 1M H₂SO₄ solution," *Prog. Org. Coatings*, vol. 64, pp. 435–445, Mar. 2009.
- [4] R. Hasanov, S. Bilgiç, G. Gece, "Experimental and theoretical studies on the corrosion properties of some conducting polymer coatings," *J. Solid State Electrochem.*, vol. 15, pp. 1063–1070, May 2011.
- [5] N.C.T. Martins, T. Moura e Silva, M.F. Montemor, J.C.S. Fernandes, M.G.S. Ferreira, "Polyaniline coatings on aluminium alloy 6061-T6: electrosynthesis and characterization," *Electrochim. Acta*, vol.55, pp. 3580–3588, Apr. 2010.
- [6] S. Chaudhari, P.P. Patil, "Inhibition of nickel coated mild steel corrosion by electrosynthesized polyaniline coatings," *Electrochim. Acta*, vol. 56, pp. 3049–3059, Mar. 2011.
- [7] A.H. El-Shazly, A.A. Wazzan, "Using polypyrrole coating for improving the corrosion resistance of steel buried in corrosive mediums," *Int. J. Electrochem. Sci.*, vol. 7, pp. 1946–1957, Mar. 2012.
- [8] I.L. Lehr, S.B. Saidman, "Bilayers polypyrrole coatings for corrosion protection of SAE 4140 steel," *Port. Electrochim. Acta*, vol. 32, pp. 281–293, Jan. 2014.
- [9] Y. Dai, "Electrosynthesis and characterization of polythiophene and corrosion protection for stainless steel," *Int. J. Electrochem. Sci.*, pp. 4084–4091, Apr. 2016.
- [10] E. McCafferty, "Validation of corrosion rates measured by the Tafel extrapolation method," *Corros. Sci.*, vol. 47, pp. 3202–3215, Dec. 2005.
- [11] P. Herrasti, P. Ocón, "Polypyrrole layers for steel protection," *Appl. Surf. Sci.*, vol. 172, 276–284, Mar. 2001.
- [12] J.O.M. Bockris, A.K.N. Reddy, *Modern Electrochemistry 2A*, Kluwer Academic/Plenum Publishers, Boston, 1977..
- [13] J.E. Huheey, "Inorganic chemistry principles of structure and reactivity," Harper&Row. Publishers, New York, 1972.
- [14] P.A. Kilmartin, L. Trier, G.A. Wright, "Corrosion inhibition of polyaniline and poly(o-methoxyaniline) on stainless steels," *Synth. Met.*, vol. 131, pp. 99–109, Nov. 2002.
- [15] A.A. Hermas, M. Nakayama, K. Ogura, "Formation of stable passive film on stainless steel by electrochemical deposition of polypyrrole," *Electrochim. Acta*, vol. 50, pp. 3640–3647, June 2005.
- [16] M. Kraljić, Z. Mandić, L. Duić, "Inhibition of steel corrosion by polyaniline coatings," *Corros. Sci.*, vol. 45, pp. 181–198, Jan. 2003.

Analysis of Carrier Based Discontinuous PWM Method for Cascaded H-Bridge Multilevel Inverter Based D-STATCOM

M. Mustafa Ertay^{1}, Ahmet Zengin¹, Murat Kale¹, Murat Karabacak¹, Ihsan Pehlivan¹*

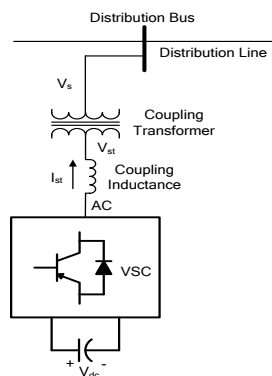
Abstract

Demand of electrical energy is increasing day by day. For this reason, nowadays, energy efficiency on power systems submit the major emphasis. Power electronics based compensation devices are developed to minimize the losses and provide energy efficiency on power systems in parallel with the development of power electronics technology. Distribution static synchronous compensator (D-STATCOM) is one of the custom power devices used in solving the power quality issues and reactive power compensation on distribution systems. In recent years various kinds of multilevel inverters have been used in D-STATCOM circuit structure in different power system applications. In this study, the analysis of cascaded h-bridge inverter D-STATCOM system controlled with proposed carrier based discontinuous pulse width modulation (DPWM) method which is based alternative phase opposition disposition (APOD) is performed. As it is known, DPWM methods are energy efficient PWM methods. D-STATCOM system controlled with proposed DPWM method is modelled in MATLAB-Simulink environment and simulations are accomplished. Proposed DPWM method is compared with continuous PWM methods in terms of harmonic distortion and losses. It is observed in simulations that proposed method with high modulation indexes provides lower harmonic distortions than proposed method with low modulation indexes. Moreover, it is determined that proposed DPWM method significantly reduces inverter losses compared with continuous PWM methods.

Keywords: *Energy demand, Energy efficiency, power systems, Power quality, D-STATCOM, Distribution systems*

1. INTRODUCTION

In recent years the interest on the electrical power and its quality has increased due to the growing energy demand. Therefore this concern has caused to the development of power electronics equipments, which connected to the network to improve the electrical energy transmission and distribution capability of the distribution and transmission networks and also the power quality of the system. These equipments or devices are known as FACTS (Flexible AC Transmission Systems) and CP (Custom Power) devices which are based on power electronics technology. The FACTS and CP devices are utilized in transmission and distribution systems respectively. Also CP devices are known as DFACTS (Distribution FACTS) [1]. The STATCOM (Static Synchronous Compensator) is one of the FACTS controllers that is used for reactive power compensation and to improve voltage stability in transmission systems. The STATCOM utilized in distribution system in low to medium rating is called D-STATCOM [2]. The D-STATCOM (Distribution Static Synchronous Compensator) is constitutively one of the shunt connected CP controllers [1]. The D-STATCOM is used to solve power quality problems and to provide reactive power compensation in distribution systems [2]. Generally power stage of D-STATCOM consists of voltage source converters (VSCs) as seen in Fig. 1 [3]. The D-STATCOM generates three phase output voltages almost in phase with ac network through a coupling inductance [2], [3]. In addition it requires only a small dc capacitor in VSC [2,3].



¹ Corresponding author: Düzce University, Department of Electrical and Electronics Engineering, 81620, Düzce, Turkey.
mustafaertay@duzce.edu.tr

Figure 1 General configuration of D-STATCOM.

Different VSC configurations have been used in D-STATCOM power stage. In addition multilevel VSC have been widely used and studied due to its ability of eliminating the bulky zig-zag transformer. In multilevel VSC based D-STATCOM section, there are mainly three different VSC configurations. These are diode-clamped converter [4-5], flying-capacitor converter [6-7] and cascaded converter configuration [8]. The diode clamped and flying capacitor configurations are require a very large number of clamping diodes or flying capacitors, respectively. But the multilevel cascaded converter has the advantage of using small number of diodes and capacitors. Furthermore, it has a modular structure so its packaging and physical layout is very easy [4].

VSC losses are an important part of total losses of D-STATCOM [9]. In [10], [11] phase shift SPWM method has been used for multilevel converter configurations of STATCOMs. In [12] space vector PWM (SVPWM) method has been utilized for different power circuit and different usage fields of STATCOMs such as wind power. In [13] DC capacitor voltage balance method based on Carrier phase shifted PWM is introduced. In [14] three converter structures (diode clamped, cascaded and hybrid converter) used in STATCOM have been investigated against losses and different load conditions; in that study SVPWM is used in STATCOMs. In [8] authors proposed the cascaded inverters for power applications such as power quality, series compensation, photovoltaic systems as well as FACTS applications; in this work analyses, simulation and experimental studies are carried out for the STATCOM device. In [15] multi-pulse GTO inverter, cascaded inverter and binary inverter utilized in STATCOM configurations have been investigated against losses. In [16] Discontinuous pulse width modulation (DPWM) methods have been utilized in active power filters; in addition the authors proposed a generalized DPWM strategy which reduces switching losses up to 46% as compared to Continuous PWM methods. There are no studies seen in the literature that investigate the effects of using DPWM in cascaded multilevel converter based D-STATCOM. However DPWM methods have been widely used in motor drives in the literature [16,17].

This paper discusses the utilization of carrier based DPWM methods in cascaded multilevel converter based D-STATCOMs in order to reduce the switching losses and analyze its performance on reactive power compensation. For this purpose a simulation model is developed to investigate these characteristics. In this study also reactive power compensation characteristic of D-STATCOM while utilizing DPWM methods is reported.

2. OPERATING PRINCIPLE OF D-STATCOM

According to the application, in distribution systems the D-STATCOM can be operated to for the purposes below [18], [30]:

- a. Voltage control at a specific ac bus
- b. Reactive power compensation of a specific load
- c. Reactive power compensation and/or harmonic compensation of a specific load

The operation principle of D-STATCOM can be explained simply according to Fig.2. In Fig.2 I_{st} is the D-STATCOM injected current which is in quadrature with the system voltage V_s ; it can be lagging (Fig.2. (b)) or leading current (Fig.2 (a)) depending on the operation. Therefore the D-STATCOM current acts as a capacitive or an inductive reactance. R_s corresponds to losses of D-STATCOM system that includes transformer, coupling inductance and converter losses, X_s is the total reactance of D-STATCOM system that includes source, leakage and coupling inductance reactance [2]. V_{st} is the D-STATCOM voltage. If $V_{st} > V_s$ D-STATCOM operates in capacitive mode. While if $V_{st} < V_s$ D-STATCOM operates in inductive mode. If $V_{st} = V_s$ reactive power exchange is zero as seen in Fig.2(c). The magnitude and phase angle of V_{st} against system voltage V_s is determined the D-STATCOM current magnitude and phase angle [2],[3]. This is achieved by providing a small quantity of active power flow in or out of the D-STATCOM. This control method of D-STATCOM is called phase angle control [3]. If we suppose $R \gg X$ the active and reactive power flow between D-STATCOM and ac system can be given in (1) and (2) [2], [3]

$$P = \frac{V_s V_{st}}{X} \cdot \sin \delta \tag{1}$$

$$Q = \frac{V_s}{X} \cdot (V_s - V_{st} \cdot \cos \delta) \tag{2}$$

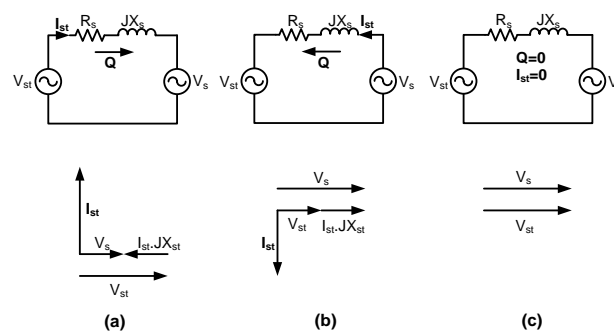


Figure. 2. Basic operating principle of D-STATCOM (a) Capacitive mode and phasors (b) Inductive mode and phasors (c) no compensation [2].

2.1. Cascaded Multilevel Converter Based D-STATCOM and Multilevel PWM strategies

Power stage of three-level H-bridge converter based D-STATCOM is indicated in Fig. 3. As shown D-STATCOM consists of three H-bridge converters [19]. A series connection of H-Bridge converters creates cascaded multilevel converter. Each full bridge consists of a dc capacitor and four power switches that can produce three levels of voltage at its terminals [19]. According to literature, several modulation strategies have been developed for multilevel converters including the following methods: multilevel sinusoidal pulse width modulation (PWM), multilevel selective harmonic elimination (SHEM), space-vector modulation (SVM) [20] and multilevel DPWM [21]-[23].

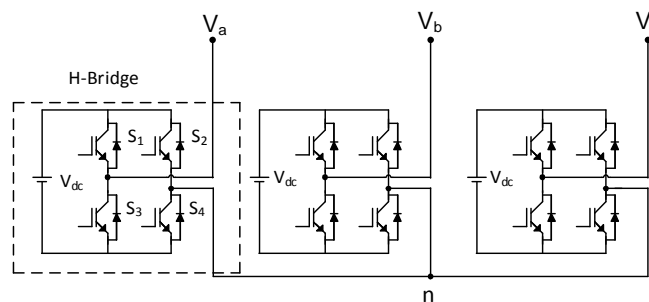


Figure3. Three phase three level cascaded converter

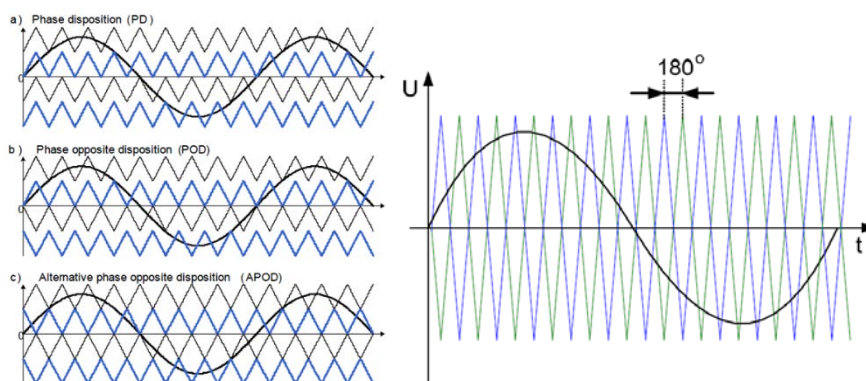


Figure 4. Carrier based PWM schemes for five level converter a) PD b) POD c) APOD d) PSC (For three level) [25].

Carrier based modulation schemes can be classified into two groups a) Phase shifted PWM (PSPWM) b) Level shifted PWM (LSPWM). Various LSPWM based modulation strategies have been developed for multilevel sinusoidal PWM (SPWM), such as alternative phase opposition disposition (APOD), phase opposition disposition (POD), and phase disposition (PD) techniques have been developed for single-phase and three-phase diode clamped inverters [20]-[22]. For the cascaded converter, PSPWM is the common strategy [20]-[24].

As seen in Fig 4. in APOD modulation, where each carrier signal is phase shifted by 180° from adjacent carrier; In POD modulation, where the carrier signals above the sinusoidal reference zero point are 180° out of phase with those below the zero point; In PD modulation, where all carrier signals are in phase. In Phase-Shifted PWM (PSCPWM), where shift N carrier waves by $360/N$ in order to provide $N+1$ level PWM pattern in each phase [20]-[24]. The carrier based DPWM methods for multilevel converters are being derived, in principle, similar to a two-level converter [20]-[24]. In this paper

POD modulation used for generating switching signals of multilevel cascaded converter based D-STATCOM. Since in three level converter APOD and POD modulations are the same.

2.2. Discontinuous PWM Modulation

DPWM is firstly proposed by Depenbrock [26] in 1977. The main idea behind the DPWM is reducing the switching number in every switching period. Hence for 1/3 of the switching period one phase is clamped to positive ($+V_{dc}/2$) or negative ($-V_{dc}/2$) dc bus. During this time of period, modulation is performed by the other two phases. It is clear that there are no switching losses of corresponding clamped phase at this time of period. Therefore total switching losses can be reduced theoretically an average of 33% as compared to CPWM methods [26]-[30].

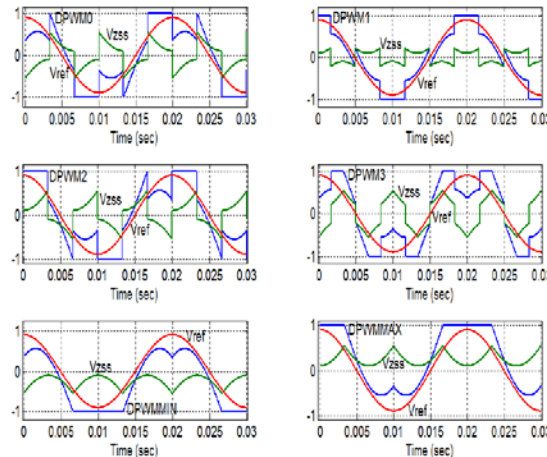


Figure 3. Modulation waveforms of DPWM methods with voltage reference and zero sequence signals ($M_i=0.9$).

There are many DPWM algorithms in the literature. According to distribution of zero vectors and different shape of V_{zss} signals, different DPWM modulation waves can be generated by using the method given in [27]. By using [27] one can obtain modulation waveforms of DPWM methods in MATLAB-Simulink as shown in Figure 5. The carrier based DPWM methods for multilevel converters are being derived, in principle, similar to a two-level converter [20]-[24].

3. MODELING AND CONTROL OF D-STATCOM SYSTEM

In this paper the D-STATCOM system which is illustrated in Fig.6 [30] is modelled in Matlab-Simulink environment. R_{st} and X_{st} is the coupling inductance resistance and reactance of the D-STATCOM respectively. The rating of the D-STATCOM in this system is 250kVAr. The power factor of the system without D-STATCOM is 0.7682 leading/lagging.

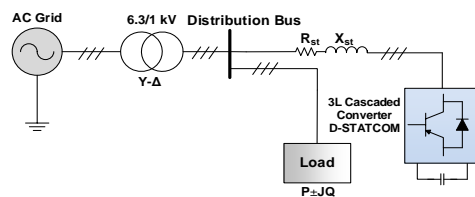


Figure 6 The D-STATCOM system under study.

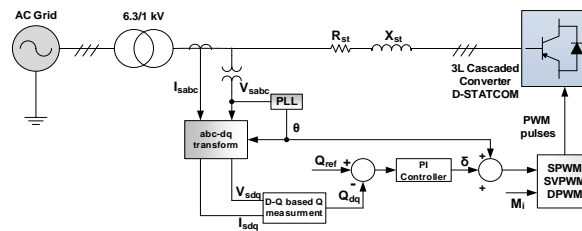


Figure 4 The principle scheme of the phase angle control of the D-STATCOM.

In this paper phase angle control method which is depicted in Fig. 7 is used in the outer control of D-STATCOM [3],[20],[30]. In this control technique the angle (δ) between the system voltage (V_s) and D-STATCOM voltage (V_{st}) changes for accomplishing the reactive power compensation while the modulation index is kept constant [3],[20],[30]. Due to the space constraints some formulations have not shown.

4. THE SIMULATION RESULTS AND DISCUSSIONS

To investigate the performance of carrier based DPWM methods on controlling the D-STATCOM, numerous simulations have been carried out. In these simulations, firstly for capacitive and inductive operation of D-STATCOM; voltage and current harmonics of system, power losses of D-STATCOM have been calculated and analyzed for $M_i = 0.94$. Secondly by changing the M_i of D-STATCOM, the analyzing of voltage and current harmonics of system, have been realized according to capacitive and inductive operation of D-STATCOM. In Fig. 8 the results of reactive power compensation performance of D-STATCOM (in inductive mode when $M_i = 0.94$) in the case of using SPWM method is illustrated. In Fig. 8 (a) active and reactive power variation at distribution bus (DB) is illustrated. D-STATCOM consumes reactive power from the system. Reactive power of DB becomes zero. In Fig. 8 (b) active and reactive power variation of the system before the TR is illustrated. In Fig. 8 (c) active and reactive power variation of the D-STATCOM is illustrated. In Fig. 8 (d) and (e) D-STATCOM phase voltage and line voltage is demonstrated respectively. active and reactive power variation of the system before the TR is illustrated. In Fig. 8 (f) DB voltage and current variation is demonstrated. It is clear that D-STATCOM provide the DB voltage and current at unity. In Fig. 9 the results of reactive power compensation performance of D-STATCOM (in capacitive mode when $M_i = 0.94$) in the case of using SPWM method is illustrated such as Fig.8. Similarly in Fig.10 and Fig.11 the results of reactive power compensation performance of D-STATCOM in inductive and capacitive mode when $M_i = 0.94$ in the case of using DPWM3 method is illustrated respectively. In Fig. 12 (a) Generation of DPWM3 modulation wave is demonstrated. In Fig.12 (b) variation of D-STATCOM current and DPWM3 modulation wave is illustrated. It is clear that clamping is realized at the high values of D-STATCOM current. According to table 1. SPWM and SVPWM methods have good performance in DB harmonic current values against DPWM methods bot in inductive and capacitive operation mode. It is clear that DPWM methods have poor harmonic performance in low modulation indexes. in high modulation indexes especially after $M_i=1$ they have good performance. In table 2. It was shown that when modulation index is increased the harmonic values of the DPWM methods have been decreased. Thus stability of reactive power compensation is increased. In table 3 power losses of D-STATCOM is demonstrated. The switching losses of D-STATCOM reduced up to 50-75% of CPWM methods DPWM3 is superior to the other DPWM methods in terms of reduction of switching losses and total losses.

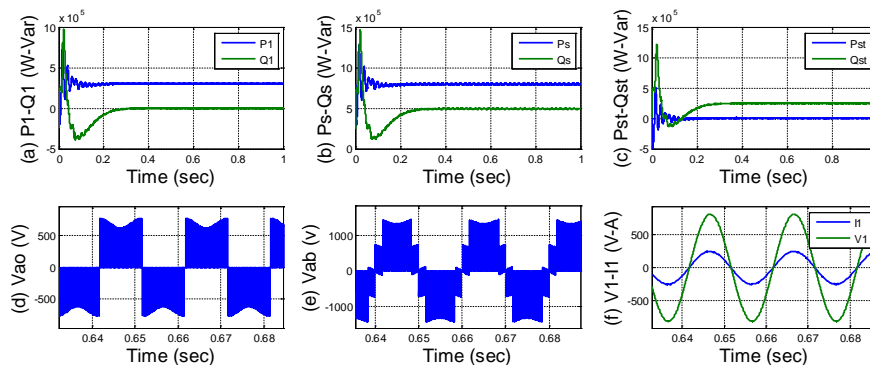


Figure. 8 D-STATCOM compensation performance in the case of using SPWM (Inductive mode) (a) Active and reactive power variation at DB. (b) Active and reactive power variation of the system before the TR (c) Active and reactive power variation of the D-STATCOM. (d) D-STATCOM phase voltage (e) D-STATCOM line voltage. (f) DB voltage and current variation

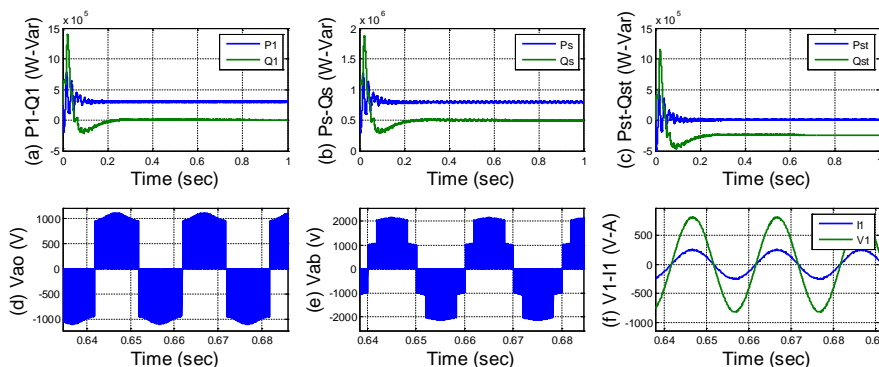


Figure. 9 D-STATCOM compensation performance in the case of using SPWM (Capacitive mode) (a) Active and reactive power variation at DB. (b) Active and reactive power variation of the system before the TR (c) Active and reactive power variation of the D-STATCOM. (d) D-STATCOM phase voltage (e) D-STATCOM line voltage. (f) DB voltage and current variation

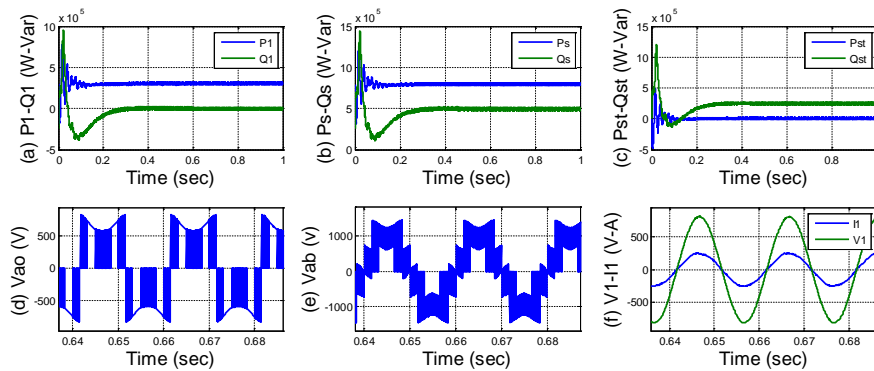


Figure. 10 D-STATCOM compensation performance in the case of using DPWM3 (Inductive mode) (a) Active and reactive power variation at DB. (b) Active and reactive power variation of the system before the TR (c) Active and reactive power variation of the D-STATCOM. (d) D-STATCOM phase voltage (e) D-STATCOM line voltage. (f) DB voltage and current variation.

Table 1. Variation of harmonic values of DB voltage and current and D-STATCOM current ($M_i=0.94$)

PWM Meth	D-STATCOM Operation Mode	D-STATCOM	Distribution Bus	
			THD_V	THD_I
SPWM	Harmonic Distortion			
	THD_I			
SPWM	Capacitive	2.35	0.50	1.89
	Inductive	1.57	0.27	1.05
SVPWM	Capacitive	3.40	0.64	2.75
	Inductive	2.25	0.33	1.60
DPWM0	Capacitive	3.73	0.53	3.01
	Inductive	2.76	0.29	2.11
DPWM1	Capacitive	3.02	0.41	2.43
	Inductive	1.96	0.23	1.47
DPWM2	Capacitive	3.45	0.52	2.8
	Inductive	2.92	0.28	2.28
DPWM3	Capacitive	5.80	0.61	4.61
	Inductive	4.64	0.34	3.72

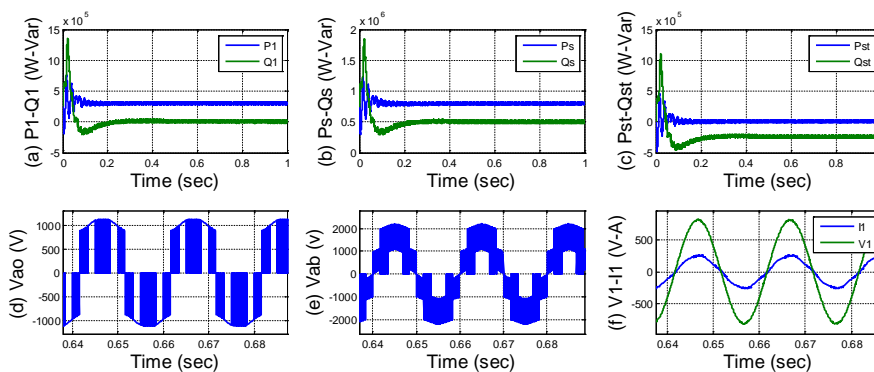


Figure. 11 D-STATCOM compensation performance in the case of using DPWM3 (Capacitive mode) (a) Active and reactive power variation at DB. (b) Active and reactive power variation of the system before the TR. (c) Active and reactive power variation of the D-STATCOM. (d) D-STATCOM phase voltage (e) D-STATCOM line voltage. (f) DB voltage and current variation

Table 2. Variation of harmonic values of DB voltage and current and D-STATCOM current

PWM Method	Distribution Bus				D-STATCOM		M_i
	Capacitive		Inductive		Capacitive	Inductive	
	THD_I	THD_V	THD_I	THD_V	THD_I		
SPWM	1.65	0.40	1.07	0.22	2.06	1.49	1
	3.11	0.29	1.59	0.18	3.89	2.04	1.155
SVPWM	2.37	0.54	1.77	0.29	2.95	2.38	1
	1.73	0.29	1.96	0.19	2.16	2.45	1.155
DPWM0	2.75	0.47	1.99	0.26	3.41	2.61	1
	2.06	0.28	1.81	0.19	2.57	2.31	1.155
DPWM1	1.81	0.37	1.2	0.21	2.24	1.62	1
	1.33	0.24	1.26	0.17	1.65	1.64	1.155
DPWM2	2.60	0.46	2.06	0.26	3.22	2.63	1
	1.71	0.27	2.06	0.19	2.11	2.57	1.155
DPWM3	4.18	0.54	3.35	0.30	5.21	4.19	1
	2.49	0.31	2.56	0.20	3.10	3.19	1.155

Table 3. Variation of power losses of D-STATCOM ($M_i:0.94$)

PWM Method	D-STATCOM Operation Mode	Power Losses (Watt)		
		Switching	Conduction	Total
SPWM	Capacitive	1300	1576	2875
	Inductive	1348	1650	2998
SVPWM	Capacitive	1187	1588	2775
	Inductive	1198	1647	2844
DPWM0	Capacitive	455	1598	2053
	Inductive	431	1650	2081
DPWM1	Capacitive	596	1589	2185
	Inductive	633	1667	2300
DPWM2	Capacitive	405	1580	1985
	Inductive	429	1680	2109
DPWM3	Capacitive	337	1586	1923
	Inductive	315	1673	1988

5. CONCLUSION

A three level cascaded converter based D-STATCOM is modelled in MATLAB-Simulink. In the inner control carrier based POD-DPWM methods are used. In this paper using of carrier based POD-DPWM methods in the D-STATCOM for reactive power compensation applications is analyzed. The results have been reported. As a result, it is found that POD-DPWM3 method is gives the significant result in the reduction of switching losses against the CPWM methods. As a

general result DPWM methods can be applied to D-STATCOM in high modulation indexes, especially after the modulation index of 1.

ACKNOWLEDGMENT

This study was supported by Scientific Research Projects (SRP) committee of Sakarya University in Turkey. (Project number :2013-09-00-002)

REFERENCES

- [1]. J. A. Barrena, L. Marroyo, M. Á. Rodríguez, Ó. Alonso, J. R. Torrealday, "DC Voltage Balancing for PWM Cascaded H-Bridge Converter Based STATCOM", IECON 2006 - 32nd Annual Conf. on IEEE Industrial Electronics, 1840 – 1845, 2006
- [2]. B. Singh, R. Saha, A. Chandra, K. Al-Haddad, "Static synchronous compensators (STATCOM): a review", IET Power Electron., Vol. 2, Iss. 4, pp. 297–324,2009.
- [3]. A. Çetin, M. Ermis, "VSC-Based D-STATCOM With Selective Harmonic Elimination" IEEE Trans. On Ind. Applications, Vol. 45, No. 3, 1000-1015, 2009.
- [4]. Wanki Min, Joonki Min, Jaeho Cho, "Control of STATCOM Using Cascade Multilevel Inverter for High Power Application", IEEE 1999 International Conference on Power Elec. and Drive Sys., PEDS'99, July 1999, Hong Kong.
- [5]. L. H. Walker, et. al., "Force-commutated reactive power compensator," IEEE Trans. Ind. Appl., vol. IA-22, no. 6, pp. 1091-1 104, Nov./Dec. 1986.
- [6]. Nam S. Choi, et. al., "Modeling and analysis of a static var Compensator using multilevel voltage source inverter", IEEE/IAS'94 Annual Meeting, pp. 946-953,1994.
- [7]. C. Hochgraf, et. al., "Comparison of multilevel inverters for static var compensation," in Conf. Rec. IEEE/JAS Annual Meeting., 1994, pp. 921-928.
- [8]. F. Z. Peng, al., "A multilevel voltage-source inverter with separate DC sources for static var generation," IEEE Trans. on Industry Applications, vol. 32, no. 5, pp.1130-1 138, September/October, 1996.
- [9]. N.G. Hingorani, L. Gyugyi. "Understanding FACTS:concepts and technology of flexible ac transmission systems",IEEE Press. New York, 1999.
- [10]. K. Sundararaju, A. Nirmal Kumar", Control Analysis of STATCOM with Enhanced Methods for Compensation of Load Variation", European Journal of Scientific Research Vol.53 No.4, pp.590-597,2011.
- [11]. H. Masdi, N. Mariun, S.M. Bashi, A. Mohamed, S. Yusuf "Construction of a Prototype D-Statcom for VoltageSag Mitigation", European Journal of Scientific Research, Vol.30 No.1, pp.112-127, 2009.
- [12]. Z., Shu, N. Ding, J. Chen, H. Zhu, X. He, "Multilevel SVPWM with DC-Link Capacitor Voltage Balancing Control for Diode-Clamped Multilevel Converter based STATCOM", IEEE Trans. On Ind. Electronics, Issue: 99, Vol. 60, No. 5, 1884-1896, 2013.
- [13]. M. Saeedifard, R. Iravani, J. Pou, "Control and DC-capacitor voltage balancing of a space vector-modulated five-level STATCOM",IET Power Electronics, Vol. 2, Iss. 3,p 203-215, 2009.
- [14]. Zeng Guang Yang Bo Zhong Yanru, Cascaded Multilevel STATCOM DC Capacitor Voltage Balance Method Based on CPS-PWM, IEEE Power Engineering and Automation Conference (PEAM), 2011
- [15]. P. Lauttamus,H. Tuusa, "Comparison of Five-Level Voltage-Source Inverter Based STATCOMs", Power Conversion Conf., P., 659 – 666, 2007.
- [16]. Lee, C.K.; Leung, J.S.K.; Hui, S.Y.R.; Chung, H.S.-H., "Circuit-level comparison of STATCOM technologies" IEEE Transactions on Power Electronics, Volume: 18, Issue: 4, P.,1084 – 1092, 2003.
- [17]. L. Asiminoaei, P. Rodríguez, F. Blaabjerg, "Application of Discontinuous PWM Modulation in Active Power Filters", IEEE Trans. on Power Electronics", Vol. 23, No. 4, 2008.
- [18]. A. M. Hava, R. J. Kerkman, T. A. Lipo, "Simple and Analytical and Graphical Methods for Carrier-Based PWM-VSI Drives", IEEE Trans. On Power Electro. vol.14, no. 1, pp. 49-60, 1999.
- [19]. G. Ledwich, A. Ghosh, "A flexible D-STATCOM operating in voltageor current control mode" IEE Proc.-Gener. Transm. Distrib. Vol. 149, No. 2, 215-224, 2002.
- [20]. R. Coteli, E. Deniz, B. Dandil, S. Tuncer, F. Ata,"Phase Angle Control of Three Level Inverter Based D-STATCOM Using Neuro-Fuzzy Controller", Advances in Elect. and Comp. Eng.Vol. 12, NO 1, 77-84, 2012.
- [21]. Roozbeh Naderi and Abdolreza Rahmati, Phase-Shifted Carrier PWM Technique for General Cascaded Inverters IEEE TRAN. ON INDUSTRIAL ELECTRONICS, VOL. 58, NO. 9, SEPTEMBER 2011
- [22]. Poh Chiang Loh, Donald Grahame Holmes, Yusuke Fukuta, and Thomas A. Lipo, "Reduced Common-Mode Modulation Strategies for Cascaded Multilevel Inverters", IEEE TRAN. ON INDUSTRY APP., VOL. 39, NO. 5, SEPT./OCTOBER 2003, 1386-1395.
- [23]. N. V. Nguyen, B. X. Nguyen, H. H. Lee, "An Optimized Discontinuous PWM Method to Minimize Switching Loss for Multilevel Inverters", IEEE TRANSACTIONS ON POWER ELECT., VOL. 23, NO. 3, MAY 2008 1257-1269.
- [24]. B. P. McGrath and D.G. Holmes, "A Comparison of Multicarrier PWM Strategies for Cascaded and Neutral Point Clamped Multilevel Inverters", Power Electronics Specialists Conference, 2000. PESC 00. 2000 IEEE 31st Annual,674-679, 2000
- [25]. Wojciech Kołomyjski, Modulation Strategies for Three-level PWM Converter-fed Induction Machine Drives,Ph.D. THESIS WARSAW UNIVERSITY OF TECHNOLOGY, Faculty of Electrical Engineering Warsaw, 2009
- [26]. M. Depenbrock, "Pulse width control of a 3-phase inverter with nonsinusoidal phase voltages", IEEE Int. Semiconductor Power Con. Conf., 1977, pp. 399–403.
- [27]. V. Blasko," Analysis of a hybrid PWM based on modified space-vector and triangle-comparison methods", IEEE Trans. on Industry Appl., Vol.:33, Issue: 3, 756 – 764,1997.
- [28]. A. M. Hava, R. J. Kerkman, T. A. Lipo, "A high performance generalized discontinuous PWM algorithm," IEEE Trans. Ind. Appl., vol.34, no. 5, pp. 1059–1071, 1998.
- [29]. D.Graham Holmes, Thomas A. Lipo,"Pulse width Modulation for power Converters: Principles and Practice",IEEE Series on Power Engineering, IEEE PRESS, John Wiley&Sons,2003.
- [30]. M.M.Ertay, A. Zengin, "ANALYSIS OF THE DISCONTINUOUS PWM CONTROLLED D-STATCOM FOR REACTIVE POWER COMPENSATION APPLICATIONS", Tehnički vjesnik 21, 4(2014), 825-833,2014

The Selection of The Most Suitable Image Subsets for Camera Calibration

Ozkan Bingol¹, Murat Ekinci²

Abstract

Camera calibration is a pretreatment to determine the physical properties of a camera. In particularly, it has been used in the studies that are produce metric information from 2D images. In order to perform calibration, a planer calibration pattern is usually preferred. Images are taken at different angles by moving this pattern. Camera parameters are calculated with the help of the common points determined on these images. However, using different image sets may cause production of different parameters. Therefore the selection of the most suitable image subsets for camera calibration is a great importance for the success of the measurement. The complexity of creating a subset of images where the total number of images is much, increases exponentially.

In this study, it is demonstrated that the genetic algorithm can be used in order to select the most appropriate subset of the set of images. Different datasets containing chessboard pattern is used to measure the success of the genetic algorithm implemented. In the algorithm, the length of each chromosome is the same as the number of images and genes are encoded in binary. The Euclidean distance between the coordinates produced by calculated parameters and the coordinates of the original image is taken as the fitness function. The study results showed that the error rate of the selected image subsets falls below 0.1 pixel per point.

Keywords: Camera Calibration, Genetic Algorithm, Image Subsets

1. INTRODUCTION

Camera calibration is the process of determining the 3D position and extrinsic parameters with the geometric and intrinsic parameters of a camera [1]. This process, particularly, in the studies which the metric information is produced from 2D images is used as a preliminary step. Generally, the calibration process is applied only once, and the obtained values is used in all other stages. Therefore, the accuracy of this process influences measurements of the next stages significantly.

In 3D space, relation between a point $P_w[X, Y, Z]$ and its projection on the image $p_{im}[u, v]$, with the help of the homogeneous coordinates, can be defined as follows;

$$s \cdot \widetilde{p}_{im} = K[R \mid T] \widetilde{P}_w \quad (1)$$

Here s is an arbitrary scale factor, $\widetilde{p}_{im} = [u, v, 1]^T$ and $\widetilde{P}_w = [X, Y, Z, 1]^T$. K is a matrix containing the intrinsic parameters of the camera and is defined as follows.

$$K = \begin{bmatrix} \alpha_u & \gamma & u_0 \\ 0 & \alpha_v & v_0 \\ 0 & 0 & 1 \end{bmatrix} \quad (2)$$

α_u and α_v in K matrix are focal length on x and y axis of the image, γ is skew factor and (u_0, v_0) is principle point. R in equation 1, shows the orientation of the camera in 3D space and T is the position.

$$R = \begin{bmatrix} r_{11} & r_{12} & r_{13} \\ r_{21} & r_{22} & r_{23} \\ r_{31} & r_{32} & r_{33} \end{bmatrix} \quad T = \begin{bmatrix} t_1 \\ t_2 \\ t_3 \end{bmatrix} \quad (3)$$

Camera calibration is the process of finding the parameters in equation-1. Also in addition to these parameters, radial (k_1, k_2 and k_3) and tangential distortion parameters (p_1 and p_2) are found.

$$u' = u(1 + k_1 r^2 + k_2 r^4 + k_3 r^6) + 2p_1 uv + p_2(r^2 + 2u^2) \quad (4)$$

$$v' = u(1 + k_1 r^2 + k_2 r^4 + k_3 r^6) + p_1(r^2 + 2v^2) + 2p_2 uv \quad (5)$$

$$r^2 = u^2 + v^2 \quad (6)$$

¹Corresponding author: Gümüşhane University, Department of Software Engineering, 29100, Gümüşhane, Turkey. bingolo@gumushane.edu.tr

²Karadeniz Technical University, Department of Computer Engineering, 61100, Trabzon/ Turkey, ekinci@ktu.edu.tr

The methods developed for the calibration according to the commonly used calibration objects can be grouped as 3D reference object based [2], 2D plane based [1],[3],[4], 1D line based [5] and self-calibration [6]-[8]. Apart from these, there are some techniques such as vanishing points[9],[10] and pure rotation [11],[12] developed by using the features of the images [16].

2D plane based calibration techniques are widely used among these studies. Because producing planar calibration patterns is very cheap and easy [2]. Zhang[4], proposes a self-calibration approach which uses a chessboard as planar pattern. In this approach, several images in different directions of the pattern is sufficient. Moreover, there is no need to know the directions of the pattern. This approach is still used more widely. In the study, due to the calibration patterns in a plane, it is considered as $Z = 0$ and perspective transformation is defined as in equation 7.

$$s \cdot \widetilde{p}_{im} = K \begin{bmatrix} r_{11} & r_{12} & t_1 \\ r_{21} & r_{22} & t_2 \\ r_{31} & r_{32} & t_3 \end{bmatrix} \begin{bmatrix} X \\ Y \\ 1 \end{bmatrix} \quad (7)$$

Zhang[4] put forth the closed-form solution of this approach by finding the parameters that minimizes the following function using Levenberg-Marquardt algorithm. In this function, $\hat{p}(K, R_i, T_i, P_j)$ is the projection on the image i of 3D point P_j .

$$\sum_i \sum_j \left(p_{ij} - \hat{p}(K, R_i, T_i, P_j) \right)^2 \quad (8)$$

Different images that are used for calibration of a camera lead to the production of different intrinsic parameters [14]. These differences can cause serious problems especially in metric measurements. Therefore it is a need to determine the most appropriate images to set the ideal parameters. This will also cause exponentially growing calculation complexity in the case where more number of images. If m is considered as number of most appropriate ones in N image sets, the number of subset that need to be check will be $\frac{N!}{m!(N-m)!}$. Zhang[4] noted that the value of m should be at least 2. However, in the literature, there is no information about the number of images needed in order to obtain best calibration results. Therefore there is uncertainty about the number of images to choose. So entire subsets of the total number of N images are required to be controlled. In this case in order to find the best calibration parameters, $2^N - n$ number of experiments should be done. For example, for the number of 20 image, there should be 1.048.556 number of alternative calibration need to be tried to find the most appropriate one.

In order to select the most appropriate image set, Semeniuta [13] has proposed a method based on quantitative analysis of probabilistic distribution of intrinsic parameters. In this iterative method, n subsets is created from m image which the calibration pattern can be determined from. 9 intrinsic parameters obtained by calibration for each set are stored in a matrix. In each iteration, among the parameter columns of this matrix, the row that has value outside of $[\mu_p - 3\sigma, \mu_p + 3\sigma]$ range is deleted. (μ_p : Average error, σ : Standard deviation of the errors). This process is continued until there is no row to be deleted. In this approach, m which contains a subset is kept as constant. However, an images set less or more than m can produce better calibration result. Another approach is proposed by Brendan et al. [14]. In this approach, for the selection on images, Selected Image network structure is established. Then, more appropriate parameters are tried to be determined on this image network.

Selection of more appropriate images for calibration is a problem that finding the ideal subset of a set. A well-established genetic algorithm can provide an ideal solution for such problems. In this study, in order to select best images for calibration, a genetic algorithm is implemented. In this proposed approach, instead of choosing a certain number of images, a structure is provided that can be considered simultaneously for all images. In order to evaluate the results of the implementations, an image dataset containing three different chessboard is used. Two of them are well known image sets in the literature. The third one is a new dataset that we created containing 74 image. The study results show that the error rate of the selected image subsets reduce below 0.1 pixel per point.

This paper is organized as follows. In the second part, a brief information about genetic algorithm is given and how the algorithm is implemented to select the appropriate images is explained. Performance in different image sets shown in the third part. In the last part, the overall evaluation is made for the study.

2. MATERIALS AND METHODS

2.1 Genetic Algorithm (GA)

GA which was first proposed by Holland [15], is imitate the evolutionary process for the solution of problems. GA, instead of developing a single structure for the solution, form a set consisting of structures. Genetic algorithm use information of individuals which are possible solutions for the problem to achieve the optimal solution. Each individual named chromosome, comprises a gene sequence. Genes are encoded in computer form of the problem. GA seeks the solution iteratively and very basic steps shown as follows:

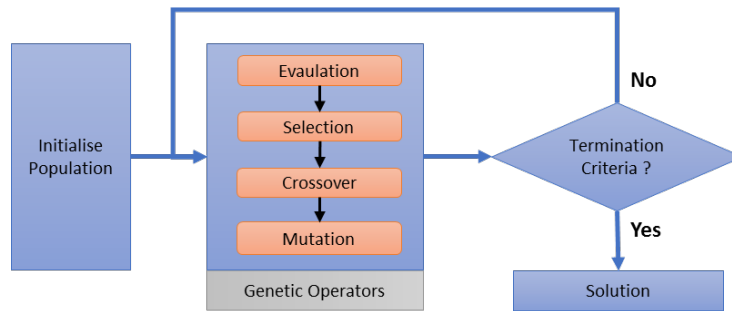


Figure 5. GA steps

- 1) **Initialize Population:** Population is a set of individuals obtained in each iteration. Initialize population is population contain randomly encoded individuals at the beginning of the algorithm
- 2) **Genetic Operators:** Operators that are representing the evolutionary process. There are different techniques to apply for each genetic operators. Which techniques will be used for in which operators usually depends on the problem and effect the success of the algorithm.
 - **Evaluation:** Evaluate the fitness value for each individuals.
 - **Selection:** Depends on the fitness value, determination of an individual will be in the next generation or not.
 - **Crossover:** The process of changing a part of gene sequence of two chromosomes. This process occurs as a result of new individuals.
 - **Mutation:** Change one or more gene of an individual is made. In this process an individual in the population is changed.
- 3) **Termination Criteria:** Usually a certain number of iteration is determined. Also the algorithm can be terminated by an expected fitness value.

2.2. Implementation of GA

- 1) **Chromosome Encoding:** Let the all images taken for the calibration create the set $A = \{I_1, I_2, \dots, I_N\}$ (N : number of images). Each individual for GA shows the images will be used. Thus each individual is coded N length in binary. Chromosome for an individual is shown in Figure 2. In a chromosome, gene which is T (True) indicates that selection of the image in the same row in the set A .



Figure 6. Structure of a chromosome

- 4) **Initial Population:** 20 individuals in the initial population is created for GA. Gene in the chromosomes of the individuals are determined randomly.
- 5) **Selection:** Individuals that will be in the new generation are selected by elitist and roulette wheel approaches. First $populationSize * \lambda$ number of individuals which has best fitness function value are added to the new population. Number of $populationSize * (1 - \lambda)$ individuals in the remaining ones are chosen by roulette wheel. Here, λ is the ratio of the elite selection ($0 \leq \lambda \leq 1$).
- 6) **Crossover:** Each two individuals in current population are group and new individuals are form by crossover operation. N -point crossover is used to cross. N is selected randomly at each crossover period. Similarly each crossover point is determined randomly. Thus it aims to increase the diversity chromosome. For $N = 3$, a crossover process is shown in Figure 3.

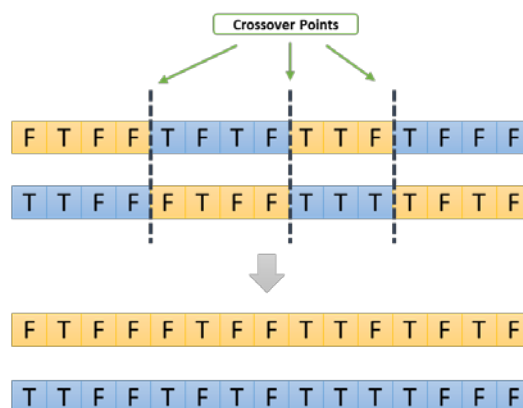


Figure 7. N-point crossover process (N=3)

- 7) **Mutation:** This process is performed in the new population which forms by individuals after the crossover process. Mutation rate is applied as 0.05. A random value (r) is selected for each individual in the population. For each individual, if r is less than the mutation rate, a random gene for the individual is changed.
- 8) **Fitness Function:** Fitness value for an individual is calculated with the help of parameters obtained by the calibration which is performed with the images according to the genes in the individuals. Euclidean distance between a point (x, y) in the original image and projected (x^r, y^r) point gives the error rate for this point. Fitness value (Root Mean Squared Error – RMS Error) is the average of the error values for all points in the chessboard pattern (equation 9).

$$fit = \frac{1}{n} \sqrt{\sum_{i=1}^n ((x_i - x_i^r) + (y_i - y_i^r))^2} \quad (9)$$

- 9) **Termination Criteria:** Max number of iterations for the GA is designated as 100. The algorithm often achieves the optimum value before the upper limit.

Determined parameter values or types for GA are given in Table 1.

Table 1. Implemented GA parameters

Parameter	Value/type
Initial population size	20
Crossover type	N-point
Crossover cut point selection	Random
Mutation type	Random
Mutation rate	0.05
Selection type	Elitist and Roulette wheel
Elitist selection rate (λ)	0.25
Roulette wheel selection rate ($1 - \lambda$)	0.75
Population size	20
Iteration Number	100

2.3. Image Datasets

To test the results of the study, initially, two open access image sets are used. These images are taken from the OpenCV library which is often preferred for camera calibration and Matlab. In addition to these datasets, there is also another dataset that we created using our camera system. Some details about the datasets are given in Table 2. Sample images can be seen in Figure 4.

Table 2. Attributes of used image datasets

Attributes	OpenCV	Matlab	Our Images
Number of images	13	28	74
Resolution	640x480	1600x480	640x480
Cheesboard size	9x6	7x6	5x4

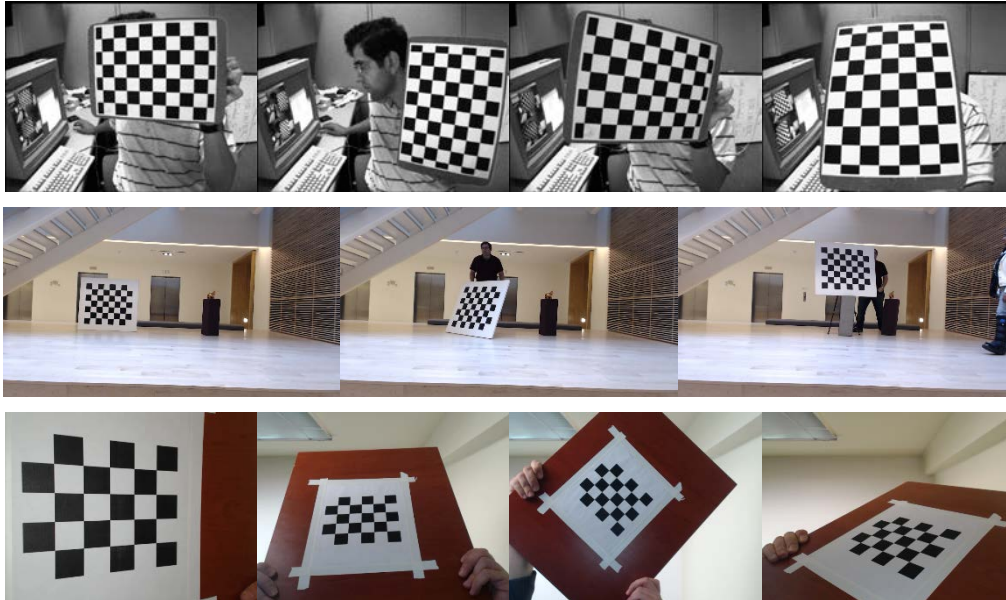


Figure 8. Calibration Images. OpenCV, Matlab and Our image samples are in first, middle, last row, respectively.

3.RESULTS AND DISCUSSION

3.1.Calibration Results without GA

In order to show the impact of the proposed method, calibrations are made for all images in each dataset. The intrinsic parameters obtained by this calibrations are shown in Table 3. Also reprojection error (RMS Error) values calculated with this parameters are in the table.

Table 3. Calibration results without GA

Parameter	OpenCV Images	Matlab Images	Our Images
α_u	535.93191	1163.12878	615.15558
α_v	535.91222	1161.23141	615.39200
u_0	342.05964	776.31139	325.01903
v_0	235.87382	459.23915	242.88648
k_1	-0.27370	0.10694	0.10455
k_2	0.01132	-0.09835	-0.21459
k_3	0.00179	-0.00391	-0.00318
p_1	-0.00033	-0.00081	-0.00051
p_2	0.14421	-0.32354	0.07772

RMS Error 0.39327 0.10308 0.62601

3.2. Calibration Results with GA

In order to evaluate the results of the research, RMS values generated by the population in each iteration are followed. Average and min RMS error values for 3 dataset are shown in Figure 5. After implementing the proposed GA approach on selected OpenCV images, it can be seen in Figure 5a that the ideal results are obtained quickly. Min RMS error value in 12th iteration is 0,15410. This value is reduced to approximately 1/3 of the value in Table 3. The developed program is repeated at different times for this dataset and reached similar RMS values between 9th and 17th iterations. The reason for reaching the ideal value very easily is due to the small number of images are used.

In the last iteration, a total of 5 images of the individual which has min RMS value are selected. Index number of these images are 3, 5, 6, 10 and 12. So that the proposed approach indicate that these images are sufficient for the ideal calibration parameters. Calibration parameters obtained from these images are shown in Table 4.

After implementing the proposed approach to Matlab dataset consisting of 28 image, average and min RMS values in each iteration are shown in Figure 5b. In this test, the best value 0.08426 is reached in 59th iteration. Comparing to the OpenCV images, it can be said that a parallel reduction is occur between average RMS errors and min RMS errors. Having a greater number of images increases chromosome diversity. Also it increases the production of individuals which has best value. This also creates a positive impact on selection of images and the success of the algorithm. Due to the distortions on Matlab images comparing to OpenCV images are less, produced RMS errors are lower. Individuals with the best RMS error obtained the algorithm, in their genes, true value is determined for 8 images (1, 2, 4, 8, 9, 10, 14 and 19). Calibration results obtained by this image set are shown in Table 4.

According to the previous two datasets, having higher number of image leads to better results as its increases alternative options. Because of that, in the scope of the study, a new dataset consisting of more images is created. There are 74 image in this set. Produced average and min RMS error values as a result of the algorithm are shown in Figure 5c. In this experiment, best RMS value (0,08501) is obtained in 99th iteration. This value is reduced to approximately 1/7 of the value in Table 3. There are 13 images in the individual with the best value (21, 22, 24, 27, 30, 34, 35, 38, 44, 48, 66, 71 and 74). Intrinsic parameters obtained from this images are shown in Table 4.

As the optimal value is achieved in 99th step in our images, it show that better results can be obtained in the next iterations. Therefore tests with 500 iterations is made on the same dataset. As a result of the tests the best RMS error value (0.06906) is obtained in 341th iteration. Produced RMS value is better the trail with 100 iteration. It indicates that in order to determine the number of iterations, a value of proportional to the number images in the dataset should be selected. In this experiment, there are 10 images in the individual with the best RMS value (21, 26, 27, 30, 34, 35, 38, 41, 48 and 65). There are same images in both experiment (21, 27, 30, 34, 35, 38 and 48). Results are shown in Table 4. and Figure 5d.

Table 4. Calibration results of image datasets with GA

Parameter	OpenCV Images	Matlab Images	Our Images (100 iter)	Our Images (500 iter)
α_u	532.07871	1173.12128	618.27861	613.89872
α_v	532.25264	1169.17999	617.36761	616.20427
u_0	341.29071	788.75975	321.45843	320.69082
v_0	233.45891	457.50886	253.29876	241.48426
k_1	-0.28190	0.06930	0.07698	0.08212
k_2	0.07940	0.46546	-0.12148	0.00341
k_3	0.00101	-0.00378	0.00401	-0.00275
p_1	-0.00010	0.00251	-0.00093	-0.00286

p_2	0.01670	-2.82264	0.23421	-0.86427
RMS Error	0.15410	0.08426	0.08501	0.06906

4. CONCLUSIONS

In the literature, very effective approaches are proposed for camera calibration. Among these approaches, in particular the ones that use a 2D plane for calibration pattern has come to the fore. Despite producing good results on sample images in order to test the success of these approaches, having similar results on real applications is sometimes difficult. This difficulty can be caused by factors such as noise or distortion in the images used. Therefore selecting the most appropriate images for calibration emerges as a problem. Also, to achieve the best calibration value how many images will be used is not clear.

In this study, it has been shown to overcome this problem by using genetic algorithm, one of the heuristic algorithm techniques. Results indicate that there are improvements on the error values obtained from the images determined by the algorithm in accordance with the error values obtained from images without being selected. These values are greatly important especially in the areas where precise measurements are made.

Selecting the most suitable images is a classic problem of finding a subset. A well-formed GA produces very good results in such problems. In fact, other heuristic approaches instead of GA can also make great improvements. In continuation of this work, different algorithms will be used to have better results.

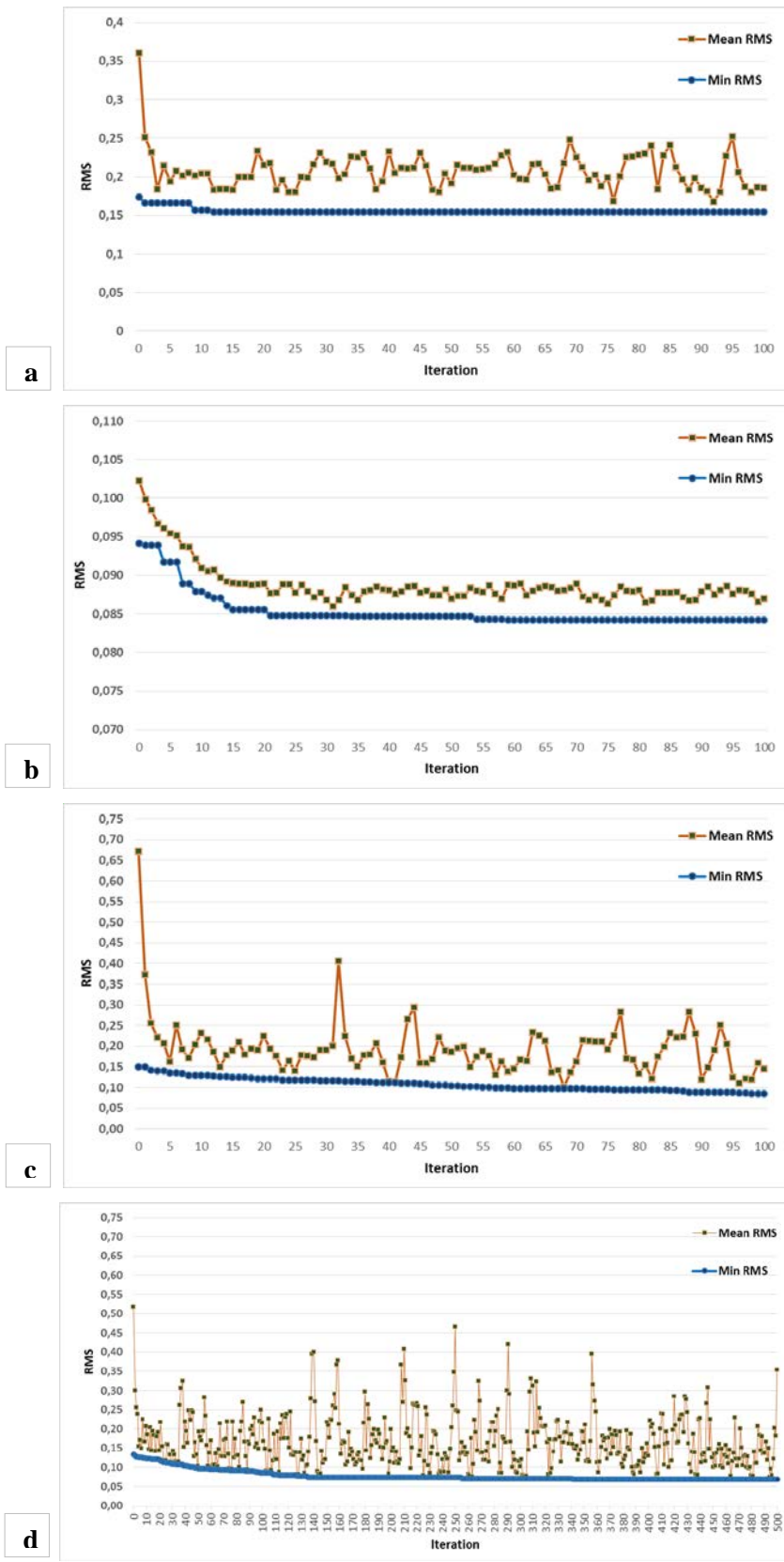


Figure 9. RMS error values of GA implementation in Image Datasets. a) OpenCV images, b) Matlab images c) Our Images (100 iteration) d) Our Images (500 iteration)

REFERENCES

- [1]. R. Y., Tsai. A versatile camera calibration technique for high-accuracy 3D machine vision metrology using off-the-shelf TV cameras and lenses. *Robotics and Automation, IEEE Journal of*, 3(4), 323-344, 1987.
- [2]. O., Faugeras. *Three-Dimensional Computer Vision: a Geometric Viewpoint*. MIT Press, 1993.
- [3]. P. Sturm and S. Maybank. On plane-based camera calibration: A general algorithm, singularities, applications. In *Proceedings of the IEEE Conference on Computer Vision and Pattern Recognition*, pages 432–437, Fort Collins, Colorado, June 1999. IEEE Computer Society Press.
- [4]. Z. Zhang. A flexible new technique for camera calibration. *IEEE Transactions on Pattern Analysis and Machine Intelligence*, 22(11):1330–1334, 2000.
- [5]. Z. Zhang. Camera calibration with one-dimensional objects. In *Proc. European Conference on Computer Vision (ECCV'02)*, volume IV, pages 161–174, Copenhagen, Denmark, May 2002.
- [6]. R. Hartley. An algorithm for self calibration from several views. In *Proceedings of the IEEE Conference on Computer Vision and Pattern Recognition*, pages 908–912, Seattle, WA, June 1994. IEEE.
- [7]. Q.T. Luong and O.D. Faugeras. Self-calibration of a moving camera from point correspondences and fundamental matrices. *The International Journal of Computer Vision*, 22(3):261–289, 1997
- [8]. S. J. Maybank and O.D. Faugeras. A theory of self-calibration of a moving camera. *The International Journal of Computer Vision*, 8(2):123–152, August 1992.
- [9]. B. Caprile and V. Torre. Using Vanishing Points for Camera Calibration. *The International Journal of Computer Vision*, 4(2):127–140, Mar. 1990
- [10]. D. Liebowitz and A. Zisserman. Metric rectification for perspective images of planes. In *Proceedings of the IEEE Conference on Computer Vision and Pattern Recognition*, pages 482–488, Santa Barbara, California, June 1998. IEEE Computer Society
- [11]. R. Hartley. Self-calibration from multiple views with a rotating camera. In J-O. Eklundh, editor, *Proceedings of the 3rd European Conference on Computer Vision*, volume 800-801 of *Lecture Notes in Computer Science*, pages 471–478, Stockholm, Sweden, May 1994. Springer-Verlag
- [12]. G. Stein. Accurate internal camera calibration using rotation, with analysis of sources of error. In *Proc. Fifth International Conference on Computer Vision*, pages 230–236, Cambridge, Massachusetts, June 1995.
- [13]. O. Semeniutar. "Analysis of Camera Calibration with Respect to Measurement Accuracy." *Procedia CIRP* 41 (2016): 765-770.
- [14]. B.P.Byrne, J. Mallon, and P.F. Whelan. "Capturing Optimal Image Networks for Planar Camera Calibration." *Machine Vision and Image Processing Conference (IMVIP)*, 2011 Irish. IEEE, 2011.
- [15]. J.H. Holland "Adaptation in Natural and Artificial Systems" MIT Press 1975.
- [16]. G. Medioni and S.B. Kang (2004). *Emerging topics in computer vision*. pg 4-43. Prentice Hall PTR.
- [17]. J.Y. Bouguet. MATLAB calibration tool. http://www.vision.caltech.edu/bouguetj/calib_doc/
- [18]. OpenCV library. <http://code.opencv.org>

A Review on Vibration Analysis of Carbon Nanotubes Based on Nonlocal Continuum Theory

*Necla Togun*¹*

Abstract

This paper reviews recent research studies on the application of the nonlocal continuum theory in vibration analysis of carbon nanotubes. Various size dependent continuum theories which are the nonlocal elasticity theory, strain gradient theory, the modified couple stress theory, the micropolar theory and the surface elasticity theory are introduced and reviewed to include the small scale effect. The applicability of size-dependent continuum theories and the necessity of the small-scale parameter are discussed. A general introduction of the nonlocal beam model for the analysis of vibration is presented. Summary and recommendations for future research are also provided.

Keywords: *Vibration, nanobeam, nonlocal continuum theory, small-scale effect*

1. INTRODUCTION

Most of the scientists have interested in carbon nanotubes (CNTs) that have been invented by Iijima [1]. CNTs have excellent mechanical and electrical characteristics and their potential applications in electronics, nanotechnology, optics and other field of material science. The size effect plays a significant role in investigating mechanical behavior of micro and nano structures due to their smaller dimensions. Conducting nanostructure experiments have both difficult and expensive, so the approximate nanostructure analysis with appropriate mathematical models is an important issue. The atomic simulation model and continuum model are used for analyzing method of nanostructures. The inherit limitations of the atomic simulation models result in time consuming and computationally expensive for large sized atomic systems. Continuum models are able to overcome these limitations to account for the length scales and time. The classical continuum (local) mechanics, scale free theory, is unable concerning the size effect. Due to this fact, various size-dependent continuum theories related with small- scale effects have been developed. These are nonlocal elasticity theory, modified couple stress theory, strain gradient theory, surface elasticity theory and micropolar theory.

CNTs consisting of covalent bonded carbon atoms behave as homogeneous and continuous macrostructure whereas their material microstructures, such as the lattice spacing between carbon atoms, are disregarded. The classical (local) continuum theory assumes that the stress at a point depends only on the strain at the same point. However, the applicability of classical (local) continuum theory to very small scales is uncertain. The limited applications of the classical continuum models result in the lattice spacing between carbon atoms at small size becomes increasingly important and the discrete structure of the material can no longer be homogenized into a continuum. In other words, the properties of material at the nanoscale are size-dependent and hence effect of small length scale should be incorporated into the equations to predict the nanomaterial mechanical behavior well. The main objective of this paper is to review the available size dependent techniques for predicting vibrational behavior of CNTs in literature. Different methods employed in the past decades are introduced.

2. APPLICATION OF CLASSICAL (LOCAL) CONTINUUM THEORY TO CNT

Continuum mechanics model with its advantages of convenience, rapidity, accuracy, low cost, ease of implementation and ease of use allows not only the straightforward generation of a structural model of a nanotube, but also enables the accurate simulation of its mechanical response [2]. In literature some researchers applied the classical continuum model to investigating the mechanical properties of the nanostructure in their studies. Resonant frequencies and the associated vibrational modes of an individual multiwall carbon nanotube (MWCNT) embedded in an elastic medium was analyzed based on a multiple elastic beam model which considers intertube radial displacements and the related internal degrees of freedom [3]. Timoshenko and Euler-Bernoulli beam model for free vibration analysis of MWCNT was compared and results show that the frequencies was significantly over-predicted by the Euler beam theory when the length-to-diameter ratios was small and when considering high vibration modes[4]. The relationship between the resonant frequency and the attached mass was established and the attached mass causes a frequency shift. Their result show that the proposed sensor equations work reasonably well when the length of the bacteria is more than 1 nm for both cantilevered and bridged configurations [5]. The vibrational behavior of SWCNTs and MWCNTs were studied to investigate their sensing characteristics when a nanoparticle is attached to them [6]. The generalized calibration constants were derived for an explicit relationship between the added mass and the frequency shift [7]. The nonlinear vibrations of MWCNTs embedded in an elastic medium [8], the nonlinear vibration of a DWCNTs embedded in a polymer matrix [9], the nonlinear vibration of DWCNTs [10], the nonlinear forced vibration analysis of curved SWCNTs on a Pasternak elastic foundation [11], the nonlinear free vibration and buckling analysis of SWCNTs resting on an elastic foundation [12], the nonlinear free vibration and post-buckling analysis of functionally graded beams on nonlinear elastic foundation [13], thermo-

mechanical buckling and nonlinear vibrations of functionally graded beams on nonlinear elastic foundation [14], the nonlinear free vibration of functionally graded nanobeams [15], effect of nonlinear elastic foundation on large amplitude free and forced vibration of functionally graded beam[16] were presented based on the classical continuum theory. The nonlinear free vibration frequency of nanotubes rises rapidly with the increment of the amplitude when the stiffness of medium is relatively small, but the nonlinear vibration will change to the linear vibration when the stiffness is large enough[17].

Buckling of single walled carbon nanotube (SWCNT) and MWCNT due to axial compressive loads was investigated and their study shows that the van der Waals forces among atoms on adjacent walls of MWCNTs play a significant role [18]. The natural frequencies were dependent on the axial load and decrease with increasing the axial load. However, the associated amplitude ratios of the inner to the outer tubes of double walled carbon nanotubes (DWCNTs) was independent of the axial load [19]. The resonant frequency shift and mode shape of the cantilever SWCNTs caused by the addition of a nanoscale particle at the free end was analyzed and results revealed that the volume of the added particle has little effect on the first resonant frequency [20]. Increasing the value of attached mass, the values of resonant frequency are decreased [21]

The influence of internal moving fluid on free vibration and flow-induced structural instability of CNTs was studied and the results indicate that internal moving fluid could substantially affect resonant frequencies especially for suspended longer CNTs of larger innermost radius at higher flow velocity and a compliant surrounding elastic medium can significantly reduce the effect of internal moving fluid on resonant frequencies [22]. Couple mode flutter may occur at higher flow velocity [23]. The structural stability of an MWCNT conveying non-viscous fluid was modeled as a Timoshenko beam theory [24]. The vibration and instability of CNTs conveying non-viscous fluid [25] and SWCNTs conveying viscous fluid [26] resting on the linear viscoelastic Winkler foundation with modulus and damping factors were studied. Free vibration of the fluid conveying SWCNT was analyzed by the Timoshenko beam model and their result show that the effects of rotary inertia and transverse shear deformation result in a reduction of the vibration frequencies, especially for higher modes of vibration and short nanotubes [27]. Dynamical behavior of triple walled CNTs conveying fluid [28] and MWCNTs conveying fluid [29] were studied and their result show that the critical velocities increase sharply as the radius becomes larger. The effect of the geometric nonlinearity and the nonlinearity of van der Waals force on the transverse vibration of the DWCNTs conveying fluid and the interaction between two types of nonlinearities were studied [30]. The effect of nanoflow viscosity is not so influential on vibration of nanotubes conveying fluid, as compared with the results of vibration of nanotubes conveying an inviscid fluid [31].

3.APPLICATION OF SIZE DEPENDENT CONTINUUM THEORY TO CNT

The application of continuum mechanics by accommodating or considering the size dependence in nanomaterials becomes another topic of major concern. Therefore, application of size dependent continuum theory allowing for the small-scale effects to analysis of nanomaterials in the study of nanostructure has been initiated. The size effect can be attributed to material length scale parameters.

3.1.Nonlocal Elasticity Theory applied to CNT

The nonlocal elasticity theory, which was introduced by Eringen[32, 33]to account for scale effect in elasticity, was used to study latticedispersion of elastic waves, wave propagation in composites, dislocationmechanics, fracture mechanics and surface tension fluids.According to the Eringen’s nonlocal elasticity theory, the stress at a reference point is considered to be a function of the strains at all other points in the body. A simplified constitutive relation in a differential form is given by Eringen[32, 33]as follows;

$$\left(1 - (e_0 a)^2 \nabla^2\right) \sigma = T \tag{1}$$

Where ∇^2 is the Laplacian operator. The nonlocal constitutive relation for the present nanobeam can be written as

$$\sigma(x^*) - (e_0 a)^2 \frac{\partial^2 \sigma(x^*)}{\partial x^{*2}} = E \varepsilon(x^*) \tag{2}$$

where E is the elasticity modulus.

The study of Peddieson et al.[34]canbe considered to be a pioneering work which first applied the nonlocalcontinuum theory to the nanotechnology to obtain the staticdeformations of beam structures by using a simplified nonlocalbeam model based on the nonlocal elasticity theory of Eringen[33]. After this study, a great deal of attention has been focused on analysis of nanostructures. Sudak [35] applied nonlocal elasticity for column buckling. Static analyses of micro-and nanostructures was studied by Wang and Liew [36] using nonlocal Euler-Bernoulli and Timoshenko beam theories. Wave

propagation in CNTs is investigated by Wang [37] and Lu et al. [38]. Vibrations of CNTs, nanobeams and rods are also studied in the previous studies using nonlocal elasticity [39-45]. Increasing nonlocal parameter (e_0a/L) decreases stiffness of the beams and bending results increase. Non-locality effects are more pronounced for point load [41].

However, the above review clearly indicates that the majority of the aforementioned works on nanostructures are related to the linear analysis of nanobeams/nanotubes. Researchers also have been studied to the nonlinear analysis of nanostructures. For example, Yang et al. [46] studied nonlinear free vibration of SWCNTs based on von-Kármán's geometric nonlinearity and Eringen's nonlocal elasticity theory. Studies related to nonlinear vibration analysis of nanotubes [47-52], functionally graded beams [53-55], nanobeams [56-59] have been reported. It has been shown that the nonlocal effect is quite significant in the vibration studies and needs to be included in the continuum model of CNTs.

3.2. Modified Couple Stress Theory applied to CNT

In the modified couple stress theory was initially proposed by Yang et al. [60], the strain energy density is a function of both strain tensor and curvature tensor. Therefore, the strain energy of a deformed isotropic linear elastic body occupying a volume Ω . λ and μ are the Lamé's constants that are defined as

$$\lambda = \frac{E\nu}{(1+\nu)(1-2\nu)}, \quad \mu = \frac{E}{2(1+\nu)} \quad (3)$$

where ν is Poisson's ratio, μ is shear modulus and E is Young's modulus.

The modified couple stress theory was initially applied by Park and Gao [61] to static deformation analysis of a micro cantilever Euler-Bernoulli beam subjected to a point load. The literature regarding the vibrations of microbeams using modified couple stress theory is quite large [62-68]. It is concluded that the dynamic deflections obtained by using the modified couple stress theory are always smaller than those by classical theory which means that the couple stresses stiffen the microbeam. The classical beam model could overestimate the dynamic deflections of the microbeam. Further, the material length scale parameter has a significant influence on the dynamic properties of microbeams whose thickness becomes equal to the material length scale parameter. Thus, modeling microscale structures based on the classical beam models is not suitable, and size dependent beam models should be used in the static and dynamic analysis of such structures. As the Poisson's ratio increases the dynamic deflections decrease for the classical beam theory. The Poisson effect should be taken into account since neglecting the Poisson effect can lead to significant errors. Some studies have been conducted on modeling the size-dependent response of nanostructures using modified couple stress theory [69-74].

3.3. Strain Gradient Elasticity Theory applied to CNT

The strain energy U in a linear elastic isotropic material occupying region U based on the modified strain gradient elasticity theory can be written by [75]

$$U = \frac{1}{2} \int_0^l [B(w'')^2 + D(w''')^2] dx, \quad (4)$$

$$\text{Where, } B = EI + 2\mu A l_0^2 + \frac{8}{15} \mu A l_1^2 + \mu A l_2^2, \quad D = I \left(2\mu l_0^2 + \frac{4}{5} \mu l_1^2 \right) \quad (5)$$

I and A are the moment of inertia and cross section area of the beam, respectively.

Lam et al. [75] proposed a modified strain gradient elasticity theory in which a new additional equilibrium equations to govern the behavior of higher-order stresses, the equilibrium of moments of couples is introduced, in addition to the classical equilibrium equations of forces and moments of forces. The theory covered three material length scale parameters in the constitutive equations to be obtained from experiments for each matter. Size dependent continuum theories have thus received increasing attention in modeling small sized structures and devices. This theory was applied extensively for micro/nano-structures [76-81]. Each of these papers considered a certain problem relating to the micro-or nano-structures such as buckling loads or natural frequency and concluded that the classical continuum theory under-estimates the numerical values of the loads and frequencies of the micro- and nano-structures. Thus, other non-classical elasticity theories such as the strain gradient theory should be applied in scrutinizing the mechanical behaviors of the micro/nano-structures.

3.4. Surface Elasticity Theory applied to CNT

To indicate the considerable influence of surface stress on elastic behaviors of nanostructures, Gurtin and Murdoch [82, 83] developed a theoretical framework based on the continuum mechanics including surface stress effects which has an excellent capability to incorporate the surface stress effects into the mechanical response of nanostructures and has been applied in many studies during the past several years. In the open literature, there are various investigations in which

surface elasticity theory have been employed to take surface stress effect into account [84-87]. It was observed that incorporating the surface stress effect may lead to increase or decrease the maximum amplitude of the stable response which depends on the sign of surface elastic constants. Moreover, it was revealed that for all types of end supports, as the length-to-thickness ratio increases, the width of frequency-response curves of nanobeams becomes larger and the maximum amplitude tends to occur at higher frequencies of excitation [84].

4. CONCLUSION

Owing to their superior mechanical and physical properties, CNTs hold many potential applications in the ever-growing nanotechnology industry. A very good understanding of mechanical behaviors of the CNTs materials is crucial. Among different approaches for modeling nanostructures, the nonlocal continuum mechanics theory allows the consideration of the small-scale effects in analysis of nano-materials. These advantages make the nonlocal continuum modeling employed as an effective way in simulating the nano-materials. The size dependent continuum models have been widely employed in analysis of the static and dynamic problems of nano/microstructures.

REFERENCES

- [1] S. Iijima, Helical microtubules of graphitic carbon, *Nature*, , 354 (1991) 56-58.
- [2] D.H. Wu, W.T. Chien, C.S. Chen, H.H. Chen, Resonant frequency analysis of fixed-free single-walled carbon nanotube-based mass sensor, *Sensors and Actuators A: Physical*, 126 (2006) 117-121.
- [3] J.R. Yoon, C.Q. Mioduchowski, A. , Vibration of an embedded multiwall carbon nanotube, *Composites Science and Technology* 63 (2003) 1533-1542, 63 (2003) 1533-1542.
- [4] C.M. Wang, Tan, V.B.C., Zhang, Y.Y. , Timoshenko beam model for vibration analysis of multi-walled carbon nanotubes *Journal of Sound and Vibration* 294 (2006) 1060-1072.
- [5] R. Chowdhury, S. Adhikari, J. Mitchell, Vibrating carbon nanotube based bio-sensors, *Physica E: Low-dimensional Systems and Nanostructures*, 42 (2009) 104-109.
- [6] S.K. Georgantzinos, N.K. Anifantis, Carbon nanotube-based resonant nanomechanical sensors: A computational investigation of their behavior, *Physica E: Low-dimensional Systems and Nanostructures*, 42 (2010) 1795-1801.
- [7] S. Adhikari, R. Chowdhury, The calibration of carbon nanotube based bionanosensors, *Journal of Applied Physics*, 107 (2010) 124322.
- [8] R. Ansari, M. Hemmatnezhad, Nonlinear vibrations of embedded multi-walled carbon nanotubes using a variational approach, *Mathematical and Computer Modelling*, 53 (2011) 927-938.
- [9] M.H. Mahdavi, L.Y. Jiang, X. Sun, Nonlinear vibration of a double-walled carbon nanotube embedded in a polymer matrix, *Physica E: Low-dimensional Systems and Nanostructures*, 43 (2011) 1813-1819.
- [10] Y. Yan, Wang, W., Zhang, L. , Applied multiscale method to analysis of nonlinear vibration for double-walled carbon nanotubes, *Applied Mathematical Modelling* 35 (2011) 2279-2289.
- [11] I. Mehdipour, A. Barari, A. Kimiaefar, G. Domairry, Vibrational analysis of curved single-walled carbon nanotube on a Pasternak elastic foundation, *Advances in Engineering Software*, 48 (2012) 1-5.
- [12] M.H. Yas, N. Samadi, Free vibrations and buckling analysis of carbon nanotube-reinforced composite Timoshenko beams on elastic foundation, *International Journal of Pressure Vessels and Piping*, 98 (2012) 119-128.
- [13] A. Fallah, M.M. Aghdam, Nonlinear free vibration and post-buckling analysis of functionally graded beams on nonlinear elastic foundation, *European Journal of Mechanics - A/Solids*, 30 (2011) 571-583.
- [14] A. Fallah, M.M. Aghdam, Thermo-mechanical buckling and nonlinear free vibration analysis of functionally graded beams on nonlinear elastic foundation, *Composites Part B: Engineering*, 43 (2012) 1523-1530.
- [15] P. Asgharifard Sharabiani, M.R. Haeri Yazdi, Nonlinear free vibrations of functionally graded nanobeams with surface effects, *Composites Part B: Engineering*, 45 (2013) 581-586.
- [16] A.S. Kanani, H. Niknam, A.R. Ohadi, M.M. Aghdam, Effect of nonlinear elastic foundation on large amplitude free and forced vibration of functionally graded beam, *Composite Structures*, 115 (2014) 60-68.
- [17] Y.M. Fu, J.W. Hong, X.Q. Wang, Analysis of nonlinear vibration for embedded carbon nanotubes, *Journal of Sound and Vibration*, 296 (2006) 746-756.
- [18] A. Sears, Batra, R.C. , buckling of multiwalled carbon nanotubes under axial compression, *Physical Review B*, 73 (2006) 085410.
- [19] Y. Zhang, G. Liu, X. Han, Transverse vibrations of double-walled carbon nanotubes under compressive axial load, *Physics Letters A*, 340 (2005) 258-266.
- [20] T.-L. Horng, Analytical Solution of Vibration Analysis on Fixed-Free Single-Walled Carbon Nanotube-Based Mass Sensor, *Journal of Surface Engineered Materials and Advanced Technology*, 02 (2012) 47-52.
- [21] I. Mehdipour, A. Barari, G. Domairry, Application of a cantilevered SWCNT with mass at the tip as a nanomechanical sensor, *Computational Materials Science*, 50 (2011) 1830-1833.

- [22] J. Yoon, C.Q. Ru, A. Mioduchowski, Vibration and instability of carbon nanotubes conveying fluid, *Composites Science and Technology*, 65 (2005) 1326-1336.
- [23] L. Wang, Q. Ni, On vibration and instability of carbon nanotubes conveying fluid, *Computational Materials Science*, 43 (2008) 399-402.
- [24] N. Khosravian, H. Rafii-Tabar, Computational modelling of a non-viscous fluid flow in a multi-walled carbon nanotube modelled as a Timoshenko beam, *Nanotechnology*, 19 (2008) 275703.
- [25] E. Ghavanloo, F. Daneshmand, M. Rafiei, Vibration and instability analysis of carbon nanotubes conveying fluid and resting on a linear viscoelastic Winkler foundation, *Physica E: Low-dimensional Systems and Nanostructures*, 42 (2010) 2218-2224.
- [26] H.L. Lee, Chang, W.J., Vibration analysis of a viscous-fluid-conveying single-walled carbon nanotube embedded in an elastic medium, *Physica E* 41 41 (2009) 529-532.
- [27] W.-J. Chang, H.-L. Lee, Free vibration of a single-walled carbon nanotube containing a fluid flow using the Timoshenko beam model, *Physics Letters A*, 373 (2009) 982-985.
- [28] Y. Yan, X.Q. He, L.X. Zhang, C.M. Wang, Dynamic behavior of triple-walled carbon nanotubes conveying fluid, *Journal of Sound and Vibration*, 319 (2009) 1003-1018.
- [29] Y. Yan, W.Q. Wang, L.X. Zhang, Dynamical behaviors of fluid-conveyed multi-walled carbon nanotubes, *Applied Mathematical Modelling*, 33 (2009) 1430-1440.
- [30] Y.D. Kuang, X.Q. He, C.Y. Chen, G.Q. Li, Analysis of nonlinear vibrations of double-walled carbon nanotubes conveying fluid, *Computational Materials Science*, 45 (2009) 875-880.
- [31] V. Rashidi, H.R. Mirdamadi, E. Shirani, A novel model for vibrations of nanotubes conveying nanoflow, *Computational Materials Science*, 51 (2012) 347-352.
- [32] A.C. Eringen, On differential-equations of nonlocal elasticity and solutions of screw dislocation and surface waves, *Journal of Applied Physics*, , 54 (1983) 4703-4710.
- [33] A.C. Eringen, *Nonlocal Continuum Field Theories*, Springer-Verlag., Newyork, 2002.
- [34] J. Peddieson, G.R. Buchanan, R.P. McNitt, Application of nonlocal continuum models to nanotechnology, *International Journal of Engineering Science*, 41 (2003) 305-312.
- [35] L.J. Sudak, Column buckling of multiwalled carbon nanotubes using nonlocal continuum mechanics, *Journal of Applied Physics*, 94 (2003) 7281-7287.
- [36] Q. Wang, K.M. Liew, Application of nonlocal continuum mechanics to static analysis of micro- and nano-structures, *Physics Letters A*, 363 (2007) 236-242.
- [37] Q. Wang, Wave propagation in carbon nanotubes via nonlocal continuum mechanics, *Journal of Applied Physics*, 98 (2005).
- [38] P. Lu, H.P. Lee, C. Lu, P.Q. Zhang, Application of nonlocal beam models for carbon nanotubes, *Int J Solids Struct*, 44 (2007) 5289-5300.
- [39] M. Aydogdu, Axial vibration of the nanorods with the nonlocal continuum rod model, *Physica E*, 41 (2009) 861-864.
- [40] M.C. Ece, M. Aydogdu, Nonlocal elasticity effect on vibration of in-plane loaded double-walled carbon nano-tubes, *Acta Mech*, 190 (2007) 185-195.
- [41] M. Aydogdu, A general nonlocal beam theory: Its application to nanobeam bending, buckling and vibration, *Physica E*, 41 (2009) 1651-1655.
- [42] P. Karaoglu, M. Aydogdu, On the forced vibration of carbon nanotubes via a non-local Euler-Bernoulli beam model, *P I Mech Eng C-J Mec*, 224 (2010) 497-503.
- [43] M. Şimşek, Large amplitude free vibration of nanobeams with various boundary conditions based on the nonlocal elasticity theory, *Composites Part B: Engineering*, 56 (2014) 621-628.
- [44] M. Şimşek, Nonlocal effects in the forced vibration of an elastically connected double-carbon nanotube system under a moving nanoparticle, *Computational Materials Science*, 50 (2011) 2112-2123.
- [45] M. Şimşek, Vibration analysis of a single-walled carbon nanotube under action of a moving harmonic load based on nonlocal elasticity theory, *Physica E: Low-dimensional Systems and Nanostructures*, 43 (2010) 182-191.
- [46] J. Yang, L.L. Ke, S. Kitipornchai, Nonlinear free vibration of single-walled carbon nanotubes using nonlocal Timoshenko beam theory, *Physica E: Low-dimensional Systems and Nanostructures*, 42 (2010) 1727-1735.
- [47] H.-S. Shen, C.-L. Zhang, Nonlocal beam model for nonlinear analysis of carbon nanotubes on elastomeric substrates, *Computational Materials Science*, 50 (2011) 1022-1029.
- [48] B. Fang, Y.-X. Zhen, C.-P. Zhang, Y. Tang, Nonlinear vibration analysis of double-walled carbon nanotubes based on nonlocal elasticity theory, *Applied Mathematical Modelling*, 37 (2013) 1096-1107.
- [49] Y.-Z. Wang, F.-M. Li, Nonlinear free vibration of nanotube with small scale effects embedded in viscous matrix, *Mechanics Research Communications*, 60 (2014) 45-51.
- [50] L.L. Ke, Y. Xiang, J. Yang, S. Kitipornchai, Nonlinear free vibration of embedded double-walled carbon nanotubes based on nonlocal Timoshenko beam theory, *Computational Materials Science*, 47 (2009) 409-417.

- [51] R. Ansari, H. Ramezannezhad, Nonlocal Timoshenko beam model for the large-amplitude vibrations of embedded multiwalled carbon nanotubes including thermal effects, *Physica E: Low-dimensional Systems and Nanostructures*, 43 (2011) 1171-1178.
- [52] R. Ansari, H. Ramezannezhad, R. Gholami, Nonlocal beam theory for nonlinear vibrations of embedded multiwalled carbon nanotubes in thermal environment, *Nonlinear Dynamics*, 67 (2011) 2241-2254.
- [53] R. Nazemnezhad, S. Hosseini-Hashemi, Nonlocal nonlinear free vibration of functionally graded nanobeams, *Composite Structures*, 110 (2014) 192-199.
- [54] F. Ebrahimi, E. Salari, Nonlocal thermo-mechanical vibration analysis of functionally graded nanobeams in thermal environment, *Acta Astronautica*, 113 (2015) 29-50.
- [55] S. Hosseini-Hashemi, R. Nazemnezhad, M. Bedroud, Surface effects on nonlinear free vibration of functionally graded nanobeams using nonlocal elasticity, *Applied Mathematical Modelling*, 38 (2014) 3538-3553.
- [56] N. Togun, Bağdatlı, S.M. , Nonlinear Vibration of a Nanobeam on a Pasternak elastic foundation based on nonlocal Euler-Bernoulli beam theory, *Mathematical and Computational Applications*, 21 (2016).
- [57] N. Togun, Nonlocal beam theory for nonlinear vibrations of a nanobeam resting on elastic foundation, *Boundary Value Problems* 57 (2016) 1-14.
- [58] S.M. Bagdatli, Non-linear vibration of nanobeams with various boundary condition based on nonlocal elasticity theory, *Composites Part B* 80 (2015) 43-52.
- [59] S.M. Bagdatli, Non-linear transverse vibrations of tensioned nanobeams using nonlocal beam theory, *Structural Engineering and Mechanics*, 55 (2015) 281-298.
- [60] F. Yang, Chong , A.C.M., Lam, D.C.C., Tong, P., Couple stress based strain gradient theory for elasticity, *Int J Solids Struct*, 39 (2002) 2731–2743.
- [61] S.K. Park, X.L. Gao, Bernoulli–Euler beam model based on a modified couple stress theory, *Journal of Micromechanics and Microengineering*, 16 (2006) 2355-2359.
- [62] H. Ma, X. Gao, J. Reddy, A microstructure-dependent Timoshenko beam model based on a modified couple stress theory, *Journal of the Mechanics and Physics of Solids*, 56 (2008) 3379-3391.
- [63] C.M.C. Roque, D.S. Fidalgo, A.J.M. Ferreira, J.N. Reddy, A study of a microstructure-dependent composite laminated Timoshenko beam using a modified couple stress theory and a meshless method, *Composite Structures*, 96 (2013) 532-537.
- [64] M. Baghani, Analytical study on size-dependent static pull-in voltage of microcantilevers using the modified couple stress theory, *International Journal of Engineering Science*, 54 (2012) 99-105.
- [65] M. Şimşek, Dynamic analysis of an embedded microbeam carrying a moving microparticle based on the modified couple stress theory, *International Journal of Engineering Science*, 48 (2010) 1721-1732.
- [66] M.H. Kahrobaiyan, M. Asghari, M. Rahaeifard, M.T. Ahmadian, Investigation of the size-dependent dynamic characteristics of atomic force microscope microcantilevers based on the modified couple stress theory, *International Journal of Engineering Science*, 48 (2010) 1985-1994.
- [67] M.H. Ghayesh, H. Farokhi, M. Amabili, Nonlinear dynamics of a microscale beam based on the modified couple stress theory, *Composites Part B: Engineering*, 50 (2013) 318-324.
- [68] Y.-G. Wang, W.-H. Lin, N. Liu, Nonlinear free vibration of a microscale beam based on modified couple stress theory, *Physica E: Low-dimensional Systems and Nanostructures*, 47 (2013) 80-85.
- [69] Y.T. Beni, I. Karimipour, M. Abadyan, Modeling the effect of intermolecular force on the size-dependent pull-in behavior of beam-type NEMS using modified couple stress theory, *Journal of Mechanical Science and Technology*, 28 (2014) 3749-3757.
- [70] J. Abdi, A. Koochi, A.S. Kazemi, M. Abadyan, Modeling the effects of size dependence and dispersion forces on the pull-in instability of electrostatic cantilever NEMS using modified couple stress theory, *Smart Materials and Structures*, 20 (2011) 055011.
- [71] E.M. Miandoab, H.N. Pishkenari, A. Yousefi-Koma, H. Hoorzad, Polysilicon nano-beam model based on modified couple stress and Eringen's nonlocal elasticity theories, *Physica E: Low-dimensional Systems and Nanostructures*, 63 (2014) 223-228.
- [72] M.M. Fakhrabadi, A. Rastgoo, M.T. Ahmadian, Size-dependent characteristics of electrostatically actuated fluid-conveying carbon nanotubes based on modified couple stress theory, *Beilstein J Nanotechnol*, 4 (2013) 771-780.
- [73] H. Zeighampour, Y. Tadi Beni, Size-dependent vibration of fluid-conveying double-walled carbon nanotubes using couple stress shell theory, *Physica E: Low-dimensional Systems and Nanostructures*, 61 (2014) 28-39.
- [74] B. Akgöz, Civalek, Ö. , Stability Analysis of Carbon Nanotubes (CNTs) Based on Modified Couple Stress Theory, in: 6th International Advanced Technologies Symposium (IATS'11), Elazığ, Turkey, 16-18 May 2011.
- [75] D.C.C. Lam, F. Yang, A.C.M. Chong, J. Wang, P. Tong, Experiments and theory in strain gradient elasticity, *Journal of the Mechanics and Physics of Solids*, 51 (2003) 1477-1508.

- [76] M.M.S. Fakhrabadi, A. Rastgoo, M.T. Ahmadian, Non-linear behaviors of carbon nanotubes under electrostatic actuation based on strain gradient theory, *International Journal of Non-Linear Mechanics*, 67 (2014) 236-244.
- [77] M.H. Ghayesh, M. Amabili, H. Farokhi, Nonlinear forced vibrations of a microbeam based on the strain gradient elasticity theory, *International Journal of Engineering Science*, 63 (2013) 52-60.
- [78] J. Zhao, S. Zhou, B. Wang, X. Wang, Nonlinear microbeam model based on strain gradient theory, *Applied Mathematical Modelling*, 36 (2012) 2674-2686.
- [79] H.M. Sedighi, Size-dependent dynamic pull-in instability of vibrating electrically actuated microbeams based on the strain gradient elasticity theory, *Acta Astronautica*, 95 (2014) 111-123.
- [80] S. Kong, S. Zhou, Z. Nie, K. Wang, Static and dynamic analysis of micro beams based on strain gradient elasticity theory, *International Journal of Engineering Science*, 47 (2009) 487-498.
- [81] B. Akgöz, Ö. Civalek, Strain gradient elasticity and modified couple stress models for buckling analysis of axially loaded micro-scaled beams, *International Journal of Engineering Science*, 49 (2011) 1268-1280.
- [82] M.E. Gurtin, Ian Murdoch, A. , A continuum theory of elastic material surfaces, *Archieve for Rational Mechanics and Analysis*, 57 (1975) 291-323.
- [83] M.E. Gurtin, Ian Murdoch, A., Surface stress in solids, *Int J Solids Struct*, 14 (1978) 431-440.
- [84] R. Ansari, V. Mohammadi, M. Faghih Shojaei, R. Gholami, S. Sahmani, On the forced vibration analysis of Timoshenko nanobeams based on the surface stress elasticity theory, *Composites Part B: Engineering*, 60 (2014) 158-166.
- [85] R. Ansari, V. Mohammadi, M. Faghih Shojaei, R. Gholami, S. Sahmani, Postbuckling characteristics of nanobeams based on the surface elasticity theory, *Composites Part B: Engineering*, 55 (2013) 240-246.
- [86] B. Gheshlaghi, S.M. Hasheminejad, Surface effects on nonlinear free vibration of nanobeams, *Composites Part B: Engineering*, 42 (2011) 934-937.
- [87] Y. Fu, J. Zhang, Y. Jiang, Influences of the surface energies on the nonlinear static and dynamic behaviors of nanobeams, *Physica E: Low-dimensional Systems and Nanostructures*, 42 (2010) 2268-2273.

Design and Developer for Disaster Management Information System

*Mehmet Alkan ^{*1}, Havva Guzel²*

Abstract

Disasters are the events which have negative effects on the life. Turkey generally is subject to large scale natural disasters due to negative effects of its geological, topographical and climatic characteristics. The loss can be minimized by working and measurements which should be taken before, during and after the catastrophe. The work which should be done before and after a disaster is examined in "design and development for disaster management information system". The primary mission of the disaster management is to reduce the loss of life and property. to be ready for rescue in every case is possible by very well organization before the disaster.

Large earthquakes that occurred in 1999 in Turkey revealed the need to review the concept of disaster management, Law No. 5902 was put into practice in our country, a new model of disaster management. This model is referred to as 'Integrated Disaster Management System', for the prevention of damage caused by the disaster and emergency situations early detection of hazards and risks, disaster losses that may occur before the measures to be taken to prevent or minimize, effective intervention and coordination in disaster and emergency situations in an integrated manner to ensure the execution of the work and the aftermath of a disaster requires improvement.

In this study, for the disaster recovery and reconstruction efforts aim to make a disaster management information system design and develop via using relational database schemas. The data needed for this study were primarily post-disaster. Then, selected as a pilot area Eregli Sofular Village, in Eregli District Temenler Village in Çaycuma District introduced. The data used in the studies were identified and added to the system software.

Keywords: *Disaster management information system, Recovery and reconstruction*

1. Introduction

Our country, geological and topographical structure and natural disasters leading to meteorological characteristics because of the huge losses of life and property is one of the countries often encounter. Earthquakes occurred in 1999, when the existing disaster management in our country, just a crisis management covering the aftermath of a disaster and to reconsider this system has revealed the necessity and 5902 with Act No (URL-1) have been restructured. With this restructuring 'Integrated Disaster Management System "as the so-called disaster management model; pre-disaster, disaster and memories are considered as a whole, including the aftermath of a disaster.

Disasters are events that profoundly affect social life and public structure. Natural or human-induced disasters, people, institutions, affect the nature of things and is even open the way to major disasters. And repeated natural disaster events, as well as a disaster caused by man's activities and behavior. This aspect of the disasters of nature, life and society is an

¹ Yildiz Technical University, Civil Engineering Faculty, Geomatics Department

² Disaster and Emergency Management Office of Zonguldak City

inevitable part. A life is not possible without exposure to disasters and always be under the encounter with disaster risk and danger, society requires the development of life skills along with disaster (Akyel 2007).

Natural, technological or losses that may arise as a result of human-induced disasters and the damage cannot, in terms of possessions and environment are known to be very large in size. Effects and caused the early threat, a natural disaster occurring in our country because of the size of the losses earthquake, the second landslide, flooding third in revenue and is followed by an avalanche with her rock fall (Disaster and Emergency Management Authority 2013). (See Table 1.)

Table 1. Disaster occurring in our country and the number of victims means (Disaster and Emergency Management Authority 2013)

Disasters	Number of victims	Percentage (%)	Suffering The Number of Settlements
Earthquake	158.214	% 58	3.942
Landslide	59.345	% 22	5.472
Flood	22.157	% 8	2.924
Falling Rock	19.422	% 7	1.703
Snow Slide	4.384	% 2	605
Other Disasters	9.237	% 3	992

Turkey was in the earthquake region of 92%, the country has lived under the threat of earthquakes of 95% of the population and is also known as major industrial centers of 98% and to 93% of the dam earthquake region .In this case, Figure 1. which is the shown for Turkey earthquake zones map.

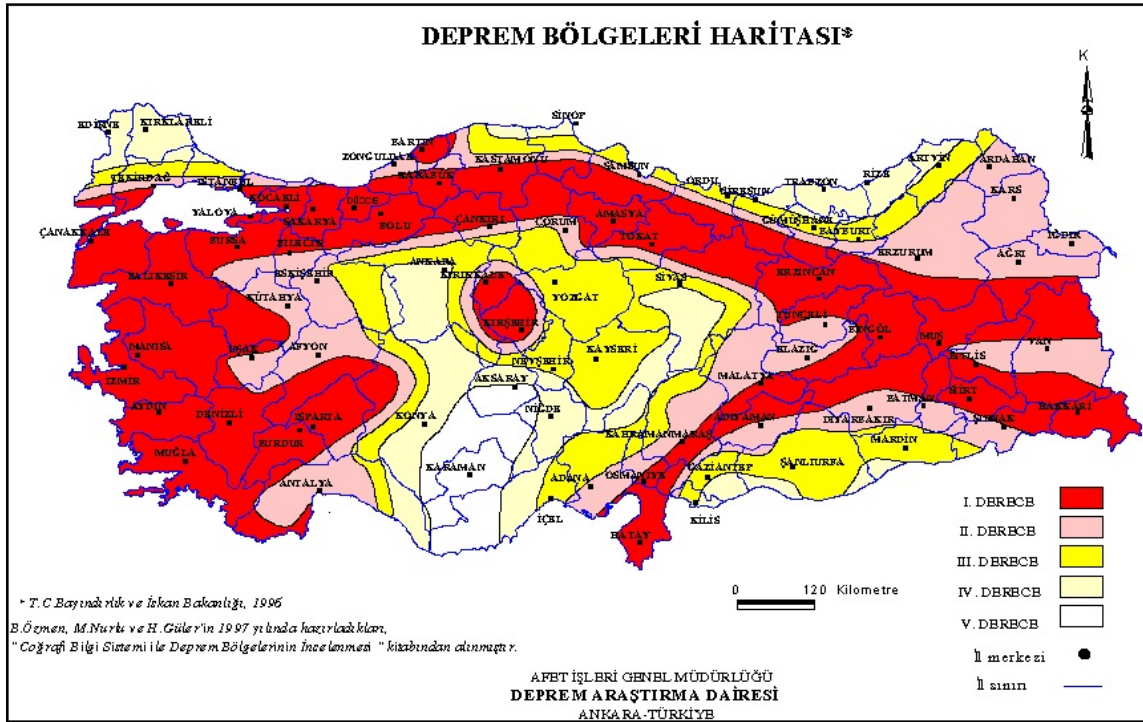


Figure 1. Turkey earthquake zones map.

2. Study Area and Materials

In this study the Disaster Management Information System database design is made towards the realization of the target application. In this context, landslides and earthquakes to test the designed system affected by the disaster Ereğli district of pious village and exposed to landslide disaster Çaycuma District Temir village who have been selected. The geographical location of the province of Zonguldak is given in Figure 2.

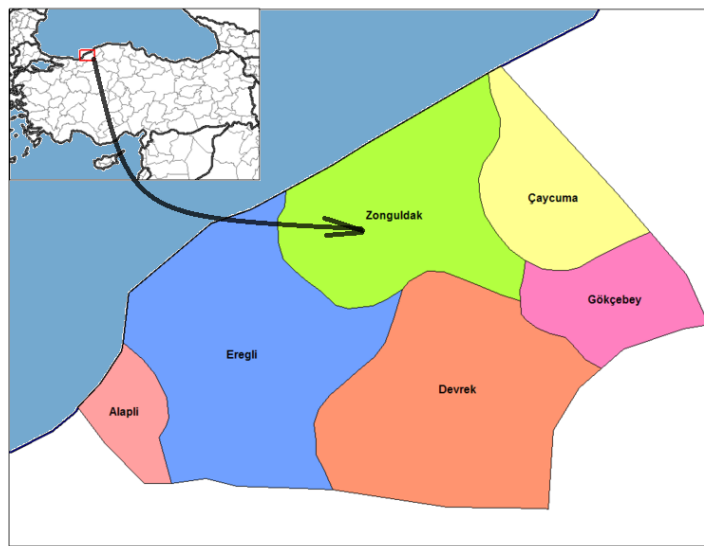


Figure 2. Geographical location of the Zonguldak city.

Sofular village Kdz.Ereğli depends on the district. District 40 km, Zonguldak province is 80 km away from the stop number 130 households. Çayırılı village north of the village, south Emirali village, east Yesilköy village, and west there is Osmans village. According to the 2000 census, the population of 550 is. Sloping topography of the village is covered with forests.

July also is connected to the village of Çaycuma County town 14 km and 59 km away from Zonguldak. Derecikör village north of the village, south Akpınar village, east village potter, a village west of Esenyurt. The population data for the year 2000 396 80 the number of households is. The economy of a village depends on agriculture and husbandry.

3. Toward Disaster Management Information Systems Database Design

3.1. Requirements Analysis

Requirements analysis is the first step in the process of creating a database. At this stage of forming the object of database and application desired to be performed in the database and which is judged by the analysis of the data must be present (Alkan 2005).

This work created in the data base of information, improvement of post-disaster AFAD Prime Minister and the Provincial Disaster and Emergency Directorate and the data will be used in reconstruction work it has been identified. Requirement analysis for Disaster Management Information Systems conducted and the results are described below as articles.

- ✓ Preliminary damage, injury and certain objections damage assessment reports; earthquakes are lists that determine those affected by the disaster in disasters such as fire. Geological survey reports; landslide, which contains maps showing the effects of disasters such as flood disaster areas, report that contains the list are in the affected disaster victims means.
- ✓ The decision of disaster-prone regions; According to Article 2 of Law No. 7269 Council of Ministers decisions are taken.
- ✓ The border regions are exposed to hazards; restricted area boundaries are determined by the structure and residence in the geological survey report.
- ✓ The type of plots and fields
- ✓ The number of apartment buildings, floor units and are field.
- ✓ The following queries can be performed with this data.
- ✓ Temporary or permanent settlement of the post-disaster plots can be made; over a certain square meters to be used in improvement work of the Treasury, or CML, in particular slope, the flood limit, etc. certain distance. Plots used for feature selection.
- ✓ An owner in exchange of real estate; in the study it can be used to examine the entitlement of ownership status.
- ✓ Parcels and buildings affected by a disaster; this question may be prohibited by the plot structure affected by disasters, hazardous and can be identified buildings that require immediate demolition.
- ✓ A building owner in exchange of inquiry; In the study entitlement with this question in that it can be questioned whether or not the owner in exchange a solid second house belonged to his wife.

3.2. Toward Disaster Information System Relational Database Design

Conceptual Data Model Data Model perform the next stage of the design is the design. Relational Data Model Implementation of the data model in this study is preferred. Relational Data Model after completion diagram was carried out using the relational database design. Relational Database Model basic concept "table" stop. A table consists of rows and columns. Database also a relational beings, all of the attributes and relationships found in the data table. Located presence and relationship type attributes in the table column. The data for each entity creates a separate row of the table. Data of an asset can be found in multiple table (Alkan, 2005 ; Elmasri and Navathe, 2000; Batini et.al., 1992).

Figure 3. shows the results of relational Database design. In addition figure 3. underlined values 'key' values. Each row of keys are the values that allows navigation between one significant defining and tables. For owners in the database in this study, TC Identification Number for owners, tas_id for real estate, building_id for buildings, BB_id for individual departments (condominium), was selected as the key value for the parcel registration_date process.

PARCELS

<u>Tas_id</u>	City	Town	District	Section Number	Parcel Number	Area	Identify
---------------	------	------	----------	----------------	---------------	------	----------

BUILDINGS

Tas_id	<u>Building_id</u>	Total Floor	Type of structure	Number of flats	Number of Condominium
--------	--------------------	-------------	-------------------	-----------------	-----------------------

CONDOMINIUMS

Tas_id	<u>Building_id</u>	<u>BB_id</u>	Flat No	Department Number	<u>TC ID</u>	Tenant
--------	--------------------	--------------	---------	-------------------	--------------	--------

OWNERS

<u>TC ID</u>	Name	Surname	Farther_Name	Date of birth	Adress	Telephone
--------------	------	---------	--------------	---------------	--------	-----------

Figure 3. A portion of database schema

4. RESULTS

In this study obtained results and considerations are discussed in here. For this study in this part of the SQL held in applied and performed system design and analysis of the samples are given.

4.1. SQL Sampling and Analysis

A building owner in exchange of more than one inquiry; offered guaranteed to be the rightful entitlement to work in the same village, the building should not be affected by the disaster. In this case, an example is given in figure 4.

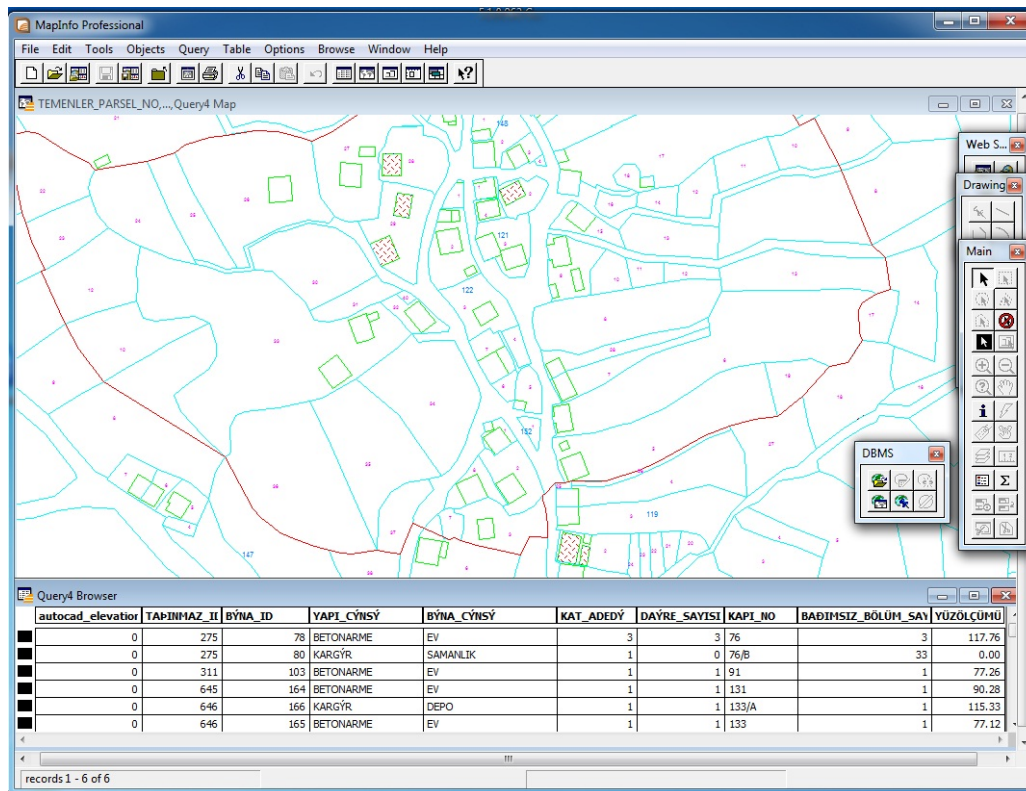


Figure 4. The questioning of the owner in exchange of a building of Temenler village

1999 interrogation of buildings affected by the earthquake; this type of disaster is displayed with query data attributes of the affected building a disaster when entered (Figure 5).

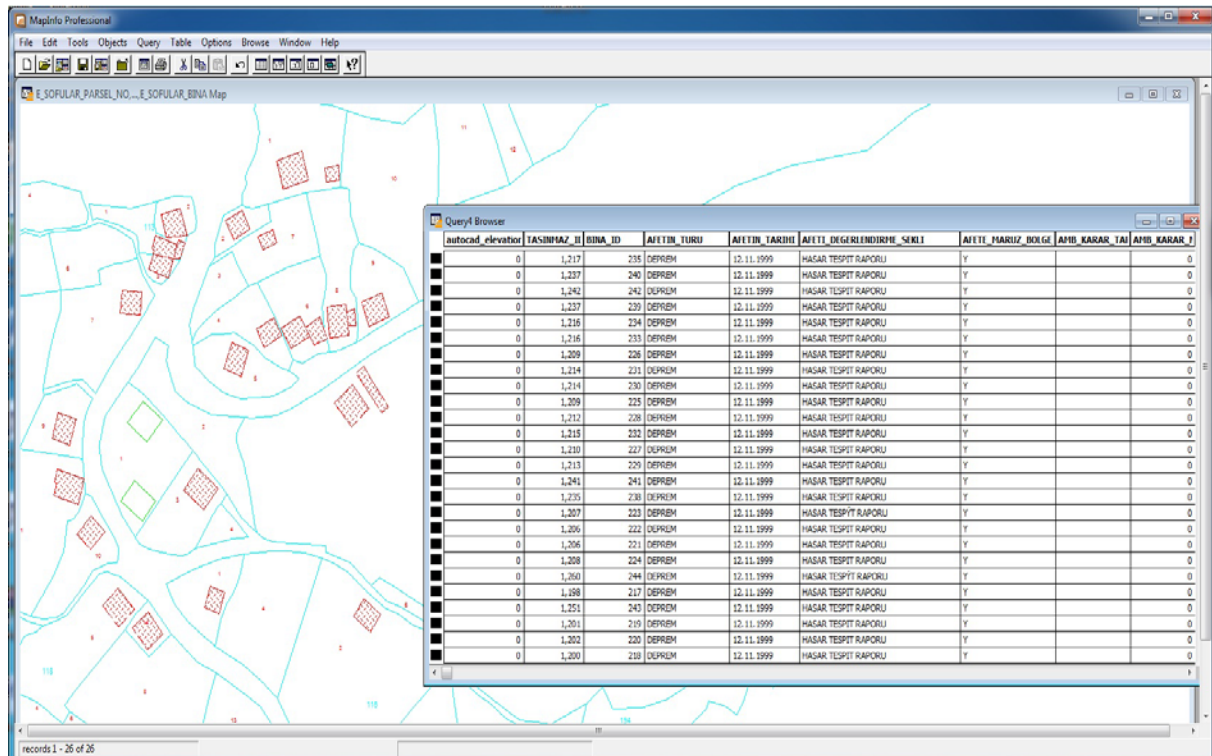


Figure 5. Querying the pious buildings in the village affected by the 1999 earthquake disaster

5. CONCLUSIONS

In this study, established by Law No. 5902 of the Prime Ministry Disaster and Emergency Management Presidency and examined duties, powers and responsibilities of the Provincial Disaster and Emergency Directorate and investigated. This is in the context, Prime Ministry Disaster and Emergency Management Presidency in the Inventory Information System to create a disaster information system and carried out work for the establishment. As the name implies, this program is an inventory program, there is no vision, like disaster management. Prime Ministry Disaster and Emergency Management Presidency in 1958, based on the nature and application of the legislation is to remain a major renovation. This study described the legislation to be included in the AFAD and the Provincial Disaster and Emergency Directorate, studies, information about the current operation has been described and study topic improvement work.

In the context of this study, the results obtained with the system design and implementation carried out in this study are given in the item below.

- Disaster Information Management System data and analysis of the requirements needed data used in establishing the post-disaster rehabilitation work has been done. Disaster Information Management System for design improvements after the needs analysis was conducted. Karadeniz Ereğli Çaycuma County District Sofular village and village who Timur examples of selected pilot regions are given the necessary inquiries and analysis.

- Perform the elimination of confusion in this application due to improvement work, especially after the disaster to disaster management, establishing a system for the rapid adoption of the necessary measures have been tried to be given to the quick and accurate decisions.

REFERENCES

- [1]. Alkan M (2005). Tapu ve Kadastro Verilerine Yönelik Zamansal Coğrafi Bilgi Sistemi Tasarımı, *Doktora Tezi*, Karadeniz Teknik Üniversitesi, 181 s. (In Turkish)
- [2]. Afet ve Acil Durum Yönetimi Başkanlığı(2013)Bireyler ve Aileleri İçin Afet Bilinci
a. Eğitimi Sunusu.
- [3]. Akyel R (2007) Afet Yönetim Sistemi: Türk Afet Yönetiminde Karşılaşılan Sorunların Tespit ve Çözümüne İlişkin Bir Araştırma, Yüksek lisans Tezi, Ç.Ü, Sosyal Bilimler
a. Enstitüsü.
- [4]. Batini C Ceri Sand Navathe S (1992) Conceptual Databsae Design : An Entity
a. Reletionship Approach, The Benjamin/Cummings Publishing Company, Inc.,
b. Redwood City, CA.
- [5]. Elmasri and Navathe (2000) Fundamentals of Database Systems, Addison-Wesley, Third
a. Eddition, California, USA, s. 48-66
- [6]. URL-1(2013) Afet ve Acil Durum Yönetimi Başkanlığının Teşkilat ve Görevleri
a. Hakkında Kanun , <http://www.mevzuat.gov.tr/Metin.Aspx?MevzuatKod=1.5.5902&MevzuatIliski=0&sourceXmlSearch=>.
- b. MevzuatIliski=0&sourceXmlSearch=.

Cooling of Plastic Injection Moulds Using Conformal Cooling Canals

Mustafa Goktas¹, Abdulmecit Guldas¹, Omer Bayraktar²

Abstract

This study has been done to increase the effect of the cooling stage which is one of the most critic stages during plastic injection moulding. A practical way for conformal cooling canal has been presented to increase the production quality and reduce the production time. Firstly, a conformal cooling canal surface to the cavity surface has been created to produce this system. The roots which have been created by offsetting the edge of surface have been converted to cooling canals. An algorithm has been developed to preserve the distance between the canals and the distance between mold canals for the plastic parts which have a complicated geometry. The cooling performance of these cooling canals has been examined by conducting numerical analysis. It has been noticed that the cycle time has decreased by increasing the cooling effect with conformal cooling canals.

Keywords: Injection molding, conformal cooling, canal design, high speed molding

1. INTRODUCTION

Plastic injection moulding is one of the most common plastic processing methods. This method consists of stages such as melting of the plastic material, filling the mould, cooling and de-moulding. One of the most time consuming stage of the moulding cycle is the cooling process. Besides reducing the cooling time, an effective cooling process also reduces the possibility of injection errors of sinking and warpage which depends on the thickness. Moreover, it also effects the rate of crystallization of particularly the semi-crystalline plastics during the solidification stage of the molten plastic.

An effective cooling system is required to reduce the cycle time and production of high quality plastic part. Traditionally, cooling process is provided by cooling canals which are obtained by drilling the mould plate which is close to the mould cavity. Although this method is compatible with plastic parts, it does not provide regular and homogeneous cooling to parts with complex surface [1]. This results in problems such as warpage, sink and irregular withdrawal on the plastic part [2, 3]. Lack of uniform results to non-homogenous pressure and temperature distribution in the mould cavity. This causes undesired results on production of quality product and moulding errors. Also, channels which are obtained by conventional drilling becomes insufficient for uniform cooling if the thickness of the plastic part is not same everywhere.

Various studies in literature have been conducted to create cooling canals in regards to plastic part geometry and thickness as well as providing cooling compatible to mould cavity geometry [1-3, 7-12]. Cooling holes following the outline of part geometry to provide effective cooling have been used in literature. But, these drilled holes which have linear line do not provide effective cooling to complex parts with concave and convex surfaces [4-7]. Instead of these classic holes, curtain and fountain methods have been used to cooling mould cores but homogenous temperature distribution was not fully obtained [8, 9].

It is known that cooling canals obtained by linearly drilling are insufficient for plastic part production of complex parts and variable thicknesses. Due to developing manufacturing technologies, it is possible to create cooling canals with different ways depending on the manufacturing technology instead of the conventional drill holes. One of the possibility is production with metal laser sintering technology. With the development of metal laser sintering technology, it is possible to create cooling canals which are conformal cooling (shape adaptive), have desired geometry, desired frequency and the most effective cooling ducts. Although the high cost of metal sintering method creates a limitation, cooling canals with desired geometry can be produced. Besides, one of the advantages of metal sintering technology is using metal powder with desired ratio which provides creating an effective heat transfer within the mould. Different geometries to the cooling canals are being tested due the possibility of creating mould cores with metal sintering. In this regard, various methods have been proposed in literature for conformal cooling canals to create effective cooling [1, 10-13]. Voronoi curve and contour lines have been used in several proposed methods. However, the distance between the canals regarding to the surface curve are ever-changing and the flow in the canals cannot be fully controlled. Furthermore, topologic optimisation studies have been conducted to reduce to mould cores produced by incremental production method [12, 13].

¹ Corresponding author: Gazi University, Technical Sciences Vocational School, 06374, Yenimahalle/Ankara, Turkey.
mustafagoktas@gazi.edu.tr

Regular and effective cooling to mould cores and mould cavity with complex geometry is intended in this performed study. Conformal cooling canal design method is proposed to provide effective cooling. Firstly, in CAD, part surface has been offset to the outside and an offset algorithm has been used for removal of errors [14, 15]. Then, the edges of the newly formed faces were offset onto itself. The path which the cooling canal will follow was determined by combining the obtained offset lines. By using Moldflow software, the analysis reports of the designed canals have comparatively examined [16].

2. MATERIAL AND METHOD

2.1. Plastic Part and Canal Dimensions

Plastic parts with curve surface geometries were addressed and studied to analyse in the scope of this study (Figure 1). The reason for choosing plastic parts with curved surface geometry is to select a geometry which cooling cannot be done effectively with the conventional drilling method. The thickness of the part is 2mm and the outer dimensions are 188 x 120 x 116mm. The mould cavity needs to be filled to conduct cooling analysis. Polypropylene (PP) is selected as the plastic material for this procedure.

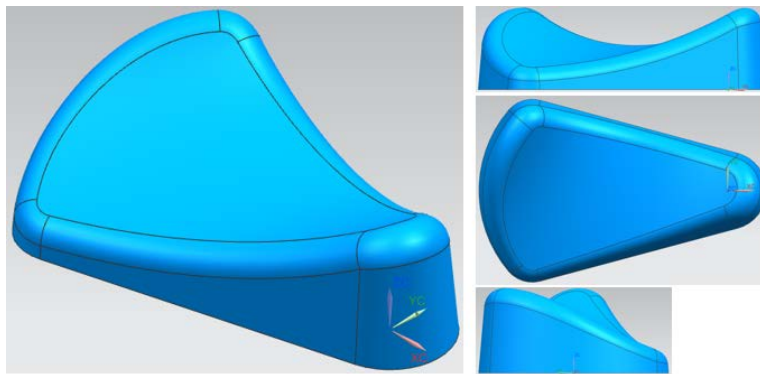


Figure 1. Plastic part

Circular cross section cooling canal has been chosen as cooling canals and the most widely used hole diameter and spacing in literature and industry were chosen (Figure 2).

As shown in Figure 2; canal diameter is $d=8\text{mm}$, distance between canal axis $b=20\text{mm}$, distance between canal axis and mould surface $a=14\text{mm}$ and plastic part thickness $t=2\text{mm}$.

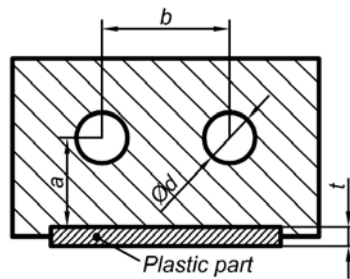


Figure 2. Dimensions of cooling canal

2.2. Creation of Cooling Canals

Firstly, during creation of cooling canals, internal and external surfaces of the plastic part have been offset in regards to the distance between the canal axis and mould surface being (a) as shown in Figure 3. The distance of the canal to the mould surface have been identified due to canal axis being created on this surface.

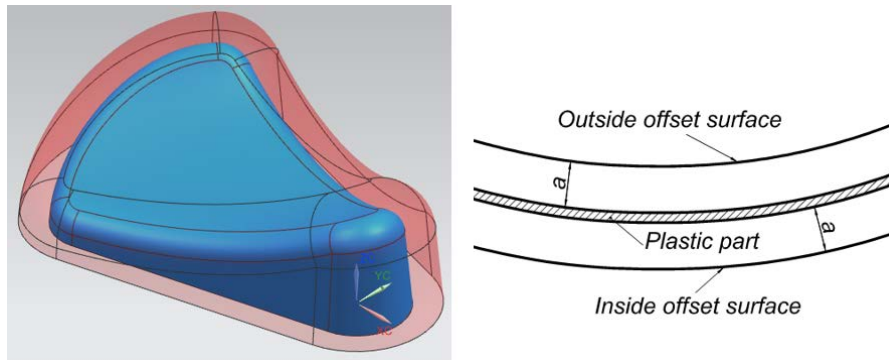


Figure 3. Offsetting of plastic part surface

After surface offset, the slopes of the boundary edge are offset to surface for identifying the canal paths. During this offset process, offset distance "b" has been defined as the distance between the cooling canal paths. During conducting the offset procedure, a plane surface which is perpendicular to a point within the boundary curve has been identified. A circle with a radius of "b" has been created with the centre being on the boundary curve. This circle can be seen in Figure 4.

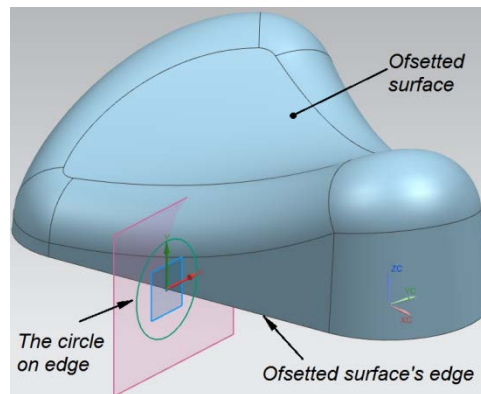


Figure 4. Circle created on the boundary curve

A tube with a radius of "b" has been created by sweeping the circle throughout the boundary curve as shown in Figure 5. The curve inter section between the generated tube and offset surface has been identified. This curved offset is the offset of the boundary curve on the surface. The self-intersections occurred during inter section procedure have been removed by creating an offset algorithm [15, 16]. The results of offsetting of boundary curve can be seen in Figure 6.

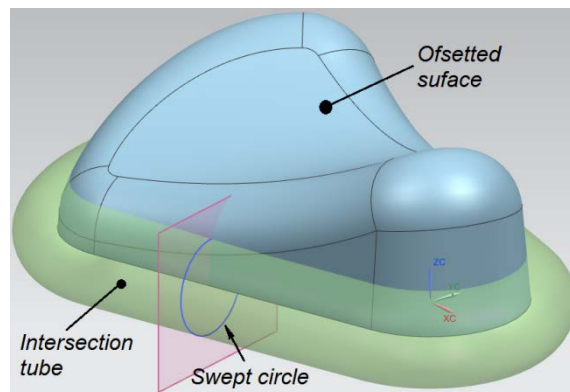


Figure 5. Obtaining the inter-section tube

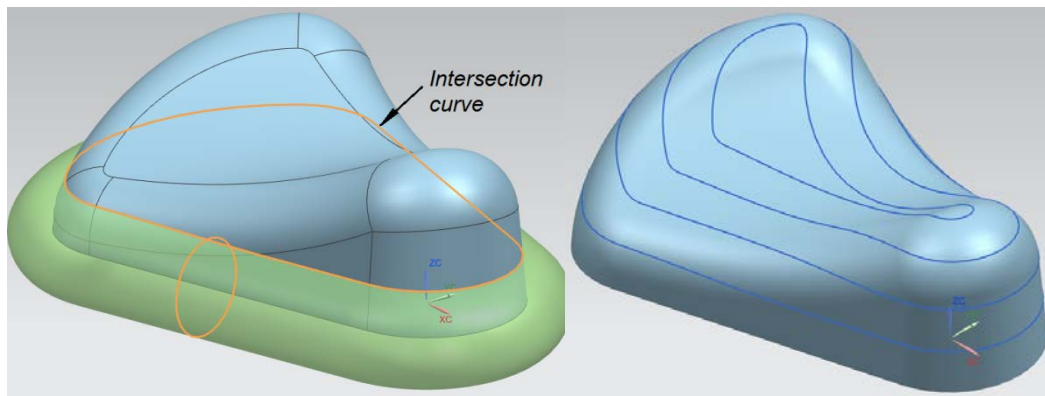


Figure 6. Obtained offset curves

Other canal paths were obtained by repeating the sweeping and taking cross-section using offset curves. The canal curves which are obtained during this procedure were combined to create a spiral. The spiral-formed canal paths are shown in Figure 7. sharp turns which might hamper the flow of the coolant have been softened by rounding.

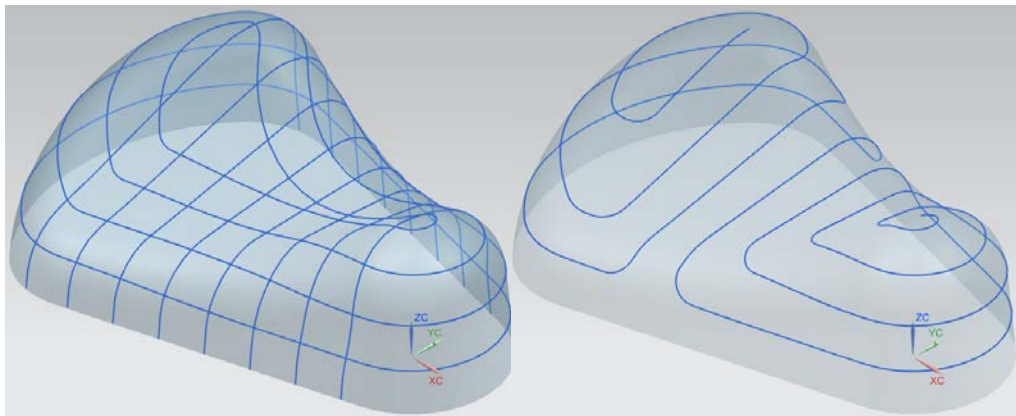


Figure 7. Spiral-formed canal paths

In order to prevent growth differences between inlet and outlet temperature of cooling water, flow line has been converted parallel line by line dividing. Distance from each other and cavity wall of canal are maintained at fix. Cavity and conformal cooling canal are shown in Figure 9.

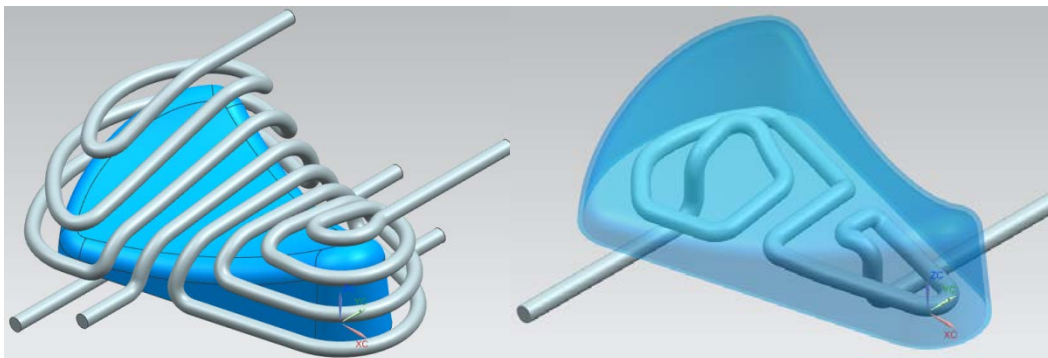


Figure 8. Conformal cooling canals in both sides

3.RESULTS

Both typical cooling canal and conformal cooling canal are designed and modelled with CAD software and then cooling analysis of these canals have been performed. Polypropylene (PP) Hostacom G2 U02 are used as a plastic material to filling of cavity and cooling analyses. Mesh generation is produced before cooling and filling analysis. In context, 685000 mesh element are generated for conformal cooling canal and 292000 mesh elements are generated for typical canal. As recommended processing parameters, melt temperature 230°C, injection temperature 160°C, and mould temperature 40°C are used. 5 lt/min is determined for flow rate of cooling water. Three inlet and three outlet are determined in conformal cooling canal, and also two inlet and outlet are used in typical canal. Cooling analysis results of conformal cooling canal and typical cooling canal (straight line) have been presented in Figure 9. In Figure 9, average temperatures distribution of

plastic part at 7th second have been shown to conformal cooling and typical cooling canal. According to cooling analysis, it is determined that average temperature value of plastic part having conformal cooling canal is less than typical cooling canal. While average temperature using conformal cooling canal is 106.9 °C, average temperature was measured as 115.9 °C using typical canal.

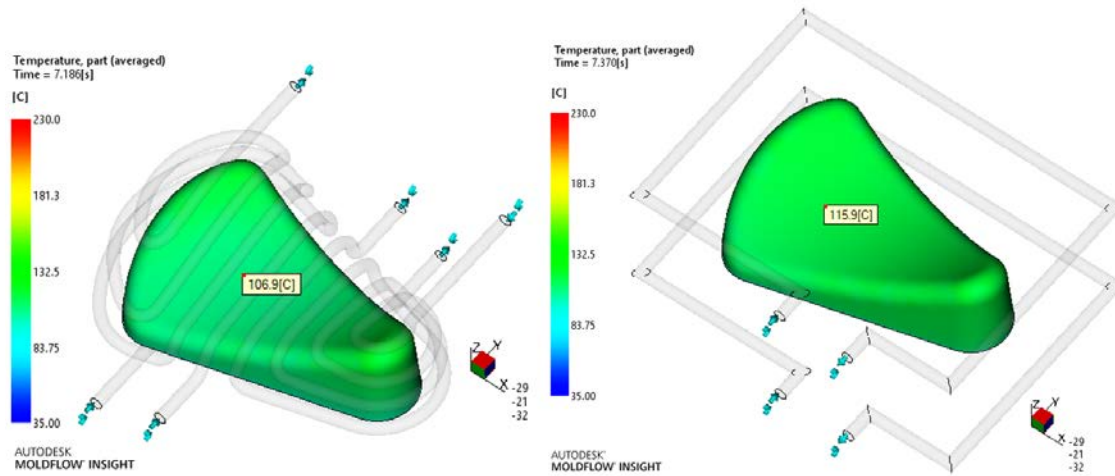


Figure 9. Temperature distribution on plastic part in the same time steps

As shown in Figure 10, temperature distribution of mould surface was determined. Accordingly, conformal cooling system is more effective than classic/typical cooling canal.

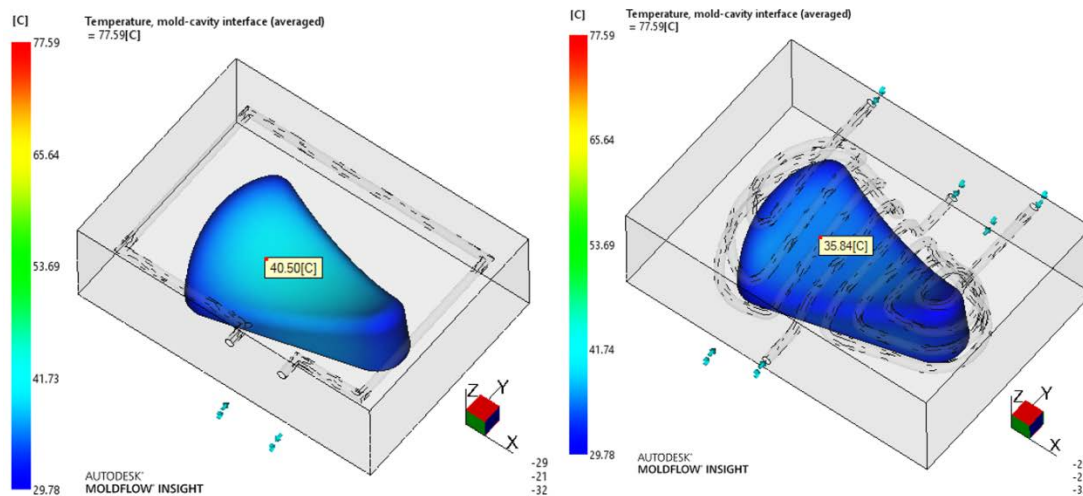


Figure 10. Comparison of the mould surface temperature distribution for both cooling canal type

Ejection time of plastic part from mould for both conformal cooling and typical cooling type were determined as shown in Figure 11. According to this, conformal cooling system has less ejection time then typical cooling canal. Thus, mold having conformal cooling canal has shorter time for one cycle which can affect the cost of plastic part.

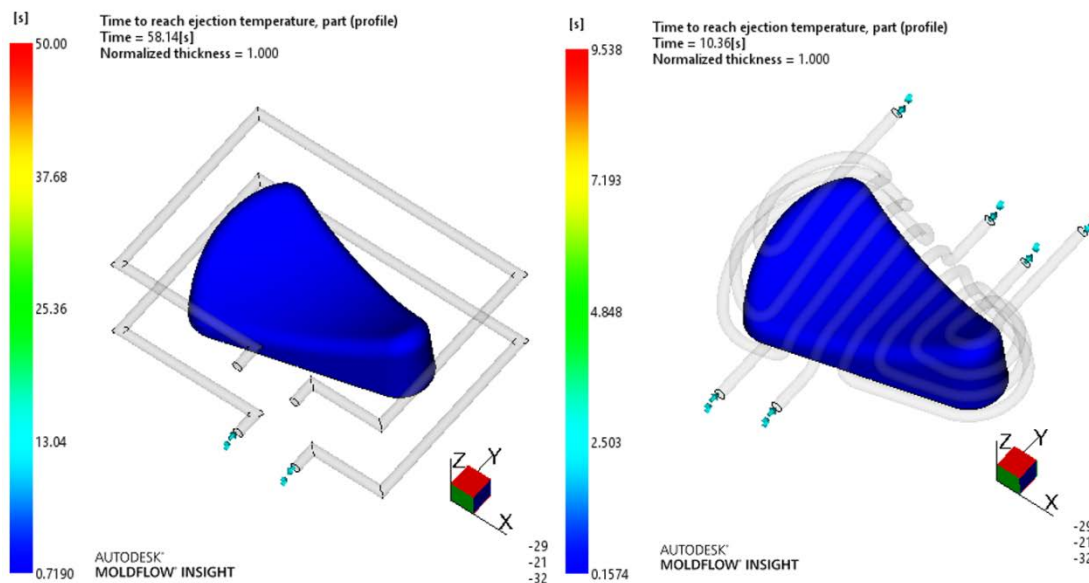


Figure 11. Comparison of the time to reach ejection temperature

4. CONCLUSIONS

A method for conformal cooling canals of plastic injection moulds has been presented in this study. Offset surface of the plastic part has been used in the proposed method. Thus, the distance of the cooling canals from the mould surface is maintained neatly. The boundary curves of the offset surface has been offset to the offset surface to regulate the distance of the cooling canals from each other. The resulting offset curves were combined to create a spiral and the parts with high curve were softened. Cooling canals were obtained extending along the resulting curves. Conformal cooling canals for complex geometries can be created with the proposed method. Moldflow software was used to analysed the effect of cooling canals designed for plastic parts with curved surface. Typical linear cooling canal created for the same part was compared. According to the analysis reports, conformal cooling canals are more effective than linear hole method.

Manufacturing of plastic injection moulds using laser metal powder sintering method is planned to be studied experimentally for the later stages in the study. Development of a software to make the designing of conformal cooling canals more practical is intended.

REFERENCES

- [1]. Sachs, E., Wylonis, E., Allen, S., Cima, M., Guo, H., Production of Injection molding tooling with conformal cooling channels using the three dimensional printing process, *Polym Eng Sci*, 40, 5, 1232–47, 2000.
- [2]. Sánchez, R., Aisa, J., Martínez, A., Mercado, D., On the relationship between cooling setup and warpage in injection molding, *Measurement* 45, 1051–1056, 2012.
- [3]. Hassan, H., Regnier, N., Pujos, C., Arquís, E., Defaye, G., Modelling the effect of cooling system on the shrinkage and temperature of the polymer by injection molding, *Applied Thermal Engineering*, 30(13), 1547–1557, 2010.
- [4]. Zhang, Y., Huang, Z., Zhou, H., Li, D., A rapid BEM-based method for cooling simulation of injection molding, *engineering Analysis with Boundary Elements*, 52, 110 – 119, 2015.
- [5]. Wang, G., Zhao, G., Wang, X., Development and evaluation of a new rapid mold heating and cooling method for rapid heat cycle molding, *International Journal of Heat and Mass Transfer* 78, 99–111, 2014.
- [6]. Jauregui-Becker, J., Tosello, G., Houten, F., Hansen, H., Performance evaluation of a software engineering tool for automated design of cooling systems in injection moulding, *Procedia CIRP* 7, 270–275, 2013.
- [7]. Li, C.G., Li, C.L., Liu, Y., Huang, Y., A new C-space method to automate the layout design of injection mould cooling system, *Computer-Aided Design*, 44, 811–823, 2012.
- [8]. Wang, G., Zhao, G., Wang, X., Heating/cooling channels design for an automotive interior part and its evaluation in rapid heat cycle molding, *Materials and Design*, 59, 310–322, 2014.
- [9]. Eiamsa-ard, K., Wannissom, K., Conformal bubbler cooling for molds by metal deposition process, *Computer-Aided Design*, 69, 126–133, 2015.
- [10]. Wang, Y., Yu, K., Wang, C., Spiral and conformal cooling in plastic injection molding, *Computer-Aided Design*, 63, 1–11, 2015.
- [11]. Xu, X., Sachs, E., Allen, S., The Design of Conformal Cooling Channels in Injection Molding Tooling, *Polymer Engineering and Science*, 41, No. 7, 2001.
- [12]. Wu, T., Jahan, S., Kumar, P., Tovar, A., El-Mounayri, H., Zhang, J., Acheson, D., Brand, K., Nalim, R., A Framework for Optimizing the Design of Injection Molds with Conformal Cooling for Additive Manufacturing, *Procedia Manufacturing*, 1, 404–415, 2015.
- [13]. Agazzi, A., Sobotka, V., LeGoff, R., Jarny, Y., Optimal cooling design in injection moulding process A new approach based on morphological surfaces, *Applied Thermal Engineering* 52, 170–178, 2013.
- [14]. Göktaş, M., Dilipak, H., Gültaş, A., “The Development of a New Algorithm for Tool Path and Offsetting of Two Dimension Profiles Machining”, *J. Fac. Eng. Gazi Univ.*, 25, 179, 1–187, 2010.

- [15]. H. Dilipak, A. Gültaş, M. Göktaş, “A New Algorithm for Offsetting Features Containing Arc”, e-Journal of New World Sciences Academy-Technological Applied Sciences, 5, 3, 212-219, 2010.
- [16]. Autodesk, MoldFlow Insight, 2010. <http://www.autodesk.com>

Chemically Color Removal from Textile Wastewater with Oxidizing and Reducing Agents

Mustafa Karaboyaci¹, Mesut Uysal¹, Aziz Sencan¹, Mehmet Kilic¹

Abstract

The textile industry consume large amounts of water and chemicals for dyeing and finishing processes. Due to the variety of organic and inorganic compounds both the dyeing as well as used in other operations, influences the resulting wastewater's characteristics. Colored wastewaters which discharged to recipient waters, reduces the light transmission in water medium, and thus adversely affect the photosynthetic activity. Also accumulation of dyes in some aquatic organisms, increases the risk of toxic and carcinogenic products occurrence. In this context, color removal processes of the textile industry wastewaters which containing dyes have ecologically importance. Chemical purification methods for the textile wastewaters, has been the most sought-after method for many years. Because, the changes which needs to be made in the quality of wastewater, can be easily adjusted with the chemical type and dose. Chemical methods such as chemical precipitation, oxidation and flocculation has been used for the textile waste water treatment, but fragmentation of dye molecules by the reduction have not been studied. Also there are many oxidizing agent has to work on. In this study, chemically color removal of textile wastewater which obtained from a cotton dyeing plant were studied with a strong oxidizing agent and a strong reducing agent. Sodium hydrosulfite was used as strong reducing agent and sodium perchlorate monohydrate was used as strong oxidizing agent. After adding 1,3,5 g/L of chemicals, color removal values were determined with Hach DR 5000 spectrophotometer according to Pt-Co unit. Also organic material removal potentials were determined with GC-MS headspace analysis. Results shows that sodium hydrosulfite has a good potential for both color and organic material removal from textile wastewater..

Keywords: *Textile Wastewater, Color Removal, Oxidizing Agent, Reducing Agent*

1. INTRODUCTION

The rapid development of the world and rapid population growth increases industrial waste and wastewater generation and it results exceeding the waste elimination tolerance level of nature. The contamination of this wastes to the natural environment, is causing adverse effects on the ecology. Major environmental balance deteriorates and discharge of this wastewaters the the receiving environment results directly or indirectly side effects on human health, fisheries and water quality. So these reasons limits the use of water for watering and similar purposes.

Due to the aforementioned reasons, especially treatment of industrial water is of great importance today.. We can define industrial wastewater as, every kind of process water formed after production, washing and cleaning from large industrial companies factories, small industries or organized industrial zones.. Compared to others, textile industry produces more wastewater.

The textile industry consumes a considerable amount of water in the manufacturing process. The water is primarily used in the dyeing and finishing operations in which the cloths are dyed and processed to finished products. In a typical dyeing and finishing mill, about 100 l of water are consumed on the average for every ton of cloth processed [1].

In the dyeing process, the dye is dissolved into the process water and at the end of dyeing process still there are some dyestuff in the when the process water is released as effluent. The wastewater contains, dyestuff and auxiliaries such as surfactants, dispersant, fatty acids that are derived from organic compounds. Most of them have very complex chemical structure. Also main environmental concern of textile wastewater lies in the dissolved organic dye compounds as some of them are aromatics and considered carcinogenic. This complex structured chemicals in the wastewater are resistant to light, acids, bases and oxidation. Because commercial needs to have this properties. Most of this chemicals have poor biodegradability so treatment of textile wastewater need special treatment methods. Treatment of textile wastewater by chemical methods has been the most sought after method for many years. The most important reason is the changes in the quality of wastewater is easily tolerable with chemical dosage and chemical kind. Most commonly used chemical methods in the textile industry wastewater treatment are oxidation methods, chemical precipitation and the flocculation methods. However decomposition of dye molecules in the textile wastewater has not been studied much. Legislation about toxic substances in industrial wastewaters is becoming increasingly strict; consequently, a large number of researchers are address- ing the variety of issues in this area [2].

In this study sodium hydrosulfite ($\text{Na}_2\text{S}_2\text{O}_4$) was used as strong reducing agent. It is a water soluble salt, and can be used as a reducing agent in aqueous solutions. The reduction properties of sodium dithionite eliminates excess dyes, residual

¹ Corresponding author: Süleyman Demirel University, Department of Chemical Engineering, 32260, Çünür / Isparta, Turkey.
mustafakaraboyaci@sdu.edu.tr

oxide, and unintended pigments, thereby improving overall effluent quality. Sodium perchlorate monohydrate (NaClO₄·H₂O) was used as strong oxidizing agent. It is the most water soluble perchlorate salt and perchlorate consists of chlorine in its highest oxidation number. Color removal potential of these chemical were performed with a textile wastewater obtained from cotton dyeing company.

2. MATERIALS AND METHODS

In this study effluent is obtained from which emerged after dyeing cotton fibers. pH of the wastewater is over 8.5. Sodium hydrosulfite BASF %88 used as reducing agent and sodium perchlorate monohydrate (Merck) %99 used as oxidizing agent. 1,3,5 mg/L of solid chemicals was added in the spectrometer tubes which includes 20 ml of wastewater. Color measurements were made according to the Platinum-Cobalt unit with Hach DR 5000 UV-Vis spectrometer at 465 nm.

Color removal percentage was calculated using the following equation.

$$\% \text{ Color removal} = (A_0 - A) / A_0 * 100$$

A₀ is the Pt Co value of raw wastewater and A is the Pt Co value of the chemical added wastewater

3. RESULTS AND DISCUSSION

Table 2 shows the color removal performance of sodium dithionite. Wastewater Pt-Co value is 3341 and it is so reddish contaminated wastewater. Table 2 shows the color removal percentage of sodium dithionite. It is clear from the table all results are about %85 so the best chose is 1 minute and 1 g/l sodium dithionite dosage. [3] performed a study involving oxidation and coagulation, for the removal of color and chemical oxygen demand from synthetic textile wastewater containing polyvinyl alcohol and a reactive dyestuff, R94H. The color removal reached with combined method maximum of 90% at a reaction time of 5 min under low dosages of H₂O₂ and Fe²⁺. [4] performed a study combined reduction-biological treatment system for the decolorization of non-biodegradable textile dyeing wastewater. They used a bisulfite-catalyzed sodium borohydride reduction followed by activated sludge technique in order to remove the color at ambient temperature and pressure. The results of this study demonstrated that the newly developed treatment technique decreased color about % 74-88. Sodium dithionite removes color in a very short time only by adding in to wastewater. So it is a good alternative for removing color from textile effluent.

Table 5. Color removal performance of sodium dithionite

Raw Pt-Co	Dosage	0 min.	1 min	5 min	10 min.
3341	1 g/L	620	485	476	454
	3 g/L	568	491	484	475
	5 g/L	506	477	457	451

Table 2. Color removal percentage of sodium dithionite

Raw Pt-Co	Dosage	0 min.	1 min	5 min	10 min.
3341	1 g/L	81,5	85,5	85,75	86,4
	3 g/L	83	85,3	85,5	85,7
	5 g/L	85	85,7	86,3	86,5

Table 3 shows the Pt-Co values of the effluent treated with sodium perchlorate and table 4 color removal percentage of sodium perchlorate. As seen from table 4 sodium perchlorate removes about %55 of color from wastewater for all time intervals and fro all doses. Perchlorate performance appears lower than dithionite. Perchlorate is an house hold bleacher and it is not directly used for textile effluent bleaching. Perchlorate can occur during the electrolysis of chlorine containing solutions but it is a undesired side product while color removal from textile wastewater with electro chemical degradation [5]. Color removal performance of sodium perchlorate can be tried with high temperatures. Or it can be used not to much contaminated effluents [6].

Table 3. Color removal performance of sodium perchlorate

Raw Pt-Co	Dosage	0 min.	1 min	5 min	10 min.
3341	1 g/L	1475	1472	1461	1461
	3 g/L	1472	1471	1459	1458
	5 g/L	1467	1468	1458	1454

Table 4. Color removal percentage of sodium perchlorate

Raw Pt-Co	Dosage	0 min.	1 min	5 min	10 min.
3341	1 g/L	55,85	55,94	56,27	56,27
	3 g/L	55,94	55,97	56,33	56,36
	5 g/L	56	56	56,95	56,48

Table 5. GC-MS headspace analysis result of untreated effluent

Peak	R.Time	Name	Area	Area%
2	1.240	(3a.alpha.,4.beta.,6a.alpha.)-hexahydro-4-methyl-5-methylene-1(2h)-	136762	1.21
5	1.567	Hexane (CAS) n-Hexane	88863	0.78
6	1.645	Butanoic acid, 2,2-dimethyl-	60094	0.53
7	1.709	Chloroform	88131	0.78
8	1.973	1,3-Dioxolane, 4-methyl-	82867	0.73
10	2.373	Ethene, trichloro- (CAS) Tri	234780	2.07
11	3.404	Benzene, methyl- (CAS) Toluene	45672	0.40
12	6.270	Isoamyl acetate	124540	1.10
13	6.330	2-Methylbutyl acetate	56675	0.50
15	13.565	Triplal 1 (iff)	104222	0.92
21	21.471	2-tert-Butylcyclohexanol	8376619	73.89
22	22.191	4-tert-Butylcyclohexanol	1267875	11.18
23	27.845	Cycloheptasiloxane, tetradecamethyl-	59775	0.53
27	35.879	Alpha. Hexylcinnamic aldehyde	58819	0.52
			11336023	100.00

Table 6. GC-MS headspace analysis result of sodium perchlorate treated effluent

Peak	R.time	Name	Area	Area%
1	1.054	Methane, tetranitro- (CAS) Tetranitromethane	390607	3.95
8	1.966	1,3-Dioxolane, 4-methyl- (CAS) 4-Methyl-1,3-dioxolane	69919	0.71
11	2.367	Heptane (CAS) n-Heptane	118858	1.20
13	6.260	Isoamyl acetate	115834	1.17
17	13.559	Triplal 1 (IFF)	107959	1.09
23	21.463	2-tert-Butylcyclohexanol	7384763	74.71
24	22.184	4-tert-Butylcyclohexanol	1131168	11.44
29	36.458	Lixetone	12231	0.12
			9884313	100.00

Table 7. GC-MS headspace analysis result of sodium dithionite treated effluent

Peak#	R.Time	Name	Area	Area%
1	1.209	Oxirane, ethyl- (CAS) 1,2-Epoxybutane	57131	0.63
7	2.370	Ethene, trichloro- (CAS) Tri	73198	0.80
9	6.262	1-Butanol, 3-methyl-, acetate (CAS) Isoamyl acetate	95263	1.05
11	16.283	Acetic acid, 2-ethylhexyl ester (CAS) Acetic acid, octyl ester (CAS) 2-Ethylhexyl acetate	99229	1.09
15	19.616	2-Ethyl-1-hexyl propionate	98325	1.08
16	21.462	2-tert-Butylcyclohexanol	7317418	80.37
17	22.182	4-tert-Butylcyclohexanol	1053792	11.57
21	35.867	Octanal, 2-(phenylmethylene)-	25184	0.28
			9105079	100.00

Table 5-7 shows the GC-MS headspace analysis results of untreated, sodium perchlorate treated and sodium dithionite treated effluents respectively. Less than 0.5 percent of the components were deleted from the table in order to shorten. In the raw water there are 27 components and of them is Benzene, methyl- (CAS) Toluene. Bot of the chemical treatment remove this carcinogenic chemical from effluent. Major component of all three effluent is butylcyclohexanol. This is an surface active agent may occur in wetting agent or in softener. It is not a dangerous substance according to 67/548/EEC and %89 of it easily biodegradable. There are 21 components in the effluent treated with dithionite. Dithionite has broken many of the components in the effluent. The separation of large molecules into smaller pieces may increase the biodegradability.

4. CONCLUSIONS

When the above statements are examined It is observed that the color removal process with hydrosulfite fairly efficient. Instant color removal in all three concentrations are similar. So for the continuous fluid system for only 1 g / L can be realized by means of color removal. Treatment of aromatic azo dyes with sodium dithionite results in a reductive cleavage of the nitrogen-nitrogen double bond [7]. So the color removal efficiency is very high. According to GC-MS headspace analysis result dithionite breaks molecules and reduce the number of compounds in the effluent. Color removal performance of perchlorate is not as efficient as dithionite but it removes about %55 of the color at room temperature. Also at the GC-MS headspace analysis about %4 of the tetra nitro methane is seen. We can interpret this result, perchlorate break down the azo dye molecules in to little pieces and it has oxidized it to nitro methane. So it can be a good chemical agent for removal of azo dyes.

ACKNOWLEDGEMENTS

This study is a part of the project supported by Suleyman Demirel University 3701-YL1-13 research project coordination unit

REFERENCES

- [1]. Lin, Sheng H., and Ming L. Chen. "Purification of textile wastewater effluents by a combined Fenton process and ion exchange." *Desalination* 109.2 (1997): 121-130.
- [2]. Slokar, Y. March, and A. Majcen Le Marechal. "Methods of decoloration of textile wastewaters." *Dyes and pigments* 37.4 (1998): 335-356.
- [3]. Kang, Shyh-Fang, Chih-Hsaing Liao, and Mon-Chun Chen. "Pre-oxidation and coagulation of textile wastewater by the Fenton process." *Chemosphere* 46.6 (2002): 923-928..
- [4]. Ghoreishi, S. M., and R. Haghghi. "Chemical catalytic reaction and biological oxidation for treatment of non-biodegradable textile effluent." *Chemical engineering journal* 95.1 (2003): 163-169.
- [5]. Brazil Maljaei, Ata, Mokhtar Arami, and Niyaz Mohammad Mahmoodi. "Decolorization and aromatic ring degradation of colored textile wastewater using indirect electrochemical oxidation method." *Desalination* 249.3 (2009): 1074-1078.
- [6]. Trumpolt, Clayton W., et al. "Perchlorate: sources, uses, and occurrences in the environment." (2005).
- [7]. *Colorants for Non-Textile Applications*, H.S. Freeman, A.T. Peters Elsevier, 3 May 2000 page 549

Finite Element Modeling of Residual Stresses and Cutting Temperature in Hard Turning

M. Erdi Korkmaz¹, Nafiz Yaşar², Mustafa Gunay³

Abstract

Hard turning and grinding are the most important finish processes for manufacturing of precision mechanical components such as bearings, gears and cams. However, hard turning has much more advantages than grinding with higher metal removal rate, shorter setup time, less machine investment and also no usage of coolant. The residual stresses and cutting temperature which are induced by hard turning affects fatigue life, corrosion crack resistance and part distortion. Therefore, they should be predicted better and the cutting parameters should be adjusted according to that. This paper presents the finite element analysis (FEA) on cutting temperatures and residual stresses in hard turning of AISI H13 tool steel to hardened 56 HRC with uncoated CBN tools. The cutting parameters are chosen as feed rate and cutting speed with three levels and constant depth of cut. The analyses are performed with Advantedge software in 2D orthogonal cutting. The adaptive remeshing are applied to workpiece for more accurate results although it requires much more time. After the cutting process is finished, both the chip and tool are removed and the workpiece is allowed to thermo-mechanically relax. The average of three extraction points on eight different depths of machined surface for residual stresses is calculated for better results. Besides, cutting temperatures obtained from tool-chip interface were evaluated according to cutting parameters. FEA results showed that both tangential and axial residual stresses act as compressive in the depths near the surface until about 75 μm while they act as tensile stress after the depth of 100 μm until about 300 μm . Also, increasing feed rate has decreasing effect on compressive residual stresses while increasing effect on tensile residual stresses. Finally, both increasing feed rate and cutting speed lead to increase in cutting temperature.

Keywords: Hard turning, AISI H13, Finite element method, Residual Stress, cutting temperature

1. INTRODUCTION

Manufacturing of hardened steel parts known as hard turning with high accuracy and surface quality is commonly replaced by grinding because of the comparatively high cost and setup time of the grinding process. Flexibility and positive ecological effects are other advantages of dry hard machining [1]. Surface integrity of components affects their service life and dimensional stability, so it is extremely important to control the final surface state of parts after hard machining. Among the properties commonly enclosed in the surface integrity of a component, the most relevant are residual stresses, roughness, hardness and microstructure followed by cutting temperature and forces. Particularly, residual stresses play a key role in the service life of components, because they add up to the external stresses acting over the part during service, leading to a real stress higher than the applied stress, and therefore the fatigue resistance of the component is reduced, leading to possible premature failure of the components during its service life [2]. Therefore, a lot of machining studies have been performed in order to control the residual stresses or cutting temperatures which determine the fatigue life. Navas et al. [3] studied the effects of cutting speed, feed, tool nose radius, geometry of the tool chip breaker and coating of the cutting tool on the final surface stress state and cutting temperature in AISI 4340 steel.

In all cases surface tensile residual stresses have been measured, tending to be more or less tensile (and consequently more or less detrimental to the service life of the machined component) depending on the cutting conditions and the characteristics of the cutting tool. The authors stated that when feed increases, residual stresses tend to be more tensile due to an increase in cutting temperature with feed, and also surface roughness increases. Therefore, surface integrity of the part deteriorates with the increase in cutting feed. Also, maximum stresses are located near cutting direction, approaching this direction slightly as cutting speed and feed increase. Smith et al. [4] investigated the relationship between fatigue life and surface integrity of hard turned AISI 52100 steel (60–62 HRC) characterized via residual stress measurements with five distinct surface conditions, namely, hard turned with continuous white layer, hard turned with no white layer, ground, and super finished hard turned and ground specimens. The results suggested that the effect of residual stress on fatigue life is more significant than the effect of white layer. For the hard turned surfaces, the fatigue life is found to be directly proportional to both the surface compressive residual stress and the maximum compressive residual stress. Jafarian et al. [5] estimated and optimized the effect of machining parameters including cutting speed, depth of cut and feed rate on induced tensile residual stresses measured by X-ray Diffraction (XRD) method in the finish/semi-finish turning process of Inconel718. Then, the experimental results were introduced to the intelligent systems including artificial neural network

¹ Corresponding author: Karabük University Engineering Faculty, Karabük/TURKEY, merdikorkmaz@karabuk.edu.tr

(ANN) and genetic algorithm (GA) to estimate residual stress at the various machining parameters and optimize the process. It was shown that, implemented efficient intelligent techniques in this paper are remarkably appropriate for machining of Inconel718.

There can be a lot of time and material saving if these machining processes including residual stresses and cutting temperatures were performed and supported with finite element modeling which predicts and controls the machining characteristics. Therefore, many finite element modeling studies have been performed with this purpose. Abboud et al. [6] developed a finite element model of orthogonal cutting using DEFORM-2D in order to build a predictive tool for machining-induced residual stresses in titanium alloy Ti-6Al-4V. A full factorial orthogonal cutting experiment is conducted using sharp tools to investigate the effect of feed rate (f) and cutting speed (v) on residual stresses under finish-turning conditions. The results show that experimental and finite element modeling results are compatible for forces, temperatures and residual stresses. It was also observed that residual stresses become more compressive with increasing feed rate and less compressive with increasing edge radius or cutting speed. Ratchev et al. [7] presented a finite element model with ABAQUS 2D for prediction of turning induced residual stresses of Ti6Al4V alloy in two cutting depths (100 and 500 μm). Dynamic thermo-mechanical FE analysis using explicit integration is performed. The workpiece is modelled as an isotropic thermal-elastic-plastic model using the Johnson-Cook constitutive equation. The near-surface residual stresses are predicted and compared with experimentally measured results. It can be seen from results that the measured and the predicted stresses are compressive near the machined surface and the predicted stresses from FEM are in very good agreement with the experimentally measured stresses in the minimum and maximum principal directions for both depths of cut (100 and 500 μm). Stenberg and Proudian [8] presented a thermo-mechanical numerical simulation of the machining operation to obtain the impacts of parameters on residual stresses and compare these stresses to measurements of a machined axis. The simulations were performed with the software package DEFORM which has a remeshing function that, for practical reasons, is necessary when forming chips. The large deformations will make the FE-analysis to costly otherwise. The simulation results showed that the residual stresses are however a bit hard to extract since the re-mesh function moved the nodes around and thereby adding extra work in the post processing phase. Therefore, 2-D simulations were used instead of 3-D simulations because of relatively low on calculation time. Özel and Ulutan [9] presented experimental investigations and finite element simulations on turning of Ti-6Al-4V titanium alloy and IN100 nickel based alloy with uncoated and TiAlN coated tools. Face turning of Ti-6Al-4V and IN100 using uncoated tools with various edge radii and TiAlN coated carbide tools was conducted; and residual stresses were measured in radial and circumferential directions using X-ray diffraction technique. The authors stated that predicted residual stresses are influenced by the tool micro-geometry as they become more compressive with increased edge radius but more tensile at the surface when coated. The results also showed that the experimental results are compatible with FEM results.

These studies preferred finite element analysis of residual stresses and cutting temperature due to the fact that the conventional way to measure these characterizations is difficult manner. The studies showed that the modelling of such characterizations is highly compatible with experimental results. Therefore, this study presents FE modeling of residual stresses and cutting temperatures in hard turning of AISI H13 tool steel with uncoated CBN tools.

2. MATERIAL AND METHOD

The aim of this study was to investigate the effects of cutting parameters on residual stresses and cutting temperatures in hard turning of AISI H13 steel with uncoated CBN tools. The finite element analyses were performed with Advantedge software with 2D orthogonal turning instead of 3D turning due to low calculation time. The following cutting conditions were used for the experiments: feed rate (f) of 0.1, 0.15 and 0.2 mm/rev and cutting speed (V) of 150, 200 and 250 m/min with constant cutting depth (a) of 0.2 mm.

2.1. Workpiece material

The workpiece material has the following chemical composition: 0.4% C, 1.0% Si, 0.40% Mn, 5.1% Cr, 1.3% Mo, 1.0% V and the balance is Fe. The workpiece was hardened to 55 ± 1 HRC by means of heat treatment by quenching in a vacuum atmosphere. The Johnson-Cook model [10] widely-used material model for machining simulations is given in Eq. 1. This material model is particularly suited to model high strain rate deformation of metals. It is generally used in adiabatic transient dynamic analysis. The hardening is a particular type of isotropic hardening in which the yield stress σ^0 is assumed as [11]:

$$\sigma^0 = (A + B(\varepsilon^p)^n) \left(1 + C \log \left(\frac{\dot{\varepsilon}^p}{\dot{\varepsilon}_0} \right) \right) \left(1 - \left(\frac{T - T_r}{T_m - T_r} \right)^m \right) \quad (1)$$

In equation (1), material parameters obtained from mechanical tests that are A , B , C , n and m are yield stress below room temperature, strain hardening, strain rate constant, strain hardening constant and thermal softening constant, respectively. The other parameters ε^p , $\dot{\varepsilon}^p$, $\dot{\varepsilon}_0$, T_r , T_m and T are equivalent plastic strain, plastic strain rate, reference strain rate, room temperature, melting temperature and reference temperature, respectively. Also, $\dot{\varepsilon}_0$ and C are usually measured at or below the reference temperature. The Johnson-Cook parameters and the other material properties for AISI H13 steel was given in Table 1 and Table 2, respectively.

Table 1. The Johnson–Cook parameters for the AISI H13 steel material

AISI H13	A (MPa)	B (MPa)	C	n	m	T_r (°C)	T_m (°C)	$\dot{\epsilon}_0$
	908.54	321.39	0.028	0.278	1.18	27	1428	1

Table 2. Physical and mechanical properties for the workpiece material

AISI H13	Density (g/cm ³)	Poisson's ratio	Young's modulus (GPa)	Thermal conductivity (W/m.K)	Specific heat (J/kg°C)	Thermal expansion (10 ⁻⁶ °C)
	7.8	0.3	215	28.6	460	10.4

2.2. The cutting tool

The low-content uncoated (KBN510) with the code of DNGA 150404S01225 from KYOCERA have been used as cutting tools in 2D orthogonal analyses. Tool holder used was DDJNR 2525M-12 coded external tool holder clamping cutting tools strictly. The combination of tool holder and cutting tool has negative rake angle (γ)= -6° and clearance angle (α)= 6° with the edge radius (r) of 0.02 mm because edge radius is used instead of tool nose radius in 2D orthogonal turning (Fig. 1). The material parameters for CBN cutting tool was given in Table 3.

Table 3. Physical and mechanical properties for cutting tool

CBN	Density (g/cm ³)	Poisson's ratio	Young's modulus (GPa)	Thermal conductivity (W/m.K)	Specific heat (J/kg°C)	Thermal expansion (10 ⁻⁶ °C)
	3.48	0.22	760	450	670	4.7

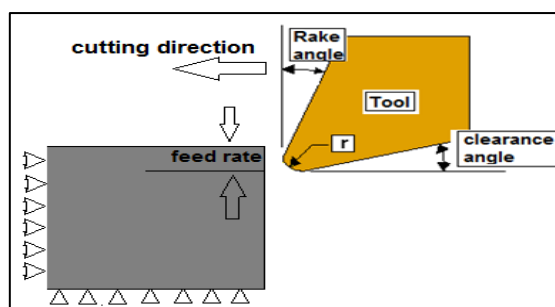


Figure 1. 2D model of orthogonal turning

2.3. FE simulations

The finite element analyses of residual stresses and cutting temperatures were performed with Advantedge software depending on finite element method. Advantedge uses an Arbitrary Lagrangian solver and it has adaptive remeshing function to provide more accurate results although it takes more time. The first stage of simulation is to determine the workpiece length (5 mm) and height (2 mm) with workpiece material. The second stage is determining the tool parameters (rake angle, clearance angle and edge radius) with tool material. The final stage is to enter required simulation parameters such as feed rate, depth of cut, length of cut and cutting speed after meshing parameters and coefficient of friction is adjusted.

The interface between tool and work piece is modelled with a standard Coulomb friction which is assumed as 0.6. The meshing parameters are used as 0.1 mm and 0.02 mm for maximum and minimum element size, respectively. The cutting parameters for finite element analyses were given in Table 4.

Table 4. Cutting parameters

<i>Levels</i>	<i>1</i>	<i>2</i>	<i>3</i>
<i>Feed rate (mm/rev)</i>	0.1	0.15	0.2
<i>Cutting speed (m/min)</i>	150	200	250
<i>Depth of cut (mm)</i>	0.2		
<i>Coefficient of friction</i>	0.6		

The workpiece was cut off 2mm in analyses of residual stresses and cutting temperatures. After the cutting process is finished, both the chip and tool are removed and the workpiece is allowed to thermo-mechanically relax. The residual stresses were obtained from three extraction levels (%20, %50 and %80) of workpiece starting point. The average of these values then calculated for more accurate results. The eight depth of workpiece were considered for residual stress analyses. The simulation model and cutting scheme were shown in Fig. 2.

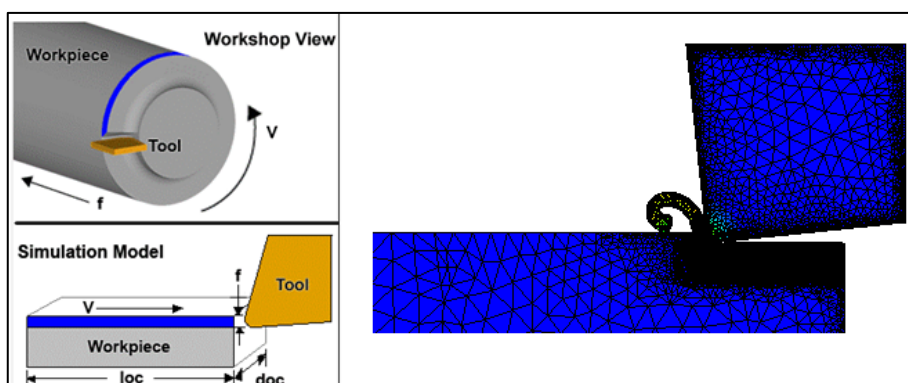


Figure 2. 2D simulation model

3. RESULTS AND DISCUSSION

In this study, only 2D simulation was performed instead of 3D simulation due to low calculation of time. As shown from Fig 3-5, the eight depth of workpiece were considered for residual stress analyses. The residual stresses were obtained from three extraction levels (%20, %50 and %80) of workpiece starting point and then average of these values calculated for evaluating precisely influence of residual stresses on workpiece materials.

3.1. Evaluating of residual stresses

The influences of cutting parameters (feed rate and cutting speed) on residual stresses were assessed by means of the figures. In general, Fig. 3-5 display similar tendency. Both tangential and axial residual stresses act as compressive in the depths near the surface until about 75 μm while they act as tensile stress after the depth of 100 μm until about 300 μm without considering the change of feed rate and cutting speed.

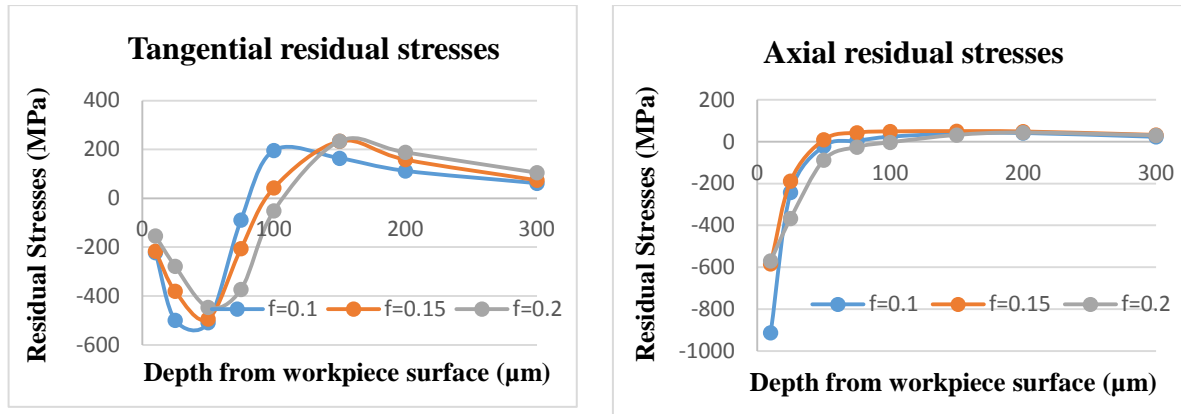


Figure 3. Residual stresses for $V=150$ m/min

The compressive residual stresses in cutting speed of 150 m/min decrease with increasing feed rate for tangential direction according to Fig.3. However, the tensile residual stresses increase with increasing feed rate. The tangential compressive residual stress decrease about %24 and %27 when the feed rate increase from 0,1 to 0,15 and 0,15 to 0,2 mm/rev, respectively in 25 μm depth from workpiece surface. The tangential tensile residual stresses increase about %41 and %20 when the feed rate increase from 0,1 to 0,15 and 0,15 to 0,2 mm/rev, respectively in 200 μm depth from workpiece surface. The axial residual stresses have not an important change for all cutting speed with increasing feed rate except for the surface in depth of 10 μm .

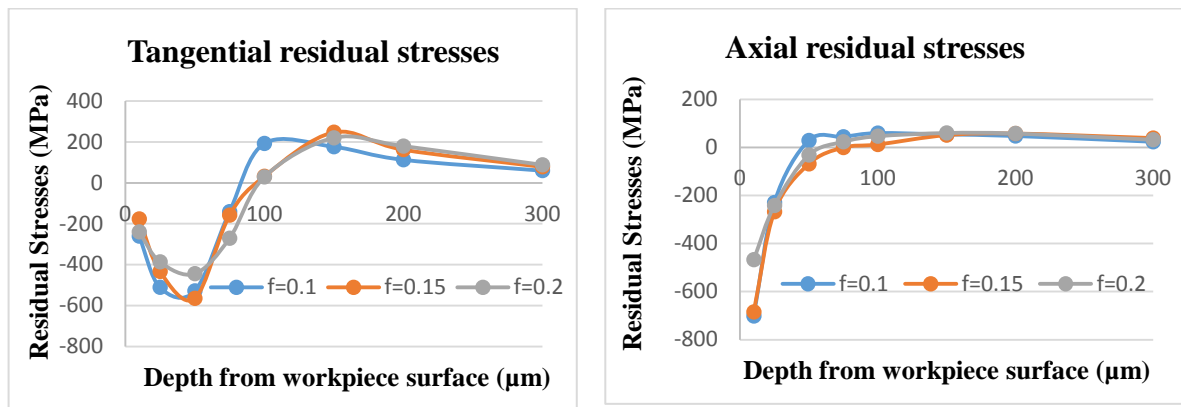


Figure 4. Residual stresses for $V=200$ m/min

Fig. 4 acts similar tendency like Fig. 3. The tangential compressive residual stress decrease about %15 and %11 when the feed rate increase from 0,1 to 0,15 and 0,15 to 0,2 mm/rev, respectively in 25 μm depth from workpiece surface. The tangential tensile residual stresses increase about %44 and %10 when the feed rate increase from 0,1 to 0,15 and 0,15 to 0,2 mm/rev, respectively in 200 μm depth from workpiece surface.

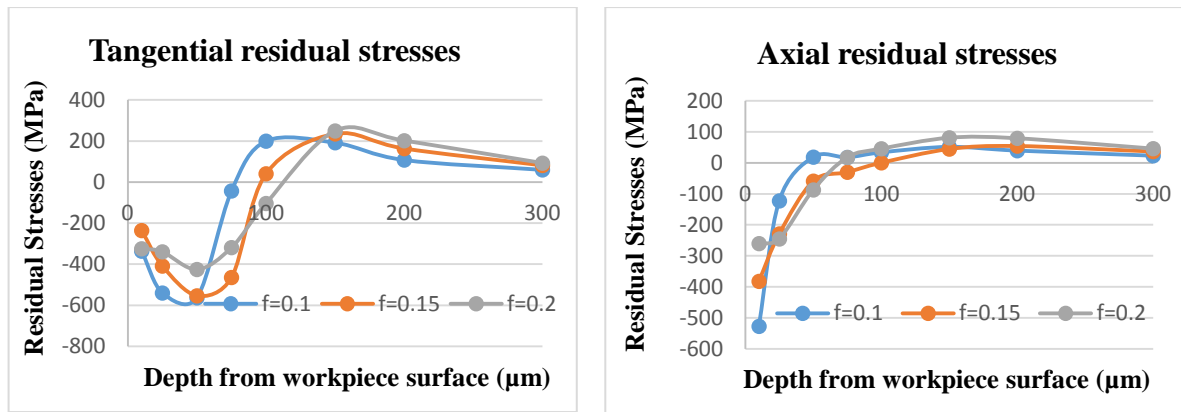


Figure 5. Residual stresses for $V=250$ m/min

The tangential compressive residual stress decrease about %24 and %17 when the feed rate increase from 0,1 to 0,15 and 0,15 to 0,2 mm/rev, respectively in 25 μm depth from workpiece surface. The tangential tensile residual stresses increase about %52 and %23 when the feed rate increase from 0,1 to 0,15 and 0,15 to 0,2 mm/rev, respectively in 200 μm depth from workpiece surface.

The cutting speed has a little change on residual stresses when examining Fig. 3-5. The tangential compressive residual stresses increase about %10 and %7 when the cutting speed increase from 150 to 200 and 200 to 250 m/min, respectively. However, the cutting speed has no important change on axial residual stresses in these conditions.

3.2. Evaluating of cutting temperature

Although a large amount of the cutting temperature occurred during metal cutting is dissipated by chip, as for the rest of temperature is transferred proportionally the cutting tool and workpiece. Hence, the temperature distribution is important because of the cutting temperature effects hot hardness of cutting tool, indirectly cutting performance and tool life. On the otherhand, temperature measurement during metal cutting are too difficult due to a thin shear zone, chip problems, and the phenomena of the tool-chip interface. Therefore, numerical analysis based on finite element method is widely used for predicting the stress, strain and temperature distributions in plastic deformation zones (primary, secondary and tertiary) as well as cutting forces. Figure 6 shows the variation by cutting speed and feed rate of cutting temperature which are acquired by numerical analysis studies. In 2D simulations both feed rate and cutting speed have increasing effect on cutting temperature in tool-chip interface.

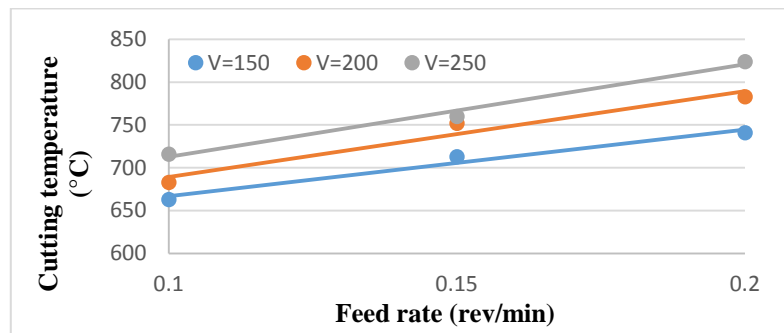


Figure 6. Cutting temperature on tool-chip interface

As can be seen from Fig. 6, cutting temperature increases about %4.7 and %3.7 when the cutting speed increases from 150 to 200 and 200 to 250 m/min, respectively. Moreover, cutting temperature increases about %7.9 and %5.5 when the feed rate increase from 0,1 to 0,15 and 0,15 to 0,2 mm/rev, respectively. The feed rate is more effective than cutting speed on cutting temperature in tool-chip interface as understood from increasing ratios.

4. CONCLUSION

In this study, the effects of cutting parameters on residual stresses and cutting temperature on tool-chip interface have been analyzed with finite element method in hard machining of AISI H13 tool steel workpieces with 55 ± 1 HRC hardness using CBN inserts. 2D orthogonal cutting has been used instead of 3D cutting due to low calculation of time in finite element analyses. The following conclusions are drawn from this study:

- Both tangential and axial residual stresses act as compressive in the depths near the surface until about 75 μm while they act as tensile stress after the depth of 100 μm until about 300 μm without considering the change of feed rate and cutting speed.

- The compressive residual stresses decrease with increasing feed rate while the tensile residual stresses increase with increasing feed rate for tangential direction. The axial residual stresses have not an important change for all cutting speed with increasing feed rate except for the surface in depth of 10 μm .
- Cutting temperature on tool-chip interface increases with increasing either feed rate or cutting speed.
- The feed rate is more effective than cutting speed on cutting temperature in tool-chip interface as understood from increasing ratios in Fig. 6.

REFERENCES

- [1] H.K. Tonshoff, C. Arend, R.B. Amor, "Cutting of hardened steel", *CIRP Annals- Manufacturing Technologies* 49 (2) (2000) 547–566.
- [2] G.K. Dosbaeva, M.A. El Hakim, M.A. Shalaby, J.E. Krzanowski, S.C. Veldhuis, "Cutting temperature effect on PCBN and CVD coated carbide tools in hard turning of D2 tool steel", *International Journal of Refractory Metals and Hard Materials*, 50 (2015) 1–8.
- [3] V.G. Navas, O. Gonzalo, I. Bengoetxea, "Effect of Cutting Parameters in Surface Residual Stresses Generated by Turning in AISI 4340 Steel", *International Journal of Machine Tools and Manufacture*, 61 (2012) 48-57.
- [4] S. Smith, S.N. Melkote, E.L. Curzio, T.R. Watkins, L. Allard, L. Riester, "Effect of surface integrity of hard turned AISI 52100 steel on fatigue performance", *Materials Science and Engineering A*, 459 (2007) 337–346.
- [5] F. Jafarian, H. Amirabadi, J. Sadri, "Experimental measurement and optimization of tensile residual stress in turning process of Inconel718 superalloy", *Measurement* 63 (2015) 1-10.
- [6] E. Abboud, B. Shi, H. Attia, V. Thomson, Y. Mebrahtu, "Finite element-based modeling of machining-induced residual stresses in Ti-6Al-4V under finish turning conditions", *Procedia CIRP*, 8 (2013) 63-68.
- [7] S.M. Ratchev, S.M. Afazov, A.A. Becker, S. Liu, "Mathematical modelling and integration of micro-scale residual stresses into axisymmetric FE models of Ti6Al4V alloy in turning", *CIRP Journal of Manufacturing Science and Technology*, 4 (2011) 80–89.
- [8] N. Stenberg, J. Proudian, "Numerical modelling of turning to find residual stresses", *Procedia CIRP*, 8 (2013) 258-264.
- [9] T. Özel, D. Ulutan, "Prediction of machining induced residual stresses in turning of titanium and nickel based alloys with experiments and finite element simulations", *CIRP Annals – Manufacturing Technology*, 61 (2012) 547–550.
- [10] G.J. Johnson, W.H. Cook, "A constitutive model and data for metals subjected to large strains, high strain rates and high temperatures". In: *Proceedings of the Seventh International Symposium on Ballistics, The Hague*, (1983) 541–547.
- [11] A. Dorogoy and D. Rittel, "Determination of the Johnson–Cook Material Parameters Using the SCS Specimen", *Experimental Mechanics*, 49 (2009) 881–885.

Experimental and Numerical Analysis of Cutting Forces in Machining of Hardened X40CrMoV5-1 Steel

Nafiz Yasar^{1,}, Hakan Yurtkuran², M. Erdi Korkmaz³, Mustafa Gunay⁴*

Abstract

The production time and cost of machine parts decrease while fatigue strength increase in manufacturing of cylindrical parts from hardened steels when hard turning is preferred instead of grinding. X40CrMoV5-1 hot work tool steels are commonly used in manufacturing of injection and extrusion mold, and also in process which require high toughness and wear resistance in high temperature. In this study, the main cutting force (F_c) in machining of X40CrMoV5-1 tool steel hardened to 55 ± 1 HRC in vacuumed heat treatment with uncoated ceramic tools were experimentally measured. The machining experiments were performed according to Taguchi L9 orthogonal array with different cutting parameters (cutting speed, feed rate and depth of cut). Kistler 9257B type of dynamometer and its equipments were used for measuring of cutting forces. The numerical analysis for cutting forces was carried out with DEFORM 3D software which has solutions according to finite element method. Moreover, the effects of cutting parameters on cutting forces has been specified with ANOVA in %95 confidence level. It was determined that average of %94 similarity between experimental and numerical analysis results for cutting forces. It was shown that the most important factor on F_c is depth of cut according to ANOVA results conducted based on experimental data.

Keywords: *Hard turning, Deform 3D, Tool steel, Finite element method, Taguchi method*

1. INTRODUCTION

Manufacturing of hardened steel parts with high accuracy and surface quality is widely provided by grinding. Hard machining has been suggested to partially replace grinding owing to the relatively high cost of the grinding process. Flexibility and positive ecological effects are other advantages of dry hard machining [1]. Additionally, the surfaces by hard turning may have a longer fatigue life when compared with grinding parts [2].

Recently, machining of hardened steel is a subject of concern for industrial fabrication and scientific investigation as it presents a number of probable advantages, involving high accuracy, lower tooling costs, shorter setup time, less process step, flexibility of larger part geometry, and generally the usage of cutting fluid is unrequired during turning of hardened steel. Manufacturing costs are expected to be reduced by up to 30% once hard turning is used for producing complex parts [3]. Besides, the main concerns of hard turning are the tool materials cost and the effect of the cutting conditions on machinability characteristics. The machining of hardened steels using cubic boron nitride, polycrystalline cubic boron nitride and ceramic tools is commonly known as a best replacement instead of grinding cost in order to reduce the tooling time and keep off the lubrication [4]. In this regard, Aouici et al. [5] mentioned about the optimization of cutting conditions in order to decrease the cost and time in mass production. For this purpose, authors performed an optimization study in hard turning of AISI H11 tool steel with CBN insert by using the response surface methodology (RSM). The results show that the cutting force components are influenced principally by the depth of cut and workpiece hardness. Bouacha et al. [6] focused on variation of tool wear and cutting forces in different workpiece hardness and cutting speed on hard turning. Moreover, the relationship between cutting parameters (cutting speed, feed rate and depth of cut) and cutting forces were analyzed. Results show that the thrust force is the highest cutting force components, and it is highly sensitive to workpiece hardness, negative rake angle and tool wear evolution. Also, the depth of cut was the most effective parameter on cutting forces as compared to the feed rate and cutting speed. Oh [7] examined the cutting force in order to determine the processing properties at hard turning of SKD 11 high hard steels with CBN. The results show that it was

effective to do cutting with low cutting speed and high transfer ratio in order to cut a large quantity of SKD 11. Also, it was demonstrated that cutting forces increased with increasing feed rate or decreasing cutting speed.

Experimental methods have many difficulties in the cutting process for analysis of machinability characteristics, namely, cutting force, temperature, strain, strain rate, and stress. Thus, the finite element models predicting these characteristics have been performed to increase the production capacity by uncompromising their required values. The techniques such as finite element method, regression analysis and artificial neural network etc. are used. Finite element method is the most commonly used among these techniques in order to forecast the machining characteristics. Many modelling research have been studied for the performance of different tool grades in cutting process of several materials. Vijayaraghavan et al. [8] investigated a finite element model used to predict the cutting force while Genetic Programming was used to obtain the mathematical relation between the process variables and the cutting force. Authors emphasized the validity of finite element model with ABAQUS 3D when compared with experimental data. Yaşar et al. [9] investigated the experimental and numerical analysis results of main cutting force (F_c) in turning of AISI P20 steel with carbide cutting tool. F_c values increased with increasing feed rate and depth of cut while F_c values decreased with increasing cutting speed in both experimental and numerical analysis results. It was determined that experimental cutting forces is %8 lower than numerical analysis results when comparing experimental and numerical analysis. This difference is referred to Johnson-Cook material model of AISI P20 and tool-workpiece friction model in simulations. Gök [10] modelled metal turning processes in three dimensional (3D) by using DEFORM 3D that may be useful for validation of experimental studies. Parameters such as cutting forces, tool wears, temperature and shear angle, which are difficult to determine analytically and experimentally during turning processes, can be easily identified by using simulation tools based on FEM on the computer. The author emphasized that the 3D FE model gives reasonable results with experimental results in view of temperature, main cutting force, thrust force, shear angle. There is a little study on FE modelling of cutting forces in hard turning although there is a lot of studies on hard turning as can be understood from mentioned literature. In this study, the changes of main cutting force depending on cutting conditions (cutting speed, depth of cut and feed rate) has been investigated during the machining of X40CrMoV5-1 tool steel (55 ± 1 HRC) with CBN inserts. Finally, the main cutting forces were analyzed based on finite element method by using DEFORM 3D and compared with experimental data.

2. MATERIAL AND METHOD

2.1. Experimental procedure

The purpose of this study was investigating the effects of cutting parameters on main cutting force in hard turning of X40CrMoV5-1 steel using CBN tools. The workpiece material has the following chemical composition: 0.4% C, 1.0% Si, 0.40% Mn, 5.1% Cr, 1.3% Mo, 1.0% V and the balance is Fe. The workpiece was hardened to 55 ± 1 HRC by means of heat treatment by quenching in a vacuum atmosphere. The experiments were carried out using a CNC lathe with 20 HP spindle power. The cutting parameters used for the experiments were given in Table 1.

Table 1. Cutting parameters and their levels

Cutting parameters	Levels
V (m/min)	150-200-250
f (mm/rev)	0.05-0.15-0.2
a (mm)	0.1-0.2-0.3

CBN inserts with 0.4 mm tool nose radius (DNGA 150404 T02020) were used to machining of X40CrMoV5-1 tool steel. The cutting tool was fixed to tool holder which has ISO code of DDJNR 2525M15. Combination of the cutting tool and the tool holder resulted in effective rake angle $\gamma = -26^\circ$, clearance angle $\alpha = -6^\circ$, inclination angle $\lambda = -6^\circ$ and approaching angle $\chi_r = 93^\circ$. The workpiece was clamped into the machine to minimize run-out and maximize rigidity. The measurement of the cutting forces was done by the Kistler piezoelectric dynamometer type 9257B which was connected to a Kistler 5070A of multi-channel charge amplifier. The measured values were continuously monitored and recorded throughout the Dynaware software. Also, the analysis of variance (ANOVA) was used to find the relative contribution of the cutting parameters in controlling the response of hard turning process.

2.2. Finite Element Analysis

The cutting simulations for hard turning were performed with DEFORM 3D software based on finite element method. Some preparations were adjusted in order to make solid models for cutting tool and determine the material models for cutting tool and workpiece before numerical analysis. 3D model of cutting tool were created in SolidWorks software in line with information from cutting tool catalogue and data from sensitive measurement devices. Lagrangian Incremental mesh model were used in simulations for 3D meshing structure for cutting tool and workpiece.

Cutting simulations were performed via Machining (Cutting) module in DEFORM 3D by choosing turning for machining type with SI units. The cutting parameters in Table 1 were considered for each simulations. Sliding friction coefficient of cutting tool-workpiece interface, heat transfer coefficient and room temperature for hardened AISI H13 steel were chosen as 0.5, 45 W/m²K and 20°C, respectively. The material models for cutting tool and workpiece were given in Table 2.

Table 2. The material models for cutting tool and workpiece [11]

Material	AISI H13	CBN
Density (Kg/m ³)	7800	3120
Young's Modulus (GPa)	211	680
Poissons Ratio	0,28	0,22
Thermal Expansion (10 ⁻⁶ /°C)	10,4 e-06	4,9e-06,25
Thermal Conductivity	37	100
Specific Heat (J/kg°K)	560	960

Mesh structure of cutting tool-workpiece modelled in DEFORM 3D were adjusted as 0.1 mm of minimum element size for cutting tool. The number of elements for cutting tool and workpiece occurred as 31582 and 70832, respectively. The finite element mesh model of cutting simulation for CBN insert and workpiece is given in Figure 1.

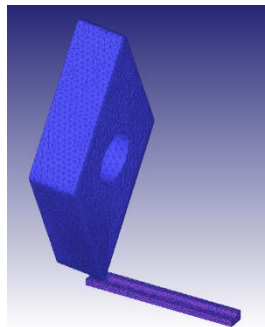


Figure 1. Mesh model for cutting tool and workpiece.

The Johnson–Cook model [12] widely-used material model for machining simulations is given in Eq. 1. This material model is particularly suited to model high strain rate deformation of metals. It is generally used in adiabatic transient dynamic analysis. The hardening is a particular type of isotropic hardening in which the yield stress σ^0 is assumed as [13]:

$$\sigma^0 = (A + B(\epsilon^p)^n) \left(1 + C \log \left(\frac{\dot{\epsilon}^p}{\dot{\epsilon}_0} \right) \right) \left(1 - \left(\frac{T - T_r}{T_m - T_r} \right)^m \right) \quad (1)$$

In equation (1), material parameters obtained from mechanical tests that are A, B, C, n and m are yield stress below room temperature, strain hardening, strain rate constant, strain hardening constant and thermal softening constant, respectively. The other parameters ϵ^p , ϵ^p , ϵ_0 , T_r , T_m and T are equivalent plastic strain, plastic strain rate, reference strain rate, room temperature, melting temperature and reference temperature, respectively. Also, ϵ_0 and C are usually measured at or below the reference temperature. The Johnson-Cook parameters parameters for X40CrMoV5-1 steel was given in Table 3.

Table 3. The Johnson-Cook parameters parameters for X40CrMoV5-1 steel [14]

Material	A	B	n	C	m	Tm
AISI H13	715	329	0.28	0.03	1.5	1427

3.RESULTS AND DISCUSSION

The main cutting force (F_c) which has primarily importance in terms of energy consumption in turning method were taken into account in the assessment of experimental and numerical analysis. Interaction graphics given in Figure 2 is shown the variations on F_c values according to cutting parameters. As seen from Figure 2 that F_c values increases with increasing depth of cut and feed rate, but this increase exhibits an irregular trend. This irregular tendency of F_c values is attributed to the randomized distribution of the depth of cut due to design of experiment (L9 orthogonal array). The variation of obtained F_c values according to cutting parameters to evaluate experimental and numerical analysis results were given in Figure 3. It was obtained that both experimental and numerical F_c values show similar tendency when both of two methods were compared. It was determined that experimental F_c values is %2-8 lower than that of numerical analysis results.

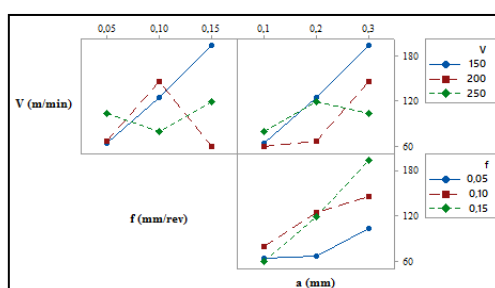


Figure 2. Interaction plots for the main cutting force

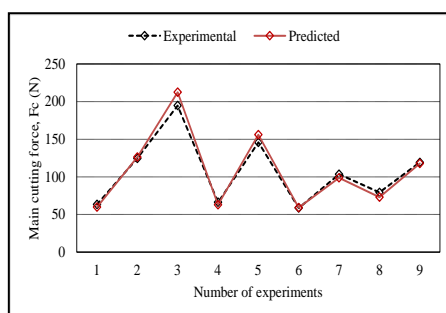


Figure 3. Comparison of experimental and numerical analysis results

The similarity between experimental and numerical F_c values in the result of cutting simulations on X40CrMoV5-1 steel in DEFORM 3D showed the suitability of FE model. On the other hand, it was determined a maximum difference of %8 between experimental and numerical results in the result of assessment according to cutting parameters. This result may arise from that Johnson-Cook model for workpiece and coefficient of friction in tool-workpiece interface were assumed from data in literature. It was referred in literature [15,17] that metallurgical structure and chemical composition of the standard manufactured material may be different. Mechanical and physical properties that generate material models should be determined according to related experimental workpiece in cutting simulations.

The analysis of variance (ANOVA) was used to find which cutting parameters significantly affect the main cutting force. This statistical analysis was carried out at the 95 % confidence level. Table 4 shows the degree of freedom (DF), the sum of squares (SS), the mean square (MS), the F-values (F) and the percentage-contribution ratio (PCR) of each factor. The F-ratios and their PCR were taken into consideration to identify the significance levels of the variables. Table 4 indicates that the most effective variable for the F_c is depth of cut with PCR of 63.96%. The other variables having an effect on F_c are the feed rate with a PCR of 22.10% and the cutting speed with a PCR of 12.14%.

Table 4. Results of ANOVA for main cutting force

Source	DF	SS	MS	F ratio	PCR (%)
V	2	12.551	6.276	6.30	12.04

f	2	23.043	11.521	11.57	22.10
a	2	66.696	33.348	33.50	63.96
Error	2	1.991	0.995		1.90
Total	8	104.281			100

4. CONCLUSIONS

In this study, main cutting force was investigated in hard machining of X40CrMoV5-1 tool steel workpieces with 55±1 HRC hardness using CBN inserts. The main cutting force was analyzed with DEFORM 3D based on finite element method. Finally, the results from experimental and numerical analysis were compared. The following conclusions are drawn from this study; the main cutting force (F_c) increased with increasing feed rate and depth of cut according to both experimental and numerical results. This results show parallelism with literature and validity of this numerical modelling study. It was also determined that experimental F_c values is %2-8 lower than that of numerical analysis when both of two methods were compared. This result was referred that Johnson-Cook model for workpiece and coefficient of friction in tool-workpiece interface were assumed from data in literature.

REFERENCES

- [1]. Tonshoff, H.K.; Arend, C.; Amor, R.B., "Cutting of hardened steel", *CIRP Annals- Manufacturing Technologies* 49 (2): 547–566, 2000
- [2]. Hashimoto, F.; Guo, Y.B.; Warren, A.W., "Surface integrity difference between hard turned and ground surfaces and its impact on fatigue life", *CIRP Annals- Manufacturing Technologies* 55 (1): 81–84, 2006.
- [3]. Huang, Y.; Chou, Y.K.; Liang, S.Y., "CBN tool wear in hard turning: a survey on research progresses", *International Journal of Advanced Manufacturing Technology* 35: 443–453, 2007.
- [4]. Meddour, I.; Yaltese, M.A.; Khattabi R.; Elbah, M.; Boulanouar, L., "Investigation and modeling of cutting forces and surface roughness when hard turning of AISI 52100 steel with mixed ceramic tool: cutting conditions optimization", *International Journal of Advanced Manufacturing Technology* 77: 1387–1399, 2015.
- [5]. H. Aouici, M.A. Yaltese, K. Chaoui, T. Mabrouki, J.F. Rigal, Analysis of surface roughness and cutting force components in hard turning with CBN tool: prediction model and cutting conditions optimization, *Measurement*, 45 (2012), 344–353, 2007.
- [6]. K. Bouachaa, M. A. Yaltese, T. Mabrouki, J.F. Rigal., "Statistical analysis of surface roughness and cutting forces using response surface methodology in hard turning of AISI 52100 bearing steel with CBN tool", *International Journal of Refractory Metals and Hard Materials*, Volume 28, Issue 3, Pages 349–361, 2010.
- [7]. S. H. Oh, "A Study on Cutting Force Characteristics in Hard Turning, *International Journal of Control and Automation*", Vol.7, No.3 pp.137-146, 2014.
- [8]. V. Vijayaraghavan, A. Garg, L. Gao, R. Vijayaraghavan, G. Lu, "A finite element based data analytics approach for modeling turning process of Inconel 718 alloys", *Journal of Cleaner Production*, doi:10.1016/j.jclepro.2016.
- [9]. N. Yaşar, M. Sekmen, M.E. Korkmaz, M. Günay, "AISI P20 çeliğinin işlenmesinde kesme kuvvetinin deneysel ve nümerik analizi", *GU J Sci Part:C*, 4(1), 625-631, 2016.
- [10]. K. Gök, "Development of three-dimensional finite element model to calculate the turning processing parameters in turning operations", *Measurement* 75, 57–68, 2015.
- [11]. H. Yan, J. Hua, R. Shivpuri, "Flow stress of AISI H13 die steel in hard machining", *Materials and Design* 28 272–277, 2007.
- [12]. G.J. Johnson, W.H. Cook, "A constitutive model and data for metals subjected to large strains, high strain rates and high temperatures. In: *Proceedings of the Seventh International Symposium on Ballistics*", The Hague, 541–547, 1983.
- [13]. A. Dorogoy and D. Rittel, "Determination of the Johnson–Cook Material Parameters Using the SCS Specimen", *Experimental Mechanics* 49, 881–885, 2009.
- [14]. Y. Karpat, T. Özel, "3-D FEA of Hard Turning: Investigation of PcBN cutting tool micro- geometry effects", *Trans NAMRI/SME* 35, 9-16, 2007.
- [15]. Bil H., Kılıç S.E., Tekkaya A.E., "A comparison of orthogonal cutting data from experiments with three different finite element models", *International Journal of Machine Tools and Manufacture*, 44 (9), 933-944, 2004.
- [16]. Özel T. and Zeren E., "Finite element method simulation of machining of AISI 1045 steel with a round edge cutting tool", *Proceedings of 8th CIRP International Workshop on Modeling of Machining Operations*, Germany, 533-542, 2005.
- [17]. Özel T., "The influence of friction models on finite element simulations of machining", *International Journal of Machine Tools and Manufacture*, 46, 518, 2006.

Optimization of Drilling Parameters for Thrust Force in Drilling of AA7075 Alloy

Mustafa Gunay¹, Nafiz Yasar², Mehmet Erdi Korkmaz³

Abstract

AA7075 aluminum alloy has been attracted considerable interest in the production of structural components in marine, automotive and aviation applications due to its high strength-to-weight ratio, good plasticity and better machinability comparable to many metals. Especially, final products must have uniformly high quality to ensure essential safety standards in the aircraft industry. The cutting forces during the machining processes is machinability criteria due to the fact that the magnitude of cutting forces have a direct influence on the tool wear, quality of machined surface and dimensional accuracy of finish product. Therefore, the optimization of hole quality which can variable according to tool geometry and drilling parameters is important in spite of high machinability rate of AA7075 alloy. In this study, the effects of drilling parameters on thrust force (F_z) has been investigated in drilling of AA7075 with tungsten carbide drills. Machining experiments were performed with three different drill point angles (120° , 130° and 140°) and three different levels of cutting parameters (cutting speed, feed rate). Kistler 9272 type of dynamometer and its equipments have been used for measuring of feed forces. The effects of drilling parameters on F_z has been determined with ANOVA in %95 confidence level. Feed rate was determined as the most important factor on F_z according to ANOVA results. Moreover, it was shown that increasing feed rate leads to increase of F_z while increasing drill point angle leads to decrease of F_z . The highest thrust force was obtained with highest point angle and lowest feed rate and cutting speed according to Taguchi optimization method.

Keywords: AA7075, Drilling, Thrust force, Optimization, ANOVA

1. INTRODUCTION

Aluminum and its many alloys are commonly used in aerospace, aircraft, computer and medical industries due to their lower weight, high strength and electrical, thermal conductivity [1]. Machining of aluminum became an important research manner because of its behavior during its machining. Tool wear, burr formation and hole surface quality are the most common problems in drilling of aluminum and its alloys. These materials adhere to cutting tool due to their smearing properties. This situation cause to change in cutting tool geometry. Thus, thrust force and surface roughness increase, too. The surface of machined part is one of the most important criteria in terms of quality. The cutting parameters used during machining of materials are important factors affecting surface accuracy [2]. Surface quality can be obtained by right choice of machining parameters.

Cutting force is known as related with tool-chip contact length in machining process. According to that adhering chip on tool change tool nose geometry. Thus, that cause to a change of force on cutting tool. Although aluminum is a ductile material, machining of these alloys will affect tool life more than expected. In recent years, many research are done in order to measure the force on tool in adequate accuracy. The forces on tool compose an important part of machining. Measuring of cutting forces is useful in optimizing of tool design and necessary for scientific analysis of cutting [3].

Drilling of hole is one of the most common machining processes applied to aluminum alloys [4]. Drilling is the most problematic machining process in removal of chips from cutting region. The leading reason is that chip forming is in closed area and not seen [5].

Rivero et al. described an experimental research study on machinability in the dry drilling of aluminium alloys (AA7075-T6) and on the potential of the new design of tools and coatings. Dry drilling tests were performed using uncoated drills and two different coatings produced by means of an arc evaporation PVD process. Experiments consisted of machining with a 10-mm diameter three-edged drill to produce 25-mm deep holes. Tool wear evolution and burr size were analyzed, as well as the impact of the process parameters on torque, power, feed force and tool temperature. The authors stated that drilling of aluminum alloys effectively in dry condition is possible [6].

Kılıçkap [7] investigated the influence of cutting parameters, such as cutting speed and feed rate, and point angle on burr height and surface roughness produced when drilling Al-7075. All tests were run without coolant at three different levels of cutting speed, feed rate and point angle. The orthogonal array, signal-to-noise ratio, and analysis of variance (ANOVA) were employed to investigate the optimal drilling parameters of Al-7075. The optimization results showed that the combination of low cutting speed, low feed rate, and high point angle is necessary to minimize burr height. The best results of the surface roughness were obtained at lower cutting speed and feed rates while at higher point angle. The predicted values and measured values are quite close to each other. The author indicated that the developed models can be effectively used to predict the burr height and the surface roughness on drilling of Al-7075. Kannan et al. [8] observed that AA7075 alloy has less burring when comparing with pure aluminum in their study. Hanyu et al. [9] studied that shaft tools with new coatings were applied to dry and semi-dry machining of highly adherent aluminum alloys whose efficient means

of dry machining have not yet been established for. In comparison to the case of conventional diamond coatings with rough surfaces, more than four times longer durability of drills was realized in perfectly dry condition. In the case of minimum quantity of lubricant condition, the lifetime was found again to be more than four times longer and successfully achieved the largest improvement of diamond-coated drills ever reported in semi-dry condition. Kurt et al. investigated the effects of cutting parameters on drilling temperature, cutting force and surface roughness in drilling of Al 2024 with DLC coated drills. In their study, it was determined that the most significant parameters on surface quality is feed rate and drill diameter. Also, author observed that the change in feed rate and drill diameter affect average surface roughness considerably in high cutting speed [10].

It is noticed that there is not sufficient study about 7000 series of aluminum alloys whose usage is increasingly spreading. In this study, the effects of cutting parameters (cutting speed, feed rate and point angle) on Fz were examined in dry drilling of AA7075 aluminum alloy.

2. MATERIALS AND METHOD

In this study, drilling processes of AA7075 alloy in three different levels of point angle (120°, 130° and 140°), cutting speed (40, 80 and 120 m/min) and feed rate (0.05, 0.1 and 0.15 mm/rev) were performed in CNC vertical drilling machine (Johnford VMC-550). Karcan branded tungsten carbide drills were used as cutting tool in experiments. Drills had diameters of 5 mm, helical angle of 30° and geometry of 2 cutting edge. Each drilling process was repeated three times and evaluations were done by taking arithmetic average of drilling outputs. The drilling parameters (factors) were given in Table 1.

Table 1. Drilling parameters and levels

Factor	Level
Point angle	120° - 130° -140°
Cutting speed (m/min)	40 – 80- 120
Feed rate (mm/rev)	0,05 – 0,1 – 0,15

Proper number of revolutions according to cutting speed by using speed head were obtained due to the fact that CNC milling machine in experiments has 6000 rev/min as a maximum number of revolution. Thrust force (Fz) values in drilling experiments were obtained by Kistler 9272 type dynamometer and Kistler Type 5070 amplifier with Dynoware software. The experimental setup for drilling tests was given in Figure 1.



Figure 1. The experimental setup for drilling tests

Three different levels of feed rate, cutting speed and point angle were chosen as cutting parameters in experimental design according to full factorial. The levels of these parameters were determined by considering cutting tool company and other AA7075 studies in literature. The experimental design according to full factorial was given in Table 2. In the light of experimental results, the effects of parameters on Fz were determined by analysis of variance (ANOVA) performed with %95 confidence level.

Table 2. Experimental design

Exp. No	P	f	V	Exp. No	P	f	V
1	120	0,05	40	15	130	0,1	140
2	120	0,05	80	16	130	0,15	60
3	120	0,05	120	17	130	0,15	100
4	120	0,1	40	18	130	0,15	140
5	120	0,1	80	19	140	0,05	60
6	120	0,1	120	20	140	0,05	100
7	120	0,15	40	21	140	0,05	140
8	120	0,15	80	22	140	0,1	60
9	120	0,15	120	23	140	0,1	100

10	130	0,05	40	24	140	0,1	120
11	130	0,05	80	25	140	0,15	40
12	130	0,05	120	26	140	0,15	80
13	130	0,1	40	27	140	0,15	120
14	130	0,1	80				

3.RESULTS AND DISCUSSION

3.1.Experimental Results

The variations of thrust force (F_z) values according to drilling parameters in experimental results were given in Figure 2. F_z values increased with increasing feed rate when examining of graph and this result show similar tendency with literature. Generally, decreasing of F_z values with increasing point angle can be referred to that tool-chip contact area decrease with increasing point angle. However, increasing of point angle from 120° to 130° in $0,1$ mm/rev feed rate lead to increase in F_z values. This situation can be referred to that built up edge change tool geometry and so has negative effect on forces.

Ancak $0,1$ mm/rev ilerleme miktarında uç açısının 120° den 130° ye artmasıyla F_z değerlerinde artış olduğu, bu işleme değerlerinde talaş yapışmasının takım geometrisini değiştirerek kuvvet üzerinde olumsuz etkisine atfedilebilir [2].

It was seen that F_z values increased with increasing cutting speed in feed rate of $0,05$ mm/rev and $0,15$ mm/rev for 120° point angle while it decreased in feed rate of $0,1$ mm/rev (Figure 2a). The experiments performed with point angle of 130° and 140° had similar tendency with point angle of 120° , but F_z values decreased when cutting speed increased from 80 m/min to 120 m/min with point angle of 130° and 140° with feed rate of $0,05$ mm/rev and $0,15$ m/rev, respectively. The smallest F_z value was obtained as 151 N (feed rate of $0,05$ mm/rev, cutting speed of 40 m/min and point angle of 140°) while highest value was obtained as 564 N (feed rate of $0,15$ mm/rev, cutting speed of 120 m/min and point angle of 120°).

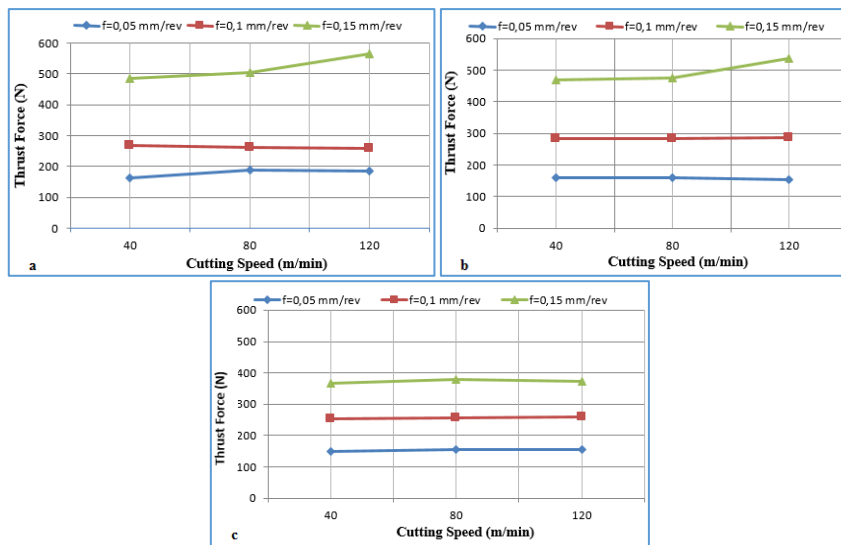


Figure 2. The variation of F_z according to drilling parameters
a) 120° , b) 130° , c) 140°

3.2. Analysis of Variance (ANOVA)

Additionally, analysis of variance (ANOVA) results performed on the 95% confidence level in order to determine the effects of factors on the F_z are given in Table 3. Here, the probability (P) values indicating the importance level of each factor, degree of freedom (DoF), the sum of squares (SS), F values and the percent contribution ratio (PCR) is shown. P value should be lower than $0,05$ in 95% confidence level in order to determine that any factor acting on the force is effective on it. Table 3 indicates that the most effective factor on the thrust force is feed rate with 94.43 % PCR. The cutting speed and point angle have effect on thrust force with 2.01 % and 3.02 % PCR, respectively. According to that, statistical analysis results confirm the experimental results.

Tablo 3. F_z için ANOVA sonuçları

Faktör	DF	SS	F	P	%PCR
f	2	1314,21	177,36	0,006	94,43
V	2	28,00	3,78	0,209	2,01

P	2	42,06	5,68	0,15	3,02
Error	2	7,41			0,54
Total	8	1391,68			100

3.CONCLUSIONS

In this study, In this study, the effects of cutting parameters (cutting speed, feed rate and point angle) on Fz were examined in dry drilling of AA7075 aluminum alloy according to full factorial experimental design.

It was seen that Fz values increased with increasing feed rate in drilling of AA7075 aluminum alloys. The most effective factor on the thrust force is feed rate with 94.43 % PCR according to ANOVA results. The low feed rate and high point angle are suggested in order to obtain minimum surface roughness in drilling of AA075 aluminum alloy. The smallest Fz value was obtained as 151 N (feed rate of 0,05 mm/rev, cutting speed of 40 m/min and point angle of 140°)

REFERENCES

- [1]. ASM Handbook, Machining, Printed in USA, Volume: 16, 761-804,1999.
- [2]. Griffiths, B.J., Manufacturing Surface Technology, in: Surface Integrity and Functional Performance, Penton Press. London, 2001.
- [3]. Çakır, A., Al 7075 ve Al 6013 Alüminyum Malzemelerin Delme Operasyonları Esnasındaki Kesme Parametrelerinin İncelenmesi, Gazi Üniversitesi Fen Bilimleri Enstitüsü, Yüksek Lisans Tezi, Ankara, Türkiye, 2009.
- [4]. Kim J, Dornfeld DA., Development of an Analytical Model for Drilling Burr Formation in Ductile Materials. Trans ASME 124:192–198, 2002.
- [5]. Akkurt, M., Talaş Kaldırma Yöntemleri ve Takım Tezgahları, 23-90, 117-181, Birsen Yayınevi, Ankara, Türkiye, 1998.
- [6]. Rivero, A., Aramendi, G., Herranz, S., Lopez de Lacella, L.N., An Experimental Investigation of the Effect of Coatings and Cutting Parameters on the dry Driling Performance of Aluminum Alloys. The International Journal of Advanced Manufacturing Technology, 28 (1), 1-11, 2006.
- [7]. 7. Kılıçkap E., Modeling and Optimization of Burr Height in Drillingof Al-7075 Using Taguchi Method and Response Surface Methodology., Int J Adv Manuf Technol, 49:911–923, 2010.
- [8]. 8. Suresh Kannan, I., Ghosh, A., Dry Machining of AA7075 by H-DLC Coated Carbide End Mill., Procedia Materials Science 5., 2615-2621, 2014.
- [9]. 9. Hanyu H., Kamiya S., Murakami Y.; Saka M., Dry and Semi-Dry Machining Using Finely Crystallized Coating Cutting Tools., Surface and Coatings Technology 173-174, 992-995, 2003.
- [10]. 10. Kurt M., Kaynak Y., Bakır B., Köklü U., Atakök G. ve Kutlu L., Al 2024-T4 Alüminyumun Elmas Benzeri Karbon (DLC) Kaplanmış Matkaplarla Delinmesinde Kesme Parametrelerinin Deneysel İncelenmesi ve Taguchi Optimizasyonu, 5. Uluslararası İleri Teknolojiler Sempozyumu (IATS'09), 13-15, Karabük, Türkiye, 2009.

Effect of fly ash on rheological properties of epoxy based polymers

Tayfun Uygunoglu¹, Ibrahim Gunes²

Abstract

Polymer matrix composites are used to make very light bicycles that are faster and easier to handle than standard ones, fishing boats that are resistant to corrosive seawater, and lightweight turbine blades that generate wind power efficiently. Υσαγε οφ φιλλερ ματεριαλισ ισ ιν πρεστιγιατεδ ιν πολυμερσ φορ both reducing the cost of the material and increase the strength. One of the fillers is fly ash. In the study, rheological properties of polymer-based composite materials such as viscosity, flow velocity and flow diameter that was produced using fly ash was characterized. According to the results, it was observed that fly ash can be used in the polymer based composite material. In this way, both environmental pollution would be decreased by evaluation of fly ash fly ash which is an environmental problem in world.

Keywords: Epoxy, fly ash, rheological properties, surface coating.

1. INTRODUCTION

Epoxy coatings are formulated based upon the performance requirements for the end product. When properly catalyzed and applied, epoxies produce a hard, chemical and solvent resistant finish. They are typically used on concrete and steel to give resistance to water, alkali and acids [1,2]. Polymer composites generally are reinforced with fiber or fillers to impart good mechanical properties. Composite properties depend on the size, shape and other physical properties of the reinforcements. The size and the aspect ratio of the reinforcing filler/fiber not only influence the mechanical properties directly but also through another factor involving the rheology of the system which affects the distribution of filler/fiber and hence the mechanical performance [3].

The most important one among the properties of epoxy coating is workability. Fresh epoxy based polymer is deformed when it is mixing or placing by effect of self weight or vibration. Protection of desired properties of epoxy based polymer against these affect is depending on its uniformity as rheological. For a fresh polymer mix is being a self consolidate able polymer should have low yield stress and optimum viscosity [4-6]. It is known that workability or rheology is effected its component such as resin dosage, binder to powder ratio and gaps between the powder particles.

Generally, the flow behavior of epoxy based polymer (EBP) approximates that of a Bingham fluid. Therefore, at least two parameters, yield stress and viscosity, are necessary to characterize the flow [4]. Viscosity is a measure of the resistance of a fluid which is being deformed by shear stress. Tendency of deformation versus shear stress gives the plastic viscosity of a liquid. However, polymer suspensions such as EBP is more appropriate the Bingham model. The most important factor which affects the viscosity is internal friction which occurs between the particles that used as filler. The increase of friction between the filler particles and escape of mortar from between the fillers resulted with an increase of yield stress and also in viscosity. EBP provides homogeny distribution of filler particles in epoxy resin by surround them. These filler particles that pasted the filler surface can occur lubrication between the particles [6]. Thus, internal friction between the particles should be decreased significantly by using of EBP. In this study, the rheological properties of EBP with fly ash was investigated.

¹Afyon Kocatepe University, Department of Civil Engineering, 03200 Afyonkarahisar, Turkey. uygunoglu@aku.edu.tr

²Afyon Kocatepe University, Technology Faculty, Metallurgical and Material Science Engineering Department, 03200 Afyonkarahisar, TURKEY, igunes@aku.edu.tr

2. EXPERIMENTAL STUDY

2.1. Materials

The fly ash used in the study was provided by the Tunçbilek Thermal Power Plant in Tavşanlı/Kütahya. It's maximum particle size was 113.78 μ . Chemical component of fly ash is presented in Table 1.

Table 1. Chemical content of fly ash

Oxide	CaO ₂	SiO ₂	Al ₂ O ₃	Fe ₂ O ₃	K ₂ O	Na ₂ O	MgO	LOI
Content, %	6.66	47.4	19.8	11.8	2.62	0.57	4.76	6.39

Commercially available epoxy resin along with hardener was used as matrix material in fabrication of different specimens. Epoxy resin has modulus of 3.42 GPa, and possess density of 1100 kg/m³. For processing the mix ratio (by weight) of epoxy resin (4 parts) and hardener (1 part) were used as specified. The required mixture of resin and hardener (Table 2) were made by mixing them in (2:1) parts in a beaker by stirring the mixture in a beaker by a rod taking into care that no air should be entrapped inside the solution. Production of the polymer matrix composite was done at room temperature. The required ingredients of resin, hardener and fly ash were mixed thoroughly and the mixture so made was transferred to mould cavity of the mould which is coated with separator.

Table 2. Composition of epoxy based polymer composites

Mixture code	Epoxy resin*, %	Fly Ash, %
FA0	100	-
FA10	90	10
FA20	80	20
FA30	70	30

*Epoxy resin was used with hardener (2:1)

2.2. Method

Following the mixing of mortar, viscosity of epoxy based polymer pastes with and without fly ash was determined by using the Brookfield RV-II type viscometer in order to establish the effect of fly ash on resistance to flow on polymer pastes in accordance with ASTM D 1824 [7]. The viscosity measurements were carried out by disc spindles at rotational speed of 10, 20, 30, 40 and 50 in laboratory temperature of 20±2 °C. Also, the fluidity was evaluated by measuring the slump-flow. The slump-flow was measured using a cylindrical frustum. The tested volume in the frustum was 0.287 L. The slump measurement consisted of filling a cylindrical frustum with the freshly polymer composite to be tested in the specified way, slowly lifting the frustum off and allowing the polymer composite to collapse under its weight. In order to prevent any thixotropic effect, the frustum mold was lifted immediately after having been filled with the polymer composite as similar to cement based composites. Slump-flow measurements were carried out on a flat and transparent sheet. The slump-flow (SF) of the final deformed, or slumped, polymer composite paste was measured from two perpendicular diameters 2 min after cone lifting.

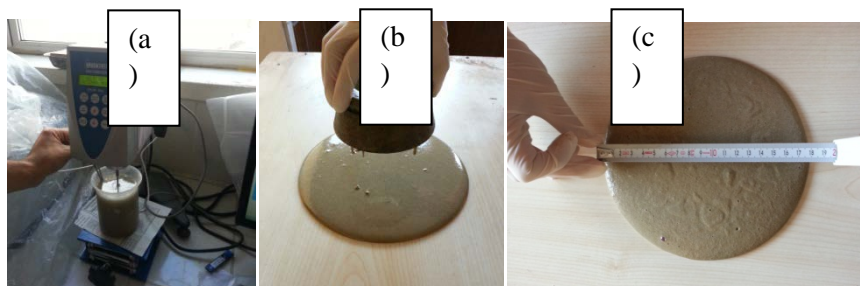


Figure 1. Rheological measurements on polymer mortar (a: viscosity; b: slump; c: spreading measurement)

3.RESULTS AND DISCUSSION

The flow properties of PCBs incorporating fly ash are defined by slump-flow (SF). The SF test results are presented in [Figure 2](#) relating to fly ash content. It is clearly seen that the slump flow diameter increases as the fly ash content.

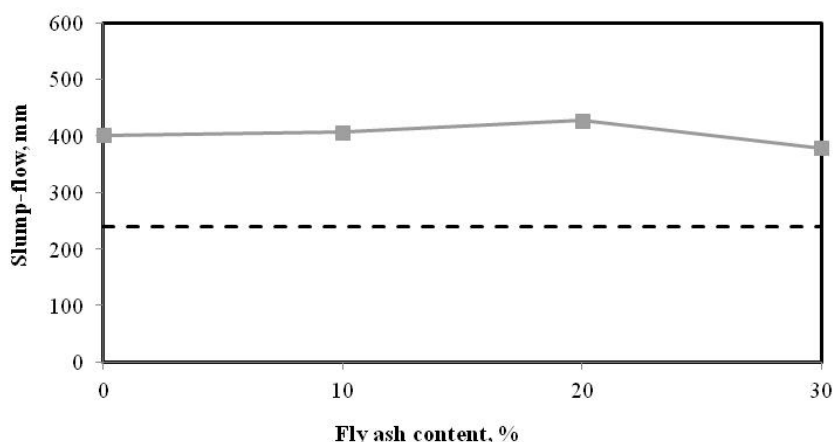


Figure 2. Slump flow of fly ash blended polymer mortar

The SF was observed at the control mixtures (without fly ash additive) as 420 mm. On the other hand, the SF increased to 427 mm with use of the fly ash in ratio of 20%. This was due to the lubrication between the particles with spherical shapes of fly ash. Thus, yield stress of composite decreases depending on movement of particles in the mixture (Fig. 3). However, the highest yield stress was obtained on polymer mortars with 30% fly ash content. Yield stress is the minimum stress to flow on a material. In the slump flow experiment, flow of mixtures depends on exceeding of yield stress. Yield stress whatever is low; mixture should much flow under self weight, and flow stops when yield stress and other stress that occurring due to self weight of polymer mixture became equal [8]. The most important factor which affects the yield stress is internal friction which occurs between the particles. The increase of friction between the particles and escape of polymer resin from between the particles resulted with an increase of yield stress. In the experiment of slump flow of fresh polymer based mixture, when the flow of mixture stops, it is accepted that yield stress and shear stress are equal. When high SF represents that yield stress of fresh mixture is low; low SF indicates that yield stress of mixture is high [9].

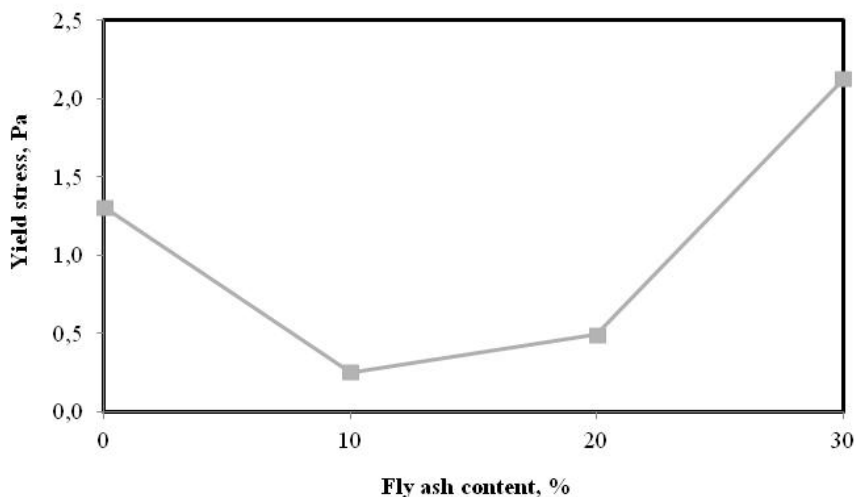


Figure 3. Yield stress of fly ash containing polymer composites

The other rheological properties is viscosity for fluid materials. Viscosity describes the resistance of a mixture to flow under external stress. Viscosity is caused by internal friction. The speed of flow of mixture is related to its viscosity [10,11]. All the apparent viscosities measured are plotted in Fig. 4 depending on fly ash using ratios and deformation speed. It can be clearly seen that all viscosity values are decreased by increasing of the rotational speed of spindle from 10 rpm to 100 rpm, i.e. increasing of the shear rates in high fly ash content. It was also observed that viscosity values increased by increasing of fly ash content, and they are inversely proportioned with slump-flow. In other words, viscosity

was decreased by increasing of slump flow. The binder content can drastically alter the rheological properties of the pastes, as they typically absorb on the particle surfaces, thus influencing both yield stress and plastic viscosities [12,13].

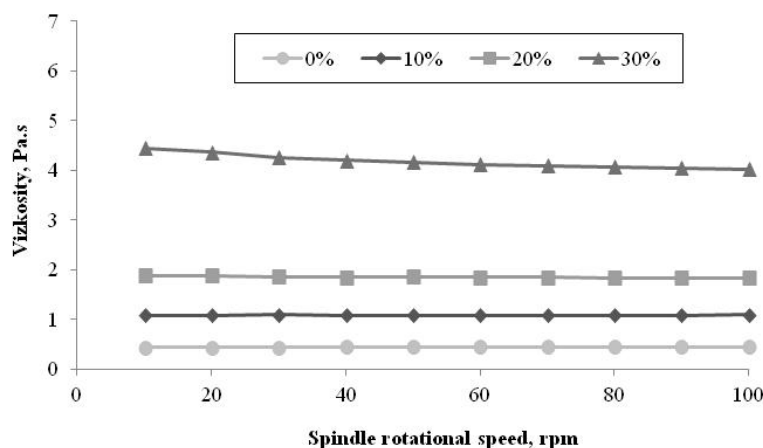


Figure 4. Viskoziteta of fly ash containing polymer composites depending on speed

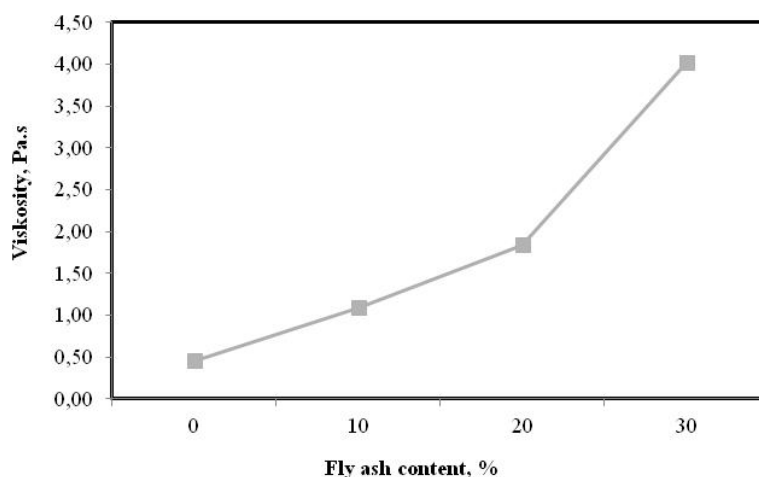


Figure 5. Viskoziteta of polymer composites depending on fly ash content

The highest viscosity values are obtained in the highest fly ash content when regardless of rotational speed (Fig. 5). This is probably because the fly ash material requires more binder than control mixtures. The increase of fly ash material content resulted with the increase of internal friction between particles and thus, polymer mortar has higher viscosity values when compared to control mixtures. For the polymer composite with fly ash using ratio of from 0% to 30%, viscosity values are ranged between 0.45 and 4.0 Pa.s at 100 rpm.

4. CONCLUSIONS

In this study it was investigated to determine the effect of fly ash content on rheological properties of epoxy based polymer composites. To evaluate the possible effects, fresh state tests were conducted as slump flow and viscosity. Based on the experimental results, the following conclusions are drawn:

The experimental results showed that epoxy based polymer mortar can flow easily when fly ash was used up to 20%. It prevent to segregation and blocking of mortar. The using of fly ash is fairly important for good rheological properties of self-consolidating polymer mortar. So, the selection of a typical powder is largely based on required qualities of polymer mixtures in fresh state. The role of filler is to improve packing and hence reduce the binder resin demand of the system.

ACKNOWLEDGMENT

This work was supported by Afyon Kocatepe University Scientific Research Fund (AKU BAP) under the project code 15.TEKNOLOJİ.02. The authors wish to express their gratitude to the AKU for its financial assistance.

REFERENCES

- [1] B Bilyeu, W Brostow, KP Menard. Epoxy thermosets and their applications. III. Kinetic equations and models. *J. Mater. Ed.* 2001;23:189-197
- [2] BZ.Jang Advanced polymer composites: principles and applications. Materials Park, OH, USA, ASM International, 1994
- [3] R.N. Rethon, Particulate Fillers for Polymers, Elsevier, New York, 2002.
- [4] M.B.,Roller,Rheology of curing thermosets: A review, *Polymer Engineering and Science*, 26(6), p.432, 1986.
- [5] M Schatzmann, P Fischer, GR Bezzola. Rheological behavior of fine and large particle suspensions. *Journal of Hydraulic Eng-ASCE.* 2003;129(10):796–803.
- [6] E. G. Kogan, S. A. Kutseba, V. G. Kulichikhin, Effect of the nature of the filler on rheological and rheokinetic properties of composites based on epoxy resins, *Fibre Chemistry*, 1989, 20(3); 206-209.
- [7] ASTM D 1824-95, Test method for apparent viscosity of plastisols and organosols at low shear rates by Brookfield Viscometer, **USA, 2010.**
- [8] Roussel N, Stefani C, Leroy R. From mini-cone test to Abrams cone test: measurement of cement-based materials yield stress using slump tests. *Cement and Concrete Research.* 2005; 35: 817-822.
- [9] T.H. Le, Rheology and microstructure of polymer matrix composites filled thermosetting minéralement and reinforced by glass fibers, Thesis, University JOSEPH Fourier - Grenoble I, 2008.
- [10] W., Borstow, T.Uygunoğlu, , Influence of chemical admixture content particle and grade on viscosity of self-leveling mortar, *El-Cezerî Journal of Science and Engineering*, 2014, 1(2); 12-21.
- [11] I. Amar , H. Brahim, A. Chouaib, B. Boudjema, B. Ibtissem, Rheological Behavior of the Epoxy Resin Loaded with the Pozzolan, *Journal of Materials Science and Engineering A 2 (7) (2012) 519-524.*
- [12] L.L. Pluart, Rheological properties of organoclay suspensions in epoxy network precursors, *Applied Clay Science* 25 (2004) 207-219.
- [13] R.P. Theriault, T.A Osswald, J.M.Castro, Numerical model of viscosity of an epoxy prepreg resin system, *Polymer Composites*, 20(5), pp.628-633, 1999.

Compensating Corruptive Influence Of Antenna System in UWB Systems

Yasin Oguz¹

Abstract

Ultra Wideband (UWB) communication systems are based on communicating with the base band signals that spread over a wide frequency band. One of the major problems in UWB systems is radiation of the UWB signal from transmitter antenna with high spectrum utilization efficiency. Ideally, in UWB systems, the used antenna for signal radiation having a flat amplitude response is requested in the operation frequency band. But all antenna's properties vary greatly depending on the frequency. Therefore, the waveform of radiated signal undergoes some kind of filtering process by the antenna structure. Deviations from the ideal situation occur in the filter characteristic known as antenna transfer function. These deviations cause distortions in the spectral distribution of the signal produced by high spectrum utilization efficiency. Consequently, the spectrum utilization efficiency of the signal radiating in the antenna output decreases.

In this study, to minimize the above mentioned problem, an optimization solution depend on antenna transfer function is presented. With the proposed method, original signal multiplies by a preliminary signal that the waveform will be changed properly before being fed into the antenna input. The production of the preliminary signal is based on obtaining the inverse of antenna transfer function with combination of gaussian signals. In this way, multiplied signal is filtered by antenna transfer function while passes through the antenna and only original signal is radiated from the antenna output.

With the suggested optimization, spectrum utilization efficiency of the radiated signal is greatly protected as highly eliminate distortion of the original signal in the antenna output.

Keywords: *Antenna Transfer Function, Optimization, UWB.*

1.INTRODUCTION

Ultra Wideband (UWB) communication is one of the wireless communication technologies that attract attention greatly in recent years and therefore have been improving rapidly. UWB communication is based on the communication principle with nano-second diverse pulse formats that usually have a frequency band up to range of several GHz from a few Hz [1,2].

One of the main problems in UWB applications is proper antenna use for radiation of UWB signal with high spectrum utilization efficiency. Therefore, in UWB applications, used antenna system having flat amplitude and a linear phase response in accordance with frequency is requested in operation frequency band, as much as possible. All of antenna's properties greatly depend on the frequency. Because of this dependence, the waveform of radiated signal undergoes some kind of filtering process by the antenna structure. Impulse response of the channel is only dependent on the filter characteristic of the antenna for free space propagation channel. Deviations from ideal situation in the filter characteristic cause distortions in spectral distribution of the antenna output signal. At this point, the antenna transfer characteristic considerably influences radiation of UWB signal in terms of spectrum utilization efficiency [3,4].

In this study, with a optimization solution, it has been aimed to minimize distorting effects that deviations from ideal situation in the antenna transfer function cause on the spectral distribution of antenna input signal. Thus It has been worked to ensure the spectrum utilization efficiency of signal on antenna output and the spectrum utilization efficiency of the initial input waveform are the same.

2.MATERIALS AND METHODS

2.1.Antenna Transfer Function Optimization Model

The proposed model is based on the principle that total transmitter system transfer function has a flat amplitude distribution with pre-input signal that will be used in antenna input for an operation frequency band.

¹ Corresponding author: Gumushane University, Department of Electrical and Electronics Engineering, 29100, Gumushane, Turkey.
yasin.oguz@gumushane.edu.tr

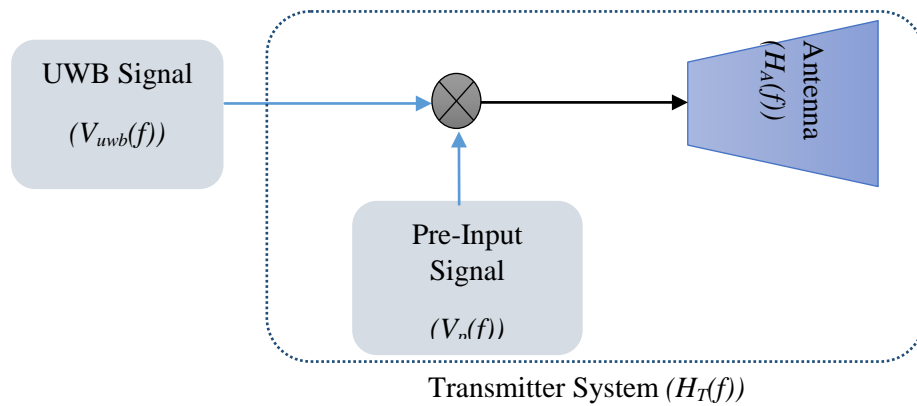


Figure 1. Block diagram of transmitter system for transfer function optimization

In Figure 1,

- $H_A(f)$: Transmitter Antenna Transfer Function
- $H_T(f)$: Transmitter System Transfer Function
- $V_p(f)$: Pre-input signal for transfer function optimization
- $V_{uwb}(f)$: UWB signal for the operation frequency band

In ideal solution case, normalized amplitude value of $H_T(f)$ transfer function is 1 is aimed in the operation frequency band. In this case, normalized spectral power distribution of $V_{uwb}(f)$ signal given from transmitter system input and normalized Equivalent Isotropically Radiated Power (EIRP) spectral distribution will be obtained in the antenna output are the same. Thus, input signal that has specific spectrum utilization efficiency will be the same efficiency in the antenna output for the operation frequency band[5].

Transmitter system transfer function can be written as

$$H_T(f) = V_p(f)H_A(f) \quad (1)$$

Main problem that have to be solved here is to obtain $V_p(f)$ pre-input signal that make $H_T(f)$ transmitter system transfer function has a flat amplitude distribution as spectral.

2.2.Obtaining Optimum Pre-Input Signal

Ideally, it is sufficient to use the inverse of amplitude of the frequency response as pre-input signal to flatten frequency response of an antenna system with this model.

In other words, the pre-input signal is obtained with expression (2) to the ideal case.

$$V_{ideal}(f) = \frac{1}{|H_A(f)|} \quad (2)$$

The main problem here is to produce inverse of the antenna frequency response as a signal [6]. This problem has been converted into an optimization problem in this study. A model has been established to obtain $V_p(f)$ pre-input signal that has the same distribution with $V_{ideal}(f)$ signal from known functions and the solution has been carried out with this model. Gaussian modulated sinusoidal signals given in expression (3) have been chosen as the known function. $V_p(f)$ signal that has distribution of $V_{ideal}(f)$ has been obtained with combination of gaussian modulated sinusoidal signals.

$$V_{gms}(f) = \sqrt{\frac{\pi}{2}} A\tau (e^{-\pi\tau(f-f_c)^2} + e^{-\pi\tau(f+f_c)^2}) \quad (3)$$

$$V_p(f) = \sum_{n=1}^N \sqrt{\frac{\pi}{2}} A_n \tau_n (e^{-\pi\tau_n(f-f_{cn})^2} + e^{-\pi\tau_n(f+f_{cn})^2}) \quad (4)$$

A_n , τ_n , and f_{cn} values in equation (4) are unknown signal parameters. N is number of base signals that generate $V_p(f)$. The solution can be performed as the problem discussed for estimation of unknown signal parameters convert to the non-linear least squares problem.

For the estimation problem, the objective function can be defined as equation (5).

$$\min \sum_{i=1}^M [V_{ideal}(f_i) - V_p(f_i)]^2 \tag{5}$$

In equation (5),

M : Number of sample frequencies in operation frequency band

f_i : Value of i . sample frequency

The minimization problem in expression (5) can be solved as using non-linear least squares algorithms and values of A_n , τ_n , and f_{cn} obtain with an accuracy rate [5]. In this study, this problem has been solved by Trust-Region method [7] as using MATLAB.

3.RESULTS AND DISCUSSION

In Figure 2, transfer function of a Log Periodic Dipole Array (LPDA) antenna that is designed for 3.1-6.2 GHz operation frequency band has been given. The fluctuations seen in the frequency response of the antenna system will cause distortion of spectral distribution of input signal in antenna output.

In Figure 3, It is observed the normalized EIRP spectral distribution that has been obtained in LPDA antenna output for UWB signal that spectrum utilization efficiency is 0.84. The spectrum utilization efficiency of this signal in antenna output is 0.64.

As shown at the example result, divergency from the adoption of the transfer function of antenna system having a flat amplitude response withdraws to a lower spectrum utilization efficiency for the spectral distribution of EIRP of the radiated signal.

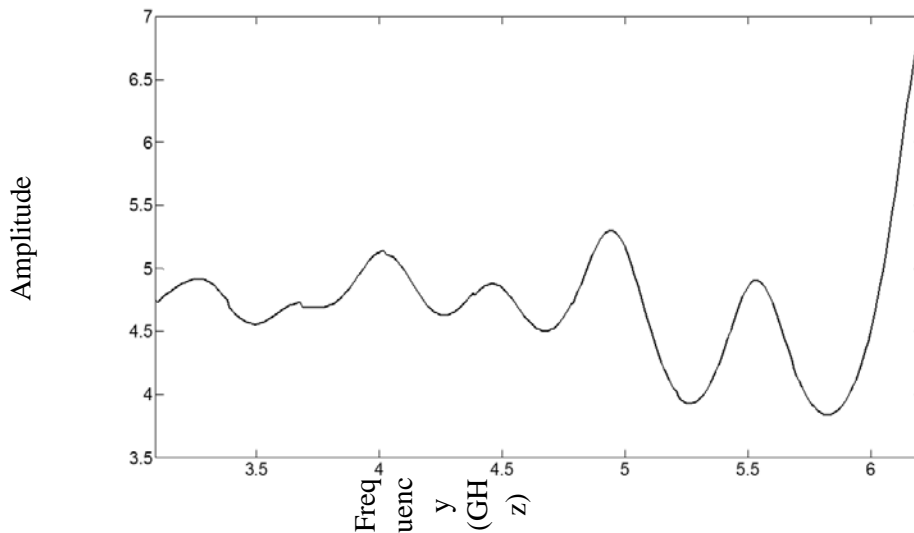


Figure 2. Far field frequency response of LPDA for 3.1-6.2 GHz

Amplitude (dB)

Signal at antenna output

Subband normalized EIRP
mask

Frequency (GHz)

Figure 3. Spectral distribution of normalized EIRP at LPDA output for 3.1-6.2 GHz

The optimization of the transfer function on the proposed model has been realized for the LPDA that is operated in 3.1-6.2 GHz. $V_{ideal}(f)$ is obtained like Figure 4 with reference to the frequency response $H_A(f)$. $V_p(f)$ signal has been produced with 8 piece gaussian modulated sinusoidal signals.

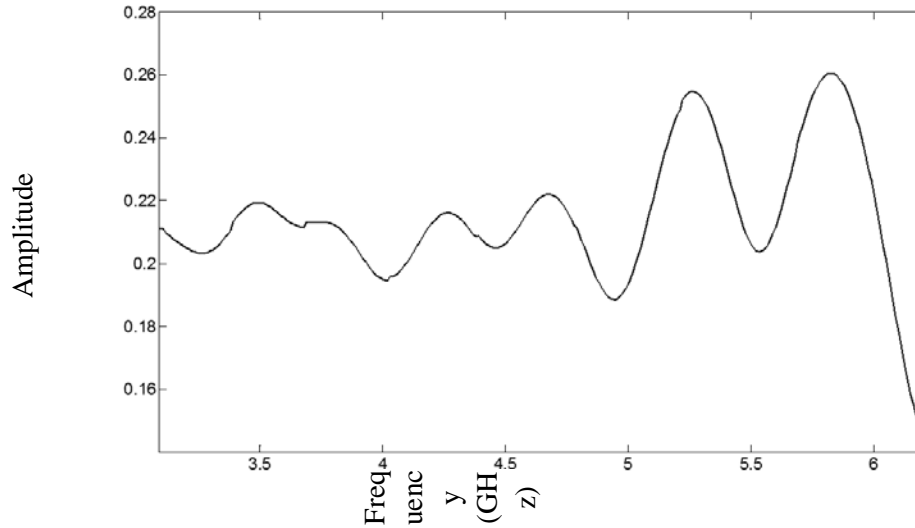


Figure 4. $V_{ideal}(f)$ distribution for 3.1-6.2 GHz

When solution of objective function in expression (5) is achieved, estimated values of A_n , τ_n and f_{cn} parameters have been given in Table 1.

Table 1. Parameter values of the $V_p(f)$ signal obtained for $V_{ideal}(f)$

n	A_n	τ_n (ns)	f_{cn} (GHz)
1	1.92×10^{12}	0.64	6.00
2	1.68×10^{12}	1.07	5.25
3	1.63×10^{12}	1.00	4.69
4	1.12×10^{12}	1.23	3.46
5	1.22×10^{12}	1.16	4.22
6	1.37×10^{12}	1.12	3.04
7	1.04×10^{12}	1.25	3.82
8	8.09×10^{11}	1.20	5.79

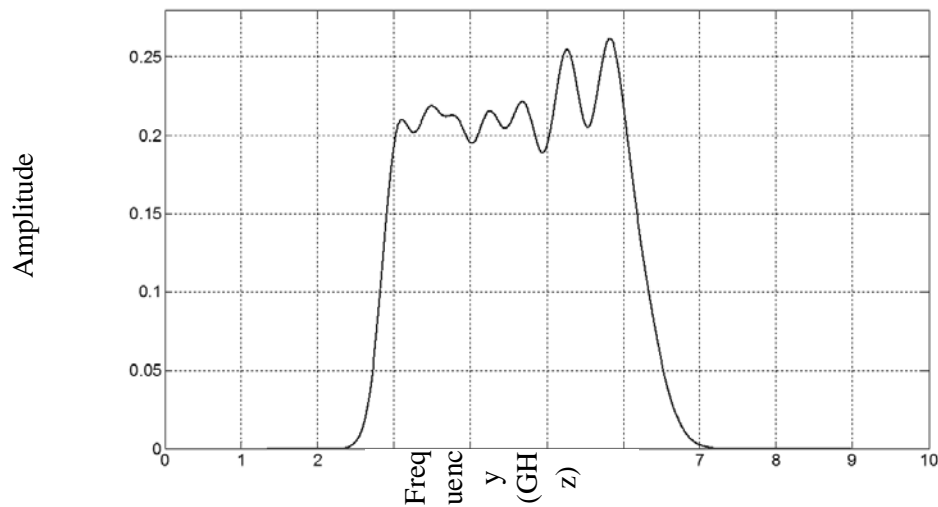


Figure 5. The spectral distribution of the $V_p(f)$ signal obtained for Table 1

When $V_p(f)$ is applied to antenna system input, transfer function of total transmitter system is obtained like Figure 6.

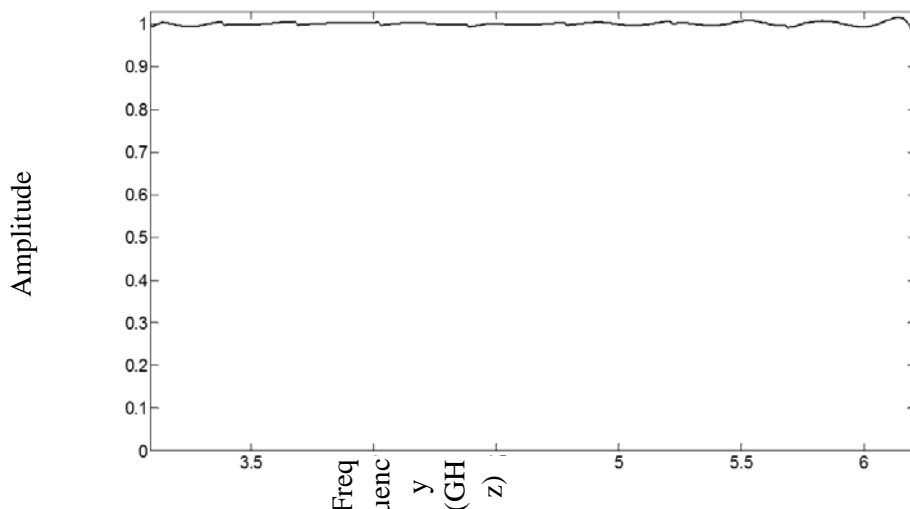


Figure 6. $H_T(f)$, Transfer function of transmitter system for $V_p(f)$ in Figure 5

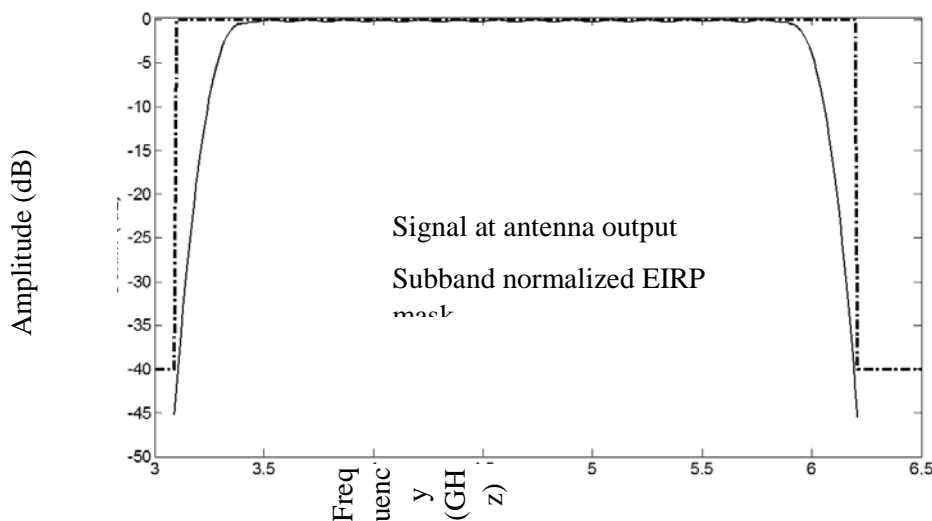


Figure 7. The spectral distribution of normalized EIRP in the output of the transmitter system to the transfer function in Figure 6.

Spectrum utilization efficiency of spectral distribution in Figure 7 is 0.83.

As result in here, due to the corruptive influence of the transfer function of the antenna system, spectrum utilization efficiency that is 0.64 upgraded to 0.83 as decreasing the mentioned corruptive influence with proposed model.

4. CONCLUSIONS

In this study, it has been focused on corruptive influence of antenna system in signal radiation in UWB systems and has been presented a optimization solution to decrease the corruptive influence. With presented model, some results have been obtained for transfer function of an example antenna. When the results are analyzed, the ideal situation is to achieve very close when using the proposed model.

REFERENCES

- [1]. M. Z. Win, and R. A. Scholtz, "Impulse radio: How it Works", IEEE Communications Letters, Vol. 2, Number 2, pp. 36-38, February 1998.
- [2]. R. A. Scholtz, and M. Z. Win, "Impulse Radio", in 8th IEEE International Symposium on Personal, Indoor and Mobile Radio Communications, PIMRC'97, 1997, p. 245-267.
- [3]. W. Sörgel, and W. Wiesbeck, "Influence of Antennas on the Ultra-Wideband Transmission", EURASIP Journal of Applied Signal Processing, Vol. 3, Number 1, pp. 296-305, March 2005.
- [4]. N. Ni, and H. Grebel, "Independently Center-Fed Dipole Array", Microwave and Optical Technology Letters, Vol. 45, Number 6, pp. 545-548, April 2005.

- [5]. Y.Oğuz, “Designing Waveform and Compensating Corruptive Influence of Antenna System in Ultra Wideband Systems”, PhD thesis, K.T.U., Institute of Science, Trabzon, Turkey, July 2008.
- [6]. A.O. Boryssenko, and D.H. Schaubert, Electromagnetics-Related Aspects of Signaling and Signal Processing for UWB Short Range Radios, Journal of VLSI Signal Processing, Vol. 43, Number 1, pp. 89-104, April 2006.
- [7]. W.Sun, and Y. Yuan , Optimization Theory and Methods: Nonlinear Programming, USA, Springer, 2006.

Ultra-Wideband Waveform Design on Artificial Bee Colony Optimization

Yasin Oguz¹, Hasan Eroglu²

Abstract

The signals, used for UWB communication cover a wide spectrum, spread over a wide frequency range. So they are likely to make a distortionary interference with other existing communication systems. In order to reduce or prevent this interference, the change of EIRP distributions' limit values for UWB systems according to the frequency had been determined by Federal Communications Commission (FCC) in 2002. Also, the UWB signal generation suitable for the spectral distribution mask has become one of the major working area.

One of the main methods used in the literature related to the signal generation suitable for the UWB spectral distribution determined by FCC is the signal combination method. In this method, the signals that meet the emission mask limits are generated by handling different combinations of a selected base signal. In this study, the design of the waveforms suitable for FCC mask was handled for UWB signal emission. In the suggested method, the gaussian signals were used as the base signal. UWB signals were designed to meet FCC emission mask with linear combination by optimizing the amplitudes, spectral positions and bandwidths of these signals. The Artificial Bee Colony (ABC) algorithm is used as the optimization method.

With the proposed model, a linear signal combination model that generates UWB signals that have high spectrum utilization efficiency and compliant with FCC emission mask has been demonstrated. With the implemented method, optimum combination of the gaussian signals produced as analogue has been provided in certain number.

Keywords: Artificial Bee Colony, Ultra Wide Band, UWB Pulse Shaping, UWB Waveform Design

1. INTRODUCTION

In recent years, the development of ultra wideband (UWB) systems have gained importance for increasing the data transmission capacity at wireless communication applications [1,2]. The UWB signals are typically the signals that have absolute bandwidth greater than 500 MHz or relative bandwidth greater than 20 % [3,4]. So one of the important issues that should be considered in UWB applications is frequency region sharing. In order to prevent the interference in the current systems, the spectral limit values of Equivalent Isotropically Radiated Power (EIRP) distributions' limit values for UWB applications had been determined by Federal Communications Commission (FCC) [5].

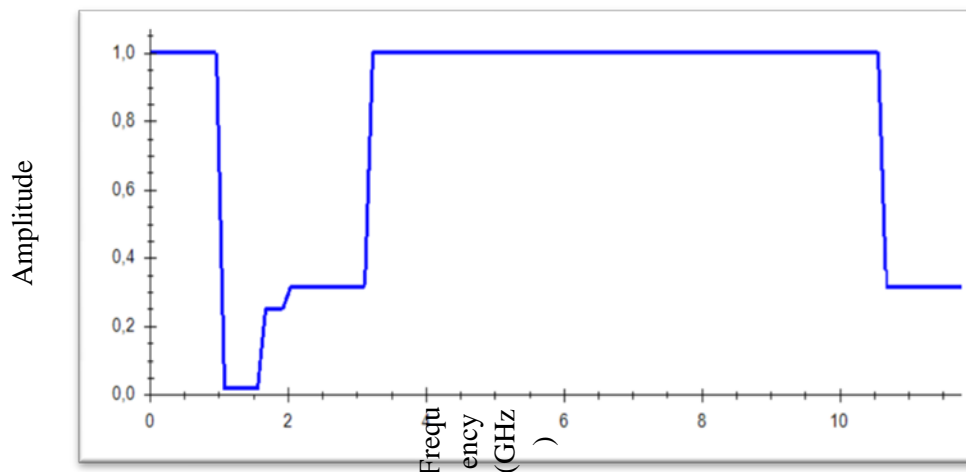


Figure 1. Normalized FCC UWB emission mask as signal amplitude for indoor communication, $V_{FCC}(f)$

¹ Corresponding author: Gumushane University, Department of Electrical and Electronics Engineering, 29100, Gumushane, Turkey.
yasin.oguz@gumushane.edu.tr

² Gumushane University, Department of Electrical and Electronics Engineering, 29100, Gumushane, Turkey.
hasan.eroglu@gumushane.edu.tr

The generation of the waveforms appropriate for this FCC mask is one of the widest area of study in literature. In this study, a generation model is presented based on linear signal combination for composing the waveforms that have high spectrum utilization efficiency [6] and compliant with the FCC mask.

2. MATERIALS AND METHODS

2.1. UWB Signal Generation Model with Linear Combination Method

Linear combination method is based on producing wanted signal waveform by sum of many base signals after optimum amplitude values, bandwidths, and spectral positions of the base signals are determined in frequency domain.

In this study, gaussian signal given with equation (1) has been chosen as base signal.

$$V_{gauss}(f) = A\tau\sqrt{\pi}e^{-(\pi\tau f)^2} \quad (1)$$

With established model, UWB signal is obtained by sum of gaussian signals in a number with optimum amplitude values, located different spectral positions in frequency domain like equation (2).

$$V_{uwb}(f) = \sum_{n=1}^N \sqrt{\frac{\pi}{2}} A_n \tau_n (e^{-(\pi\tau_n(f-f_{cn}))^2} + e^{-(\pi\tau_n(f+f_{cn}))^2}) \quad (2)$$

Main problem have to solve in here is estimation of A_n , τ_n , and f_{cn} values in equation (2) for a particular value of N. The problem has been converted to an optimization problem in expression (3) for estimation.

$$\begin{aligned} \min \sum_{i=1}^M [V_{FCC}(f_i) - V_{uwb}(f_i)]^2 \\ \text{s.t. } V_{uwb} \leq V_{FCC} \end{aligned} \quad (3)$$

The objective function given with expression (3) under the given restrictions has been solved by using Artificial Bee Colony (ABC) algorithm. All parameters that belong to equation (2) can be find as estimate amplitude, bandwidth, and spectral position of each gaussian signal as optimum with made solution.

2.2. ABC Algorithm

ABC algorithm defined by Karaboğa in 2005 has captured much attention and used in many optimization studies [7].

There are three types of bees in the hive: the employed bees, the onlooker bees and the scouts. The employed bees find the food sources and memorize the surroundings' food information in order to give the information to the onlooker bees in the hive. The onlooker bees select one of the food sources from the information taken from the employed bees and gather the nectar. The finding the new nectars, foods and sources duty is made by scouts. When a scout or onlooker bee finds a food sources it becomes an employed bee.

As shown in Figure 2, every solution consists of the sum of more than one signal. Every signal consist of different A, and f_c values.

3. CONCLUSION

In this paper, we demonstrate fault tree analysis for transformers in figure 3. The demonstrated analysis shows that transformer faults has been occurred from many basic faults. Especially, winding fault has many sub-branches. When table 2 and table 3 are examined, winding failures cause vital problems for transformers. Also, when there is considered that power transformers are a critical role for power systems, they should be monitored against any unplanned outage. Due to this reasons, some monitoring methods are utilized in thermal analysis, vibration analysis, dissolved gas analysis, partial discharge analysis, and frequency response analysis. If transformers have any hot spot temperature condition, we can find it owing to thermal analysis. In this way, overheating failures will be prevented. Vibration analysis prevents wall and winding vibration faults. Dissolved gas analysis (DGA) prevents failures comes from winding and some partial discharge failures. In [11], condition monitoring with DGA is explained in detailed. Partial discharge analysis demonstrates partial discharges before any partial discharge failures. And Frequency response analysis is served to preventing of determination the winding movements and deformations.

REFERENCES

- [1]. Transformer Handbook, ABB, Switzerland.
- [2]. S. Singh, and M. Bandyopadhyay, "Dissolved Gas Analysis Technique for Incipient Fault Diagnosis in Power Transformers: A Bibliographic Survey," *Int. IEEE Electrical Insulation Magazine*, vol. 26, pp. 41-46, 2010.
- [3]. R. Murugan, and R. Ramasamy, "Failure Analysis of Power Transformers for Effective Maintenance Planning in Electric Utilities," *Engineering Failure Analysis*, vol.55, pp. 182-192, 2015.
- [4]. F.C. Sica, F.G. Guimarães, and R.O. Duarte, "A Cognitive System for Fault Prognosis in Power Transformers," *Electric Power Systems Research*, vol. 127, pp. 109-117, 2015
- [5]. I.A. Metwally, "Failures, monitoring and new trends of power transformers," in *IEEE Potentials*, vol. 30, pp. 36-43, May-June 2011.

- [6]. M. İlkahman, "Güç Transformatör Arızalarının İncelenmesi," M. Tr. Thesis, Institute of Science and Technology, Gazi University, Eskişehir, Turkey, Jan. 2008.
- [7]. E. Gençaydın, "Hata Ağacı ve Blok Diyagramı Yöntemi İle Koruma Sistemlerinde Güvenilirlik Analizi ve Çözüm Önerileriyle Türkiye Elektrik İletim Sistemine Uygulanması," PhD. Tr. Thesis, Graduate School of Natural and Applied Sciences, Yıldız Technical University, İstanbul, Turkey, 2012.
- [8]. L. Harms-Ringdahl, *Safety Analysis Principles and Practice in Occupational Safety*, 2nd ed., New York, USA: Taylor&Francis, 2005.
- [9]. W.S. Lee, D.L. Grosh, F.A. Tillman, C.H. Lie, "Fault Tree Analysis, Methods, and Applications- A Review," *IEEE Transactions on Reliability*, Vol. R-34, No. 3, Aug. 1985.
- [10]. W. Dietrich, "An International Survey on Failures in Large Power Transformers in Service," *CIGRE Final Report of Working Group 05 of Study Committee 12*, Electra no. 88, pp. 23-48, France, 1983.
- [11]. H. de Faria, J. Costa, and J. Olivas, "A Review of Monitoring Methods for Predictive Maintenance of Electric Power Transformers Based on Dissolved Gas Analysis," *Renewable and Sustainable Energy Reviews*, Vol. 46, pp. 201-209, March 2015.

Simulation Modelling for Worker Assignment and Machine Scheduling in a Job Shop Environment: A Case Study

Gul Didem Batur¹, Emre Caliskan²

Abstract

Job shop models, consisting of multiple part types and multiple operations, are widely used in real life manufacturing systems. In this study we consider a job shop environment in which different types of electronic components are processed at a leading electronic company in Turkey. Considered system has two lines that the components have to be assigned to exactly one of them. At each line, assigned components are processed according to a fixed operation route for each job in a given schedule. Besides, since some operations can be performed only by the skilled workers, worker assignments have also been taken into consideration. The aim of the study is to balance the utilization for the described system. It has been modeled by simulation using the data obtained from the company. Results obtained from the simulation model have been analyzed to determine the wastes affecting the efficiency. Finally, suggestions related to obtaining an active schedule and good assignments together with the best possible objective function value, have been presented.

***Keywords:** Job Shop, Scheduling, Simulation, Skilled Worker*

1. INTRODUCTION

Job shop scheduling problems have been studied by many researchers since the early 1950s. These problems are generally defined as the combinatorial optimization problems. The classical job shop scheduling problem is one of the most well-known machine scheduling problems. The problem can be described as follows: there are a set of jobs and a set of machines. Each job consists of a set of operations, each of which needs to be processed during an uninterrupted time period of a given length on a given machine and the operation order on machines is prespecified. A schedule is an allocation of the operations to time intervals on the machines. Complexity in such environment arises when the assignment of operations to workers is skilled dependent. Under such situation, efficient scheduling of orders and allocation of workers at different work centers play a major role to improve system performance.

Electronic manufacturing systems are taken into consideration in the literature commonly due to their complex structure and real world applications. In a manufacturing system, production process involves the use of resources from personnel to materials so that finished products are ready to be delivered according to the specified schedule. Such systems contain many different types of problems to be solved. Production scheduling is one of the most famous topics that is studied commonly in the literature. The decision problem includes assignment of confirmed orders to the production periods and to the workers with different skills. Due to the impact of level of skilled workers on the efficiency of production system, many researchers have devoted their attention towards scheduling of workers. In this area of research, workers are classified into various classes depending on their level of education, experience, performance and/or ability to do different job. The schedule aims at properly assigning the right person to the right job at the right time, which consequently will minimize the processing time and/or the associated production costs.

In the literature there are different studies related to the subjects of job shop environments and simulation studies. Reference [1] reviewed scheduling articles in order to summarize how job shop scheduling with material handling problems are solved in dynamic and static problem settings, as well as how simulation models play a role in solving this type of problems. Reference [2] focused on the production scheduling of job-shops under the restriction of hierarchical nature of workforce where a higher qualified worker type can substitute a lower qualified one, but not viceversa. They solved the problem of assigning confirmed orders to the production periods and to the workers at different work centers. Reference [3] presented a solution method using simulation-based optimization for solving the job shop scheduling problem. Reference [4] used discrete event simulation software ARENA as a planning tool for job shop production environment together with the aim of identifying options to improve machines utilization, reducing job waiting times at bottleneck machines. Reference [5] used discrete event simulation for stochastic dynamic job shop scheduling problem with sequence-dependent setup times. They assess the performance of six dispatching rules from makespan, mean flow time, mean tardiness, number of tardy jobs, total setups, and mean setup time performance measures viewpoint. In another study, Reference [6] developed a discrete event simulation model of a stochastic dynamic job shop manufacturing system

¹ Corresponding author: Gazi University, Department of Industrial Engineering, 06570, Ankara, Turkey. dbatur@gazi.edu.tr

² Gazi University, Department of Industrial Engineering, 06570, Ankara, Turkey. ecaliskan@gazi.edu.tr

in order to assess the performance of nine dispatching rules, i.e. makespan, mean flow time, maximum flow time, mean tardiness, maximum tardiness, number of tardy jobs, total setups and mean setup time. Reference [7] evaluated 44 dispatching rules with the classification of hybrid and single rules using a set of data from an automotive industry to simulate the job shop production environment. Reference [8] presented a simulation study to investigate the interaction between due-date assignment methods and scheduling rules in a typical dynamic job shop production system. They observed seven scheduling rules for the scheduling of jobs on machines, where the performance of the system is evaluated using measures based on flow time and tardiness of jobs.

In this study, we consider a job shop environment in which different types of electronic components are processed at a leading electronic company in Turkey. Considered system has two lines that the components have to be assigned to exactly one of them. At each line, assigned components are processed according to a fixed operation route for each part in a given schedule. Besides, since some operations can be performed only by the skilled workers, worker assignments have also been taken into consideration. In Section 2, the simulation model of the problem is given. Section 3 is devoted to the results obtained from the model using the data obtained from the company, and the suggestions related to obtaining an active schedule and good assignments together with the best possible objective function value. Section 4 summarizes the contributions and the concluding remarks of this study.

2. MATERIALS and METHODS

In this study, a job shop manufacturing system is taken into consideration. Production system includes two production lines which have two sub-stages; i.e. assembly and test. As there are enough machines to complete the necessary operations, worker assignment is the main problem. In the company, lots of different parts are produced, whereas we consider mostly produced ten of these parts. The number of operations varies between 10 to 20 different steps, each of which is assigned to exactly one worker. It has been pointed out by researchers that six operations are sufficient to represent the complex structure of a job shop manufacturing system [9,10] and most of the researchers addressed a job shop scheduling problem with less than ten operations [11,12,13].

Each part arrives to the system according to a predefined production plan, so the time between arrivals are considered to be constant. In deterministic scheduling problems, processing and setup times of the parts on the machines are fixed. But the real world problems are stochastic in nature. Thus, in the present work, the processing times of parts are considered stochastic and assumed to be triangularly distributed. For example, processing time $TRIA(a,b,c)$ means that the processing time of the operation has lower limit a , upper limit c and mode b , where $a < c$ and $a \leq b \leq c$. There are also setup times for all operations which are constant. Processing and setup times change according to the part type. Parts are sequenced according to the FIFO (first-in-first-out) rule of scheduling. According to this option, arrival dates, which indicate the time at which parts enter the system, are considered.

Complexity in the system arises according to decision of when to perform the next operation of an order and the part assignments depending on the skills of workers. Test operations can only be performed by specific workers, while assembly operations are completed by almost any one of them. Therefore, worker assignment is encountered to be an important decision problem to be solved. The aim of the study is determined according to the feedback taken from the company, which is to balance the utilization of workers.

2.1. Simulation

The study of large and complex manufacturing systems is possible only with simulation modelling [6]. In the present study, using ARENA software, a discrete event simulation model for the operations of a workplace in an electronic company in Turkey, is developed. The part flow in the modeled system is shown in Fig. 1. Priorities of the parts are determined according to the arrival dates in the production plan. In the first step, parts arrive to the system in the predetermined time of the planning horizon. Parts go through their own route which is known in consistent with the job shop production environment. Worker assignments are performed randomly among the available workers at any time, considering whether the operation is skill-dependent or not.

The assumptions made while developing a simulation model are as follows. System has two lines containing 15 and 17 workers, respectively. Each worker can perform only one operation on any part at a time. An operation cannot be performed until the previous operation is completed. Buffer capacity is considered to be unlimited. Processing times of each part are stochastic while setup times are known. Preemption is not allowed.

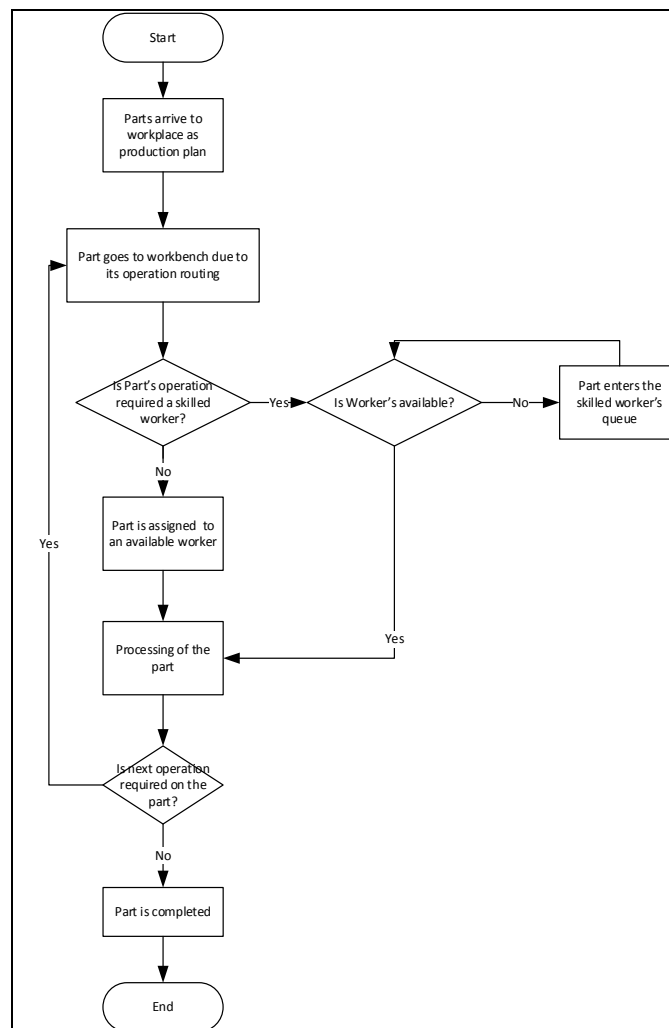


Figure 1. Flow of modeled system

Simulation model is developed using the assumptions mentioned above. The model is debugged and checked with real data, in order to obtain validation. The main performance measure used for evaluation is the utilization of workers, which can be defined as the percentage of time during when a worker is productive. It also represents the idle time of workers in the production period.

3.RESULTS and DISCUSSION

Results obtained from the simulation model have been analyzed to determine the wastes affecting the efficiency.

In order to obtain an active schedule and good assignments together with the best possible objective function value specific rules, for both worker assignment and part sequencing, are proposed. Current utilization rates of the workers in both of the two lines are given in Figure 2.

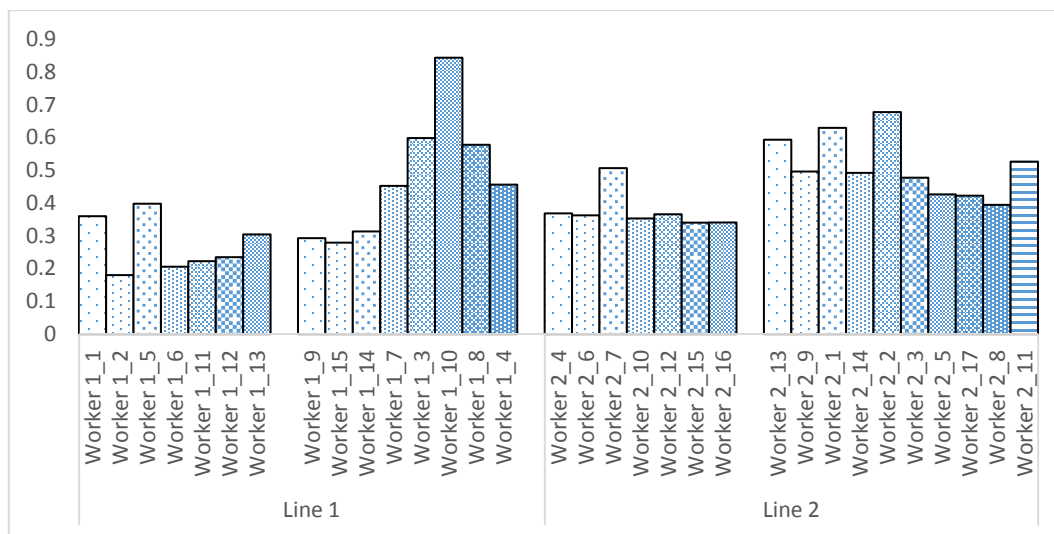


Figure 2. Utilization rates for the current system with respect to the workers

In Figure 2, the 1st and 3rd groups of columns indicate the workers of assembly of Line 1 and Line 2 respectively, whereas the 2nd and 4th groups indicate the workers of test of the two lines. In the current system, simulation results show the average utilization rates given in Table 1.

Table 1. Average utilization rates for the current system

	Line 1		Line 2	
	Assembly	Test	Assembly	Test
Utilization Rate	0,27	0,48	0,38	0,52

In order to improve the system's behavior, rearrangements are performed for worker assignment and part sequencing problems. The first rule that is applied for worker assignments is named as Largest Remaining Capacity (LRC) which assigns the workers to the operations taking the already assigned operations' into account. Second, parts waiting for some specific operations are considered and they are sequenced according to the processing times for that operation; this rule is named as Shortest Processing Time (SPT). Using these approaches, it is expected to have more *balanced* results with respect to the worker utilizations. Simulation is studied using these two rules. Results obtained are given in Table 2. According to these data, more *balanced* results are obtained with respect to the comparisons between the assembly and test workers for each of the two lines. The gap between the assembly and test workers was 0,21 and 0,14 in Lines 1 and 2 respectively, whereas the new gaps are 0,12 and 0,15 for the first rule, and 0,12 and 0,14 for the second, in Lines 1 and 2 again.

Table 2. Results obtained by using LRC and SPT

		LRC	LRC+SPT
Line 1	Assembly	0,32	0,31
	Test	0,44	0,43
Line 2	Assembly	0,37	0,38
	Test	0,52	0,52

4. CONCLUSION

In this study we consider a job shop environment in which different types of electronic components are processed at a leading electronic company in Turkey. The main purpose is to improve the utilization rates in a specific workplace in the company and a simulation study is performed taking the part sequencing and worker assignments into account. In the first stage, system simulation is used in order to see how it works in the current situation. With the help of the ARENA simulation program, model is proposed and debugged. Then, two different heuristic rules; i.e. LRC and SPT, are used to see whether the system can be improved or not. Finally, these newly proposed working decisions are analyzed and it is observed that more balanced results are obtained with respect to the comparisons between the assembly and test workers for each of the two lines. As a future research direction, system decisions are planned to be given using exact solution approaches like mathematical programming.

REFERENCES

- [1]. C. Xie and T.T. Allen, "Simulation and experimental design methods for job shop scheduling with material handling: a survey", *The International Journal of Advanced Manufacturing Technology*, vol. 80(1-4), pp. 233-243, 2015.
- [2]. N. Al-Hinai and S. Piya, "Jobshop scheduling for skill-dependent Make-to-order system", in *International Conference on Industrial Engineering and Operations Management (IEOM)*, 2015, pp. 1-5.
- [3]. K. Kulkarni and J. Venkateswaran, "Hybrid approach using simulation-based optimisation for job shop scheduling problems", *Journal of Simulation*, vol. 9(4), pp. 312-324, 2015.
- [4]. V. Maram, M.K.B.M. Nawawi, S.A. Rahman and S.J. Sultan, "Simulation as a planning tool for job-shop production environment", in *Innovation and Analytics Conference And Exhibition (IACE 2015): Proceedings of the 2nd Innovation and Analytics Conference & Exhibition*, vol. 1691, p. 030018, 2015.
- [5]. P. Sharma and A. Jain, "Stochastic Dynamic Job Shop Scheduling with Sequence-Dependent Setup Times: Simulation Experimentation", *Journal of Engineering and Technology*, vol. 5(1), pp. 19-25, 2015.
- [6]. P. Sharma and A. Jain, "Performance analysis of dispatching rules in a stochastic dynamic job shop manufacturing system with sequence-dependent setup times: Simulation approach", *CIRP Journal of Manufacturing Science and Technology*, vol. 10, pp. 110-119, 2015.
- [7]. A.K. Kaban, Z. Othman and D.S. Rohmah, "Comparison of Dispatching Rules in Job Shop Scheduling Problem Using Simulation: A Case Study", *International Journal of Simulation Modelling*, vol. 11(3), pp. 129-140, 2012.
- [8]. V. Vinod and R. Sridharan, "Simulation modeling and analysis of due-date assignment methods and scheduling decision rules in a dynamic job shop production system", *International Journal of Production Economics*, vol. 129(1), pp. 127-146, 2011.
- [9]. Wilbrecht, J.K., Presscott, W.R., "The influence of setup time on job shop performance", *Management Science*, vol. 16(4), pp. 274-280, 1969.
- [10]. Baker, C.T., Dzielinski, B.P., "Simulation of a simplified job shop", *Management Science*, vol. 6(3), pp.311-323, 1960.
- [11]. Dominic, P.D.D., Kaliyamoorthy, S., Saravana Kumar, M., "Efficient dispatching rules for dynamic job shop scheduling", *The International Journal of Advanced Manufacturing Technology*, vol. 24(1-2), pp. 70-75, 2004.
- [12]. Yu, X., Ram, B., "Bio-inspired scheduling for dynamic job shops with flexible routing and sequence dependent setups", *International Journal of Production Research*, vol. 44(22), pp. 4793-4813, 2006.
- [13]. Rossi, A., Dini, G., "Flexible job shop scheduling with routing flexibility and separable setup times using ant colony optimisation method", *Robotics and Computer-Integrated Manufacturing*, vol. 23(5), pp. 503-516, 2007.

BIOGRAPHY

Gül Didem Baturis a Dr. Research Assistant at Gazi University, Ankara, Turkey. He earned B.S. in Industrial Engineering from Gazi University, Turkey, Masters in Industrial Engineering from Bilkent University, Turkey and PhD in Industrial Engineering from Gazi University. He has published journal and conference papers. His research interests include scheduling and optimization.

Emre Çalışkan is a Dr. Research Assistant at Gazi University, Ankara, Turkey. He earned B.S. in Industrial Engineering from Gazi University, Turkey, Masters in Industrial Engineering from Gazi University, Turkey and PhD in Industrial Engineering from Gazi University. He has published journal and conference papers. His research interests include supply chain management, logistics and optimization.

An Experimental Investigation on The Aeration Efficiency of Stepped Spillways

Tuba Bostan¹, Asli Sari²

Abstract

Although hydraulic structures are used these days for a variety of purposes, including drinking water supplies, electricity generation, and irrigation, the fact that these structures help increase the aeration efficiency of water and therefore provide natural water treatment is normally ruled out. On the other hand, cascades, especially on stepped spillways, and the subsequent hydraulic jump, decrease the amount of required dissolved oxygen, and thus contribute to the permanence of natural life. The stepped structures that are widely used, especially in drinking water treatment facilities, can also be used for aeration purposes in the vicinity of rivers or on the coastline. Natural aeration is defined as the process of oxygen passing into the water, without the use of special equipment. There are three mechanisms that enable natural aeration; these include jet streams, hydraulic jumps, and cascades. To ensure natural aeration, hydraulic jumps and jet streams are used together with hydraulic structures, such as stepped channels (cascades) or spillways, depending on the location and purpose of aeration.

The aeration efficiency was investigated in two different structures for different flow rate values. In the stepped structures, nappe, transition, and skimming flow regimes were generated, and the effect of these flow regimes on oxygen gain was examined.

Keywords: *Aeration efficiency, stepped spillways, dissolved oxygen, nap flow regime, skimming flow regime*

1. INTRODUCTION

Natural resources are being depleted quickly due to the rapid growth of urbanization and industrialization. Environmental pollution and consequent degradation are also increasing rapidly every day. Contamination of natural water resources are of great importance on the lives of living organisms from the viewpoint of the environmental pollution. One of the most important parameters in determining the quality of the water on Earth is the amount of oxygen dissolved in water (DO). For living organisms, the concentration of dissolved oxygen in the water must be greater than 5 mg/L to sustain their lives in a healthy way.

The natural aeration can be provided by aeration with air bubbles, aeration with hydraulic jump, aeration of the water flowing through a spillway, oxygen transfer in stepped structures, and oxygen transfer with a free-fall water jet in a shaft system.

The experimental studies show that there is a linear correlation between the energy lost in natural aeration applications and the amount of oxygen ingress into the water. This implies that the aeration efficiency increases with increasing amounts of lost energy of water.

The particles floating on the water surface and suspended particles have an impact on the hydrodynamic properties and aeration efficiency of the stream by decreasing the surface tension and impeding air-water surface area. The salt and chlorine content of the water increases the solubility rate.

2. STUDIES ABOUT THE AERATION

The studies of natural aeration have been generally performed on the high-slope ($Jo > 0.002$ m/m) hydraulic structures such as embankments, gates and stepped spillways. Gameson (1957), Gulliver et al. (1998), Ervine (1998) and Chanson (1995) were conducted studies on the aeration performance of the hydraulic structures.

Gameson is the first researcher, who worked on the oxygen transfer in hydraulic structures such as water gates, hatchways, and spillways in 1957. Gameson, who took upstream and downstream measurements of dissolved oxygen concentrations, showed that the aeration performance of stepped spillways and water gates was better than the other hydraulic structures.

In Rajaratnam study in 1961, he observed the point distribution of air content in the water, for a variety of Fr_1 values inside the hydraulic jump. In this study, the greatest air ingress was shown to take place at the beginning of the jump (Küçükali, 2006).

¹ Corresponding author: Yildiz Technical University, Department of Civil Engineering, 34220, Esenler/Istanbul, Turkey. bostan@yildiz.edu.tr

² Department of Survey and Projects, Istanbul Metropolitan Municipality, Turkey, asli.sari@ibb.gov.tr

Stepped spillways are among the most widely used hydraulic structures recently in open channels and dams, due to their advantages in relation to energy loss and aeration. On the other hand, these structures have been used for centuries. The oldest stepped spillway is found in Greece (Akarnanian).

In recent years, spilled channels are used not only for civil engineering applications, but also within the realm of environmental engineering, in treatment systems, and for aesthetic purposes.

Stepped spillways are basically constructed by stepping the spillway (Ağralioğlu, 2007). In stepped spillways, the total cascade is divided into a number of smaller cascades. In the design of a stepped spillway, a number of factors, including economic, hydraulic, geologic, hydrologic, social, and environmental factors, should be taken into consideration.

In the design of a stepped spillway, firstly, the flow regime is determined. There are three possible flow regimes in stepped spillways. These are nappe flow regime, transition flow regime, and skimming flow regime. The flow regimes in a stepped spillway can be seen in Figure 1.

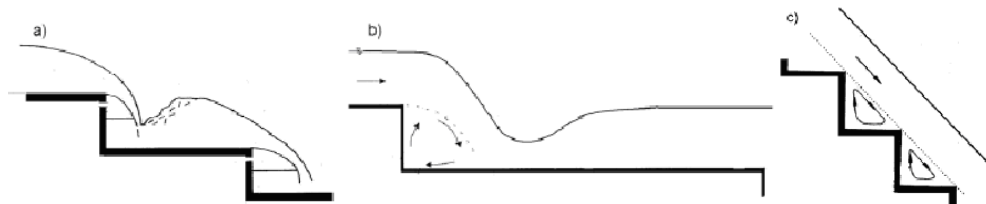


Figure 1. The flow regimes in stepped spillways (Murillo, 2006)
a) Nappe flow regime b) Transition flow regime c) Skimming flow regime

3 TESTING SYSTEM

The tests that were carried out in order to identify the effect of hydraulic structures in open channels on oxygen transfer took place in the Yıldız Technical University, Faculty of Civil Engineering, Hydraulic, Coastal, and Harbor Engineering Laboratories. In these tests, different hydraulic structures were placed inside the open channel, and the effect of these on aeration efficiency was examined through oxygen measurements before and after the structures.

The tests were carried out inside the linear open channel with a rectangular section, which was 12 m long, 40 cm wide and 65 cm high. The channel floor is horizontal and the sides of the channel are made of glass (Figure 2).



Figure 2. Channel used for tests

The flow inside the channel was provided by means of two tanks placed on the bottom and top segments of the channel. The water stored in the bottom tank was pumped to the top tank, and transferred to the channel from here. In this way, the water was circulated throughout the system. The amount of the flow through the channel can be adjusted using the valve at the egress of the top tank. The rate of the flow inside the channel was determined by means of the triangular weir placed at the entrance to the channel and the rating curve. The flow depths in the channel, on the other hand, were measured by a limnimeter. A water gate was placed at the end of the channel so that the flow depths can be adjusted.

In the experimental part of this study, two different hydraulic structures, both made of sheet steel, were used. The first of these was a 30 cm high and 60 cm long three-step spillway. In this spillway, the step widths were 20 cm while step heights were 10 cm. The second hydraulic structure that was used for testing purposes, on the other hand, was a 30 cm high and 60 cm long five-step spillway. In this spillway, the step widths were 12 cm, while step heights were 6 cm. In order to ensure that all three flow regimes can be observed during the tests, different flow rates were used.

A hydraulic structure constructed in an open channel helps the water gain oxygen through the formation of turbulence and air bubbles in the channel. These two hydraulic structures were placed at a distance of 3 m from the beginning of the channel and oxygen measurements were taken before and after placing the structure. In order to prevent oxygen intake during water flow from the tank to the channel and to calm the flow, a brick was placed at the entrance to the channel.

The dissolved oxygen and temperature measurements before and after the structure in the flow were made by means of two YSI EcoSense DO200 manual oxygenmeters. Before the tests began, the oxygenmeters were calibrated at the Yildiz Technical University's Environmental Engineering Department.

The measurement range of the oxygenmeter for dissolved oxygen was 0-20 mg/L with $\pm 2\%$ sensitivity. These values were $(-6) - (46) ^\circ\text{C}$ and $\pm 0.3 ^\circ\text{C}$, respectively, for temperature measurements.

To be able to determine the aeration efficiency of the hydraulic structures used in the tests, the dissolved oxygen concentration in the inflow should be below the saturation level. In order to reduce the dissolved oxygen concentration, sodium sulfite (Na_2SO_3), and cobalt chlorite (CoCl_2) as a catalyzer were added to the bottom tank. As oxygen is consumed during this reaction, the dissolved oxygen amount inside the water is reduced. On the other hand, dissolved oxygen values were not able to be reduced to zero, due to oxygen gain in the tank entrance and exit, as well as inside the channel.

In order to calculate the oxygen efficiency of hydraulic structures used in these tests, the dissolved oxygen values in the water, before and after the structures were placed in the channel, were measured every 30 seconds. The dissolved oxygen amounts were measured for each structure for different flow rate values, and E_{20} values were calculated.

4 INVESTIGATION OF AERATION EFFICIENCY IN SPILLWAYS

The aeration efficiency was investigated in two different structures for different flow rate values. In the stepped structures, nappe, transition, and skimming flow regimes were generated, and the effect of these flow regimes on oxygen gain was examined.

The hydraulic structures used for testing purposes and the changes that occurred on flow regimes are shown in Figure 3.



Figure 3. Five-step system (nappe, transition, and skimming flow)

In the case of the nappe flow regime, the flow behaves like a different cascade system in each step. The nappe flow is observed in small flow rate values. With increasing flow rate values, the nappe flow regime changes first into the transition flow regime, and then into the skimming flow regime.

The flow in the transition flow regime looks like a skimming flow in the first step of the hydraulic structure, while it looks more like a nappe flow in the following steps. Vortices are observed on the steps.

In the skimming flow regime, on the other hand, a straight flow is observed on the steps, almost as if there were no steps at all. With increasing flow rates, the flow regime changes from transition flow to skimming flow, and the flow becomes steadier.

The oxygen measurements were taken for each structure for each flow rate value, before and after the placement of the structure inside the channel. For each data series, a aeration efficiency value was calculated. Because different temperatures are generated during the tests, E_{20} values were calculated using the Equation (1) for 20°C , so as to allow a comparative analysis (Gulliver, 1990).

$$1 - E_{20} = (1 - E_T)^{1/f_T} \quad (1)$$

where, f_T is the temperature correction factor and is calculated using Equation (2)

$$f_T = 1 + 0.02103(T_w - 20) + 8.261 \times 10^{-5} (T_w - 20)^2$$

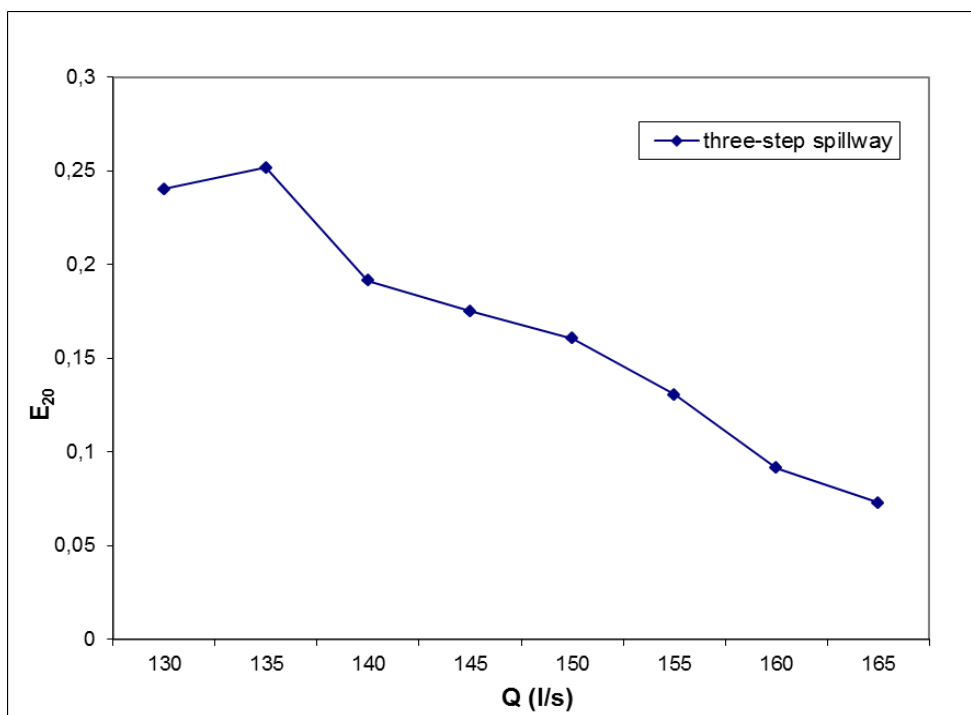
(2)

Table 1 shows the flow conditions and results obtained from different testing systems.

Table 1. Flow regimes in three-step spillway and five-step spillway systems

Three-Step Spillway System				Five-Step Spillway System			
Nappe (cm)	Q (l/s)	E ₂₀	Flow Regime	Nappe (cm)	Q (l/s)	E ₂₀	Flow Regime
3.5	130	0.240291	Nappe	3.6	130	0.26299	Nappe
4.5	135	0.251822	Nappe	4.6	135	0.280632	Nappe
5.5	140	0.191603	Nappe - Transition	5.5	140	0.221217	Nappe - Transition
6.5	145	0.175214	Nappe - Transition	6.7	145	0.186518	Nappe - Transition
7.5	150	0.160589	Transition - Skimming	7.5	150	0.169734	Transition - Skimming
8.5	155	0.130633	Transition - Skimming	8.5	155	0.12267	Transition - Skimming
9.5	160	0.091698	Skimming	9.5	160	0.08291	Skimming
10.5	165	0.072981	Skimming	10.2	165	0.060565	Skimming

The flow rate and E₂₀ values obtained for each structure are graphically shown below. As can be seen from Figure 4, the highest aeration efficiency value was obtained for lowest flow rate level, where the contact duration was the maximum. With increasing flow rate values, the aeration efficiency was observed to decrease.



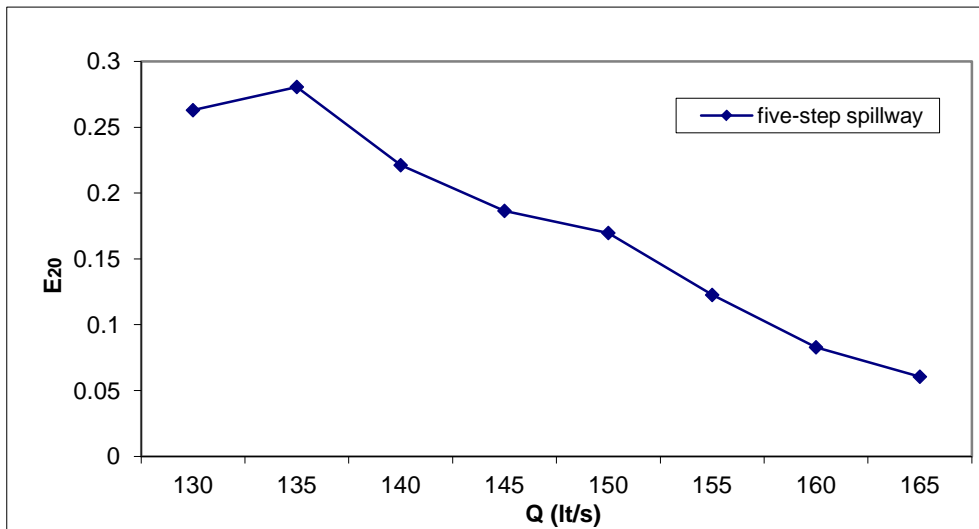
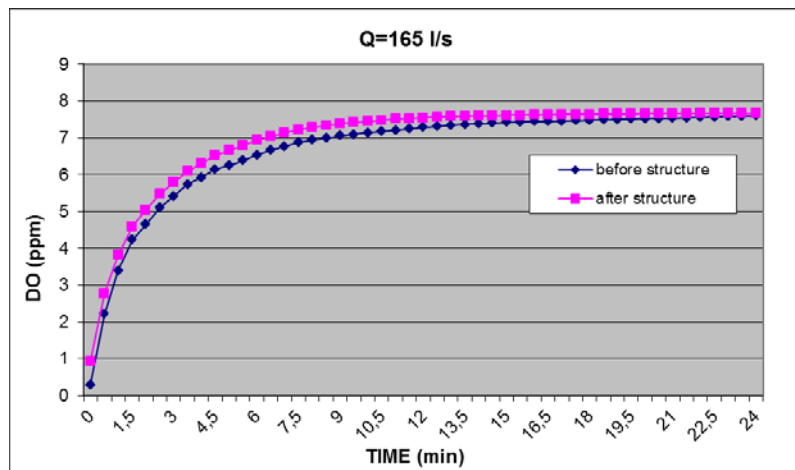


Figure 4. Change in E_{20} with flow rate values three-step spillway systems and five-step spillways

In the nappe flow regime, a certain amount of increase was observed in the aeration efficiency with increasing flow rates. As the flow changed into the transition flow regime, the aeration efficiency began to decrease. During the skimming regime, on the other hand, the aeration efficiency decreased with increasing flow rate values.

In addition, the tests showed that the saturation level is generally achieved to a large extent in the first 20 minutes. The oxygen gain is quite rapid in the beginning, while the gain becomes gradually slower as the saturation level is approached, because the need for oxygen decreases. This shows that the oxygen transfer rate between water and air is a function of dissolved oxygen content in the water (Figure 5-6). In addition, the amount of this difference varied based on flow conditions (nappe flow, transition flow, and skimming flow), changing depending on increasing flow rate values. The highest gain value was observed in the nappe flow regime. The gain level was smaller in the transition flow, and the lowest gain values were obtained in the skimming flow regime.



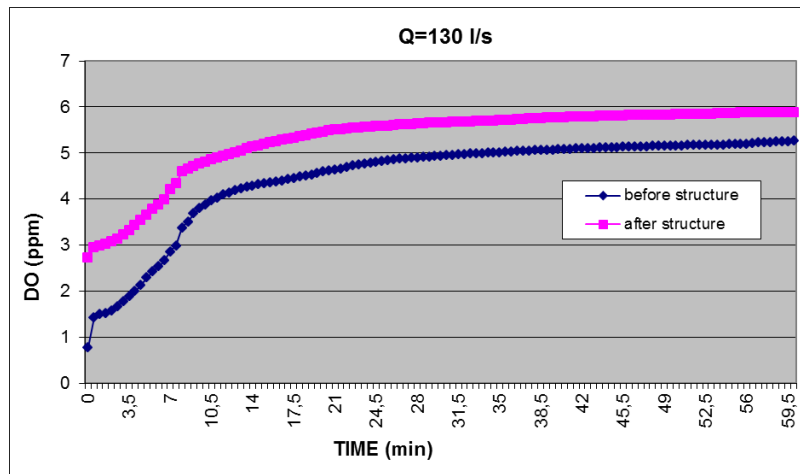
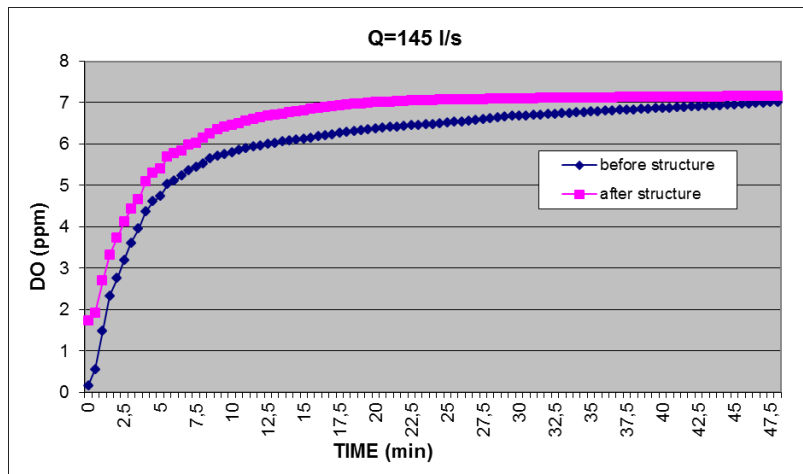
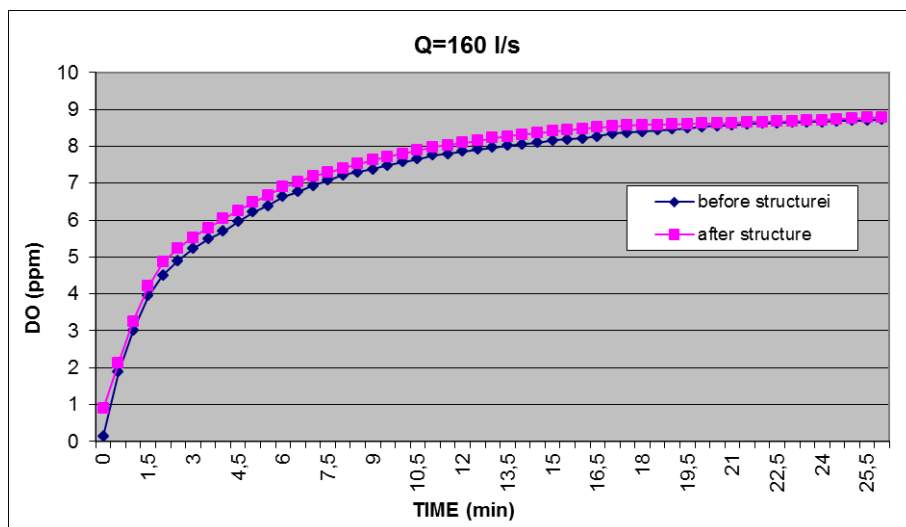


Figure 5. Time-dependent change in dissolved oxygen concentration in the three-step spillway (for different flow rate values)



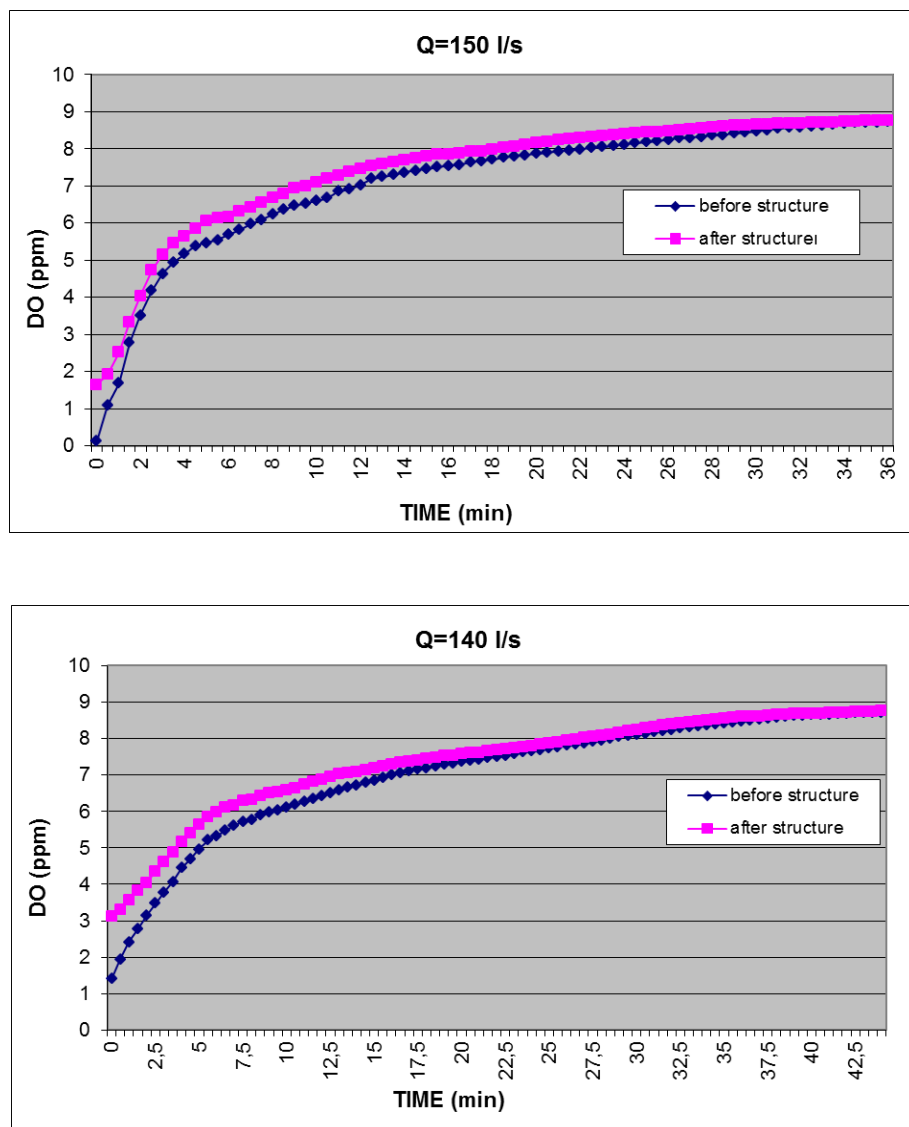


Figure 6. Time-dependent change in dissolved oxygen concentration in the five-step spillway (for different flow rate values)

5 RESULTS

In this study, the aeration efficiency of different hydraulic structures was experimentally investigated, and the following results were obtained:

1. During the study, the nappe flow regime was observed to have the lowest flow rates. As the flow rate increased, the flow regime first changed into the transition flow, and then into the skimming flow regime.
2. The aeration efficiency values were different in all three flow regimes. The results showed that the highest amount of aeration takes place in the nappe flow regime. This is because in the nappe flow regime, aeration takes place at every step via plunge jet and hydraulic jump, and therefore turbulence and contact duration is higher.
3. Within the same system, aeration efficiency decreases with increasing flow rates and with changing flow regimes (transition flow, skimming flow).

REFERENCES

- [1]. Ağırlioğlu N., (2007). *Baraj Planlama ve Tasarımı* (Cilt 1), Su Vakfı Yayınları, İstanbul.
- [2]. Chanson H. (1995). *Hydraulic Design of Stepped Cascades, Channels, Weirs and Spillways*, Pergamon, Oxford, UK, Jan., 292 pages (ISBN 978-0-08-041918-3).
- [3]. Ervine, D. A. (1998). Air entrainment in hydraulic structures: a review. *Proc. Instn Civ. Engrs Wat., Marit. & Energy.*, 130, 142-153.

- [4]. Gameson, A.L.H. (1957). Weirs and aeration of rivers., *J.Inst. Water Engrg*, 11 : 477-490
- [5]. Gulliver, J.S., Wilhelms S. C., and Parkhill K.L. (1998). Predictive capabilities in oxygen transfer at hydraulic structures. *J. Hydr. Engrg., ASCE*, 124, pp. 664-671.
- [6]. K uc kali, S., (2006). *Hidrolik Sıçramanın Havalandırma Verimliliğinin İncelenmesi*, Doktora Tezi, İT , Fen Bilimleri Enstit s , İstanbul.
- [7]. Murillo, R. E. (2006). *Experimental Study of The Development Flow Region on Stepped Chutes*. Doctoral Thesis, Department of Civil Engineering University of Manitoba Winnipeg, Manitoba, Canada.
- [8]. Rajaratnam, N., (1961). An Experimental Study of Air Entrainment Characteristics of Hydraulic Jump. *J. Institution of Engineers (India)*, 42, 247-273.

Experimental and Numerical Analysis of Cutting Force in Hard Turning of AISI 52100

Mehmet Boy¹, Ibrahim Ciftci²

Abstract

Hard turning process is widely used as an alternative machining process to grinding. Hard machining has many advantages over grinding such as short cycle time, process flexibility, better surface finish and higher material removal. In this paper, numerical analysis and experimental investigation of hard turning were studied to investigate the effects of cutting parameters on cutting forces in machining of AISI 52100 steel using coated and uncoated Cubic Boron Nitride (CBN) inserts. Machining tests were carried out to study and evaluate the effect of cutting parameters on cutting force. The Johnson-Cook plasticity model was used to describe the work material behaviour. A three dimensional (3D) finite element analysis (FEA) model to predict cutting forces in hard turning was developed and validated with the extensive experimental data. The results of FEA simulation and machining tests were compared. The obtained cutting force measurement tests and numerical results showed that the feed rate and coating have a great influence on the cutting forces. The predicted forces are similar to the measured ones in magnitudes and trends.

Keywords: *Cutting Force, DEFORM 3D, Finite Element Analysis, Hard Turning, CBN Cutting Tool*

1. INTRODUCTION

Hard part machining is a very popular manufacturing process for production of high precision metallic parts. Today, the hard turning process has been increasingly used as an alternative to grinding of hardened steel components. The hard turning process has the capacity of machining the hardened components such as roller bearings, gears, shafts, cams, axles requiring a low surface roughness and high dimensional accuracy. Hard turning can produce a better surface finish than grinding operations using the right combination of cutting parameters, cutting edge geometry, nose radius and other factors. Hard turning, compared to grinding operations, has many advantages such as higher material removal rates, more flexibility, short cycle time, lower energy consumption, elimination coolants, shorter set up time in complex parts and better surface integrity. Hard turning significantly reduces the production time, tooling costs and the machine tool investment, also presents a great contribution to sustainable manufacturing [1-5].

Cubic boron nitrite (CBN) and ceramics are usually employed in hard turning operations, due to their high hardness, high abrasive wear resistance and high thermal, physical and chemical stability. Although tools with ceramic inserts are employed, the most common tool material employed in hard turning is CBN. CBN tool performance is affected by cutting edge geometry, coating type, CBN content, type of binder, grain size of CBN, use of cooling methods and variation in cutting parameters. There are several types CBN tools depending on the percentage of CBN, the grain size, the binder and coating type. Cutting edges of CBN inserts are especially prepared with a sharp edge, chamfers, hones, and chamfers plus edge hones. However, chamfer plus hone cutting edge preparation is usually preferred in hard turning operations. Cutting edge preparations plays a crucial role in the workpiece surface properties and the performance of the cutting tool. The design of cutting edges may affect the chip formation mechanism, cutting forces, surface integrity and tool life [6-8].

Modelling and simulation of metal cutting operations have become very popular to understand of the cutting process in recent times. Several numerical and analytical approaches have been applied to simulate the machining process. Due to the complexity of the chip formation process, finite element modelling has been widely used to predict the critical mechanisms of stress & strain variations, thermal variations, residual stress formation, chip formation, tool-chip contact length. These mechanisms are difficult to visualize and realize by experimental techniques. The advancement in computers and the development of complex codes have increased the popularity of the finite element modelling. The finite element method is a very suitable tool to obtain approximate solutions for engineering problems. Furthermore, FEM reduces also the experimental costs. Finite element method (FEM) solutions with different softwares such as DEFORM 2D/3D, ABAQUS, ADVANTEDGE, ANSYS etc. have been used in numerical modelling for the metal cutting process. The main features of these software packages to simulate the metal cutting process includes Finite Element and Meshless methods, Lagrangian and Arbitrary Lagrangian-Eulerian (ALE) formulations, implicit and explicit time integration algorithms, constitutive and damage models and, friction models. DEFORM uses a Lagrangian formulation together with implicit time integration to simulate both 2D and 3D metal cutting processes. This software has a relatively better user-

¹ Corresponding author: Karabük University, TOBB Technical Sciences Vocational College, 78050, Karabük, Turkey, mboy@karabuk.edu.tr

² Karabük University, Department of Manufacturing Engineering, 78050, Karabük, Turkey, iciftci@karabuk.edu.tr

friendly interface to set-up the model and to analyse the results of the simulations [9-14]. Several constitutive models are embedded in the graphical interface, including the well-known Johnson–Cook constitutive model. Other models can be implemented in the software by developing simple subroutines. The chip formation process is modelled using a remeshing procedure, where the chip is formed due to continuous indentation of the tool in the workpiece, and by applying a frequent remeshing procedure to minimize the penetration of the tool in the workpiece’s mesh. Deform has two friction models embedded in the graphical interface, the Coulomb and shear friction models, while other models can be implemented in the software by developing simple subroutines [15].

In literature, there are many studies using numerical analysis with FEM, and experimental method in relation to hard turning. The available research on hard turning includes tool wear, cutting force, temperature, residual stresses, microstructural and phase changes, cutting parameters selection, mechanism of chip formation, cutting tool geometry and workpiece hardness effects on cutting performance. Guo and Liu proposed a 3D FE model for hard turning of AISI 52100 steel using PcBN tools. The model was used to predict the temperature distribution over the cutting edge, the residual stress distribution on the machined surface and cutting forces. They also presented a basic sensitivity analysis for flow stress and friction [16]. Khalili and Safaei investigated the effects of chamfer width and chamfer angle on process variables in machining of a mild carbon low alloy steel by using finite element method. The simulation results showed that as the cutting speed increases, cutting forces remain almost the same at a constant chamfer width or angle. The results of the simulations also showed that the effect of width or angle is more pronounced on the thrust force than the cutting force. It was observed that with increase in chamfer width, the shear angle increases and the chip thickness decreases [11]. Qian and Hossain performed tests on hard turning of AISI 52100, AISI H13, AISI D2 and AISI 4340 hardened steels at different cutting speed, feed rate, tool geometry and workpiece hardness. Numerical simulations with FEA were performed using the 2D Lagrangian FE modeling software ADVANTEDGE. Cutting forces and feed forces were determined in the numerical simulations. The process parameters, tool geometry and workpiece hardness, were the most significant factors on cutting and feed forces. Cutting force and feed force were increased with increasing feed, tool edge radius, negative rake angle, and workpiece hardness. The simulation results are compared to the experimental results reported in the literature [5]. Yaşar et al. investigated the effects of machining parameters (cutting speed, feed rate and depth of cut) on cutting force of P20 steel by experimentally and numerically. The numerical simulations with FEA were performed using the DEFORM 3D software. As a result, they stated that the percentage error between simulation and experiment results on cutting force came out to be 8 % [17].

Özel also used a 2D FEM model to simulate orthogonal cutting of AISI H13 steel using honed and chamfered PCBN tools. Both models simulated the continuous chip formation and predicted forces, temperature and stress distributions [9]. Arrazola and Özel performed 3D FEA modelling of precision hard turning of AISI 52100 steel and investigated the effects of chamfered edge geometry. Because the complicated chip shape is difficult to predict, they presented a hybrid approach for the FEA simulations. In their approach, initially a manual remeshing stage is performed and finally an arbitrary Lagrangian-Eulerian step with Eulerian boundaries is used to reach the steady state condition [12]. Özel carried out cutting experiments and 3D finite element simulations to compare uniform and variable edge preparations. The most important finding was that variable micro-geometry insert edge design reduces heat generation and stress concentration along the tool cutting edge, whereas tool wear depth and predicted wear rate decreased with the use of a variable micro-geometry insert [10]. Kurt and Şeker investigated the effect of chamfer angle of polycrystalline cubic boron nitride cutting tool on the cutting forces and the tool stresses in finish hard turning of AISI 52100 steel. The results obtained by them show that an angle of 20° has a major influence on the cutting forces and on Von Mises stresses [18]. Al-Zkeri et al. investigated the effects of edge radius of a round-edge coated carbide tool on chip formation, cutting forces, and tool stresses in orthogonal cutting of an alloy steel of 42CrMo4. They used 2D finite element cutting simulations based on Lagrangian thermo-viscoplastic formulation to predict the cutting temperatures and tool-stress distributions within the tool coating and substrate. Their study demonstrated that finite element analysis can significantly help in optimizing the design of coated cutting tools through the prediction of tool stresses and temperatures, especially within the coating layer [19].

In designing machine tools and cutting tools for hard turning, knowledge of the cutting forces for various cutting conditions is necessary. Besides, selection of suitable cutting conditions affect surface integrity and cutting tool life. In this paper, a series of numerical analysis and experimental investigation of hard turning were carried out to investigate the effects of cutting parameters (cutting speed and feed rate) on the tangential cutting forces in machining of AISI 52100 steel using coated and uncoated Cubic Boron Nitride (CBN) inserts. The machining tests were carried out to study and evaluate the effect of cutting parameters on cutting force. The Johnson-Cook plasticity model was used to describe the work material behaviour. A three dimensional (3D) finite element analysis (FEA) model was used to predict cutting forces in hard turning of AISI 52100 and the simulation results are compared with the experimental results.

2. EXPERIMENTAL

2.1. Experimental Conditions and Equipment

In this study, AISI 52100 bearing steel was used as the workpiece material. The cylindrical AISI 52100 workpieces utilized in these experiments had a diameter of 40 mm and length of 200 mm. The workpieces were through-hardened and tempered to obtain the hardness value of 60 ± 2 HRC. The hardness values were defined by the mean values of the measured workpiece hardness. The cutting tools used were commercial grade CBN inserts produced by Kyocera with the geometry of DNGA 150404 S01225ME KBN10M. CBN cutting tools with uncoated and special coating called “Megacoat” were used for the tests. These inserts were clamped mechanically on a rigid tool holders with an ISO designation of DDJNR 2525M-1504. The inserts were positioned into a tool holder characterized by a negative rake angle of $\gamma=-6^\circ$, clearance angle of $\alpha=-6^\circ$, and an approach angle of $\chi=93^\circ$. Three different cutting speeds and feed rates with a fixed depth of cut were used. The selected cutting parameters are given in Table 1. The machining tests were carried out on the Johnford TC35 CNC turning centre. The coolant was not used, and all the tests were performed in dry cutting conditions. Cutting forces were measured with a Kistler 9257 B piezoelectric dynamometer and an associated 5019B130 charge amplifier connected to PC employing Kistler Dynoware software. During turning tests, the cutting forces known as the primary cutting force F_c , the feed force F_f , and the radial force F_p were recorded.

Table 1. Machining parameters and their values.

Parameter	Value
Cutting speed, V_c (m/min)	140,180,220
Feed rate, f (mm/rev)	0.06, 0.08, 0.1
Coating	Uncoated, Coated
Depth of cut (mm)	0.1
Lubrication	Dry

2.2. FEM modelling

The commercial FEA software DEFORM-3D was used to simulate the three-dimensional cutting process of AISI 52100 steel. A Lagrangian formulation was used and the automatic remeshing capability of the software was used for creation of a dense mesh at the vicinity of the cutting edge. CBN cutting insert was dimensioned using measurement device and catalogue information according to ISO standards. Solid model of the CBN cutting insert was prepared according to the obtained dimensions using SolidWorks software, then the prepared solid model was imported from SolidWorks to DEFORM 3D. The cutting tool was modelled as a rigid body. The mesh density is defined with a minimum input size of 0.2 mm and size ratio of 4 for cutting tool. The workpiece was considered as an elasto-plastic body with a mesh of 0.04 mm and size ratio of 4. Fig. 1 shows the mesh structure of the tool and the workpiece FEM modelling.

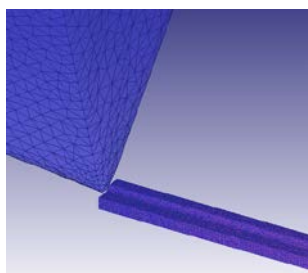


Figure 1. Mesh structure of cutting tool and workpiece.

Material properties are essential inputs for an FEA simulation of a machining process. To represent the constitutive behaviour of the workpiece material under specific cutting conditions, it is necessary to have an accurate and reliable flow stress model that is capable of representing hardening, strain hardening rate and thermal softening. The Johnson–Cook material model is commonly used as flow stress model of work material in FEM modelling. The Johnson–Cook material model is applicable to high rate deformation of many materials, including AISI 52100. Johnson–Cook model is given Eq.1.

$$\bar{\sigma} = [A + B (\bar{\epsilon})^n] \left[1 + C \ln \left(\frac{\dot{\bar{\epsilon}}}{\dot{\bar{\epsilon}}_0} \right) \right] \left[1 - \left(\frac{T - T_r}{T_m - T_r} \right)^m \right] \quad (1)$$

In the Johnson–Cook model, the constant A is in fact the initial yield strength of the material at room temperature, B is the strain hardening factor, n is the strain hardening index, C is the strain rate sensitivity parameter, T is the homologous

temperature, and m is the thermal softening coefficient. T_r is the ambient temperature during the test and T_m represents the melting temperature of the workpiece material. $\bar{\epsilon}$ is the plastic strain, $\dot{\bar{\epsilon}}$ is the strain-rate (s^{-1}), $\dot{\bar{\epsilon}}_0$ is the reference plastic strain-rate [12].

Friction on the tool-chip interface is a major input which determines the output of the FEA simulations. The constant Coulomb friction model is the most widely used in the simulation of metal cutting process [10–12]. In the cutting simulation, tool–chip friction was modelled with Coulomb friction model. The Coulomb friction model defines the shear stress, τ , at which sliding of the surfaces starts as a fraction of the contact pressure, σ , between the surfaces ($\tau = \mu\sigma$). Material and cutting tool properties for the process simulations, taken from the literature sources, used in FEM simulation are mentioned in Table 2.

Table 2. Input parameters for the FE models, materials and cutting properties [12, 20].

Plasticity Johnson-Cook Law	A [MPa]	2482,4
	B [MPa]	1498,5
	n	0,19
	C	0,027
	m	0,66
Inelastic heat fraction (β)		0,9
Density (ρ) (kgm^{-3})	Tool (PCBN)	3120
	Workpiece (AISI 52100 62HRC)	7827
Young's Modulus (E) (GPa)	Tool (PCBN)	680
	Workpiece	201,33 f(T)
Poisson's rate	Tool	0,22
	Workpiece	0,277
Conductivity (k) ($Wm^{-1} K^{-1}$)	Tool	100
	Workpiece	43
Specific heat (c) ($JKg^{-1} K^{-1}$)	Tool	960
	Workpiece	458
Expansion (K^{-1})	Tool	$4,9 \times 10^{-6}$
	Workpiece	$11,5 \times 10^{-6}$ f(T)
Thermal conductance, (Ki) [$W m^{-2} K^{-1}$]		1×10^8
Heat Partition coefficient (Γ)		0,5
Friction coefficient (μ)		0,35

3.RESULTS AND DISCUSSION

Cutting forces should be considered as the most important technological parameters in machining processes. Cutting forces are essential in minimizing energy consumption and distortion of the machine components, withstanding these forces to avoid excessive distortion of workpiece and cutting tools, and selection of machine tool power. Since tangential force is dominant in the orthogonal cutting of the hard materials. Effect of cutting parameters on tangential cutting force were measured by experimentally and numerically. Experimental results are compared with the prediction of the finite element results. In this study, the evaluation of experimental and numerical analysis results tangential cutting force is considered.

The tangential cutting forces that have been obtained from the measurements and the FE simulations for the cases of using uncoated CBN tool were presented in Figure 2. As can be seen in Figure 2, F_c decreases with increasing cutting speed. This decrease is explained by the thermal softening of machined material by the increasing cutting temperature, as mentioned by Kountanya et al [7]. That is, the shearing forces in the primary deformation zone and the friction force in the secondary deformation zone (tool–chip interface) were reduced. Consequently, the tangential cutting force decreases as the shear angle increases and the chip thickness decreases. As can be seen in Figure 2, F_c increases with increasing feed rate. This can be attributed to the increase in chip cross-sectional area with increasing feed rate. In this case, more plastic deformation energy is required for chip formation which leads to increase in main cutting force. In Fig. 2, the F_c decrease in 7–10 % level with increasing of cutting speed from 140 to 220 m/min. When evaluating Fig. 2, the minimum cutting force is obtained in finish turning with feed rate of 0.06 mm/rev, and cutting speed 220 m/min.

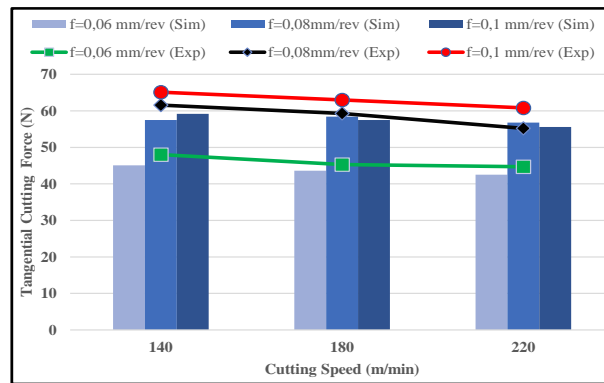


Figure 2. Comparison of tangential cutting forces between numerical and experimental results for uncoated cutting tool.

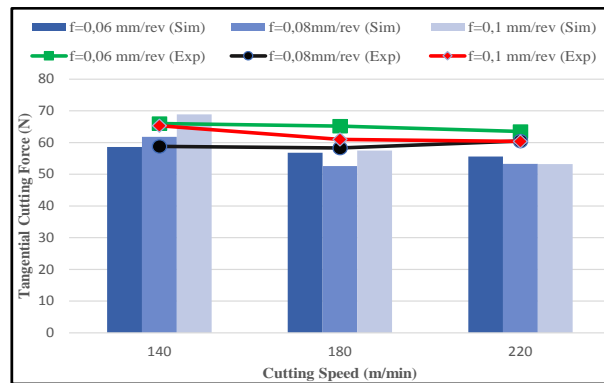


Figure 3. Comparison of tangential cutting forces between numerical and experimental results for coated cutting tool.

In Fig. 2, the experimental values of the tangential cutting force (F_c) are compared to the predicted from the simulations. It was found that forces obtained from the simulations showed a similar trend when compared with the experimental ones. The F_c from the simulation are lower than those from the experimental. The differences between numerical and experimental results were determined to be 9% lower. However, the trends observed in the cutting forces between the simulation and experimental results are similar. As shown in Fig. 2, the cutting forces are closer to those from the measurement than from the simulation, indicating that the numerical model can be used for prediction of cutting forces for hard turning.

Figure 3 shows the comparison of F_c obtained for coated cutting tool. When the coated and uncoated cutting tools are compared, it can be seen that the average F_c obtained with coated cutting tool was higher than those obtained with uncoated cutting tool at all cutting speeds (Fig. 2 and 3). Experimental and simulated results show the same tendencies on F_c using coated tool. The minimum F_c is obtained in finish turning with feed rate of 0.08 mm/rev, and all cutting speed. The F_c measured by experimentally for coated cutting tool is about 30% higher than the measured value for uncoated tool at cutting speed of 140 m/min. This result is mainly caused by low friction at chip-tool interface due to coating. Coating material affect the coefficient of friction and thermal conductivity. The thermal conductivity increases with increasing temperature for WC, TiCN, and TiN [8]. The temperature in primary deformation zone decreases and the cutting force is increased. The maximum differences predicted F_c is about 13% lower than the measured value for coated cutting tool at cutting at same cutting condition. On the contrary, for coated insert, the difference between numerical and experimental results is about 6 % at cutting speed of 220 m/min. The difference between numerical and experimental results decrease with increasing feed rate. The numerical values seem to alteration the experimental ones while the discrepancies are larger for low or higher cutting speeds; this may be attributed to the large strain-rates developed during the process that alters the material behaviour in such a way that they cannot be taken into account by the model or to inadequate friction modelling, which means that a more advanced friction theory needs to be modelled.

4. CONCLUSIONS

In this study, effects of cutting speed and feed rate on tangential cutting forces in hard turning of AISI 52100 were measured and predicted using DEFOM 3D. The results obtained from this study are given below:

1. According to the results, predicted cutting forces agree well with measured experimental data available in the literature with reasonable accuracy.

2. The decreasing trends of tangential cutting forces with increasing speed is consistent with experimental and numerical results reported by other. It was also observed that cutting forces increased with increasing feed rate.
3. The uncoated and coated CBN tools have similar trends on tangential cutting force. The lower tangential cutting forces were obtained by the uncoated tool.
4. It is important to note that further work needs to be carried out to determine the correct material and coating properties of CBN tools. This work will be carried out in the near future.

ACKNOWLEDGEMENTS

The authors would like to express their thanks to the Unit of Scientific Research Projects of Karabük University in Turkey for financial support.

REFERENCES

1. Tönshoff, H.K., Arendt, C., Amor, R.B. "Cutting of hardened steel", *Annals of the CIRP*, vol. 49(2), pp.547-566, 2000.
2. Byrne, G., Dornfeld, D., Denkena, B. "Advancing cutting technology", *Annals of the CIRP*, vol. 52(2), pp. 483-507, 2003.
3. König, W., Berkold, A., Koch, K.F. "Turning versus grinding - a comparison of surface integrity aspects and attainable accuracies", *Annals of the CIRP*, vol. 42(1), pp. 39-43, 1993.
4. Klocke, F., Brinksmeier, E., Weinert, K. "Capability profile of hard cutting and grinding processes", *Annals of the CIRP*, vol. 54(2), pp. 22-45, 2005.
5. Qian, L., Hossain, M.R. "Effect on cutting force in turning hardened tool steels with cubic boron nitride inserts", *Journal of Materials Processing Technology*, vol. 191, pp. 274-278, 2007.
6. Dogra, M., Sharma V. S., Sachdeva A., Suri M. N., Dureja J. S. "Tool Wear, Chip Formation and Workpiece Surface Issues in CBN Hard Turning: A Review", *International Journal of Precision Engineering and Manufacturing*, vol. 11(2), pp. 341-358, 2010.
7. Kountanya, R., Al-Zkeri, I., Altan, T. "Effect of tool edge geometry and cutting conditions on experimental and simulated chip morphology in orthogonal hard turning of 100Cr6 steel", *Journal of Materials Processing Technology*, vol. 209, pp.5068-5076, 2008.
8. Özel, T., Karpas, Y., Srivastava, A. "Hard turning with variable micro-geometry PcBN tools", *Ann CIRP*, 57(1), pp.73-76, 2008.
9. Özel T. "Modeling of hard part machining: effect of insert edge preparation for CBN cutting tools", *Journal of Materials Processing Technology*, Vol.141, pp. 284-93, 2003.
10. Özel, T. "Computational modelling of 3D turning: influence of edge microgeometry on forces, stresses, friction and tool wear in PCBN tooling", *Journal of Materials Processing Technology*, vol. 209, pp. 5167-5177, 2009.
11. Khalili, K., Safaei, M., "FEM analysis of edge preparation for chamfered tools", *Int J Mater Form*, vol.2, pp.217-224, 2009.
12. P.J. Arrazola, T. Özel, "Numerical modelling of 3D hard turning using arbitrary Lagrangian Eulerian finite element method", *Int. J. Machining and Machinability of Materials*, Vol. 3(3), pp.238-249,2008.
13. P.J. Arrazola, T. Özel "Investigations on the effects of friction modelling in finite element simulation of machining", *International Journal of Mechanical Sciences*, vol. 52, pp.31-42, 2010.
14. Mamalis, A. G., Kundrač J., Markopoulos, A., Manolagos D. E., "On the finite element modelling of high speed hard turning", *Int J Adv Manuf Technol*, vol.38 pp. 441-446, 2008.
15. Outeiro, J. C., Umbrello, D., M'Saoubi, R., Jawahir, I.S., "Evaluation of Present Numerical Models for Predicting Metal Cutting Performance And Residual Stresses", *Machining Science and Technology*, vol.19 (2), pp.183-216, 2015.
16. Guo, Y., and C.R. Liu, "3D FEA modelling of hard turning", *ASME Journal of Manufacturing Science and Engineering*, Vol. 124, pp. 189-199 , 2002.
17. Nafiz
18. Kurt, A., Şeker, U. "The effect of chamfer angle of polycrystalline cubic boron nitride cutting tool on the cutting forces and the tool stresses in finishing hard turning of AISI 52100 steel", *Materials and Design*, vol. 26, pp. 351-356, 2005.
19. Al-Zkeri, I., Rech, J., Altan, T., Hamdi, H., Valiorgue, F. "Optimization of the cutting edge geometry of coated carbide tools in dry turning of steels using a finite element analysis", *Machining Science and Technology*, Vol.13 (1), pp. 36-51, 2009.
20. Y. B. Guo Y.B., Liu C.R., "Mechanical Properties of Hardened AISI 52100 Steel in Hard Machining Processes", *Journal of Manufacturing Science and Engineering*, Vol. 124, pp.1-9, 2002.

BIOGRAPHY

Mehmet Boy, born in 1978, he received Ph.D. degree from Karabük University in 2015, Now, he is an Ass. Prof. Dr. in Vocational College in Karabük University. His main research interest is manufacturing technology. He is working on machining of hardened steels.

Dry Sliding Wear Behaviour and Mechanical Properties of Mg-Al-Ti Alloys with Zn Addition

H Cug, Y. Tren, H. Ahlatci, Y. Sun, E. Cevik*

Abstract

Magnesium is receiving great attention for engineering applications, particularly its cast alloys. This investigation focuses on the as-cast microstructure and mechanical properties of permanent-mould cast Mg–Al alloys. In this study, the effects of Zn additions with varying amounts on the microstructure, tensile strength and wear resistance of the Mg5Al1Ti alloy produced by casting method were investigated. The percentages of Zn added to the master alloy are 0.5%, 1%, 2% and 4%. Optical microscope (LOM), X-ray diffraction analysis (XRD) and SEM were used for microcharacterization. The sample investigated by means of X-ray diffraction (XRD), optical microscopy (OM), scanning electron microscopy (SEM), energy dispersive spectroscopy (EDS) and standard tensile testing. Hardness test with the low-force hardness scale of 0.5 HV and wear test in pin-on-disk type testing machine under the loads of 5N-40N in total 12000 m slide distance. As a result of the microstructural characterization, Mg17Al12 grain boundary intermetallic was formed in α -Mg matrix by small amount of Zn additions whereas the microstructures having higher Zn additions showed differences. MgZn phase was formed by 4% Zn addition. The tensile strength and wear resistance of Mg5Al1Ti alloys has increased with %4 Zn addition.

Keywords: *Magnesium alloys, Casting, Microstructure, Wear.*

1. INTRODUCTION

As the most promising lightweight materials, magnesium (Mg) alloys have high specific strength and specific stiffness, good yield strength, excellent machinability and good damping capacity. So, more and more magnesium alloy products have been used in automobile, aerospace and communication industries [1,2] Although Mg has numerous favourable properties as listed above, its usage is limited in engineering applications due to the low wear resistance. It is possible to improve the mechanical and wear properties of these alloys by means of adding alloying elements along with a proper casting procedure [3]. Aluminium (Al), Silicon (Si), Zinc (Zn) and Manganese (Mn), Titanium (Ti) are the main alloying elements in Mg based alloys [4,5].

As an alloying element in Mg based alloys, Al improves the solid precipitation hardening and castability of molten Mg and reduces the micro-pores of casting alloys. Additionally, while Al additive increases the hardness, strength and solidification time of the alloy; it decreases ductility of the alloy. In Mg alloys, Al improves the strength of the alloy by composing Mg₁₇Al₁₂ intermetallic at low temperatures. Nonetheless, the alloys that include excess Al become vulnerable to micro-pores. Mn, which added to Mg alloys, mostly enhances corrosion resistance and creep resistance [6].

Corresponding author: Karabuk University, Department of Metallurgical and Material Engineering, 78150,

Karabuk/Turkey. hahlatci@karabuk.edu.tr

Zn reduces the solidification temperature of the alloy by increasing the amount of eutectic in grain boundaries. Zn increases the hardness, tensile strength and at the same time fluidity of the melt [7-9]. Ti element have excellent properties such as high corrosion resistance, good mechanical properties [10]. Our previous work showed Ti element could refine the as-cast microstructure and changed the morphology of β phases. There are various studies in literature about reproducibility and characteristics of AZ and AM series alloys. There are but a few studies about Mg-Al-Ti based alloy. This is caused by the existence of consistent intermetallic compounds in grain boundaries at high decomposition temperature. In this present study, the influence of Zn additions up to 4% on the mechanical properties and wear behaviour of Mg-Al-Ti-based alloy was investigated.

2. MATERIALS AND METHODS

The alloys in this study were produced in an atmospheric controlled 1200 °C capacity electric resistance furnace. Commercially pure (99,8%) Mg and Al10Ti were used as starting materials to prepare the Mg5Al1Ti code alloys. After that Zn ranging between 0.5%-4% was added to the master alloy remelting at 800°C. Chemical compositions of the produced alloys determined by optic emission methods are given in Table 1.

Table 1. Chemical composition of alloy.

No	Alloy	Alloying Elements
----	-------	-------------------

		Al	Ti	Zn	Mg
1	Mg5Al1Ti	4,6	1,1	-	Rest
2	Mg5Al1Ti-0,5Zn	4,7	0,9	0,4	Rest
3	Mg5Al1Ti-1Zn	4,7	0,9	1,0	Rest
4	Mg5Al1Ti-2Zn	4,6	1,0	1,9	Rest
5	Mg5Al1Ti-4Zn	4,8	1,0	3,9	Rest

In accordance with the standard metallographic procedure, including a grinding process up to 1200 mesh and a following polishing process with a diamond solution and then etching with 2% nitric acid, conducted on the specimens. Microstructural analysis on the prepared specimens was conducted using light optical microscopy (LOM) and a scanning electron microscope (SEM). XRD analyses were carried out by Rigaku Ultra IV model X-ray diffractometer using Cu K α radiation. Diffraction patterns were obtained over range of Bragg angle from 20° to 90°. The LOM (Nikon Epiphot 200 Model) and SEM (Carl Zeiss Ultra Plus Gemini Fesem) images were taken. Energy Dispersive Spectroscopy (EDS) analyses were carried out on the light and grey coloured spots in the microstructural images captured. The dry environment wear tests (ASTM: G99 – 05(2010)) of the investigated alloys were carried out using a pin-on-disc type wear device. The pin samples were 30 mm in length and 7 mm in diameter. The specimens were tested under 5 N, 10 N, 20 N and 40 N, at a sliding rate of 0.5 m/s, and a sliding distance of 12000 m. The weights of the samples were measured before and after the experiment using electronic scales with 0.1 mg accuracy, after which the results of the experiment were evaluated according to the loss in weight. The surface of the specimens were analysed using SEM in order to determine the post-experimental wear mechanisms.

3.RESULTS AND DISCUSSION

3.1.Microstructural analysis

The results of microstructures and XRD analysis of the alloys produced by casting method are given in Figure 1 and Figure 2, respectively. Microstructure analysis revealed that the microstructure was comprised of mainly intermetallic phases arranged predominantly along grain boundaries in primary α -Mg matrix. The results of XRD analysis presented that the formation of Mg₁₇Al₁₂ phases in primary α -Mg matrix occurred with addition of alloying elements up to 4%. MgZn phase was formed with addition of 4% Zn in the matrix.

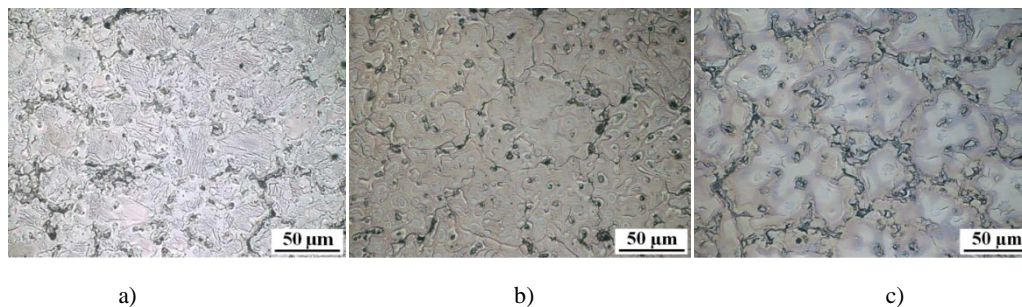


Figure 1. Microstructure of a) Mg5Al1Ti, b) Mg5Al1Ti-0,5Zn, c) Mg5Al1Ti-4Zn.

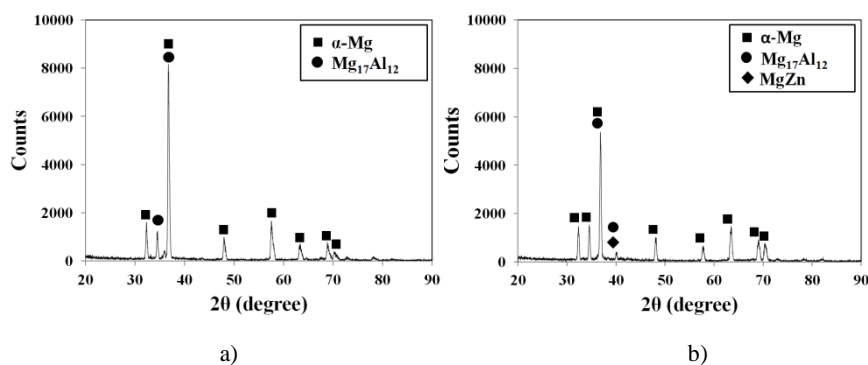
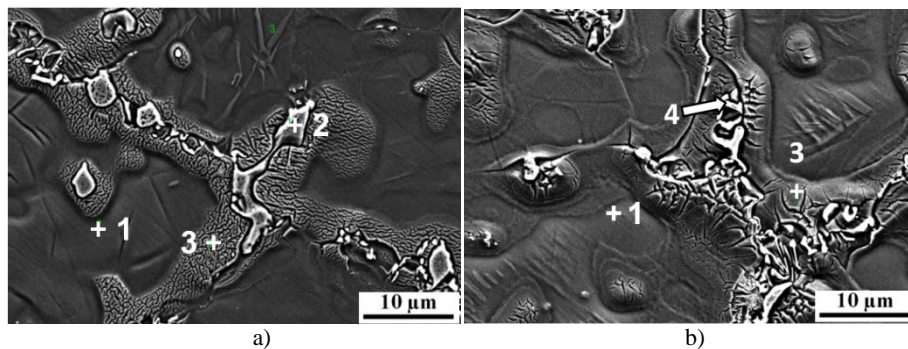


Figure 2. XRD patterns of alloys



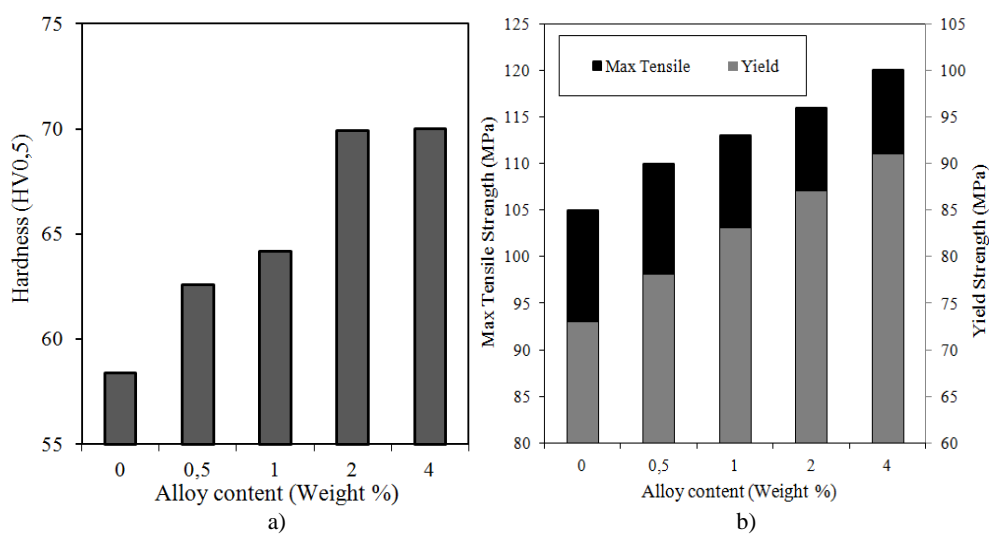
	Mg5Al1Ti			Mg5Al1Ti-4Zn		
	1	2	3	1	2	4
Mg	97,1	63,4	83,8	97,6	66,2	52,2
Al	2,1	36,6	16,2	2,4	30,2	3,0
Ti	0,8	-	-	-	2,5	-
Zn					0,9	44,8

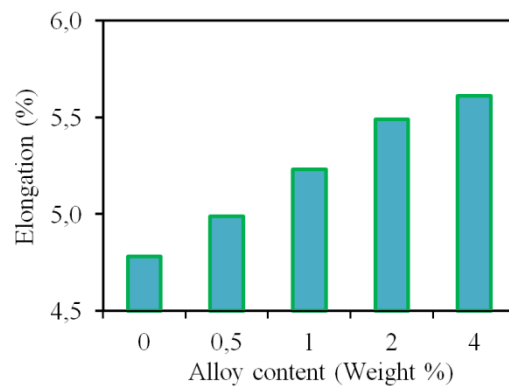
Figure 3. SEM micrographs and EDS analysis result of the microstructure a) Mg5Al1Ti, b) Mg5Al1Ti-4Zn

SEM microphotograph and EDS analysis, shown in Figure 3, identified the $Mg_{17}Al_{12}$ and MgZn phases formed on grain boundaries. MgZn phase was mainly observed in the microstructure of the Mg5Al1Ti alloy with Zn addition. The chemical compositions of the phases stated above and the morphological characteristics of these intermetallic phases showed similarities to those in literature [11,12].

3.2. Mechanical properties

The hardness values of the alloys are represented in Figure 4a. In Mg5Al1Ti matrix, the effect of Zn addition on the increase in hardness. The hardness of Mg5Al1Ti alloy was 58,4 HV. and Zn addition by 4% resulted in a 20% increase in hardness (to 70 HV).





c)

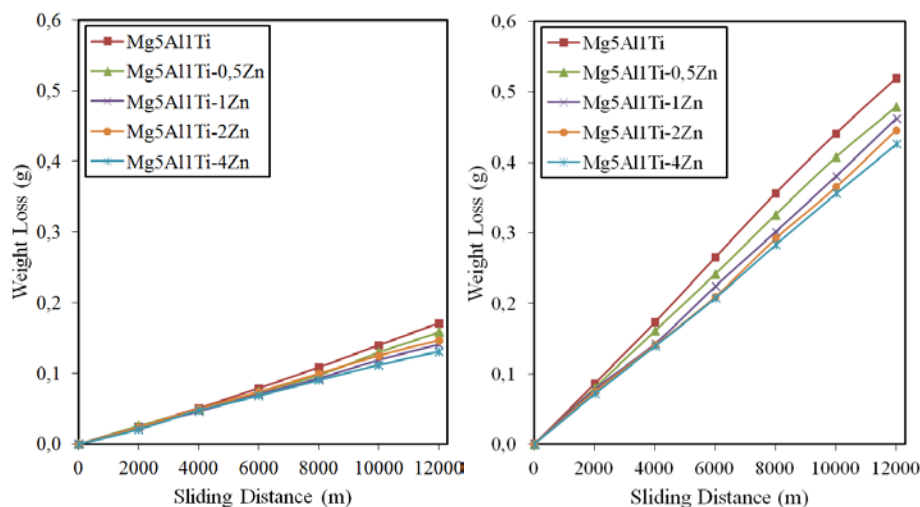
Figure 4. Mechanical properties of the alloys; a) Hardness, b) Tensile test result and c) Elongation.

The dependence of ultimate tensile strength, yield strength and elongation of Mg5Al1Ti alloy on the additions of Zn is shown in Figure 4b,c. Significant enhancement of tensile strength and yield strength was achieved by increasing Zn addition in the alloy. The ultimate tensile strength rose by 15% to 120 MPa with addition of 4% Zn. Similar studies have mentioned this enhancement of tensile strength by Zn addition [13-15]. An improvement in ductility was also achieved besides the tensile and yield strength.

Guangyin et al. made addition of Zn by 4%-8% in their study of the mechanical properties of Mg alloy [5]. They reported that a decrease in the amount of elongation was observed with Zn addition above 4%, and when the amount of Zn reached 8%, a 40% loss in the elongation was measured. In the present study, even though an increase in the amount of elongation was achieved with Zn addition of up to 4% (Figure 4c), it is predicted in regard to the studies of Guangyin et al that the amount of elongation will fall when Zn addition exceeds 4% [5].

3.3. Wear behaviour

Figure 5 presents the results of cumulative weight loss in Mg5Al1Ti alloys with Zn additions which obtained by the pin-on-disk wear testing with a sliding speed of 0.5 m/s, under the loads of 5N-40N. The weight loss showed a linear change with sliding distance at constant sliding speed. The highest weight loss was exhibited by Mg5Al1Ti alloy whereas the minimum weight loss was measured in Mg5Al1Ti-4Zn alloy at a given load and a sliding distance. The slope of the graph of Weight loss (g) versus Sliding distance (m) determined the wear rate as g/m. The variation in wear rate due to alloying content is shown in Figure 6. As it can be seen from Figure 6, the wear rate showed a decrease at a medium rate in the alloy with an alloying content of up to 2% while a constant and stable decrease in wear rate was observed in that of between 2% and 4%. The wear rate of Mg5Al1Ti master alloy with addition of XZn under a given load was slightly. All in all, a better wear resistance under all the loads was obtained by the addition of 4%. As seen in the literature, the higher the load, the larger the amount of weight loss [12]. Asla et al. studied the wear characteristics of Mg-Al-Zn alloy by testing at different sliding speeds. They reported that a stable wear behaviour was obtained under the loads of between 10N and 30N whereas the loads of 50N-100N resulted in a severe wear at a sliding speed of 0.5 [17].



a)

b)

Figure 5. The effect of sliding distance on the weight loss of the Zn content alloys; a) 5N and b) 40N.

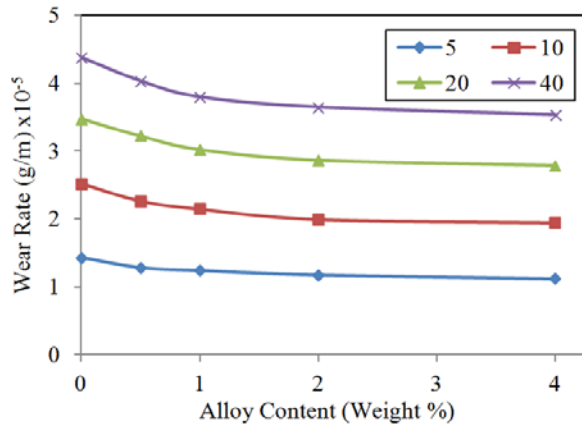


Figure 6. Relationship between wear rate and alloy contents in the investigated alloys.

An increase in the wear resistance of Mg5Al1Ti master alloy was observed with Zn addition in relation to volume fraction of MgZn intermetallics. As it is seen, the improvement of mechanical properties provided by the addition of Zn was made up primarily the increase in wear resistance.

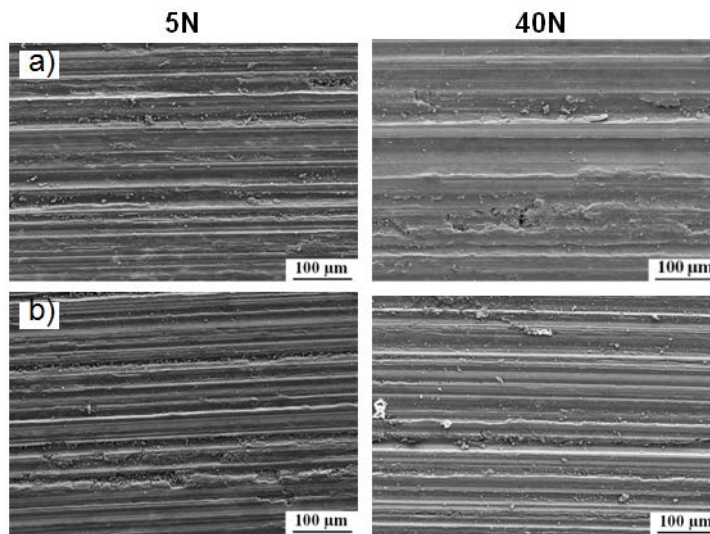


Figure 7. SEM micrographs of the worn surfaces of the investigated alloys, a) Mg5Al1Ti, b) Mg5Al1Ti-4Zn

SEM images showing the worn surfaces after wear testing are presented in Figure 7. Surface analyses were made in terms of minimum (5N) and maximum (40N) applied loads. Adhesive wear marks and small cavities as a light wear mechanism were formed at low loads. However, at high loads, as a severe wear mechanism, large pits and cavities occurred because of the formation and propagation of surface cracks [18].

4. CONCLUSIONS

The primary conclusions that can be derived from the present study are as follows:

1. Compared with the Mg5Al1Ti matrix by small amount of Zn additions the microstructures showed differences. MgZn phase was present in α Mg matrix by the addition of 4% Zn.
2. The highest hardness value was obtained by adding the 4% Zn. A significant enhancement of tensile strength and yield strength was achieved by increasing Zn addition in the alloy.
3. The wear rate of the alloy with an alloying content of approximately up to 2 % showed a decrease at a medium rate while a constant and stable decrease of the wear rate was observed in the alloying content of between 2% and 4%.

ACKNOWLEDGMENT

This study is a part of project which has been supported by Karabük University.

REFERENCES

- [1]. X. Xiaoling, L. Ping, L. Jiangwen, W. Dongxiao, N. Jianfen, BC. Muddle "Structure of hcp/bcc Inter-Phase Boundaries in AZ91 Mg-Al Alloy". *Chin J Nonferrous Met* 2003; 13: 15-20.
- [2]. M. Regev, E. Aghion, A. Rosen, "Creep studies of AZ91D pressure die casting". *Mater Sci Eng* 2001; A234-236: 46-50.
- [3]. W. Minmin, Z. Yongqing, Z. Lian., "Factor analysis on creep behavior of titanium alloys". *Rare Met Mater Eng* 2002; 31: 135-9.
- [4]. C. Blawert, N. Hort, K. Ku, "Automotive applications of magnesium and its alloys," *Transactions of The Indian Institute of Metals*, vol. 57, pp. 397-408, 2004.
- [5]. G. R. Ma, X. L. Li, L. Li, X. Wang, Q. F. Li, "Modification of Mg₂Si morphology in Mg-9%Al-0.7%Si alloy by the SIMA process," *Materials Characterization*, vol. 62, pp. 360-366, 2011.
- [6]. Y. Guangyin, L. Manping, D. Wenjiang, A. Inoue, "Mechanical properties and microstructure of Mg-Al-Zn-Si-base alloy," *Materials Transactions*, vol. 44, pp. 458-462, 2003.
- [7]. P. Cao, M. Qian, H. David, "Effect of manganese on grain refinement of Mg-Al based alloys," *Scripta Materialia*, vol. 54, pp. 1853-1858, 2006.
- [8]. J. Zhang, Z. X. Guob, F. Pan, Z. Li, X. Luoa, "Effect of composition on the microstructure and mechanical properties of Mg-Al alloys," *Materials Science and Engineering A*, vol. 456, pp. 43-51, 2007.
- [9]. G. A. Santos, C. M. Neto, W. R. Osorio, A. Garcia, "Design of mechanical properties of a Zn27Al alloy based on microstructure dendritic array spacing," *Material Design*, vol. 28, pp. 2425-2430, 2007.
- [10]. Sun, X. Sui, H. Li, Q. Wang, "Interface microstructure and mechanical properties of zinc-aluminum thermal diffusion coating on AZ31 magnesium alloy," *Material Design*, vol. 67, pp. 280-284, 2015.
- [11]. Y. Mingbo, S. Jia, "Modification and refinement mechanism of Mg₂Si phase in Sr containing AZ61-0.7Si magnesium alloy," *China Foundry*, vol. 6, pp. 37-42, 2009.
- [12]. K. Chen, Z. Q. Li, J. S. Liu, J. N. Yang, Y. D. Sun, S. G. Bian, "The effect of Ba addition on microstructure of in situ synthesized Mg₂Si/Mg-Zn-Si composites," *Journal of Alloys and Compounds*, vol. 487, pp. 293-297, 2009.
- [13]. S. Cai, T. Lei, N. Li, F. Feng, "Effects of Zn on microstructure, mechanical properties and corrosion behavior of Mg-Zn alloys," *Materials Science and Engineering C*, vol. 32, pp. 2570-2577, 2012.
- [14]. Z. Yu, H. Y. Zhao, X. D. Hu, D. Y. Ju, "Effect of elements Zn, Sn and In on microstructures and performances of AZ91 alloy," *Transactions of Nonferrous Metals Society of China*, vol. 20, pp. 318-323, 2010.
- [15]. M. Cong, Z. Li, J. Liu, M. Yan, K. Chen, Y. Sun, et al, "Effect of Ca on the microstructure and tensile properties of Mg-Zn-Si alloys at ambient and elevated temperature," *Journal of Alloys and Compounds*, vol. 539, pp. 168-173, 2012.
- [16]. S. Dasa, A. T. Morales, A. T. Alpasa, "Microstructural evolution during high temperature sliding wear of Mg-3% Al-1% Zn (AZ31) alloy," *Wear*, vol. 268, pp. 94-103, 2010.
- [17]. K. M. Asla, A. Masoudib, F. Khomamizadehb, "The effect of different rare earth elements content on microstructure, mechanical and wear behavior of Mg-Al-Zn alloy," *Materials Science and Engineering A*, vol. 527, pp. 2027-2035, 2010.
- [18]. A. Palta, Y. Sun, H. Ahlatci, "Effect of copper addition on wear and corrosion behaviours of Mg₂Si particle reinforced composites," *Material Design*, vol. 36, pp. 451-458, 2012.

BIOGRAPHY

Assist. Prof. Yunus Türen was born in Konya in 1969 and completed his elementary, middle and high school education in there. After graduating from Gazi University Faculty of Technical Education Casting Metallurgy Department in 1993, he started working as a research assistant in Zonguldak Karaelmas University Karabük Faculty of Technical Education in 1994. He gained his master's degree and doctorate in Metal Education from Gazi University Graduate School of Natural and Applied Sciences in 1998 and in 2003 respectively.

In 2004, he was appointed to Karabük University Faculty of Technical Education, Department of Metal Education as assistant professor. As from the beginning of 2015, he was appointed to Faculty of Engineering, Department of Metallurgy and Materials Engineering as assistant professor and currently keeping at this position.

Asst. Prof. Yunus Türen had 22 academic papers in total. 6 of them are indexed in SCI and SCI-Expanded journals, 1 of them is an article in a national peer-reviewed journal and 15 of them are full-text published proceedings in national and international conferences. He worked as a researcher in 3 different projects within university. Besides, he participated in British Council, Science Partnership Programme projects as a researcher. 4 master's theses have been completed under his supervision.

Asst. Prof. Yunus Türen is currently giving the lectures on Casting Technologies, Casting Techniques, Cast Iron, Casting Defects, Solidification at undergraduate level and Metal Casting Techniques, Industrial Light Metals and Their Alloys and Continuous Casting Technology of Metals at postgraduate level.

Vibration Control of A Semi-Trailer Truck for Comfort with An Output Feedback H_{∞} Controller

A. Oguzhan Ahan¹, Dogan Onur Arisoy², Kenan Muderrisoglu³,
Hakan Yazici⁴, Rahmi Guclu⁵

Abstract

Driver comfort is a fundamental parameter in large goods vehicles. Drivers working under uncomfortable driving conditions, experience ergonomic problems over long periods of time. Unless these conditions are overcome, drivers confront fatigue and require additional rests. Consequently, these rests increase both in time and numbers resulting with lost logistics time and reduced efficiency. On the other hand, drivers encounter medical issues and reduced life quality over time. Drop in medical status of drivers and efficiency of logistics increase the expenditure via hidden costs. Therefore an uncomfortable driving experience becomes an economical inconvenience. To prevent these issues, in this study a dynamic output feedback H_{∞} controller is designed via Linear Matrix Inequalities (LMI) approach and implemented on a model of a half semi-trailer truck augmented with a human model, to measure the change in the comfort level of the driver. To address the comfort level, acceleration and displacement values from passive and active systems are presented in graphics with contrast to each other. Finally, acceleration values under different speeds have been gathered from the human body model and evaluated with respect to the ISO 2631 specification to acquire comfort parameters, which then discussed accordingly.

Keywords: Driver Ergonomics, Vehicle Vibrations, Multi-Body Analysis, Optimal Control, LMI, Output Feedback Control, H_{∞} Controller, Comfort

1. INTRODUCTION

Overland logistics is a large employment area for drivers [1]. Hence human ergonomics and comfort become important. Driver ergonomics is an often studied topic in the literature. Kyung G., et al. report their findings on the experiment done on 27 participants which evaluates the effect of 6 different driver seats on comfort [2]. Participants are interviewed after their driving sessions for their body comfort mapping. In the same study Kyung G., et al. present measurements done via pressure sensors placed on driving seats [3]. Their deduction is that uncomfortable driving experience is a result of the pressure between hip and seat. Tiemessen I.J., et al. suggest that full-body vibrations in humans are a main cause for lumbago (lower back pain) and labor time loss [4]. Thamsuwan O., et al. relate lumbago often seen in bus drivers with full-body vibrations and measure it for different bus and road types. Additionally, these measurements are evaluated with ISO2631-1/5 specification to mark their risk on driver health [5]. Wolfgang R. and Limerick R.B. discuss measured full-body vibrations that drivers in coal mines experience and propose suggestions [6]. Ab Aziz S.A., et al. report full-body vibration measurements done with a heavy duty military vehicle in Malaysia. In the study, vibrations are gathered three dimensionally using Z-notch filter method [7]. Blood R.P., et al. measure the differences of driver full-body vibrations with different wheels and evaluate under both ISO 2631-1 and ISO 2631-5 specifications. As a result they state that evaluations using ISO 2631-1 specification are more viable in terms of health focused assessments [8].

Control is a tool which may be used to reduce full-body vibrations experienced by drivers. Therefore increasing their health condition and reducing their fatigue [2, 3]. In this perspective, Guclu R. suggests a fuzzy logic controller for a half-vehicle model [9]. Guclu R. and Gulez K. realize a control method both for driver seat vibration and vehicle vibration in a full-vehicle model with an artificial neural network, using linear permanent magnet synchronous motors [10]. Paksoy M., et al. in their study, control a full vehicle model augmented with magnetorheological damper utilizing a fuzzy logic controller [11]. With the advancements in control theory, especially in modern control theory, applications which utilize Lyapunov stability theorems are quite common today. H_{∞} controllers are an effective method for suppression of the fundamental mode. Kau S.W. et al., suggest a fuzzy-static-output-feedback H_{∞} controller for a semi-trailer truck to

¹ Corresponding author: Yildiz Technical University, Department of Mechanical Engineering, 34349, Beşiktaş/İstanbul, Turkey. ahan@yildiz.edu.tr

² Author: Yildiz Technical University, Department of Biomedical Engineering, 34220, Esenler/İstanbul, Turkey. arisoy@yildiz.edu.tr

³ Author: Yildiz Technical University, Department of Mechatronic Engineering, 34349, Beşiktaş/İstanbul, Turkey. kenan.muderrisoglu@gmail.tr

⁴ Author: Yildiz Technical University, Department of Mechanical Engineering, 34349, Beşiktaş/İstanbul, Turkey. hyazici@yildiz.edu.tr

⁵ Author: Yildiz Technical University, Department of Mechanical Engineering, 34349, Beşiktaş/İstanbul, Turkey. guclu@yildiz.edu.tr

address cruise and maneuver conditions. Controller is designed simplistically with relaxed border conditions, which mentioned as to have increased applicability [12]. Li H., et al. report reduced suspension displacement, body displacement and body acceleration values, after the implementation of their H_∞ controller to a quarter-vehicle model [13]. Sun W., et al. present a dynamic output feedback H_∞ controller for a quarter-vehicle model augmented with a human model [14]. Zhao Y., et al. realize control of a human-seat model with state feedback H_∞ controller. This controller is designed with actuator saturation, time dependent input delays and parameter uncertainties in mind [15].

In this study, firstly, design of a half semi-trailer truck model augmented with a human-seat couple suggested by Zhao Y., et al., is realized using an output feedback H_∞ controller. The controller is designed using LMI method. Secondly, road irregularities are defined as indicated in ISO 2631 specification. Finally, comfort parameters are evaluated in parallel to ISO 2631-1 specification both from the uncontrolled and controlled model between 0-100 km/h velocities. This presented the efficiency of the controller for increased comfort.

2. MATERIALS AND METHODS

2.1. Modelling

In this paper, comfort of a semi-trailer truck driver is studied. For convenience only vertical and pitch motions are considered in the model. Therefore any instances such as roll, yaw, maneuver etc. are neglected. Model is designed with 5 axel shafts each having a delayed road irregularity input relative to previous one. Human model is placed inside the cabin of the tractor. In the model, m_1 represents tractor mass, m_2 represents semi-trailer mass, m_3, m_4, m_5, m_6 and m_7 present wheel masses, m_{s1} represents seat chassis mass, m_{s2} represents combined seat cushion and hip mass and m_{s3} represents combined human torso and head mass. Values given with k and c represent stiffness and damper values between the masses respectively. Length values are shown with L . Angular displacements are denoted with θ and linear displacements are denoted with x for vehicle model and z for human-seat model. Road irregularity inputs are shown with Xy . Controller actuator is placed between m_1 and m_{s1} and denoted with u . Your paper must use a page size corresponding to A4 which is 210 mm wide and 297 mm long. The margins must be set as follows:

Equations of motion of the model are gathered using 2nd kind Lagrange equations, then converted into state-space form. State matrix is obtained as,

$$A = \begin{bmatrix} [0]_{nxn} & I_{nxn} \\ -M^{-1}K & -M^{-1}C \end{bmatrix}_{2nx2n} \quad (1)$$

State-space equations are defined as,

$$\dot{x}(t) = Ax(t) + Bu(t) \quad (2)$$

$$y(t) = Cx(t) + Du(t) \quad (3)$$

Where states of the vehicle defined as,

$$x_t = \{x_{t1} x_{t2} \dots x_{t20}\}^T \quad (4)$$

and states of the human-seat couple defined as,

$$x_{s1} = z_1 - z_0, x_{s2} = \dot{z}_1, x_{s3} = z_2 - z_1, x_{s4} = \dot{z}_2, x_{s5} = z_3 - z_2, x_{s6} = \dot{z}_3 \quad (5)$$

Here z_0 indicates the linear displacement of the tractor frame displacement. Also may be defined as $z_0 = x_{t1}$. Model parameters are presented in Table 1. Figure 1 exhibits the mentioned model.

Table 1 Semi-Trailer Truck and Human-Seat Couple Model Parameters [15, 16]

m1=4892,5 kg	k=155800 N/m	c1=20000 Ns/m	V=60 km/h
m2=13000 kg	k1=300000 N/m	c2=10000 Ns/m	L1=1,2 m L2=3,6 m
m3=270 kg	k2=847000 N/m	c3=0 Ns/m	L3=4,8 m L4=4,13 m
m4=520 kg	k3=967430 N/m	c4=27627 Ns/m	L5=6,97 m
m5=520 kg	k4=2000000 N/m	c5=0 Ns/m	L6=4 m
m6=270 kg	k5=967430 N/m	c6=27627 Ns/m	L7=0,685 m
m7=270 kg	k6=2000000 N/m	c7=0 Ns/m	L8=0,7 m
ms1=15 kg	k7=155800 N/m	c8=44506 Ns/m	
ms2=8,8 kg	k8=2000000 N/m	c9=0 Ns/m	

ms3=43,4kg	k9=155800 N/m	c10=44506 Ns/m
J1=9155 kgm ²	k10=2000000 N/m	c11=0 Ns/m
J2=125950 kgm ²	ks1=31000 N/m	cs1=830 Ns/m
J3=3300 kgm ²	ks2=18000 N/m	cs2=200 Ns/m
	ks3=44130 N/m	cs3=1485 Ns/m

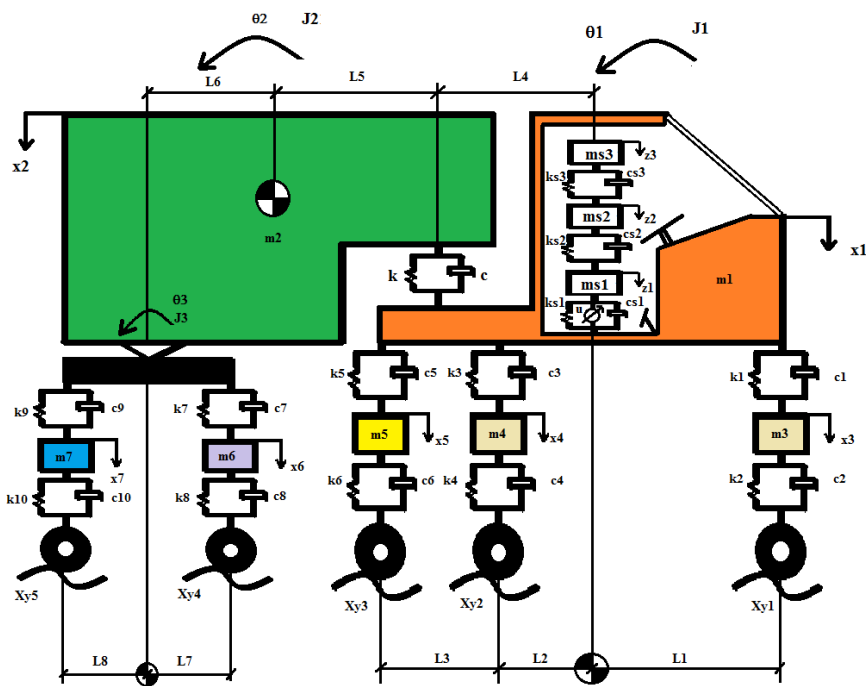


Figure 1. Semi-trailer truck model with human-seat couple

2.2. Controller Design

As a part of the study, a dynamic output feedback H_∞ controller is designed. State-space model of the system is given as below.

$$\dot{x}(t) = Ax(t) + B_1w(t) + B_2u(t) \tag{6}$$

$$z(t) = C_1x(t) + D_{11}w(t) + D_{12}u(t) \tag{7}$$

$$y(t) = C_2x(t) + D_{21}w(t) + D_{22}u(t) \tag{8}$$

Where w defines exogenous input and z defines exogenous output.

As there is no direct transmission between inputs and outputs, therefore D_{22} can be represented with a zero matrix. Hence $y(t)$ can be simplified as following,

$$y(t) = C_2x(t) + D_{21}w(t) \tag{9}$$

In this model, states of the human-seat couple have been chosen as performance criteria. Therefore C_1 matrix is defined as,

$$C_1 = [0_{6,20} I_6] \tag{10}$$

C_2 matrix determines which states are the observers. In this case, x_{s1} and x_{s2} are chosen as observers. Hence C_2 matrix is defined as,

$$C_2 = \{0_{2,20} I_2 0_{2,4}\} \tag{11}$$

D_{11} , D_{12} and D_{21} matrices are defined as zero matrices. Controller matrices of the output feedback control is demonstrated as

$$\dot{x}_k(t) = A_k x_k(t) + B_k y(t) \quad (12)$$

$$u(t) = C_k x_k(t) + D_k y(t) \quad (13)$$

Performance of the controlled system is provided with γ which can be defined as

$$\|G\|_\infty = \frac{\|z\|_2}{\|w\|_2} \leq \gamma \quad (14)$$

And this approximation can be written as below.

$$\|z\|_2 \leq \gamma \|w\|_2 \quad (15)$$

This formula can be rewritten with norm properties of a vector.

$$g(x, w) = z^T z - \gamma w^T w \leq 0 \quad (16)$$

With this performance criterion, Lyapunov inequality can be rewritten for H_∞ controller design as,

$$\dot{V}(x) + g(x, w) < 0 \quad (17)$$

$$\dot{V}(x) + z^T z - \gamma^2 w^T w < 0 \quad (18)$$

where $P = P^T > 0$ and $V(x) = x^T P x$. If this Hamiltonian inequality are to be written with these Lyapunov inequality, the following can be provided. (19)

Thence arranged and evaluated with Schur-Complement formula, following can be obtained.

$$\begin{bmatrix} PA + A^T P & PB & C^T \\ B^T P & -\gamma I & D^T \\ C & D & -\gamma I \end{bmatrix} < 0 \quad (20)$$

When above expression evaluated with Similarity transformation and then with the proper Congruence transformation as given in [17], following can be gathered.

$$\begin{bmatrix} XA + A^T X + \bar{B}C_2 + C_2^T \bar{B}^T & \bar{A} + A^T + C_2^T \bar{D}^T B_2^T & XB_1 + \bar{B}D_{21} & C_1^T + C_2^T \bar{D}^T D_{12}^T \\ * & AY + YA^T + B_2 \bar{C} + \bar{C}^T B_2^T B_1 + B_2 \bar{D} D_{21} & Y C_1^T + \bar{C}^T D_{12}^T \\ * & * & -\gamma I & D_{11}^T + D_{21}^T \bar{D}^T D_{12}^T \\ * & * & * & -\gamma I \end{bmatrix} < 0 \quad (21)$$

where $X = X^T > 0$ and $Y = Y^T > 0$ which can be obtained with the several similarity transformation of the P matrix. To obtain coupling condition of the X and Y,

$$\begin{bmatrix} X & I \\ I & Y \end{bmatrix} > 0 \quad (22)$$

can be defined. With (21) and (22) constraints, LMI problem can be solved with semi definite optimization in according to minimize γ parameter. With optimization, $X, Y, \bar{A}, \bar{B}, \bar{C}$ and \bar{D} matrices can be found as a local minima. Thence, control matrices can be found as below, where $Z = Y - X^{-1}$

$$D_k = \bar{D} \quad (23)$$

$$C_k = -\bar{C}Z^{-1} + D_k C_2 Y Z^{-1} \quad (24)$$

$$B_k = X^{-1} \bar{B} - B_2 D_k \quad (25)$$

$$A_k = -X^{-1} \bar{A} Z^{-1} + (A + B_k C_2) Y Z^{-1} - B_2 C_k \quad (26)$$

Thence A_{cl}, B_{cl}, C_{cl} and D_{cl} matrices of the controlled model can be gathered as,

$$D_{cl} = D_{11} + D_{12} D_k D_{21} \quad (27)$$

$$C_{cl} = [C_1 + D_{12} D_k C_2 D_{12} C_k] \quad (28)$$

$$B_{cl} = \begin{bmatrix} B_1 + B_2 D_k D_{cl} \\ B_k D_{21} \end{bmatrix} \quad (29)$$

$$A_{cl} = \begin{bmatrix} A + B_2 D_k C_2 & B_2 C_k \\ B_k C_2 & A_k \end{bmatrix} \quad (30)$$

Therefore the state-space model of the controlled system can be defined as following.

$$\begin{cases} \dot{x}_{cl} \\ z \end{cases} = \begin{bmatrix} A_{cl} & B_{cl} \\ C_{cl} & D_{cl} \end{bmatrix} \begin{cases} x_{cl} \\ w \end{cases} \quad (31)$$

2.3. Definition of the ISO 2631-1 (1994) Technical Specification

ISO 2631-1 1994 technical specification defines a methodology to analyze human-machine interaction under vibrations. One of the fundamental tool of this specification is the comfort and health analysis method. Furthermore specification provides a technique to analyze kinetosis (motion sickness). ISO 2631-1 specification is only interested in human related vibrations and their effect on health and comfort; on the other hand does not concern about general vehicle performance.

Firstly, road irregularities has been defined with the specification. To define irregularity, randomness has been created with methodology, which had been studied by [18]. In Figure 2, example road profile has been defined with 60 km/h simulated vehicle from Matlab/Simulink.

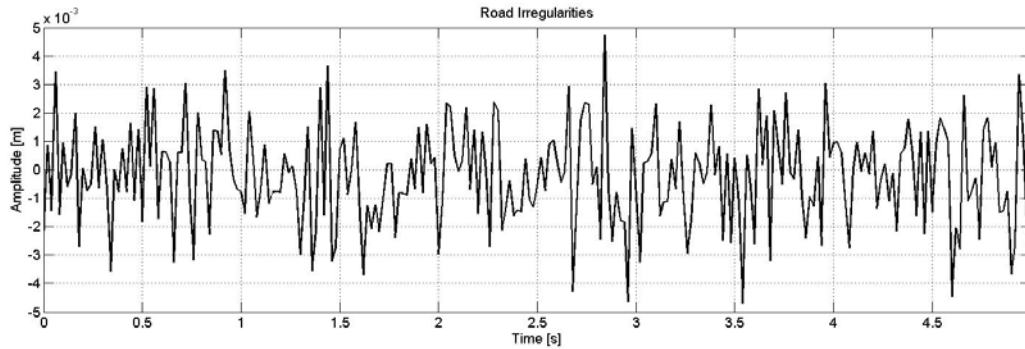


Figure 2. Road Irregularity

ISO 2631-1 specification handles vibration effects on humans as full body vibrations. In this perspective, frequencies between 0.5 Hz and 80 Hz are related with health, comfort and perception; also frequencies between 0.1 Hz and 0.5 Hz are related with kinetosis.

RMS value of acceleration is used in the evaluation of vibration, which defined as,

$$a_{rms} = \frac{1}{T} \sqrt{\int_0^T a_w^2(t) dt} \quad (32)$$

where a_w is weighted acceleration measurement, T is the measurement period. To obtain a_w , 3 types of filters are used which are,

$$H_H(s) = \frac{s^2}{s^2 + \frac{2\pi*100}{0,71}s + (2\pi*100)^2} \quad (33)$$

$$H_L(s) = \frac{(2\pi*100)^2}{s^2 + \frac{2\pi*100}{0,71}s + (2\pi*100)^2} \quad (34)$$

$$H_{TV}(s) = \frac{(s+2\pi*16)^2}{s^2 + \frac{2\pi*16}{0,63}s + (2\pi*16)^2} \cdot \frac{s^2 + \frac{2\pi*2,5}{0,8}s + (2\pi*2,5)^2}{s^2 + \frac{2\pi*4}{0,8}s + (2\pi*4)^2} * 32,768\pi \quad (35)$$

Where H_L is a low-pass filter, H_H is a high-pass filter and H_{TV} is a filter which is defined for vertical comfort investigation [19]. When generalized, filter can be shown as,

$$H_{vertical}(s) = H_H(s)H_L(s)H_{tv}(s) \quad (36)$$

3. RESULT AND DISCUSSION (SIMULATION STUDIES)

Simulations are conducted with 5 seconds of measurement period to provide admissible comfort analysis, in conjunction with the ISO 2631-1 Specification [20]. After the simulation, two cases are investigated. First being controlled and uncontrolled semi-trailor truck model has been simulated with 60 km/h vehicle velocity. As result, time and frequency responses of the human-seat couple with all states are obtained comparatively.

Secondly, comfort during both controlled and uncontrolled situations are calculated and evaluated for 0-100 km/h velocity range with 1 km/h interval. Comfort parameter has been provided from interpretation of human torso acceleration. Then, results are interpreted with ISO 2631-1 technical specification.

In Figure 3, responses of the first case is demonstrated in time domain.

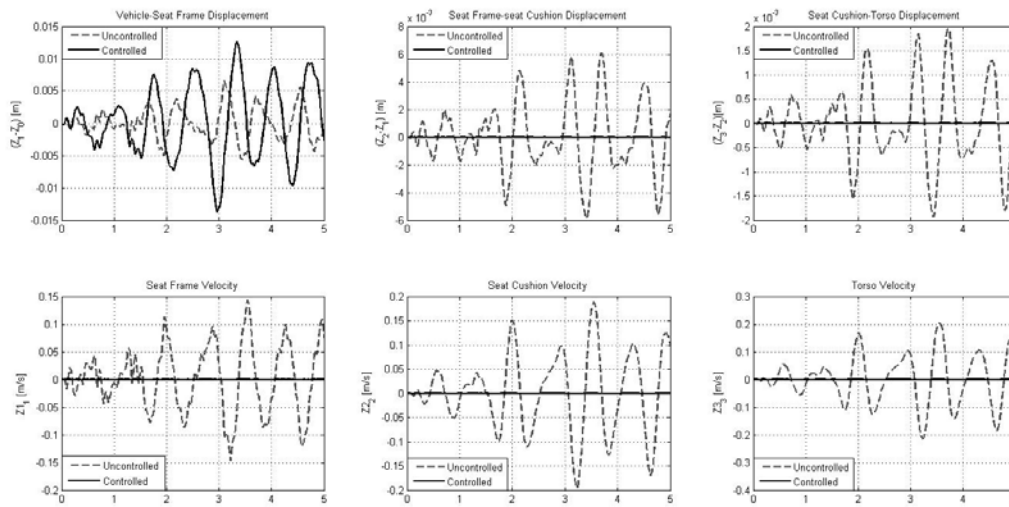


Figure 3. Time Domain Responses of the human-seat couple

Time responses show that, seat frame and vehicle relative displacement, also seat frame velocity are decreased, when controller is on. Subsequently, relative displacement of seat frame and seat cushion is attenuated. Also seat cushion velocity is decreased. Moreover, human torso velocity and relative displacement is decreased dramatically. This result immerge an idea, that comfort condition has increased with the implementation of the controller. In Figure 4, Frequency response of the first case is shown.

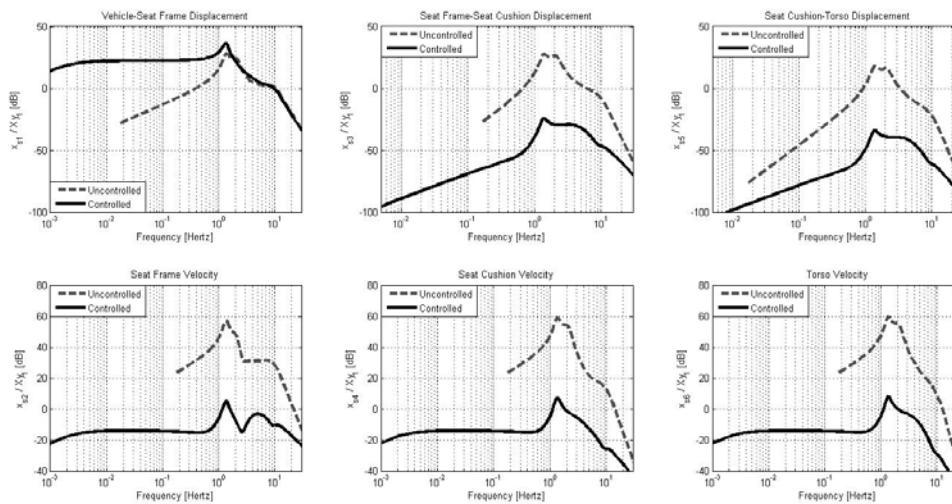


Figure 4. Frequency Responses of the human-seat couple

Similar results can be seen in the frequency responses. Seat frame and vehicle relative displacement frequency response increased, however, all of the other states decreased dramatically. This means, controller create force signal to attenuate the seat vibration relative to the vehicle. In result, seat and driver does not effect the road irregularites. In Figure 5, controller force is presented.

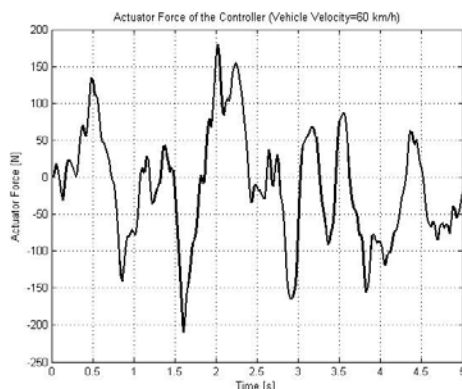


Figure 5. Actuator Force of the Controller

With the second case, more generalized form of the simulation has been tested. Main purposes of the second case is to obtain comfort parameter and mean generalized actuator force according to vehicle velocity. With this analysis, it can be said that, controller methodology may provide suitable comfort condition with rational force generation for this model. Simulations are conducted with 5 seconds of measurement period, in result comfort parameter and mean generalized force are gathered. In Figure 6 (a), comfort parameter for controlled and uncontrolled situations relative to vehicle velocity are shown. In Figure 7 (b), mean actuator force relative to vehicle velocity is given.

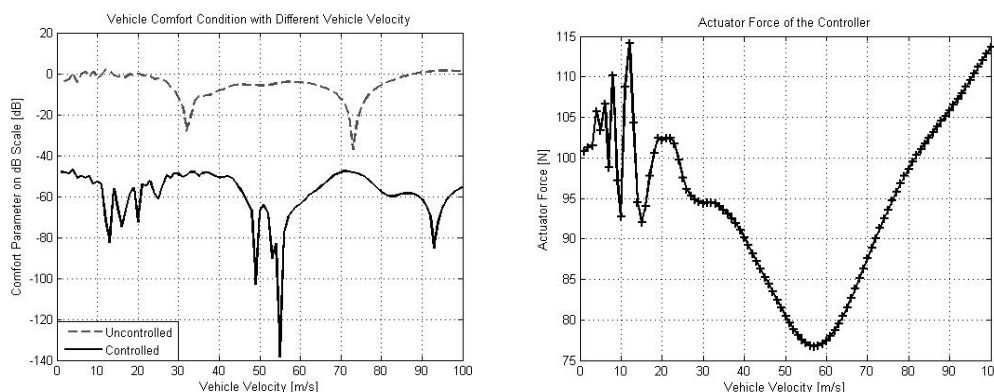


Figure 6. (a) Comfort Parameter Relative to Vehicle Velocity (b) Mean Actuator Force Relative to Vehicle Velocity

Figure 6 (a) shows that, comfort parameter is affected from various speed values. Table 2 displays the comfort condition for different weighted mean acceleration values, which is cited before as comfort parameter. Evaluation of Figure 6 (a) with respect to Table 2 presents that, uncontrolled vehicle has uncomfortable conditions for 0-20 km/h, after this velocity, vehicle becomes comfortable, but higher speeds cause vehicle to become uncomfortable again. In contrast when the controlled situation in Figure 6 (a) evaluated, it can be seen that it has almost zero weighed mean acceleration through the whole velocity spectrum given. Therefore it is possible the say that controlled vehicle is comfortable indeed with respect to Table 2.

Table 2. ISO 2631-1 Comfort Condition According to Mean Weighted Acceleration on dB Scale

Acceleration of Vibration (m/s ²)	Travel Comfort
<(-10,034)	Comfortable
(-10,034) - (-4,0132)	Quite Comfortable
(-6,0206) - 0	Quite Uncomfortable
(-1,9382) - 4,0824	Uncomfortable
1,9382- 7,9588	Very Uncomfortable
>6,0206	Extremely Uncomfortable

4. CONCLUSION

In this study, 10 DOF half semi-trailer truck vehicle model augmented with a human-seat couple has been investigated for comfort and health analysis in controlled and uncontrolled cases. Firstly, Lagrangian model of the system has been obtained. Controller has been designed with norm interpretation of the dynamic output feedback method. Then, using ISO 2631-1 specification, comfort analyzer has been built with filters. Lastly, components have been implemented with using Simulink. In the sake of the comfort analysis, torso acceleration has been observed.

As a result, controlled system has conducted a notable performance. Comfort parameter decreased at all velocities. Especially, the lower velocity region has a right to be highlighted. Comfort analysis shows that, worst comfort conditions are at 0-20 km/h for uncontrolled case. As traffic congestion is an inevitable problem for crowded cities and happens to be overlapping with uncomfortable velocity regions; it is possible to say that, why traffic congestion affect the life quality and productivity especially for professional drivers. With this perspective, it can be thought that, traffic congestion caused economic burden is much more than the assumed one.

ACKNOWLEDGMENT

There is no conflict of interest.

REFERENCES

- [1]. Bureau of Labor Statistics (2015), Occupational Employment and Wages, May 2015: 53-3032 Heavy and Tractor-Trailer Truck Drivers, [Online]. Available: <http://www.bls.gov/oes/current/oes533032.htm>
- [2]. G. Kyung, M. A. Nussbaum, K. B. Reeves, "Driver sitting comfort and discomfort (part I): Use of subjective ratings in discriminating car seats and correspondence among ratings", *International Journal of Industrial Ergonomics*, vol. 38, pp. 516–525, 2008
- [3]. G. Kyung, M. A. Nussbaum, K. B. Reeves, "Driver sitting comfort and discomfort (part II): Relationships with and prediction from interface pressure", *International Journal of Industrial Ergonomics*, vol. 38, pp. 526–538, 2008
- [4]. I. J. Tiemessen, C. T. J. Hulshof, M. H. W. Frings-Dresen, "An overview of strategies to reduce whole-body vibration exposure on drivers: A systematic review", *International Journal of Industrial Ergonomics*, vol. 37, pp. 245–256, 2007
- [5]. O. Thamsuwan, R. P. Blood, R. P. Ching, L. Boyle, P. W. Johnson, "Whole body vibration exposures in bus drivers: A comparison between a high-floor coach and a low-floor city bus", *International Journal of Industrial Ergonomics*, vol. 43, pp. 9-17, 2013
- [6]. R. Wolfgang, R. Burgess-Limerick, "Whole-body vibration exposure of haul truck drivers at a surface coal mine", *Applied Ergonomics*, vol. 45, pp. 1700-1704, 2014
- [7]. S. A. A. Aziz, M. Z. Nuawi, M. J. M. Nor, "Predicting whole-body vibration (WBV) exposure of Malaysian Army three-tonne truck drivers using Integrated Kurtosis-Based Algorithm for Z-Notch Filter Technique 3D (I-kaz 3D)", *International Journal of Industrial Ergonomics*, vol. 52, pp. 59-68, 2016
- [8]. R. P. Blood, P. W. Rynell, P. W. Johnson, "Whole-body vibration in heavy equipment operators of a front-end loader: Role of task exposure and tire configuration with and without traction chains", *Journal of Safety Research*, vol. 43, pp. 357–364, 2012
- [9]. R. Guclu, "The Fuzzy-Logic Control of Active Suspensions without Suspension-Gap Degeneration", *Journal of Mechanical Engineering-Strojnicki Vestnik*, vol. 50(10), pp. 462-468, 2004
- [10]. R. Guclu, K. Gulez, "Neural Network Control of Seat Vibrations of a Non-linear Full Vehicle Model using PMSM", *Mathematical and Computer Modelling*, DOI: 10.1016/j.mcm.2007.08.013, vol. 47(11-12), pp. 1356-1371, 2008
- [11]. M. Paksoy, R. Guclu, S. Cetin, "Semiaactive Self-Tuning Fuzzy Logic Control of Full Vehicle Model with MR Damper," *Advances in Mechanical Engineering*, DOI:10.1155/2014/816813, vol. 2014, Article ID 816813, 2014
- [12]. S. W. Kau, H. J. Lee, C. M. Yang, C. H. Lee, L. Hong, C. H. Fang, "Robust H_∞ fuzzy static output feedback control of T-S fuzzy systems with parametric uncertainties", *Fuzzy Sets and Systems*, vol. 158, pp. 135 – 146, 2007
- [13]. H. Li, X. Jing, H. R. Karimi, "Output-Feedback-Based H_∞ Control for Vehicle Suspension Systems With Control Delay", *IEEE Transactions On Industrial Electronics*, vol. 61(1), pp. 436-446, 2014
- [14]. W. Sun, J. Li, Y. Zhao, H. Gao, "Vibration control for active seat suspension systems via dynamic output feedback with limited frequency characteristic", *Mechatronics*, vol. 21, pp. 250–260, 2011
- [15]. Y. Zhao, W. Sun, H. Gao, "Robust control synthesis for seat suspension systems with actuator saturation and time-varying input delay", *Journal of Sound and Vibration*, vol. 329, pp. 4335–4353, 2010
- [16]. G. Tsampardoukas, C. W. Stammers, E. Guglielmino, "Hybrid balance control of a magnetorheological truck suspension", *Journal of Sound and Vibration*, vol. 317, pp. 514–536, 2008
- [17]. I. Polat, "LPV Control of Two Link Flexible Manipulator", M. Sc. Thesis, Bogazici University, Istanbul, Turkey, 2006
- [18]. H. Du, W. Li, N. Zhang, "Integrated seat and suspension control for a quarter car with driver model", *IEEE Transactions On Vehicular Technology*, vol. 61(9), pp. 3893–3908, 2012
- [19]. A. Orvnas, "On Active Secondary Suspension in Rail Vehicles to Improve Ride Comfort", PhD Thesis, KTH School of Engineering Science, Stockholm, Sweden, 2011.
- [20]. *Mechanical vibration and shock - Evaluation of human exposure to whole-body vibration. Part 1: General requirements. International Organization for Standardization (ISO), ISO 2631-1, 1997.*

BIOGRAPHY

A. Oguzhan Ahanis born in 1990. He received his B.Sc. degree from Yildiz Technical University, Department of Mechanical Engineering in 2012 and his M.Sc. degree from Istanbul Technical University, Department of Mechanical Engineering in 2015. He is currently studying for his Ph.D. degree in Yildiz Technical University, Department of Mechanical Engineering. He is a Research Assistant in Yildiz Technical University, Department of Mechanical Engineering. His current research interest includes biomechanical system dynamics and optimal control, as well as structural modal testing and vibration theory.

Dogan Onur Arisoy is born in 1990. He received his B.Sc. degrees from Yildiz Technical University, Department of Mechanical Engineering and Department of Electrical Engineering in 2012 and 2014 respectively. He is currently studying for his M.Sc. degree in Bogazici University, Institute of Biomedical Engineering. His M.Sc. research is about modelling of human cardiovascular system. He is a Research Assistant in Yildiz Technical University, Department of Biomedical Engineering. His current research interest includes physiological systems modelling, also system dynamics and control.

Kenan Muderrisoglu born in 1990. He received his B.Sc. degree from Yildiz Technical University, Department of Mechanical Engineering in 2012. He is currently studying for his M.Sc. degree in Yildiz Technical University, Department of Mechatronics Engineering. His M.Sc. research is about adaptive and robust control of biped robots. He is working as a Systems Engineer in Tumosan Motor ve Traktor A.S. His current research interest includes system kinematics, kinetics and modern control methods.

Hakan Yazici received his M.Sc and Ph.D. from Yildiz Technical University, all in Mechanical Engineering, in 2006 and 2011, respectively. He conducted post-doctoral research at Southern Illinois University Edwardsville, USA, from 2011 to 2012. He is currently an Assistant Professor at Yildiz Technical University, Department of Mechanical Engineering. His current research interest includes robust and optimal control of time-delay systems with actuator saturation, stability of functional differential equations with time delays, and active vibration control and its applications.

Rahmi Guclure received his B.Sc. degree from Yildiz Technical University, Department of Mechanical Engineering in 1985, his M.Sc. degree from Yildiz Technical University, Department of Naval Architecture and Marine Engineering in 1988 and his Ph.D. degree from Yildiz Technical University, Department of Mechanical Engineering in 1996. He is a Professor in Yildiz Technical University, Department of Mechanical Engineering and head of the Sub-Department of Machine Theory, System Dynamics and Control. His current research interest includes mechanical vibrations, system dynamics and control, vehicle dynamics, structural vibrations and rail system dynamics.

The Effects of Synthetic and Steel Fibers Admixtures to the Abrasion Resistance of Normal and Vacuum Concrete

Hakan Bolat¹, Mustafa Cullu²

Abstract

Although the most important mechanical properties of the concrete compressive strength, many times which is exposed to abrasion by means of friction, wetting-drying and freeze-thaw. Therefore, concrete is also need to be extra reinforced for the exposed abrasion. The concrete strength class to be high, is not a factor that increases the abrasion resistance by itself. Abrasion resistance should be increased with also admixtures and application methods besides being concrete compressive strength is high. Fiber admixtures and the vacuum dewatering are two methods which increase the abrasion resistance of concrete. This study parameters are; normal production of concrete, vacuum dewatered concrete, steel fibers, polyester fibers, 3 different rates of fiber, 2 different fiber length and 3 different concrete strength classes. The aim of the study, the effects of the rates and lengths of steel and polyester fibers to determine abrasion resistance on the normal and vacuum concrete according to ASTM C944 standard. Consequently, of all the study parameters has been shown to influence of abrasion resistance all of the concrete types.

Keywords: vacuum concrete, steel, polyester, fiber admixtures, abrasion

1. INTRODUCTION

Concrete is a building material that needs to be protected. The deterioration of concrete often consists of a combination of several negative factors. Generally factors causing deterioration of the concrete can be summarized as that in Figure 1 [1-3].

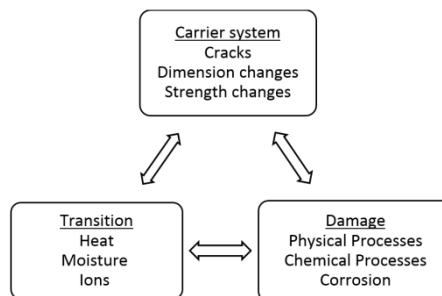


Figure 1. Causes of deterioration of concrete

Fibres have been used as additives to concrete for long times. Generally they are used to increase bending resistance of concrete and increase capacity of energy muffle under loading for long time [6-8]. Steel fibres are oldest fibres that are used in concrete. Steel concretes gain the concrete a big energy in first times and they can lose their physical structure under negative weather conditions by time. Especially their physical appearance spoils by rusting and they lose their effect in short time. Synthetic fibres increase the capacity of concretes absorbing energy in long times thanks to that their structure does not spoil in negative conditions although they are not like steel fibres [9-11].

Using of concrete fibres can decrease wear resistance depending on factors such as mixture percentage, resistance class, cement type and percentage, features of fibres, time of cure and conditions, environmental conditions, surface behaviour, water-cement percentage, percentage of air and penetrability. Attenuation which is in wear resistance depending on these factors effect concrete compressive strength the most

In this study, compressive strength of concretes which has steel and polyester fibres, normal and produced with vacuum is aimed. The parameters of the study are concretes which have three compressive strength, short and long steel and

¹ Corresponding author: Gumushane University, Department of Civil Engineering, 29100, Gumushane, Turkey. hb@gumushane.edu.tr,
² mcullu@hotmail.com

polyester fibres, three different fibre percentage and vacuum application. As a part of these parameters, type of fibres, length of fibres and vacuum application's effects to compressive strength are determined.

2. MATERIALS AND METHODS

2.1. Materials

2.2.1. Fibers

In this study, short and long steel and polyester fibers were used (Fig 2). The properties of fibers are given in Table 1. TS 10514 [19] offers that the highest amount per metercube of steel fibers to be used in the concrete is 50 kg. There isn't any standard related to synthetic fibers, so three ratios including 15-30-45 kg/m³ (A-B-C) were specified in the study by taking account of the highest fiber ratio based on by steel fiber standard. Volume was specified by considering the density, quantity and dimensions of steel fibers prepared on the basis of kg, and the quantity of polyester fiber was considered in the same volume.

Table 1. Fiber admixtures properties

Fiberproperties	Polyester	Steel
Ratio (dm ³ A-B-C)	1.91-3.81-5.72	1.91-3.81-5.72
Length (mm)	25-50	30-60
Width (mm)	0.9	-
Thickness (mm)	0.5	-
Diameter (mm)	-	0.9
Density (g/cm ³)	1.36	7.87
Tensile Strength (MPa)	400-800	~1100
Elastic modulus (MPa)	17237	200000
Ultimate elongation (%)	> 8	< 2
Fire point temperature (°C)	537	-
Melting, oxidation and decomposition temp (°C)	253	800
Water absorption according to ASTM D 570 (% - by weight)	0.4	0



Figure 2. Fiber admixtures

2.1.2. Concrete

In the study, normal and vacuumed concretes of C16/20 (low-L), C25/30 (normal-N) and C35/45 (high-H) strength classes were used. Long and short polyester and steel fibers in three different volumes (A-B-C) (Table 1) were added to the concretes. Fiber volume and the excess total concrete volume were balanced by deducting from sand volume. 79 types of concrete with the parameters including type of application, type of fiber, length of fiber, ratio of fiber and concrete strength class were prepared (Fig 3). Mixture ratios of the concretes by strength classes were specified in Table 2 by considering TS 802 [20] and TS 10514 standards. Granulometry of the aggregates used in the concretes are shown in Fig 4. CEM II/A-M (P-LL) 42,5 R type cement was used.

Table 2. Concrete mix design

Concrete components	Concrete types (1000 dm ³)		
	Low	Normal	High
Water	301	260	280
Cement	94.3	115.7	153.3
Air	14	14	14
Fluidisation	-	4.4	5.8
Aggregates	590.7	608.7	546.9
Fly ash	56.7	58.5	52.5
0-2 mm	-	-	120
0-4 mm	215	199	-
2-4 mm	-	-	110
4-8 mm	106	120	-
4-11.2 mm	-	-	140
8-16 mm	106	117	-
11.2-32 mm	-	-	124.4
16-32 mm	107	117	-
Total	1000	1000	1000



Figure 3. Vacuum concrete

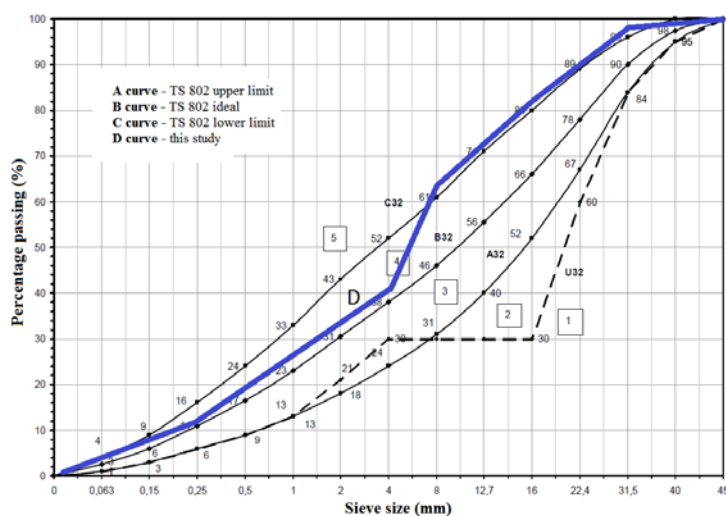


Figure 4. Aggregate granulometry

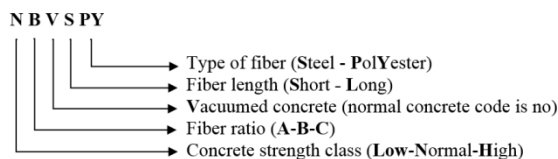
The concrete samples were coded in 2 different ways as reference concrete sample without fiber and concrete samples with fiber, as shown below.

Nonfiber reference concretes:

LR-NR-HR: Low-Normal-High strength reference concretes

LVR-NVR-HVR: Low-Normal-High strength reference vacuumed concretes

Fiber reinforced concretes (example):



2.2.Method

Compressive strength of concretes is determined according to standard of ASTM C944 [21]. Samples which are 10 cm in diameter and 20 cm height were obtained from produced concretes with coring machine. Dry weigh of samples were determined. Then they were placed in abrasion machine and corroded two minutes in 200 rev/min speed (Fig 5). This procedure was done three times and dusting was done each time and their weigh were set. Three pieces of concrete sample from each concrete type were underwent abrasion test and arithmetical average of loss of determined weight was shown in graphics.



Figure 5. Abrasion test procedure

3.RESULTS and DICUSIONS

Steel and Polyester FRC (SFRC and PYFRC)) abrasion test were showed in separate graphics. Parameters of graphics are C16/20 (Low), C25/30 (Normal) and endurance class C35/45 (H) and they are kinds of concrete productions (vacuumed and normal). So that it was aimed short and long and fibre ratio is aimed. Then argument of vacuumed and normal concretes that were in same shape was done. The last argument was done on SFRC and PYFRC abrasion value.

In figure 6, abrasion value of vacuumed and normal concretes was showed. Abrasion which was nearly half of normal concretes was seed in vacuumed concrete types. Although both short SFRVC and SFRC abraded nearly twice times that long SFRC, variability of fibres percentage did not give any idea about abrasion value.

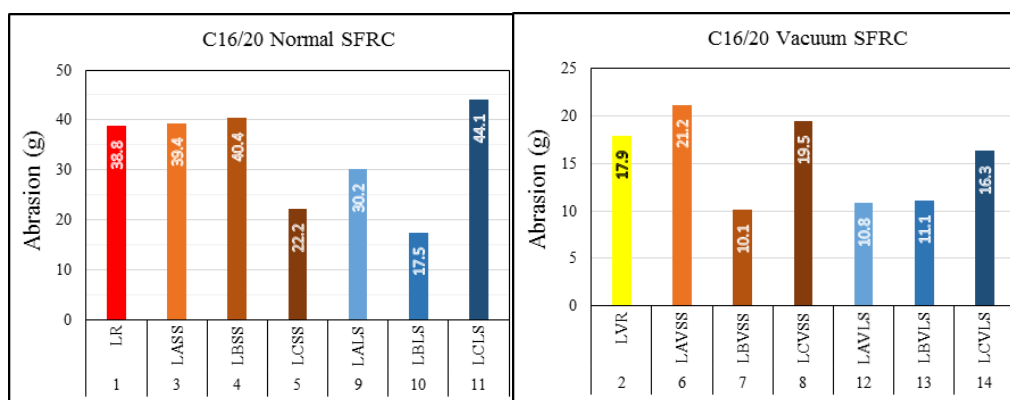


Figure 6. C16/20 Normal and Vacuum SFRC abrasion values

In figure 7, abrasion values of C25/30 vacuumed and normal concretes were showed. SFRVC abraded ~%30-65 less than Normal Short SFRC. However long SFRC is opposite to this. Long SFRC abraded more than short SFRC.

In figure 8, while abrasion values of vacuumed and normal concrete were showed. In HVR, ~%60 less abrasion was seen compared to HR concrete, abrasion values of SFRVC and SFRC was determined as so close to each other. As strength of concrete increase, abrasion values of SFRVC and SFRC are close to each other. When normal concrete is looked, short SFRC has the lowest abrasion values. When vacuumed concretes is looked, the more fibres percentage the more abrasion values in long SFRVC.

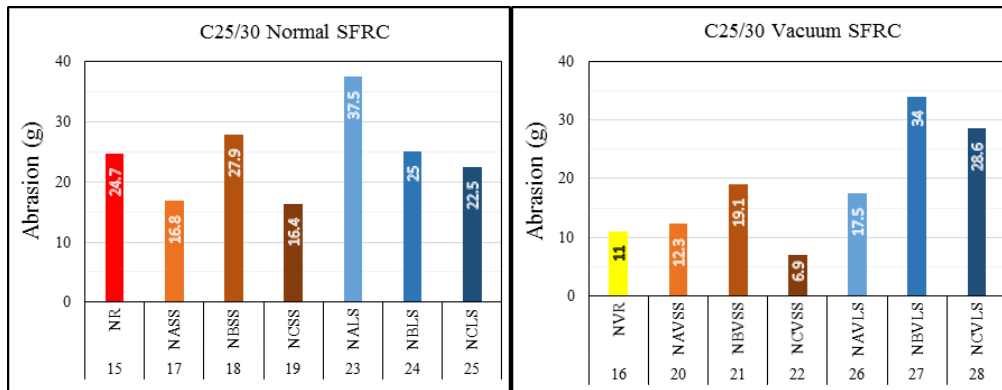


Figure 7. C25/30 Normal and Vacuum SFRC abrasion values

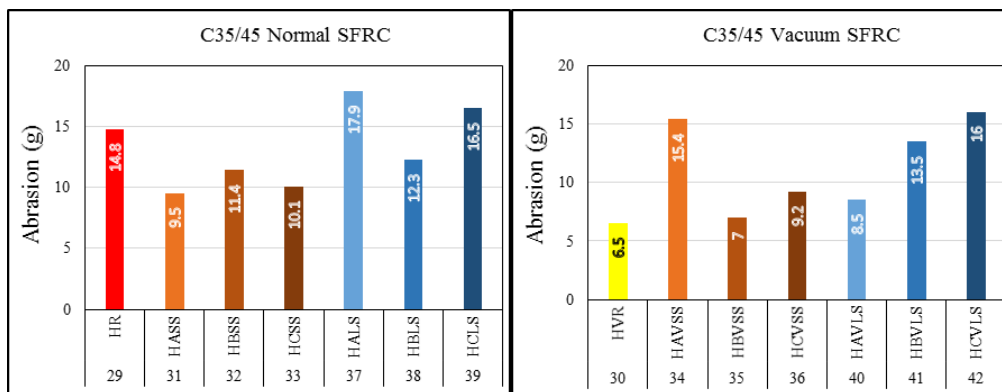


Figure 8. C35/45 Normal and Vacuum SFRC abrasion values

In figure 9, abrasion values of PYFRVC and PYFRC are showed. There was half abrasion in vacuumed concrete types compared to normal concretes. Long PYFRC abraded more than short PYFRC. Abrasion values decreases in both vacuumed and normal concretes. Abrasion of polyester fibre concretes is more regular than steel fibre concretes. In C16/20, short SFRC abraded ~%18 more than short PYFRC. As there were no relations between long SFRC and PYFRC, there is a complicated relation between abrasion values. SFRVC abraded more than PYFRVC. Long PYFRVC abraded more than long SFRVC.

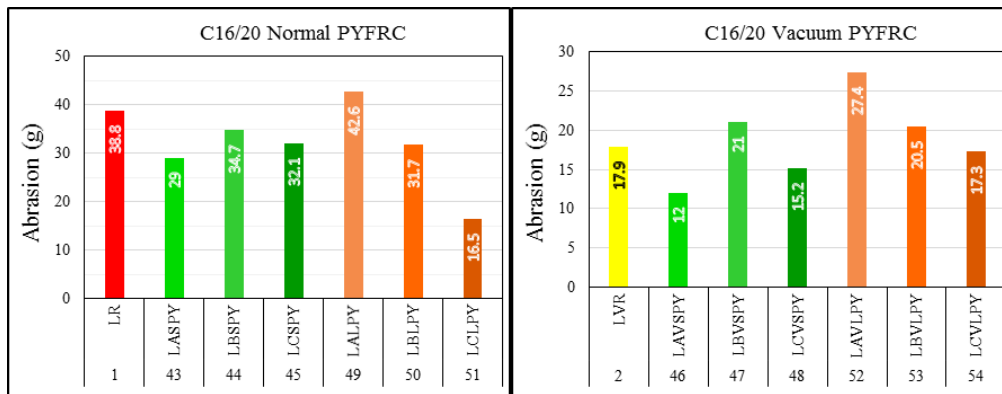


Figure 9. C16/20 Normal and Vacuum PYFRC abrasion values

In figure 10, abrasion value of C25/30 PYFRVC and PYFRC was showed. Short PYFRVC abraded ~%40-70 less than long PYFRC. Long PYFRVC and PYFRC had similar abrasion. Short PYFRVC and PYFRC abraded ~%15-35 less than long PYFRC. Short PYFRC abraded more compared to NR in C25/30 normal concretes. In vacuumed concretes, long and short SFRVC abraded more. PYFRVC had similar results with NVR. Long SFRC abraded ~%60 more than long PYFRC.

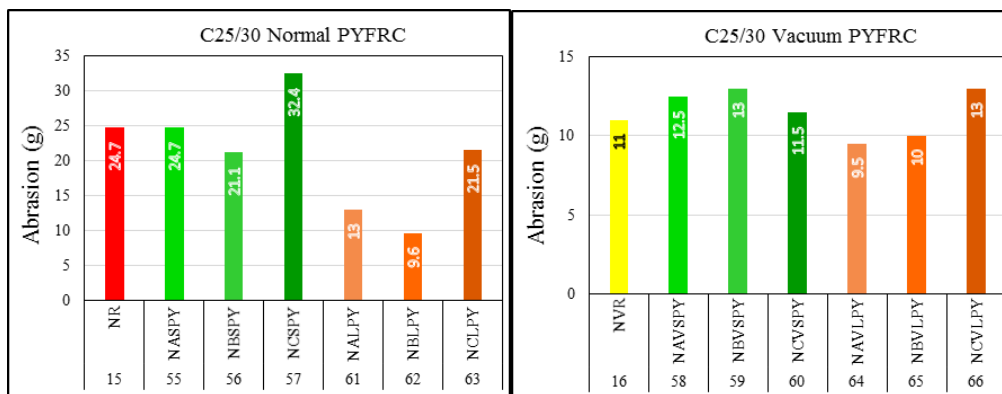


Figure 10. C25/30 Normal and Vacuum PYFRC abrasion values

In figure 11, abrasion values of C35/45 PYFRVC and PYFRC was showed. PYFRVC abraded ~%33-66 less than PYFRC. Short PYFRC abraded ~%15-50 more than long PYFRC. In vacuumed concretes, a concrete which has long and short polyester fibres is most in percentage. Long steel fibres and polyester fibres did not have an important effect on abrasion values. However in short SFRC and PYFRC, there is a complicated situation. However there is no important difference in YVR.

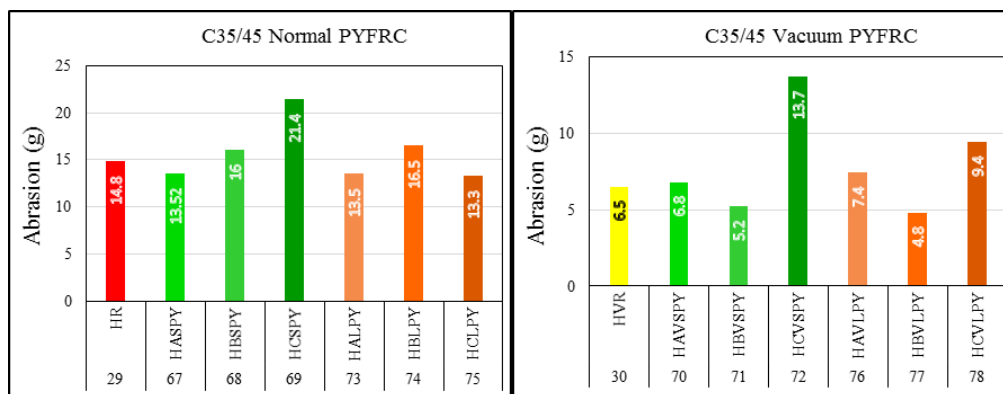


Figure 11. C35/45 Normal and Vacuum PYFRC abrasion values

In general, abrasion was seen as dusting in concretes which has steel and polyester fibres (figure 12). There were some breaking in C25/30 and C35/45 steel fibre concretes. In steel fibre concretes, a better bonding appeared in parallel to increase of strength. It is thought that breakings were because of breakings of steel fibres during abrasion.



Figure 12. Steel and polyester fibre concrete samples after the abrasion test

4 CONCLUSIONS

Vacuum application provided nearly half abrasion in C16/20 concretes. It can be said that there was an opposite relation between abrasion height and vacuum application of polyester fibre and steel fibre in abrasion values of concretes. While long SFRC had the least abrasion values compared to NR, short PYFRVC and long SFRVC was seen as the least. The opposing in abrasion values is thought to be that C16/20 concrete class has lower strength class. Bonding of fibres with concrete because of little percentage of cement and non-homogeneous distribution of fibres in sample concretes caused this result.

Vacuum application in C25/30 concretes decreases abrasion values in half percentage. In normal concretes, while there were long PYFRC, polyester fibres did not have effect on vacuum concretes steel concretes caused more abrasion.

Vacuum application in C35/45 concretes showed ~%65 less abrasion in general. There were no important values in normal concretes according to Yr except steel fibres. In vacuumed concretes, the more steel and polyester fibres' height and percentage the more abrasion is.

As a result, the more strength class of concretes, the less abrasion in concretes. It is thought because of increase in cement percentage. The more concrete's strength class increase, the less steel and polyester fibres' abrasion value. It can be said that the more fibres, the more abrasion in concretes. Abrasion values in SFRC were seen complicated compared to polyester fibre concretes. It is thought because of abrasion that occurred breaking with dusting which happened in abrasion of concretes. Steel fibres can give more damage in concretes where there was abrasion like friction. Vacuum application is seen to decrease abrasion in % 50 levels nearly in all concretes. Also, piece number of concretes, percentage of fibres in concrete, fibre concretes being in negative conditions is thought to effect concretes' abrasion.

ACKNOWLEDGMENT

This study was supported by TUBITAK (The Scientific and Technological Research Council of Turkey). Project number: 212M012.

REFERENCES

- [1]. B.Baradan, H.Yazıcı, Ün H. *Betonarme Yapılarda Kalıcılık (Durabilite)*, DEÜ Fac. Eng. Publishing, no: 298.2002.
- [2]. H.Bolat, S.Subaşı, M Çullu, U.Akkaya. *Concrete Roads Pending Hazards*, Electronic Journal of Construction Technologies Vol: 6, No: 1, 2010 (p.30-37)
- [3]. H.Yalçın, T.Koç. *Betonarme Demirlerinin Korozyonu ve Önlenmesi*, CMS Ltd. Publishing, Ankara2004,.
- [4]. N. Kabay. *Abrasion resistance and fracture energy of concretes with basalt fiber*, Construction and Building Materials 50 (2014) 95–101.
- [5]. B.Li, K.Guoju, Z.Ming kai. *Influence of manufactured sand characteristics on strength and abrasion resistance of pavement cement concrete*. Construction and Building Materials 25 (2011) 3849–3853.
- [6]. A.M. Neville, J.J.Brooks. *Concrete technology*. Malaysia: Pearson Education Asia Pte Ltd. PP(CTP); 2008.
- [7]. P.K. Mehta, J.M.P. Monteiro. *Concrete: microstructure, properties and materials*. The McGraw-Hill Companies; 2006 [p. 33–187].
- [8]. T.Y. Erdoğan. *Concrete*. 3rd ed. Metu Advances Foundation Publications; 2010 [p. 66–115].
- [9]. H.Bolat, O.Şimşek, M.Çullu, G.Durmuş, Ö.Can. *The effects of macro synthetic fiber reinforcement use on physical and mechanical properties of concrete*. Composites: Part B 61 (2014) 191–198.
- [10]. H.Bolat, O.Şimşek, *Evaluation of Energy Absorption of Macro Synthetic and Steel Fiber Reinforced Concretes* Romanian Journal of Materials 2015, 45 (2), 123 – 132.
- [11]. A. Caggiano, M. Cremona, C. Faella, C. Lima, E. Martinelli. *Fracture behavior of concrete beams reinforced with mixed long/short steel fibers*. Constr Build Mater 2012;37:832–40.
- [12]. Z.J Grdic, G.A.T Curcic, N.S. Ristic, I.M. Despotovic. *Abrasion resistance of concrete micro-reinforced with polypropylene fibers*. Constr Build Mater 2012;27:305–12.
- [13]. E. Horszczaruk. *Abrasion resistance of high-strength concrete in hydraulic structures*. Wear 2005;259:62–9.
- [14]. H. Li, M.H. Zhang, J.P. Ou. *Abrasion resistance of concrete containing nanoparticles for pavement*. Wear 2006;260:1262–6.
- [15]. R. Siddique, K. Kapoor, E.H. Kadri, R. Bennacer. *Effect of polyester fibres on the compressive strength and abrasion resistance of HVFA concrete*. Constr Build Mater 2012;29:270–8.
- [16]. C.D. Atis. *High volume fly ash abrasion resistant concrete*. J Mater Civ Eng 2002;14 (3): 274–7.
- [17]. B. Felekoğlu, S. Türkel, F.Y. Altuntas. *Effects of steel fiber reinforcement on surface wear resistance of self-compacting repair mortars*. Cem Concr Compos 2007;29:391–6.
- [18]. S.K Rao, P. Sravana, T.C Rao. *Abrasion resistance and mechanical properties of Roller Compacted Concrete with GGBS* Construction and Building Materials 114 (2016) 925–933.
- [19]. TS 10514. *Concrete-Steel Fibre Reinforced-Rules for Mixing Concrete and Control*. Turkish Standards Institute. (1992) 1–23.
- [20]. TS 802. *Design concrete mixes*. Turkish Standards Institute. (2009) 1–18.
- [21]. ASTM C 944. *Standard Test Method for Abrasion Resistance of Concrete or Mortar Surfaces by the Rotating-Cutter Method*. 1999.

BIOGRAPHIES

Hakan Bolat was born in 1977 in Ankara-Turkey. Received his BA(1999), MA (2002) and PhD (2010) education in Gazi University Institute Of Natural Sciences Department of Construction Education in Ankara-Turkey. His MA Thesis is about Vacuumed Concrete and PhD Thesis is about Energy Absorption of Different Fiber Reinforced slab concrete.

He gave undergraduate and graduate lessons such as Construction Drawing, Material Science, Concrete Technology and Engineering Management in Hacettepe and Gumushane. Currently he has been worked as an Assistant Professor at Gumushane University in Turkey since 2010. He continue to researches of about different fiber reinforced concrete energy bsorption and durability, different fiber reinforced granul and fluid foam concrete and effects of water properties on concrete. major publications are as follows listed:

Mustafa ÇULLU was born in 1975 in Adana-Turkey. Received his BA(2001), MA (2004) and PhD (2010) education in Gazi University Institute Of Natural Sciences Department of Construction Education in Ankara-Turkey. His MA Thesis is about Alkali-silica reaction and PhD Thesis is about antifreeze for concrete.

He gave undergraduate and graduate lessons such as Construction Drawing, Material Science, Concrete Technolgy and construction management in Hacettepe University and Gumushane University. Currently he has been worked as an Assistant Professor at Gumushane University in Turkey since 2010. He continue to researches of about heavy aggregate and radiation shielding:

Reducing Motion Blur by Constrained Control of Helicopter Vibration

Harun Celik¹, Tugrul Oktay², Ilke Turkmen³, Metin Uzun⁴

Abstract

In this paper, image blur which is the result of the relative motion between the camera mounted helicopter and the imaging scene during exposure time is modeled and studied to be reduced by controlling the helicopter. Initially, helical and level banked turns are considered for physics-based, control-oriented, and complex helicopter models to satisfy constraints on tight controlled flight. By using these models, a variance-constrained controller is designed to minimize the vibrations. Since the blur is a function of the motion of helicopter, in order to reduce motion blur from the taken images, the motion of helicopter in exposure time is constrained via autonomous performance maximization. Then, the blur is modeled by estimating the blur kernel using the motion of helicopter during camera integration time. After that the motion blur is added to images using the estimated blur kernel. Lastly, the performance of the constrained helicopter control is measured by the motion blur occurring in taken images.

Keywords: helicopter vibration, motion blur, constrained control

1. INTRODUCTION

Up to the present, helicopter flight control systems (HFCS) have been designed to satisfy various tasks. While the majority of these studies investigated control systems to provide flight safety and slung-load carrying in early years, there have been many researches in designing HFCS to accomplish further steps in recent years. For instance; [1] proposed HFCS to reduce helicopter noise/vibration for comfortable flight, in [2] HFCS was developed to save more energy.

Until now various control systems have been developed to control the flights. Historically, the first techniques are pole placement [3, 4] and simple feedback [5, 6] methods. After them, Linear Quadratic Regulator (LQR) and Linear Quadratic Gaussian (LQG) controllers [7, 8] established over linear matrix algebra, H_∞ control synthesis [9, 10], Neural Network (NN) controller [11], Model Predictive Control (MPC) [12], and variance constrained controllers (VCCs) [13–14] were investigated and applied to flights. Also several optimal, adaptive, sliding and feedback control approaches were investigated.

VCCs have been studied by various researchers to be applied for helicopters [15–17]. The advantages of VCCs can be emphasized as: initially, as VCCs are modified from LQG controllers which can estimate the states by Kalman filters, they are very beneficial for helicopters whose states are difficult to calculate; then, they utilize the state covariance matrix which is crucial for stability to be physically meaningful; Lastly, they are capable of capturing constraints with high temporal behavior of separate variables. With all of these reasons, VCCs are applied for our HFCS.

In order to build up a helicopter model that physics-based and control-oriented, a fully articulated main rotor, main rotor downwash, blade flexibility, and fuselage and tail rotor aerodynamics are involved. Moreover, some trim and modal data are given for Puma SA 330 to show how the dynamics of realistic helicopters are achieved by the model.

In this conference paper, two output variance constrained controllers (OVCs) are used for helicopter trajectory tracking. One of these is soft while and the other one is as tight as possible to reduce the vibrations into minimum values. Since helicopter using tight OVC is tracking trajectory better autonomous performance, the blur caused by the motion of helicopter is less than the one heavy soft OVC. Thus, the motion blur resulted from helicopter vibration is reduced by designing tight OVC and better constrained control of helicopter.

2. HELICOPTER MANEUVERS AND MODEL

2.1. Maneuvers

In this paper, level banked turn and helical turn without sideslip are considered. The helicopter linear velocities for maneuvering flight as depicted in Figure 1 are

¹ Erciyes University (ERU), Department of Aircraft Electric and Electronic, 38039, Kayseri, Turkey. haruncelik@erciyes.edu.tr

² Corresponding author: ERU, Department of Aeronautical Engineering, 38039, Kayseri, Turkey. oktay@erciyes.edu.tr

³ ERU, Department of Aircraft Electric and Electronic, 38039, Kayseri, Turkey. titi@erciyes.edu.tr

⁴ ERU, Department of Aircraft Airframe-Powerplant, 38039, Kayseri, Turkey. muzun@erciyes.edu.tr

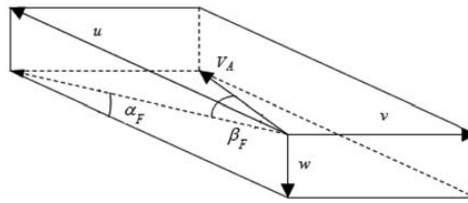


Figure 1. Fuselage angle of attack and sideslip [15].

$$\begin{bmatrix} u & v & w \end{bmatrix}^T = \begin{bmatrix} V_A \cos(\alpha_F) \cos(\beta_F) & V_A \sin(\beta_F) & V_A \sin(\alpha_F) \cos(\beta_F) \end{bmatrix}^T \quad (1)$$

where α_F and β_F denote fuselage angle of attack and sideslip, and given as below, respectively.

$$\alpha_F = \tan^{-1}(w/u), \quad \beta_F = \sin^{-1}(v/V_A) \quad (2)$$

During level banked turn, helicopter banks towards the center of turning circle. In Figure 2 (a), the axis of helicopter and forces acting on it during a level banked turn is given. In this conference article, level banked turn is the maneuver we are interested in. There is also one more focused maneuver which is helical turn. During this motion, helicopter rotates around a helix with a stationary speed. In Figure 2 (b), a helicopter in a helical turn is depicted.

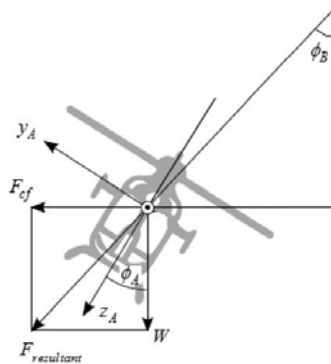
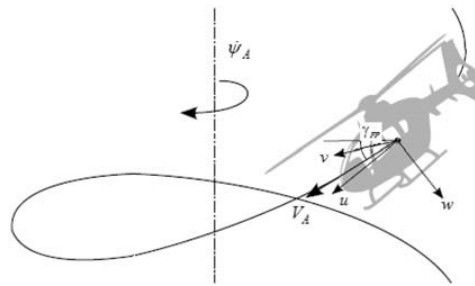


Figure 2.(a) Level banked turn.



(b) Helical turn.

2.2. Model

The mathematical model of the maneuvering helicopter has 9 fuselage equations, 16 blade flapping and lead-lagging equations, 16 blade flexibility equations, 3 static main rotor downwash equations, and 1 algebraic flight path angle equation [15]. These equations of motion can be expressed in implicit form as

$$f(\dot{x}, x, u) = 0 \quad (3)$$

where $f \in R^{45}$, $x \in R^{41}$ (x is the nonlinear state vector), and $u \in R^4$ (u is the nonlinear control vector)

2.3. Trim and linearization

In this conference paper, the condition for which zero sideslip and level banked or helical turn with stationary \mathbf{v}_A are achieved is assumed as trim. For our helicopter model, 29 trim equations and 29 unknowns were obtained. Flight path angle required for helical turn maneuver is illustrated in Figure 3.

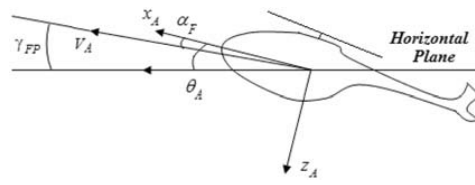


Figure 3. Angle of flight path [15].

The 29 trim equations were solved by using `f solve` command in Matlab. The results, thus, found were verified by inserting them into the governing equations of motion given in (3). Very small numbers (around 10^{-10}) were obtained showing that the trimming procedure is correct. Numerous numerical experiments resulted in trim values that are in the range reported in the literature [15]. After calculating trim values, the mathematical model was linearized using via benefiting Maple, yielding continuous linear time-invariant (LTI) systems

$$\dot{\mathbf{x}}_p = \mathbf{A}_p \mathbf{x}_p + \mathbf{B}_p \mathbf{u} \quad (4)$$

where $\mathbf{x}_p = \Delta \mathbf{x}$ and $\mathbf{u} = \Delta \mathbf{u}$. The obtained modes (flight dynamics modes, flapping, and lead-lagging modes) are very close to the modes proposed in [15] for straight level flight which were validated against available data in the literature.

3. CONTROLLERS AND OVC APPROACH

In this article, output variance-constrained control (OVC) was investigated. The OVC problem is stated next. Given a continuous LTI system

$$\dot{\mathbf{x}}_p = \mathbf{A}_p \mathbf{x}_p + \mathbf{B}_p \mathbf{u} + \mathbf{D}_p \mathbf{w}_p, \mathbf{y} = \mathbf{C}_p \mathbf{x}_p, \mathbf{z} = \mathbf{M}_p \mathbf{x}_p + \mathbf{v}_s \quad (5)$$

and a positive definite input penalty $\mathbf{R} > 0$, find a full order dynamic controller

$$\dot{\mathbf{x}}_c = \mathbf{A}_c \mathbf{x}_c + \mathbf{F} \mathbf{z}, \mathbf{u} = \mathbf{G} \mathbf{x}_c \quad (6)$$

to solve the problem

$$\min_{\mathbf{A}_c, \mathbf{F}, \mathbf{G}} E_\infty \mathbf{u}^T \mathbf{R} \mathbf{u} \quad (7)$$

subject to

$$E_\infty \mathbf{y}_i^2 \leq \sigma_i^2, \quad i = 1, \dots, n_y \quad (8)$$

where \mathbf{z} represents sensor measurements, \mathbf{w}_p and \mathbf{v}_s are zero-mean uncorrelated Gaussian white noises with intensities \mathbf{W} and \mathbf{V} , respectively. σ_i^2 is the upper bound imposed on the i th output variance, and n_y is the number of outputs. OVC solution reduces to a LQG problem solution by choosing output penalty $\mathbf{Q} > 0$ depending on the inequality constraints. An algorithm for the selection of \mathbf{Q} is presented in [13]. After converging on \mathbf{Q} , OVC parameters are

$$\begin{aligned} \mathbf{A}_c &= \mathbf{A}_p + \mathbf{B}_p \mathbf{G} - \mathbf{F} \mathbf{M}_p, \mathbf{F} = \mathbf{X} \mathbf{M}_p^T \mathbf{V}^{-1} \\ \mathbf{G} &= -\mathbf{R}^{-1} \mathbf{B}_p^T \mathbf{K} \end{aligned} \quad (9)$$

where \mathbf{X} and \mathbf{K} are solutions of two algebraic Riccati equations

$$\begin{aligned} 0 &= \mathbf{X} \mathbf{A}_p^T + \mathbf{A}_p \mathbf{X} - \mathbf{X} \mathbf{M}_p^T \mathbf{V}^{-1} \mathbf{M}_p \mathbf{X} + \mathbf{D}_p \mathbf{W}_p \mathbf{D}_p^T \\ 0 &= \mathbf{K} \mathbf{A}_p + \mathbf{A}_p^T \mathbf{K} - \mathbf{K} \mathbf{B}_p \mathbf{R}^{-1} \mathbf{B}_p^T \mathbf{K} + \mathbf{C}_p^T \mathbf{Q} \mathbf{C}_p \end{aligned} \quad (10)$$

3.1. BLUR MODEL

The blur resulted from the motion of the helicopter can be expressed as

$$\mathbf{B} = \mathbf{I} * \mathbf{H} + \mathbf{N} \quad (11)$$

where \mathbf{B} designates blurred image, \mathbf{I} denotes underlying latent image, \mathbf{H} is the blur kernel or point spread function that expresses how the effect of the motion spreads over the image and \mathbf{N} denotes noise. The most important step in deblurring

images is estimation of blur kernel; H . Blur kernel is proportional to the motion of the camera. Blur increases as well as the motion of camera during exposure time increases.

Since the motion of the helicopter during exposure time cause motion blur, adjusting the exposure time of the camera is very important. While shorter exposure time which means faster shutter speed reduces blur by indicating a small part of motion, faster shutter speed results to more image noise by increasing the sensitivity of imaging sensor. On the other hand, longer exposure time means slower shutter speed reduce image noise, but leads to more motion blur by including a bigger movement of helicopter. Thus, the optimum value of exposure time plays a big role in imaging.

In this study, exposure time is set to be 0.3 seconds and blur kernel is estimated from 2D helicopter motion that is converted from 3D motion by using camera projection model [18] as seen in Figure 4.

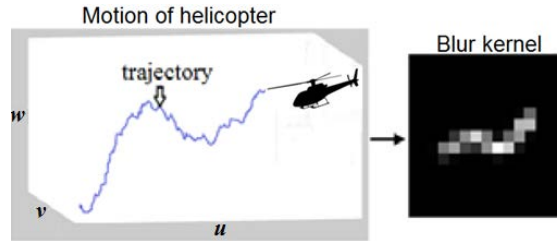


Figure 4. An estimated blur kernel from a motion of helicopter.

Estimation of blur kernel is very difficult and complex process if the latent image or the motion of camera is unknown. However, with a known 2D motion $s(t)$ projected from 3D motion of helicopter, the blur is estimated as

$$H = \int_0^T \delta_{s(t)} dt \tag{12}$$

where T is the exposure time, 0.3s.

4.RESULTS

In order to determine possible motion during exposure time, the trajectory of helicopter lasts 60 seconds is scanned and divided to 0.3 s intervals. Eventually, 200 intervals are obtained. Each interval indicates the occurred motion of helicopter during exposure time approximately. The movement occurred during each exposure time calculated as

$$motion_i = \sqrt{(u_{(i-1)t} - u_{it})^2 + (v_{(i-1)t} - v_{it})^2} \tag{13}$$

where $i = 0, 1, 2, \dots, 200$ is the number of time interval. $t = 0.3$ is exposure time. w is neglected as it has very small effect on blur, relatively. Here, the biggest two movements are selected by scanning the maximum value of motion in (2) for both controllers.

The output of interests are roll, pitch and yaw angles (ϕ_A, θ_A, ψ_A). For the first OVC, the constraint on these outputs is $\sigma^2 = 10^{-1} [1 \ 1 \ 1]$ for the helicopter using soft OVC. For the second OVC which is tight, the outputs are constrained with $\sigma^2 = 10^{-3} [1 \ 1 \ 1]$. First two maximum motion ranges during exposure time are determined from the responses of applying these OVSSs, and these two maximum motions in soft and tight controlled flights are depicted in Figure 5 and Figure 6.

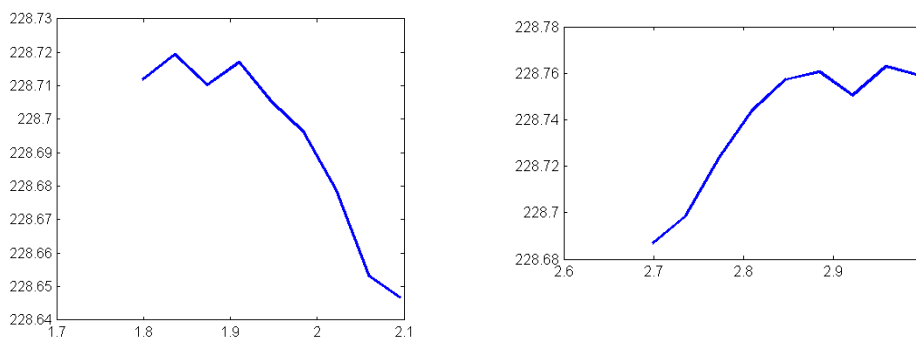
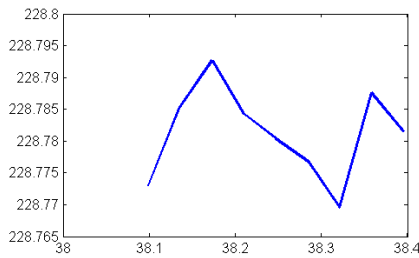


Figure 5. (a) First maximum motion for soft OVC



(b) second maximum motion for soft OVC

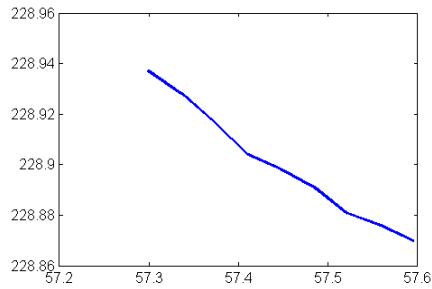


Figure 6. (a) First maximum motion for tight OVC

(b) second maximum motion for tight OVC

After examining (12), for soft OVC, the maximum first and second movements are found at $i = 6$ and 9 , and 6.47 and 6.45 meters, respectively. Likewise, the maximum first and second movements are detected at $i = 127$ and 191 , and 5.67 and 4.45 meters for tight OVC, respectively. Then, for relative exposure time interval, blur kernel is estimated by camera projection model from these motions and convolved with latent images as modeled in (11) and (12). The results are illustrated in Figure 7 and Figure 8 for helicopter using soft and tight OVC, respectively.



Figure 7. (a) latent image

(b) second biggest vibration convolved with latent image

(c) the biggest vibration convolved with latent image



Figure 8. (a) latent image

(b) second biggest vibration convolved with latent image

(c) the biggest vibration convolved with latent image

Real sharp latent aerial images are illustrated in Figure 7 (a) and Figure 8 (a). In Figure 7 (c) and (b), and Figure 8 (c) and (b), latent images convolved with the modeled blur corresponding to the biggest two motion of helicopter in trajectory tracking are given, respectively. It can be seen from the real image results that the image taken by helicopter using soft OVC is more degraded by motion blur. The motion blur is reduced by designing tight OVC. Also the values of peak signal-to-noise ratio are 19.12 dB, 18.23 dB, 29.86 dB and 24.75 dB for Figure 7 (b), Figure 7 (c), Figure 8 (b) and Figure 8 (c), respectively. Thus, the biggest two vibrations of helicopter using soft OVC are bigger than the biggest two vibrations of helicopter using tight OVC. Also the biggest two vibrations of helicopter using soft OVC are closed to each other while the second biggest vibration of helicopter using tight OVC is smaller than the first biggest vibration of helicopter using tight OVC. That means tight controlled helicopter rarely vibrates abruptly while soft controlled helicopter always has big vibrations.

5.CONCLUSIONS

In this study, motion blur caused by the vibration of helicopter is reduced by designing the tight OVC. In order to design control system, physics-based, control-oriented, and complex helicopter models are implemented for helical and level

banked turns. Models are linearized for these flight conditions to design the OVC. The performance of designed control system is measured by the caused motion blur in the most vibrating exposure times in flights. The motion blur is modeled by using camera projection model. As the blur is proportional to the movement of the helicopter, the biggest two moves during exposure time are added to images taken by the helicopter using soft and tight OVC, respectively. The blur caused by the vibrations of the soft and tight controlled helicopters are studied and compared. The results show that when the helicopter is modeled physics-based and control-oriented to satisfy constrains on tightly controlled flights, the blur is reduced by decreasing vibrations of helicopter via tight controller.

REFERENCES

- [1]. T. Oktay and C. Sultan, "Comfortable helicopter flight via passive/active morphing", *Aerospace and Electronic Systems, IEEE Transactions on*, 51(4), 2876-2886, 2015.
- [2]. T. Oktay and F. Sal, "Combined passive and active helicopter main rotor morphing for helicopter energy save", *Journal of the Brazilian Society of Mechanical Sciences and Engineering*, 1-15, 2015.
- [3]. D. Fusato and R. Celi, "Multidisciplinary design optimization for aeromechanics and handling qualities", *Journal of aircraft*, 43(1), 241-252, 2006.
- [4]. D. Fusato and G. Guglieri and R. Celi, "Flight dynamics of an articulated rotor helicopter with an external slung load", *Journal of the American Helicopter Society*, 46(1), 3-13, 2001.
- [5]. P. Apkarian, C. Champetier and J. F. Magni, "Design of a helicopter output feedback control law using modal and structured-robustness techniques", *International Journal of Control*, 50(4), 1195-1215, 1989.
- [6]. E. Altuğ, J. P. Ostrowski and R. Mahony, "Control of a quadrotor helicopter using visual feedback" in *IEEE Int. Conf. on Robotics and Automation*, pp. 72-77, 2002.
- [7]. J. Zarei, A. Montazeri, M. R. J. Motlagh and J. Poshtan, "Design and comparison of LQG/LTR and H_∞ controllers for a VSTOL flight control system", *Journal of the Franklin Institute*, 344(5), 577-594, 2007.
- [8]. S. Park, J. Bae, Y. Kim and S. Kim, "Fault tolerant flight control system for the tilt-rotor UAV", *Journal of the Franklin Institute*, 350(9), 2535-2559, 2013.
- [9]. C. C. Luo, R. F. Liu, C. D. Yang and Y. H. Chang, "Helicopter H_∞ control design with robust flying quality", *Aerospace science and technology*, 7(2), 159-169, 2003.
- [10]. C. C. Kung, "Nonlinear H_∞ robust control applied to F-16 aircraft with mass uncertainty using control surface inverse algorithm", *Journal of the Franklin Institute*, 345(8), 851-876, 2008.
- [11]. K. P. Tee, S. S. Ge and F. E. Tay, "Adaptive neural network control for helicopters in vertical flight" *Control Systems Technology, IEEE Transactions on*, 16(4), 753-762, 2008.
- [12]. K. Dalamagkidis, K. P. Valavanis and L. A. Piegl, "Nonlinear model predictive control with neural network optimization for autonomous autorotation of small unmanned helicopters", *Control Systems Technology, IEEE Transactions on*, 19(4), 818-831, 2011.
- [13]. C. Hsieh, R. E. Skelton and F. M. Damra, "Minimum energy controllers with inequality constraints on output variances", *Optimal Control Applications and Methods*, 10(4), 347-366, 1989.
- [14]. G. Zhu, M. A. Rotea and R. Skelton, "A convergent algorithm for the output covariance constraint control problem", *SIAM Journal on Control and Optimization*, 35(1), 341-361, 1997.
- [15]. T. Oktay, "Constrained control of complex helicopter models", PhD Dissertation, Virginia Tech, Blacksburg, 2012.
- [16]. T. Oktay and C. Sultan, "Variance constrained control of maneuvering helicopters", in *Proceedings of the 68th American Helicopter Society International Annual Forum*, 2012.
- [17]. T. Oktay, "Combined output variance constrained and input variance constrained design for flight control", *Proceedings of the IMechE, Part G: J. Aerospace Engineering*, 2015
- [18]. O. Faugeras, *Three-dimensional computer vision: a geometric viewpoint*, MIT press, 1993.

Appendix

Notation

- E_∞ expected value operator
- p, q, r angular velocities of helicopter in aircraft frame, (rad/s)
- u, v, w linear velocities of helicopter in aircraft frame, (m/s)
- V_A flight speed of helicopter, (kts)
- γ_{FP} flight path angle, (rad)
- ϕ, θ, ψ Euler angles of helicopter (roll, pitch, and yaw), (rad)
- $(.)^T$ transpose

The Effect of Variation of Peak Ground Velocities of Near Field Earthquakes on Mid-Rise Reinforced Concrete Buildings

Serkan Engin¹

Abstract

The most important parameter of nonlinear time history analysis is the earthquake record that will be used in the analysis. Many of the characteristics of an earthquake such as its magnitude, displacement and acceleration, can extremely be different from others. Despite the fact that the number and range of the records in the earthquake database increase with every new earthquake and there exist many studies performed with several different earthquake records, there is no general opinion about which characteristics of an earthquake effect the reaction of a building. For this reason, there still exists a requirement to studies about determining the effect of characteristics of earthquakes on structural response. In this study, nonlinear time history analysis of a reinforced concrete mid-rise building are performed by using two different record sets with different peak values, that are recorded from near field. From the results of the analyses, shear force, moment and interstory drift ratio values are obtained for each storey level. When the results obtained from each set are compared to each other, it is observed that shear force, moment and interstory drift ratio of the building increase as the peak ground velocity (PGV) value of the earthquake increase.

Keywords: *Near field, mid-rise reinforced concrete building, peak ground velocity, time history analysis.*

1. INTRODUCTION

Despite deeming the time history analysis (THA) method as the most reliable method being used in the analysis of structures, the reliability of results obtained from this analysis method depends on the characteristics of acceleration record being used in the analysis. For this reason, it is extremely important for the earthquake records - to be used in the THA method - to have characteristics suiting the structure to be analyzed and the area where the structure will be constructed [1]. Due to its nature, each earthquake has many various characteristics, and many characteristics such as peak ground acceleration (PGA), peak ground velocity (PGV), peak ground displacement (PGD) and frequency obtained from each earthquake are able to be different. And it is still unable to be completely known how these different earthquake characteristics are affecting the response to be given structure [2].

Since the first earthquake record, the number of records taken from many places in the world has reached to thousands. The researchers have grouped these recorded earthquake characteristics such as PGA, PGV, PGD and frequency as per their possible damage potential. Despite this grouping, it is still not possible to make a generalization regarding which characteristic of the earthquake record will cause what kind of an effect. For this reason, in order to be able to select the earthquake record as per the quality of structure to be analyzed, it is required to make studies peculiar to the site and structure [3], [4].

In this study, peak ground velocity (PGV) was recorded from the changing near field, record groups were formed, and by using these records, non-linear analyses of a typical reinforced concrete mid high structure were realized by the time history analysis (THA) methods, and as the result of the analyses, the shear force, bending moment and interstory drift ratio values of the structure at the floor levels were obtained. "Shear Force", "Bending Moment", and "Interstory Drift Ratio" – "Story" change curves were formed by these obtained data, and the effects of change of PGV on the response of the structure were discussed.

¹ Corresponding author: Kocaeli University, Umuttepe Campus Department of Civil Engineering, 41380, İzmit/Kocaeli, Turkey.
serkanengintr@yahoo.com

2. ANALYTICAL STUDY

In this part of the study, analytical model of the structure, selection of earthquake records, analyses made and the data obtained from these analyses have been explained.

2.1. Analytical Model of Structure

A typical frame reinforced concrete building was selected for the study. The concrete compressive strength of the building was taken as $f_{ck}=40$ MPa, and its longitudinal and transverse reinforcement yield strength was taken as $f_y=420$ MPa. The building's importance coefficient was taken as $I=1$, its earthquake load reduction coefficient was taken as $R=8$, its effective ground acceleration coefficient was taken as $A_o=0.40$, and its soil characteristic periods were taken as $T_A=0.15$, $T_B=0.40$ (Z2 soil class), and a linear dynamic analysis was realized in order to obtain the vertical load values of the columns. In this analysis, the increased load obtained by adding 30% of live loads (Q) - which was taken as 7.50 kN/m²- to dead loads (G) - which was taken as 3.00 kN/m²- was applied on the slab.

In the study, story of the structure was taken as 5, the height of each floor was taken as $h_f=3$ m, the span of the structure in both directions was taken as 3, the distance in between axes was taken as 6 m, the slab thickness was taken as 0.20 m, beam sizes at each floor were taken as $b_w=0.30$ m, $h_k=0.60$ m, and the column sizes were taken as $b=0.50$ m, $h=0.50$ m. The floor plan of the study's structure has been provided in Figure 1, and reinforcement layout of the column and beam cross-sections has been provided in Figure 2. As the result of linear dynamic analysis realized under these conditions, the axial loads applied on the vertical elements of the building were obtained, and the predominant periods on both directions of the building were found as $T_x=0.52$ sec, $T_y=0.52$ sec.

Confined and unconfined Mander concrete model [5], [6] was used for the concrete behavior, and the reinforcement steel behavior model - defined in Turkish Earthquake Code 2007 [7] - was used for the reinforcements at concrete cross-sections.

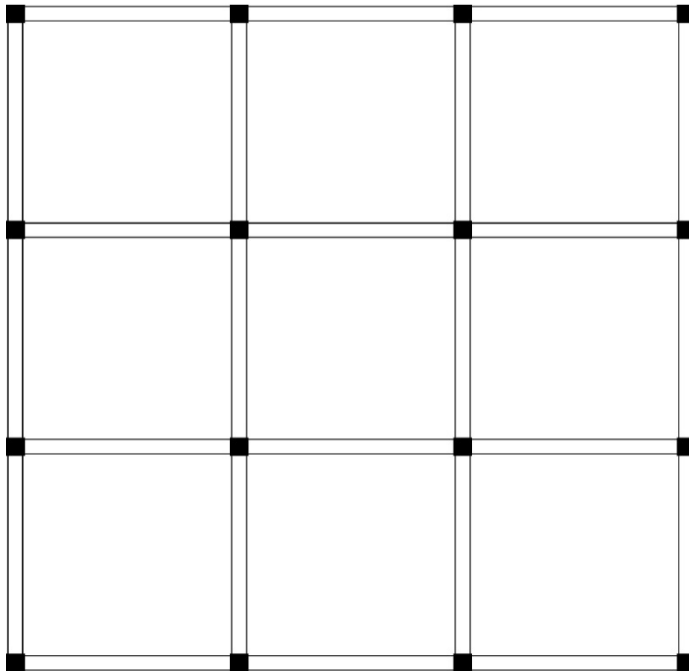


Figure 1. Floor Plan

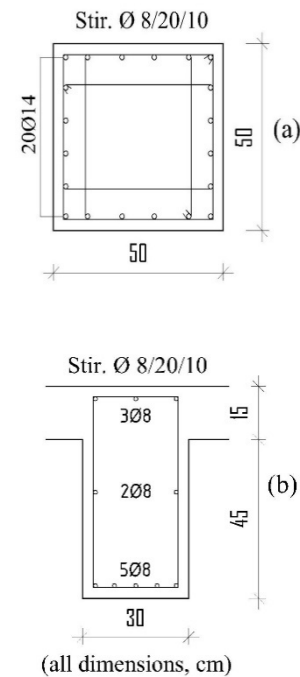


Figure 2. a-) Beam; b-) Column reinforced configuration

As the result of the referred cross-section analyses, yield and curvature moment values of the structural components were determined. By all this data, the analytical model of the structure was formed in the SAP2000NL analysis program. The column and beam members were defined as frame element in the analytical model, and the capacity diagrams of each defined member were obtained by the XTRACT [8] cross-section analysis program. Columns axial loads required for the

cross-section analysis were obtained as the result of linear dynamic analysis. On the beam, the capacity curve was determined by taking the axial load as zero.

The earthquake records used in the study were selected from the database formed by Pacific Earthquake Engineering Research Center (PEER) [9]. The selected records were divided to two groups each consisting of seven earthquake records. The PGV values of the records in the first group were separated as to change in between 20 cm/sec and 40 cm/sec (PGV₂₀₋₄₀), and the PGV values of the records in the second group were separated as to change in between 40 cm/sec and 60 cm/sec (PGV₄₀₋₆₀). The soil classes -from where the selected records were obtained - were in groups C (shear wave velocity in between 360 m/sec and 760 m/sec) and D (shear wave velocity in between 180 m/sec and 360 m/sec). The magnitudes of earthquakes generating the records under the groups were changing in between $M_w=6.5$ and $M_w=7.6$, and the distance of epicenter of the earthquake was less than R , 20 km.

From among the selected records, the ones included in the PGV₂₀₋₄₀ group have been provided in the below Table 1. For the records in this group, the distance R was changing in between 0.96 km and 14.70 km, and the PGV values were changing in between 20.60 cm/sec and 39.30 cm/sec..

Table 1. Characteristics of ground motion records at PGV₂₀₋₄₀ group

Earthquake	Station	Component	Soil Type	Magnitude (M_w)	R (km)	PGV (cm/s)
Tabas-Iran (TI-D)	Dayhook	LN	C	7.3	13.94	20.60
Northridge (N-HCC)	Hollyw. Cold.C.	180	C	6.7	12.51	25.00
Chi-Chi (CC-TCU)	TCU	N	C	7.6	5.18	28.10
ImperialVall (IV-C)	Chihuahua	282	D	6.5	7.30	30.10
Northridge (N-CP)	Canoga Park	106	D	6.7	14.70	32.10
Kobe (K-K)	KJMA	090	D	6.9	0.96	37.20
Chi-Chi (CC-ALS)	ALS	E	C	7.6	10.8	39.30

The records under PGV₄₀₋₆₀ group have been provided in Table 2. For the records in this group, the distance R was changing in between 2.68 km and 15.37 km, and the PGV values were changing in between 42.10 cm/sec and 60.00 cm/sec

Table 2. Characteristics of ground motion records at PGV₄₀₋₆₀group

Earthquake	Station	Component	Soil Type	Magnitude (M_w)	R (km)	PGV (cm/s)
Kocaeli (K-S)	Sakarya	090	C	7.5	3.12	42.10
Imperial Vall. (IV-BC)	Bonds Corner	140	D	6.5	2.68	45.20
Chi-Chi (CC-CHY024)	CHY024	N	C	7.6	9.64	48.90
Imperial Vall. (IV-ECA4)	El Centro Ar.#4	140	D	6.5	3.86	54.30
Düzce (D-B)	Bolu	000	D	7.1	12.04	56.40
Kocaeli (K-D)	Düzce	180	D	7.5	15.37	58.80
Düzce (D-D)	Düzce	180	D	7.1	6.58	60.00

2.2. The Performed Analyses and Obtained Data

On the analytical model, non-linear time history single direction analysis was performed by using the selected earthquake records. In this analysis, it was assumed that the damages were being occurred at hinges. In the analysis, calculation was made as per the Newmark numerical integration method approach, and the critical damping ratio of the structure was assumed as 0.05. As the result of the analyses, the displacements, forces and moments of the building were obtained. In order to observe the change of building's response - obtained from the analyses made by the records whose PGV values change- at each floor, graphs of change of the values of Shear Force (V), Bending Moment (M) and Interstory Drift Ratio (δ) as per Story Level (N) were obtained. The average values of the relevant group - which are obtained by taking the average of curves formed for each record- have also been indicated. In the following Table 3, the values of maximum shear force, moment and interstory drift ratio obtained from the analyses -in which the earthquakes under group PGV₂₀₋₄₀ were used - have been given.

Table 3. Analysis results of PGV₂₀₋₄₀ group

Ground motion records of PGV ₂₀₋₄₀	V_{max} kN $\times 10^3$	M_{max} kNm $\times 10^3$	δ_{max} 10^{-3}
Tabas-Iran (TI-D)	17.57	94.74	1.23
Northridge (N-HCC)	13.14	48.19	0.95
Chi-Chi (CC-TCU)	16.23	124.94	1.48
Imperial Vall (IV-C)	21.38	147.38	1.71
Northridge (N-CP)	30.04	128.38	2.35
Kobe (K-K)	25.20	108.50	1.88
Chi-Chi (CC-ALS)	35.70	198.90	3.08
Average	22.75	121.58	1.81

In the following Table 3, the values of maximum shear force, moment and interstory drift ratio obtained from the analyses -in which the earthquakes under group PGV₂₀₋₄₀ were used - have been demonstrated. As seen in Table 3, the maximum shear force value of Tabas-Iran earthquake - whose PGV value is the minimum - was obtained as $V_{max}=17.57 \times 10^3$ kN in the Dayhook (TI-D) record, and the maximum shear force value of Chi-Chi earthquake - whose PGV value is the maximum - was obtained as $V_{max}=35.70 \times 10^3$ kN in the ALS (CC-ALS) record. Similarly, maximum moment - of the one with the minimum PGV value - was obtained as $M_{max}=94.74 \times 10^3$ kNm in the TI-D record, and the maximum moment - of the one with the maximum PGV value - was obtained as $M_{max}=198.90 \times 10^3$ kNm in the CC-ALS record. Maximum interstory drift ratio - of the one with the minimum PGV value - was obtained as $\delta_{max}=1.23 \times 10^{-3}$ in the TI-D record, and the maximum interstory drift ratio - of the one with the maximum PGV value - was obtained as $\delta_{max}=3.08 \times 10^{-3}$ in the CC-ALS record.

In Figure 3, change curves of story - shear force, bending moment and interstory drift ratio - obtained from the earthquake records under group PGV₂₀₋₄₀ - have been given. In the figures, the curves in light color specify the results of each of seven earthquakes included in the group, and the curves in dark color specify the average of the group. As per the change curves of story - shear force given in Figure 3(a), the maximum shear force (V_{max}) was obtained at the first story of the building by 17.57×10^3 kN, and the minimum shear force (V_{min}) was obtained at the 5th of the building by 5.08×10^3 kN in the TI-D record. In the CC-ALS record - having the maximum PGV value in the group - it was $V_{max}=35.70 \times 10^3$ kN at the first story, and $V_{min}=7.51 \times 10^3$ kN at the 5th story.

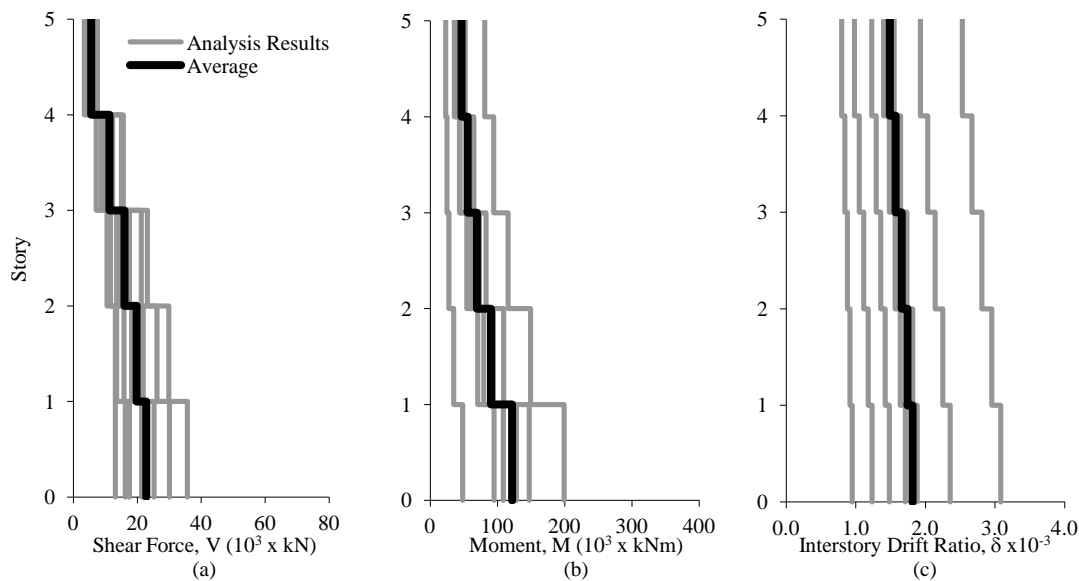


Figure 3. Group PGV₂₀₋₄₀ Story - (a) Shear Force; (b) Moment; (c) Interstory Drift Ratio Diagram

Regarding the change curves of bending moment given in Figure 3(b), it was $M_{max}=94.74 \times 10^3$ kNm at first story of the building, and it was $M_{min}=35.73 \times 10^3$ kNm at the 5th story of the building in the TI-D record. And it was $M_{max}=198.90 \times 10^3$ kNm at the first story of the building, and it was $M_{min}=81.31 \times 10^3$ kNm at the 5th story of the building in the CC-ALS record. Regarding the change curves of interstory drift ratio given in Figure 3(c), it was $\delta_{max}=1.23 \times 10^{-3}$ and $\delta_{min}=0.98 \times 10^{-3}$ in the TI-D record. And its as $\delta_{max}=3.08 \times 10^{-3}$ and $\delta_{min}=2.53 \times 10^{-3}$ in the CC-ALS record.

In the following Table 4, the values of maximum shear force, moment and interstory drift ratio obtained from the analyses -in which the earthquakes under group PGV₄₀₋₆₀ were used- have been given. According to this, it was $V_{max}=15.63 \times 10^3$ in K-S record having the minimum PGV value, and $V_{max}=30.71 \times 10^3$ kN in the D-D record having the maximum PGV value. When the moment values are considered, it is being observed that it was $M_{max}=94.49 \times 10^3$ in K-S record, and it was $M_{max}=198.05 \times 10^3$ kNm in D-D record. While it was $\delta_{max}=1.21 \times 10^{-3}$ in K-S record -where the PGV value was the minimum, it was $\delta_{max}=2.50 \times 10^{-3}$ in D-D record.

Table 4. Analysis results of PGV₄₀₋₆₀ group

Ground motion records of PGV ₄₀₋₆₀	V_{max} kN $\times 10^3$	M_{max} kNm $\times 10^3$	δ_{max} 10^{-3}
Kocaeli (K-S)	15.63	94.49	1.21
Imperial Vall. (IV-BC)	48.88	219.68	3.21
Chi-Chi (CC-CHY024)	26.87	161.42	2.53
Imperial Vall. (IV-ECA4)	37.00	221.12	2.98
Düzce (D-B)	55.56	296.03	3.25
Kocaeli (K-D)	28.84	166.21	2.27
Düzce (D-D)	30.71	198.05	2.50
Average	34.78	193.86	2.56

In Figure 4, change curves of story – shear force, bending moment and interstory drift ratio –obtained from the earthquake records under group PGV₄₀₋₆₀ (whose PGV values change in between 40 cm/sec and 60 cm/sec)- have been given. As per the change curves of story - shear force provided in Figure 4(a), the maximum shear force (V_{max}) of Kocaeli earthquake – having the minimum PGV value and obtained from the Sakarya (K-S) record- was 15.63×10^3 kN at the first story of the building, and its minimum shear force (V_{min}) was 3.75×10^3 kN at the 5th floor of the building. In the D-D record of Duzce

earthquake -having the maximum PGV value in the group- obtained from the Duzce station, it was $V_{max}=30.71 \times 10^3$ kN at the first story, and $V_{min}=7.60 \times 10^3$ kN at the 5th story. Regarding the change curves of bending moment given in Figure 4(b), it was $M_{max}=94.49 \times 10^3$ kNm at the first story, and $M_{min}=33.67 \times 10^3$ kNm at the 5th story in the K-S record. And in the D-D record, it was $M_{max}=198.05 \times 10^3$ kNm at the first story, and $M_{min}=72.79 \times 10^3$ kNm at the 5th story.

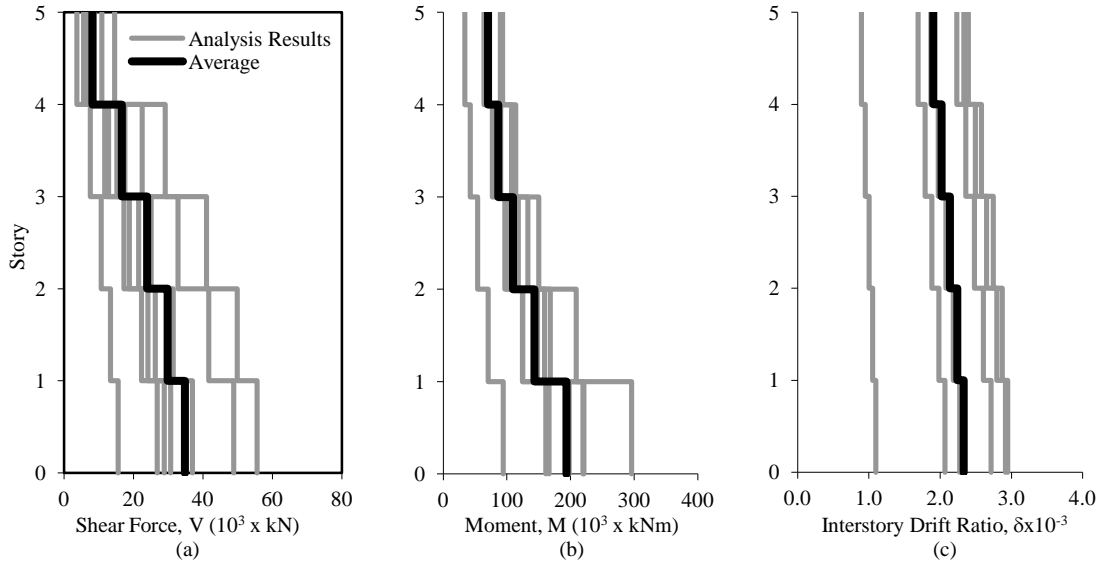


Figure 4. Group PGV₄₀₋₆₀ Story - (a) Shear Force; (b) Moment; (c) Interstory Drift Ratio Diagram

Regarding the change curves of interstory drift ratio given in Figure 4(c), it was $\delta_{max}=1.21 \times 10^{-3}$ and $\delta_{min}=0.98 \times 10^{-3}$ in the K-S record. And in the D-D record -with the maximum PGV value-, it was $\delta_{max}=2.50 \times 10^{-3}$ and $\delta_{min}=2.06 \times 10^{-3}$

When the values of shear force, bending moment and interstory drift ratio obtained from the sets are assessed together, it is being observed that as the PGV value of the earthquake record increases the obtained effects are tending to increase, and that the maximum values are being obtained at the first story of the building, and the minimum values are being obtained at the 5th story of the building.

3.ASSESSMENT OF THE DATA OF ANALYSIS

In earthquake codes [7] [10] for time history analysis, it is generally being required to obtain the parameter of the structure to be controlled by taking the average of earthquake records of seven and more. In this section, average shear force, bending moment, interstory drift ratio and story curves obtained for each group have been discussed comparatively.

In Figure 5, the curves relevant to such comparison have been given. The light colored curve in Figure 5(a), in the graph where the changes of story and shear force are compared, indicates the average of PGV₂₀₋₄₀ record group, and the dark colored curve indicates the average of PGV₄₀₋₆₀ record group. Maximum average shear force value (V_{max}) of PGV₂₀₋₄₀ group was obtained as 22.75×10^3 kN at the first story of the building. And the minimum shear force (V_{min}) on this curve was obtained as 5.53×10^3 kN at the 5th story of the building. And in the curve obtained as the average of PGV₄₀₋₆₀ group, V_{max} was 34.78×10^3 kN at the first story of the building. And the V_{min} on this curve was obtained at the 5th of the building, and it was 8.19×10^3 kN.

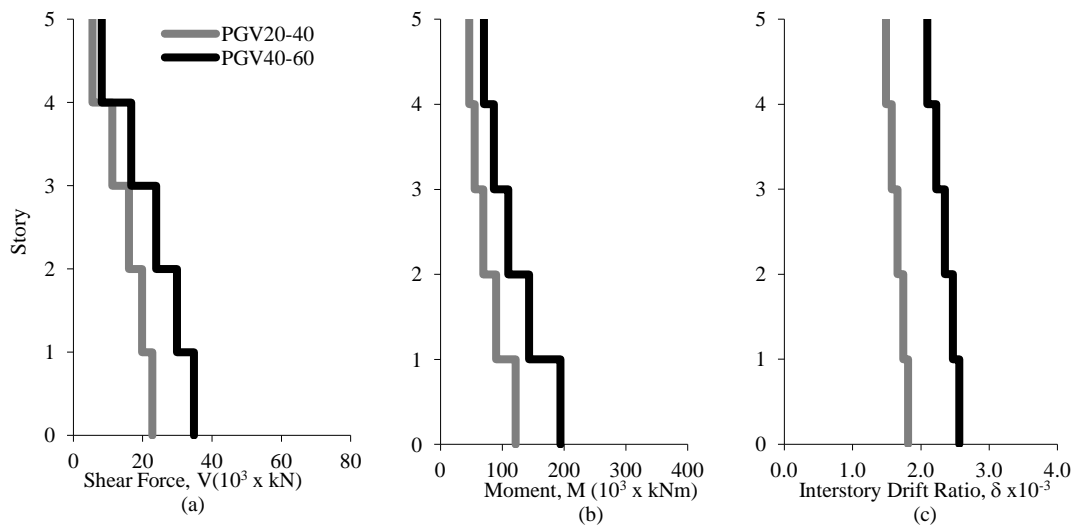


Figure 5. Comparison as per story of changes of (a) Shear Force, (b) Moment, (c) Interstory Drift Ratio obtained from record groups whose PGV values change

As per the graph in Figure 5(b), by which the changes of story and bending moment are compared, average M_{max} for the PGV₂₀₋₄₀ group was obtained as 121.58×10^3 kNm at the first story of the building, and M_{min} was obtained as 46.52×10^3 kNm at the 5th of the building. And in the curve which was obtained as the average of PGV₄₀₋₆₀ group, M_{max} was obtained as 193.86×10^3 kNm again at the first story, and M_{min} was obtained as 70.50×10^3 kNm at the 5th floor. In the graph given in Figure 5(c) by which the story and interstory drift ratio were compared, average δ_{max} for the PGV₂₀₋₄₀ group was obtained as 1.81×10^{-3} at the first story of the building, and δ_{min} was obtained as 1.49×10^{-3} at the 5th story of the building. And in the curve obtained as the average of PGV₄₀₋₆₀ group, δ_{max} was obtained as 2.56×10^{-3} again at the first story, and δ_{min} was obtained as 2.09×10^{-3} at the 5th story of the building.

Along with observing that the obtained internal force and interstory drift ratio increase along with the increase of PGV from the graphs provided for comparison, the level of increase is unable to be revealed. For this reason, graphs for the numerical comparison of two groups were formed, and the referred graphs have been given in Figure 6. In Figure 6(a), the curve in which the shear forces obtained from the PGV₂₀₋₄₀ group are compared with the ones obtained from PGV₄₀₋₆₀ group has been provided. According to this, shear force obtained from the PGV₄₀₋₆₀ group has been 53% larger than the ones obtained from the PGV₂₀₋₄₀ group at the first story of the building, and this value has been the maximum difference among the shear forces. According to bending moment curve given in Figure 6(b), the moment values obtained from the PGV₄₀₋₆₀ group have been 60% larger at the first story of the building. According to the interstory drift ratio curve given in Figure 6(c), the difference among the values obtained from the PGV₄₀₋₆₀ group has been the maximum on the 2nd story of the building, and the interstory drift ratio arising in the PGV₄₀₋₆₀ group at this story has been 42% larger compared to the PGV₂₀₋₄₀ group.

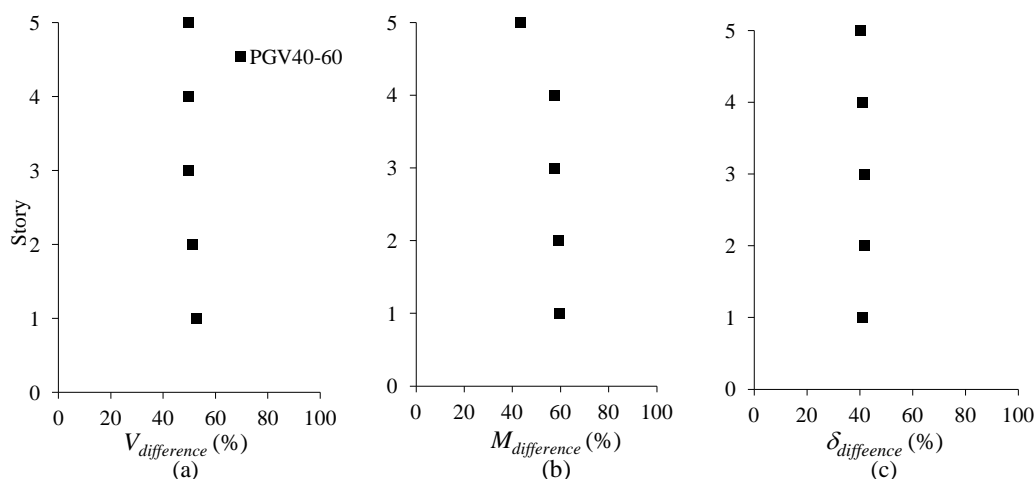


Figure 6. Proportionately comparison of changes of (a) Shear Force, (b) Moment, (c) Interstory Drift Ratio obtained from record groups whose PGV values change

4. CONCLUSIONS

In this study, where it is intended to examine the effect of change of earthquake record peak ground velocity (PGV) on mid-rise structures, two different record groups whose PGV value was changing in between 20 cm/sec and 40 cm/sec (PGV₂₀₋₄₀), and in between 40 cm/sec and 60 cm/sec (PGV₄₀₋₆₀) were formed. By using the records in these groups, non-linear time history analyses of the building were performed. Within the frame of the analyses performed, when the results of the analyses of the two groups were compared, it was determined that the shear forces obtained from the PGV₄₀₋₆₀ group were 53% larger compared to the ones obtained from the PGV₂₀₋₄₀ group, and that the bending moments were 60% larger, and that the interstory drift ratios were 42% larger among the same groups. When the results of shear force, bending moment and interstory drift ratio obtained from the earthquake records formed as per the PGV value are assessed together, it is being observed that the internal forces and drifts arising in the building remarkably increase as the PGV value of the record increases. For this reason, it will be beneficial to the select as high as possible the earthquake records' PGV values to be used in the non-linear time history dynamic analysis of mid-rise buildings.

REFERENCES

- [1]. Z. Celep, N. Kumbasar, *Yapı Dinamiği ve Deprem Mühendisliğine Giriş*, Sema Matbaacılık, İstanbul, 1996.
- [2]. J.J. Bommer and A.B. Acevedo, "The Use of Real Earthquake Accelerograms as Input to Dynamic Analysis", *Journal of Earthquake Engineering*, 2004, 8(1), 43-92.
- [3]. J.C. Anderson, V.V. Bertero, "Uncertainties in establishing design earthquakes", *Journal of Structural Engineering (ASCE)*, 1987, 113(8), 1709-1724.
- [4]. *Tentative Provisions for the Development of Seismic Regulations for Buildings*, Applied Technology Council (ATC), ATC-06, Redwood City, California, 1978.
- [5]. J.B. Mander, M.J.N. Priestley and R. Park, "Observed stress-strain behaviour confined concrete", *Journal of Structural Engineering (ASCE)*, 1988, 114(8), 1827-1849.
- [6]. J.B. Mander, M.J.N. Priestley and R. Park, "Theoretical Stress-Strain Model for Confined Concrete", *Journal of Structural Engineering (ASCE)*, 1998, 114, 1804-1826.
- [7]. *Türk Deprem Yönetmeliği (TDY)*, Bayındırlık ve İskan Bakanlığı, Ankara, 2007.
- [8]. *XTRACT v3.0.8 Section Analysis Program (2013)*, Educational Version, Imbsen Software Systems, CA.
- [9]. Pacific Earthquake Engineering Research Center Strong Motion Database, <http://peer.berkeley.edu/smcat/>
- [10]. *American Society of Civil Engineers, Minimum Design Loads for Buildings and Other Structures*, Standard ASCE/SEI 7-05, Reston, VA. 2005.

BIOGRAPHY

The author had completed his Civil Engineering education at Kocaeli University in 2000, and his post graduate study in 2005 and his doctorate study in 2014 at the same university, and he is now continuing his operations as research associate.

Manufacturing and Characterization of Self-Cleaning Air Filters Coated with Zinc Oxide Nanostructures

Mucahid Ozcan, Cansu Noberi, Cengiz Kaya, Figen Kaya*

Abstract

Zinc Oxide (ZnO) is the one of the most promising material for filtering applications due to its large surface area. It is also a well-known fact that ZnO is a polar crystal with hexagonal phase, and the high anisotropy of ZnO leads to the oriented growth along the c axis. This high anisotropy enhances nanotube formation rate during recrystallization. In this study, single crystal ZnO nanorods are successfully synthesized using $Zn(O_2CCH_3)_2(H_2O)_2$, NaOH and distilled water as precursors at ambient pressure and temperature. Synthesized nano structures are used to produce multi walled ZnO nanotubes using simple hydrothermal treatment without use of any catalysts, plates or substrates. ZnO nanotube structures are synthesized at low temperatures and calcined at 500 °C for 5 hours. Characterization result indicate that both tubular and rod structures are successfully produced. Finally, synthesized nanotubes are used for coating carbon and stainless steel based porous filter by using electrophoretic deposition. In order to assess the filtering capability of as received and coated filters, flow of air through the filter porosity is simulated. For modelling and simulation of air flow of manufactured filters Solidworks and Ansys programmes are employed. Tubular and rod like nanostructures demonstrated effective catalytic and air filtration properties at room temperature.

Key words : Zinc Oxide, Hydrothermal, Nanotubes, Nanorods

Yıldız Technical University, Department of metallurgical and materials engineering Davutpasa Campus 34210 - Istanbul

1. INTRODUCTION:

Zinc Oxide (ZnO) is one of the most important and promising materials for a large number of areas. It has distinct advantages over its competitors such as non-toxicity, low material costs, chemical stability, high transparency in the visible and near infrared spectral region [1], good electrical properties, high luminous transmittance, excellent substrate adherence, hardness, optical and piezoelectric behaviour and its low price [2]. It is also a well-known fact that ZnO is apolar crystal with hexagonal phase, and the high anisotropy of ZnO leads to the oriented growth along the c axis. [3]. ZnO is a very promising material with a wide direct band gap (3.37 eV), a large exciton binding energy (60 eV) at room temperature, and high degrees of mechanical, chemical and thermal stability [4]. Zinc Oxide has been widely investigated due to their potential wide-ranging applications [5]. It is a versatile smart material that has unique applications in catalysts, sensors, piezoelectric transducers and actuators, photovoltaic and surface acoustic wave devices. ZnO is also a biosafe and biocompatible material, which can be directly used for biomedical applications without coating [6], UV photodetectors, field emission cathodes, PH sensors, gas sensors. [4] As a biosafe and biocompatible material, ZnO can be directly used for biomedical applications without coating [5]. These properties have stimulated the search for new synthetic methodologies for well-controlled ZnO nanostructures. Synthesis of ZnO with different forms of controlled nanostructures have been widely explored in recent years and many kinds of interesting and delicate ZnO nanostructures have been obtained by using different methods based on vapor phase processes and solution processes [7].

Among heterogeneous semiconductors, TiO₂ and ZnO are the most widely used because they fulfill all the above requirements and exhibit adequate conversion values in a multitude of photochemical processes oriented to degradation and/or fine chemical synthesis. Anatase and wurtzite are typically the most active phases of these two oxides while entering in the nanometer regime. In the quest to optimize the photoactivity of such nanomaterials several research paths have been pursued. The control of the nanostructure is the first and possibly the least accurately known at this moment. However, the knowledge of the nanostructure effects on photoactivity appears as a requirement that is necessary for any other way of improving photoactivity as normally nanosized, high-surface area particles are always used in this field. The second and more broadly used is the (cationic and/or anionic) doping of the materials. Also the use of composite systems based on TiO₂ and ZnO materials can be mentioned. These two possibilities have the additional objective of producing visible light and, more interestingly, sunlight active materials, allowing in this way the use of removable energy sources in photocatalytic processes [8], [9] and [10].

ZnO has also been widely used as the photocatalyst because of its high electron mobility, diversified morphologies, low cost, high chemical stability, and environmental friendliness [11], [12], [13], [14] and [15]. Moreover, compared with the commercial TiO₂ photocatalyst, ZnO has larger quantum efficiency and higher photocatalytic activity, as reported in the literature [16] and [17].

2. EXPERIMENTAL WORKS

2.1. Fabrication of ZnO Nanoparticles

In this study, single crystal ZnO nanorods are successfully synthesized using $\text{Zn}(\text{O}_2\text{CCH}_3)_2(\text{H}_2\text{O})_2$, NaOH and distilled water as precursors at ambient pressure and room temperature. Firstly, Zinc Acetate is added to distilled water and stirred magnetically (Solution A). Then NaOH is added to distilled water and stirred magnetically as well (Solution B). Afterwards, Solution B added to Solution A, dropwisely and stirred for 2 hours. Finally obtained nano structures are calcined at 300 °C for 3 hours. [18]

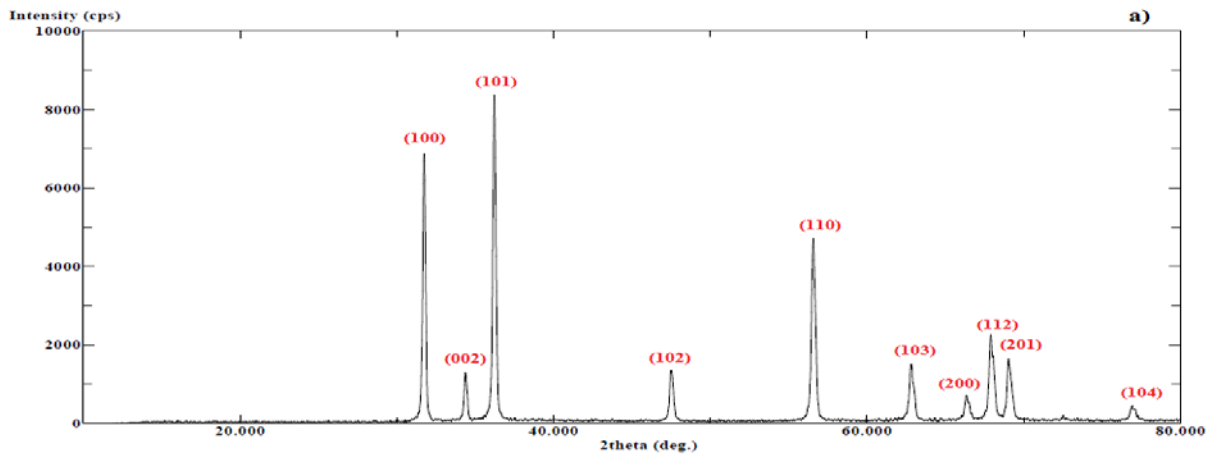
2.2. Fabrication of ZnO Nanotubes

ZnO Nanoparticles were already prepared. H_2O_2 [Hydrogen peroxide] used as a solvent. (0.8 g) of ZnO Nanoparticles were added to (40 ml) of H_2O_2 and stirred in a magnetic stirrer for 1 hour. The obtained solution was removed from the magnetic stirrer. The solution was added to a stainless steel autoclave and was heated to 180°C for 24 hours. The autoclave was removed from the furnace and was cooled to room temperature. 50 ml Distilled water was added to the resulting solution and was stirred for 30 min. The solution then was removed from the stirrer and was filtered. [pH=6]. The obtained solution was washed twice with ethanol, and twice with distilled water until pH= 5 is obtained. The final product was dried at 70 °C hours in the furnace. After drying, the product was removed from the furnace and ground to a fine powder. The final powder was calcined in the furnace at 500 °C for 5 hours. [18]

2.3. Results and Discussion

The XRD pattern of the ZnO nanotubes is shown in Fig. 1(a). All the diffraction peaks could be indexed to hexagonal wurtzite structure of ZnO. No impurities are detected in the diffraction pattern, indicating that the residual ions from both nanoparticle and nanotube synthesis processes have been successfully removed by washing with distilled water, as could be seen in Fig.1(a) . In addition, the (002) reflection plane is extremely weak compared with the standard reflection, which is due to the fact that the (00n) planes are absent in hollow or tubular ZnO structure [19].

The XRD spectrum (Fig 1.b) of the synthesized material showed diffraction peaks, which can be well indexed to the hexagonal phase of ZnO. The obtained ZnO possesses the wurtzite structure. The relative intensities of the diffraction peaks matched well with the standard diffraction pattern of crystalline ZnO (space group $P6_{3mc}$, JCPDS File no. 89-1397). The sharp diffraction peaks also indicated high crystallinity of the material. It is pertinent to mention here that the calcined material was thoroughly washed with distilled water several times to remove the excess H_2O_2 molecules. Thus, the extra peaks in the XRD spectrum may be attributed to the H_2O_2 remaining at the surfaces of ZnO nanorods.



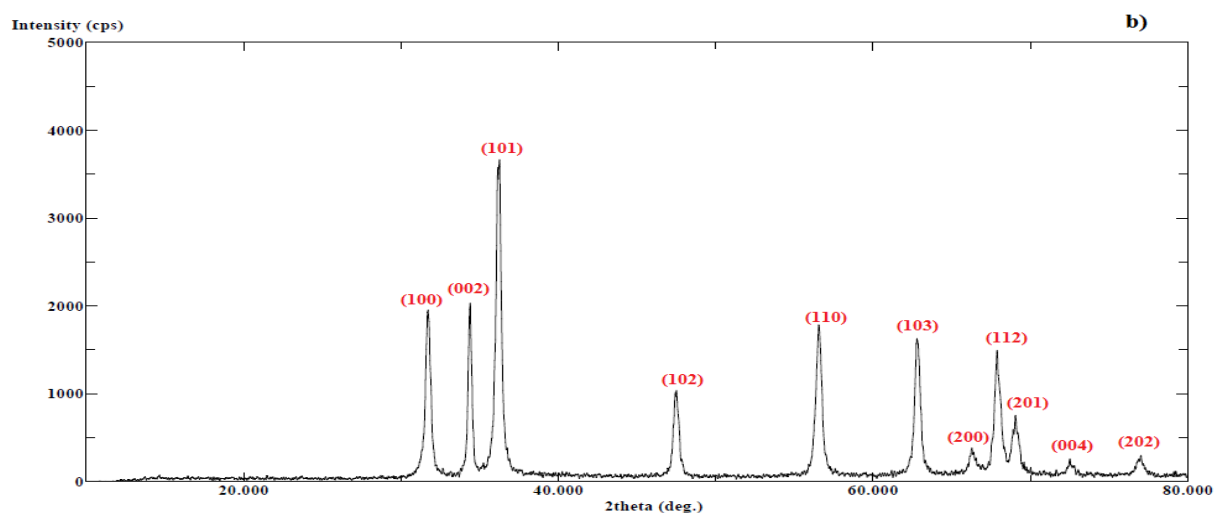


Fig. 1. (a) XRD pattern of the as-prepared ZnO tubular structures revealing the wurtzite phase and (b) XRD spectrum of ZnO nanorods

The morphology of the synthesized zinc oxide nanorods was confirmed using scanning electron microscopy (SEM). It was confirmed that nanorods were obtained as wished. Their length was more than 1 μm which can be seen at Fig.3b.

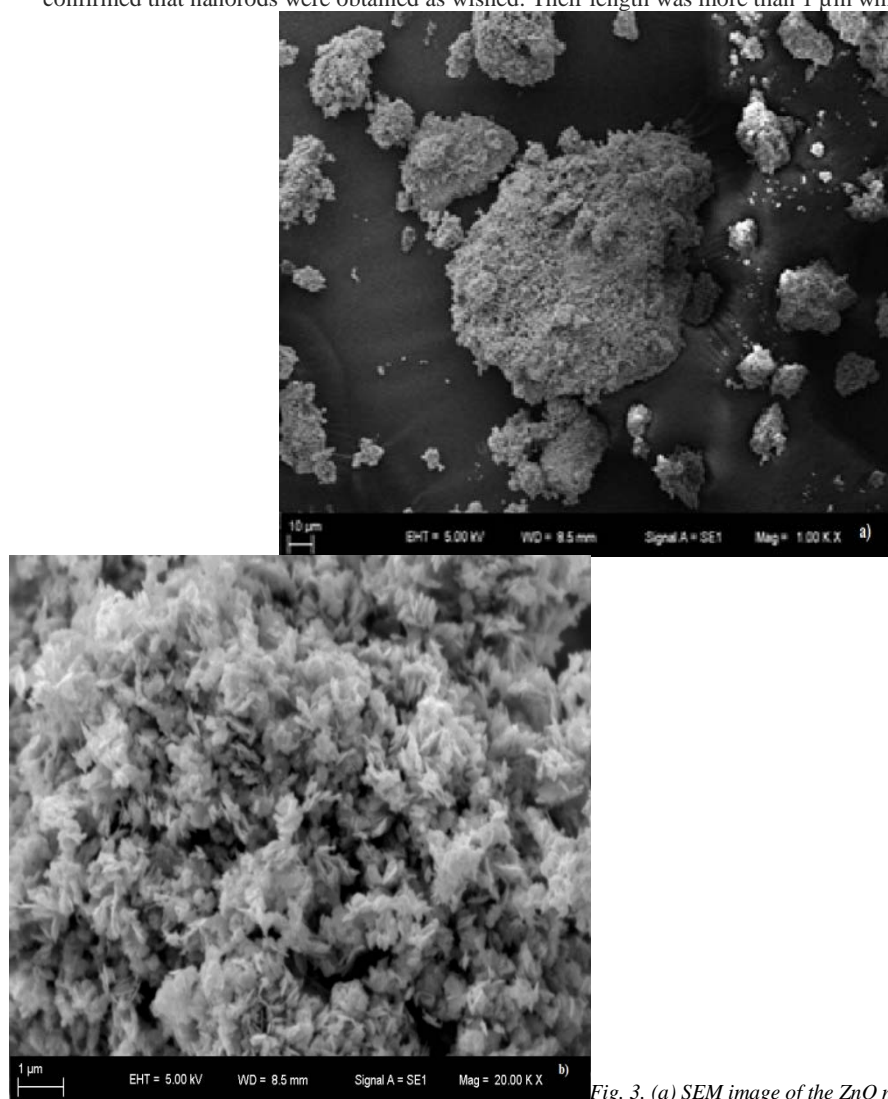


Fig. 3. (a) SEM image of the ZnO nanostructure (b) Enlarged SEM image of an individual ZnO nanostructure and non-uniform diameter along the c-axis.

The formation mechanism of ZnO nanotubes is not completely understood, however it is believed that the mechanism of ZnO nanotubes from nanowire-rod like ZnO powders can be explained with the Kirkendall effect [21,22]. In the Kirkendall effect, diffusion of atoms cause oversaturation of lattice voids. It is considered that this oversaturation cause condensation of more voids (Kirkendall voids) close to the ZnO interface. Therefore, these Kirkendall voids changes properties of the ZnO interface and force it to form multi-walled nanotubes [23].

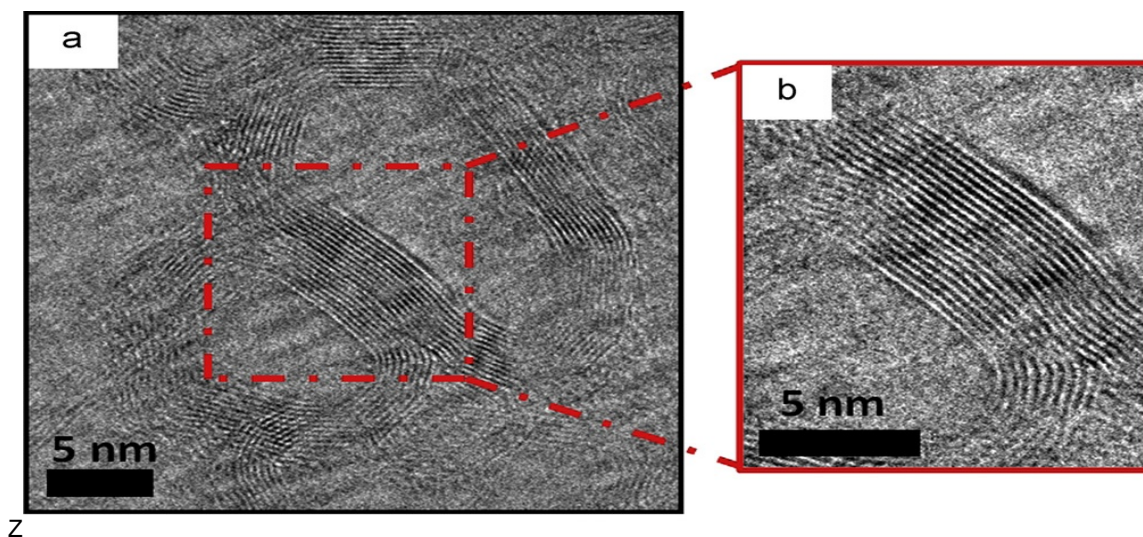


Fig. 4. TEM images of the obtained ZnO nanotubes: the cross section of the ZnO nanotubes (a, b)[18]

Fig.4(a) shows TEM micrograph of synthesized ZnO based nanotubes after hydrothermal treatment. The synthesized ZnO nanotubes were coated on 3D stainless steel filters by electrophoretic deposition (EPD) technique. It is shown that the obtained multi-walled ZnO nanotubes show antibacterial behavior and have variable inner diameters of 5–17 nm, outer diameters of 10–22 nm as could be clearly seen from Fig.4 (b) [18]

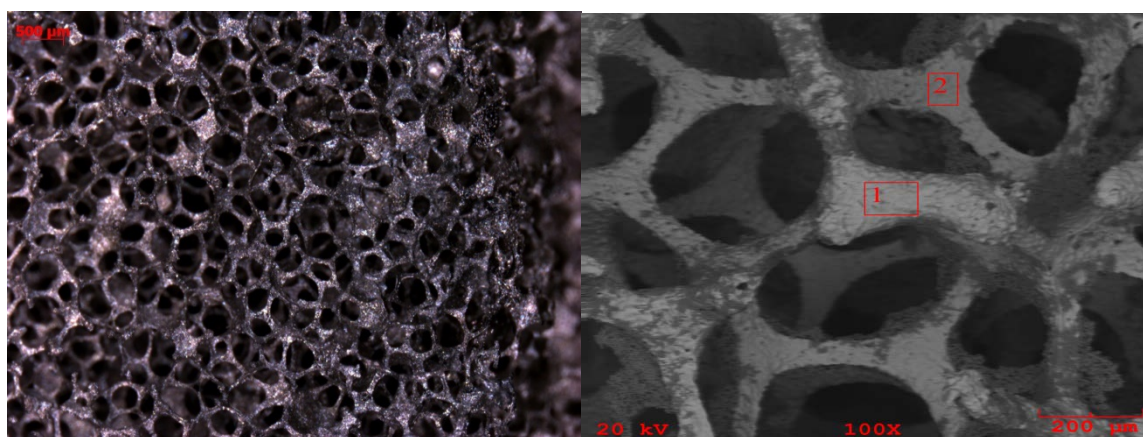


Fig. 5. Optical images of un-coated stainless steel filter and SEM image of ZnO nanotube-coated stainless steel filter.

Table 1 : EDS analysis taken from the regions 1 and 2

Region 1					
Elt.	Line	Intensity	Error	Conc	
		(c/s)	2-sig		
O	Ka	7.10	0.973	1.439	wt.%
Si	Ka	2.61	0.590	0.285	wt.%
Cr	Ka	169.87	4.759	20.374	wt.%
Mn	Ka	1.16	0.394	0.184	wt.%

Fe	Ka	306.57	6.393	58.534	wt.%
Ni	Ka	39.18	2.285	10.996	wt.%
Zn	Ka	19.32	1.605	8.188	wt.%
				100.000	wt. % Total
Region 2					
Elt.	Line	Intensity	Error	Conc	
		(c/s)	2-sig		
O	Ka	1.55	0.454	1.617	wt.%
S	Ka	1.36	0.426	0.585	wt.%
Cr	Ka	32.46	2.080	19.771	wt.%
Fe	Ka	60.99	2.851	59.326	wt.%
Ni	Ka	5.63	0.867	8.026	wt.%
Zn	Ka	4.96	0.813	10.674	wt.%
				100.000	wt. % Total

Zinc oxide nanorods are successfully coated on to stainless steel filters. EDS analysis taken from the regions 1 and 2 confirmed that coating is established. Namely, 10 wt. % Zn and 1.5 wt % O is present in EDS analysis results. Also Cr, Ni ve Fe is coming from stainless steel filters. This thin coating allows ease of filtering and provides photocatalytic activity. Stainless steel based filter shows unobstructed air flow and therefore air viscosity decreases

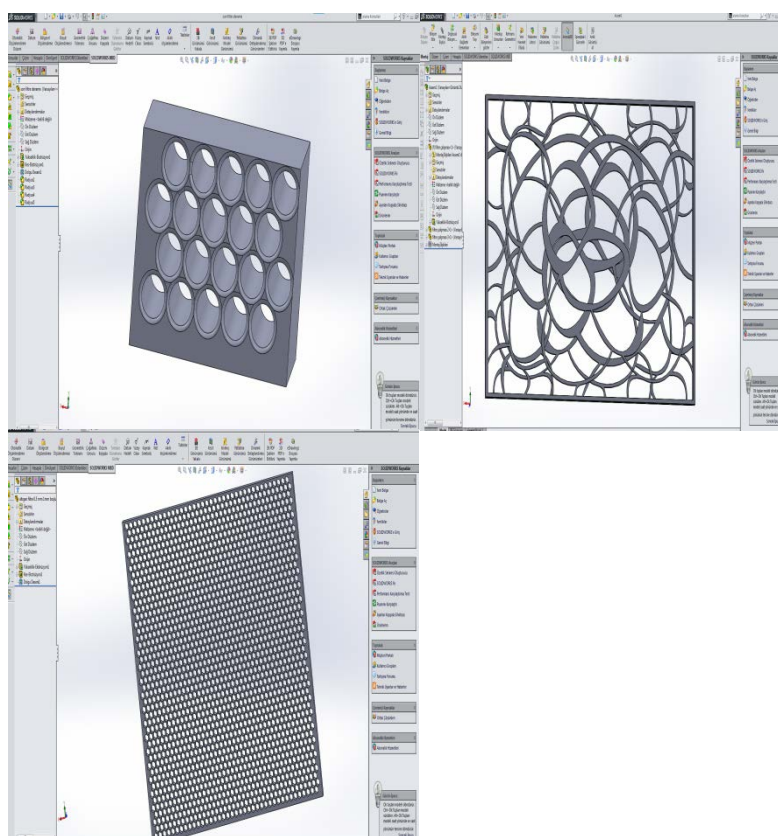


Fig. 5. Solid modeling examples of un-coated stainless steel filter

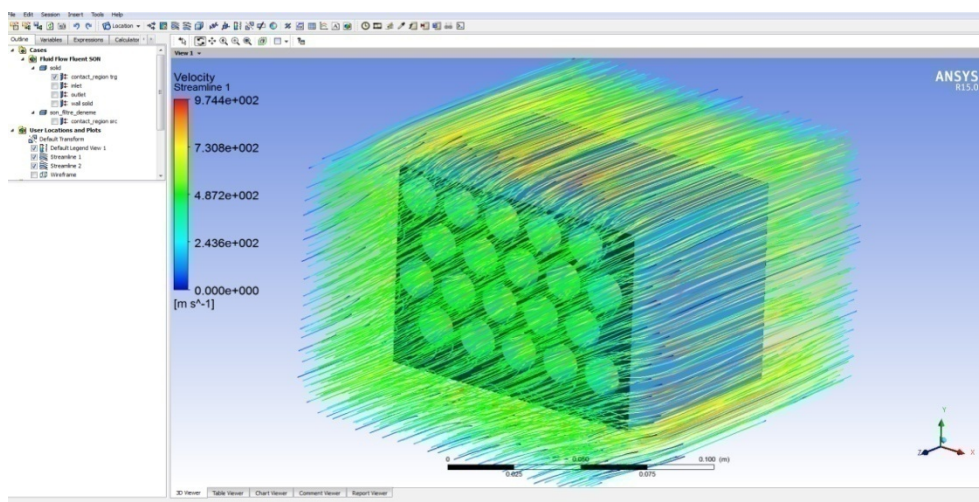


Fig. 5. Solid modeling examples of un-coated stainless steel filter

- The red line velocity : 9.744 m/s
- The yellow line velocity : 7.308 m/s
- The green line velocity : 4.872 m/s
- The light blue line velocity : 2.436 m/s

As It could be clearly seen from the simulation, the air flow varies according to the nature of filter. When the air and particulates passed through a narrow passage, air flow rate is increased. Therefore, filter models have to be complex to increase the filtration rate. The difference of between coating and uncoating samples is air flow changing. When we coated the filters, we blocked the air flow. Thus we must pay attention to the thickness of coating

3.CONCLUSIONS

ZnO nanotubes with controlled size and shape can be prepared by a simple hydrothermal method without the use of any catalysts, surfactant or substrates. The final ZnO nanotubes are considered to be suitable candidates for photocatalytic and self cleaning applications, such as filters in air conditioning systems. Finally, filtering capability of coated filters is simulated. For modelling and simulation of air flow of manufactured filters Solidworks and Ansys programmes are employed. Tubular and rod like nanostructures demonstrated effective catalytic and air filtration properties at room temperature.

ACKNOWLEDGEMENTS

This work was funded by TUBITAK – COST (The Scientific and Technological Research Council of Turkey) under the contract number 109R007 and TUBITAK 1512- 2130001.

REFERENCES

- [1] T. Touam, F. Boudjouan, A. Chelouche, S. Khodja, M. Dehimi, D. Djouadi, J. Solard, A. Fischer, A. Boudrioua, Effect of silver doping on the structural, morphological, optical and electrical properties of sol-gel deposited nanostructured ZnO thin films, *Optik - International Journal for Light and Electron Optics* (2015), <http://dx.doi.org/10.1016/j.ijleo.2015.09.066>.
- [2] Lu H, Wang Y, Lin X. *Mater Lett* 2009;63:2321.
- [3] Q. Wu, X. Chen, P. Zhang, Y. Han, X. Chen, Y. Yan, S. Li, Amino acid- assisted synthesis of ZnO hierarchical architectures and their novel photocatalytic activities, *Crystal Growth and Design* 8(2008)3010–3018.
- [4] C.-S. Chou, F.-C. Chou, Y.-G. Ding, P. Wu, The effect of ZnO-coating on the performance of a dye-sensitized solar cell, *Solar Energy Materials & Solar Cells* 98 (2012) 357–362.
- [5] M.H. Huang, S. Mao, H. Feick, H. Yan, Y. Wu, H. Kind, E. Webber, R. Russo, P. Yang, *Science* 292 (2001) 1897.
- [6] J.A. Rodriguez, T. Jirsak, J. Dvorak, S. Sambasivan, D.J. Fischer, *J. Phys. Chem. B* 104 (2000) 319.
- [7] C. Pacholski, A. Kornowski, H. Weller, *Angew. Chem. Int. Ed.* 41 (2002) 1188.
- [8] M.R. Hoffmann, B.T. Martin, W. Choi, D.W. Bahnemann *Chem. Rev.*, 95 (1995), p. 69
- [9] T.L. Thompson, *J.T. Yates Chem. Rev.*, 106 (2006), p. 4428
- [10] A. Kubacka, M. Fernández-García, G. Colón *Chem. Rev.*, 112 (2012), p. 1555
- [11] J.G. Yu, X.Y. Xiao Hydrothermal synthesis and photocatalytic activity of zinc oxide hollow spheres *Environ. Sci. Technol.*, 42 (2008), pp. 4902–4907
- [12] C.Q. Zhu, B.G. Lu, Q. Su, E.Q. Xie, W. Lan A simple method for the preparation of hollow ZnO nanospheres for use as a high performance photocatalyst *Nanoscale*, 4 (2012), pp. 3060–3064
- [13] X.H. Lu, Y.Z. Zheng, S.Q. Bi, Y. Wang, X. Tao, L.M. Dai, J.F. Chen Multidimensional ZnO architecture for dye-sensitized solar cells with high-efficiency up to 7.35% *Adv. Energy Mater.* (2014), p. 1301802

- [14] Y.C. Weng, K.T. Hsiao Composition optimization of ZnO-based photocatalyst arrays by scanning electrochemical microscopy and the characterization of efficient photocatalysts *Int. J. Hydrog. Energy*, 40 (2015), pp. 3238–3248
- [15] N.T. Khoa, S.W. Kim, D.H. Yoo, S. Cho, E.J. Kim, S.H. Hahn Fabrication of Au/graphene-wrapped ZnO-nanoparticle-assembled hollow spheres with effective photoinduced charge transfer for photocatalysis *ACS Appl. Mater. Interfaces*, 7 (2015), pp. 3524–3531
- [16] A. Akyol, H.C. Yatmaz, M. Bayramoglu Photocatalytic decolorization of remazol red RR in aqueous ZnO suspensions *Appl. Catal. B Environ.*, 54 (2004), pp. 19–24
- [17] H. Nakatani, S. Motokucho, K. Miyazaki Difference in polystyrene oxo-biodegradation behavior between copper phthalocyanine modified TiO₂ and ZnO paint photocatalyst systems *Polym. Degrad. Stab.*, 120 (2015), pp. 1–9
- [18] T. Ipeksac, C. Kaya, F. Kaya, *Materials Letters* 100(2013)11–14
- [19] L. Vayssieres, K. Keis, A. Hagfeldt, S.E. Lindquist, *Chem. Mater.* 13 (2001) 4395;
- [20] J.J. Benitez, M.A. San-Miguel, S. Dominguez-Meister, J.A. Heredia-Guerrero, M. Salmeron *J. Phys. Chem. C*, 115 (2011), p. 19716
- [21] Wei A, Sun XW, Xu CX, et al. Growth mechanism of tubular ZnO formed in aqueous solution. *Nanotechnology* 2006;17:1740–4.
- [22] Chang Y, Lye ML, Zeng HC. Large-scale synthesis of high-quality ultralong copper nanowire. *Langmuir* 2005;21:3746–8.
- [23] Fan HJ, G'osele U, Zacharias M. Formation of nanotubes and hollow nano- particles based on kirkendall and diffusion processes: a review. *Small* 2007;3:1660–71.

Particles' Behaviour Analysis in Particle Swarm Optimization

Nihan Kazak¹, Nesibe Yalcin^{1,2}

Abstract

Particle Swarm Optimization (PSO) is an easily realizable and computationally effective heuristic optimization technique and is based on the social behaviour of a flock of birds, a school of fish or a swarm of insects while they are searching for food. This technique is very simple and it needs the small number of parameters by comparison with other optimization techniques. In the literature, the escape behaviour from bad has been modelled for the improvement of PSO. According to this behaviour, each particle moves depending on extra two best values in addition to "pbest" and "gbest", in one generation: "pworst" is the personal worst solution of each particle found so far and "gworst" is a global worst solution. In this study, a constriction factor is added into the equation of particle velocity updating to increase the speed of convergence of this PSO version. The proposed PSO in this study is compared with other PSO versions using benchmark functions and their performances are analyzed.

Keywords: *Constriction Factor, Convergence, Swarm Behaviour, Heuristic Optimization.*

1. INTRODUCTION

Particle Swarm Optimization (PSO) developed by Eberhart and Kennedy [1] is widely used to solve global optimization problems. PSO is faster and simpler than other techniques such as genetic algorithm, ant colony optimization and evolutionary computation. A new way of behaviour (escape from bad) has been modelled and proposed for the improvement of inertia weight PSO (IWPSO) algorithm by Altunöz and Yılmaz in [2]. According to this behaviour, each particle moves depending on extra two best values in addition to "pbest" and "gbest", in one generation: "pworst" is the personal worst solution of each particle found so far and "gworst" is a global worst solution.

In this study, a constriction factor is added into the equation of particle velocity updating to increase the speed of convergence of the PSO algorithm instead of inertia weight. The performances of obtained PSO algorithm, IWPSO and are compared with using benchmark functions.

2. PARTICLE SWARM OPTIMIZATION (PSO)

Particle Swarm Optimization (PSO) algorithm, a population based heuristic optimization technique has been successfully applied in the research and application areas. Each individual in PSO is denoted as particle [3]. Particles in the problem space move according to their personal best positions and best position within the particles, and the velocity and position of each particle can update using (1) and (2) equations.

$$v_{id} = v_{id} + c_1 * rand() * (p_{id} - x_{id}) + c_2 * rand() * (p_{gd} - x_{id}) \quad (1)$$

$$x_{id} = x_{id} + v_{id} \quad (2)$$

v_{id} and x_{id} indicate the velocity and position of i th ($i=1, 2, 3, \dots, N$) particle at d th dimension ($d=1, 2, 3, \dots, M$), respectively. N is the total number of particles and M is dimension size of a particle. p_{id} is personal best position and p_{gd} is global best position. c_1 and c_2 are positive acceleration constants, $c_1=c_2$. $rand()$ is a random number in the range of (0,1) [4, 5].

¹ Corresponding author: Bilecik Şeyh Edebali University, Department of Computer Engineering, 11230, Merkez/Bilecik, Turkey.
nihan.kazak@bilecik.edu.tr

² Sakarya University, Institute of Natural Sciences, 54187, Serdivan/Sakarya, Turkey.
nesibe.yalcin@bilecik.edu.tr

2.1.PSO with Inertial Weight (PSO1)

The velocity component of i th particle at d th dimension in PSO can update with inertia weight w [6] as given in Eq. (3):

$$v_{id} = (w)v_{id} + c_1 * rand() * (p_{id} - x_{id}) + c_2 * rand() * (p_{gd} - x_{id}) \quad (3)$$

Equation (4) can be used to change the value of w .

$$w = w_{\max} - \frac{w_{\max} - w_{\min}}{j_{\max}} j \quad (4)$$

w_{\max} and w_{\min} are maximum and minimum values of w , respectively. j is iteration index and j_{\max} is maximum iteration number [5].

2.2.PSO with Constriction Factor (PSO2)

Constriction factor χ [7] can preferred to update d th velocity component of i th particle as shown in Eq. (5) :

$$v_{id} = (\chi) * \{v_{id} + c_1 * rand() * (p_{id} - x_{id}) + c_2 * rand() * (p_{id} - x_{id})\} \quad (5)$$

The formula used in the calculation of constriction factor χ is described in Eq. (6).

$$\chi = \frac{2}{\left|2 - \beta - \sqrt{\beta * (\beta - 4)}\right|} \quad \beta = c_1 + c_2 \quad (6)$$

2.3.PSO with Inertial Weight and Escape Behaviour from Bad Position (PSO3)

In this PSO version, each particle moves depending on extra two worst components: k_{id} and k_{gd} are personal and global worst positions, respectively. These components are added into the equation of particle velocity updating to increase the speed of convergence of the PSO algorithm [2]. The new equation obtained is given as follows:

$$v_{id} = (w) * v_{id} + c_1 * rand() * (p_{id} - x_{id}) + c_2 * rand() * (p_{gd} - x_{id}) + c_3 * rand() * (x_{id} - k_{id}) + c_4 * rand() * (x_{id} - k_{gd}) \quad (7)$$

where c_3 and c_4 are positive acceleration constants.

2.4.PSO with Constriction Factor and Escape Behaviour from Bad Position (PSO4)

To update the velocity of each particle, constriction factor is used instead of inertia weight in Eq. (7).

$$v_{id} = (\chi) * v_{id} + c_1 * rand() * (p_{id} - x_{id}) + c_2 * rand() * (p_{gd} - x_{id}) + c_3 * rand() * (x_{id} - k_{id}) + c_4 * rand() * (x_{id} - k_{gd}) \quad (8)$$

Equations (9) is used to update the value of χ as follows.

$$\chi = \frac{2}{\left[\left(2 - \beta - \sqrt{\beta * (\beta - 4)}\right) * \left(1 - \alpha - \sqrt{\alpha * (\alpha - 1)}\right)\right]} \quad \alpha = c_3 + c_4 \quad (9)$$

The values presented in Table 1 are used for optimization of each function.

Table 6. Parameters of PSO

Parameter	Value
Run	50
Maximum iteration number	1000

Dimension of particles	20
Particle number	20
w_{max}	0.9
w_{min}	0.4
$c_1=c_2$	2.01
$c_3=c_4$	1.005

3. BENCHMARK FUNCTIONS

In this section, some standard benchmark functions applied to demonstrate PSO versions' efficiency and robustness are described. Equations, global minimum values and search domains of the functions used in our experimental study are given as follows:

Ackley function:

$$f(x) = -a \exp\left(-b \sqrt{\frac{1}{d} \sum_{i=1}^d x_i^2}\right) - \exp\left(\sqrt{\frac{1}{d} \sum_{i=1}^d \cos(cx_i)}\right) + a + \exp(1) \quad (10)$$

$a = 20$, $b = 0.2$ and $c = 2\pi$.

$x_i \in [-32, 32]$, Global Minimum=0

Rastrigin function:

$x_i \in [-5, 5]$, Global Minimum=0

$$f(x) = 10d + \sum_{i=1}^d [x_i^2 - 10 \cos(2\pi x_i)] \quad (11)$$

Rosenbrock function:

$x_i \in [-2, 2]$, Global Minimum=0

$$f(x) = \sum_{i=1}^{d-1} [100(x_{i+1} - x_i^2)^2 + (x_i - 1)^2] \quad (12)$$

Griewank function:

$x_i \in [-600, 600]$, Global Minimum=0

$$f(x) = \sum_{i=1}^d \frac{x_i^2}{4000} - \prod_{i=1}^d \cos\left(\frac{x_i}{\sqrt{i}}\right) + 1 \quad (13)$$

Sphere function:

$x_i \in [-5, 5]$, Global Minimum=0

$$f(x) = \sum_{i=1}^d x_i^2 \quad (14)$$

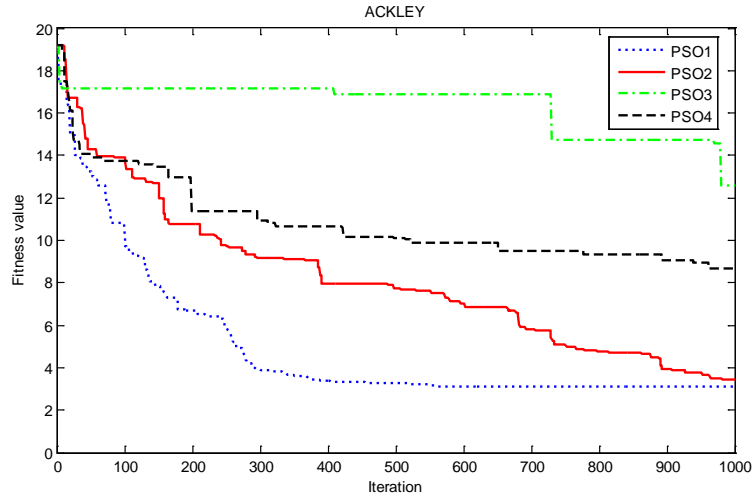
Schwefel function:

$x_i \in [-500, 500]$, Global Minimum=0

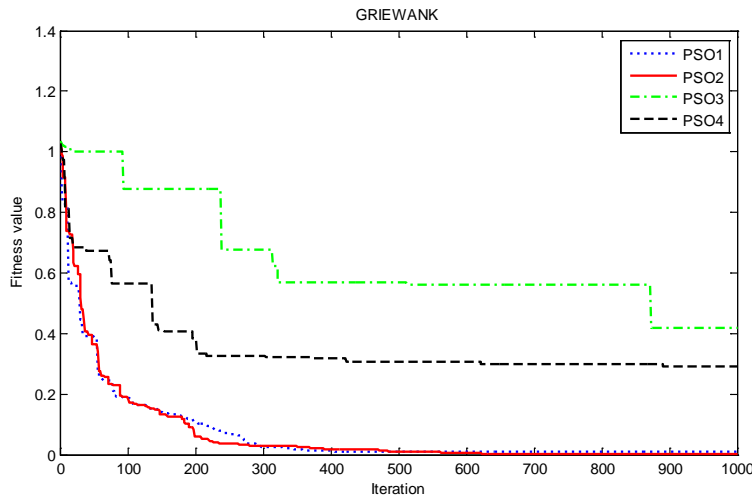
$$f(x) = 418.9829d - \sum_{i=1}^d x_i \sin(\sqrt{|x_i|}) \quad (15)$$

4.RESULTS AND DISCUSSION

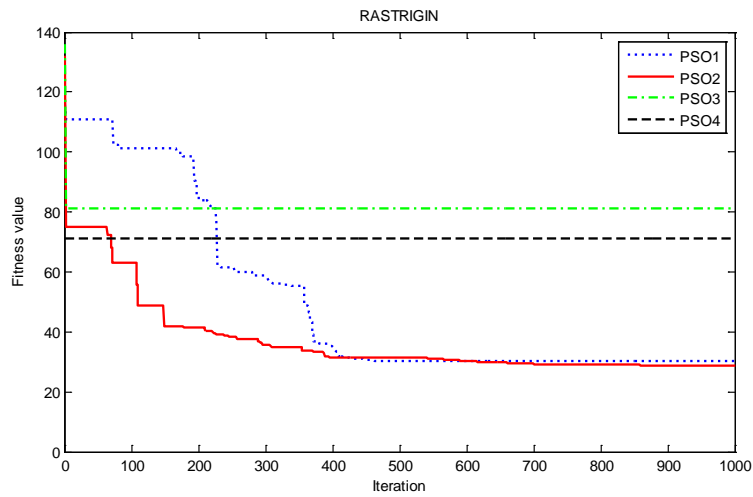
The performances of benchmark functions applied by PSO versions are compared in this section. Figure 1 shows the best run results among 50 runs about used PSO versions for the functions.



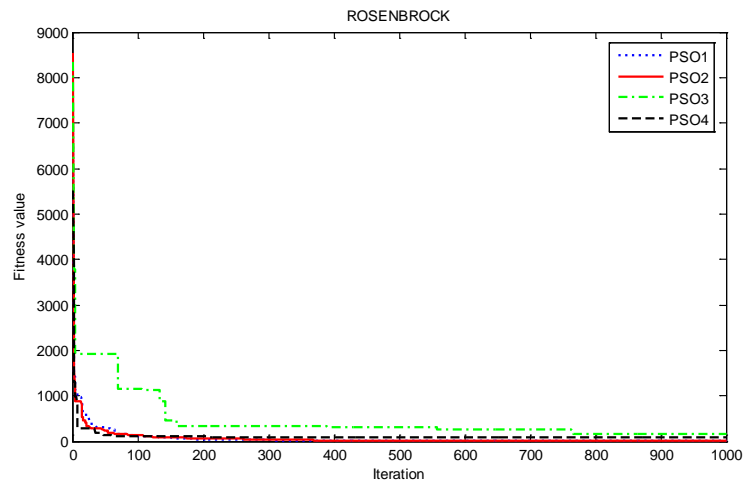
(a) The results of Ackley function



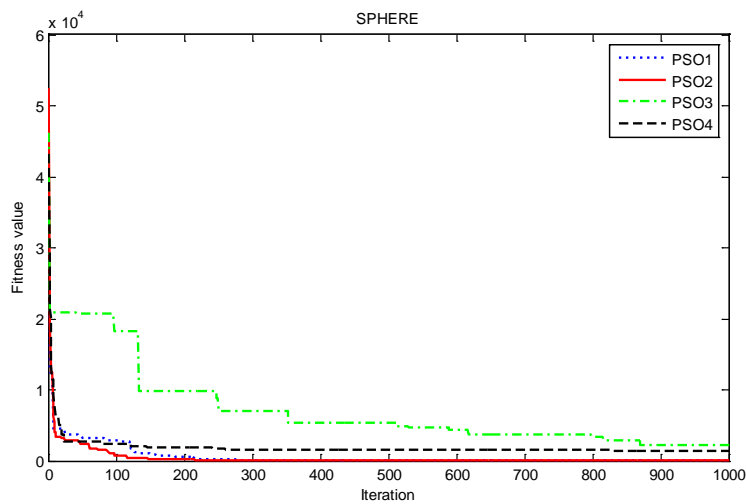
(b) The results of Griewank function



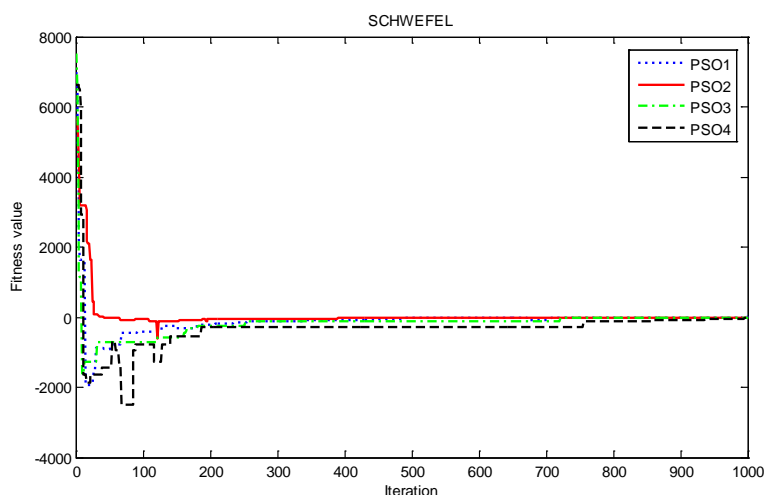
(c) The results of Rastrigin function



(d) The results of Rosenbrock function



(e) The results of Sphere function



(f) The results of Schwefel function

Figure 10. The best run results among 50 runs

Table 2 demonstrates the operation times and best values of PSO versions for test functions. When Fig 1 and Table 2 are analyzed, the comparison results show the PSO2 algorithm is faster than the other PSO versions in terms of operation time.

Table 7. Operation times (s) and best values of PSO versions for test functions

Test Function	Operation times				Best values			
	PSO1	PSO2	PSO3	PSO4	PSO1	PSO2	PSO3	PSO4
Ackley	29.796	19.13	25.505	25.791	3.112	3.417	12.583	8.6632
Rastrigin	15.866	14.808	22.337	21.256	30.249	28.683	81.054	71
Rosenbrock	16.312	15.256	23.326	21.513	19.56	16.37	165.666	79.976
Griewank	22.47	16.118	22.499	29.259	0.01	0.001	0.419	0.292
Sphere	13.795	13.118	21.596	18.927	25.583	3.963	2278.469	1423.25
Schwefel	16.162	15.185	23.689	20.636	-0.014	-6.655	-18.398	-17.789

When the results are analyzed in terms of the optimum value, all the PSO versions have not converged to optimum value for some benchmark functions like Rastrigin and Rosenbrock functions. PSO2 version has generally the best convergence for the most of the benchmark functions.

4. CONCLUSION

In this study, it has been aimed to determine the best PSO version and analyze the escape behaviour of the particles from bad position. For this purpose, the use of constriction factor instead of inertia weight is not provided the required convergence in new PSO version. As a result of global optimization studies, the way of behaviour is not suitable for PSO algorithm.

REFERENCES

- [1]. J. Kennedy and R. C. Eberhart, "Particle swarm optimization," *Proc. IEEE int'l conf. on neural networks*, vol. 4, pp. 1942–1948, IEEE service center, Piscataway, NJ, 1995.
- [2]. Ö. T. Altınöz, and A. E. Yılmaz, *Parçacık Sürü Optimizasyonunda Yeni Bir Birey Davranış Biçimi Önerisi*, EMO 13. Ulusal Kongre, Ankara, Türkiye, pp. 45-50, 2009.
- [3]. S. Helwing, F. Neumann, and R. Wanka, "Particle Swarm Optimization with Velocity Adaptation," *Proceedings of the International Conference on Adaptive and Intelligent Systems (ICAIS 2009)*, Klagenfurt, Austria, pp. 146–151, 2009.
- [4]. Q. Bai, "Analysis of Particle Swarm Optimization Algorithm", *Computer and Information Science*, vol. 3(1), pp.180–184, 2010.
- [5]. N. Yalçın, G. Tezel, and C. Karakuzu, *Epilepsy diagnosis using artificial neural network learned by PSO*, *Turkish Journal of Electrical Engineering & Computer Sciences*, 23: 421-432, 2015.

- [6]. M. Akin, M. A. Arserim, M.K. Kıymık, and İ. Türkoğlu, *A new approach for diagnosing epilepsy by using wavelet transform and neural networks*, Proceedings of the 23rd Annual EMBS International Conference, Istanbul, Turkey, pp. 1596-1599, 2001.
- [7]. Z. Wang, X. Sun and D. Zhang, *A PSO-Based classification rule mining algorithm*, *ICIC 2007*, LNAI 4682, 2007, pp. 377-384.

Assessment of Yakutiye Junction by VISSIM

O.Unsal Bayrak^{1}, F.Hattatoglu¹, H.Ferit Bayata,²M.Ali Colak²*

Abstract

There are about 150 thousand vehicles registered to traffic in Erzurum city. Although the increased traffic volume in every day, road capacity remains constant. Therefore, accident numbers are increasing every day. According to study of the number of accident in Turkey, fatal and injury accidents in city centrum occurred, especially, at junctions in the percent of 52%.

In this study, taking into consideration for number of accidents in the junction which has 3000 veh/h for peak hour Yakutiye Square that is intersection of Cumhuriyet Street-Menderes Street and Ali Ravi Street in Erzurum, different alternative solutions were modelled by changing road geometries and signalizations. These alternatives were evaluated by micro simulations technique. There are many congestions in that junction. Since the junction is in the center of commercial field, it is important to mitigate the congestion problems. VISSIM program was used for modeling. Travel time, delay, queue length, fuel consumption and CO emissions were considered as assessment criteria. As a result, optimum alternative was proposed.

Keywords: *Traffic; Junction; Microsimulation; VISSIM, Delay, Queue Length*

1.INTRODUCTION

Thousands of vehicles come into traffic every day. The increase amount of vehicles cause traffic congestion especially in junctions. Traffic congestion and delay make drivers and passengers impatient. Therefore, comfort and traffic and pedestrian safety are decreased and several fatal accidents can be occur. The solution of the traffic congestion may be seen as diverting vehicles in different roads or constructing a new roads. However this solution cannot be applicable in most cases and traffic engineers try to solve the problem by improving the junction in its current status. The junction geometry and signalization should be investigated for the roadway design to traffic accident (Goliass (1997)). The parameters such as delay, travel time and queue length are used as the evaluation criteria for improvement (Murat and Başkan (2006); Park and Schneeberger (2003)).

Microscopic simulations are widely used in transportation engineering due to its great advantages. Microsimulation is safer, less expensive and faster than field implementation (Park and Schneeberger (2003), Brought and Wahstedt (2007), Truong et al. (2015)). Moreover, it can visually reflect temporal and spatial variations of the traffic flow. One of the most used microsimulation package program is VISSIM. It is developed to model urban and public transit operations. Traffic composition, signal heads, lane configurations, each type of junctions, driver behavior etc. can be simulated by VISSIM. It can be used to analyze an intersection, a corridor, or an entire network.

Pedestrian safety is an important factor in traffic. In most countries, pedestrians are suffered from traffic accidents and are involved in the largest amount of fatal crashes. Pedestrians have to share the road spacetherefore pedestrians are exposed to high risk of being involved in a road traffic crash.Hence, it becomes crucial to provide pedestrians with safe, accessible and comprehensive facilities to reduce pedestrian crashes. In Turkey, the vehicles which turn right do not stop in pedestrian crossing. In such cases, pedestrian delay increase and also accident occurrence is inevitable. Therefore, pedestrian phase and protective time should be consider carefully in a signalized junction.

The objective of the study is to manage the Yakutiye junction with measures to be implemented in the study area. SignalizedYakutiye junction was modelled by microsimulation program, VISSIM. In the present model, 2 and 3 phase signalization program and grade separated junction is considered in terms of delay, travel time, queue length, CO emissions and fuel consumption for the junction.

¹ Corresponding author: Atatürk University, Department of Civil Engineering, 25240 Erzurum, Turkey.

* unsalb@atauni.edu.tr; hattat@atauni.edu.tr

²Erzincan University,Department of Civil Engineering, 24120, Erzincan, Turkey. hfbayata@erzincan.edu.tr, macolak@erzincan.edu.tr

2. MATERIAL AND METHOD

2.1. Study Area

Yakutiye junction is located in the center of the Erzurum (Figure 1). It is a signalized junction with four arm. There is Cumhuriyet Street in east-west direction and Menderes Street and Ali Ravi Street in north-south direction. There are commercial fields in both directions. East-west direction has two lanes while north south direction has three lanes. The first lane of each direction has parking lots along the street. Therefore, vehicles use only one lane for east-west direction and two lanes for north-south direction. In this case, travel time, queue length and hence delay of the either vehicles or pedestrians increase.



Figure 11. Yakutiye Junction

There is a two phase signalization program in the junction serves heavy volume during peak hours. The north-south direction is very intensive in the peak hours and queue length increases in these hours. The traffic composition is composed of cars and minibus and bus of public transportation. High congestion, lack of safety and traffic accidents with injuries and dead were observed at Yakutiyejunction.

2.2. Data Collection and Calibrating the Model

Traffic data collection and analysis is widely required for traffic control and management. Preliminary investigations, road and public transport inventories, traffic volume counts, intersection traffic volume counts, speed and delay studies were conducted in the area during morning and evening peak hours in the weekdays and weekend. Once data collection was done, data were analyzed and modal split graphs, frequency of vehicles have been found. These outputs were used as input data in the micro simulation software VISSIM.

Data was gathered at Yakutiye junction by means of one-hour video camera recordings. Peak hour volumes were counted either weekdays or weekend. Cars, buses and minibuses were counted separately according to their routes and general characteristic of traffic was revealed Figure 2-6.

Travel time and queue length characteristics along the critical road sections of the area were collected by the experts. This data provides the basis for better understanding and identifying the traffic bottlenecks in the routes. The junction is modeled according to field conditions by VISSIM. Peak hour volumes, signal durations, modal split, road inventory of the study area are the inputs for the microsimulation model. The calibration of the model is very important to represent the reliable results. Hence, this model was calibrated according to the GEH (Geoffry E. Havers) formula (Shankar et al., (2013)). Havers developed a continuous volume tolerance formula. In this study, gathered data was calibrated according to the Havers's study. Hence the model is said to be calibrated.



Figure 2. Routes

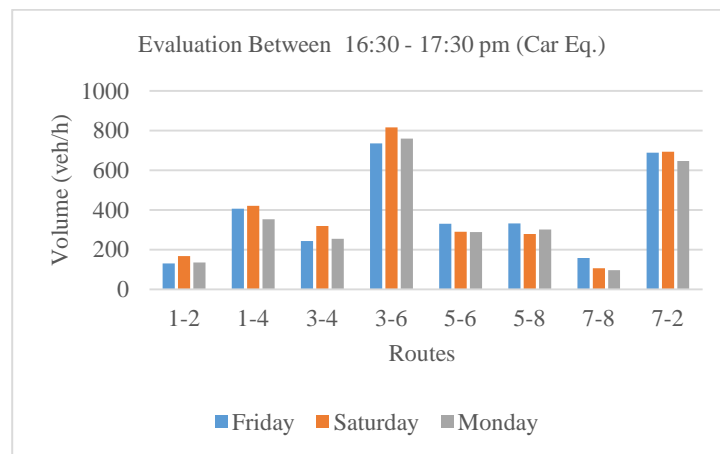


Figure 3. Peak hour volumes

The distribution of traffic volume counting has a similar trend for 3 days in the evening hours.

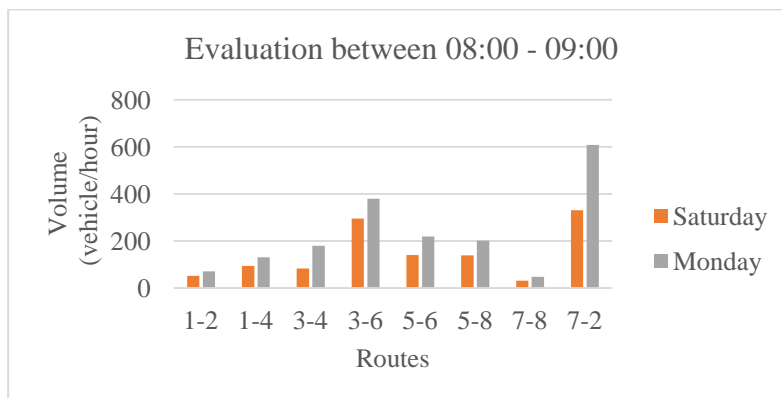


Figure 4. Peak hour volumes

For Saturday and Monday, the higher traffic volume was monitored on morning hours in weekday.

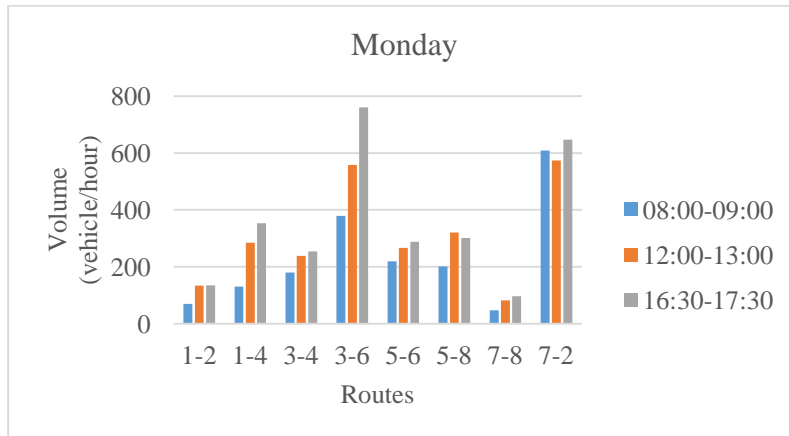


Figure 5. Peak hour volumes

On the evening hours, the higher traffic volume was monitored especially Menderes-Karayolları routes for Monday.

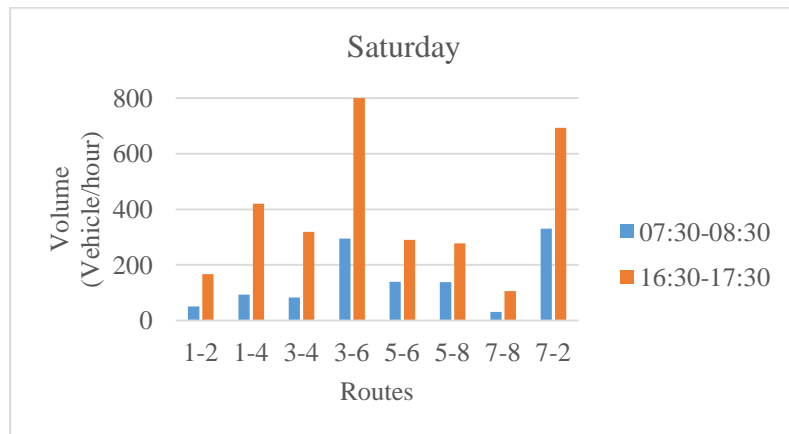


Figure 6. Peak hour volumes

Weekend traffic in the morning compared to the evening traffic at a very minimal level.

3.EVALUATION OF MEASURES AND RESULTS

After the model is calibrated, the current state was compared with the proposed results in terms of travel times, delay, queue length, CO emissions and fuel consumption. Two and three phase signalization program and grade separated junction was modeled for alternative solutions for Yakutiye junction (Figure 7-8). In the modeling, it was focused that the pedestrian safety was increased.

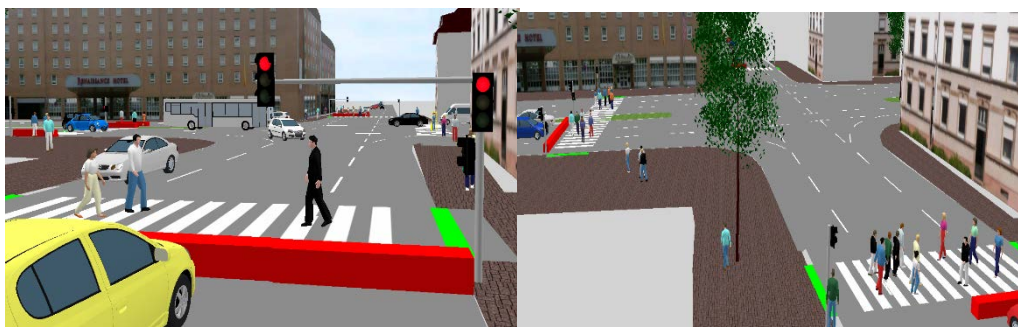


Figure 7. Current and 3 phase signalization



Figure 8. Three phase signalization and grade separated junction

In current signalization program, the vehicles which turn right, do not stop for the pedestrian crossing. Therefore, the fatal crashes for pedestrians are inevitable. The proposed alternatives were aimed to avoid the traffic accidents in the pedestrian crossing. Primarily, 3 phase signalization program was proposed for the pedestrian safety. In this signalization program, the north-south and the east-west direction are open in the first and second phase respectively. In the third phase, vehicles in all directions was stopped and pedestrians phase was opened for 10 seconds. Secondly, two phase signalization was proposed. In this signalization program, north-south and the east-west directions are open respectively. However, the vehicles which turn right wait for pedestrian crossing for 10 seconds. There is a protective time of 5 seconds between first and second phase. Therefore, no congestion occur in the junction. Thirdly, grade separated junction was proposed in the east-west direction. The results for all situations are given in Figure 9 – 13.

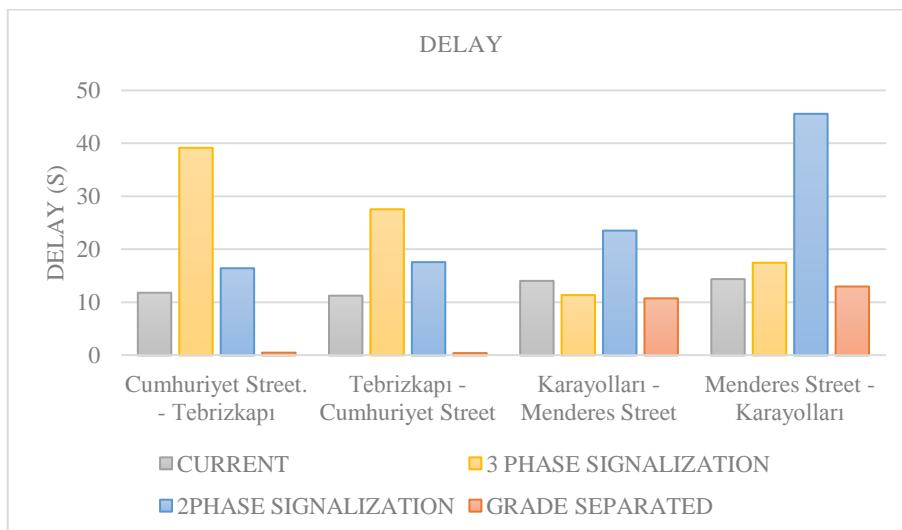


Figure 9. Delay results

According to the delay results, 2 and 3 phase signalizations have more delay time than current signalization program. Actually, this is undesirable situation. However, pedestrian safety is in the worst case in the current state. Because no pedestrian phase was included. In 2 and 3 phase signalization, pedestrian phase added to program. Therefore delay time increased as expected



Figure 10. Travel time results

According to the travel time, the results obtained were usually close to each other. Besides, the more travel time results were obtained for 3 phase alternative. The highest travel time value were found for 3 phase alternative and Menderes-Karayolları Street route. This route has the maximum traffic volume.

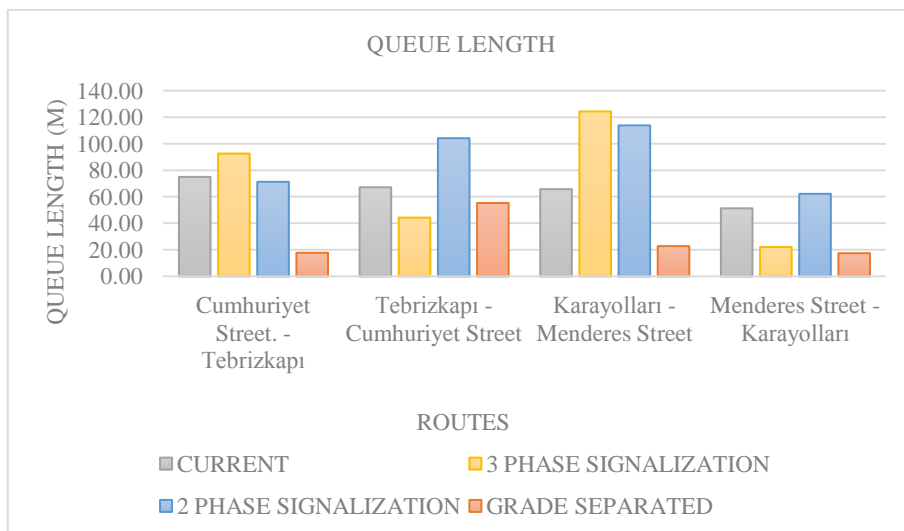


Figure 11. Queue length results

Grade-separated alternative has the best results for queue length. Generally, 3-phase option for higher queue lengths were obtained.

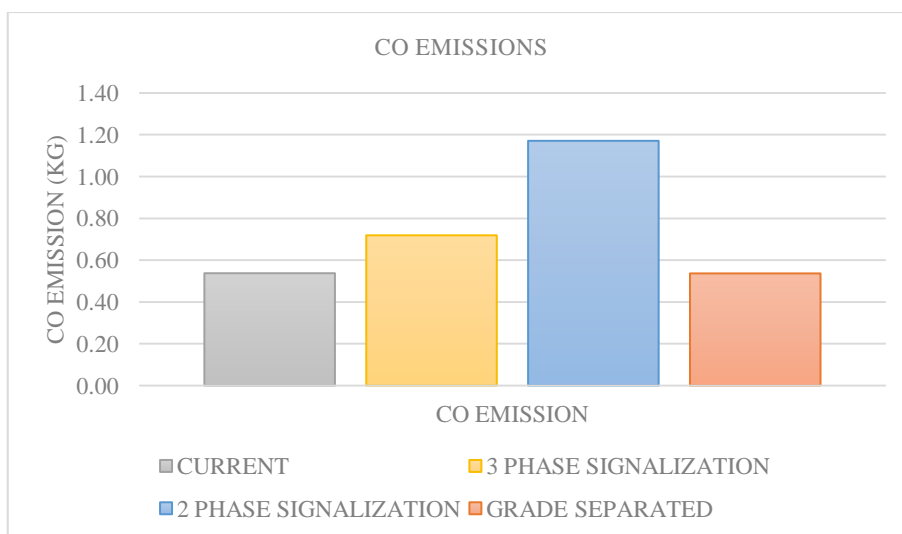


Figure 12. CO emissions results

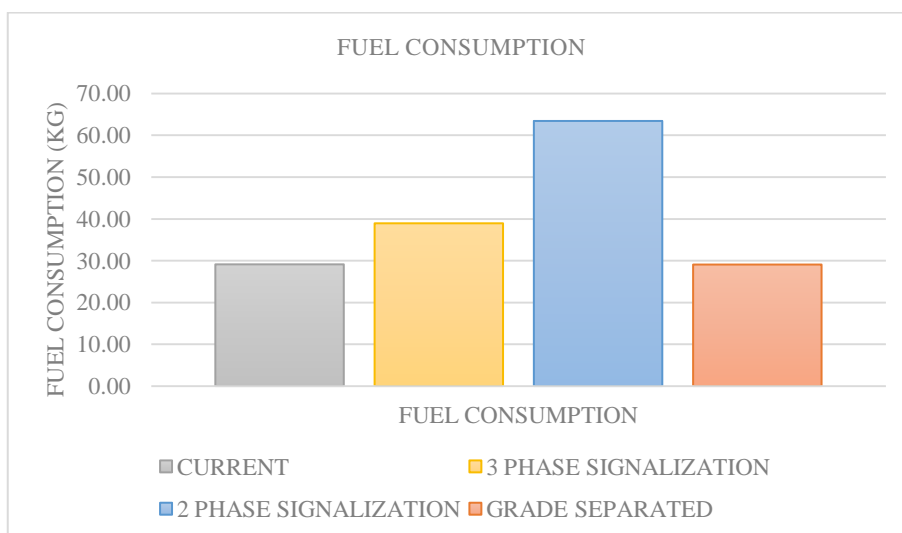


Figure 13. Fuel consumption results

For fuel consumption and CO emission, the higher results were obtained to 2 phase alternative. Because waiting again at right-turn is effected for CO emissions and fuel consumption.

4.CONSLUSION

In this study, the pedestrian safety was tried to increase by changing the current signal program with different signal programs and grade separated junction. Although the delay, travel time, queue length, CO emission and fuel consumption were increased for all alternative solutions, the pedestrian safety was ensured by adding extra pedestrian phases. The following conclusions can be drawn:

- Yakutiye Junction is analyzed with different three alternatives by VISSIM.
- The minimum delay was obtained for the alternative of grade separated junction.
- Maximum delay was occurred for the 2 phase signalization in the route of Menderes Street to karayolları.
- The travel time was increased in the range of 2% and 45%.
- Queue length was increased for some routes and decreased some routes.
- Maximum CO emissions and fuel consumption was occurred in the 2 phase signal program.
- Pedestrian safety was ensured by improving pedestrian phase signalization.

- Grade-separated alternative has the optimum results but it is not useful because of the construction cost

REFERENCES

- [1]. Y. Ş. Murat and Ö. Baskan, "Modeling vehicle delays at signalized junctions: Artificial neural networks approach", *Journal of Scientific & Industrial Research*, 2006, Vol. 65, July 2006, pp. 558-564.
- [2]. B. Park, and J. Schneeberger, Evaluation of traffic signal timing optimization methods using a stochastic and microscopic simulation program, Virginia Transportation Research Council, 2003.
- [3]. J. Golias, Effects of signalization on four-arm urban junction safety. *Accident Analysis & Prevention*, 1997, 29, 181 – 190.
- [4]. Burghout W & Wahstedt J., Hybrid traffic simulation with adaptive signal control. *Transportation Research Record*, 2007, 191-197.
- [5]. Truong LT, Sarvi M, Currie G & Garoni TM., Required traffic micro-simulation runs for reliable multivariate performance estimates. *Journal of Advanced Transportation*, 2015.
- [6]. Shankar K, Prasad C & Reddy T., Evaluation of Area Traffic Management Measures Using Microscopic Simulation Model. *Procedia-Social and Behavioral Sciences*, 2013, 104, 815-824.

A Study On Junction Performance Analysis: Dörtyol Junction Sample (Erzincan, Turkey)

Halim Ferit Bayata^{1}, Fatih Hattatoglu², Muhammed Ali Colak¹, Osman Unsal Bayrak²,
F. Irfan Bas¹*

Abstract

Erzincan city located in northeast Anatolia of Turkey has annual average daily traffic of 5250 and the road of D-80 transit interurban road pass here. 2015 central population of Erzincan is 135.000. The number of registered vehicles in traffic is about 48.166 according to the Turkish Statistical Institute. The city with high vehicle density (a vehicle per three people) is located in an earthquake zone. Therefore, settlement grow up through east to west direction. Moreover, current rural and arteries are insufficient for vehicle intensity. Thus, queue length, delay and travel time increase in junction which are more effective on capacity. It will be a rational approach to design junctions balancing the comfort expectations of drivers and safety requirements.

In this study, Dörtyol junction located on the Halit Paşa Street and intersection of Ordu St. - 13 Şubat St.- Fevzi Paşa St. was investigated. For this junction, the peak traffic value is reached at noon and approximately 3500 vehicles use the intersection during the peak hours. Due to queue lengths at this intersection, negative situations and other problems for drivers occur. It is expected that this problem will increase in the coming years and solutions would be difficult. Revision of the existing signal program, roundabout junctions, new by-pass roads in south and north side and graded junctions was proposed as a solution for the traffic problems. In this study, the junction was modeled with a microsimulation technique and compared with the proposed solutions in terms of delay, travel time, queue length, fuel consumption, CO emissions. VISSIM program was used for simulations and optimum solution was proposed according to the simulation results.

Keywords: *Erzincan, Dörtyol junction, microsimulation, traffic management*

1. INTRODUCTION

Erzincan is a city located in eastern Turkey, altitude of around 1350 m, with a population of 130.000. It is a residential area with administrative boundaries of the 11795 km² and 600 km² of lowland area. Due to its geopolitical position, it is in the city's transportation network with many of the intersections and connections. 223 km section of the E-80 (D-100) highway passes in the east-west line with 5250 vehicle Average Annual Daily Traffic (AADT) value. At the same time in the same direction, Baku-Tbilisi-Kars line connects in a railway line with the the İstanbul-Eskişehir-Mersin line. Karasu River with an international importance, the Baku-Tbilisi-Ceyhan oil pipeline, the Shah Deniz Pipeline and Iran Pipeline pass through Erzincan. Due to geopolitical situation of the province, Turkey-Austria gas line construction and two gas pipeline construction Erzincan-Trabzon and Erzincan-Rize are ongoing. At the same time, the railroad construction which will perform the connection of Trabzon port to the Mediterranean port along the north-south line is ongoing. Erzincan has an international airport and this increases the significance of the city's transport network. Besides all these developments, traffic and congestion problems have been increasing and these problems remain to be solved.

Traffic congestions are caused by insufficient capacity on the volume of traffic control and management. Although the main reasons of congestion vary from country to country, inadequate control is the main reason. Effective control mechanisms are closely related primarily with the infrastructure and junction type selection [1]. Traffic management in intersections is an issue that should be carried out with the parameters as peak hour speed limits in order to increase the capacity, delay controls, signal management and so on. In this regard, delay time of the current situation and travel time parameters are used in assessing the performance of the junction or junction capacity analysis. Delays reveal because of the time of drivers, passengers and pedestrians lost outside of their control, signalization, stop and road signs, expiry of the line capacity and unpredictable traffic accidents. Delays on the road reveal due to reduced opportunities of the vehicles to pass each other and reduced speed of the vehicles caused by the high traffic density. Any obstacles on the route also cause slowing down or stop. Intersections and pedestrian crossings on a road and / or parked vehicles are seen as an obstacle for traffic [2]. Traffic delays, occurring queues and travel time are the most important parameters in determining the evaluation of the adequacy of the line lengths, the efficiency of the intersection and fuel consumption [2].

The most appropriate junction type selection is critical for traffic management and is one of the most important criteria to create an efficient road network [3]. Using traffic signalization instead of traffic signs for a road with low volume traffic may cause redundant delays and because of this situation junction performance and capacity are reduced. Therefore,

¹ Corresponding author: Erzincan University, Department of Civil Engineering, 24100, Erzincan, Turkey. *hfbayata@erzincan.edu.tr; macolak@erzincan.edu.tr; fatihirfan@gmail.com

² Atatürk University, Department of Civil Engineering, 25240, Erzurum, Turkey. fhattat@atauni.edu.tr, unsalb@atauni.edu.tr

investors must take care of selecting the appropriate type of junction and must evaluate according to the choice with some parameters. In many regions of our country signalized intersections, roundabouts, priority intersections, four-arm junction, three-arm intersections and T-junctions are preferred. During the intersection selection process, results can be seen in advance by performing simulation before construction [4].

Usage of improved simulation programs is spreading day by day for modeling and evaluation of the traffic in the urban transportation system and the operation of the public transport systems (bus, light rail system etc.) [5]. VISSIM is one of the programs in this field which is behavior-based and discrete time microscopic simulation program. VISSIM is an important tool applied for planning urban transportation and solving a variety of traffic problems [6].

In this study, it was focused that queue lengths were investigated for Dörtüyl junction with the intersections of Ordu Street, 13 Şubat Street and Fevzipaşa Street in Erzincan city Halit Paşa Street. As a solution proposal, revision of the existing signalization program, roundabout junction construction, new by-pass roads on the south and north directions, alternatives for different level junctions were improved and simulated with micro-simulation modeling technique. Delay, travel time, queue lengths, fuel consumption, CO emissions parameters were considered for assessment. Optimum solution was proposed according to the results.

2.MATERIAL AND METHOD

2.1.Study Area

Erzincan city takes place at an important point in terms of roads and power lines and its importance is increasing with each passing day (Fig.1). 48.166 vehicles are registered in Erzincan according to 2015 TUIK data. Considering the central district population, every three people have one vehicle in Erzincan province. Due to the building density and gathering of the business centers in this location, business centers are gathered around 450 meters of the city center (Fig.2). Queue lengths have been reached 150-200 meters at peak traffic hours. Constructions have been caused east-west direction in the city and according to this; transportation network shows the development in this direction (Fig 2).

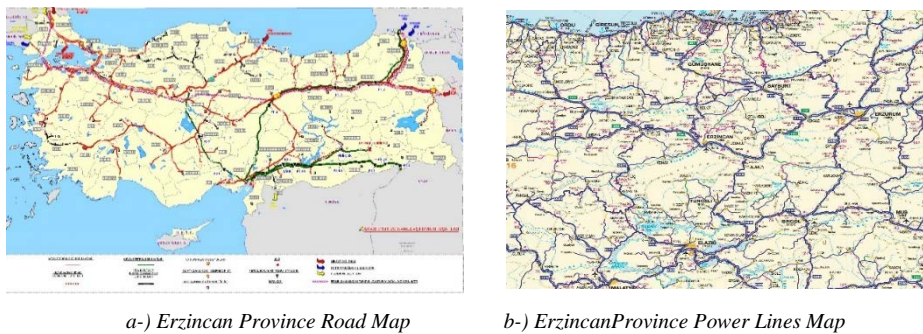


Figure 1. Erzincan City Road and Power Lines

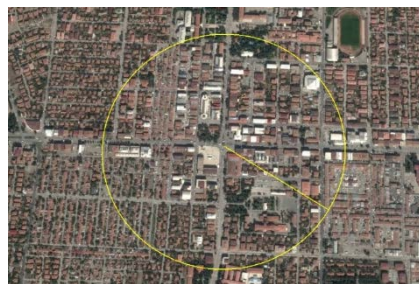


Figure 2. City Business Centers Workspace (Scaled - Business centers are gathered around 450 meters of the city center)

In the study, Dörtüyl junction located in Erzincan city center was examined. Dörtüyl junction is a mini roundabout double-lane signalized intersection. Central island circle diameter is 16.5 m, and the outer circle diameter is 46 m (Figure 3).



Figure 3. Dörtyol Junction Workspace

As a result of peak hour measurements obtained on a weekly count was given in Figure 4. The resulting counts were given in car equivalent values. Monday midday hours are the peak hours according to the traffic count. For the models prepared in this study, Monday midday counts were taken into account. In terms of being in the region's trade area, the occurrence of peak hour traffic is expected at midday.

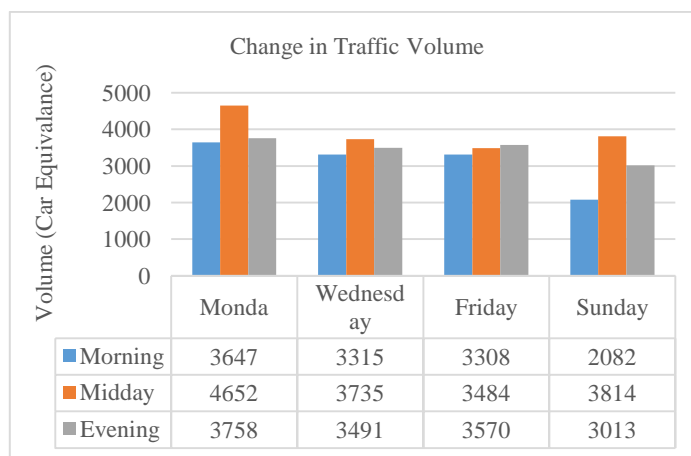


Figure 4. Change in Traffic Volume

The distribution of traffic at midday on Monday was given in Figure 5.

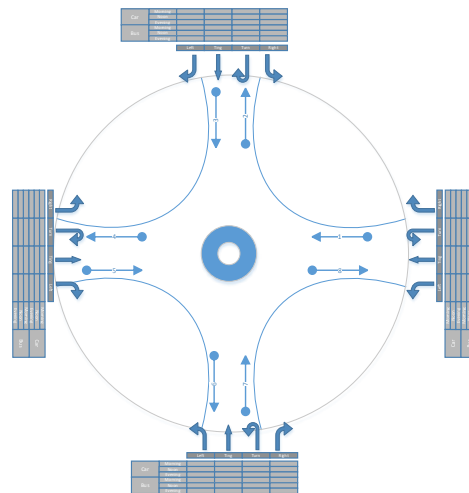


Figure 5. Distribution of traffic according to the directions at peak

Dörtyol junction is managed as signalized in the current state. In the current signalize program, uniform programming has been used for all days and same durations have been used for different hours at the junction. Because of the long queue lengths, all of the vehicles could not pass through the junction during the green traffic light. Queue lengths observed in the field for No.5 route having the highest value was given in Figure 6.

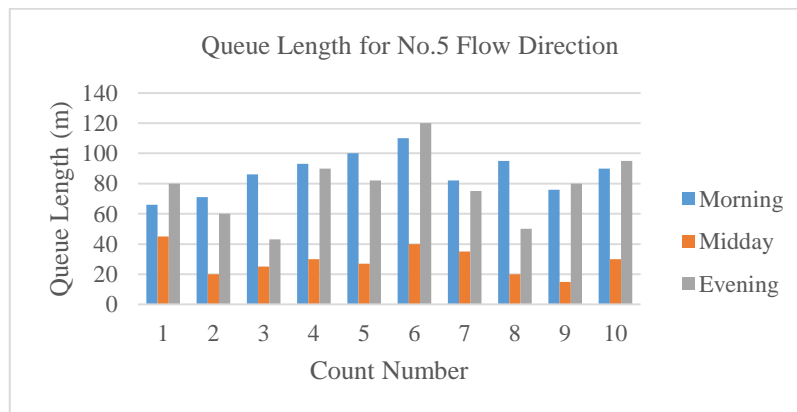


Figure 6. Average Queue Lengths at Peak Hours at No. 5 Flow Direction

Dörtyol junction was modeled with VISSIM software. The established model was given in Figure 7. For calibration, traffic counts conducted previously in the investigated corridor, traffic volumes were accepted as a parameter. In order to gather the traffic volumes from the simulation program, the collectors called as “Data Collection Point” are located. Required flow rates in the required parts of the road, so traffic volumes can be achieved with the help of these collectors. The values obtained counting results, the values derived from the simulation and their error evaluations were given in Table 1. Established simulation model for the existing situation reflected the real traffic conditions.

Table 8. Evaluation of the simulation values with counting values

Dedector No	Counting Value	Simulation Value	Relative Error
1	300	321	-0,07
2	300	321	-0,07
3	400	393,2	0,02
4	400	393,2	0,02
5	372	401,8	-0,08

2.2. Proposed Alternative Solutions

Revision of the existing signaling program of Dörtyol junction, modern roundabout, new by-pass roads at south and north directions and grade separated junction construction alternatives were investigated in this study.

Existing active signalization program for the junction is a 4-phase program, fixed termed and runs the same program for every day of the week. Same periods have been used during the day. Existing signaling periods are given in Table 2. Because of the ignorance of traffic composition and queues occurred in the junctions, rearrangement of the existing signalization programs is planned as an alternative.

Table 9. Existing Signalization Program (Red durations)

	Morning	Noon	Evening
1st arm	43	43	43
3rd arm	48	48	48
5th arm	43	43	43
7th arm	48	48	48

Roundabouts can offer higher capacities / lane opportunities due to lack of time-consuming red and yellow lights on the signalized intersections [7]. Roundabouts endorse the drivers to reduce their speeds while entering the junctions and have an aim to obviate possible accidents that may occur or to reduce the severity of the accidents [7]. It has been observed that a lot of accidents happen at this junction, because of this situation a new alternative is proposed as a roundabout style junction construction. In many researches, it is stated that this type of intersection reduces accidents and permits a more effective traffic management. In this study, modern roundabouts were examined as an alternative.

Existing roads in Erzincan city have limited lane widths and have no possibility of expansion. Therefore, the existing roads will be inadequate in a probable traffic increment which may occur in the future. In order to avoid the congestions, reducing the density of the existing roads by constructing new bypass roads alternative was examined.

As a last alternative, grade separated junction design was planned. These type of junctions have no delays but have a high construction cost and can be planned in the long term. Considering the traffic density of the other junctions on the main road, construction of grade separated junction on east-west direction was planned.

3.RESULT AND DISCUSSION

Obtained results for alternative were shown as below. The assessment of alternative was made according to the parameters of delay, travel time, queue length, Co emission and fuel consumption.

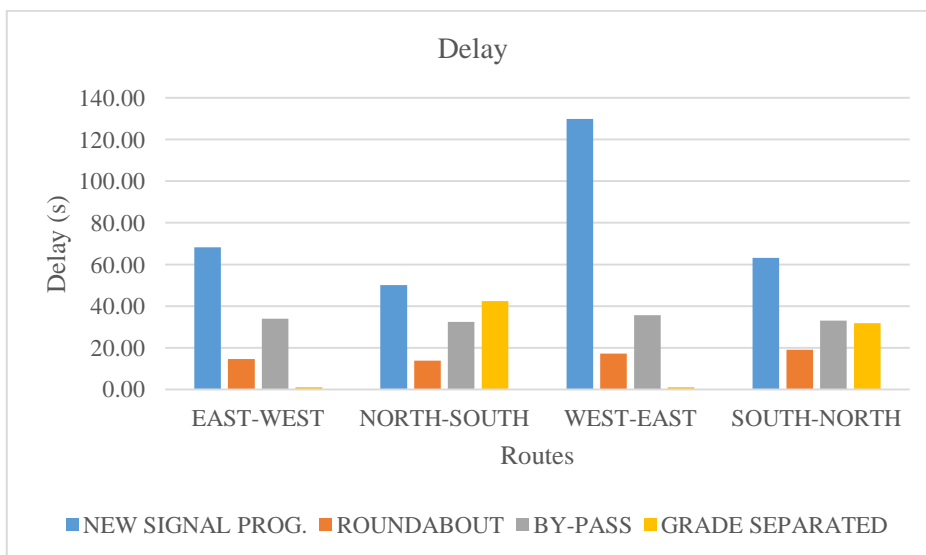


Figure 7. Delay results for alternative solutions

Minimum delays were obtained for roundabout alternative. Long delaytimes were obtained for the new signal program. There is no delay atleast-west direction for grade separated junction. The most appropriate alternative in terms of delay is roundabout junction.

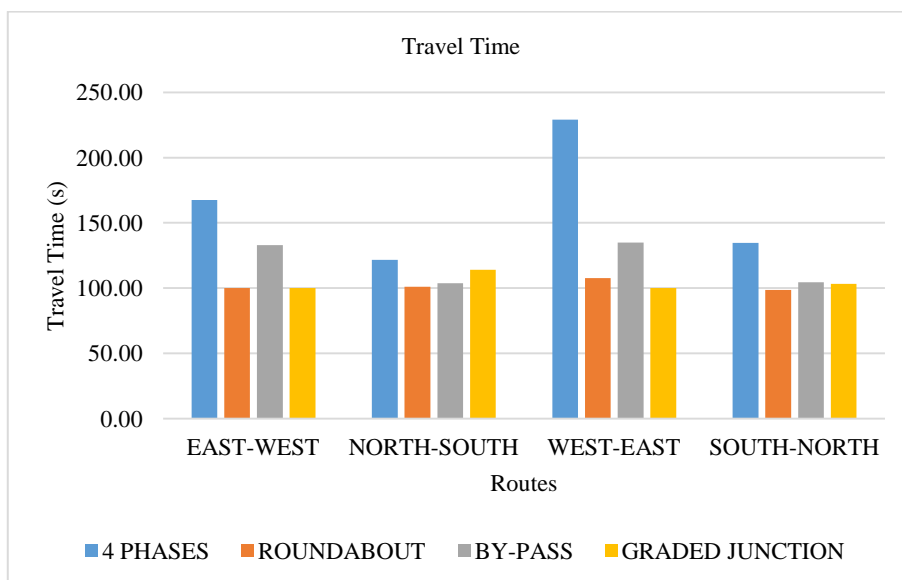


Figure 8. Travel Time results for different alternatives

Similar results were obtained for all routes except new signal program in terms of travel time. These three alternatives are found appropriate in terms of travel time.

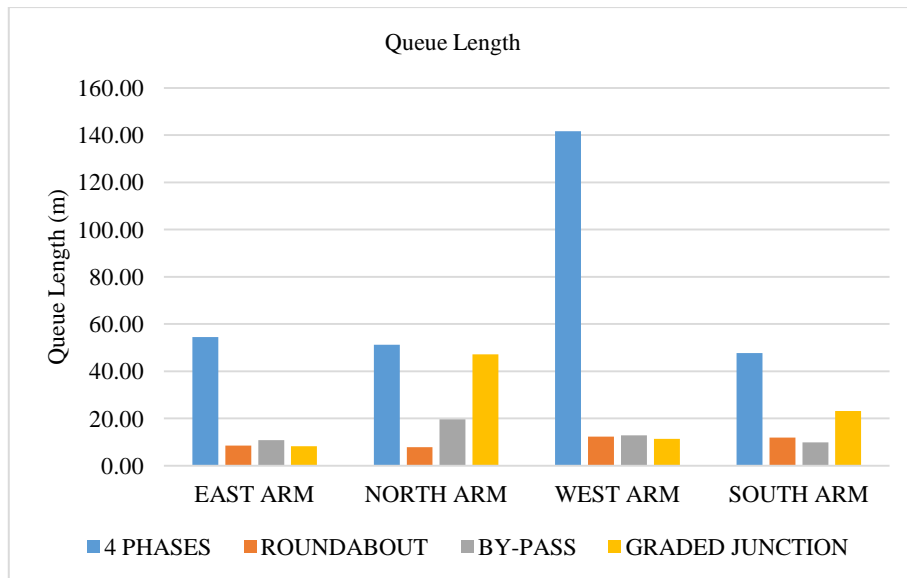


Figure 9. Queue length results for alternative solutions

High values were found for new signal program in terms of queue length. It was found to be the second most inappropriate option for grade separated junction at north and south directions.

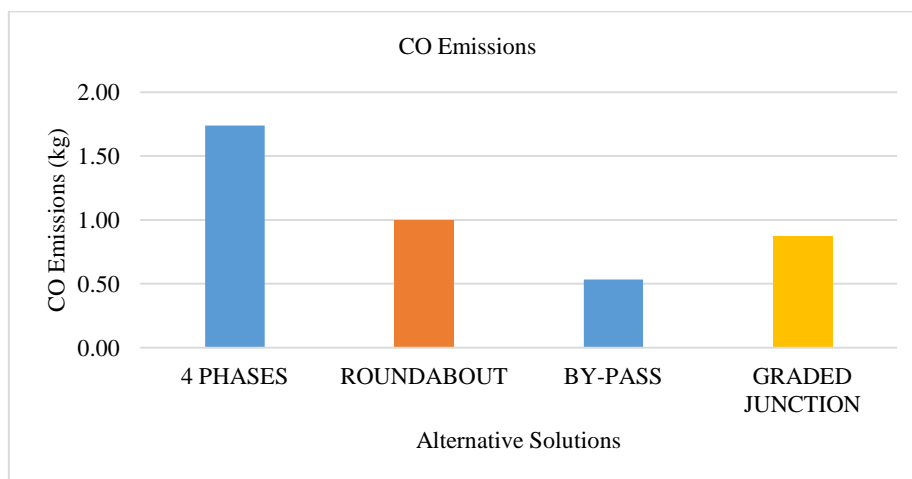


Figure 10. CO emissions results for different alternatives

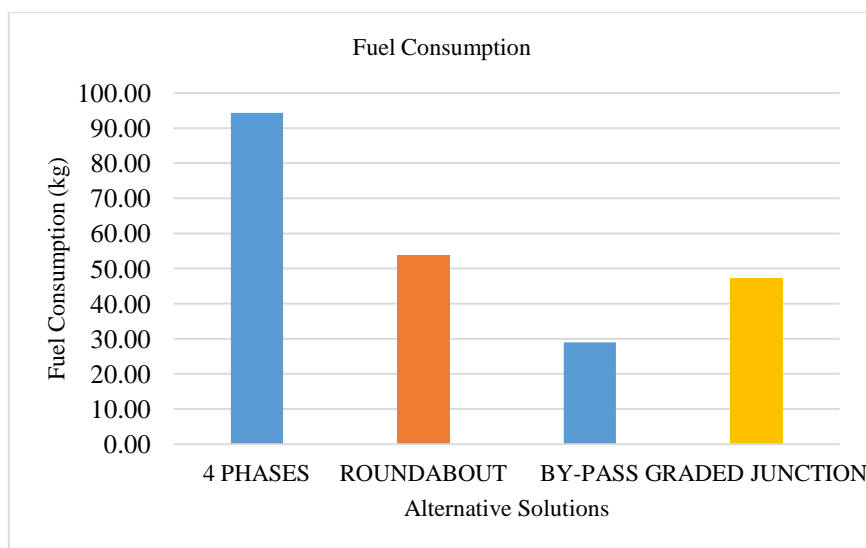


Figure 11. Fuel consumption results for different alternatives

It is the most appropriate option in terms of fuel consumption and CO emission because the decrement of the traffic volume from the junction at bypass option. New signal program was found to be the worst case and the other options were found close to each other.

4. CONCLUSION

In this study, Dört Yol junction located on the Halit Paşa Street and intersection of Ordu St. - 13 Şubat St. - Fevzi Paşa St. was investigated. Revision of the existing signal program, roundabout junctions, new by-pass roads in south and north side and graded junctions was proposed as a solution for the traffic problems. The junction was modeled with a microsimulation technique and compared with the proposed solutions in terms of delay, travel time, queue length, fuel consumption, CO emissions.

The following conclusions can be drawn:

- Dört Yol Junction was analyzed by VISSIM
- The minimum delay was obtained for roundabout alternative. New signal program has the highest delay values for all alternatives
- All alternative except for new signal program has similar travel time results for all route
- Queue length was decreased for roundabout and by-pass alternative
- Maximum CO emissions and fuel consumption was occurred in the new signal program.
- According to results, roundabout and by-pass alternatives are appropriate solutions.

REFERENCES

- [1]. A. A. Kurzhanskiy and P. Varaiya, "Traffic management: An outlook", *Tech. Rep.*, 2014
- [2]. Altun İ., 2003. Sinyalizasyon Kavşaklarında trafik akım etkileşimleri, Yüksek Lisans Tezi, Dokuz Eylül Üniversitesi.
- [3]. https://tr.wikipedia.org/wiki/Karayolu_kapasitesi
- [4]. Murat, Yetis Sazi, et al. "Analytical Hierarchy Process (AHP) based Decision Support System for Urban Intersections in Transportation Planning." *Using Decision Support Systems for Transportation Planning Efficiency* (2015): 203.
- [5]. Kopal B, 2011. Boğaziçi Köprüsü Üzerindeki Trafik Sıkışıklığının Hiz Yönetimi Yöntemiyle Azaltılması, Yüksek Lisans Tezi, Bahçeşehir Üniversitesi.
- [6]. Siddharth, S. M. P., and Gitakrishnan Ramadurai. "Calibration of VISSIM for Indian heterogeneous traffic conditions." *Procedia-Social and Behavioral Sciences* 104 (2013): 380-389.
- [7]. HAttatoglu F., Bayata HF, Çolak MA., Bayrak OU, 2015. Erzincan İli N. Muratoğlu Meydanı Kavşağı İçin Farklı Alternatiflerin Mikrosimülasyon Modellemelerinin Değerlendirilmesi, ROTRASA.

Utilization of Melamine Impregnated Paper (MIP) and Urea Formaldehyde (UF) Adhesives in Different Layers of Particleboard

Fatih Mengelolu¹, Ibrahim Halil Başboga², Kadir Karakus³, Ilkay Atar⁴

Abstract

In this study, various amount of waste melamine impregnated paper (MIP) and urea formaldehyde (UF) adhesives were used both in surface and core layers of the three layer particleboard. Four types of particleboard were manufactured. First panel had 9% UF on the surface layers and 15% MIP in the core layer while second panel had 12 % UF on the surfaces and 20% MIP in the core. In the third panel 15 MIP was used on the surfaces and 9% UF in the core layer while 20% MIP was on the surfaces and 12% UF in the core layer. Mechanical and physical properties including bending strength, modulus of elasticity, internal bond strength, surface stability, thickness swelling and water absorption of the samples were determined according to EN 310, EN 319 and EN 317 standards, respectively. As results of this study, amount of adhesives and where they used had significant effect on panel properties. Utilization of UF adhesives in surface layers and MIP in the core layer improved internal bond strength, bending strength and modulus of elasticity of the panels. For other properties, enhanced panel properties were achieved with the use of MIP on the surface layers and UF in the core layer.

***Keywords:** Particleboard layer, melamine impregnated paper waste, mechanical and physical properties, waste management*

1. INTRODUCTION

The supply of raw materials are decreasing with rapidly population growth, depletion of natural resources and increasing demand for raw material. Consequently, the costs are rising. Environmental friendly and recycling-oriented technologies are used for sustainable production due to the risk of natural resources depletion [1].

Particleboards are large surface boards which combining particles and thermoset resin (urea formaldehyde, melamine formaldehyde, phenol formaldehyde, etc.) under high temperature and pressure conditions. Particleboards generates wastes such as particles with resin, melamine impregnated paper (MIP), non-standard board, etc. Portion of them were reused in manufacturing panels while some other were utilized for generating energy [2].

Melamine impregnated paper (MIP) is decorative paper for wood based boards coating. Two different type of MIP waste occur during particleboard manufacturing. First one is obtained when the neat décor papers were impregnated (in the impregnation line) with melamine urea formaldehyde and other chemicals. Second one is from melamine press during coating with of the melamine impregnated papers on the boards. Two and half million of MIP wastes occur for a year in the middle-size middle density board plant which uses 420 million m²/year MIP, approximately.

MIP contains chemicals (adhesives, curing agents, crosslinking agents, etc.) and it is not suitable for generating energy through burning them. It is required special running boilers at higher temperatures [3]. Researches have looked for alternatives to utilize these wastes. In another study [4], grinded MIP with hammer-mill the size of 2-3mm and utilized them with glued fibers in fiberboard manufacturing. It was reported that mechanical properties approved with the adding of MIP. In another study, Alpar and Winkler [5] have used MIP powder in the manufacture of particleboard as a both filler and adhesives. As a result, no significant differences were found between particleboard manufactured with UF adhesives and the one with MIP powder. In this study, single-layer particleboards were manufactured and there is no information about MIP size. Commercial particleboards have three layers. Mechanical and physical properties show differences according to layers characterizations [6]. Akbulut [7] reported that, particle rate for between layers and also board type (three-layers or homogenous board) have significant effect on some mechanical properties of particleboards.

¹Kahramanmaraş Sutcu Imam University, Department of Forest Product Engineering, 46100, Onikişubat/Kahramanmaraş, Turkey. fmengelo@ksu.edu.tr

² Corresponding author: Kahramanmaraş Sutcu Imam University, Department of Forest Product Engineering, 46100, Onikişubat/Kahramanmaraş, Turkey. ihbasboga@ksu.edu.tr

³Kahramanmaraş Sutcu Imam University, Department of Forest Product Engineering, 46100, Onikişubat/Kahramanmaraş, Turkey. karakus@ksu.edu.tr

⁴Kahramanmaraş Sutcu Imam University, Department of Forest Product Engineering, 46100, Onikişubat/Kahramanmaraş, Turkey. iatar@ksu.edu.tr

In this study, utilization of melamine impregnated paper (MIP) and urea formaldehyde (UF) adhesives in different layers of particleboard was investigated. On this purpose, three-layer particleboards were manufactured with two different rates of MIP (15%, 20%) and UF (9%, 12%) in different layers for this study. Mechanical and physical properties of the samples were determined according to TS EN 310, TS EN 319, TS EN 311 and TS EN 317 standards.

2. EXPERIMENTAL

2.1. Materials

Particleboards were produced utilizing waste melamine impregnated paper (MIP) and urea formaldehyde (UF) as adhesives and 2 different types of particle (fine and coarse). MIP waste was got from the impregnation line of Kastamonu Integrated Adana MDF Facility. UF (65% solid content) was also prepared in the same plant. Particles were obtained from Kastamonu Integrated Tarsus Particleboards Facility.

2.2. Particleboard Manufacturing

Waste melamine impregnated paper (MIP) granulated in Pulverizator with cooling capabilities into the flour form. These flours, screened and passed from 0,1mm sieve, were used as an adhesive in this study. Urea formaldehyde (UF) was also used as an adhesive. UF was applied by spraying method. Fine particles were utilized in surface layers (SL) while coarse ones in core layer (CL). Four different particleboards with three layers (two surface layers and one core layer) were manufactured. The experimental design of the study was presented Table 1. The core layer was accounted for 67% of the total board weight. Surface layers were contained 33% of the total board weight.

Table 10. Manufacturing schedule of Particleboards

Board-Type	Layer	MIP (%)	UF (%)
I	C *	15	0
	S **	0	9
II	C	20	0
	S	0	12
III	C	0	9
	S	15	0
IV	C	0	12
	S	20	0

*C : Core Layer
**S : Surface Layer

Depending on the formulation particles and MIP were dry-mixed in a high-intensity mixer to produce a homogeneous blend. In addition, UF resin was applied with spray gun according to formulation in Table 1. Ammonium Chloride (1% for SLs, 2% for CL) was added to UF resin for short curing time in process before the spraying. The blends were laid into frame of 500mm x 500mm. A hot press was used for forming of particleboards (0,5-4,8 MPa). The target thickness was 19mm. Pressing time and temperature were 240s and 200 °C, respectively. After pressing, particleboards were conditioned at a temperature of 20 °C and 65% relative humidity. The conditioned boards were cut from four edges and grinded until their thickness was 18mm. Then test samples were cut according to TS EN standards.

2.3. Particleboard testing

Testing of the samples was conducted in a climate-controlled testing laboratory. Densities were measured by air-dried density method according to the TS EN 323 standard. Bending strength, modulus of elasticity, internal bond strength, surface stability, thickness swelling and water absorption of the samples were determined according to TS EN 310, TS EN 319, TS EN 311 and TS EN 317 standards, respectively. Five samples for each group were tested. Mechanical properties testing were performed on Zwick Z010 (10KN).

3. RESULTS AND DISCUSSION

Particleboards were produced in the density range of 657-717 kg/m³. In this study, mechanical (bending strength, modulus of elasticity, internal bond strength and surface stability) and physical (thickness swelling and water absorption) properties of all samples were determined. All data of the study were summarized in Table 2. The arithmetic mean and standard deviation values were given for each group in the table.

Table 2. Mechanical properties of Particleboards

Board-Type	Bending strength (MPa)	Modulus of elasticity (MPa)	Internal bond strength (MPa)	Surface stability (MPa)	Thickness swelling (%)	Water absorption (%)
I	14,77 (1,36)*	2739,24 (121,76)	0,405 (0,015)	0,85 (0,08)	28,09 (1,38)	77,95 (2,47)
II	18,53 (2,37)	3202,67 (190,98)	0,538 (0,08)	1,20 (0,19)	19,30 (1,27)	67,25 (0,89)
II	11,75 (1,29)	2390,06 (110,00)	0,155 (0,04)	0,61 (0,13)	36,14 (1,94)	77,44 (3,80)
IV	16,52 (2,49)	2974,90 (222,52)	0,373 (0,09)	0,90 (0,20)	19,43 (1,45)	61,88 (3,26)
Standard	≥ 13	Min. 1600	≥ 0,35	≥ 0,8	Max. 15	Max. 80

* Values in parenthesis are standard deviations.

The graph of internal bond strength was given in Figure 1. X axis refers to board-type. Based on results, internal bond strength increased with rising of both MIP and UF rate in the layers. The best result was obtained from board-type II. However, board-type I and board-type IV with 9% differences have nearly closer internal bond strength values. Coarse particles included 4,5-5% moisture while fines 4,1-4,6% moisture content. MIP also has nearly same as fine particles' moisture content (4-4,5%). The manufactured boards were formed 63% Coarse and %37 fine particles content. With the spraying of the UF resin, moisture content increases 10-12% for particles, approximately. That means particle moisture reaches 15-17%. To mention for board-type IV, using of UF in the core layer raised to moisture content from 4,5-5% to 15-17%. In addition, using of MIP in surface, that caused to low moisture content (4-5%, approximately). That is also caused to poor heat transmission for core layer. It is also mean poor curing reaction. It is thought that, this is the one of the reason for low property values when UF was used in core layer. The liquid spraying method on surface of particleboard is known as a conventional method for better plasticization on surface and high modulus of elasticity. This method also helps to heat transmission. However, Liiri reported that [8], increasing of moisture content from 10% to 15% cause to decreasing on bending strength and internal bond strength. In parallel with Liiri's study, Halligan and Schiewind [9] reported that some strength properties reduced with the rising of moisture content. In addition, it is stated in the study of Dexin and Östman [10], when the amount of moisture coming up from 7%, internal bond strength and modulus of elasticity decreased. High temperature and high moisture content are much more effective on the strength values of particleboard [10]. In our study, all board-types except type III provided standards requirements for internal bond strength except third one.

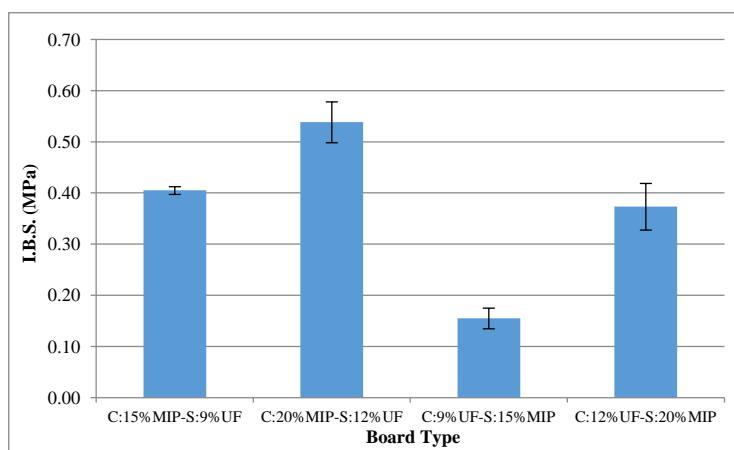


Figure 12. Bar graphs of internal bond strength

The graph of bending strength was given in Figure 2. Depending on the results, with the increasing of MIP and UF in both layers, bending strength increased. Rate of both MIP and UF is significantly effective on bending strength. The best result was observed from second board. All manufactured particleboards satisfied standards requirements for bending strength except third one, like internal bond strength.

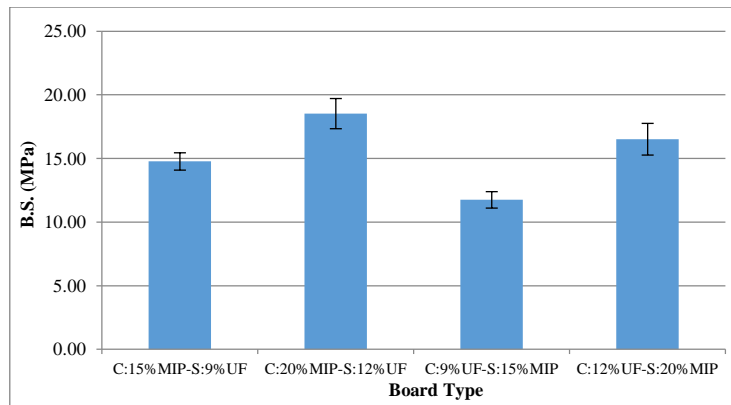


Figure 2. Bar graphs of bending strength

To mention on modulus of elasticity, all observed data was summarized on the graph which was given in Figure 3. With the rising of MIP and UF in different layers, modulus of elasticity was tightly increased. The best result was obtained from second board. The other three has closer value. By contrast with first two given strength properties, modulus of elasticity values for all produced board reached standards requirements.

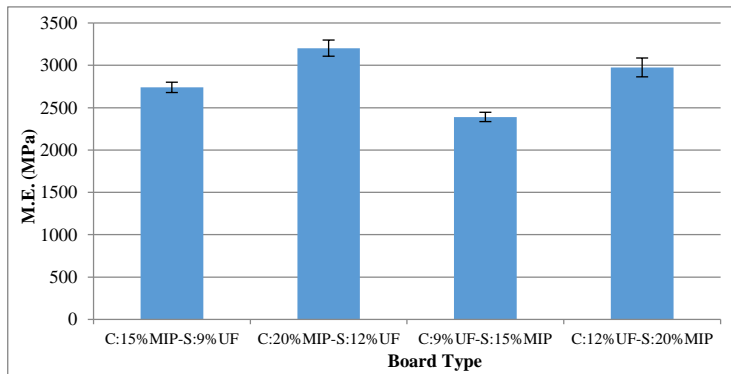


Figure 3. Bar graphs of modulus of elasticity

In figure 4. bar graphs of surface stability properties was shown. Depending on the results, which layer MIP used is effective on surface stability properties. The best result was obtained from second board. First and fourth boards have closer surface stability values. All manufactured particleboards satisfied standards requirements for bending strength except third one. It is thought that, these UF resin was properly dispersed among particles in SL. That might help to explain why the best result for surface stability properties was obtained from board which has 12% UF in SL.

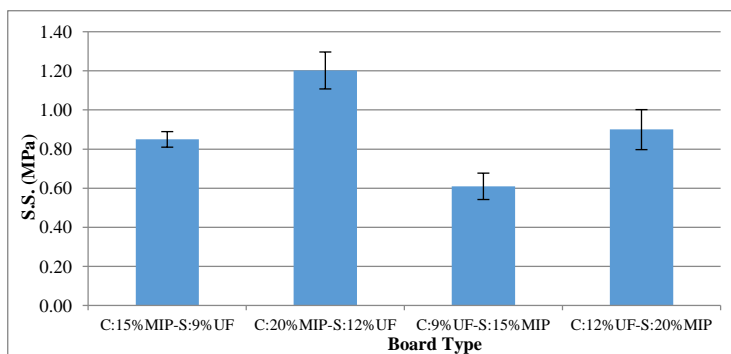


Figure 4. Bar graphs of surface stability

The graph of thickness swelling and water absorption are shown in Fig. 5, Fig. 6, respectively. To mention on the thickness swelling properties, all the manufactured boards was not satisfied standards requirements. However, for water absorption values, all produced boards were reached standards requirements. The best properties were observed from second and fourth boards. That is mean; amount of adhesive is effective on both thickness swelling and water absorption.

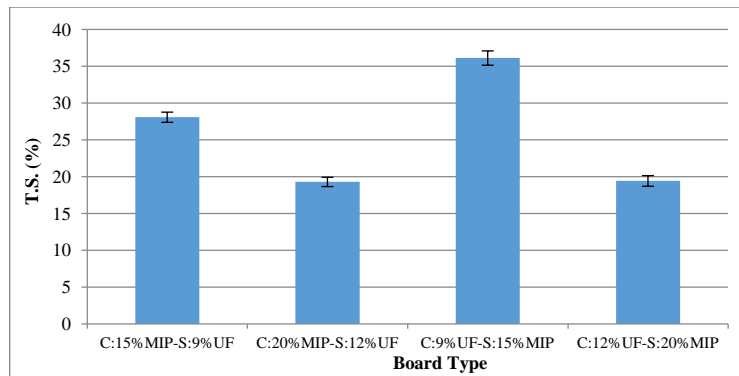


Figure 5. Bar graphs of thickness swelling

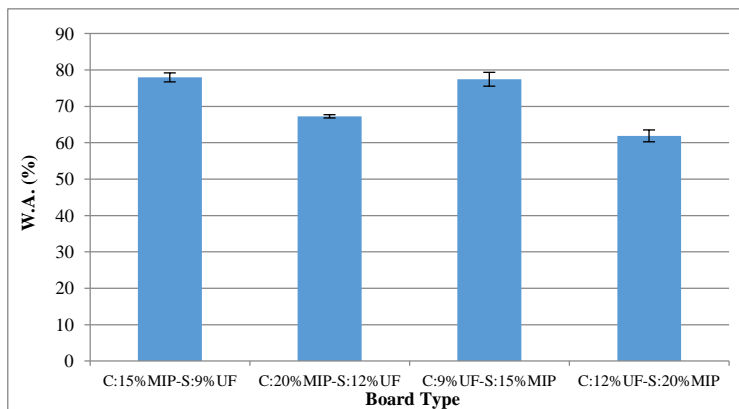


Figure 6. Bar graphs of water absorption

Moreover, all the data and standard requirement were summarized in Table 3. Values matching standards was painted in green and if not, it was painted in red.

Table 3. Summary of Mechanical and Physical properties of Particleboards

BOARD ID	B.S.	M.E.	I.B.S.	S.S.	T.S.	W.A.
1						
2						
3						
4						
Standard Values	≥ 13	Min. 1600	≥ 0,35	≥ 0,8	Max. 15	Max. 80

B.S.: Bending Strength

M.E.: Modulus of Elasticity

I.B.S.: Internal Bonding Strength

S.S.: Surface Stability

T.S.: Thickness Swelling

W.A.: Water Absorption

4. CONCLUSIONS

As results of this study, amount of adhesives and where they used had significant effect of panel properties. Utilization of UF adhesives on the surface layers and MIP in the core layer improved internal bond strength, bending strength and modulus of elasticity of the panels. For other properties, enhanced panel properties were achieved with the use of MIP on the surface layers and UF in the core layer.

Waste Melamine Impregnated Papers (MIP) and Urea Formaldehyde (UF) were successfully utilized as an adhesive in the different layers of Particleboard and the following conclusions were reached;

1. The moisture content of particles is significantly effective on mechanical properties,
2. Type I, type II and type IV boards provided standards requirements for all determined properties except thickness swelling.
3. The best result for mechanical properties was observed from type II board.
4. The effects of particles moisture content on MIP should be investigated with changing of moisture for the particle.

As a result, MIP waste and UF might utilize in different layers for particleboards industry but proper moisture content should be determined.

ACKNOWLEDGMENT

This study was supported by Ministry of Science, Industry and Technology in Ankara. Project number: 870.STZ.2015. Authors would also like to thank Kastamonu Integrated Adana MDF Facility for providing waste melamine impregnated paper (MIP) and particles.

REFERENCES

- [1]. H. Ayboğa, B. ÖKTEM, *Examining The Theoretical Framework Of The Importance Of Recycling In The Product Life Cycle*, Marmara Üniversitesi Öneri Dergisi, 11(44), pp. 173-188, 2015. ISSN 1300-0845
- [2]. F. Mengelöglu, F. Bozkurt, I.H. Başboğa, Ö. Yüce, *Waste Melamine Impregnated Paper (Mip) In Thermoset And Thermoplastic Based Composites*, Pro Ligno, 11(4), pp. 165-172, 2015. Online Issn: 2069-7430.
- [3]. M.C. Barbu, M. Steinwender, *The state of the art for the environmental protection in the European wood based panels industry*, Pro Ligno, 5(2), pp. 85-96, 2009.
- [4]. N. Ayırlmış, *Enhancement of Dimensional stability and mechanical properties of light MDF by Adding melamine resin impregnated paper waste*, International Journal of Adhesion & Adhesive, 33:4549, 2012.
- [5]. T. Alpar, A. Winkler, *Recycling of Impregnated Décor Paper in Particleboard*, Acta Silv. Lign. Hung., (2), pp. 113-116, 2006.
- [6]. T.M. Maloney, *Modern Particleboard & Dry-Process Fiberboard Manufacturing*, Miller Freeman Inc., San Francisco, Update Addition, 681p., 1993.
- [7]. T. Akbulut, *Çeşitli Üretim Değişkenlerinin Yongalevhanın Teknolojik Özellikleri Üzerine Etkisi*, PhD Thesis, İTÜ Graduate School of Natural and Applied Sciences, p268. 1999.
- [8]. O. Liiri, *Investigations on the Effect of Moisture and Wax upon the Properties of Wood Particle Board*, Paperi ja Puu, 42(2), pp 43-56, 1960.
- [9]. A.F. Halligan, A.P. Schiewind, *Prediction of particleboard Mechanical Properties at Various Moisture Content*, Wood Science of Technology, Vol. 8, pp. 68-78, 1974.
- [10]. Y. Dexin, A.L. Östman, *Tensile Strength Properties of Particle Boards at Different Temperatures and Moisture Contents*, Holz als Roh- Lind Werkstoff, Vol. 41, pp. 281-286, 1983.
- [11]. TS EN 310, *Wood based panels determination of modulus of elasticity in bending and of bending strenght*, TSE, Ankara, 1999.
- [12]. TS EN 311, *Wood-based panels - Surface soundness - Test method*, TSE, Ankara, 2005.
- [13]. TS EN 317, *Particleboards and fibreboards – Determination of swelling in thickness after immersion in water*, TSE, Ankara 1999.
- [14]. TS EN 319, *Particleboards and fibreboards- Determination of tensile strength perpendicular to the plane of the board*, TSE, Ankara, 1999.
- [15]. TS EN 323, *Wood- Based panels- Determination of density*, TSE, Ankara, 1999.

Fault Tree Analysis for Transformers and Determination of Maintenance Strategies

Mustafa Sen Yildiz¹, Mugdesem Tanrioven²

Abstract

Transformers have a critical role for power systems to ensure the high quality, continuous and economic power for increasing energy demands. Robust network infrastructure and sustainable maintenance strategy are required for economic operation of the system. Therefore, in order to determine the maintenance strategies and to monitor the strategies in whole economic operation period, it is required to classify the transformers according to the importance level. In this study, fault tree analysis is considered for the critical transformers reliability assessment. The real fault data of power transformers in transmission line is used in fault tree analysis. As a result, the possible reasons of transformer faults are identified, and maintenance strategies for the determined fault types are presented.

Keywords: *Power Transformers, Fault Data, Fault Tree Analysis, Maintenance Strategy*

1. INTRODUCTION

The power systems are complex and nonlinear systems. They include subsystems and components such as generators, switching substations, power lines and loads. Switching substations include disconnect switches, circuit breakers and transformers. The outline shows that transformers has a vital role for power systems, because they adjust electric voltage level to a suitable level on each part of the power transmission from generation to the end user. Therefore, any unplanned interruption of transformer decreases the energy reliability and to cause complexity hospitals, industries, and households. Therefore, it should be observed and to collect fault data, and some predictive methods should be developed and implemented. From this aspect, firstly, transformers should be classified and then it should be determined maintenance strategy for every class.

Transformers are utilized after generation unit to step up the electric voltage to transmission line for bringing to over long distances and to step down electric voltage to transfer distribution system, it is called power transformers. In distribution system, transformers are used different electric voltage level below 33kV for industrial and household, it is called Distribution Transformers [1]. For power transformers, several studies are achieved valuable results about aspect of protection, see for instance [2]–[5].

In this article, fault tree analysis is presented to determine fault of transformers in detailed. When fault tree is shaping, benefited from these studies [6]–[8]. After fault tree analysis, especially for power transformers, it is explained that which maintenance strategy should be used.

2. CONSTRUCTION OF FAULT TREE

Fault tree is often used method to determine causes of an undesired event or state. This method demonstrates all steps from top event to basic event with logical combinations which is explained Table 1 and graphical visualization, showed samples in figure 1 [8].

¹ Corresponding author: Kırklareli University, Department of Electrical and Electronics Engineering, 39100, Kayalı/Kırklareli, Turkey. mustafasenyildiz@klu.edu.tr

² Yıldız Technical University, Department of Electrical Engineering, 34220, Esenler/İstanbul, Turkey. tanriov@yildiz.edu.tr

Table 1. Symbols used in Fault Tree Analysis

Symbol	Designation	Function
○	Basic event	Basic event or failure
◇	Undeveloped event	Cases are not developed
□	Event	Event resulting from more basic events.
◌	Conditional event	Event can occur normally
⌒	AND gate	Output event C occurs only if all input events (A and B) occur simultaneously
⌒	OR gate	Output event C occurs if any one of the input events occurs
△	Transfer symbol	Indicates that the tree is developed further at another place

Fault tree analysis has been developed since 1960. In [9], the development of fault tree analysis and different types of this method is presented.

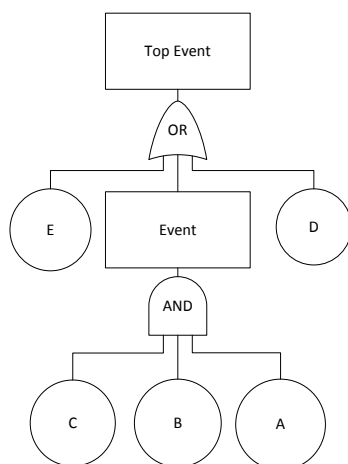


Figure 1. Sample of Fault Tree

3.CASE STUDY

In general, different types of transformers are used in power systems. Mainly, using three types, namely, oil-immersed, gas-insulated and dry-type transformers with or without cast coil insulation system [4,5].

Therefore, transformer's recognition is needed, figure 2 shows its major components. The main components that ensure the normal operating of a transformer are the windings, core, main tank, cooler, oil, and On Load Tap Changer (OLTC) [1].

Figure 3 demonstrates fault tree of transformers in detailed which is shaped with real fault data [6,7].

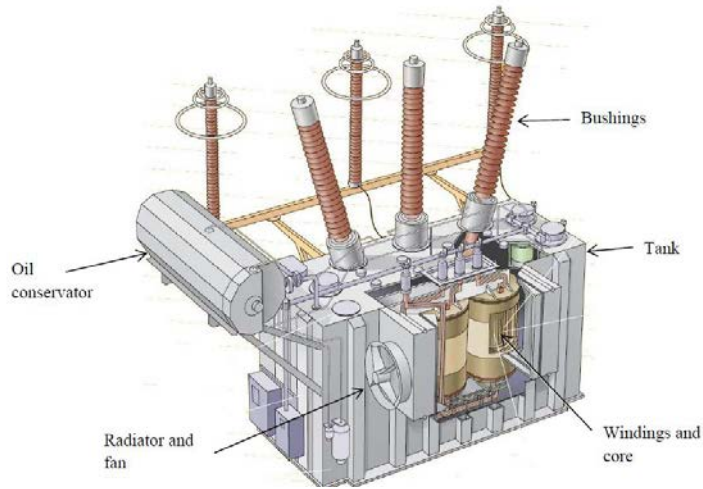


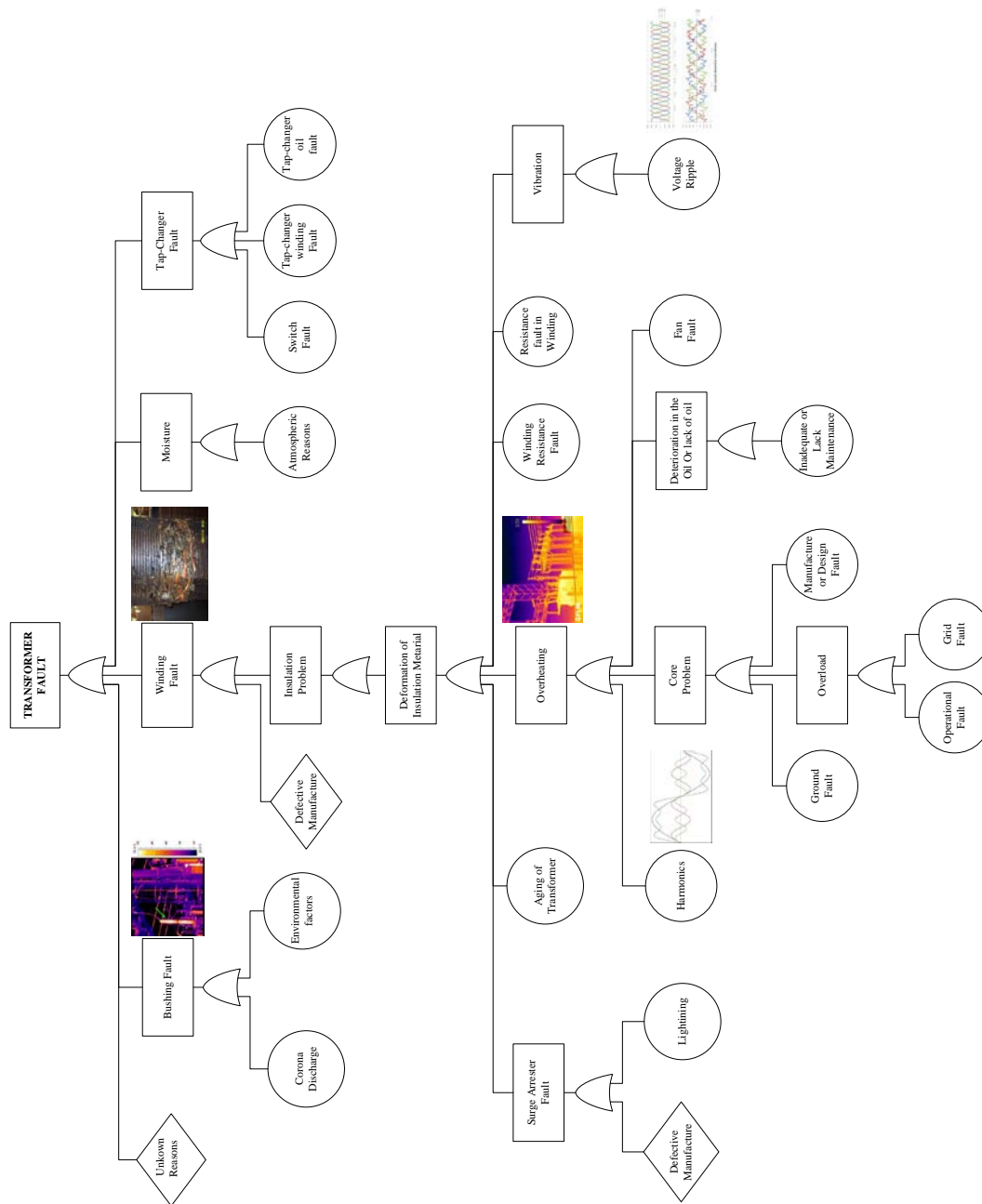
Figure 2. Major components of power transformers [5]

Table 2. Failure Rates of Power Transformers in Turkey between 1995 and 2007 [6]

Deteriorated Component	Rate
Windings	% 46.0
Tap-Changers	% 27.0
Bushings	% 15.5
Core and others	% 11.5

Table 3. Failure rates of transformers in 13 countries from CIGRE [10]

Deteriorated Component	Rate
Windings	% 30.0
Tap-Changers	% 40.0
Bushings	% 14.0
Core and others	% 16.0



4.CONCLUSION

In this paper, we demonstrate fault tree analysis for transformers in figure 3. The demonstrated analysis shows that transformer faults has been occurred from many basic faults. Especially, winding fault has many sub-branches. When table 2 and table 3 are examined, winding failures cause vital problems for transformers. Also, when there is considered that power transformers are a critical role for power systems, they should be monitored against any unplanned outage. Due to this reasons, some monitoring methods are utilized in thermal analysis, vibration analysis, dissolved gas analysis, partial discharge analysis, and frequency response analysis. If transformers have any hot spot temperature condition, we can find it owing to thermal analysis. In this way, overheating failures will be prevented. Vibration analysis prevents wall and winding vibration faults. Dissolved gas analysis (DGA) prevents failures comes from winding and some partial discharge failures. In [11], condition monitoring with DGA is explained in detailed. Partial discharge analysis demonstrates partial discharges before any partial discharge failures. And Frequency response analysis is served to preventing of determination the winding movements and deformations.

REFERENCES

- [1]. Transformer Handbook, ABB, Switzerland.
- [2]. S. Singh, and M. Bandyopadhyay, "Dissolved Gas Analysis Technique for Incipient Fault Diagnosis in Power Transformers: A Bibliographic Survey," *Int. IEEE Electrical Insulation Magazine*, vol. 26, pp. 41-46, 2010.
- [3]. R. Murugan, and R. Ramasamy, "Failure Analysis of Power Transformers for Effective Maintenance Planning in Electric Utilities," *Engineering Failure Analysis*, vol.55, pp. 182-192, 2015.
- [4]. F.C. Sica, F.G. Guimarães, and R.O. Duarte, "A Cognitive System for Fault Prognosis in Power Transformers," *Electric Power Systems Research*, vol. 127, pp. 109-117, 2015
- [5]. I.A. Metwally, "Failures, monitoring and new trends of power transformers," in *IEEE Potentials*, vol. 30, pp. 36-43, May-June 2011.
- [6]. M. İlkahırman, "Güç Transformatör Arızalarının İncelenmesi," M. Tr. Thesis, Institute of Science and Technology, Gazi University, Eskişehir, Turkey, Jan. 2008.
- [7]. E. Gençaydın, "Hata Ağacı ve Blok Diyagramı Yöntemi İle Koruma Sistemlerinde Güvenilirlik Analizi ve Çözüm Önerileriyle Türkiye Elektrik İletim Sistemine Uygulanması," PhD. Tr. Thesis, Graduate School of Natural and Applied Sciences, Yıldız Technical University, İstanbul, Turkey, 2012.
- [8]. L. Harms-Ringdahl, *Safety Analysis Principles and Practice in Occupational Safety*, 2nd ed., New York, USA: Taylor&Francis, 2005.
- [9]. W.S. Lee, D.L. Grosh, F.A. Tillman, C.H. Lie, "Fault Tree Analysis, Methods, and Applications- A Review," *IEEE Transactions on Reliability*, Vol. R-34, No. 3, Aug. 1985.
- [10]. W. Dietrich, "An International Survey on Failures in Large Power Transformers in Service," *CIGRE Final Report of Working Group 05 of Study Committee 12*, Electra no. 88, pp. 23-48, France, 1983.
- [11]. H. de Faria, J. Costa, and J. Olivás, "A Review of Monitoring Methods for Predictive Maintenance of Electric Power Transformers Based on Dissolved Gas Analysis," *Renewable and Sustainable Energy Reviews*, Vol. 46, pp. 201-209, March 2015.

